ENGINEERING STUDY OF NEAR-FIELD EARTHQUAKE GROUND MOTIONS

Thesis submitted to
THE UNIVERSITY OF LONDON
Imperial College of Science and Technology

J.M.H.MENU

for the Degree of
Doctor of Philosophy of the University of London

MAY 1986

Department of Civil Engineering
Imperial College of Science and Technology
London SW7 2BU

ACKNOWLEDGEMENT

The work of this thesis was carried out in the Department of Civil Engineering at Imperial College. It presents part of the work performed under contract with the Commissariat à l'Enérgie Atomique, département de Sureté, CEA (France) and research done for the Comitato Nazionale per la ricerca e per lo sviluppo dell'Energia nucleare e delle Energie Alternative, ENEA (Italy). The second part was supported by the Science and Engineering Research Council, SERC (U.K.).

I wish to sincerely thank Professor N.N.Ambraseys for his guidance and encouragement. I also express gratitude to Dr.S.K.Sarma for his help and comments during innumerable discussions.

Additional mention is due to the IC Computer Center, where all the computational work was carried out using the CDC 170/855 computer. The entire thesis was phototypeset using the word-prossessing package "TEX" available on this machine.

ABSTRACT

Earthquake near-field ground motion records are of vital importance for the design of large structures as well as for a better understanding of the earthquake phenomenon. Before the constitution of data banks of earthquake motions or before any subsequent use, the recorded accelerations must be carefully processed.

The first level of processing consists of producing uncorrected records. They are digitized versions of the motions usually recorded on analogue form, more suitable for mass storage and subsequent numerical treatment.

The second level of processing seeks to produce time histories of ground acceleration, velocity and displacement, corrected for undesirable distortions such as recorder imperfections and digitization noise, or solving for the unknown acceleration base line.

In a first part, this thesis discusses the various stages of the processing typical strong motion records before their entry in data banks. Particular considerations are given to the analysis of the digitization noise introduced by semi-automatic and automatic systems. A new processing procedure based on the use of efficient digital filters is introduced and compared to the standard methodologies. The work demontrates that, with careful processing, acceleration time histories of improved quality can be obtained.

The second part treats of the simulation of earthquake motions in the near-field. Empirical methods based on the statistics of the recorded motions as well as geophysical methods are discussed. In both cases, it is shown that many parameters, (most of them are not accessible experimentally), have to be assessed to generate realistic motions at particular sites. The work also shows that, in near-field studies, one must not attempt to applied the conventional seismological methods used in the far-field.

CONTENTS

PART I: STRONG MOTION RECORD PROCESSING

CHAPTER III

CHAPTER IV

CHAPTER VII

PART II: SIMULATION OF EARTQUAKE STRONG MOTIONS

CHAPTER VIII

CHAPTER IX

PART I:

STRONG MOTION RECORDS PROCESSING

SCOPE OF PART I

In the first part of this thesis, we discuss the earthquake near-field ground motion measurement. Unlike far-field measurement, the motion recorded in the near-field is the acceleration time history. At first sight, this may seem advantageous for engineering purposes since one can relate it directly to the applied force. However, it also generates many problems that are not encountered in conventional seismology. This has given birth to a new branch of seismology called *strong motion seismology*. Surely engineers and architects are primarely interested since they investigate the damage caused by earthquakes near the epicenters. Geologists and seismologists are also attracted by the wide potentiality of this new information for the studies of geomorphological and structural changes caused by earthquakes or for more accurate fault mechanism investigations.

In all the cases a good basic recorded time history is required. Unfortunalely, ground motion recording in the near-field is affected by several of types of noise which often masked the true motion. This is particularly visible when one computes the ground motion displacement from an acceleration record.

We intend to analyse the strong motion data acquisition process in order to show the order of magnitude of the accuracy which can be reached. A complete mathematical formulation is introduced to facilitate any further analysis. A thorough investigation of digitization is performed and its effect on the recorded signals is quantified. The various methods of acceleration correction are reviewed and compared. We show that the new method proposed, based on efficient filtering, is at least as satisfactory as the standard ones. It offers the possibility of permanent displacement recovery, although in many cases, with the first generation of recording intrument, no separation of this information from the processing noise seems possible.

It is believed that, with careful processing and correction, a fair description of the near-field ground motion may be obtained.

CHAPTER I

ACCELERATION GROUND MOTION ACQUISITION AND USE

1-1 Introduction

Since the early days of earthquake near field strong motion recording in the early 30's, more than 6,000 records have been recovered over the world. For most of them, the three translational components are available. There is a large disparity in the quality of the data, due to a large number of responsible agencies having each their own particular policy in the recovery process. The first records were mainly destined for the engineering community to help structural engineers in their design of structures. This is the reason why early instruments were installed in buildings, or dams. In California in particular many of the records were obtained from the basements or current floors of multistorey buildings. Today, regional and national networks are re-designed but also the location of the recording instruments has become more specialised and appropriate to specific problems like, plant sites, tectonic faults, large slopes or mountains; buildings, bridges and nuclear plants are fully instrumented.

There is also a large variety of recording instruments, having different characteristics and hence different imperfections. All the various countries are subjected to different types of earthquakes, in different geological environment and use different methods of processing. The world production of Strong Motion records is as a consequence very much ill-assorted.

In the following we shall see how the early processing stage in the recovery process is of vital importance for the quality of the final product.

1-2 Background of Strong Motion acquisition and processing

The first concern in the strong motion acceleration retrieval must be the influence of recording instrument and of its installation in the environment. We must ask ourselves to which extent the measurement is affected by the particularities of the type of recorder and by its location either in a particular building or on soft deposits.

We shall see in the next section what are the actual characteristics of available transducers. As far as the location of the instruments are concerned, it is useful to develop here some comments and definitions.

The purpose of the measurement is not always to measure the acceleration of the ground. In many cases, engineers wish to monitor structures and all they want to obtain is a passive check of an early design. Sometimes and usually for structural research purposes, a complete array of instruments is installed at various points of a construction. The aim is clearly to collect information in order to build structural response models. It is fundamental to distinguish these records from those aiming at measuring the ground motion at a given site. But then, it is a mistake to rely on such motions recorded at a specific site and/or in a particular building, in order to make use of them in a similar situation. There is no similar situation and each time it must be re-assessed. The design ground motion must then originate only from motions as "raw" as possible.

The recovery of such motions poses specific problems. A common installation for such measurements has been to fasten the acceleragraph firmly to a foundation. It is implicitely assumed that the foundation has no appreciable effect on the recording, and that such records are "good", at least in the frequency range of interest. However, this frequency range has never been accurately defined and furthermore is much dependent of the subsequent use of the record. Locating instruments in the basement of buildings or on rigid structures may well not affect the recording if the foundation lies on rock since, in general, no appreciable relative motion is likely to occur between ground and foundation, but this is not true for all frequencies. We must accept that, for the general case, little information is known about the actual closeness of our records with the true ground motions. Due to the formidable task involved, little serious field experiment has been carried out to check their truthfulness. We only can consider more confidently a "free field" record, exempt from any structural influence.

On soft soil, even in the "free field", material yielding and dynamic soil-structure interaction are expected and we are short of firm evidence about the extent of its actual influence. It is likely, based on theoretical ground, that the recovered ground motions include, not only the earthquake source information and the travel path effect, but also a strong soft soil effect which may become predominant and mask all other features. This is why the case of motions recorded on soft soil deserves particular attention. Records from soft soil deposits must not be analysed in the way as rock site records. Their specific characters may be viewed either as part of the wave travelling path or as a particular structure. In the former case, the wave propagation analysis is further complicated by the presence of an highly non-linear medium. In the latter, soils may be treated as three dimensional structures. Since, we possesses today more and more data concerning ground motions on rock, it seems preferable to consider the motion recorded on soft soil as a motion distorted by a soil structure. In that case, the definition of the "raw" ground motion is a motion recorded at a rock site in which the influence of structures, including soil layers is minimum. A "raw" ground motion is then a motion which includes only information relating to the earthquake source and the seismic wave travelling paths; this a first level motion since these features cannot be separated.

A recent fact is also creeping in the today's approach of strong motion records acquisition. There is an increasing demand for improved ground motion information. Scientists and seismologists would like to make full use of this precious type of data for earthquake source studies. Engineers expect to be able to control the risks involed in advanced structures at both ends of the spectrum. Both are looking for informations contained in frequencies as low as .05 Hz and as high as 50 Hz.

It is well known that the required information is masked by noise in these frequency ranges. The first optical-mechanical accelerometers with natural frequency as low as 10 Hz, were not intended to inform below 0.1Hz or above 10Hz. Today, the strong motion records acquisition centers are faced with a technical-economical dilemma: either they replace and improve their networks at great cost, or they try, by performing advanced signal processing methods, to extract as much information as possible from their available systems without changing the equipments. When it is known that the cost per record of an advanced processing is three to four times less than the acquistion itself, we understand why so much effort is devoted at present, to obtain from a given record the best of what is possible.

Although this situation is only temporary, one cannot say when a definite reverse trend will occur. The following chapters of this thesis will describe some of the common and advanced methods which have been generated by this situation. A fundamental question then must be asked. Is it worthwile to search for sophisticated processing procedures when the recording instruments are, by comparison, so crude? The answer is mainly of economical character. In the meantime this approach will remain relevant for many years to come in Strong Motion Seismology. The methods will also enable to extract the best from all the records that we inherited.

For the future, special efforts should be made to record the "raw free field" ground motions: the basic form of seismic loading, and with advanced recorders free from today's drawbacks. Others records, on soft sites or in various structures would provide purer information for structural respose model studies (including soil response). It is visible that they would yield better data to be treated, with full efficiency, in all subsequent analysis, up-stream for geophysical studies or down-stream for structural design.

1.3 Quality of recording instruments

1.3.1 The first generation of accelerometers

One of the parameters that limit the veracity of ground acceleration records is the intrinsic capability of the transducer to pick-up the true ground motion. The theoretical transducer principle must be thouroughly investigated. The robustness of its central parts and the reliability of its peripherical elements also play an important role in the efficiency of a network and the quality of the products.

Some of the accelerographs which recorded the first near-field earthquakes signals are still in service today; many modern ones are of the same generation: a mechanical-optical type. Table I describes their main characteristics. They all rely, for robustness reasons, on the same type of transducer: a SDOF pendulum (*fig.I.1a and 1b*). As we shall develop in chapter VI, such systems record only approximatively the ground acceleration. A deviation of the order of 10 %should be expected at the natural frequency of the instrument which remains low (10-20 Hz). Much larger errors occur in the high frequencies. As a consequence, it is imperative, if we consider 10 %accuracy as insufficient, to operate a correction in order to get better ground motions. This major aspect of instrument deconvolution will be treated in more details in chapter VI.

A general schematic picture of such mechanico-optical strong motion accelerograph is shown on *fig.I.2* and its main implementation on *fig.I.3,4,5 and 6.*

A critical part of the recording instrument is the starting system. All accelerometers of the first generation are trigerred mechanically by one of the first pulse of the seismic wave itself. As an example, the *fig.I.7* shows the pendulum starter used by the USCGS accelerograph and designed in the thirties (*Heck et al. 1936*). It consists of a vertical pendulum with natural frequency of 1 Hz and a damping ratio of 0.3. A displacement of 0.05 cm in any horizontal direction is sufficient to close the platinium contacts and start the recording cycle. The time required to trigger the recording device is of the order of 0.2 sec but depends of the amplitude of the attacking pulse. It may be estimated to be less than 0.2 sec.

This starting delay is surely not as short as might be desired and efforts have been made on the dynamic characteristics of the starters in order to reduce as much as possible the lost initial portion of the record. One must realise however, that a delay is inevitable with such devices and this will have a significant influence on the subsequent search for the true base line of the record.

Finally, one must not neglect the discrepancies of higher order like the variation of the time scale due to possible irregularities in the recording speed (*fig.I.8*), the departure of the dynamic characteristics from their nominal values or the misaligment and cross-axis sensitivity (*fig.I.9*).

The correction for variation of time scale can be achieved by digitizing the position and length of the

Table I-a

	USGS	SMAC A/B/C/D	AR-240	RFT-250	RMT-280
Manufacturer	USGS	Akashi Seisakusho	Teledyne	Teledyne	Teledyne
Country	USA	Japan	USA	USA	USA
Size (cm)	33x51x114	38x53x53	35x41x41	27x22x50	23x38x50
Weight (kg)	61	99	27	16	19
Power Supply	12 vdc	12 vdc	12 vdc	12 vdc	24 vdc
Transducer	SDOF	SDOF	SDOF	SDOF	SDOF
Natatural Frequency	adjustable 6.7/23.3	fixed 7.14	variable 12.5/18.0	variable 12.5/18.0	fixed 16.7
Damping	0.60	1.00	0.60	0.60	0.60
Sensitivity (cm/g),{g}	adjustable (6/20)	fixed (4 or 8)	fixed (7.6)	variable (1.9/3.8/7.6)	variable {.25,.2,1}
Frequency Range (Hz)	0-6.6	0-6.0	0-10/15	0-10/15	0-14
Recording Medium	6-12 inch paper	waxed paper	12 inch paper	70 mm film	3/4 inch mag.tape
Reccording Duration	1.25 mn	1.5 or 3.0 mn		30 mn	60 mn
Recording Drive	dc motor	hand wound spring	dc motor	dc motor	dc motor
Recording Speed (cm/s)	1.0	1.0	2.0	1.0	9.5
Time marking (per sec)	2	1	2	2	2
Damping Mechanism	magnetic	air piston	electro-magnetic	electro-magnetic	electro-magnetic
Sarter type	pendulum	spring	pendulum	pendulum	spring em pickup
Starter Frequency(Hz)	5.0		4.0	3.3	3.3/4.5
Starter Damping	low		1.50	unknown	1.5
Starter Control	ver.	hor.	vert.	vert.	vert.
Trigger Level (g)	0.01		adjustable 0.005/0.05	0.01	adjustable 0.005/0.05
Operational Rise time (s)	0.2	0.05	0.10	unknown	unknown

Table I-b

	MO-2	UAR	SMA-1	DC-3	SMAC E/Q
Manufacturer	Victoria Engineering	Ph.Earth Institute	Kinemetrics	Hosaka Shindo Keiki	Akashi Seisakusho
Country	New-Zealand	USSR	USA	Japan	Japan
Size (cm)	18x18x43		18x18x38	36x41x41	35x45x45/ 40dia.x32
Weight (kg)	9		9	198	70/35
Power Supply	12 vdc		12 vdc	6 vdc	12 vdc
Transducer	SDOF	SDOF	SDOF	SDOF	SDOF
Natural Frequency	33.0	fixed 20.0	variable 12.5/25.0	variable 15.4/18.2	fixed 20.0
Damping	0.60	0.70	0.60	0.60	0.60
Sensitivity (cm/g), {g}	(1.5 h.) (2.5 v.)	fixed (1.6)	variable (1.9/3.8/7.6)	adjustable (5.0/7.5)	(0.5)
Frequency Range (Hz)	0-25	0-16.0	0-10/20	0-12/15	0-16.0
Recording Medium	35 mm film	photo paper	70 mm film	smoked paper	scrach film
Reccording Duration	47 sec	1.0 mn	25 mn	3 mn	1.5 mn
Recording Drive	dc motor	spring	dc motor	dc motor	dc motor
Recording Speed (cm/s)	1.5	1.0	1.0	1.0	0.5
Time marking (per sec)	2and 0.2 coupled	none	2	5.2 or 1	2
Damping Mechanism	oil paddle	electro-magnetic	electro-magnetic	electro-magnetic	air piston
Starter Frequency(Hz)	1.0	3.3	1.0	1.0	1.0
Starter Damping	0.30	unknown	low	0.60	0.60
Starter Control	hor.	vert.	hor.	hor.	hor.
Trigger Level (g)		0.005 or 0.01	0.005 or 0.01		
Operational Rise time (s)	0.2		0.10 to 0.15	0.10	0.10

SMA-1

Strong Motion Accelerograph

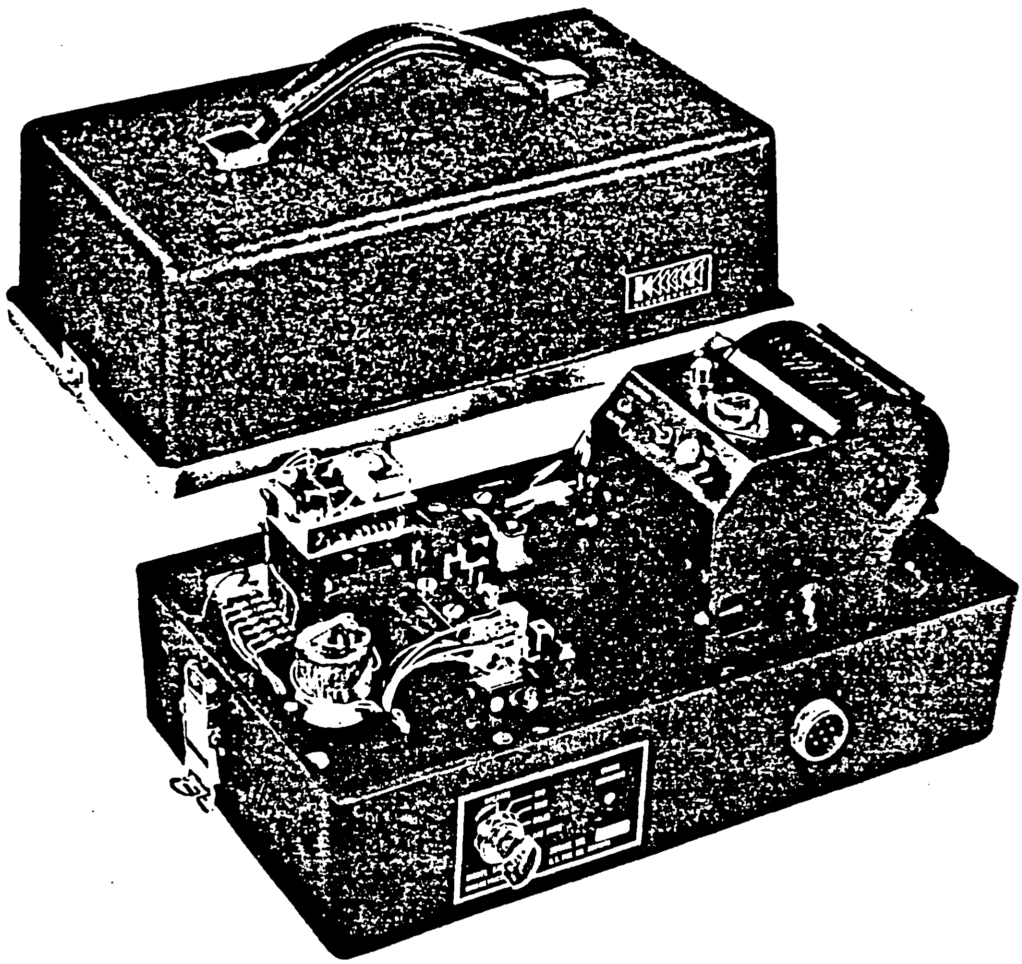

A widely used strong motion recording instrument of the first generation

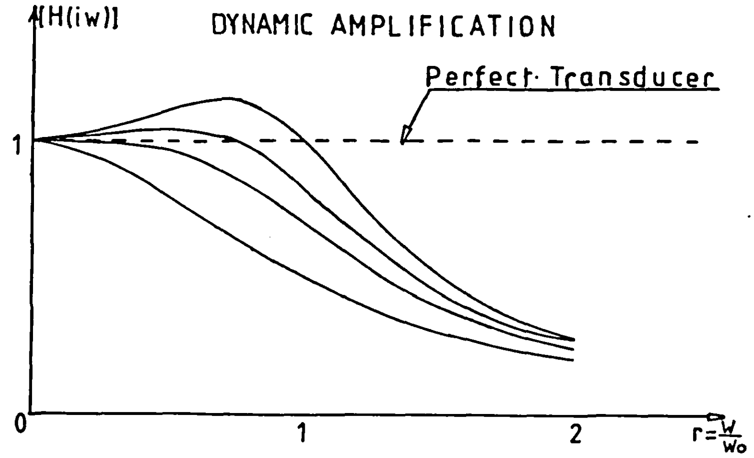

Fig.I.1

Principle of SDOF transducer

a) dynamic amplification

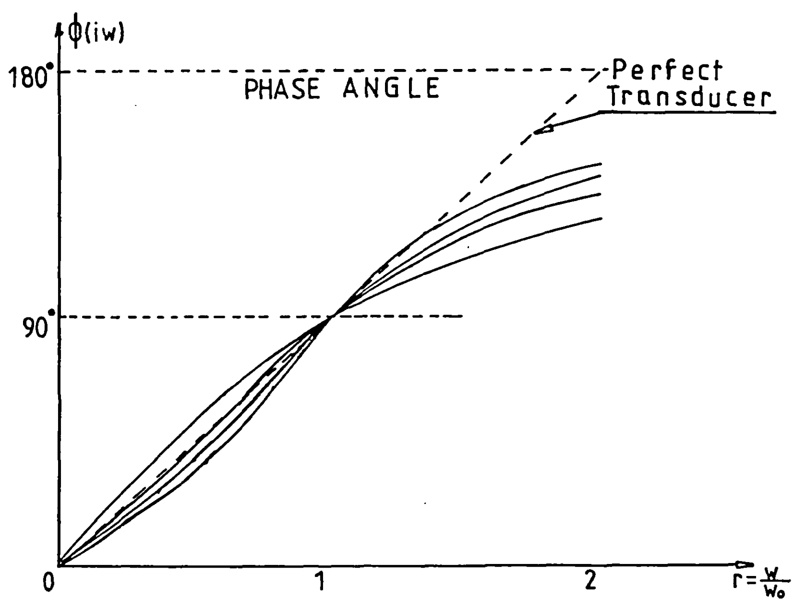

Fig.I.1

b) phase angle

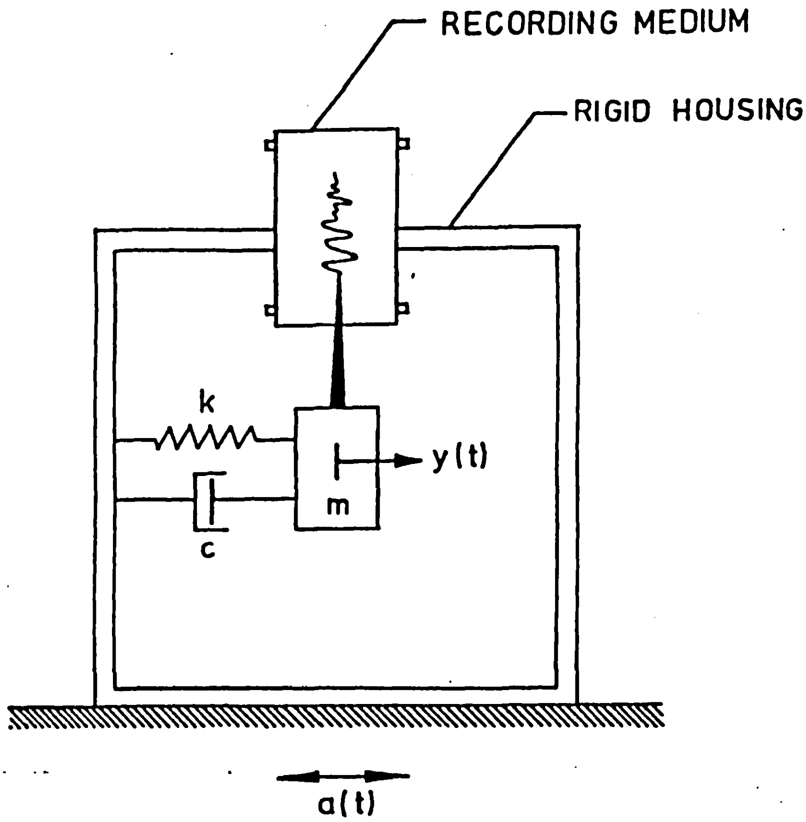

Fig.I.2

Schematic diagram of a SDOF transducer.

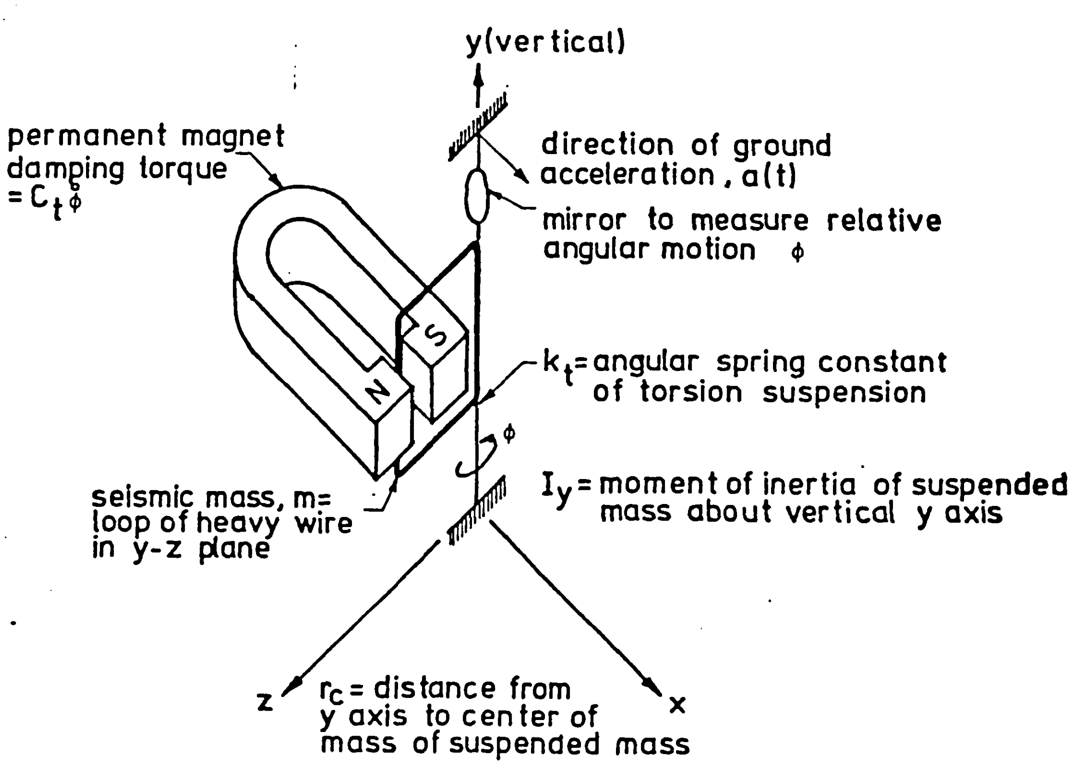

Fig.I.3

Schematic diagram of the USCGS accelerogaph.

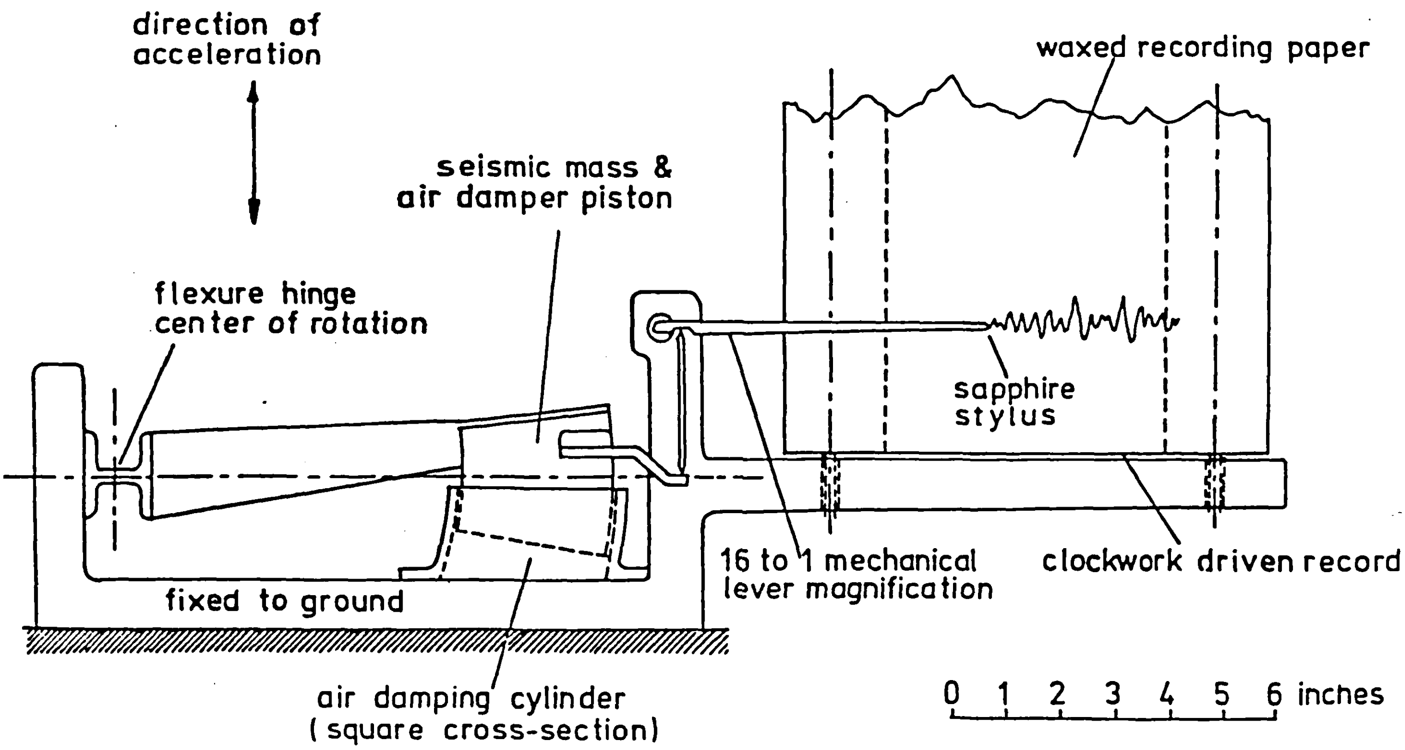

Fig.I.4

Schematic diagram of the SMAC accelerograh.

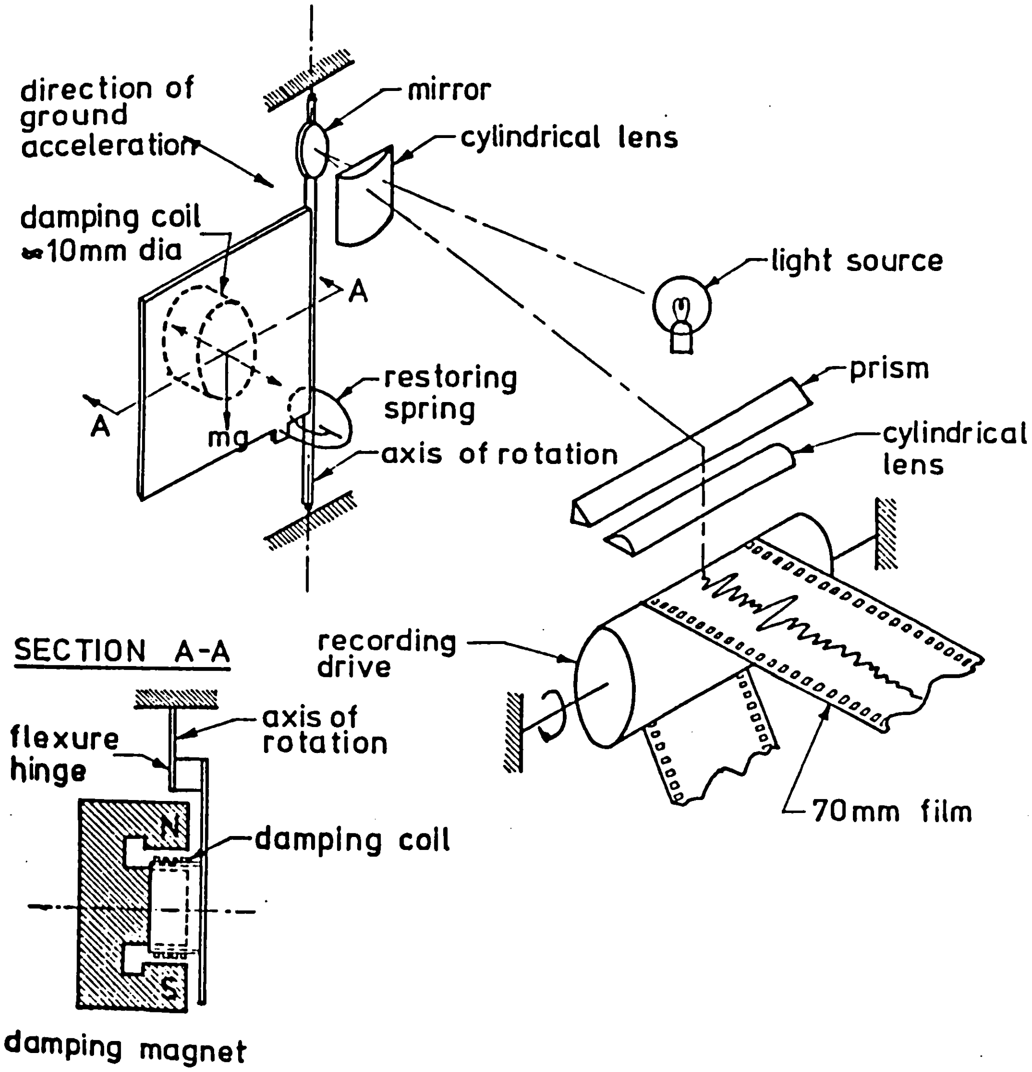

Fig.I.5

Schematic diagram of the a mechanical-optical instrument.

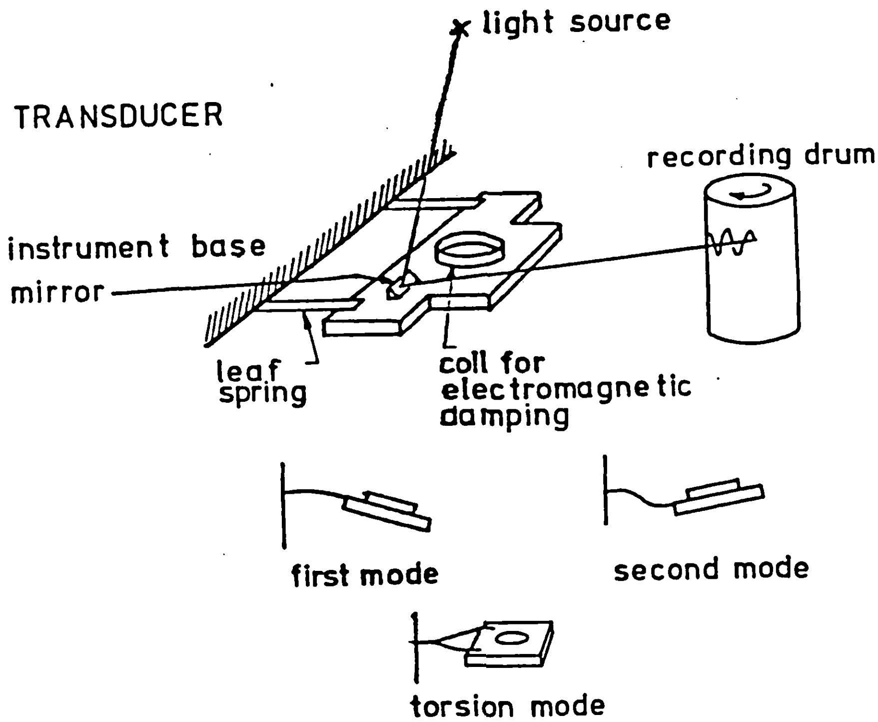

Fig.I.6

Schematic diagram of an SMA-1 instrument.

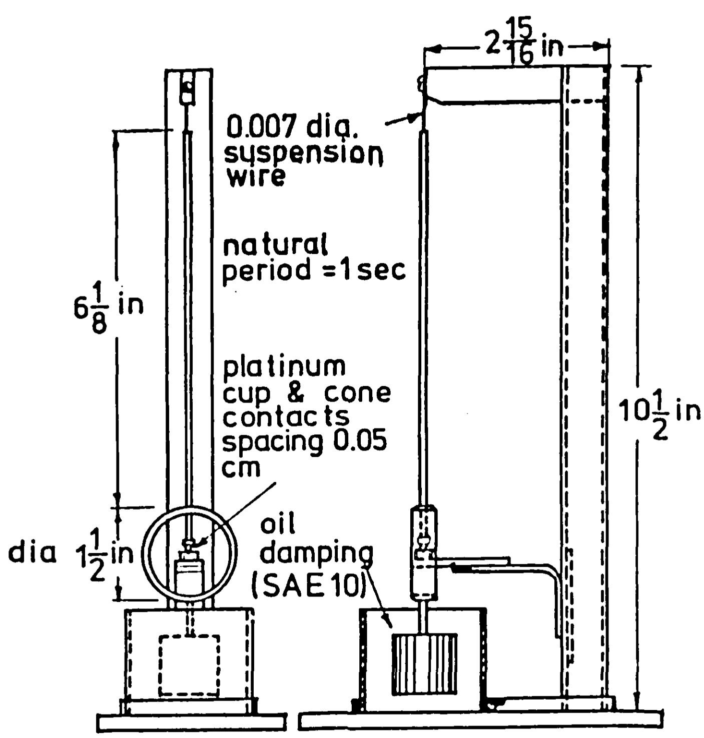

Fig.I.7

Pendulum starter for the USCGS accelerograph.

time marks available at the top and the bottom of the records (*fig. I. 10*), but it is limited by the accuracy of the digitization itself (see chapter III).

It is common practice however to measure the real values of the transducer natural frequency and damping ratio by performing a standard calibration test before and after the instrument had been triggered. *Fig. I. 11* shows a typical example of sample calibration records obtained by special tests switches on the SMA-1 instrument. The principle underlying this calibration procedure is discussed now.

The undamped natural frequency is obtained by disconnecting the transducer damping system and applying a step voltage function. The first portion of the test record shows, for the three components, a slowly decaying free vibration response to this excitation. The decay expresses a non-zero but very small residual damping λ_R due mainly to air friction . Its value is negligeable for the natural frequency computation. The equation of motion following the release of the voltage is:

$$y(t) = y_0 e^{-\lambda_R \omega_0 t} \cos\left(\omega_0 \sqrt{1 - \lambda_R} t - \Phi\right) \tag{1.1}$$

Since λ_R is small, the natural frequency f_0 is simply computed by counting the number of cycles for a given length of time:

$$f_0(Hz) = \frac{\text{number of vibration cycles}}{\text{length of time in sec.}} \tag{1.2}$$

A large value of λ_R (more than 0.01), computed by measuring the logarithmic decrement:

$$\lambda_R = \frac{1}{2\pi} \ln \frac{\text{amplitude at beginning of cycle}}{\text{amplitude at end of cycle}} \tag{1.3}$$

would indicate a malfunctioning of the instrument.

The actual transducer damping is obtained by measuring the overshoot in the response to a steady step voltage function to the damped accelerometer. The theoretical response is given by:

$$y(t) = y_0 \left\{ 1 - e^{-\lambda \omega_0 t} \left(\cos \omega_1 t + \lambda \frac{\omega_1}{\omega_0} \sin \omega_1 t \right) \right\} \tag{1.4}$$

where

λ is the search damping ratio,
$\omega_0 = 2\pi f_0$ is the natural circular frequency
$\omega_1 = \omega_0 \sqrt{1 - \lambda_R}$ is the damped natural frequency
y_0 is the static offset due to the step voltage.

At the time of the first peak, e.i, $t = \pi / \omega_1$ *Eq(1 .3)* provides the overshoot value:

$$y = y_0 \left[1 + e^{-\lambda \pi \omega_0 / \omega_1} \right] \tag{1.5}$$

The overshoot ratio:

$$\eta = \frac{y - y_0}{y_0} \tag{1.6}$$

Fig. I. 11 shows an example of such dynamic characteristics calculation can be measured accurately by means of the digitisation equipement and input into the following expression giving the damping ratio:

$$\lambda = \sqrt{\frac{(\ln \eta)^2}{\pi^2 + (\ln \eta)^2}} \tag{1.7}$$

The determination of the sensitivity is performed by a simple static test (*fig. I. 12*).

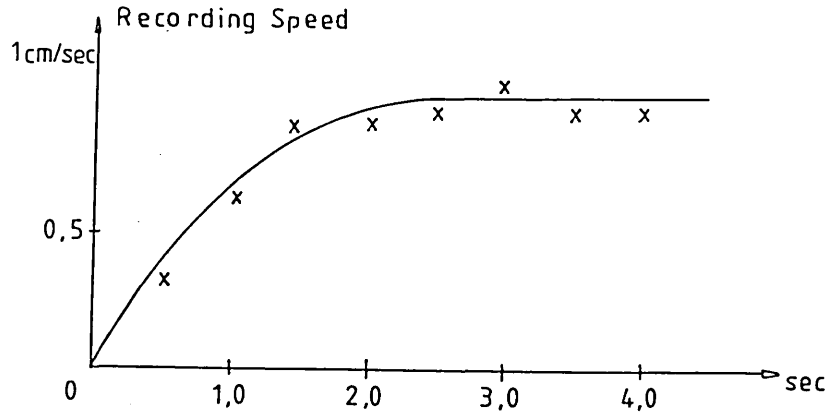

Fig.I.8

Irregularities in the recording speed.

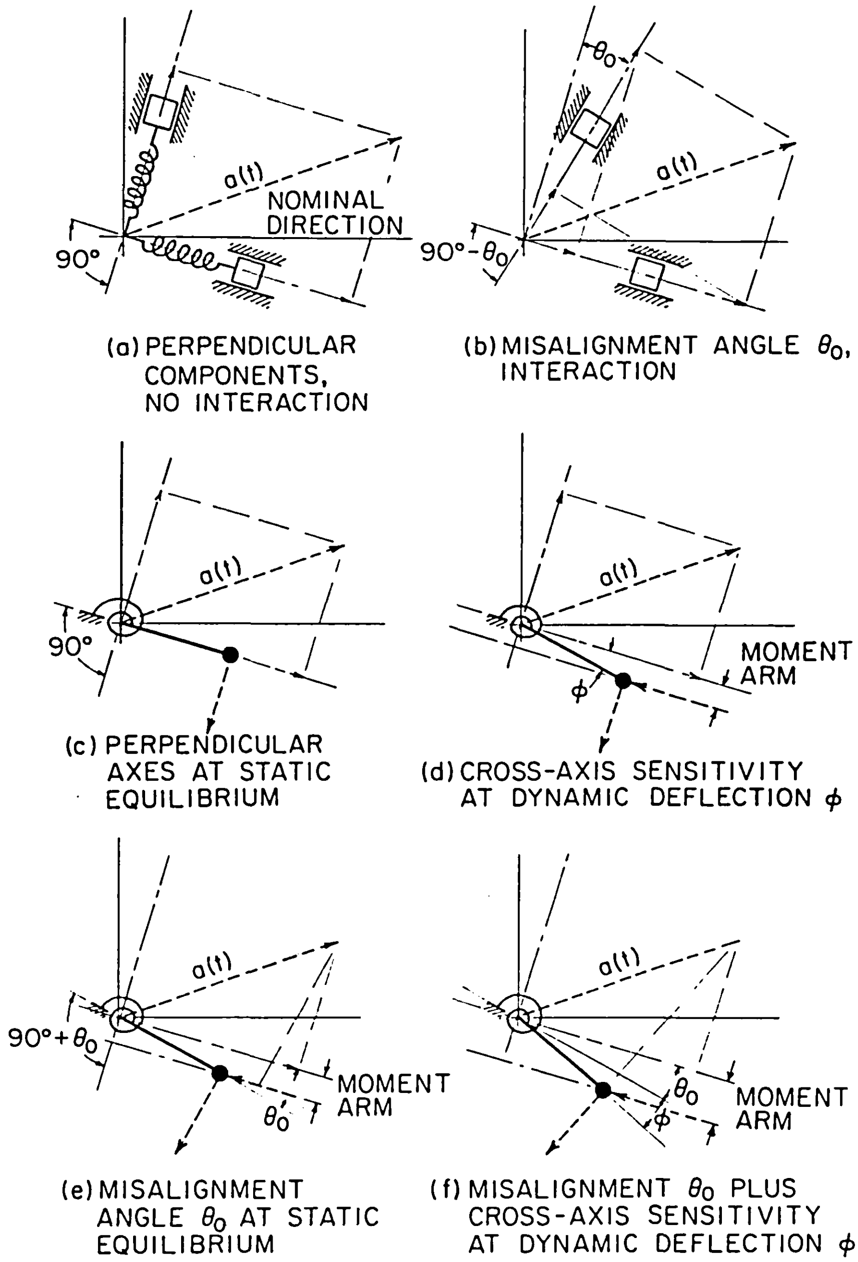

Fig.I.9

Misaligment and cross-axis sensitivity in transducers.

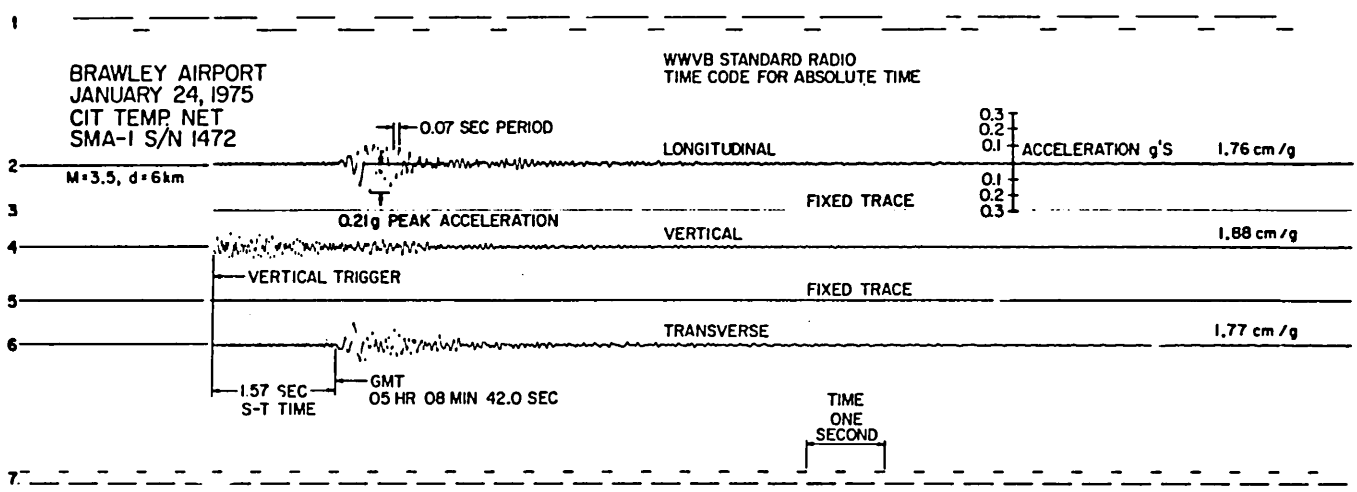

Fig.I.10

Typical earthquake analogue accelerogram.

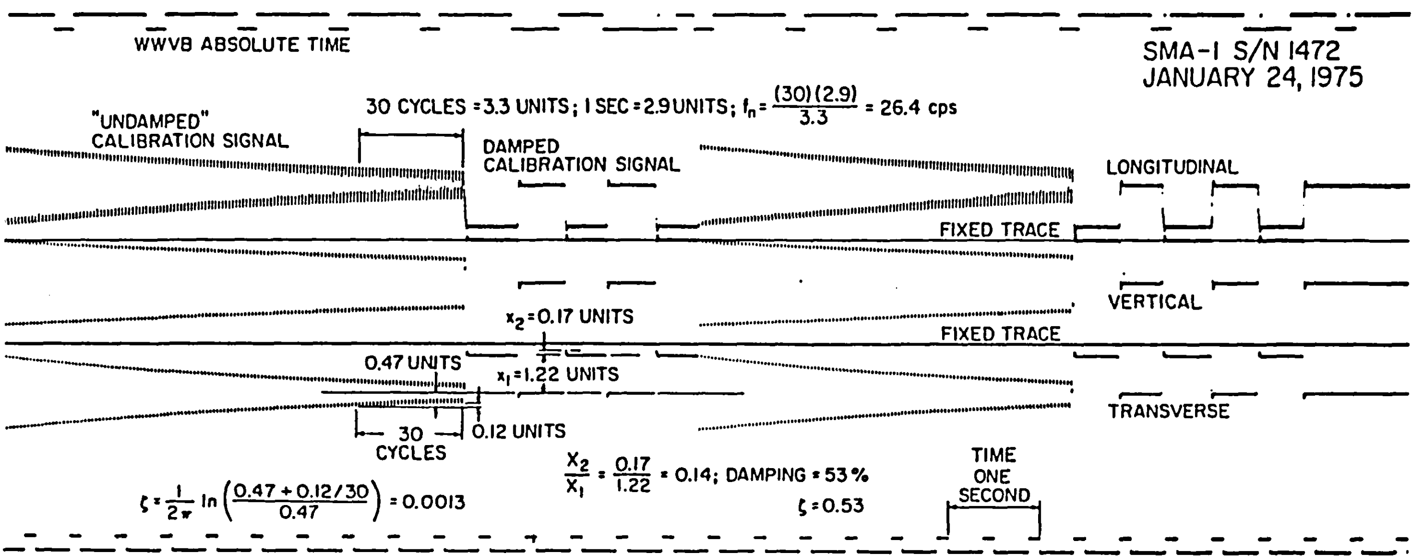

Fig.I.11

Sample calibration of SMA-1 instrument.

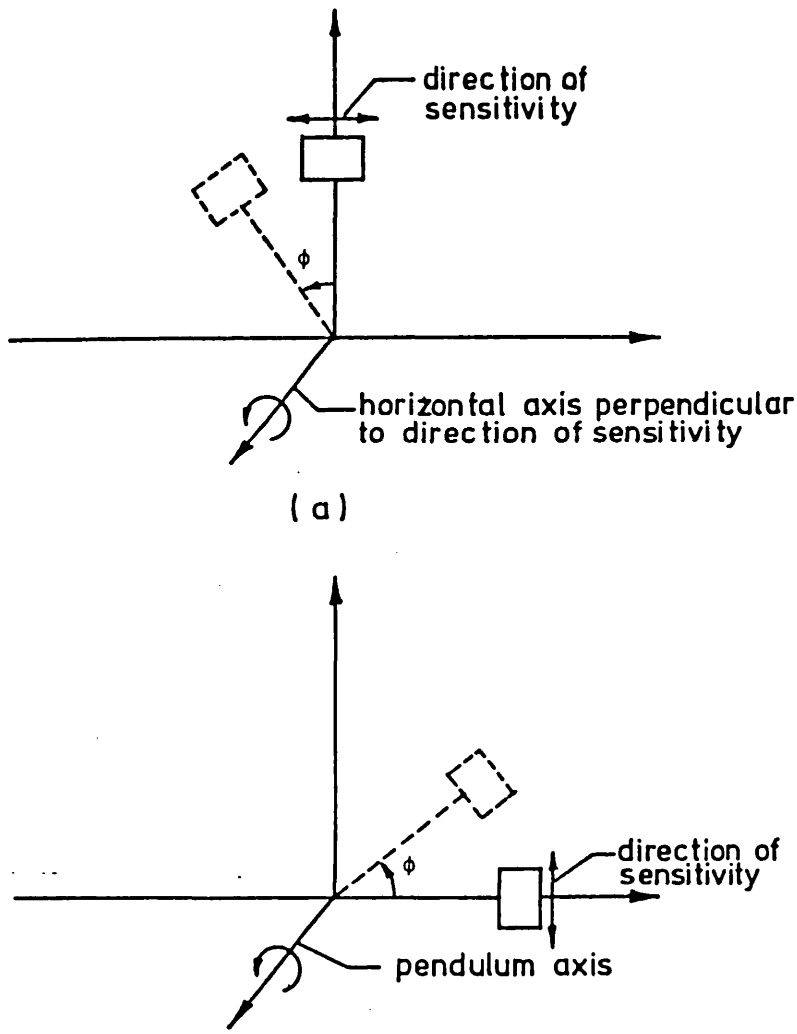

Fig.I.12

Definition diagram for sensitivity test.

1.3.2 Second generation of accelerometers

In the previous section we mentioned that mechanico-optical accelerometers yields an acceleration trace significantly distorted due to a series of insufficiencies or imperfections of the transducer. The recovered trace will also have to be processed before it reaches a state where it can be subsequently treated on computers. Amongst the various processing steps, digitisation is certainly the most critical one, as much undesirable noise is then introduced in the signal. The second generation of accelerometers based on solid state electronic digital technology is an attempt to solve many of the problems encountered with the first generation. The main attractions of the second generation reside in the following improvements:

1. the transducer becomes a force-balance servo type transducer able to extend to 50 Hz at least the recording frequency range with a better accuracy.
2. the solid state element provides the instrument with a short memory so that the onset of the ground motion can be recorded.
3. the integrated electronic circuitry makes it possible to perform the digitisation operation within the instrument itself, avoiding most of the basic noise problem.

Table II catalogues the characteristics of these advanced available acceleration recorders.

The force-balance servo-type transducer or feed back transducer is a device whose behaviour is very similar to the SDOF pendulum but where the natural frequency f_0 and the damping ratio λ are governed mainly by variable electrical parameters (*fig.I.13*). Using a relatively high damping, the amplitude response can be made very constant over a much wider range of frequency (see mathematical description in chapter VI). Also the phase diagram shows that the linearity is maintained very accurately (*fig.I.14*).

The force-balance transducer involves many parameters which complicate the calibration tests as well as it requires regular checkings of the various elements.

The facilities offered by the solid state to store several kilo-bytes of information is advantageously used to record information from the actual onset of the seismic wave. Typical pre-event memories range from 1 to 5 sec and are of major importance. This limits or even supresses the uncertainties relating to the acceleration base line location. It permits also the study of the first pulses of the motion which is so needed for seismological analysis of the faulting mechanism.

Finally, the capability of these advanced instruments to produce outputs on digital form achieves a vital step in the recovery of quality ground acceleration. The dynamic range reaches currently 66 dB since 12 binary bits are used (11 bits + sign) and this corresponds to an increase of about 20 times of that of analogue instruments. A particularly apparent advantage of the avoidance of digitisation is shown on *fig.I.17a, b and c* where the Fourier Amplitude spectra of the *Irpinia 23 Nov 1980* earthquake recorded

Table II-a

	SMA-2	DSA-1	A-700
Manufacturer	Kinemetrics	Kinemetrics	Teledyne
Country	USA	USA	USA
Size (cm)	20x20x36	25x43x22	28x33x23
Weight (kg)	11.4	19.5	20
Power Supply	24 vdc	24 vdc	12 vdc
Transducer	F.B. Pendulum	F.B.Pendulum	F.B.Piezo-sensor
Natural Frequency	50.0	50.0	
Damping	0.70	0.70	
Sensitivity volt/g	2.5 full	2.5 full	2.5 full
Frequency Range (Hz)	0-50	0-50	0.1-65
Dynamic Range (dB)	46	66	66
Recording Medium	magnetic cassette	digital cassette	solid state
Reccording Duration	30 mn	20 mn	18/36 mn
Recording Drive	dc motor	dc motor	dc motor
Recording Speed	4.8 cm/sec	6.4 cm/sec	

Table II-b

Modulation type	Frequency modulation	phase encoder	
Sampling rate (Hz)	200	200	100/200
Pre-event Memory		2.5,5	2,4,8,10
Sarter type	pendulum		transducer
Starter Frequency (Hz)	4.0	15.0	6.5/13.0
Starter Damping	1.5		
Starter Control	vert.	vert.	
Trigger Level (g)	adjustable 0.005/0.05	adjustable 0.005/0.05	adjustable 0.0025/0.025
Operational Rise time (s)	0.10	0.10	

TOTALLY SOLID-STATE STRONG MOTION ACCELEROGRAPH

A-700 ACCELOCORDER

An example of the second generation of strong motion recording instrument

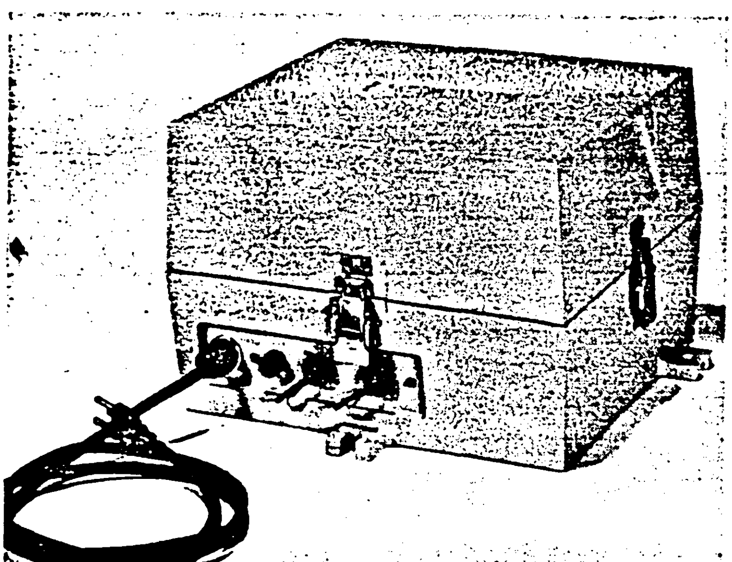

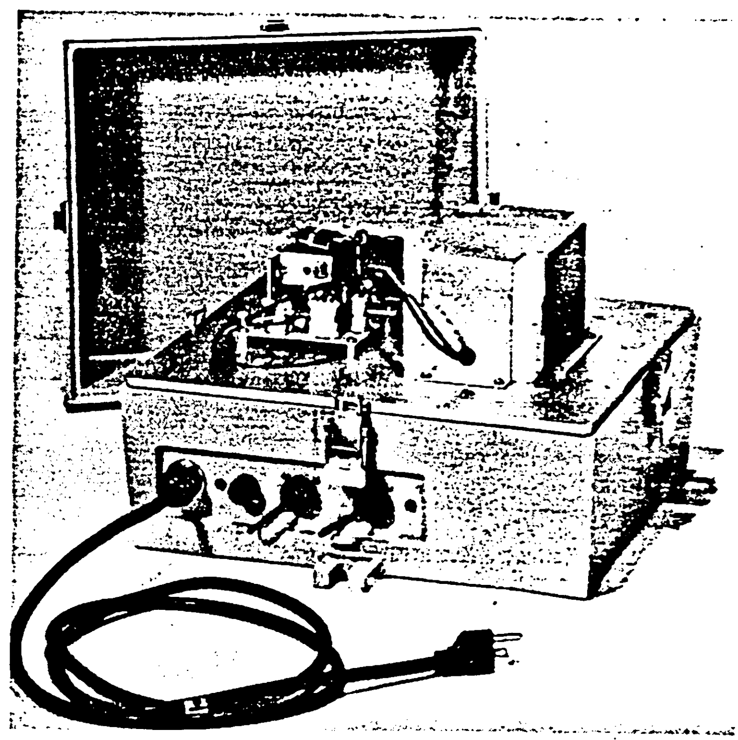

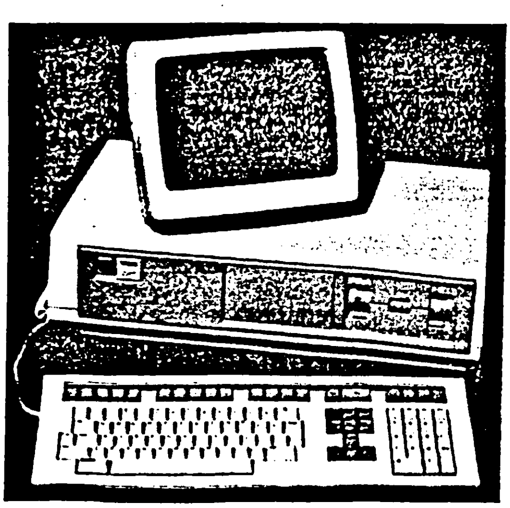

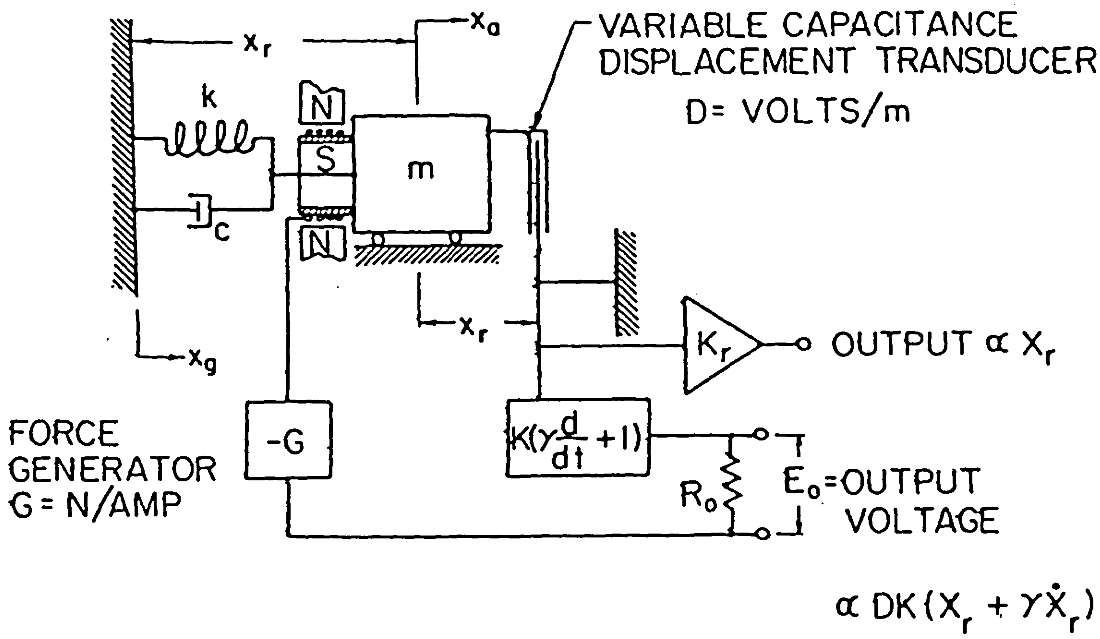

Fig.I.13

Schematic representation of a feed-back transducer.

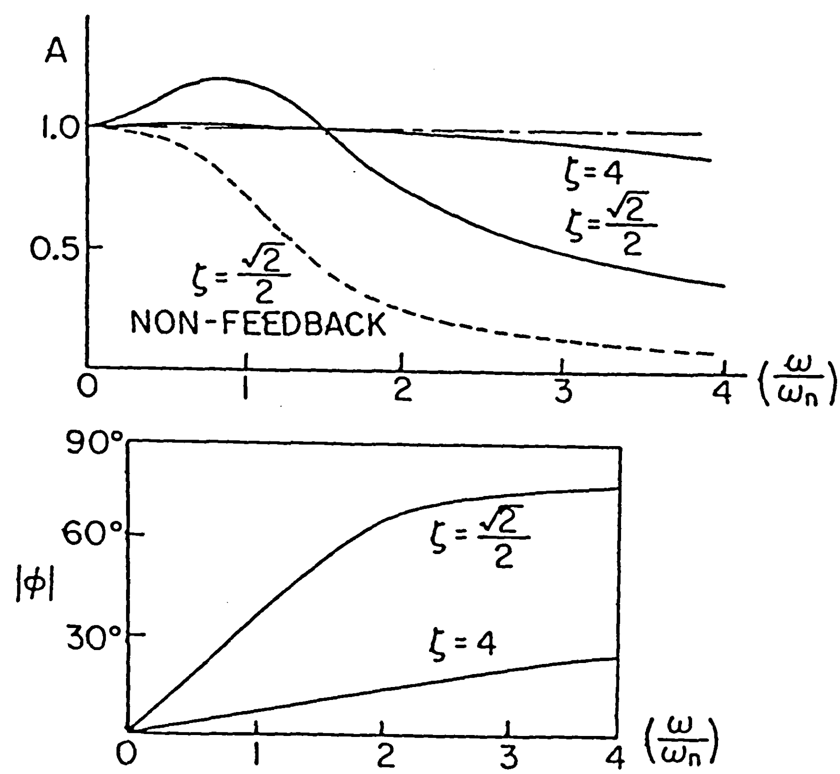

Fig.I.14

Characteristics of the feedback and non-feedback transducers.

at Procisa Nuova is shown. *Fig. I. 15a* shows the case of the acceleration recorded by a SMA-1 instrument, manually digitised and linearly interpolated. *Fig. I. 15b* represents the same case but digitised automatically at small constant interval (Δt = 0.002*sec*). *Fig. I. 15c* exhibits the same picture again but this time recorded by a DSA-1 instrument located exactly next to the SMA-1 (20 cm apart on the same foundation). The striking feature of this comparison is the level of the low frequency in the manually digitised case. This level has been significantly reduced thanks to improved digitisation but still is nowhere near the level appearing on *fig. I. 15c* believed to represent a better true frequency content of the ground motion at the site.

The quality of the information provided by the second generation of accelerometers is going to satisfy scientists and engineers both in seismology and in earthquake engineering. Too much enthusiasm, however must be cooled down since a few drawbacks have not been solved satisfactorily yet.

The major uncertainties to be anticipated with such modern equipments are related to their maintenance and cost. Their long term reliability in the field has not been demonstrated yet. Fears are founded: we observe that their standby length without recharging expresses in days rather than in months for the older instruments. Some, however, may be self rechargeable thanks to an internal panel of solar cells (A-700). The provision of simple field tests and calibration devices for adjusting and checking out the system seems to be excluded. Instrument maintenance will have to be performed both in the laboratory and in the field by technicians of high qualifications covering electronics, data processing as well as a sound knowledge of engineering seismology. Most of these instruments require complementary data retrieval units and compatible other office computing equipments which also increase significantly the total cost of such systems. It is certainly not a simple matter to decide, in the actual circumstances whether or not the setting up of new strong motion networks will prove economically adequate to record near-field events which are, by definition, unlikely to occur at high rate. There is no doubt however that further development will eventually produce reliable devices satisfying economic considerations.

In the meantime, more than 95 %of the near-field ground acceleration recorders are of the first generation, and are not likely to be replaced before several decades. All our attention and effort should be devoted to carry out, through good quality processing, the best of what can be achieved, the analogue acceleration trace being given.

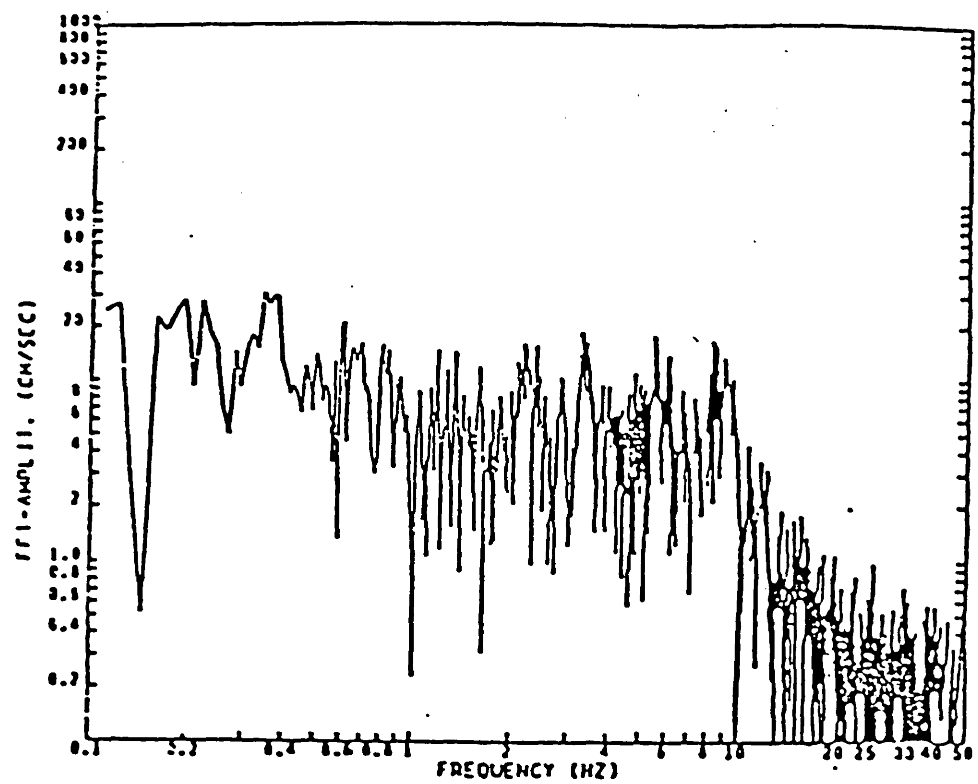

Fig.I.15

Comparison of Fourier Amplitude Spectra of the Procisa Nuaova record (Irpinia 23-11-1980)

a) SMA-1 instrument and manual digitization

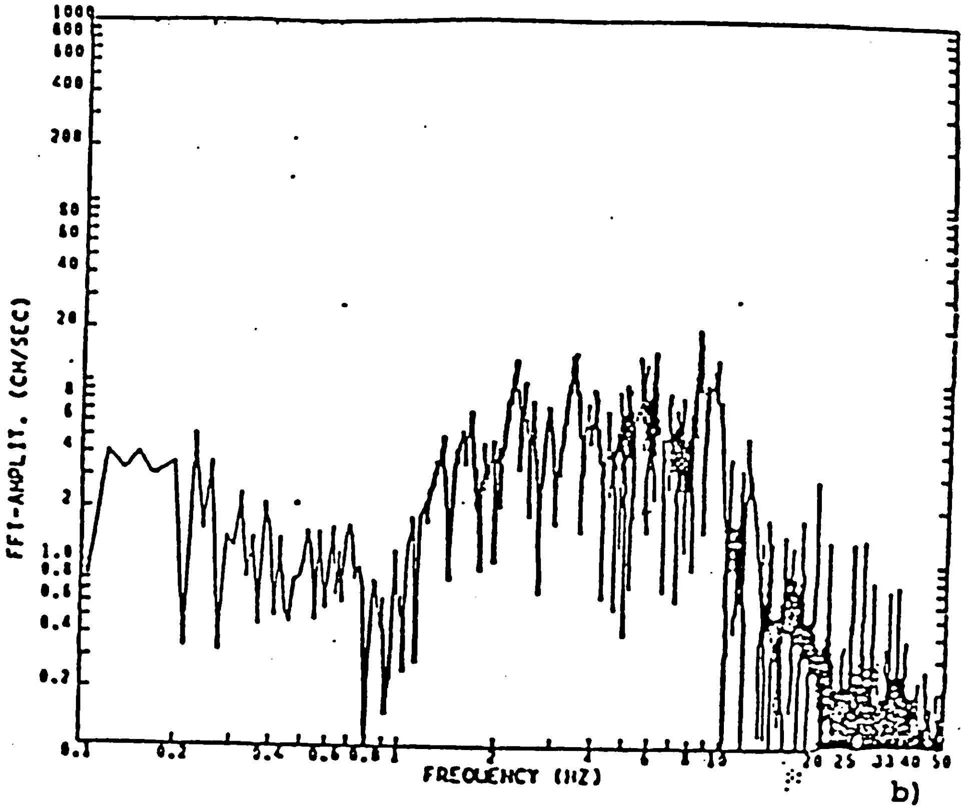

Fig.I.15

Comparison of Fourier Amplitude Spectra of the Procisa Nuaova record (Irpinia 23-11-1980)

b) SMA-1 instrument and automatic digitization

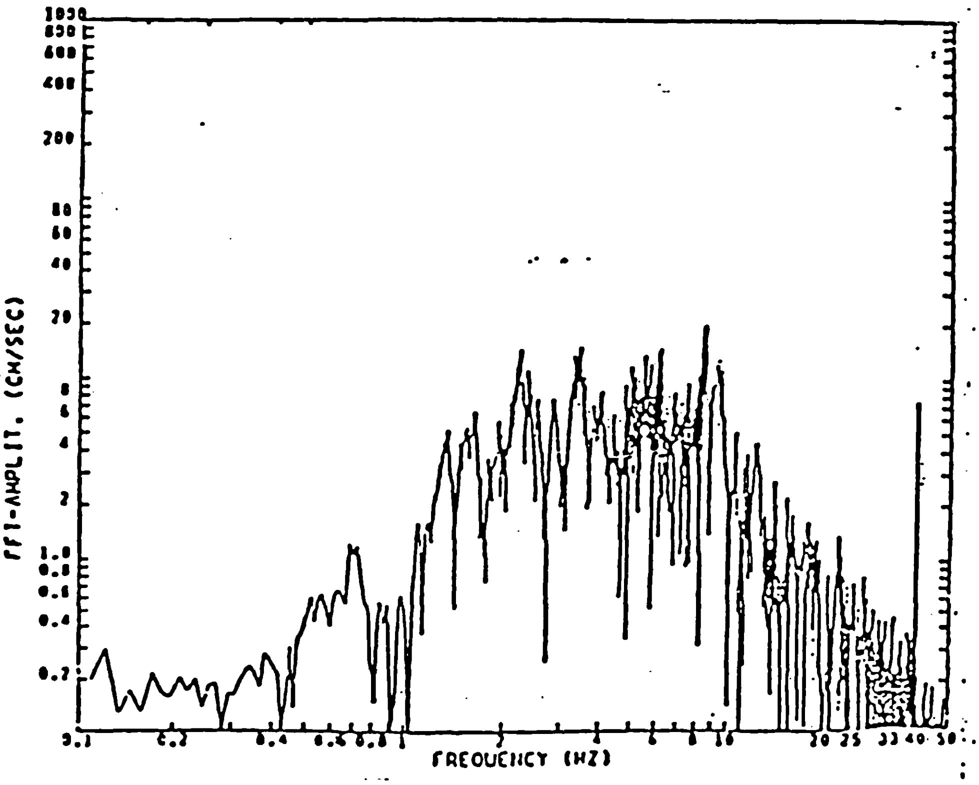

Fig.I.15

Comparison of Fourier Amplitude Spectra of the Procisa Nuaova record (Irpinia 23-11-1980)

c) DSA-1 instrument.

1.4 PURPOSES OF STRONG MOTIONS COLLECTION

1.4.1 Instrument Choice and Network Design

It is frequently observed that the two major branches of earthquake strong motion studies:

1) the ground motion acquisition,

2) the subsequent strong motion analysis,

are separated.

This widens the gap of misunderstanding between the scientists, who deal with signal acquisition problems and the research engineers who use the data without always grasping fully the limitations of the data. On one hand, the collectors, usually of seismological background, see near field acceleration records as another seismic signal but do not attempt to analyse them for engineering purposes. On the other hand, geotechnical and structural engineers, who are still rebuffed by the conventional seismological approach for their recovery, expect to be given earthquake ground motions of perfect quality capable of satisfying their design requirements.

It is clear that this excess of specialisation affects badly the strategy of recovery, the processing techniques and even limits the validity of any subsequent analysis.

If the exact purpose for the data is not known, major misinterpretations may appear:

a) in the choice of the recording instruments, by misdealing with the fundamental trade-off between cost and quality,

b) in the design of the network, by more or less abandonning to hazard or convenience the location of the recorders,

c) in the efficiency of the information recovery process by under or overprocessing the raw data.

The simple collection of strong motion recordsis, inits present form, somehow awkward, since little or no associated information, relating to the conditions of recovery, the seismological or geotechnical environment, are accurately described. It is therefore a formidable task to perform any proper analysis with a set of mixed data which may hardly be subdivided in different categories of statistical significance. The sad consequence is that we are still compelled to limit our studies making use of too little reliable parameters. Peak accelerations, peak velocities are still used too much since any other ones cannot be associated strongly enough with site or shock characteristics. Recording instruments and networks should be studied and designed according to what the profession is looking for. And today too little efforts have been made in that direction.

The exact knowledge of what may be achieved with strong motions and the difficulties that arise should be precisely understood. Such knowledge should improve tremendously both acquisition processes and subsequent treatments. In the next chapters we shall give a detailed view of the problems encoutered in the recovery of the ground motions with particular emphasis in its displacement form. In the following section, we shall outline the information that can be expected from near field records as well as the context for the need for analogue or digital instruments.

1.4.2 Types of information to be recovered

It is the basic role of Engineering Seismology to predict earthquake ground motion intensities at a specific site, for a given Magnitude, distance and local soil conditions, in order to perform safe and economic design of structures of all nature.

Until today one has searched in that direction by producing design response spectra. Although some attempts have been made to extend its application to non-linear design, they are basically applicable to structures behaving linearly, which is far from being satisfactory near collapse. They are also scaled by the peak ground acceleration expected at a given site and it is widely recognised today that better parameters should be found. Realistic time histories, based on physical parameters and scaling factors, will provide a new answer by enabling non-linear structural studies to be carried out.

In order to simulate such earthquake excitations. an immense amount of information is required, and one must stop looking at strong motions only as the provider of response spectra. They must be seen, under another angle, as the scientific source for a better understanding of the behaviour of the rupture mechanism and the seismic wave propagation through geological structures.

If, with that principle in mind, we look at what can be obtained from strong motion records, we can divide the types of retrievable information into two main categories:

1) information of geophysical nature,

2) information of engineering nature.

We shall describe now these two categories of retrievable information.

1.4.3 Geophysical information

The first category refers mainly to basic data needed for research of geophysical and seismological nature, for the purpose of understanding of the earth crust rupture mechanism.

Geophysical information is relevant in engineering since it provides the data required to simulate realistic earthquake ground motions to be used in research and design. These simulated motions are essential, in particular for areas where strong motion data are scarce or non-existant.

In order to get records free from other types of information (soft soils or structural effects, see further) the best instrument location is the free field on rock. Little "contamination" by other features is expected since rock-structure interaction is quasi-inexistant and if the instruments have been adequately positioned in basements of buildings, one can certainly rely on the recorded time histories as good ground motions. A still better location, however, would be away from any spurious influences. The work which can be performed consists mainly of modeling attempts aiming at detecting fundamental features of the rupture zones, depths, velocities and directions of the rupture front, or rise times of energy release. Also of interest are the computations of typical seimological parameters: Magnitudes, hypocenters, distances or some cross-indications for fault plane solutions. This information is today far from being obtained satisfactorily (even with advanced methods), from the far field and it is not unreasonable to believe that one might be able to improve in this field by better data acquisition and interpretation of the near field records.

In chapter X, we shall develop on the necessary parameters required to build a simulated motion based on geophysical models. Let us here,only enumerate some of them:

The radiation pattern:

The seismic energy propagation is not regularly distributed around the source. P-waves, S-waves but also surface-waves have different radiation patterns. They are usually determined from far-field measurements from a large number of stations. Studies for each type of waves are possible due to the dispersion which has separated the different phases. In the near field, the radiation patterns cannot be assumed to be the same; extra near field terms are present in the radiation and also the existence of an extended and moving source rejects all assimilation to a point source . Furthermore, dispersion is not strong enough to separate the phases which remain bundled in the same wave train.

Near field information is fundamental for the recognition of the geometry of the faulting in order to relate it to more global tectonic features. It would then allow a significant step forward in the simulation techniques. It may be obtained by instrumenting seriously all potential or suspected fault in critical areas. Strong motion recorder arrays, in particular, would provide invaluable data for this purpose.

Improved fault plane solutions

Fault plane solution is a routine determination for most of the well recorded earthquakes in the far field. However, it suffers from inaccuracies; in particular it does not permit to decide which of the two conjugate planes provided by the method, is actually the fault plane. Improved solutions may be obtained with near field data. This will be particularly efficient when rupture directions on the fault will be detected, for instance by recognising the Doppler effect in the records. But with no pre-event memory to record the P-wave onset, there is little possibility to retrieve the necessary information.

Epicenters and focal depths

These two common and fundamental parameters of seismology are incredibly badly known. It is already accepted that a more accurate determination consists of near field recordings through specially designed networks.

Rupture mechanisms

The knowledge of the features of the rupture on the fault are of major importance since they are responsible for the high frequencies which affect the engineering structures most. Also, in order to be able to carry out better seismic wave attenuation studies urgently needed for design, one must understand (and this is not the case) how high frequencies are generated on the fault and how they behave near the source. This is certainly in relation with the brittleness of the broken rocks during rupture and such evidence would provide guidance for the choice of design parameters in a particular region. The dynamics of the crust rupture also, is still poorly understood and too many assumptions have to be made. Information of dynamic nature cannot be retrieved from far field techniques since high frequencies have been absorbed by the propagating medium. Relying too much on such techniques will not enable to depart from the useful but insufficient quasi-static parameters that are the seismic moment and the corner frequency.

Wave propagation studies

There are significant differences in the propagation of seismic waves in the far field and in the near field conditions. The usual assumptions, commonly accepted for the far field, originate from the infinitesimal character of the strains encountered as the waves pass. Elastic theory has always been the rule. When anelastic absorbtion, which cannot be neglected when large distances are involved, has to be taken into consideration, one still refers to an equivalent elastic theory. It is based, for mathematical convenience, on an equivalent viscous attenuation, defined by a Q factor (or damping) typically of the order of 1000. To reflect frictional type of attenuation as well as the viscous damping and hysteretic damping Q is described as "partially" frequency dependent.

In the near field, such an approach is only a very crude approximation and a large strain propagation theory should be based on the real non-linearity of the propagating medium. Theoretical attempts have been made, based on numerical techniques but the problem is still underdeveloped. The main difficulty resides in the lack of adequately recorded signals to check possible models. Almost none of the available sets may serve as convincing data to advance in that direction. Furthermore, as stated previouly, all the wave types, which behave differently, are mixed together, and this renders the analysis formidable. As a first approximation, used by engineers, empirical global approaches based on the energy propagation are used, but they must be seen as a pragmatic solution wich should not stop us from looking further.

To perform wave propagation studies in the near field, more signal processing is required. It should serve at separating the different seismic waves in some way. This is the scientific technique to use to have access to a better and accurate understanding of their individual behaviour. Surely we must also introduce models to express the constant presence of large strains when we deal with destructive energy, since the conventional elastic theory is hardly applicable. Finally, the knowledge of the medium characterstics like density, variable with depth, the layer extents and the stress-strain laws as well as the crust state of stress are needed, and this resembles to an impossible task.

Although many practical and theoretical problems have to be solved, it is believed that, with sustained scientific and economical efforts in the search for good recorders and the design of adapted networks, much more valuable information could be obtained from the near field. The immediate result would be to insure a wealth of geophysical parameters to be used progressively in realistic simulated ground motions both for modelling earth rupture and for design.

1.4.4 Engineering Information

The second category is associated with applied research, for the direct safety of structures (buildings, dams, plants, etcæ.), generating hazard for lives or for our economy.

One may split these Engineering studies into two subcategories:
1) the geotechnical studies,

2) the structural response studies.

It is preferable to include here, in the "geotechnical studies" at the recording site, the soft soil effects on ground motions, when they are present. Therefore, in the following, geotechnical structures as soil layers or dams etcæ. will be viewed in the same ways as other structures. The reason for this is that they may be analysed using the same modelling approaches.

Here, one does not aim at discoursing about the nature of the ground motions but one seeks to trace the features of the motions which have destructive effects on structures. One has to ask the following fundamental questions:

1) What are the mechanism of attenuation and low energy transfer in soft soil media?

2) Should one depart from the conventional equivalent elastic theory of wave propagation in strongly non linear and anisotropic soil deposits and what are the basic physical laws?

3) What are the intrinsic characteristics of a time history which have predominant effect on specific structures?

4) Are isolation and ductility always the economial answers in aseismic design?

To answer these questions, one has to rely on the information obtained from strong motion recordings on structures, which are of three types: peak values, information for model verification, information for systems identification. It must be realised that in the case of buildings as well as for other similar structures one does not always record the ground motion in the geophysical sense, since in many cases, it is rather the floor motion which is of interest and hence recorded.

Peak values are the simplest quantities to obtain from strong motion records. In fact, they can be obtained directly from simple peak value recorders which could cover a very wide area. Significant, useful data could be obtained cheaply from such a cover.

Peak accelerations only are still used in almost all building codes, and structures have been built safely to such standards for many years. Even for structures for which dynamic amplification is significant, the peak response is rarely more than three times of the peak ground motion. This is due to both the usually short duration of the excitation and the non-zero damping of most of the structures. One rarely obtains the high dynamic amplification associated with resonant mechanical vibrations of lightly damped systems. This is the reason why peak values studies alone are of great importance for building design. Also of interest are the peak relative displacements to provide the necessary gaps between structural elements which, otherwise, would touch each other generate large accelerations and provoke collapse. This is particularly true for big towers or bridges which must have, for other reasons, free displacements allowances. Peak values alone may be of vital interest for many structures and should not be overlooked particularly if sets of peak values are available where the time histories may not be.

For more advanced understanding of structural behaviour under earthquake excitation one must go into model verification studies. The process of model verification is defined as follows:

1) complete input time histories are recorded.

2) at least one time correlated response time history is recorded.

3) a mathematical model for for the structure is formulated.

4) the model is subjected to the recorded input motion.

5) the model response is compared to the recorded response.

If the two responses do not match well, then the model is not verified and a new and improved model must be found. This is a trial and error procedure which may identify the best model after some attempts and is applicable for structures with relatively few degrees of freedom.

The likelihood of identifying a good structural model from model verification gets smaller when the degrees of freedom becomes larger. A more advanced technique, called system identification consists of finding the pre-determined model parameters by some goodness of fit criteria. Such techniques have been first sucessfully used in the frequency domain when one only required the linear or equivalent linear part of the behaviour. Today the identification of structural response parameters assuming a non-linear model is of particular importance because we are more closely looking at the ultimate behaviour of the structures and their ultimate capacity to withstand earthquake depends upon their behaviour at high amplitudes of motion.

The fundamental point to make here is that the techniques used to obtain such identification are based on non-linear regression analysis. Those analysis are very sensitive to any variation of the input excitation and may generate results far from the true searched model due to the many interactive constraints involved.

The earthquake excitations used as inputs for such studies must definitively be as reliable as it can possibly be. It would be unwise and in some cases useless to perform any non-linear analysis with records whose contamination may annihilate the conclusions of the so sophisticated (and expensive) structural analysis.

CHAPTER II

DESIGN OF AN EARTHQUAKE-LIKE SIGNAL

2.1 INTRODUCTION

In the following chapters, we shall be studying various aspects of the acceleration record processing techniques. Chapter III relates to the first step of the processing consisting in producing a discrete version of the signal. Different categories of noise are introduced at this stage. Chapters IV through VI concern individual key points of the signal processing itself, like digital to analogue conversion, the use of digital filters, the instrument deconvolution or the problem of permanent displacement recovery. In Chapter VII a comparison of of the different processing technique procedures will be performed.

In order to control the transformation of an acceleration signal when it is submitted to these various types of processing, a well defined earthquake-like motion has to be designed. The advantage of such a signal over any recorded one lies in the fact that it is perfectly described through mathematical formulation. We shall see, for example, that it is possible to control the onsets of phase arrivals and their energy variation with time. Recorded accelerations on the other hand, may only be expressed numerically by approximate methods based on restricted assumptions.

This chapter is devoted to the design of an earthquake-like signal, which will be used at the different stages of the study. It will be defined analytically and will represent the main features of a real earthquake, although no emphasis will be given to the real source or travel path effect in particular. What is wished, is an acceleration function whose main characteristics are close to what is typically recorded as an earthquake near-field ground motion.

This approach may also be followed when one whishes to design a realistic acceleration function of known frequency content. The *Boore's Model* for acceleration Fourier Amplitude Spectra (see Ch.III) is suitable for such time history generation. To take full advantage of the method, realistic phase arrival times must be assessed, for example at a given distance, from the knowledge of an approximate (or typical) crust velocity model.

2.2 CONSTRAINTS IMPOSED TO THE SYNTHETIC SIGNAL

Before describing the signal itself, we shall discuss the general constraints which have governed the design.

The signal must be viewed as a reference motion of the ground during an earthquake, and as such it must reflect its typical characteristics. It is, however, recognised that it could not represent a real earthquake (or very unlikely) since features which originate in a vast range of situations connot be met at the same time.

Although strong ground motions are recorded in the form of acceleration time histories, we wished to initiate the ground motion function from a displacement time history. The main reason for this is that displacement is the final stage of the recovery process and as such is most affected by the numerous errors introduced at the different steps of the processing. Comparisons of "true" and "recovered" displacements functions will provide an extensive field of analysis.

The frequency content must be as wide as to extend inside the unexplored domains of low and high frequencies, and that without too many points. It was chosen to limit the number of frequencies to $N =$ 28 . This should avoid frequency interaction which renders the spectrum rather confused. The Fourier amplitude spectrum is following a typical shape for earthquake displacement ground motion, i.e, a constant energy level up to a "corner frequency", followed by decays of ω^{-2}

or ω^{-3} types. Reasonable limits for the spectrum were found

to be at $F_{min} = 0.05Hz$ and $F_{max} = 50.0Hz$.

In the time domain, the simulation of sudden arrivals of P and S phases was considered necessary. A "T" phase was also added to represent low frequencies, sometimes apparent in strong motion records

and associated with multiple reflections of waves within the soft soil layers and baptised here the "tail" of the record.

All the phases are mixed and the total duration of the motion is limited to $20sec$.

Those constraints produce a synthetic signal which possesses the following "wished difficulties" during the processing:

-presence of high frequencies at a low energy level,

-presence of small amplitudes of low frequencies at the end of the record,

-sufficient duration to create "fatigue" of the operator which results in non equal accuracy at the beginning and at the end of the record,

-mixtures of low and high frequencies in the middle part of the signal,

-possibility of cutting the first seconds of the record to re-create the loss of the initial part due to low trigerring level (also valid for the tail),

-inclusions of frequencies much higher than the natural period of the instrument,

-simulation of sharp phase onsets, (here S-waves were selected for this purpose) to affect the true signal during long sequence filtering processes.

In the following, only the basic signal is described. It is referred to as:

$$A/V/D/S = 0.052/8.7/3.5/1.0$$

corresponding to the peak values of acceleration in *g.*, velocity in *cm/sec* and displacement in *cm* respectively. S is a scaling factor.

Other versions of proportional signals are refered to according to the scaling factor replacing 1.0 in their code as in:

$$A/V/D/S = 0.130/21.8/8.7/2.5$$

which means that the basic signal is multiplied by a factor of 2.5.

The technique used here to generate an earthquake-like signal may be used to simulate realistic strong ground motions time histories.

The required Fourier Amplitude Spectrum has to be given, to represent the expected frequency content at a site. It may be obtained from various available models like the *Trifunac and Lee, 1978* model or the *Boore, 1983* model. The required durations for each frequency and their onset have to be assessed independently. They may be based on the work of *Brady and Trifunac, 1975.*

2.3 ANALYTICAL DESCRIPTION

2.3.1 Basic Formulation

The synthetic signal is basically a Fourier series in which only one period, corresponding to the fundamental period T_1 has been retained. T_1 is then the duration of the signal:

$$T_1 = \frac{1}{f_1} = 20sec.$$

For the purpose of the investigation, we have chosen to originate the formulation in terms of the displacement time history, we then have:

$$d(t) = \sum_{k=1}^{N} D_k \sin(2\pi f_k t - \Psi_k) \tag{2.1}$$

$$0 \le t \le T_1$$

$f_1 = 1/T_1$ is the fundamental frequency,

D_k and Ψ_k are respectively the modulus and phase of the frequency f_k,

N is the number of frequencies included in the signal.

Once the values of f_1, D_k, and Ψ_k are defined, the velocity and acceleration functions are immediately deduced:

$$v(t) = \sum_{k=1}^{N} (2\pi f_k) D_k \cos(2\pi f_k t - \Psi_k) \tag{2.2}$$

$$a(t) = -\sum_{k=1}^{N} (2\pi f_k)^2 D_k \sin(2\pi f_k t - \Psi_k) \tag{2.3}$$

$$0 \le t \le T_1$$

In the following, we show how the coefficients:

$$f_k,\ N,$$
$$D_k,\ \Psi_k, \quad (k = 1,2,.\ \ ,N)$$

are computed according to the constraints listed above.

Although the upper frequency limit of $50.0Hz$ requires only a $\Delta t = 0.01 sec.$, the displacement function was generated with $\Delta t = 0.001 sec.$ This small time increment was retained to avoid noise in the highest part of the spectrum in the digital-to-analogue conversion in the preparation of the signal on film (see Chap.III).

Fig. II.4 shows the frequency content of the displacement before windowing, and values of D_k and

Ψ_k appear in Table III.

Fig. II. 2a and II. 2b represent respectively the Fourier amplitude spectrum of the acceleration function and the associated phase spectrum before windowing. It can be seen that Δf is not constant over the total range of frequencies, but has three values:

$$\Delta f_1 = 0.05Hz \quad \text{for} \quad 0.05Hz \le f_k \le 0.5Hz$$

$$\Delta f_2 = 0.5Hz \quad \text{for} \quad 0.5Hz \le f_k \le 5.0hz$$

$$\Delta f_3 = 5Hz \quad \text{for} \quad 5Hz \le f_k \le 50Hz$$

The total number of frequencies is $N = 28$.

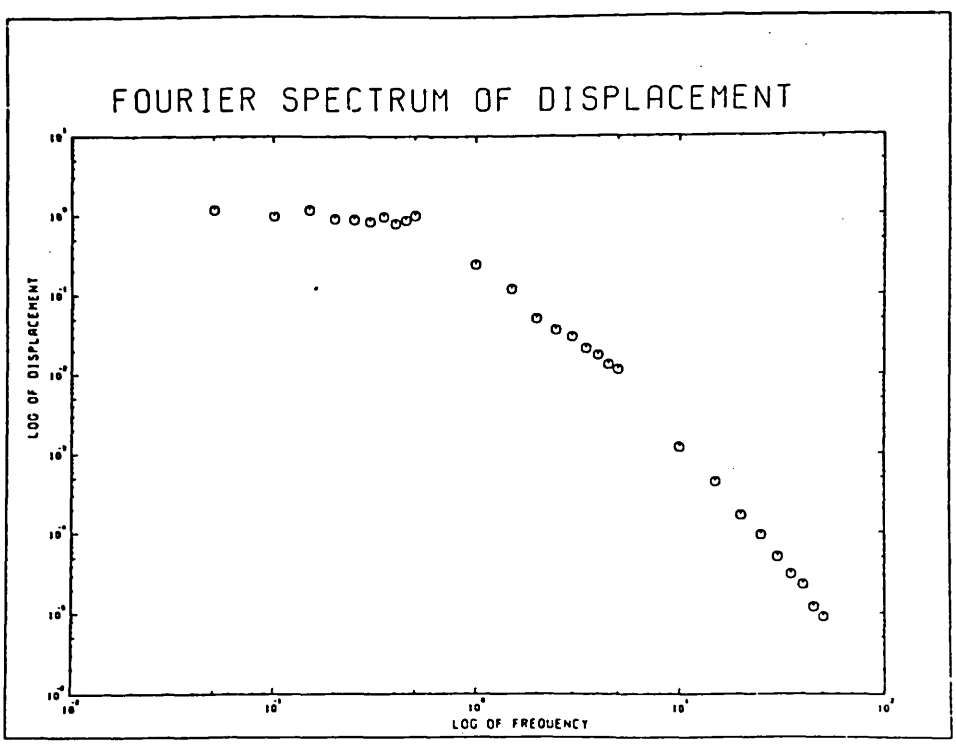

Fig.II.1

Frequency content of the basic displacement function before windowing

Numerical values were chosen normally distributed about the ω^0, ω^2, ω^3 trends.

$F_{min} = 0.05Hz$, $F_{max} = 50Hz$, Corner frequency $= 0.5Hz$.

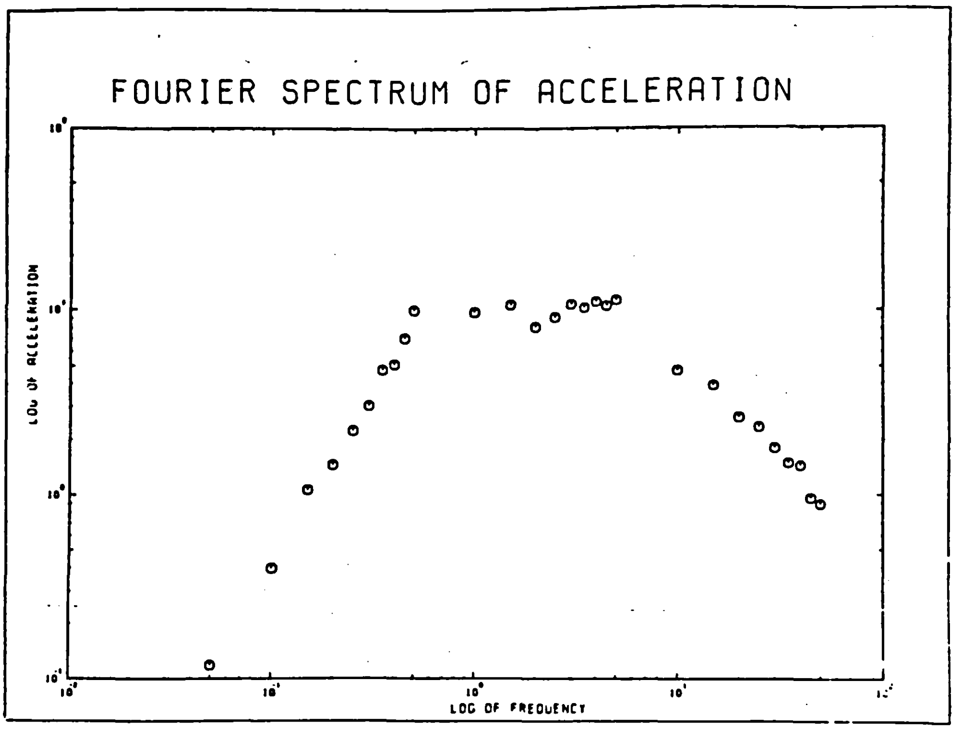

Fig.II.2a

Frequency content of the basic acceleration function before windowing.

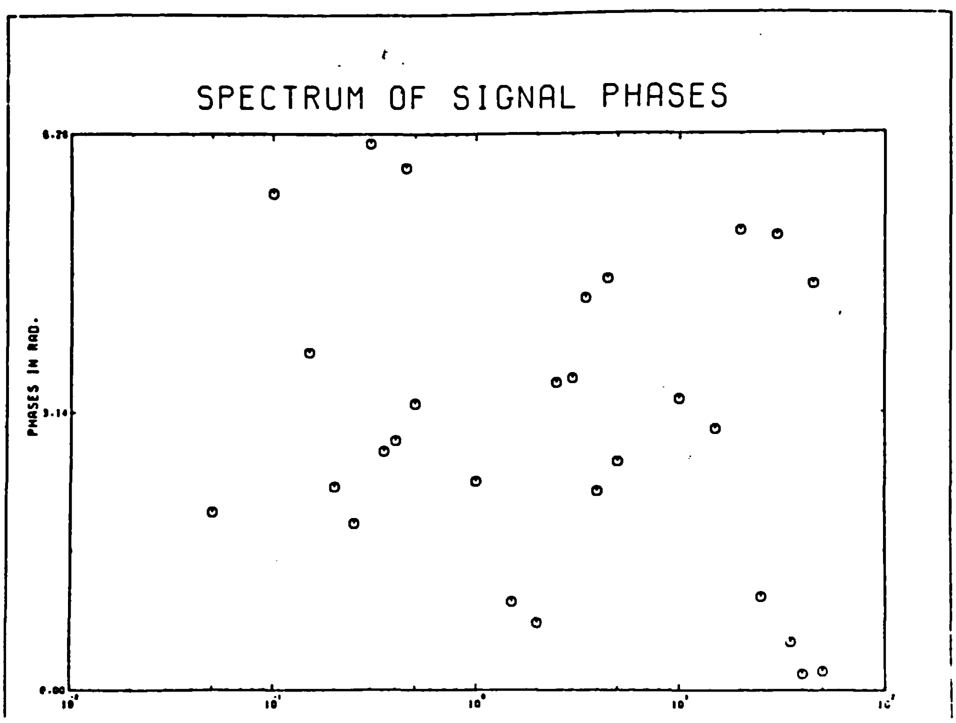

Fig.II.2b

Phase delays of the various frequencies of the basic signal

They were chosen randomly distributed following a uniform distribution between 0 and 2π.

2.3.2 Phase Windowing

In order to simulate the arrivals of the different phases, windowing in time is applied. The columns (6), (7), (8) in Table III give the time of onset of each particular frequency as well as each time of maximum intensity and end time.

Simplification in the nomination of the phases prompted the definition of three wave groups codified in column (3):

P-waves assumed to be the high frequencies ($5 \;\; to \;\; 50Hz$)

T-waves assumed to be low frequencies ($0.05 \;\; to \;\; 0.45Hz$)

S-waves assumed to be the medium frequencies ($0.5 \;\; to \;\; 4.5Hz$)

Table III also indicates that only the P-waves and the T-waves have a symetric window, extending respectively from $T_0 = 0sec.$ to $T_f = 14sec.$ and $T_0 = 0sec.$ to $T_f = 20sec.$ The S-waves exhibit a sharp onset from $T_0 = 3sec.$ to $T_m = 4sec.$ and a slow decay from $T_0 = 4sec.$ to $T_m = 18sec.$

The choice of a particular time window was determined by the fact that their effect in the frequency domain should not allow significant leakage which would smear neighbouring frequencies. A three term cosine window was chosen. Its expression is:

$$w(t) = A_0 - A_1 \cos\frac{2\pi t}{T} + A_2 \cos\frac{4\pi t}{T} \tag{2.4}$$

T is the window length.

It gives a very good efficiency, both in lobe width and sidelobe level if we use:

$$A_0 = 0.42323$$
$$A_1 = 0.49755$$
$$A_2 = 0.07922$$

as proposed by Harris (1978).

Figures 2.3*a and* 2.3*b* show the time window used and their frequency effects, both on amplitudes and phases. For the P-waves and T-waves the fall-off is of the order of $-6dB/oct$ and the sidelobe level is if $-61dB$. Due to dissymmetry of the S-waves these characteristics are altered. The separation of the various frequencies is well achieved in the high frequency range and sufficient in the medium frequency range. The low frequencies, however suffer from severe interaction due to leakage.

The final expression for the displacement time history can be written:

$$d(t) = w_T(t)T_0(t) + [w_{S_1}(t) + w_{S_2}(t)]S_0(t) + w_P(t)P_0(t) \tag{2.5}$$

where

$$T_0(t) = \sum_{k=1}^{9} D_k \sin(2\pi f_k t - \Psi_k) \tag{2.6a}$$

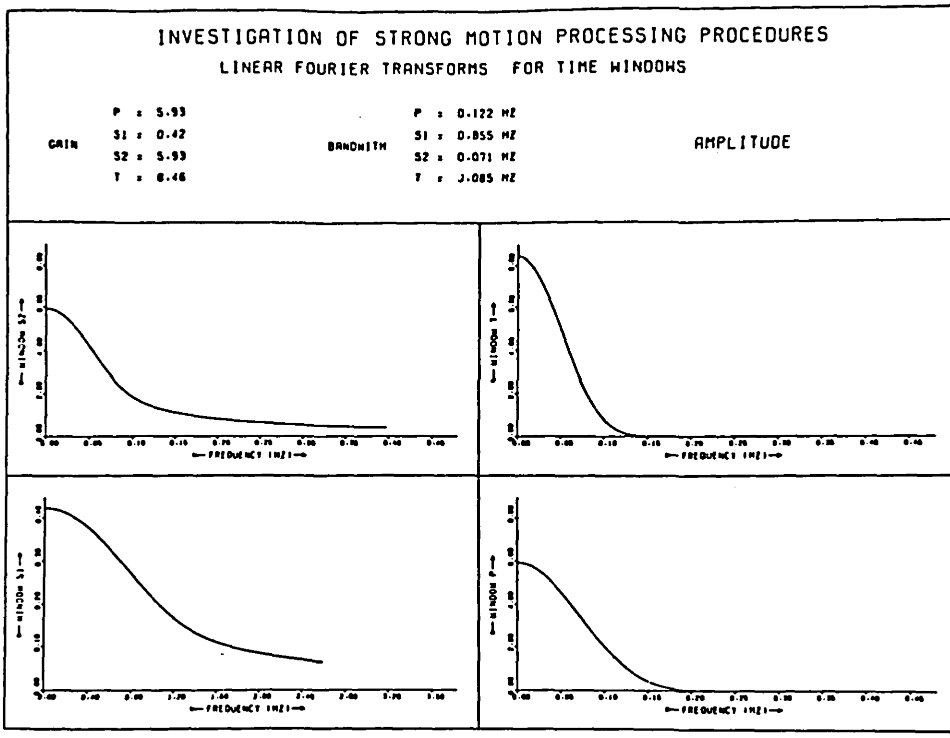

Fig.II.3a

Frequency effect of the time windows used to simulate T, P, and S-waves.

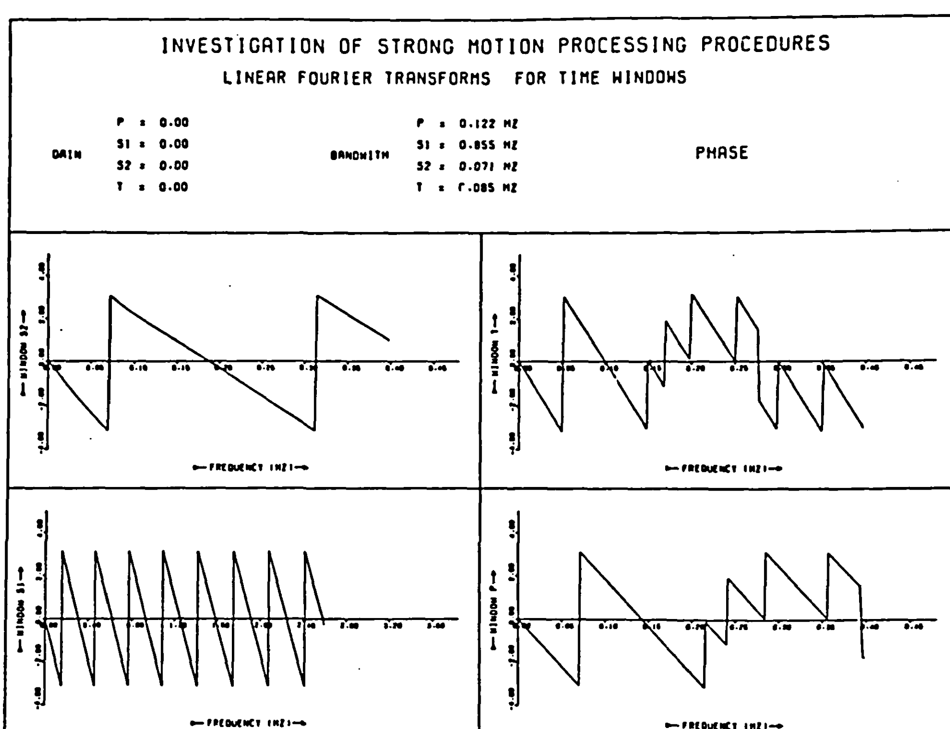

Fig.II.3b

Phase functions introduced by the time windows of T, P, and S-waves.

$$S_0(t) = \sum_{k=10}^{18} D_k \sin(2\pi f_k t - \Psi_k) \tag{2.6b}$$

$$P_0(t) = \sum_{k=19}^{28} D_k \sin(2\pi f_k t - \Psi_k) \tag{2.6c}$$

are respectively the T-waves, S-waves anf P-waves of the synthetic signal before windowing,

and

$$w_T(t) = \begin{cases} A_0 - A_1 \cos\frac{2\pi t}{20} + A_2 \cos\frac{4\pi t}{20} & 0 \le t \le 20sec. \\ 0 & if \quad t < 0 \quad or \quad t > 20sec. \end{cases} \tag{2.7a}$$

$$w_{S_1}(t) = \begin{cases} A_0 - A_1 \cos\frac{2\pi(t-3)}{2} + A_2 \cos\frac{4\pi(t-3)}{2} & 3 \le t \le 4sec. \\ 0 & if \quad t < 3sec. \quad or \quad t > 4sec. \end{cases} \tag{2.7b}$$

$$w_{S_2}(t) = \begin{cases} A_0 - A_1 \cos\frac{2\pi(t+10)}{28} + A_2 \cos\frac{4\pi(t+10)}{28} & 4 \le t \le 18sec. \\ 0 & if \quad t < 4sec. \quad or \quad t > 18sec. \end{cases} \tag{2.7c}$$

$$w_P(t) = \begin{cases} A_0 - A_1 \cos\frac{2\pi t}{14} + A_2 \cos\frac{4\pi t}{14} & 0 \le t \le 14sec. \\ 0 & if \quad t < 0 \quad or \quad t > 14sec. \end{cases} \tag{2.7d}$$

Expressions for velocity and acceleration time functions are readily obtained:

$$v(t) = w'_T T_0 + w_T T'_0 + [w'_{S_1} + w'_{S_2}]S_0 + [w_{S_1} + w_{S_2}]S'_0 + w'_P P_0 + w_P P'_0 \tag{2.8}$$

$$\begin{aligned} a(t) = & w''_T T_0 + 2w'_T T'_0 + w_T T''_0 + w''_S S_0 + 2w'_S S'_0 + w_S S''_0 \\ & + w''_P P_0 + 2w'_P P'_0 + w_P P''_0 \end{aligned} \tag{2.9}$$

where $w_S = w_{S_1} + w_{S_2}$ and ' and " denote successive differentiation with respect to time.

Figures 2.4*a*, 2.4*b and* 2.4*c* show the individual time functions composing the signal before windowing. *Figure* 2.4*d* shows the sum of all the components.

After windowing is applied, these functions transform into those on figures 2.5*a*, 2.5*b* and 2.5*c* respectively. The final earthquake-like signal is shown on figure 2.5*d*.

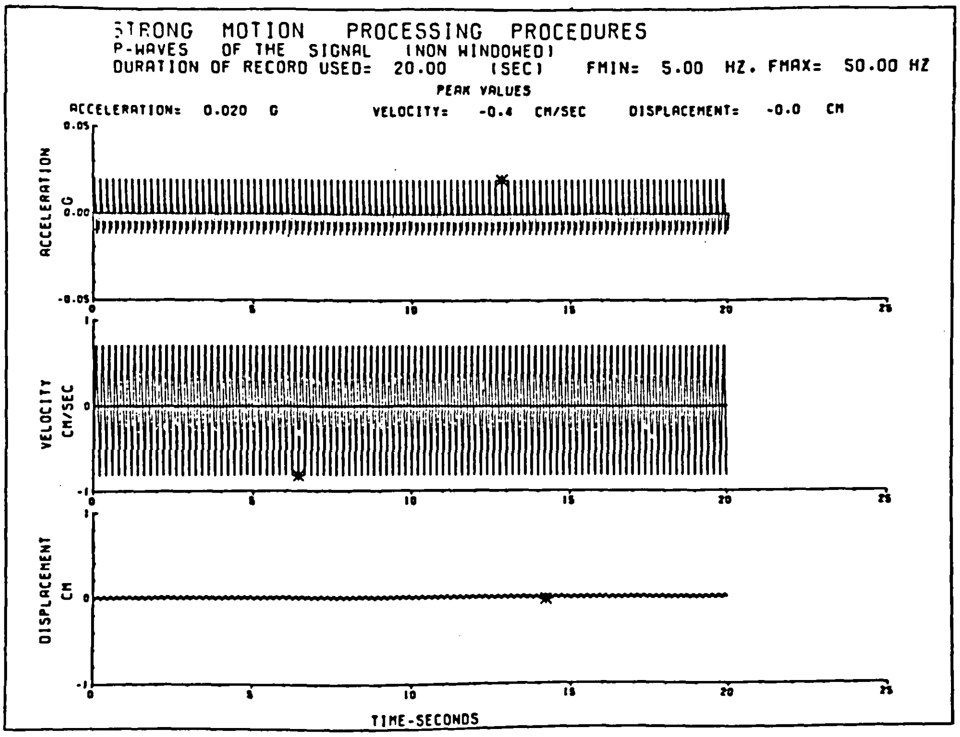

Fig.II.4a

P-waves before windowing

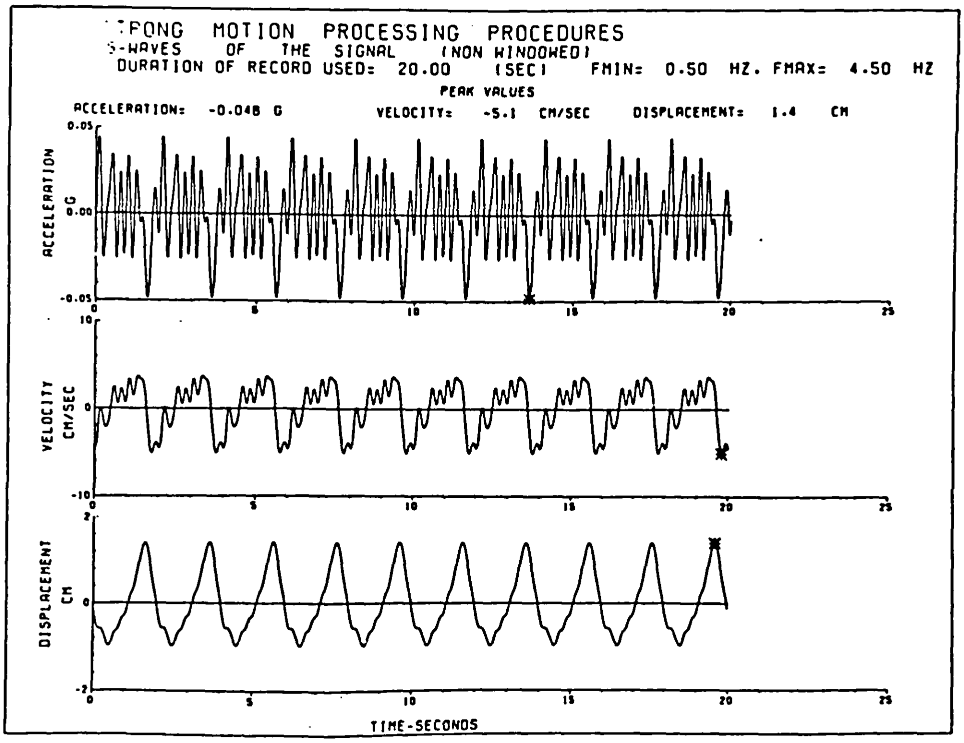

Fig.II.4b
S-waves before windowing

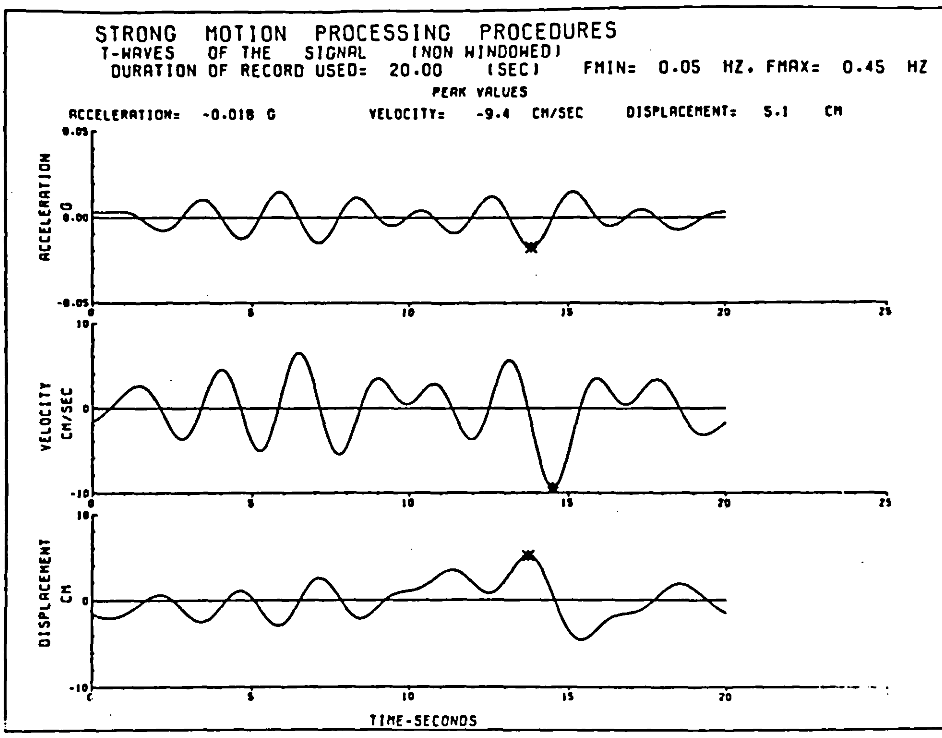

Fig.II.4c

T-waves before windowing

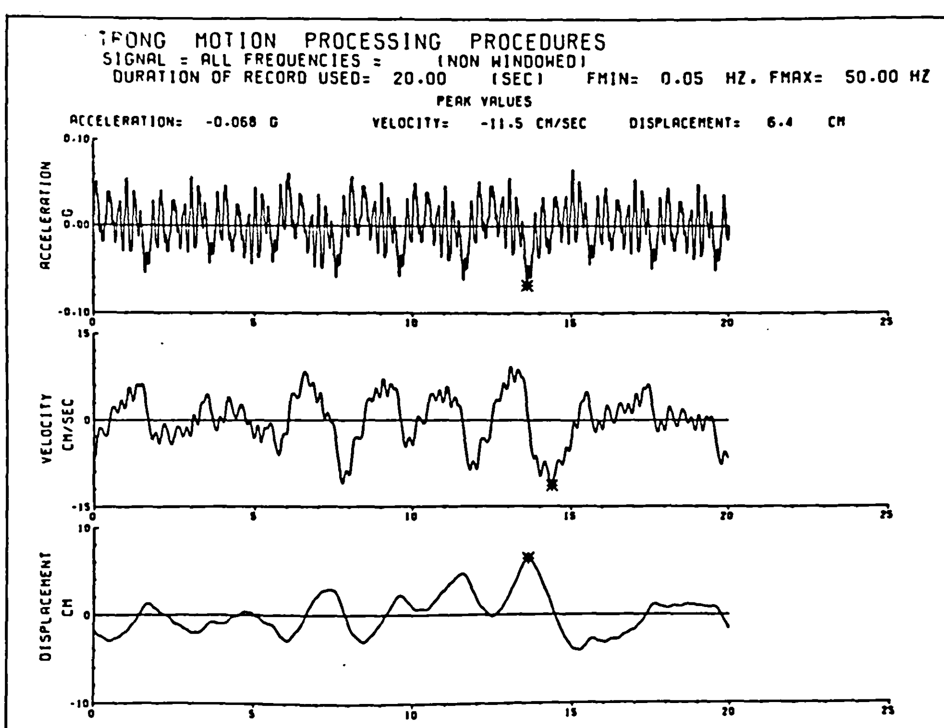

Fig.II.4d

Final time histories, including all frequencies of table III, before windowing.

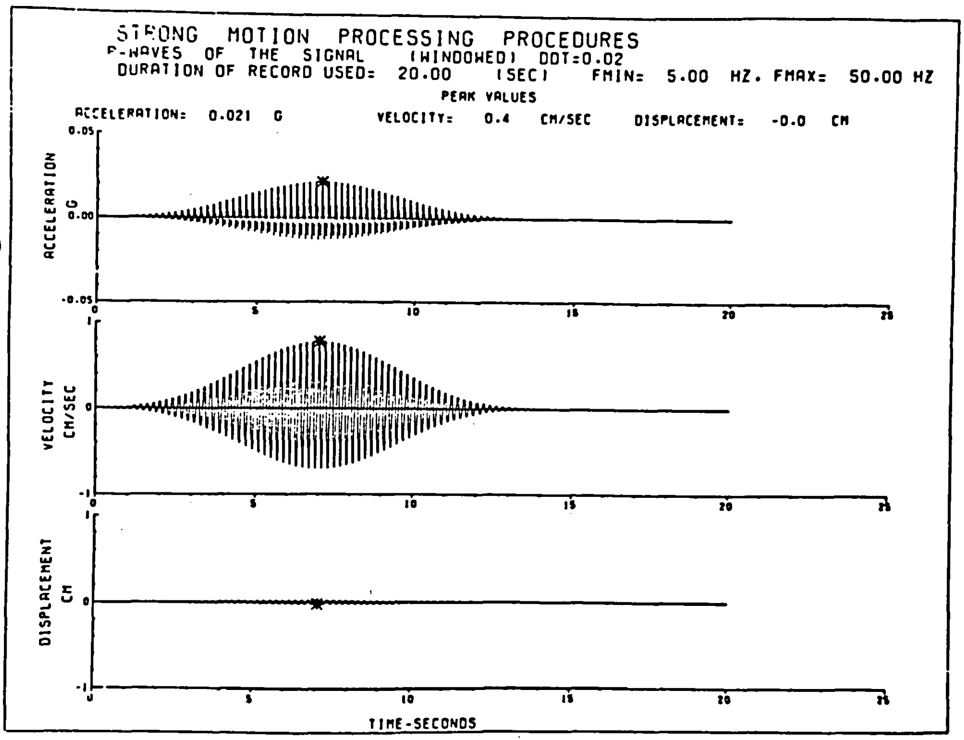

Fig.II.5a

Windowed P-waves. $T_0 = 0$ sec, $T_f = 14$ sec.

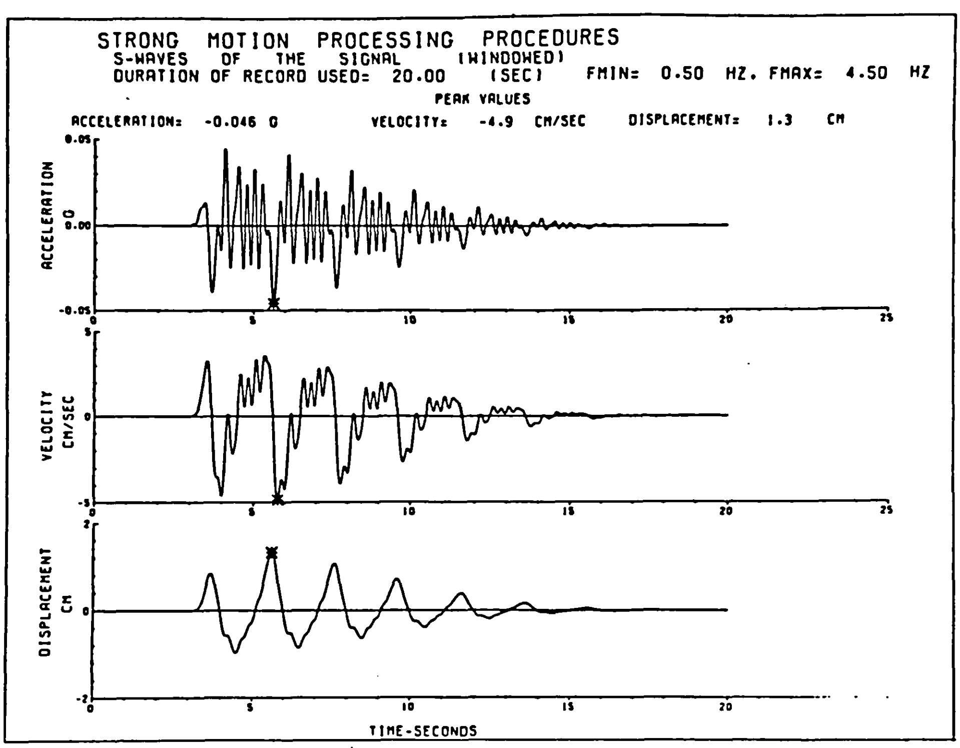

Fig.II.5b

Windowed S-waves. $T_0 = 0$ sec, $T_f = 3$ sec, $T_m = 4$ sec, $T_f = 18$ sec.

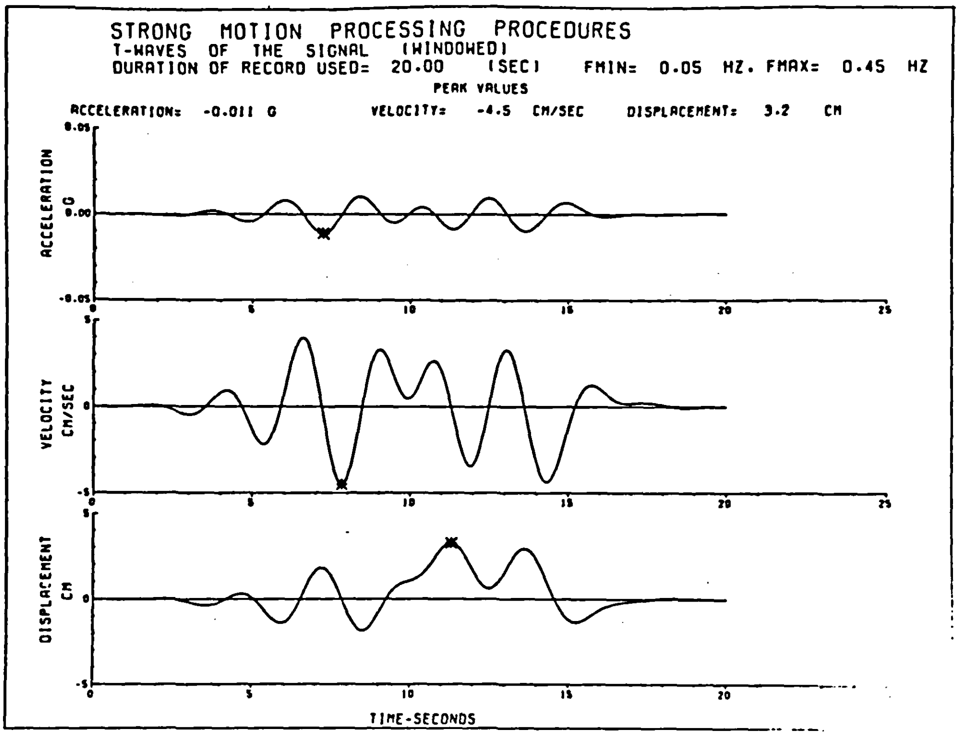

Fig.II.5c

Windowed T-waves. $T_0 = 0$ sec, $T_f = 20$ sec.

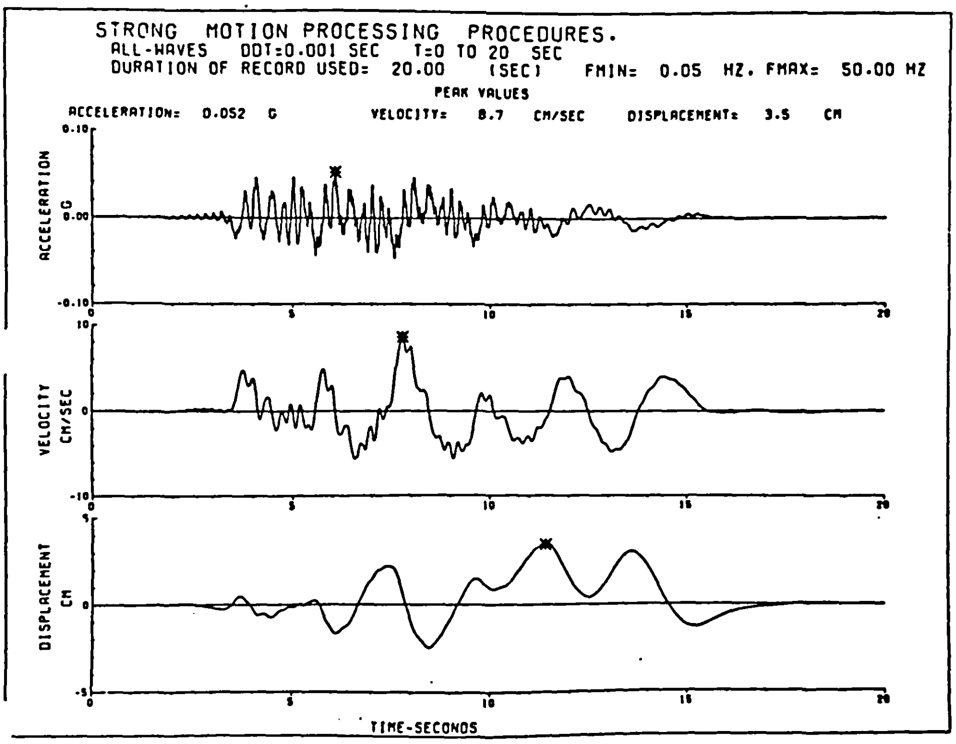

Fig.II.5d
Final time domain of the designed earthquake-like signal.

2.3.3 Frequency Domain Formulation

The accurate frequency content of the signal can be computed directly as a linear combination of shifted Dirichlet functions.

Calling $D(i\omega)$ the complex Fourier spectrum of the non-windowed displacement signal, we knwow that the weighted truncation introduced by the window transforms $D(i\omega)$ into a new spectrum $D_R(i\omega)$ such that:

$$D_R(i\omega) = \frac{1}{2\pi i} \int_{c-i\infty}^{c+i\infty} D(is) \quad W[i(\omega - s)] \quad ds \tag{2.10}$$

where $s = c + i\Omega$ with $c \rightarrow 0$

$W(i\omega)$ is the complex frequency representation of the window, expressing that $D_R(i\omega)$ is the convolution product of the original complex spectrum $D(i\omega)$ and the window $W(i\omega)$.

In the case of our particular signal, $D(i\omega)$ is discrete and we have three groups of frequencies, affected by three different windows: $W_T(i\omega)$, $W_S(i\omega)$ and $W_P(i\omega)$ whose expressions are given in the next section.

The general expression (2.10) becomes:

$$\begin{aligned} D_R(i\omega) = & \sum_{k=1}^{9} D_k W_T(i\omega - i\omega_k) \\ & + \sum_{k=10}^{18} D_k W_S(i\omega - i\omega_k) \\ & + \sum_{k=19}^{28} D_k W_S(i\omega - i\omega_k) \end{aligned} \tag{2.11}$$

which is also a continuous complex spectrum.

The exact analytic expressions for velocity and acceleration complex Fourier spectra are:

$$V_R(i\omega) = i\omega D_R(i\omega) \tag{2.12}$$

$$A_R(i\omega) = -\omega^2 D_R(i\omega) \tag{2.13}$$

Figures 2.6*a and* 2.6*b* show the frequency content of the signal in terms of displacement and acceleration.

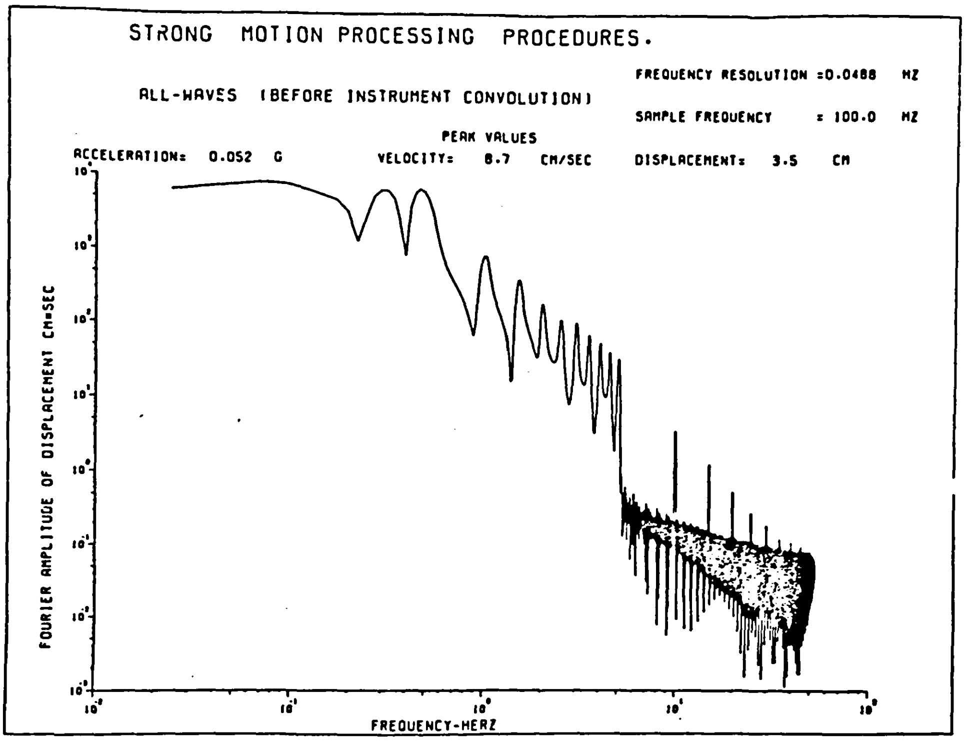

Fig.II.6a

Fourier amplitude spectrum of the displacement function after windowing.

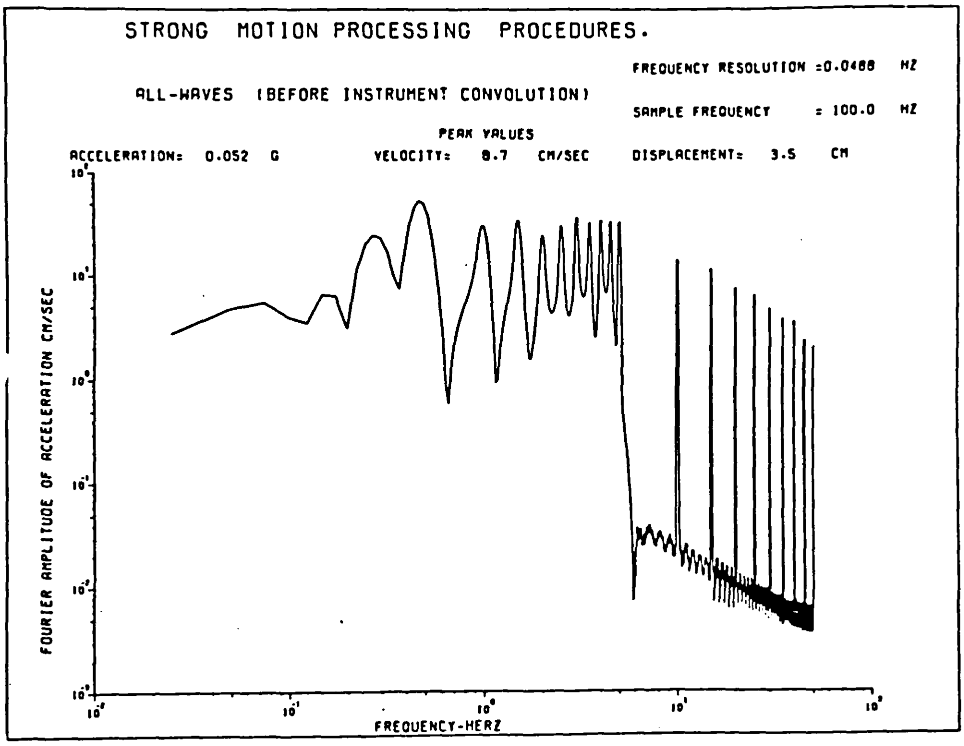

Fig.II.6b

Fourier amplitude spectrum of the acceleration function after windowing.

2.4 WINDOW EXPRESSIONS IN FREQUENCY

2.4.1 General Equations

In this section, we shall develop the expressions for $W_T(i\omega)$, $W_{S_1}(i\omega)$, $W_{S_2}(i\omega)$ and $W_P(i\omega)$.

All these windows have the same form and since computations are achieved from an incremental file, must be expressed with discrete time variable $n\Delta t$:

$$w(n\Delta t) = A_0 - A_1 \cos\frac{2\pi n}{N_L} + A_2 \cos\frac{4\pi n}{N_L} \tag{2.14}$$

$$n = 0,. \quad ,N_L - 1 \qquad T = N_L \Delta t$$

Its frequency domain equivalent is:

$$W(i\omega) = \Delta t \sum_{n=0}^{N_L-1} w(n\Delta t) \quad \exp -i\omega n\Delta t \tag{2.15}$$

which can be computed from a combination of the well-known Dirichlet kernel.

$$W_0(i\omega) = \frac{1}{N_L} \exp\frac{i\omega\Delta t}{2} \frac{\sin\frac{\omega N_L \Delta t}{2}}{\sin\frac{\omega\Delta t}{2}} \tag{2.16}$$

Δt is the working time increment,

N_L is the associated number of points,

where N_L may be N_T, N_{S_1}, N_{S_2} or N_P.

We obtained after some algebra:

$$\begin{aligned} W(i\omega) = A_0 W_0(i\omega) - \frac{A_1}{2}\left[W_0(i\omega - \frac{2\pi i}{N_L\Delta t}) + W_0(i\omega + \frac{2\pi i}{N_L\Delta t})\right] \\ + \frac{A_2}{2}\left[W_0(i\omega - \frac{4\pi i}{N_L\Delta t}) + W_0(i\omega + \frac{4\pi i}{N_L\Delta t})\right] \end{aligned} \tag{2.17}$$

2.4.2 Frequency windows for T-waves and P-waves

They are obtained by substitution of N by N_T or N_P in equation 2.17;

we get:

$$\begin{aligned} W_T(i\omega) = A_0 W_{0T} - \frac{A_1}{2}\left[W_{0T}(i\omega - \frac{2\pi i}{T_T}) + W_{0T}(i\omega + \frac{2\pi i}{T_T})\right] \\ + \frac{A_2}{2}\left[W_{0T}(i\omega - \frac{4\pi i}{T_T}) + W_{0T}(i\omega + \frac{4\pi i}{T_T})\right] \end{aligned} \tag{2.18}$$

$$W_P(i\omega) = A_0 W_{0P} - \frac{A_1}{2}\left[W_{0P}(i\omega - \frac{2\pi i}{T_P}) + W_{0P}(i\omega + \frac{2\pi i}{T_P}) \right] + \frac{A_2}{2}\left[W_{0P}(i\omega - \frac{4\pi i}{T_P}) + W_{0P}(i\omega + \frac{4\pi i}{T_P}) \right] \quad (2.19)$$

Table III

COMPOSITION OF THE BASIC SIGNAL, (before windowing).

Nber (1)	Freq.Hz (2)	Wave (3)	D_k (4)	A_k (5)	Ψ_k (6)	T_0 (7)	T_m (8)
1	0.05	T	1.199211	0.118357	2.005	0.0	10.0
2	0.10	T	1.006645	0.397407	5.616	0.0	10.0
3	0.15	T	1.199199	1.065204	3.820	0.0	10.0
4	0.20	T	0.923047	1.457615	2.293	0.0	10.0
5	0.25	T	0.898514	2.216990	1.876	0.0	10.0
6	0.30	T	0.849212	3.017294	6.173	0.0	10.0
7	0.35	T	0.976224	4.721115	2.701	0.0	10.0
8	0.40	T	0.801443	5.062343	2.821	0.0	10.0
9	0.45	T	0.875775	7.001266	5.899	0.0	10.0
10	0.50	S	0.999587	9.865512	3.231	3.0	4.0
11	1.00	S	0.244018	9.633428	2.354	3.0	4.0
12	1.50	S	0.119585	10.622292	0.991	3.0	4.0
13	2.00	S	0.051209	8.086587	0.756	3.0	4.0
14	2.50	S	0.036967	9.121226	3.473	3.0	4.0
15	3.00	S	0.030221	10.737677	3.524	3.0	4.0
16	3.50	S	0.021304	10.302823	4.435	3.0	4.0
17	4.00	S	0.017574	11.100681	2.247	3.0	4.0
18	4.50	S	0.013224	10.571749	4.651	3.0	4.0
19	5.00	P	0.011508	11.357921	2.587	0.0	7.0
20	10.00	P	0.001204	4.753193	3.292	0.0	7.0
21	15.00	P	0.000443	3.935005	2.956	0.0	7.0
22	20.00	P	0.000167	2.637154	5.196	0.0	7.0
23	25.00	P	0.000095	2.344027	1.053	0.0	7.0
24	30.00	P	0.000051	1.812056	5.138	0.0	7.0
25	35.00	P	0.000031	1.499190	0.545	0.0	7.0
26	40.00	P	0.000023	1.452803	0.184	0.0	7.0
27	45.00	P	0.000012	0.959324	4.584	0.0	7.0
28	50.00	P	0.000009	0.8882629	0.216	0.0	7.0

2.4.3 Frequency window for S-waves

In the case of S-waves, the frequency window is the sum of two semi-windows having different parameters:

$$S\,1 \text{ from } T_0 = 3sec. \text{ to } T_m = 4sec.$$
$$S_2 \text{ from } T_m = 4sec. \text{ to } T_f = 18sec.$$

Equation 2.14 becomes:

$$w_{S_1}(n\Delta t) = A_0 - A_1 \cos\frac{2\pi(n-N_1)}{N_{S_1}} + A_2 \cos\frac{4\pi(n-N_1)}{N_{S_1}} \tag{2.20}$$

$$N_1\Delta t = 3sec. \qquad N_{S_1}\Delta t = 2sec.$$

$$N_1 \leq n \leq N_1 + \frac{N_{S_1}}{2}$$

for the S_1 case.

$$w_{S_2}(n\Delta t) = A_0 - A_1 \cos\frac{2\pi(n-N_2)}{N_{S_2}} + A_2 \cos\frac{4\pi(n-N_2)}{N_{S_2}} \tag{2.21}$$

$$N_2\Delta t = -10sec. \qquad N_{S_2}\Delta t = 28sec.$$

$$N_2 + \frac{N_{S_2}}{2} \leq n \leq N_2 + N_{S_2}$$

for the S_2 case.

We finally obtain:

$$\begin{aligned} W_{S_1}(i\omega) = \exp(-3i\omega)\ & A_0 W_{0S_1}(i\omega) - \frac{A_1}{2}\left\{ W_{0S_1}(i\omega - \frac{2\pi i}{T_{S_1}}) + W_{0S_1}(i\omega + \frac{2\pi i}{T_{S_1}}) \right\} \quad \exp(-i\pi) \\ & + \frac{A_2}{2}\left\{ W_{0S_1}(i\omega - \frac{4\pi i}{T_{S_1}}) + W_{0S_1}(i\omega + \frac{4\pi i}{T_{S_1}}) \right\} \end{aligned} \tag{2.22}$$

$$\begin{aligned} W_{S_2}(i\omega) = \exp(-4i\omega)\ & A_0 W_{0S_2}(i\omega) - \frac{A_1}{2}\left\{ W_{0S_2}(i\omega - \frac{2\pi i}{T_{S_2}}) + W_{0S_2}(i\omega + \frac{2\pi i}{T_{S_2}}) \right\} \quad \exp(i\pi) \\ & + \frac{A_2}{2}\left\{ W_{0S_2}(i\omega - \frac{4\pi i}{T_{S_2}}) + W_{0S_2}(i\omega + \frac{4\pi i}{T_{S_2}}) \right\} \end{aligned} \tag{2.23}$$

Figures II.3a and II.3b show the windows W_T, W_S and W_P of the three phase groups.

2.5 OUPUT OF COMPUTER SIMULATED TRANSDUCER

When the designed ground motion is fed into a recording instrument, the displacement of the single harmonic oscillator is assumed to represent the acceleration time history of the ground motion. This is achieved with a typical instrument when its natural frequency f_0 is high and its viscous damping, the percentage of critical value, λ is near $\sqrt{2}/2$. We have retained, for the computer simulated recorder, values close to the characteristics encounted in practice:

$$f_0 = 20Hz.$$

$$\lambda = 0.600$$

When activated by the designed ground motion input, the "perfect" instrument having these characteristics will give the acceleration time history called here signal after convolution with instrument, since this function is actually obtained by convolution of the input (2.9) with the impulse response of the oscillator:

$$h(t) = \frac{1}{\omega_D} e^{-\lambda\omega t} \sin \omega_D t \tag{2.24}$$

where

$$\omega_D = \omega\sqrt{1-\lambda^2} \quad \text{is the damped natural frequency}$$

λ is the percentage of critical damping.

The displacement output of the transducer is a close approximation of the ground acceleration:

$$a_g(t) = \int_0^t a(\tau)h(t-\tau) \; d\tau \tag{2.25}$$

which is represented on *Fig. II.7a.*. It can be noted that the time functions of the input and output are very similar (as expected); no major difference can be detected even in the time sequence of the pulses. The peak value transforms from 0.052g before convolution to 0.048g after convolution, showing a variation of the order of ten percent.

Fig. II.7b represents the Fourier Amplitude of the transformed acceleration. Also as expected, there is little difference with *figure* 2.6*b* except in the high frequency range where some attenuation is visible.

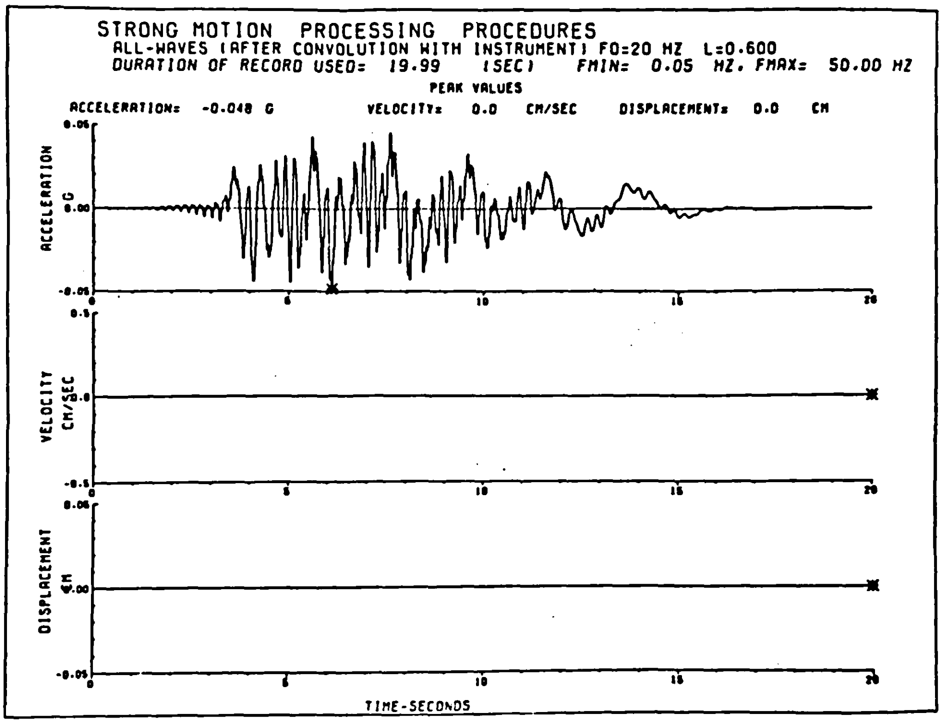

Fig.II.7a

Designed signal after convolution with recording instrument.

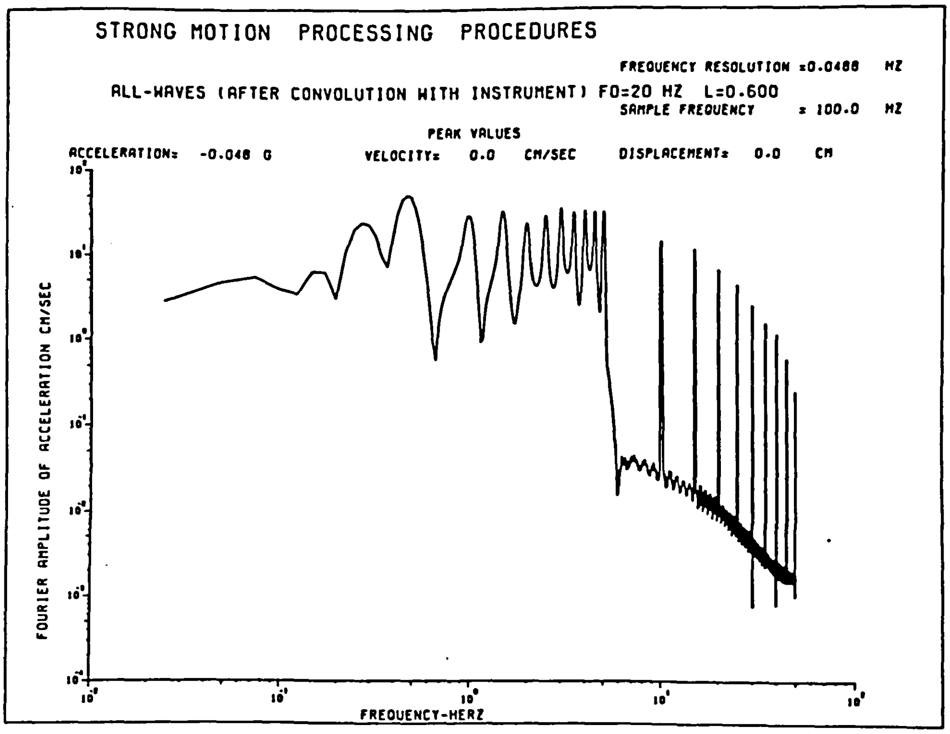

Fig.II.7b

Fourier amplitude of acceleration after convolution with recording instrument.

CHAPTER III

ANALOGUE TO DIGITAL CONVERSION

3.1 INTRODUCTION

Most of the accelerogram recorders in use produce analogue traces of the acceleration time histories in three perpendicular directions. The recording media are, for instance, 35*mm* (*M02* New Zealand), 70*mm* (*SMA1* and *RFT-250*, USA) film negative, 92*mm* waxed paper (*SMAC-B2* and *ERS-B*, Japan) or 12 inch photo-paper (*AR-240* USA).

The first stage of accelerogram processing consists of transforming the acceleration time function into a digital form, which presents many advantages. It is imperative that this operation be reduced to its simplest form, to limit signal distorsion. The digitized version of the analogue record enables:

1. easy storage of magnetic discs or tapes necessary for the constitution of earthquake record banks.
2. simple data transfer through digital channels.
3. numerical computations like correction, filtering or interpolation etcæ. to determine ground velocities displacements as well as many other signal descriptions.

Any other subsequent calculations can easily be achieved from the digital form: the Fourier spectra, response spectra or structural response. It also permits the carrying out of many statistical studies for engineering or geophysical research purposes and enables to prepare graphic representations in any desired form or scale.

However, it must be realised that this digitized version, which is a fundamental step in the production of the so called "uncorrected record", is not exactly equivalent to the original analogue. The digitized version is affected by the various operations required to reach the digital stage. Firstly, when the recording medium is a film negative it must be developed and in some cases enlarged. This photographic processing introduces undesirable distorsions, mainly in the low frequency range. Secondly, during the digitization process itself, many factors have significant influence on the final result:

- the *sampling* which defines the time instants at which the signal is to be mesaured. It has been shown explicitely (*J. Shoha-Jabean, 1980*) that the sampling is a sensitive factor which affects any subsequent analysis.
- the *quantization* which is the measurement decision from a continuous space, to a discrete sequence

of numbers. Several quantization rules (sign and magnitude, two's - complement, one's complement representation) are commonly used and introduce different types of quantizing errors.

Finally, the most important source of errors is relating to semi-automatic digitization, where the operator is a vital agent of the processing chain. What is called *Raw data* may be severely affected by several human types of mistakes, such as bad point positioning due to variable trace thickness, lack of concentration or tiredness.

In this Chapter, we shall discuss the effects that these imperfections have on the recorded acceleration in order to understand to what extent commonly used records are reliable. It is believed that analogue to digital conversion is responsible for most of the limitations of our current available records.

3.2 MATHEMATICAL FORMULATION OF DIGITIZATION OPERATIONS AND ERRORS

In strong motion record processing, as in many applications of signal processing, one visualises input and output as continuous time signals. It is most important, however, to differentiate between analogue and digital form. The records are originally analogue; they become digital after digitization. As a result, they must be treated as a sequences, according to the mathematics of discrete (and not analogue) functions; these sequences are numerically processed to yield corrected sequences which are finally converted back, according to some interpolation rule, to continuous time signals.

As mentioned above, the digitization operation generates various types of distortions. In this paragraph, we shall give a mathematical formulation to digital signals in order to be in a position to formulate analytically the consequences that such discretization has on the recorded acceleration signals.

3.2.1 Sampling

Although most subsequent treatments of the data require a constant sampling interval, manual digitization generates sampling at a variable interval of time. This is advantageous in the sense that points of particular interest, like peaks, throughs or inflection points, are picked up and also that the operator can decide on the number of points to digitize. He can increase the rate of sampling when the curvature increases and he will reduce it when he finds it less necessary.

Since the frequency content of the digitized version is closely related to the smallest interval of time, variable sampling requires less points as it adapts to the frequency content of the original analogue. On the other hand, when digitized at a constant intervals of time, the same highest frequency information is obtained by chosing a Δt equal to the smallest value existing in the variable interval of time ensemble. This obviously assumes that the operator does not miss any of the highest frequencies. It is possible, with regard to some assumptions, to obtain a uniform sampling from a non-uniform one. This is achieved by interpolation. All the strong motion processing centres have opted for linear interpolation between points since it is certainly the simplest type of interpolation; this is also what, consciously or not, the operator has in mind when digitizing.

It has often been said that the choice of the new Δt in the case of linear interpolation cannot be smaller than the smallest sampling interval, since frequency information above the corresponding frequency is absent. In fact, if we accept that the analogue function re-formed from the digitized version consists of piecewise linear segments (crude approximation, but other interpolation are also possible), it is legitimate to reduce the interval of time. But, during interpolation, the particular points like peaks or throughs are likely to be truncated since they will not in general correspond to a multiple of the chosen interval of time.

Linear interpolation is certainly valid when the original chosen interval is very small, like in the case of an accurate automatic digitization. When the number of points is limited, like in most manual digitization, many advantages will be found in the use of non linear interpolation. In Chapter IV, we shall study several methods of non-linear interpolation of acceleration records digitized at large intervals of time.

Interpolation may be seen as a new sampling after a reconstitution of a realistic analogue function from a given discrete set of points has been performed. Once done, we can carry out subsequent analysis, either with this analogue function or from any new constant sampling interval. One can therefore consider that the restriction on Δt is not a strict one. In general, one may feel free to choose new values, but one must be aware of the actual limitation: the small high frequency noise introduced by the particular interpolation.

Let $a(t)$ be the analogue output signal and $a_s(t)$ one sampled version. Furthermore, let $s(t)$ be the sampling function: a continuous infinite trace of unit amplitude impulses and finite width τ, non-uniformly spaced (*fig. III. 1*):

$$(...\Delta t_{n-1}, \Delta t_n, \Delta t_{n+1}, ...) \qquad with \quad \tau << \Delta t_i.$$

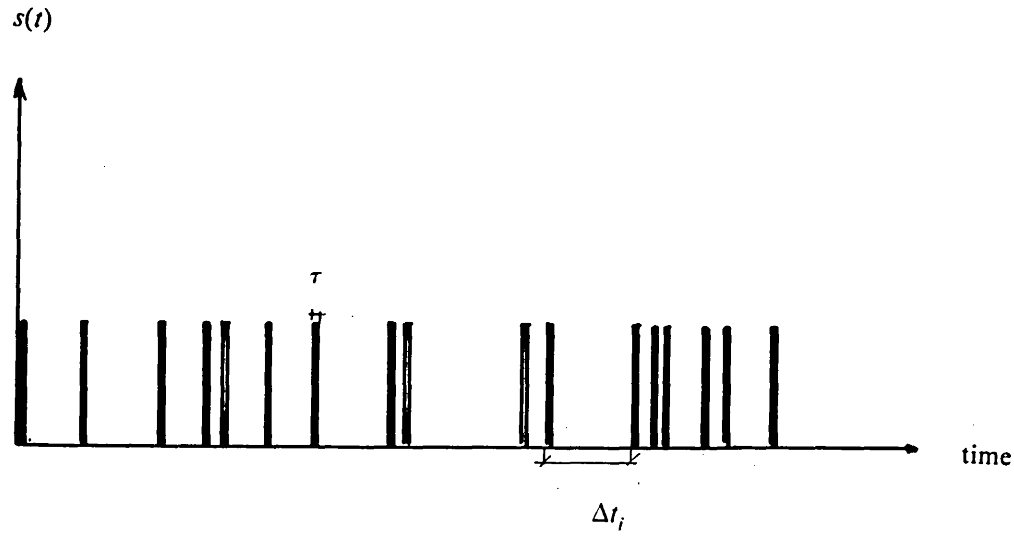

Fig.III.1

Sampling functiom $s(t)$ a variable interval of time

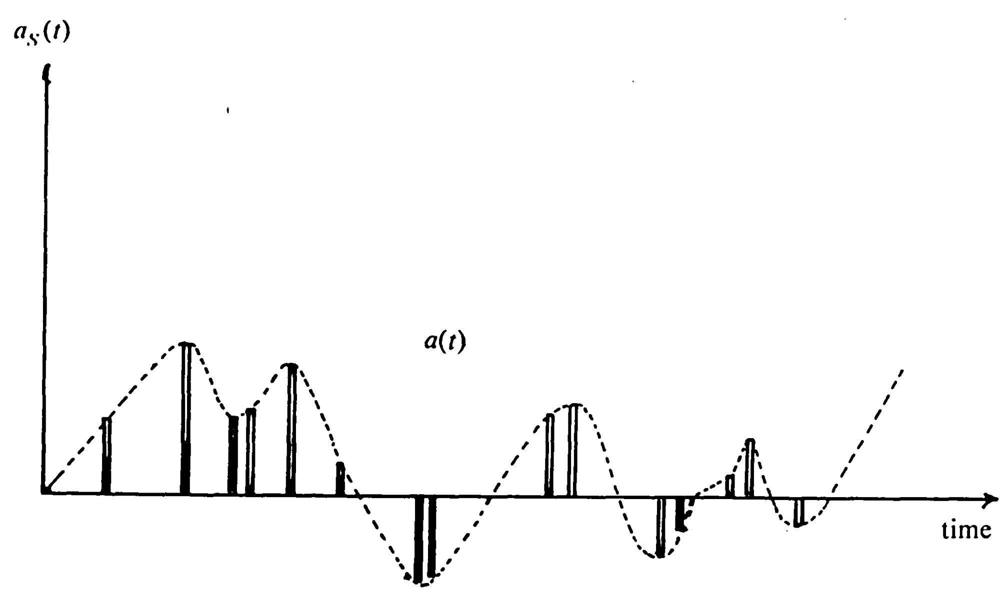

Fig.III.2

Digitized version $a_S(t)$ of an analogue $a(t)$

It is apparent that the sampled signal $a_s(t)$ may be represented by the product of $a(t)$ and the sampling function $s(t)$ (*fig. III. 2*):

$$a_s(t) = a(t) \times s(t) \tag{3.1}$$

In the following however, we shall consider uniform sampling with constant period Δt, since it is frequently the working state of the digitized signals. The interpolation rules, mentioned above and examined in the next chapter enable the passage from a variable to a constant sampling. The sampling wave form $s(t)$ then becomes the natural sampling $s_{\Delta t}(t)$, periodic and continuous. It is composed of a sum of shifted elementary pulses s_τ (fig.III.3) and can be written:

$$s_{\Delta t}(t) = \sum_{n=-\infty}^{+\infty} s_\tau(t + n\Delta t) \tag{3.2}$$

where $s_\tau(t)$ is defined as:

$$s_\tau(t) = \begin{cases} 1, & \text{if } \; -\tau/2 < t < \tau/2 \\ 0, & \text{if } \; t < -\tau/2 \;\; or \;\; t > \tau/2 \end{cases} \tag{3.3}$$

Sampled with the natural sampling function, the digitized signal can be written:

$$a_{\Delta t} = a(t) \times s_{\Delta t}(t) \tag{3.4}$$

It is seen on *fig. III. 4.*

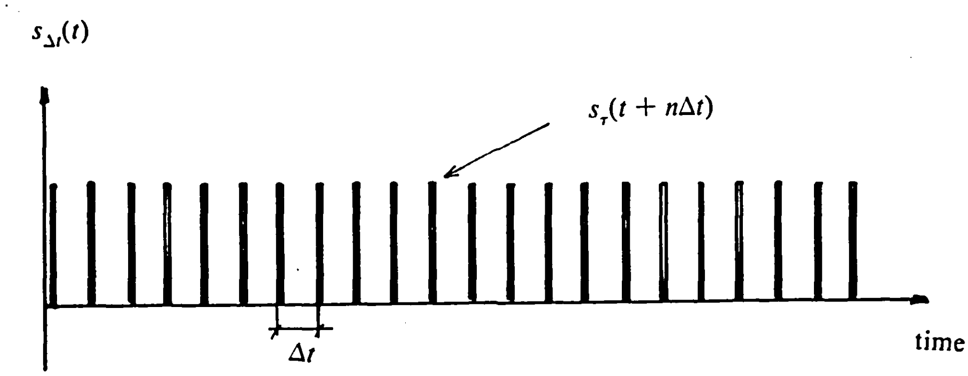

Fig.III.3
Sampling function $s_{\Delta t}(t)$ at constant interval of time

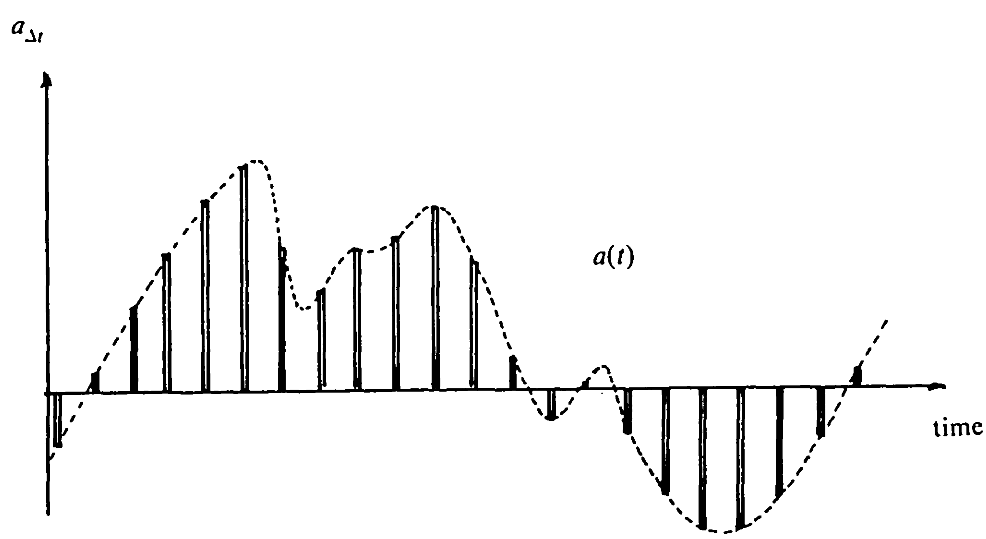

Fig.III.4
Digitized version $a_{\Delta t}(t)$ of an analogue $a(t)$
sampled at constant interval of time

3.2.2 Effects of sampling on Fourier Spectrum

It is worthwhile to look at the effects of sampling in the frequency domain. The Fourier Transform of the analogue function $a(t)$ is:

$$A(i\omega) = \int_{-\infty}^{+\infty} a(t)e^{-i\omega t}\,dt \tag{3.5}$$

and the Fourier Transform of the sampled signal $a_{\Delta t}(t)$ is the convolution of $A(i\omega)$ with the Fourier Transform $S_{\Delta t}(i\omega)$ of the sampling function:

$$A_{\Delta t}(i\omega) = \frac{1}{2\pi}A(i\omega)*S_{\Delta t}(i\omega) \tag{3.6}$$

We see that the true spectrum $A(i\omega)$ is affected by the sampling function. We shall present here the analytic formulation of this effect.

The frequency spectrum $S_{\Delta t}(i\omega)$ is not continuous: Since it is periodic with period Δt, it only exists at certain discrete values $\omega_n = 2\pi n/\Delta t$, $n = -\infty, ..., -1, 0, +1, ..., +\infty$. It may be graphically represented as a series of equally spaced lines, whose heights are proportional to the amplitude of the continuous spectrum of the individual pulse:

$$S_\tau(i\omega) = \int_{-\tau/2}^{+\tau/2} s_\tau\, e^{-i\omega t}\,dt = \frac{2}{\omega}\sin(\frac{\omega\tau}{2}) \tag{3.7}$$

These amplitudes S_n are the terms of the Fourier series coefficients of the sampling function. They are expressed in complex form as:

$$S_n = \frac{1}{\Delta t}\int_{-\tau/2}^{\Delta t-\tau/2} s_{\Delta t}(t)e^{-\dfrac{2\pi i n t}{\Delta t}}\,dt \tag{3.8a}$$

$$= \frac{1}{\Delta t}S_\tau(\frac{2\pi i n\tau}{\Delta t}) \tag{3.8b}$$

$$= \frac{1}{n\pi}\sin(\frac{n\pi\tau}{\Delta t}) \tag{3.8c}$$

The spectrum of the sampling signal is represented in *fig. III.5* where it is seen that it has an envelope proportional to the well known *sinc* function.

It is possible to express the periodic sampling function on time, from its Fourier coefficients, as:

$$s_{\Delta t}(t) = \sum_{n=-\infty}^{+\infty} S_n e^{2\pi i n t/\Delta t} \tag{3.9}$$

Now, taking the Fourier Transform of both sides, and with $\omega_s = 2\pi/\Delta t$, the sampling circular frequency, we obtain an expression for $S_{\Delta t}$, the Fourier Transform of the sampling function:

$$S_{\Delta t}(i\omega) = \int_{-\infty}^{+\infty} \left(\sum_{n=-\infty}^{+\infty} S_n e^{in\omega_s t} \right) e^{-i\omega t} dt \tag{3.10a}$$

$$= 2\pi \sum_{n=-\infty}^{+\infty} S_n \delta(\omega - \omega_s) \tag{3.10b}$$

and substituting *Eq. 3.8c* into *Eq. 3.10b*:

$$S_{\Delta t}(i\omega) = 2 \sum_{n=-\infty}^{+\infty} \frac{1}{n} \sin(\frac{n\pi\tau}{\Delta t}) \delta(\omega - \omega_s) \tag{3.11}$$

This equation consists of impulses that exist at:

$$\omega = 0, \quad \pm\, \omega_s, \quad \pm\, 2\omega_s, \quad \pm\, ..., \quad \pm\, n\omega_s, ...$$

whose amplitudes at $\omega = n\omega_s, (n = -\infty, ..., -1, 0, +1, ..., +\infty)$ are:

$$\frac{2\pi\tau}{\Delta t} sinc(\frac{n\tau}{\Delta t}) \tag{3.12}$$

We then obtain the frequency spectrum of the sampled signal by substituting *Eq. 3.11* into *Eq. 3.6*:

$$A_{\Delta t}(i\omega) = \sum_{n=-\infty}^{+\infty} \frac{1}{n\pi} \sin(\frac{n\pi\tau}{\Delta t}) A(i\omega - ni\omega_s) \tag{3.13}$$

Eq. 3.13 may be simplified if we assume that our sampling is perfect. This case, also refered to as an ideal or an instantaneous sampling is, of course, physically impossible. It is defined as the limiting case when τ tends to zero. The term,

$$\frac{1}{n\pi} \sin(\frac{n\pi\tau}{\Delta t})$$

can be substituted by:

$$\frac{1}{\Delta t} S_\tau(i\omega)$$

which tends to $1/\Delta t$ as τ tends to 0. Since $S_\tau(i\omega)$ tends to the Fourier Transform of the Dirac function $\delta(t)$, *Eq. 3.13* becomes:

$$A_{\Delta t}(i\omega)_{\text{perfect}} = \frac{1}{\Delta t} \sum_{n=-\infty}^{+\infty} A\left[i(\omega - n\omega_s) \right] \tag{3.14}$$

and is represented in *fig. III.6* where the spectrum of the original analogue signal appears at the same location on natural sampling, while the amplitude remains constant.

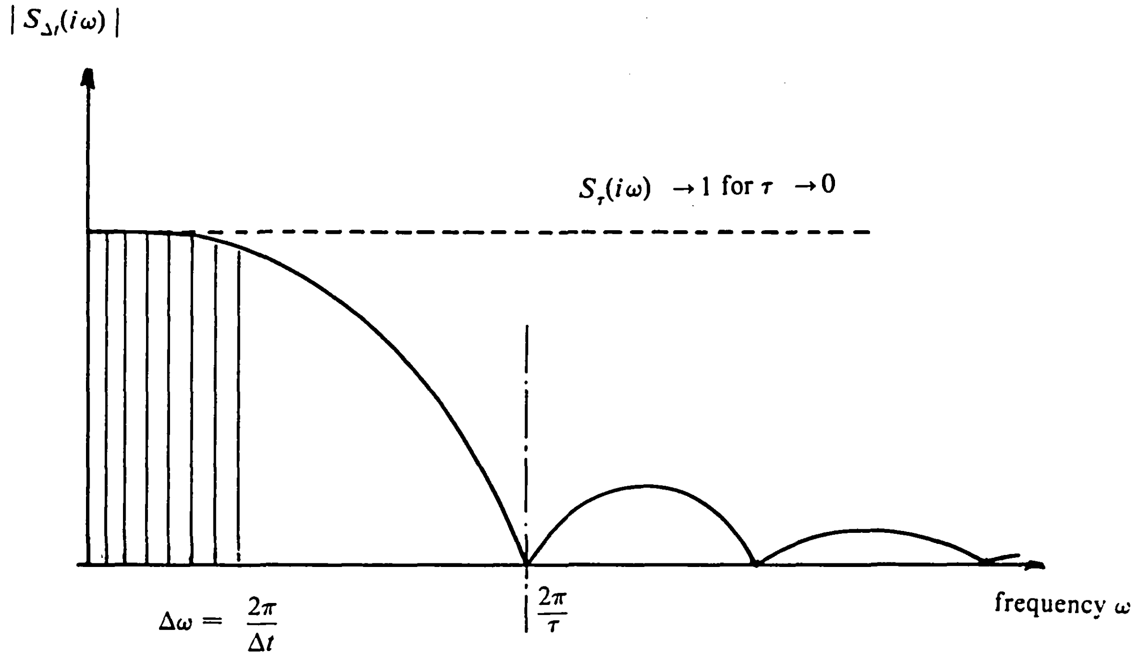

Fig.III.5

Spectrum of a constant interval sampling signal

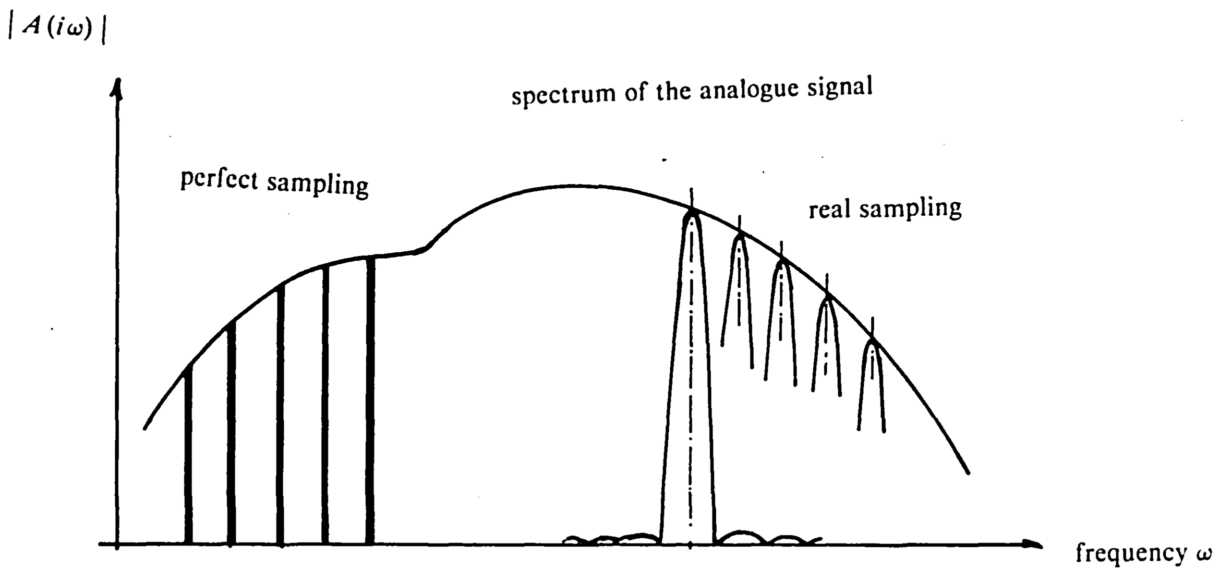

Fig.III.6

FAS of analogue and sampled signals

3.2.3 Aliasing Error due to Sampling

At this stage of the development, we should recall the uniform sampling theorem :

"If a message signal $f(t)$ is band limited to a frequency ω_m, then it is completely charaterised by samples taken at uniform intervals less that π/ω_m."

The sampling theorem may also be interpreted as follows:

Let ω_s be the sampling rate of a signal $a(t)$. If this signal does not contain information above the frequency $\omega_N = \omega_s/2$, it may be recovered fully by the digitization at constant intervals $\Delta t = \pi/\omega_s$.

ω_N is called the Nyquist frequency.

If, however, there is in the signal information beyond ω_N, then the digitized version will be contaminated by the frequencies above ω_N. *Fig.III.7* shows such a case in the frequency domain where the true spectrum expands far beyond the Nyquist frequency: the signal "energy" contained in these frequencies is re-distributed in the lower ones by folding about the Nyquist frequency. In the case of strong ground motions, typical sampling intervals of $\Delta t = 0.02sec$ and $\Delta t = 0.01sec$ are used; this means that it is implicitely considered that no frequency components are present above $25Hz$ or $50Hz$ respectively. The term band-limited implies that there should be absolutely no frequency components in the spectrum above ω_N. However, typical strong motion acceleration signals do not have such sharp frequency cutoffs and will contain components at all frequencies. For this reason it is imperative to treat the acceleration before sampling to ensure that the band-limited condition is fulfilled. The phenomenon of aliasing results from the discrete character of the signal as a direct consequence of the digitization of the records; it introduces a distorsion of the spectrum called aliasing error.

Methods to avoid aliasing exist and will not be described here. Let us only indicate the main anti-aliasing techniques:

- reduction of the sampling interval Δt,
- use of a randomly distributed time sampling function $s(t)$,
- pre-filtering of the contaminating frequencies above ω_N.

These techniques will have to be used whenever accurate processing procedures are required.

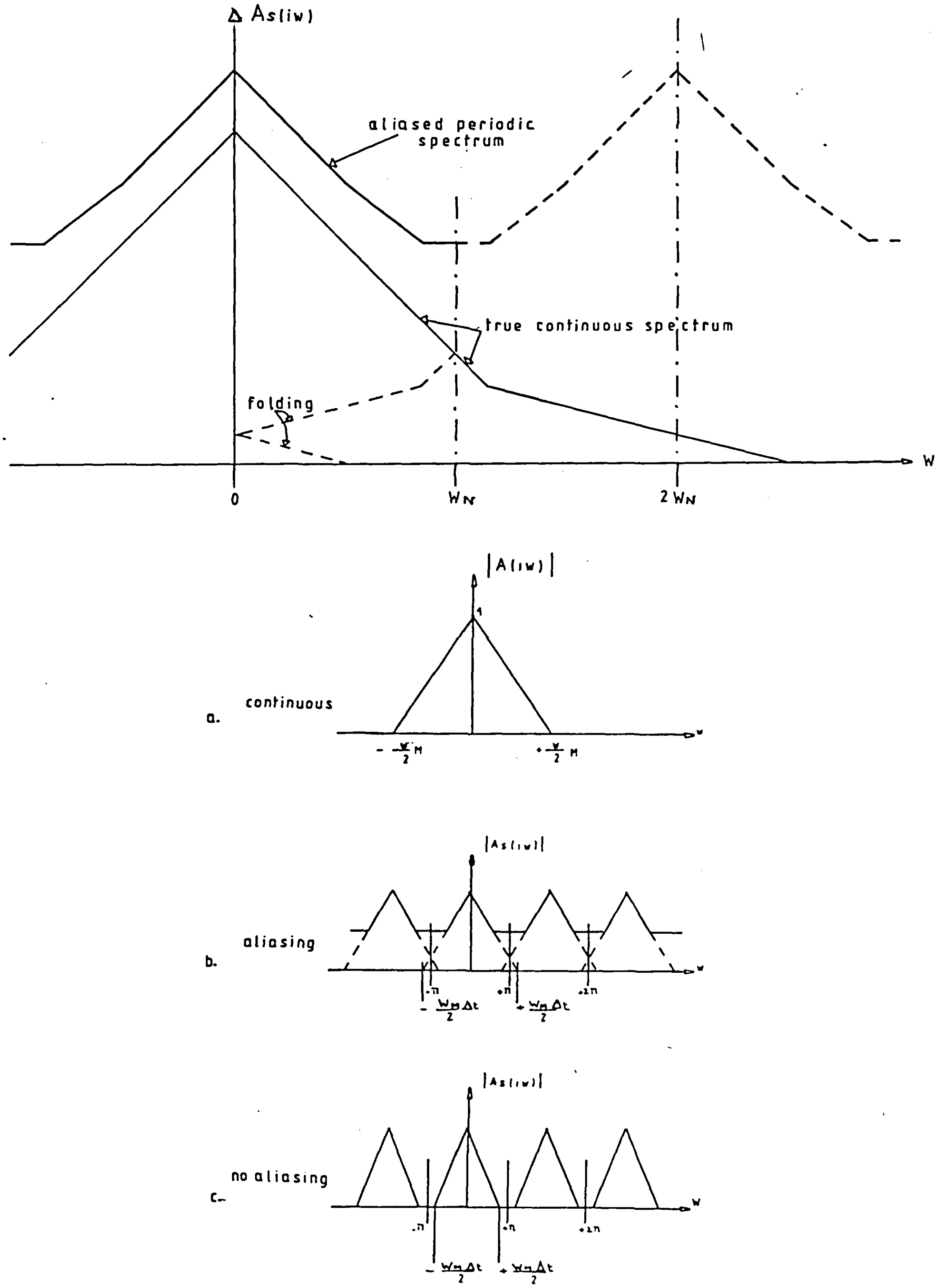

Fig.III.7

Aliasing contamination effect

3.2.4 Spectral leakage

Leakage of spectral amplitudes towards neighbooring frequencies is a particularly significant effect in earthquake Strong Motion studies. It is due to the short length of the analysed signal. It is also known as the *uncertainty principle.* It may be expressed as follows:

Let us call "energy" of an acceleration signal the quantity:

$$\int_{-\infty}^{+\infty} |a(t)|^2 dt = \frac{1}{2\pi} \int_{-\infty}^{+\infty} |A(i\omega)|^2 d\omega \tag{3.15}$$

We define the "*time duration* of $a(t)$ by:

$$D_t^2 = \int_{-\infty}^{+\infty} t^2 |a(t)|^2 dt \tag{3.16}$$

and the *frequency duration* of its Fourier Transform $A(i\omega)$ by:

$$D_\omega^2 = \int_{-\infty}^{+\infty} \omega^2 |A(i\omega)|^2 d\omega \tag{3.17}$$

The *uncertainty principle* states that:

$$D_t D_\omega = \text{constant} \geq \sqrt{\frac{\pi}{2}} \tag{3.18}$$

(The equality holds only for Gaussian functions).

Since the product is finite, this means that a good resolution in frequency, e.i., D_ω small, can only be achieved with large D_t. In other words, if the duration D_t is small, as most acceleration records are, then little accuracy in frequency should be expected; long duration records, with significant "energy", will produce better frequency descriptions.

The *uncertainty principle* presents a theoretical limitation in the search for time dependent frequency analysis of Strong Motion signals. Such analysis would be of value in Engineering since it is well known that the frequency content of earthquake ground motions vary with time. The first P-waves, for example, contain more high frequencies than the following S-waves or any subsequent refracted or reflected waves. In order to perform a time dependent frequency analysis, we would be lead to analyse short lengths of time, successively along the record. The *uncertainty principle*, however, shows that, the frequency resolution would be inversely proportional to the *time duration* of each portion analysed.

This reduction of the accuracy is also accompanied by frequency leakage as is shown in the following equations.

A time dependent signal $a(t)$, non-zero between $t = 0$ and $t = T$, may be viewed as an infinite function $a_\infty(t)$ windowed by the box-car function $w(t)$:

$$a(t) = a_\infty(t) \times w(t) \tag{3.19}$$

where

$$w(t) = \begin{cases} 0 & t \le 0 \\ 1 & 0 \le t \le T \\ 0 & t \ge T \end{cases} \tag{3.20}$$

and its Fourier Transform $A(i\omega)$ is the convolution of $A_\infty(i\omega)$ with $W(i\omega)$ the Fourier Transforms of $a_\infty(t)$ and $w(t)$ respectively.

In *fig. III.8*, we have shown the leakage effect on one particular frequency $\omega_0 = 2\pi f_0$. It is seen that, when the signal has an infinitely long duration D_t, the frequency is picked up by the perfect δ-Dirac pulse $\delta(\omega - \omega_0)$. When D_t is finite due to a record of length T, the Dirac transforms into:

$$|A(i\omega)| = \frac{2\sin(\omega - \omega_0)T}{(\omega - \omega_0)} \tag{3.21}$$

Not only the width of the main lobe has increased, but also sidelobes have appeared. They are responsible for the distorsion of the neighbooring frequencies.

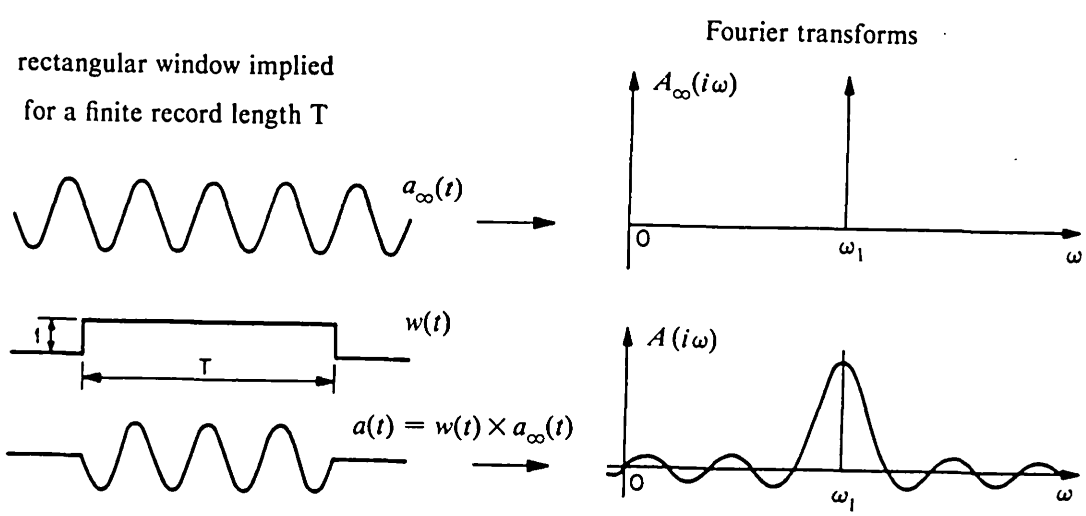

Fig.III.8
Leakage effect

3.2.5 Z-transform representation of a discrete signal

Section 3.2.2 has simply expressed the relationship between continuous and discrete acceleration signals both in time and frequency. As frequency domain will be fully required in the following, it is convienient to make use of the Z-transform, defined here for completion.

The concept of perfect sampling will enable the use of the following digital notation: given an analogue function $a(t)$, its perfect sampled version at constant interval Δt is:

$$a_{\Delta t}(t) = \int_{-\infty}^{+\infty} a(\tau)\delta(t-\tau)\,d\tau \tag{3.22}$$

where $\tau = k\Delta t$, $t = n\Delta t$, and $\delta(t)$ is the Dirac delta function.

$a_{\Delta t}(t)$ is a continuous function, non zero only at $t = \tau$ and whose digital expression is $a(n\Delta t)$ also written $a[n]$ (circular brackets for continuous function and squared brackets for digital function). With this notation, *Eq. 3.22* becomes:

$$a[n] = \sum_{n=-\infty}^{+\infty} [k]\delta[n-k] \tag{3.15}$$

where the interval of time Δt = constant is implicit and assumed to be 1.

$a[k]$ is the amplitude (digitized numerical value) of the sequence $\delta[n-k]$ (with square brackets).

$\delta[n-k]$ is the *Kronecker symbol* defined only for integers as:

$$\delta[n-k] = \begin{cases} 1 & \text{if } n = k \\ 0 & \text{if } n \neq k \end{cases}$$

It can be seen that *Eq. 3.22* represents the complete sequence of digitised points $a[k]$ since the term $a[k]\delta[n-k]$ equals $a[n]$ if $k = n$ and vanishes for $k \neq n$. *Fig. III.9* shows how the sequence $a[n]$ is constructed.

The Z-transform of a sequence of numbers $x[n]$, $n = -\infty, ..., -1, 0, 1... + \infty$, which is, for instance, a sample set (digital) of a continuous function $x(t)$ is the digital equivalent of the Laplace transform of the function $x(t)$ known to be:

$$X(p) = \int_{-\infty}^{+\infty} x(t)e^{-pt}\,dt \tag{3.23}$$

the Z-transform (bi-lateral) of $x[n]$ leads to the complex function:

$$X_s(z) = \sum_{n=-\infty}^{+\infty} x[n]z^{-n} \tag{3.24}$$

where z is a complex variable.

When an acceleration $a[n]$ is causal i.e. when $a[n] = 0$ for $n < 0$ and the signal is zero after its duration $T = N\Delta t$, as in the case of strong motion acceleration records, the sum in *Eq.3.24* becomes unilateral and always converges.

The interest of the Z-transform is multi-fold:

1. It is a series (polynominal in the case of a signal limited to $N + 1$ points like acceleration signal) in z^{-1} whose coefficients are the digitized values of the signal:

$$A_s(z) = a[0] + a[1]z^{-1} + a[2]z^{-2} + a[3]z^{-3} + ... + a[N]z^{-N} \tag{3.25}$$

2. It possesses transform pairs similar to the Laplace transform pairs.
3. It allows the solution of recursive equations through the shifting theorem:

$$a[n-1] \quad \longrightarrow \quad z^{-1}A_s(z) + a[-1] \tag{3.26}$$

4. The Laplace transform or the Fourier transform of a sequence is obtained by giving to z, respectively the values $e^{p\Delta t}$ or $e^{i\omega\Delta t}$.

This last point mentioned is fundamental in the search for the Fourier Spectrum of a ground acceleration signal. The following development will show it in detail. The sequence of digitized points, viewed as a continuous time signal is given by *Eq.3.22*. It has therefore a Laplace transform:

$$A_{\Delta t}(p) = \int_{-\infty}^{+\infty} a(t)e^{-pt}\,dt \tag{3.27}$$

and with $t = n\Delta t$, ($n = 0, 1, ..., N$ we get:

$$A_{\Delta t}(p) = \Delta t \sum_{n=0}^{N} a(n\Delta t)e^{-pn\Delta t} \tag{3.28}$$

The Z-transform of the sequence $a[n]$ is given by *Eq.3.24*:

$$A_s(z) = \sum_{n=0}^{N} a[n]z^{-n} \tag{3.29}$$

The examination of *Eq 3.28c* and *Eq.3.29* leads to the conclusion that:

$$A_{\Delta t}(p) = \Delta t\, A_s(e^{p\Delta t}) \tag{3.30a}$$

$$= \Delta t\, A_s(z)\,\big|_{z=e^{p\Delta t}} \tag{3.30b}$$

and in particular, on the frequency axis:

$$A_{\Delta t}(i\omega) = \Delta t\, A_s(z)\ \Big|_{z=e^{i\omega\Delta t}} \tag{3.31}$$

The mapping from the p-plane onto the Z-plane is defined by:

$$z = e^{p\Delta t}$$

It characterises the link between the Laplace transform of a sampled signal and its Z-transform.

The periodic character of $A_{\Delta t}(i\omega)$ is again observed through the periodicity of $e^{i\omega\Delta t}$, and we also notice the presence of the proportionality factor is $F_s = 1/\Delta t$. The Z-transform provides an easy way to compute the frequency function of a digital signal or filter. It will be extensively used in Chapter V for the design of the digital elliptic filter.

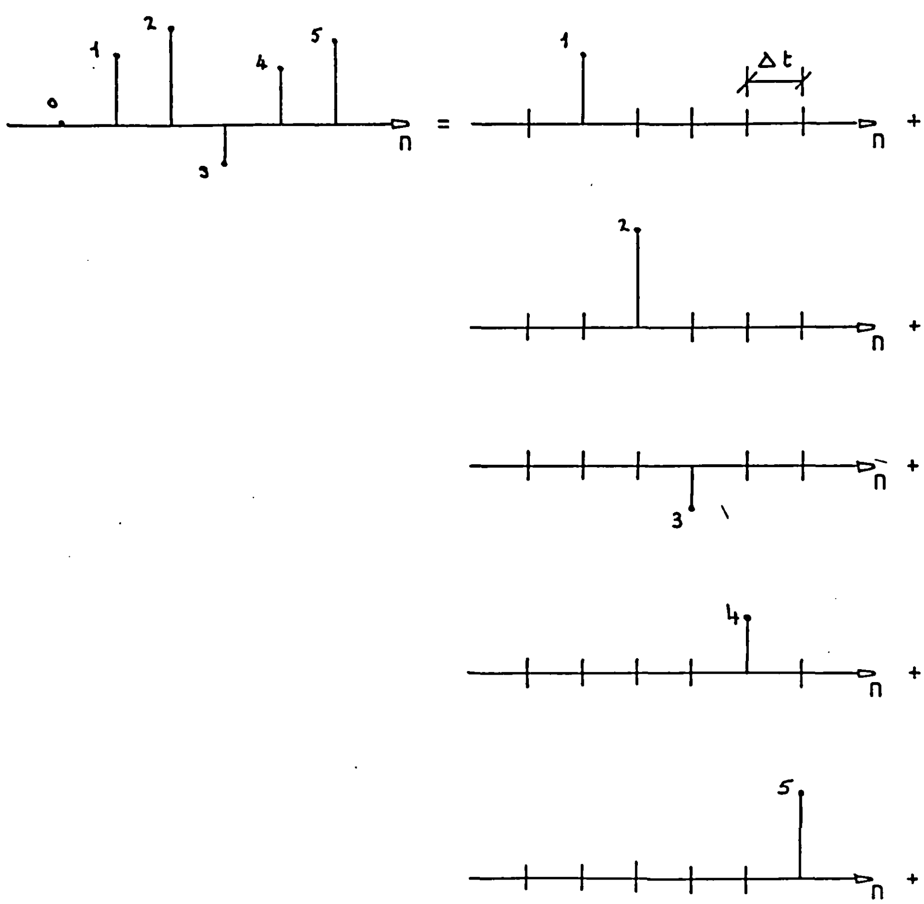

fig.III.9

Construction of a digital sequence

3.3 DIGITIZATION ANALYSIS

3.3.1 Background of the problem

Surprisingly digitization analysis has never been performed thoroughly. Several investigators have been working on this subject for the last 15 years, but they have not analysed the expected spread of errors introduced during the digitization stage by the various processing centres.

The only study involving accurate experiments was achieved by *Trifunac et al. (1973)* and their results have served as a basis for the understanding of the effect of digitization on accel2ration signals. Later, *Arias and Sandoval (1979)* used their data to investigate further, analytically. They concluded that the confidence of the digitized records in the medium and high frequencies was much lower than what one has been normally expecting.

In this section, we shall examine the digitization errors making use of our specially designed earthquake-like signal (described in Chapter II). It has been digitized, exactly as a real record, by various operators in Europe, and using different digitization equipments. A comparison between the obtained versions with the target will be presented here with particular emphasis on the spread of the results.

3.3.2 Digitization equipments

Digitization equipment is a complex piece of hardware whose control device is an analogue to digital (A/D) converter. It is often associated with several computer codes necessary to handle and arrange the data. *Fig. III.10* shows schematically a complete digitization complex. Some of these elements are sometimes suppressed from the chain.

Before describing the digitization equipments used in the study, it is worthwhile to define the terms that are used since confusion sometimes occurs.

The fundamental characteristic of the Analogue-to-Digital converter is its resolution. Resolution (RES) is the distance in mm that the cursor has to move to jump one less significant digit to the next. Resolution capacities depend, in practice, on the distance units used and are expressed in either SI or Imperial system. When SI units are used, a $RES = 0.1mm$ is commonly encountered. When Imperial units are used the less significant digit may represent a $RES = 0.01inch$ or a $RES = 0.001inch$. It can be seen that this enables equipment to jump progressivley from 0.01 inch, to 0.1mm, 0.001 inch and 0.01mm, thus avoiding the too high "order of magnitude jump".

If ENL is photographic enlargement of the film and SEN and SPE respectively the sensitivity of the recording instrument expressed in mm/g and the recording speed expressed in mm/sec, The Global Enlargement is defined by $GE = SEN*ENL$ in acceleration and $GE = SPE*ENL$ in time.

Table IV gives the full characteristics of the equipments used by comparison with the well known ones

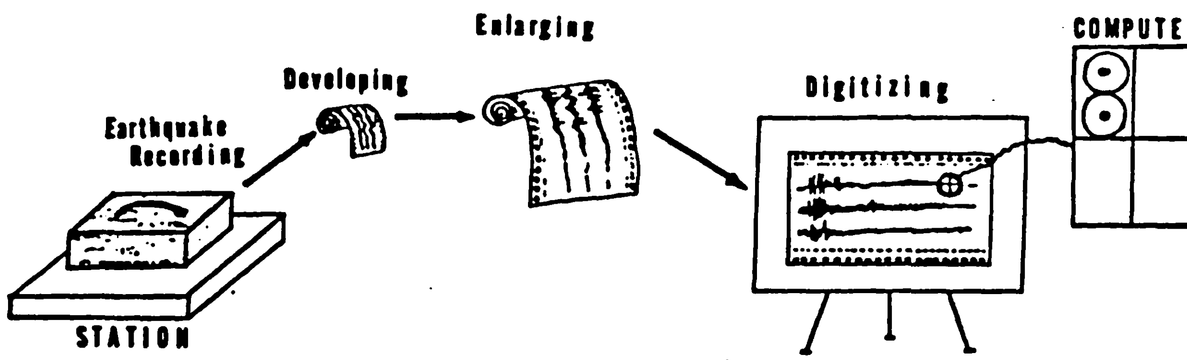

Preliminary Phases to Obtain the Uncorrected Accelerogram

Fig.III.10

A digitazation complex

used in California.

Finally, the Digitization Error (DE) involves a new factor. Errors are usually introduced during the positionnig of the points to digitize, in particular in the case of semi-automatic digitization, where the human operator decides which points are to be measured. They are due to several causes like variable thickness of the trace or operator tiredness and have a significant effect on the final product. Misjudgements or lack of concentration may also result in errors, sometimes far more desruptive than the hardwave inperfections. In the case of automatic digitization, the human eye is replaced by a photocell (*fig. III. 11*) and hence is more reliable. The same concept may however be applied, if one considers that automatic machine decisions, on the level of grey which falls into white (no trace) or black (trace present), generates some uncertainties. Also it is not certain, as is commonly assumed, whether the wished point to digitize lies in the centre of the trace.

In both cases the digitization "mistakes", associated with the limited Digitization Accuracy produce at each point an offset between the aimed value and its digitized representation. This ensemble of offsets constitutes a stochastic process, which follows some, so far badly known, probability distribution. *Trifunac et al.* believe that such noise is Gaussian and normally distributed in the time space (*Fig. III. 12*), but *Basili* showed a significant departure from this finding. In *section 3.4*, we shall propose a power density distribution in the frequency space, depending on two variables: the acceleration frequency ω and the record length T.

Table IV

Range of the digitization equipment used

		$\Delta a(10^{-2}g)$			$\Delta t(sec)$			
Semi − automatic	*RES (mm)*	$ENL = 1$ $SEN = 10$	$GB = 80$	$ENL = 4$ $SEN = 80$	$ENL = 1$ $SPE = 10$	$GB = 40$	$ENL = 4$ $SPE = 20$	
D.Mac(Italy, UK)	0.1	1.0	0.125	0.050	0.010	0.0025	0.00125	DIG2 3
Altek(France)	0.020	0.2	0.025	0.006	0.002	0.0005	0.00025	DIG4
Lehner(Calif.)	0.032	0.32	0.040	0.010	0.0032	0.0008	0.00040	
Automatic	*RES (mm)*	$ENL = 1$ $SEN = 10$	$GB = 20$	$ENL = 1$ $SEN = 80$	$ENL = 1$ $SPE = 10$	$GB = 10$	$ENL = 1$ $SPE = 20$	
Contraves(Italy)	0.0248	0.25	0.124	0.031	0.00248	0.00248	0.00124	DIG1
P.1000(Calif.)	0.0500	0.50	0.250	0.063	0.0050	0.0050	0.0025	

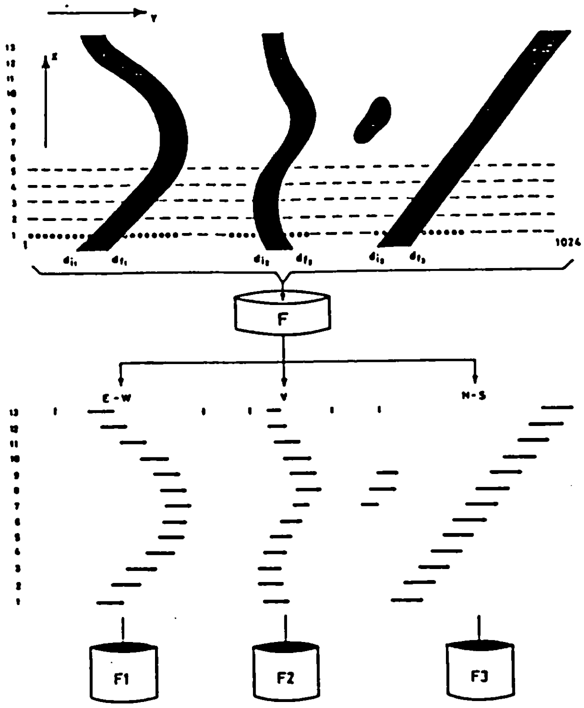

a) Photocell locations

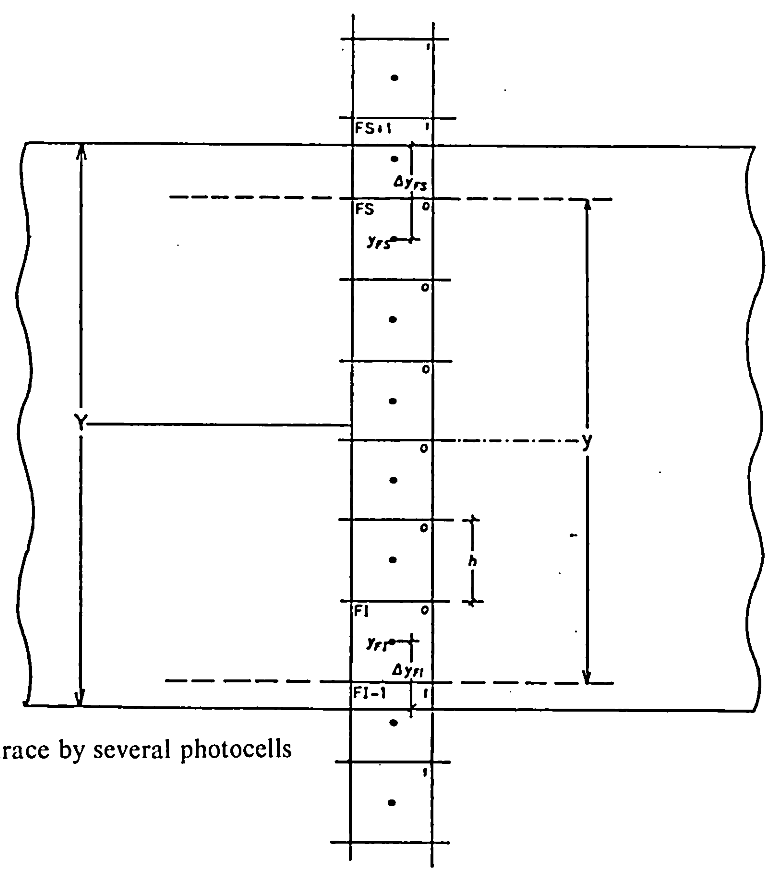

b) Coverage of the trace by several photocells

Fig.III.11

Automatic digitazation

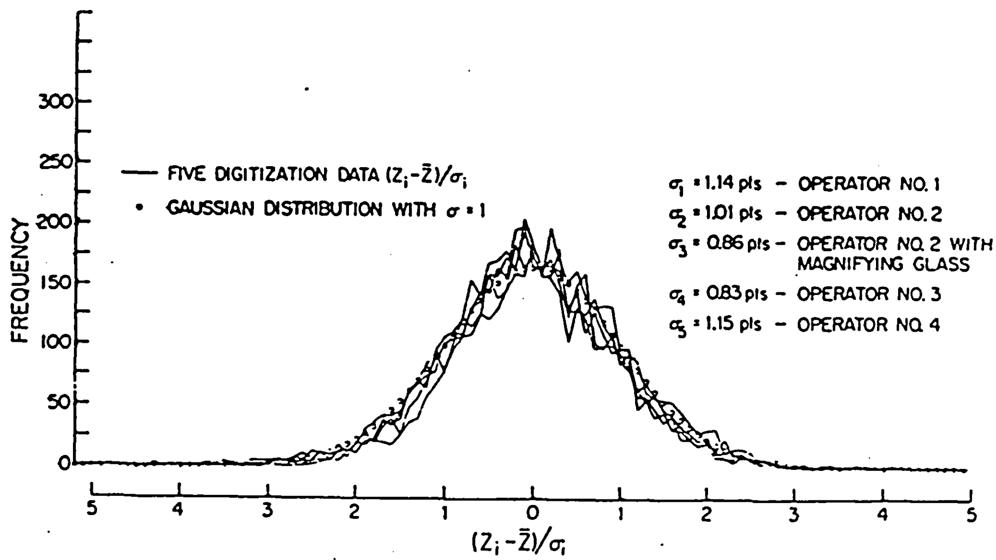

a) Gaussian distribution (after Trifunac et al. 1971)

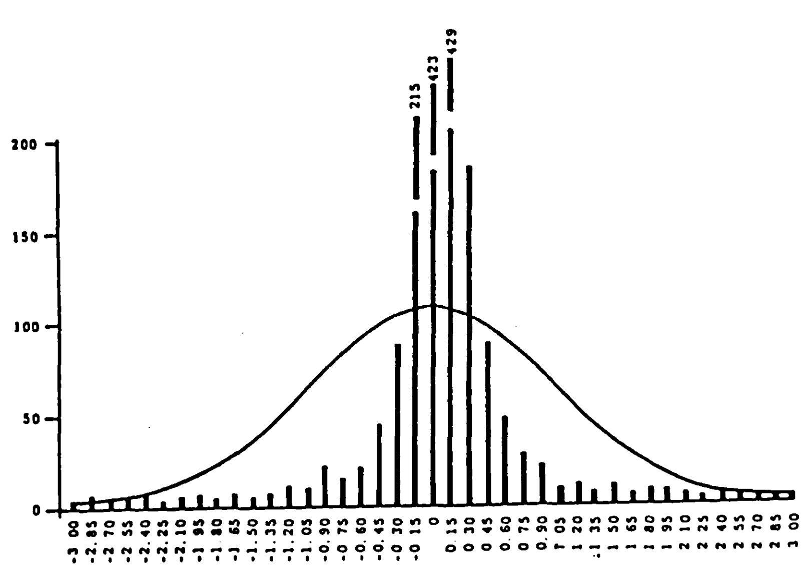

b) Non Gaussian distribution (after Basili and Mariano 1982)

Fig.III.12

Digitization noise distribution

3.3.3 Digitization comparisons

Although the original earthquake-like signal is known analytically, the comparison between the digitized versions and the original presents some difficulties for the following reasons:

1) a digitized version is known from a set of points arbitrarily chosen by the operator and these points cannot be easily associated with the corresponding points of the target. This is particularly true for semi-automatic digitization since each operator decides on the location of the points to digitize.

2) In any analogue trace of acceleration signal, the base line is unknown , so it is for our designed signal (*fig.III.13*). It is usually assumed to be a straight line, determined from compatibility conditions on velocity (see $KK = 0$ in chapter IV). This straight line is not unique and clearly depends on the particular choice of the digitized points as shown by *Soha-Jabean (1980)* by using the jack-knife technique on the point set.

The following data analysis have been performed:

For each digitized version (DIG1 to DIG4, see table IV), a "true time series" was generated from the analytic signal at the same time points as the version studied. A first comparison was carried out by plotting the analytic against the measured accelerations. *Fig. III.14a* shows such a graph. A cross-correlation function (*fig.III.14b*) enabled to determined a time shift (peak of the function) representing the overall translation between the two signals. After correction, the same graph has been replotted. An improvement in the fitting is clearly visible and allows for a better assessment of the pure effect of digitization, including hardware imperfections and operator intervention. In the case of real records, however, this time shift is not accessible and plot a) should be retained. The various values of the fitting are presented in table VI. It may be observed that semi-automatic digitizations with low resolution equipment (DIG2, DIG3) are far less reliable than the other two. It is also interesting to note the good result of DIG4, (high resolution equipment) by comparison with DIG1 (automatic equipment).

The comparison in frequency is presented in the form of zero damping acceleration response spectra. *Fig.III.15a* shows the picture on the raw data where a simple signal mean value has been subtracted. *Fig.III.15b* shows the case where the conventional technique to get "uncorrected" records has been performed. No significant differences between all the versions occur in the middle frequency range, between 0.3Hz and 5Hz. A systematic loss of amplitude reaching an order of magnitude is observed on both sets of curves in the high frequencies. Again, DIG2 and DIG3 are the most affected (*fig.III.16*).

In the low frequency range, departure from the target starts between 0.3 to 0.4 Hz depending on the digitization. An increase in signal energy is visible, indicating a strong low frequency digitization noise in this band. The plots of *fig.III.16a and b* show the variation on the zero damping pseudo-velocity response spectra. An average digitization noise value of 5cm/sec may be observed for DIG2 and DIG3, whereas a very good fit with a variation of the order of 0.5cm/sec is obtained for DIG1 and DIG4.

These observations quantify the immense benefit of improved digitization, both in the high frequency and in the low frequency ranges. Conventional equipments, with low resolution and/or little global enlargements are seen to be unacceptable below 0.3/0.4 Hz Modern semi-automatic digitizers with enlargement and automatic digitizers with no enlargements are comparable, and increase drastically the reliability in this range. It must be said, however, that the trace used was more uniform than real traces. In this latter case, the DIG4 results will certainly not exhibit as good performance.

As an overall comparison, table VI shows the RMS of the various versions and their relative differences with the target. Variations increase with the less accurate equipments up to 8.2 %. Also in this table, are the base line coefficients A and B. They vary immensely from one digitization to the other, confirming the previously mentioned work of *Soha-Jabean*, and emphasizing the influence of the choice of digitized points to define the base line. It is therefore not surprising, as will be seen in next chapter, that velocity and displacement time histories always remain far from the true function, whatever the efforts put in the correction types.

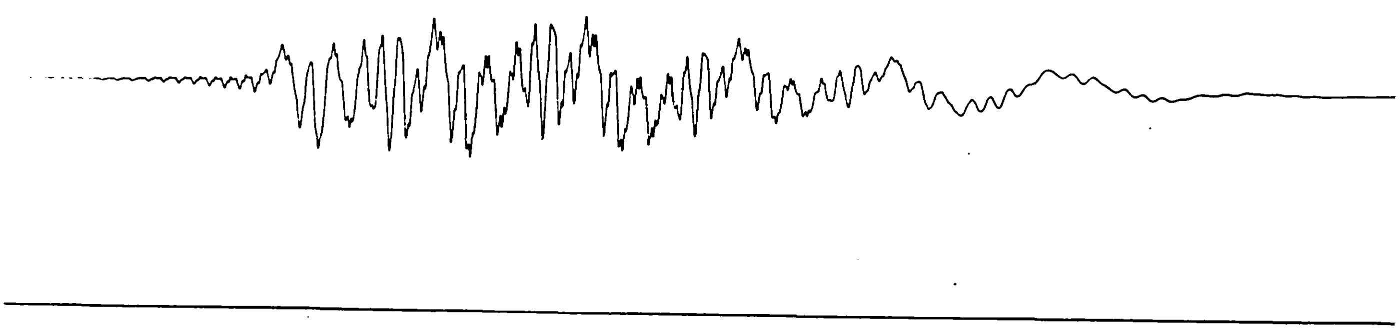

Fig.III.13
Copy of the Earthquake-like signal
with its fixed trace

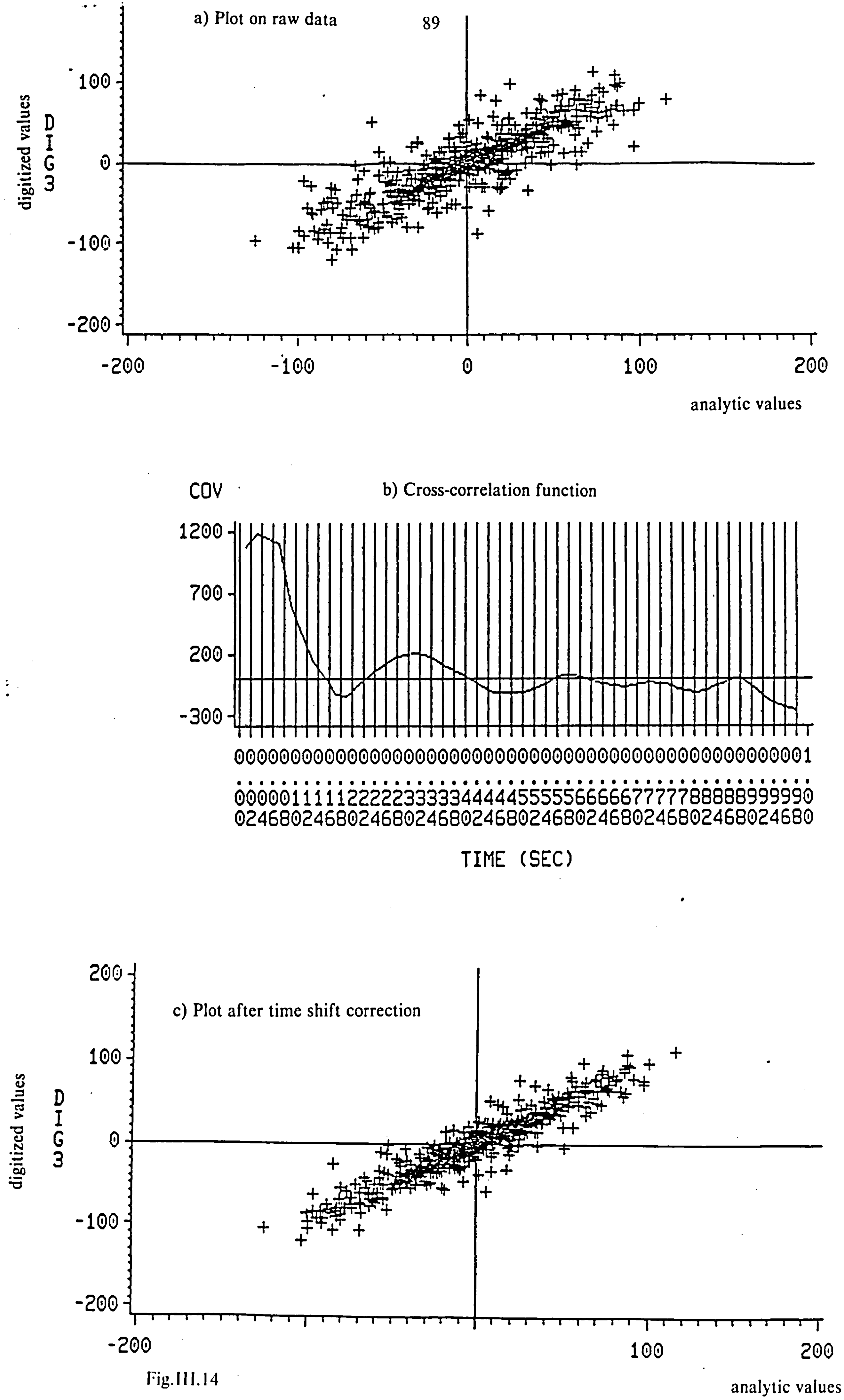

Fig.III.14

Correlation between a digitized signal and its true analytic values

Table V

Comparison between analytic and digitized values
for the various digitizations,
before and after time shift correction.

Digitized signal	Correlation coefficient		Straight line coefficients				Shift (sec) (3)
			Intercept		Slope		
	Before shift(1)	After shift(2)	Before shift	After shift	Before shift	After shift	
DIG1	0.960	0.976	−0.029	−0.030	0.986	0.994	−0.005
DIG2	0.839	0.933	−0.751	−0.759	0.898	0.947	0.030
DIG3	0.744	0.896	−0.235	−0.190	0.866	0.951	0.030
DIG4	0.945	0.976	−0.143	−0.145	0.966	0.979	0.005

Table VI

Valuesof the straight line adjustment parameters
yielding an uncorrected digitized version,
and RMS of the signals.

Signal S1

	A	B	RMS	%
$ORIG$	0.6	−0.06	30.19	
$DIG1$	−0.77	0.09	30.22	+0.1
$DIG2$	−1.98	−0.35	27.7	−8.2
$DIG3$	3.58	−0.40	29.5	−2.3
$DIG4$	−0.72	0.07	29.9	−1.0

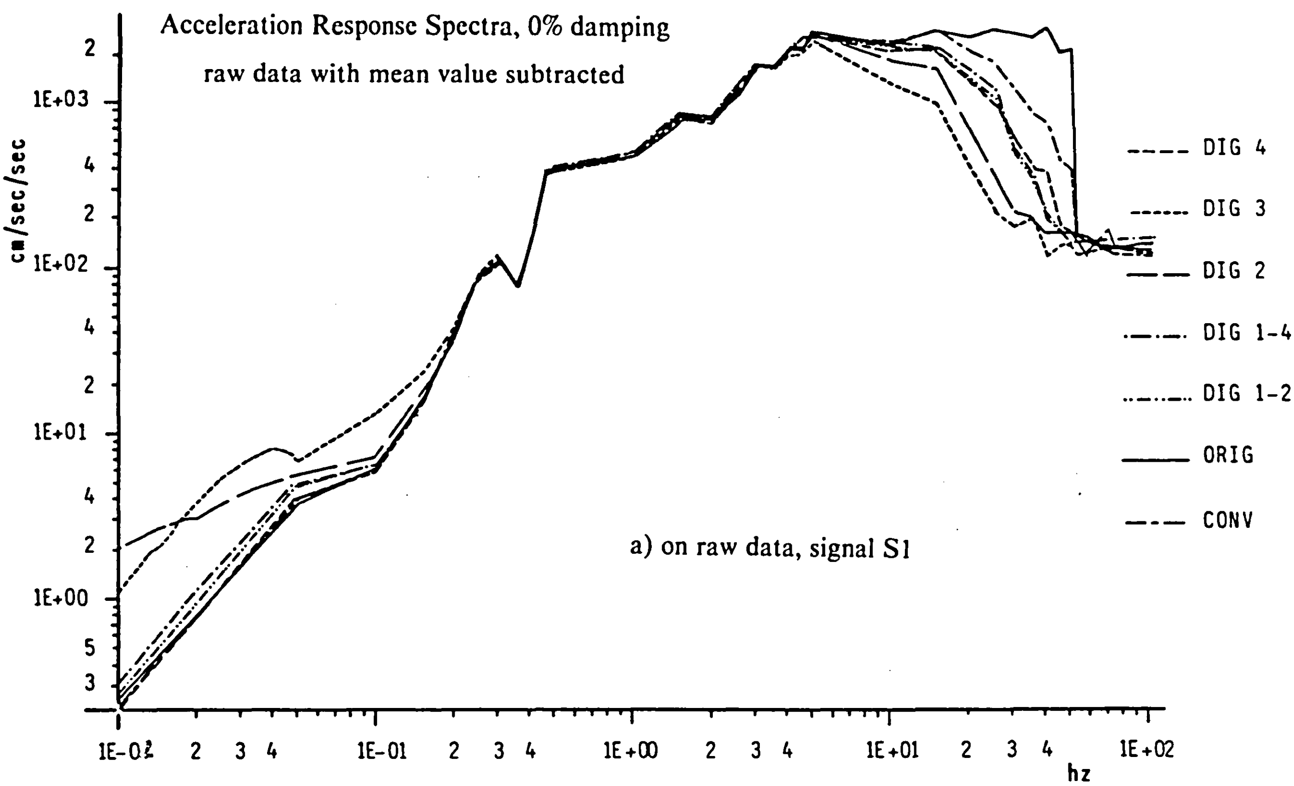

Fig.III.15a

Comparison of various digitizations of the designed signal
Acceleration spectra

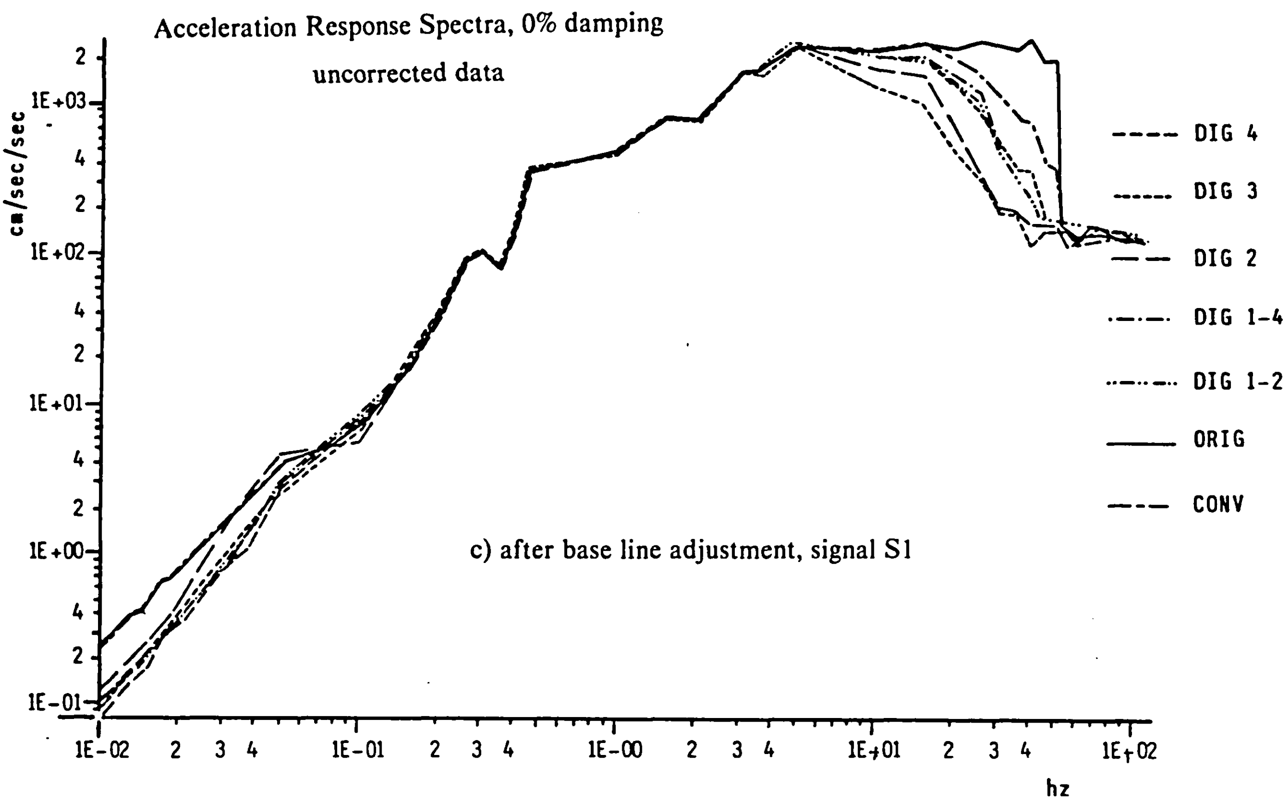

Fig.III.15b

Comparison of various digitizations of the designed signal acceleration spectra

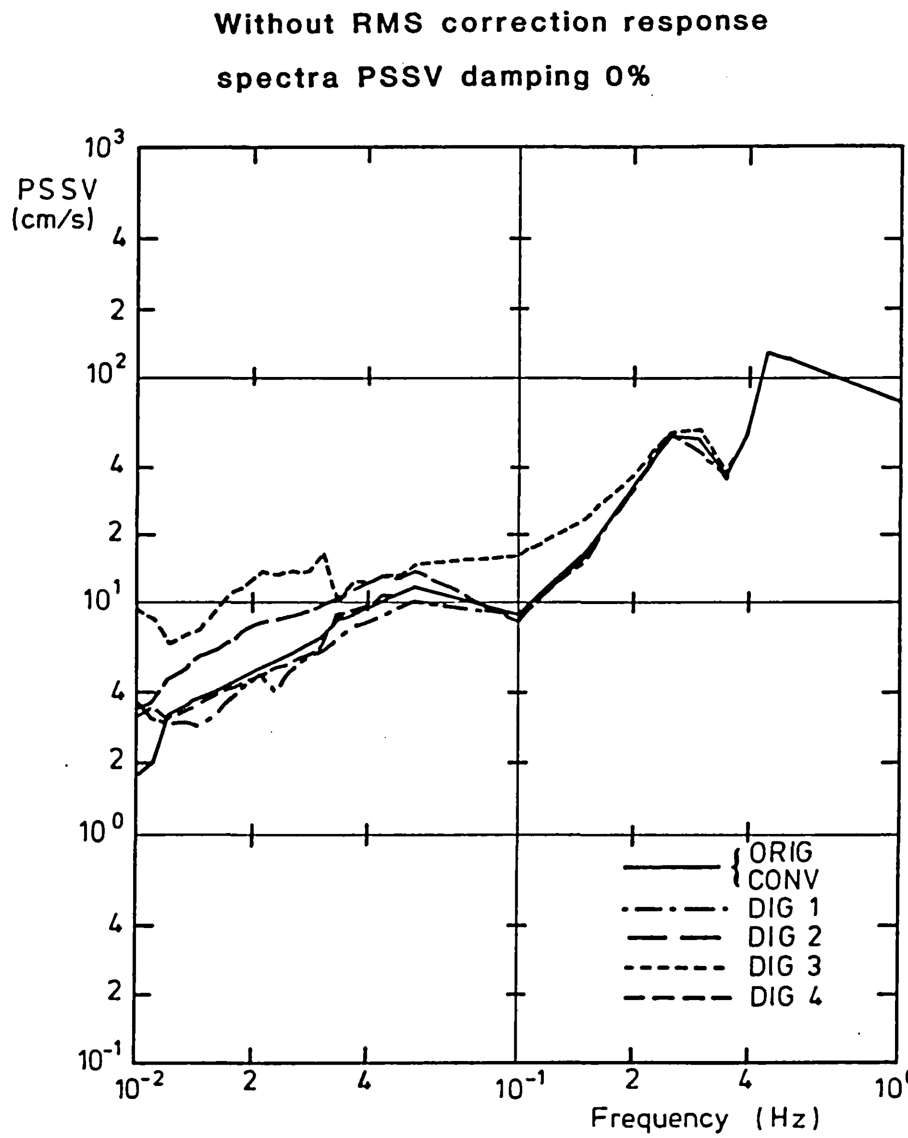

Fig.III.16a

Comparison of various digitizations of the designed signal

Pseudo-velocity spectra

on raw data

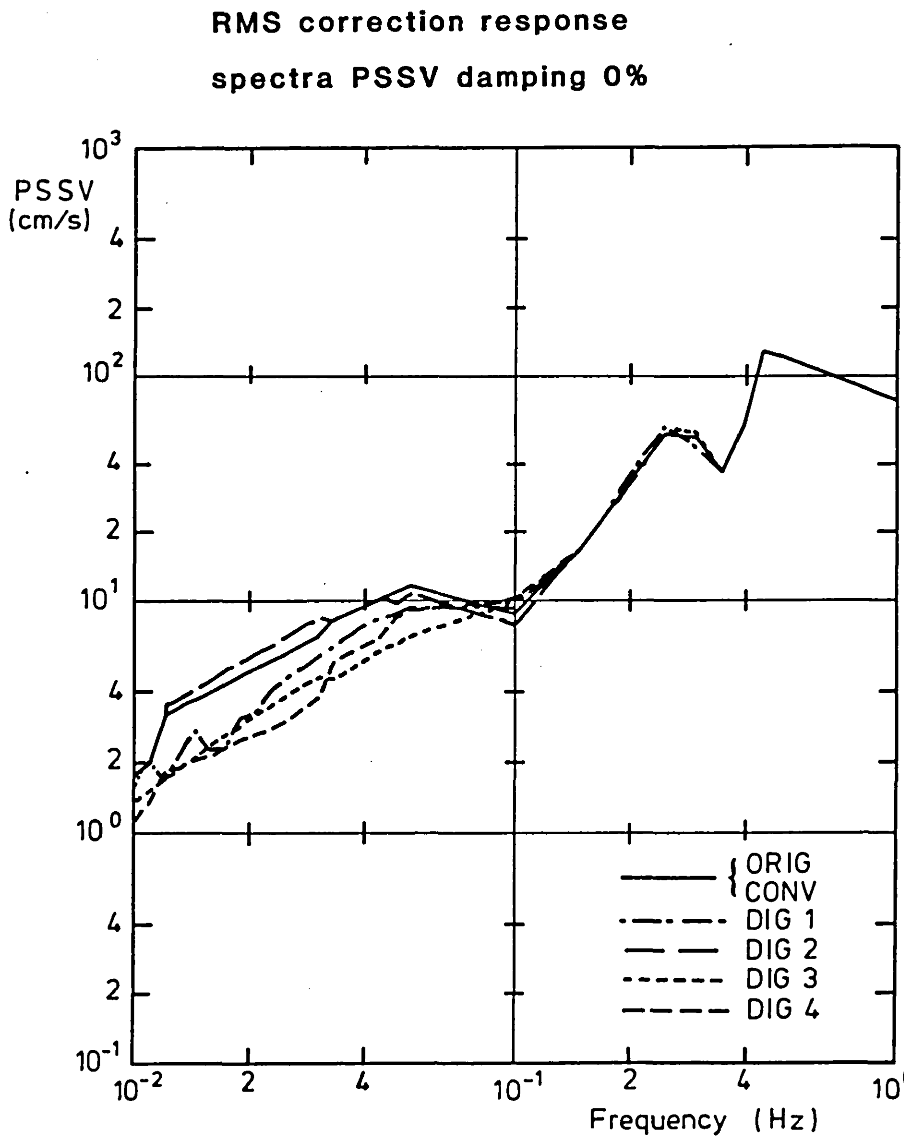

Fig.III.16b

Comparison of various digitizations of the designed signal

Pseudo-velocity spectra

after base line adjustment

Acceleration Response Spectra, 0% damping

raw data with mean value subtracted

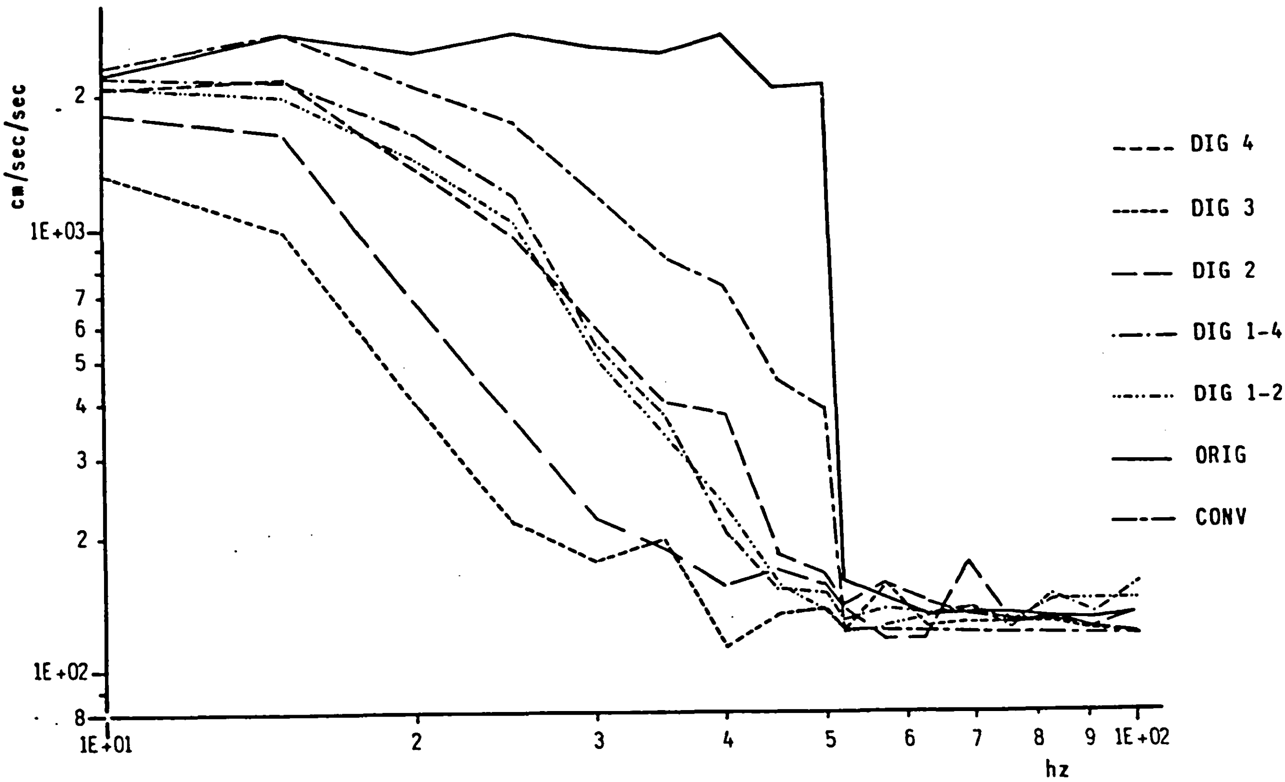

Fig.III.16c

Comparison of various digitizations of the designed signal

Detail of the high frequency range in acceleration spectra

3.4 DIGITIZATION NOISE MODEL

3.4.1 Data description and model

The analysis of the digitization noise is now presented. The work was based on an ensemble of "zero acceleration" time histories obtained by digitization of fixed traces. These digitizations constituted part of the more complete work performed for the "*Investigation of Strong Motion Processing Procedures*" involving many European Data centers, and Universities.

The fixed traces were digitized using the same assumptions as those imposed on the synthetic signal (*Menu, April 1985*). In particular the sensitivity was assumed to be 80 mm/g and the recording speed 10 mm/sec. The processing centers have chosen their own enlargement. The available global enlargements GE ranged from 8 to 26 cm/g. In addition, "zero-acceleration" time histories of 15, 20, 30 and 40 sec duration were digitized on the *D-Mac* table at Imperial College. A total of 54 "zero acceleration" time histories $n_i(t)$ were studied. (4 of 15 sec, 34 of 20 sec, 8 of 30 sec, and 8 of 40 sec).

All the functions were interpolated to a constant $\Delta t = 0.01$ sec and their Fourier spectrum systematically computed. Some of the Amplitude Fourier spectra are shown on *fig. III. 17a,b and c* using a log-log graph. After smoothing in frequency, we classified the data in the following categories:

Category I:

semi-automatic equipment
small enlargement
little operator experience

Category II:

semi-automatic equipment
big enlargement
little operator experience

Category III:

semi-automatic equipment
big enlargement
good operator experience

Category IV:

automatic equipment
no enlargement.

The main group of data consisting of 20 sec long time histories was first observed. Simplified shapes of the various smoothed curves are drawn on *fig. III. 18* where the various enlargement are indicated. These Fourier Amplitude Spectra were modeled according to the expression (for $T_0 = 20$ sec):

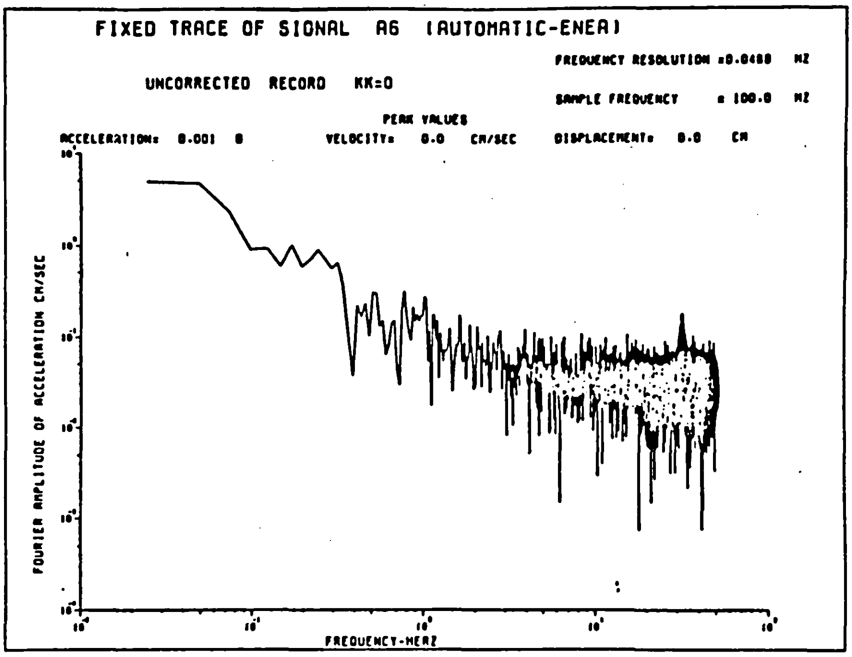

Fig.III.17a

Example of FAS of digitization noise

semi-automatic $GB = 240$

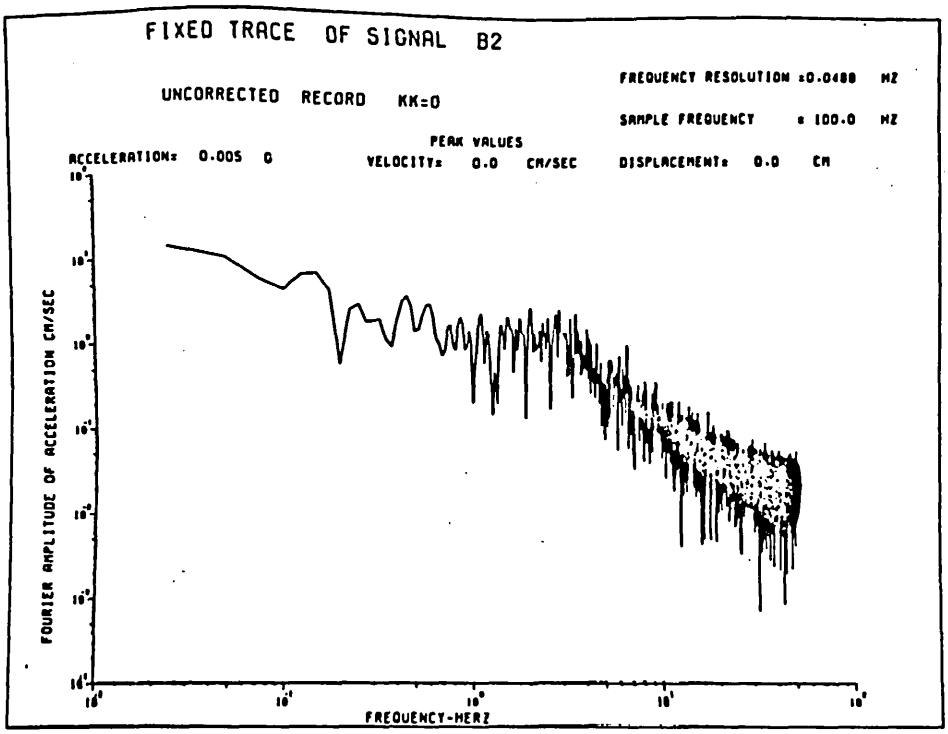

Fig.III.17b

Example of FAS of digitization noise

semi-automatic $GB = 160$

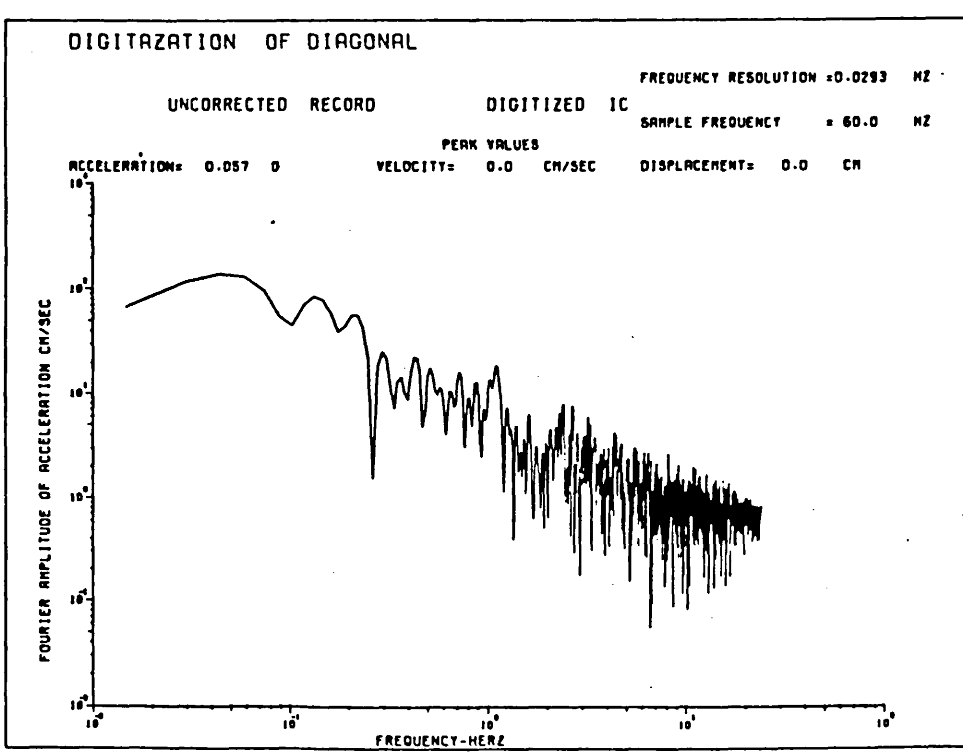

Fig.III.17c

Example of FAS of digitization noise

automatic $GB = 80$

$$N(\omega, T_0) = \frac{A_N(T_0)}{\omega^b} \tag{3.32}$$

where $A_N(T)$ reflects the variation of the noise level with other factors than frequency, and b is the parameter describing the frequency dependence as a negative power of the circular frequency ω. The values of $A_N(T_0)$ and b have been computed from the fitting of the data set to this model. Both values were found to be function of the digitizing equipment used as well as the operator experience. The global enlargement played a predominant role as multiplication factor for the function $A_N(T)$. Proposed values for b and N_1, the noise amplitude at $1Hz$ (directly equivalent to $A_N(T_0)$), are given in table VII.

In a second part of the analysis, the influence of the signal duration was investigated. Since the bulk of the data was constituted from 20 sec long time histories, an attempt to detect variation of the RMS of the noise as time elapses from 0 to 20 sec was performed. No pattern of statistical significance has been found. However, when the averages of 15 sec, 20 sec, 30 sec and 40 sec duration data were introduced, a slight increase of the noise power has been noted (noise energy increases as a power of T greater than one).

The duration dependence was assumed to be described by:

$$A_N(T) = (2\pi)^2 \left(\frac{T}{T_0}\right)^\alpha N_1 \tag{3.33}$$

where N_1 is the overall quality factor mentioned above and function of the global enlargement, the digitizer accuracy and the operator quality.

No similar data were available for the case of automatic digitization. We used results from a study by *Lee et al. (1982)* obtained on the *P. 1000 Photoscanner* of the USC. The "Zero acceleration" functions ranged from 15 sec to 90 sec. and the data used (*fig. III. 19*) are tabulated in table XII.

The final expression for the Fourier Amplitude of digitization is:

$$N(\omega, T) = \frac{a \quad T^\alpha}{\omega^b} \tag{3.34a}$$

where

$$a = (2\pi)^b \quad N_1 \quad T_0^{-\alpha} \tag{3.35.b}$$

This proposed noise model expressed by *Eq. 3.5* can be of great importance in any subsequent processing of digitized analogue acceleration signal. Only the three parameters a, b and α are needed and may be readily obtained from the knowledge of the digitizer characteristics and an assessment of the operator experience. A series of tests consisting of straigth line digitizations would yield the required information. If no tests have been carried out, Table VII may serve as a guideline for the coefficients assessment.

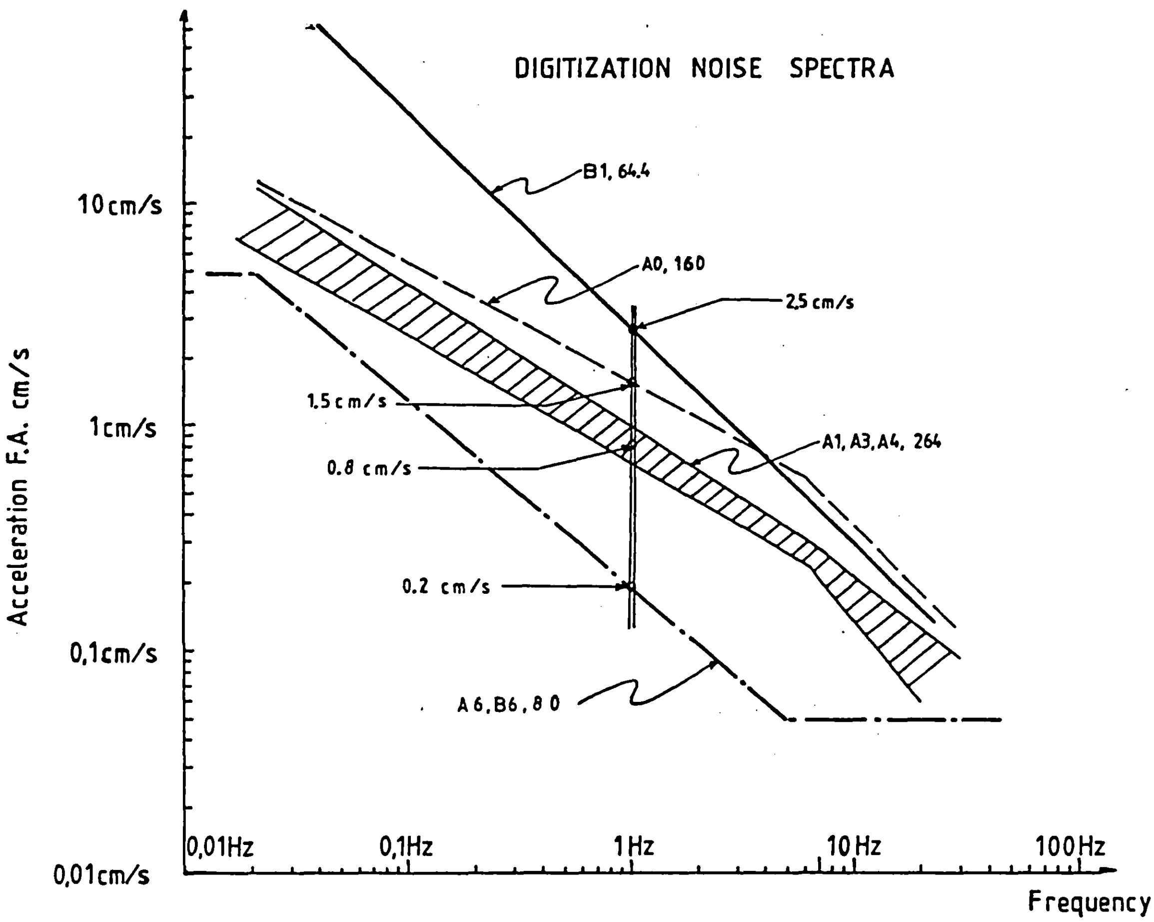

Fig.III.18a

Digitization Noise Spectra:

simplified shapes for T0=20 sec.

Semi-automatic and automatic equipments were used;

the global enlargements varied from 8 to 26.4 cm/g.;

the vertical line at 1Hz shows the N1 values.

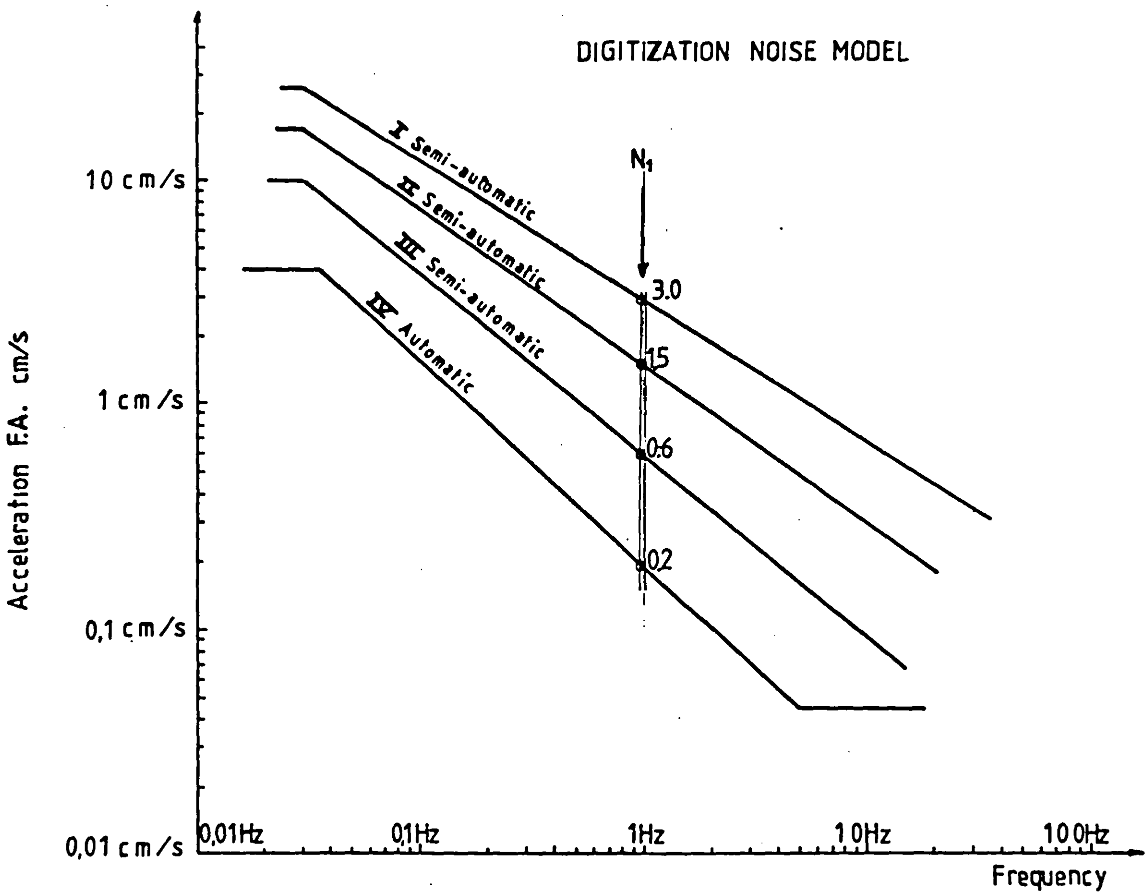

Fig.III.18b

b- noise model for a duration $T_0 = 20sec$; the curves represent the functions for the 4 categories defined in the text; Values of N_1 are the digitization quality reference points.

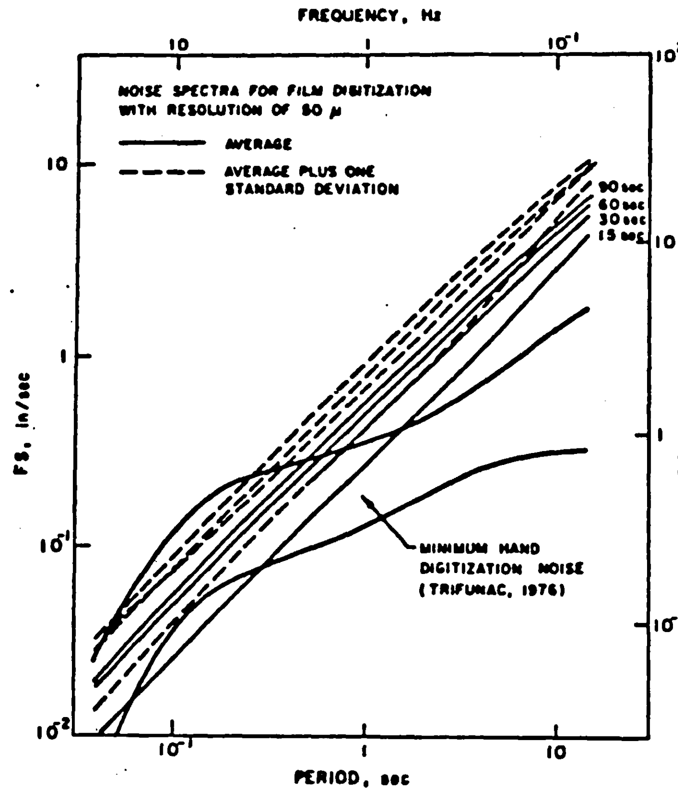

Fig.III.19

Fourier Amplitude Spectra of noise in digitization of a 70*mm* film. Spectra are shown for duration of noise of 15, 30, 60 and 90*sec*. *(after Lee et al. 1982)*

The values of N_1 ($T_0 = 20$ sec) can be evaluated from:

$$N_1(cgs) = 600\frac{IND*RES}{GE} \tag{3.36}$$

where

RES = resolution of the digitizer in mm

GE = Global enlargement in mm/g

IND = Operator quality index

The latter coefficient may be chosen from 1 (automatic equipment) to 10 (first time operator). Values varying from $IND = 4$ to 9 were observed amongst a group of students at Imperial College. A typical value for an experienced operator is $IND = 2.5$. In table VII, an example of such combinations has been given to define the four categories envisaged in this study.

Table VII

Digitization Noise Model Parameters.

Categ.	RES	IND	GE	$A_N(T_0)$	b	N_1	a	α
I	0.1	6	120	9.04	0.6	3.0	1.50	0.6
II	0.1	6	240	5.43	0.7	1.5	1.21	0.5
III	0.1	2.4	240	2.61	0.8	0.6	0.79	0.4
IV	0.02	1	80	1.05	0.9	0.2	0.43	0.3

3.4.2 Root Mean Square of noise and its influence

In this section, we shall show the effect of digitization noise as modelled by *Eq. 3.35a and b* on ground motion representations. Values of the noise variance in terms of acceleration, velocity and displacement will be readily computed. An assessment of the expected noise level induced in Response Spectra will also be obtained.

We shall consider, for our purpose that it is sufficient to define the average random power of the digitized noise as (duration T finite):

$$G_N(\omega) = \frac{1}{T} \left(\int_0^{+\infty} n(t) \ e^{-i\omega t} \ dt \right)^2 \tag{3.37a}$$

$$= \frac{1}{T} \ |N(\omega, T)|^2 \tag{3.37b}$$

Although the stochastic process is time dependent, we shall treat each subset of duration T as stationary with constant variance function of T. The following results refer to the stationary limits of the various cases envisaged. As such they constitute upper bounds of the actual variances.

The noise power spectral density, once it has passed through a linear time invariant system, is given by:

$$G_X(\omega) = G_N(\omega) \ \ |H_X(\omega)|^2 \tag{3.38}$$

where X categorizes the particular system, fully defined by its transfer function $H_X(\omega)$. The Root Mean Square of the output noise is then:

$$(RMS)_X = \left(\int_{-\infty}^{+\infty} G_X(\omega) \ \ d\omega \right)^{1/2} \tag{3.39a}$$

Noting that we are dealing with real functions of time of limited extent T, a practical calculation of this integral may be obtained as follows. The limits of integration will be limited to $\omega_L = 2\pi/T$ in the low frequency range and to $\omega_H = \pi/\Delta t$ (Nyquist Frequency) in the high frequency range. This is acceptable when the signal is free from noise energy above this limit. It has been observed however, that the integration up to $+\infty$. does not affect substancially the results, and

$$(RMS)_X = \left(2 \int_{2\pi/T}^{+\infty} G_X(\omega) \ \ d\omega \right)^{1/2} \tag{3.39b}$$

has been used.

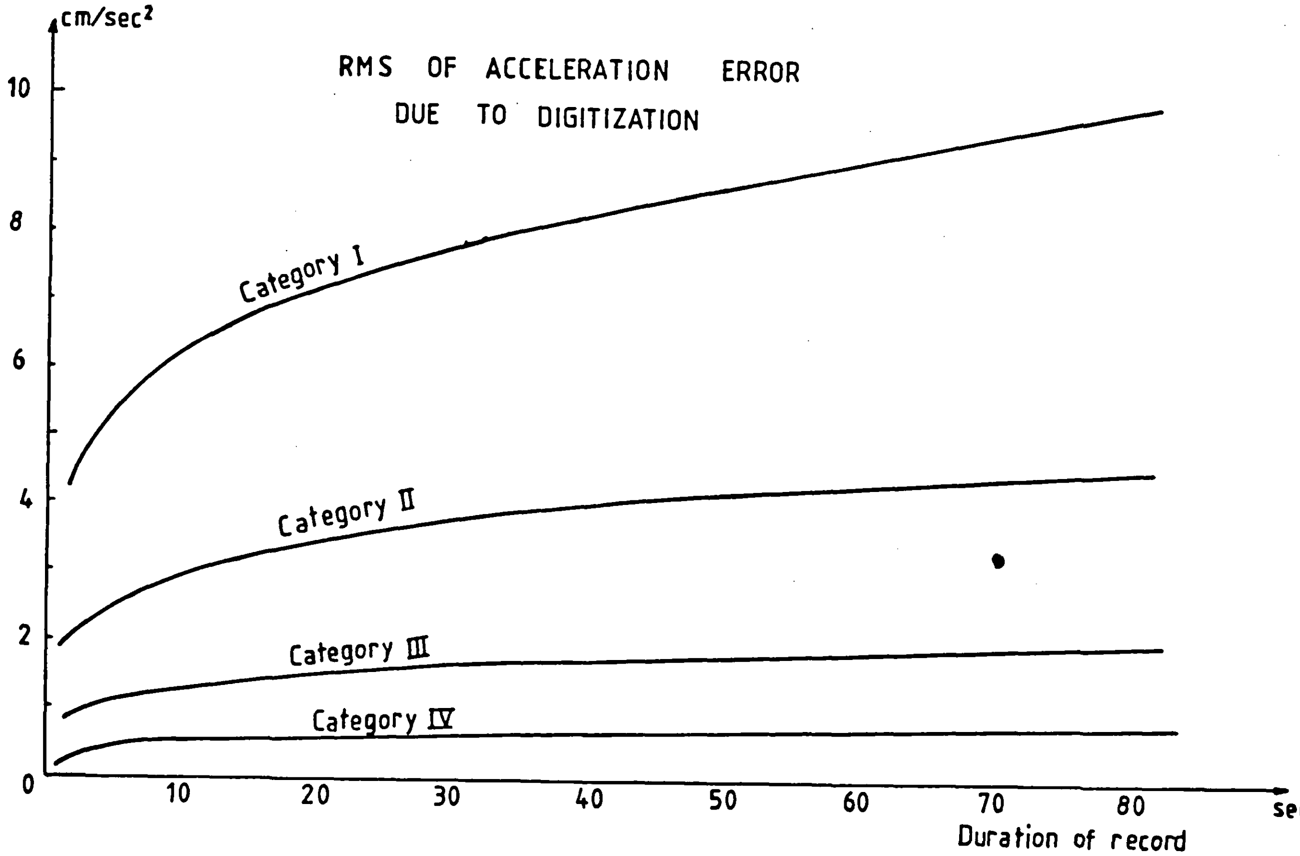

Fig.III.20a

Root Mean Square of digitization noise for the 4 categories defined in the text

a- effect of noise on acceleration

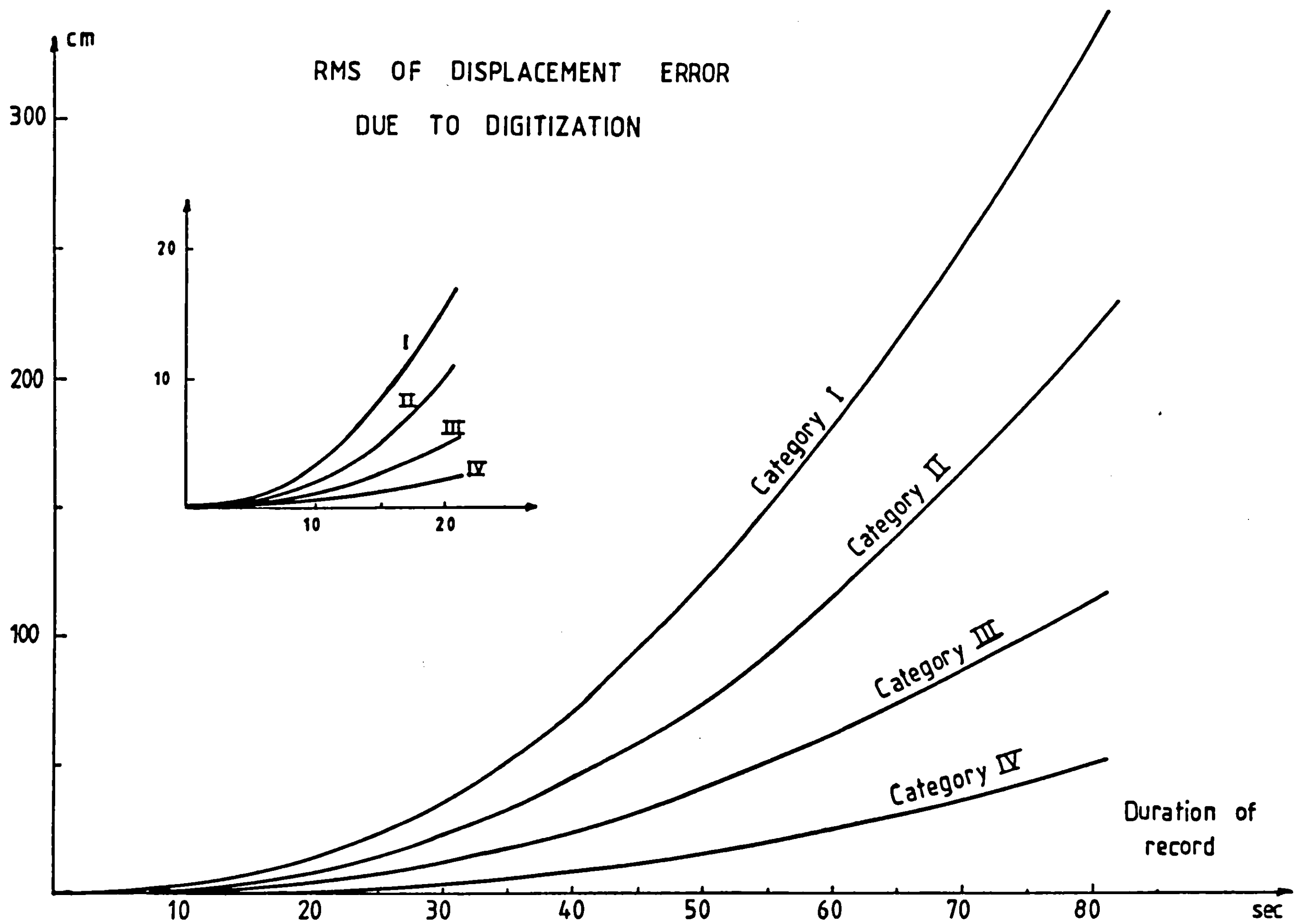

Fig.III.20b

Mean square of digitization noise

b- effect of noise on displacement

RMS of noise in time history representation

Velocity and displacement time histories may be seen as the outputs of linear time invariant systems when the acceleration functions are input. The moduli of their transfer function are $1/\omega$ and $1/\omega^2$ respectively.

The RMS of the noise are then obtained from *Eq. 3.37b/3.38/3.39b/* in which:

$$|H_X(\omega)| = |H_A(\omega)| = 1 \quad \text{for acceleration} \tag{3.40a}$$

$$|H_X(\omega)| = |H_V(\omega)| = \frac{1}{\omega} \quad \text{for velocity} \tag{3.40b}$$

$$|H_X(\omega)| = |H_D(\omega)| = \frac{1}{\omega^2} \quad \text{for displacement} \tag{3.40c}$$

Graphical representations of these RMS are shown an *Fig. III. 20a and b* for acceleration and displacement as a function of the record duration T. A crude approximation for the 95% interval of confidence for the true motion can be taken as twice these values.

RMS of noise in response spectra representation

A similar approach can be followed for the Response Spectra case. The linear time invariant systems involved here, are the simple harmonic oscillators of natural circular frequency ω_0 and percentage of critical damping λ. The amplitude of their transfer functions are:

$$|H_X(\omega)| = |H_{SA}(\omega)| = \frac{\omega^2}{\sqrt{(\omega_0^2-\omega^2)^2 + 4\lambda^2\omega^2\omega_0^2}} \quad \text{for acceleration} \tag{3.41a}$$

$$|H_{\dot X}(\omega)| = |H_{SV}(\omega)| = \frac{\omega}{\sqrt{(\omega_0^2-\omega^2)^2 + 4\lambda^2\omega^2\omega_0^2}} \quad \text{for velocity} \tag{3.41b}$$

$$|H_X(\omega)| = |H_{SD}(\omega)| = \frac{1}{\sqrt{(\omega_0^2-\omega^2)^2 + 4\lambda^2\omega^2\omega_0^2}} \quad \text{for displacement} \tag{3.41c}$$

Examples of such influence on the spectra are shown on *Fig. III. 21. a,b,c and d* when the dynamic characteristics of the oscillators, ω_0 and λ vary and for different values of the signal duration. Similarly to the previous case, it is reasonable to assess the 95% confidence interval for the Response spectra as twice the computed values.

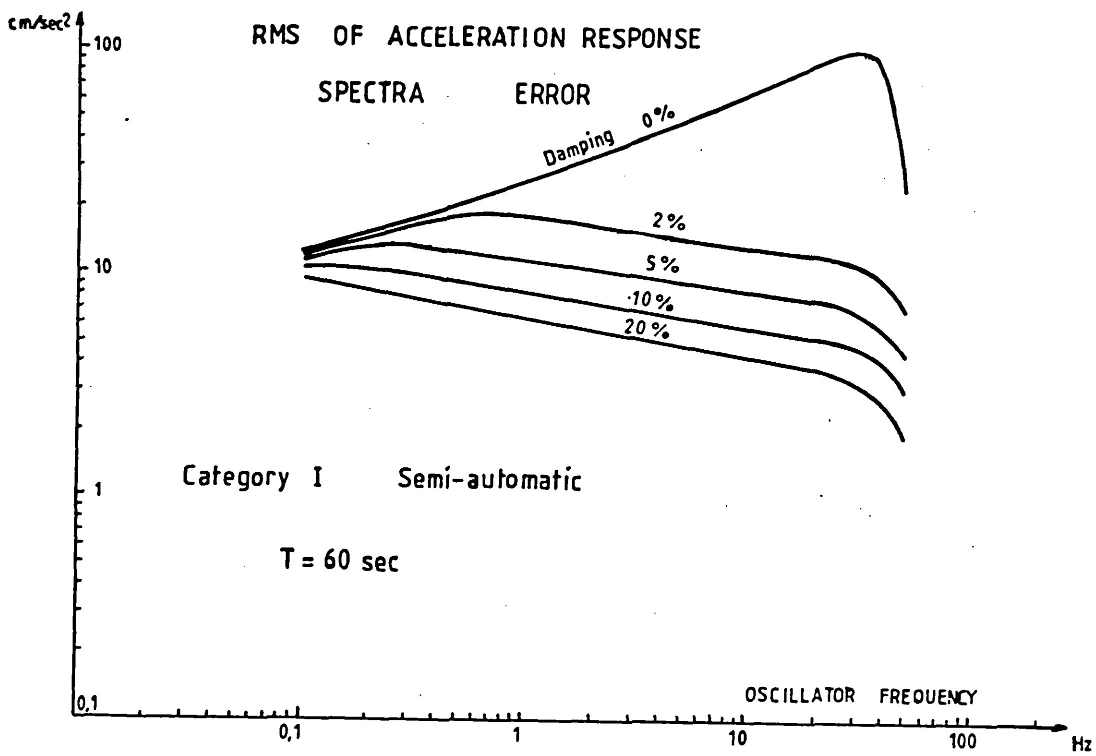

Fig.III.21a

Root Mean Square of digitization noise as output of a single harmonic oscillator.

a- effect of semi-automatic digitization noise (category I) on Acceleration response spectra (duration $T = 60sec$)

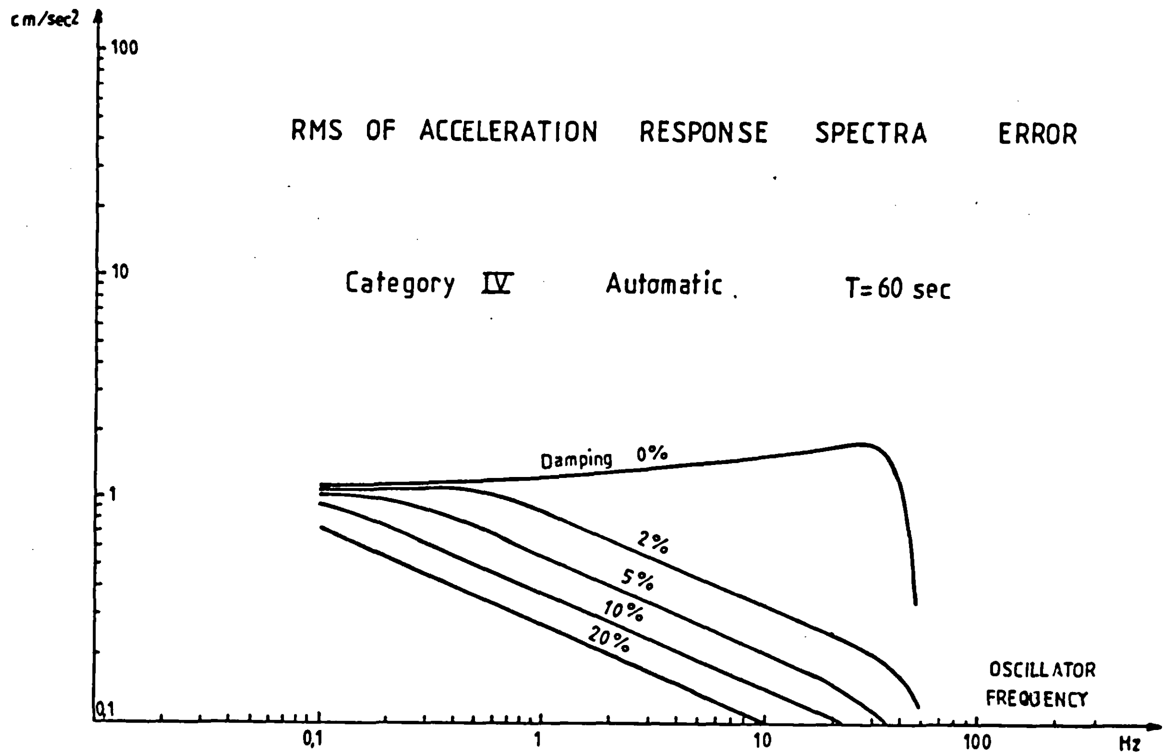

Fig.III.21b

b- effect of automatic digitization noise (category IV) on Acceleration response spectra (duration $T = 60sec$)

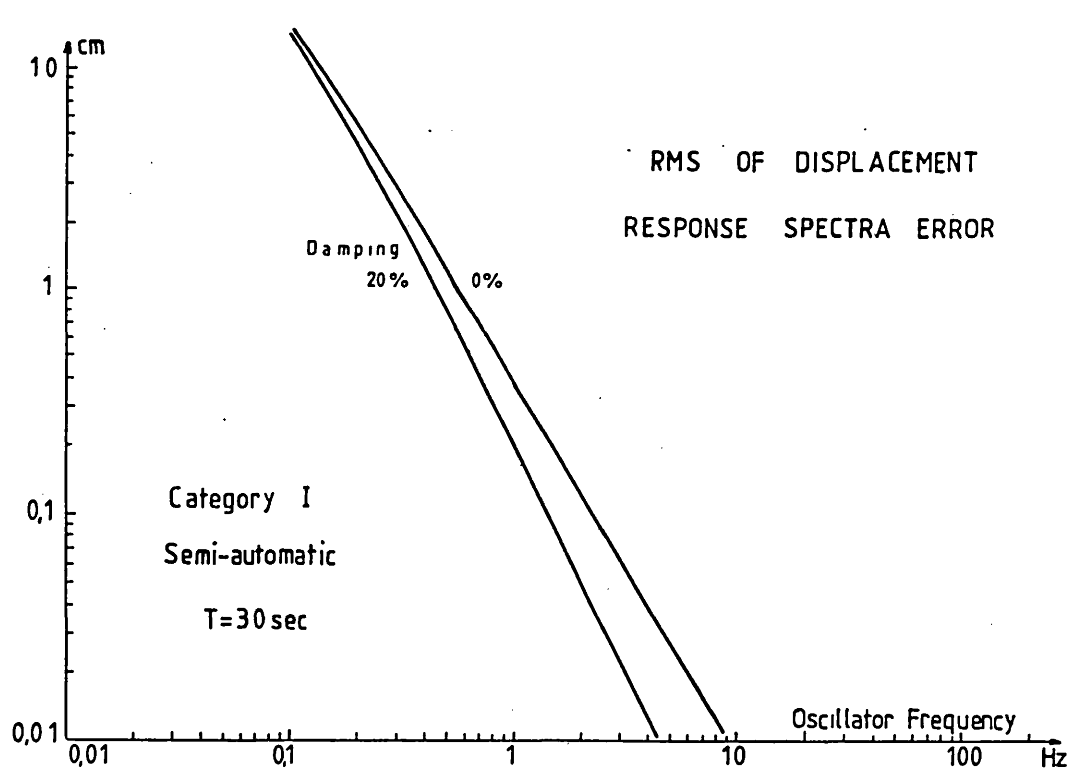

Fig.III.21c

c- effect of semi-automatic digitization noise (category I) on Displacement response spectra (duration $T = 30sec$)

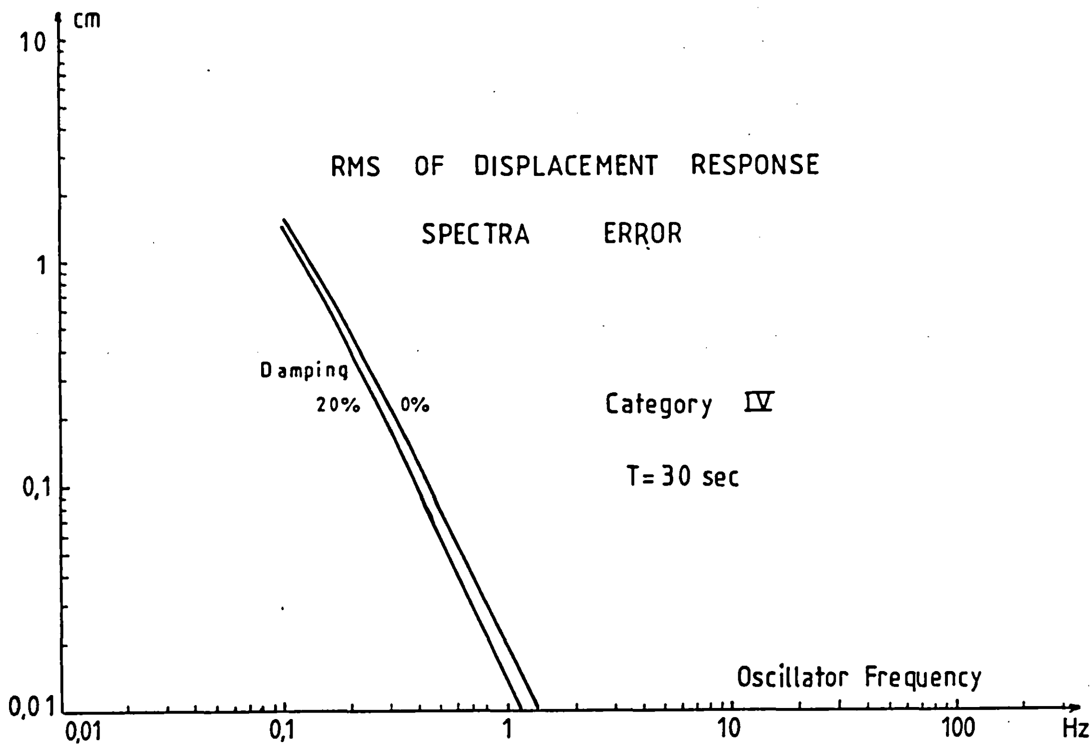

Fig.III.21d
d- effect of automatic digitization noise (category IV) on Displacement response spectra (duration $T = 30sec$)

3.4.3 Selection of the record frequency limits

Current procedures to correct for noise and distortion which contaminate the uncorrected version of the acceleration signal consists of filtering out both ends of the Fourier Amplitude Spectrum (FAS). This is indeed at the extremities that the signal-to-noise ratio decreases. The true ground motion beyond these frequencies is masked by the noise and that renders the signal unreliable. Since the expected FAS gross level depends of Magnitude and distance, it is clearly seen that, for a given digitization, the reliable frequency range will vary with these two parameters (*fig. III. 22*). In some cases, in particular for small Magnitude shocks or/and at large distance from the source, the spectrum may lie entirely below the predicted noise spectrum and no signal can be realistically recovered.

We shall consider that the low and high frequency limits within which the recovered acceleration is worth analysing are determined by the intersection of the expected FAS with the noise spectrum multiplied by a predetermined "safety factor". In the following the value of 2 will be used. The retained frequency range then complies with a signal-to-noise ratio of at least 2.

In practice, a simple examination of the FAS of the uncorrected records yields a fair indication for the choice of ω_L and ω_H. It is often visible that the shape of the spectrum departs from the theoretical one and shows the areas where the noise energy prevails over the signal energy *fig. III. 23.*

However, as the noise spectrum level reduces, in particular with automatic digitizers, the picture looses its power and an analysis becomes more helpfull. The knowledge of the source corner frequency ω_c, calculated from far field methods, and of the maximum frequency as defined by *Hanks (1982)* are of great value in such a computation.

A complete FAS model for ground motion acceleration is also required. We shall make use of the *Boore's model (1983)* developed from preliminary observations by *Hanks and McGuire (1979)* in the high frequency of Strong Motion Spectra.

BOORE'S model for ground motion FAS

This model is based on seismological models and is applied to the near field. A simple far field spectrum constitutes the basis of the expression in the frequency domain. Supplementary terms are introduced to represent attenuation and high frequency decay. The FAS of acceleration is expressed by:

$$A(\omega) = \frac{C M_0 S(\omega, \omega_c) P(\omega, \omega_m) e^{-\omega R/2Q\beta}}{R} \tag{3.42}$$

where C is a constant depending on the source-station relative geometry as well as the crust velocity model. An average value for C has been taken here as:

$$C = \frac{0.89}{4\pi\rho\beta^3} \tag{3.43}$$

M_0 is the seismic moment of the shock

β is the average shear wave velocity

The fault slip function is approximated in frequency by:

$$S(\omega, \omega_c) = \frac{\omega^2}{1 + \left(\frac{\omega}{\omega_c}\right)^k} \tag{3.44}$$

and follows the Brune's model for motion restricted to shear waves. The $\omega - square$ far field decay suggested by *Aki (1967)* is chosen by making $k = 2$. It can be easily modify up to $k = 3$ if one believes that the slip rise time, seen from the near field, is shorter than the conventional value.

The wave energy decay term is:

$$\frac{1}{R} e^{-\omega R/2Q\beta} \tag{3.45}$$

where the denominator accounts for the geometrical spreading of spherical type and the numerator is the term usually seen in far field seismology, to simulate the anelastic material absorption.

Q is the quality factor which may reach values as low as 100 in the near field, typically an order of magnitude smaller than in the far field.

This term has been found to represent inadequately the high frequency energy decay near the source and a Butterworth cutoff was added:

$$P(\omega, \omega_m) = \frac{1}{\sqrt{1 + \left(\frac{\omega}{\omega_m}\right)^{2s}}} \tag{3.46}$$

where s shapes the decay rate at high frequency. It was assigned the value $s = 4$ to comply with actual FAS of acceleration observations (*Hanks and McGuire*).

In this model, ω_m is not assumed to be a function of the earthquake size, so that the spectrum $A(\omega)$ is basically controlled by the two parameters ω_c and M_0. We know that they may be related through the equation:

$$\omega_c = 3.1\ 10^7 \quad \beta\left(\frac{\Delta\sigma}{M_0}\right)^{1/3} \tag{3.47}$$

$\Delta\sigma$ is the fault stress drop in bars

Furthermore, surface wave Magnitude is certainly a more accessible earthquake size description than the seismic moment. An empirical relationship proposed by *Udias (1971)* has been used here:

$$M_S = 0.79 \log M_0 - 13.84 \tag{3.48}$$

The two independant input data for the model become:

1- the surface wave Magnitude Ms which controls the low frequency level of the spectrum.

2- the stress drop $\Delta\sigma$ which controls the width of the acceleration frequency content.

For the subsequent computation, we fixed the following parameters which are not essential for the conclusions:

$\Delta\sigma = 40 bars$

$\beta = 3.2 km/sec$

$\rho = 2.7 g/cm3$

$F_{max} = 10 Hz$

$Q = 250$

The results obtained in the next section will then reflect the influence of the major variables in the choice for a reliable frequency range for ground motion records in the near field:

Magnitude M_S and distance R.

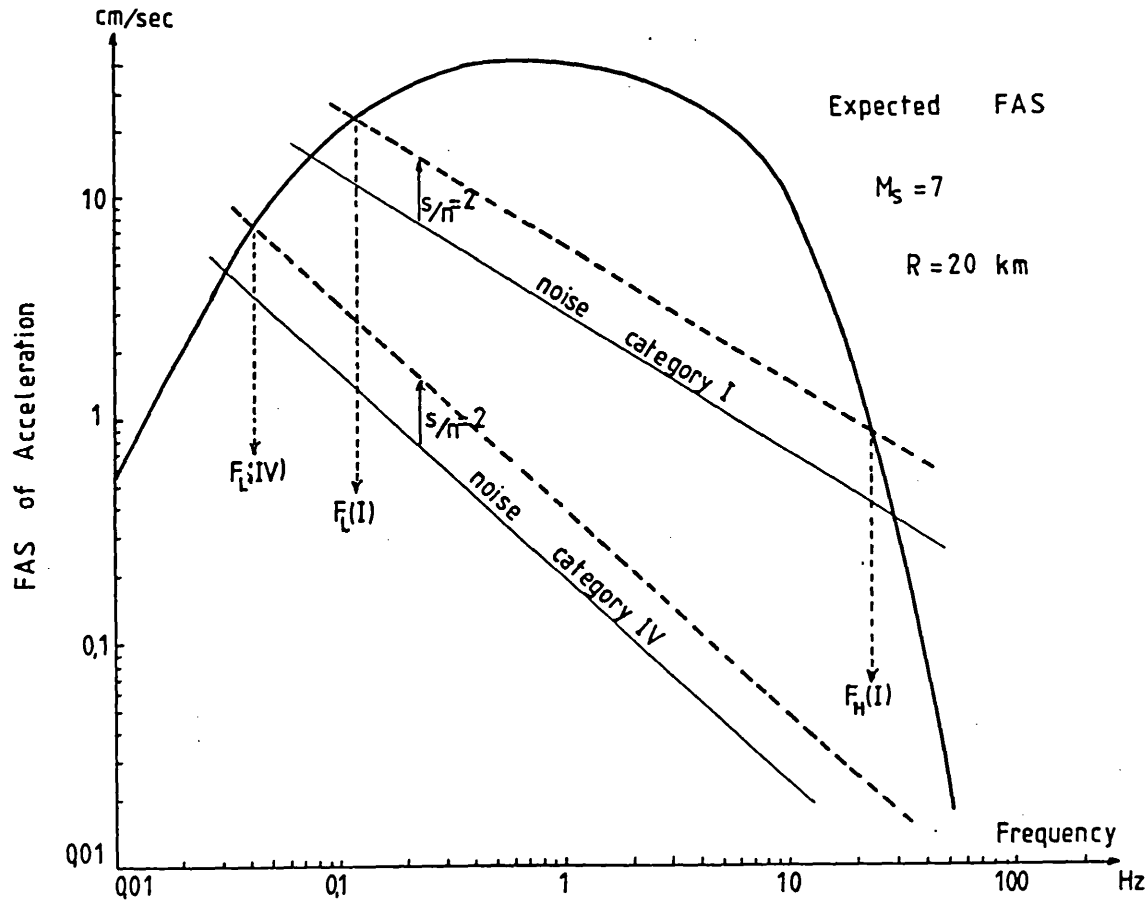

Fig.III.22

Representation of the expected FAS of a strong motion acceleration signal together with the proposed noise model. The frequency cutoffs in the low and high frequencies are defined by the intersection of the FAS with $2N(\omega, T)$ yielding, for the corrected acceleration, a signal-to-noise ratio of at least 2.

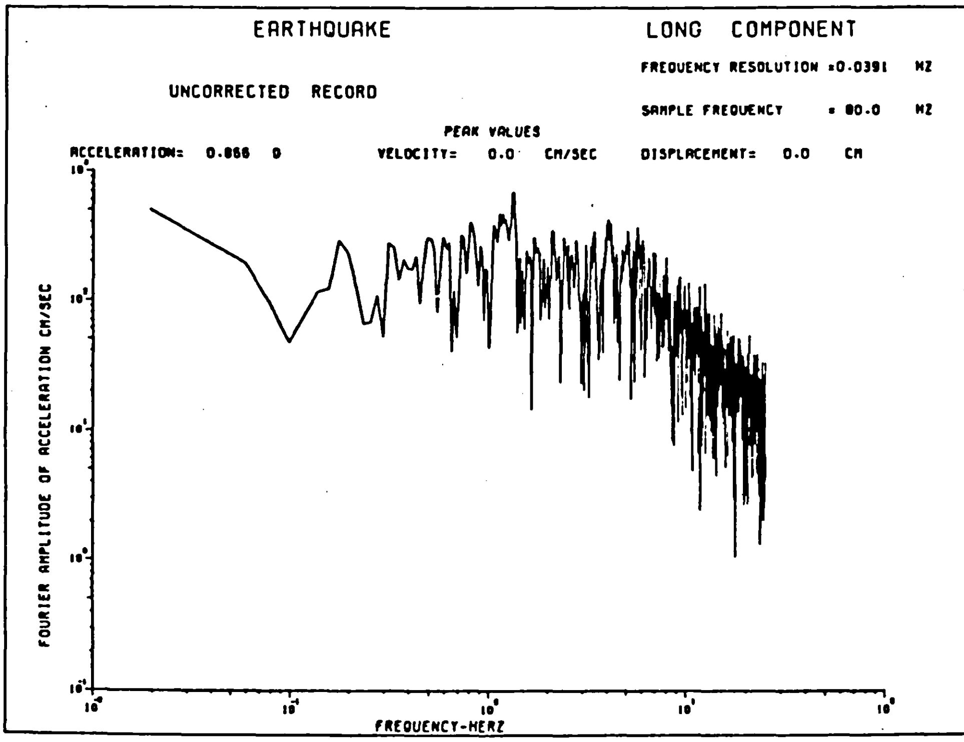

Fig.III.23

Typical FAS of an uncorrected acceleration record. Knowing that the corner frequency of this earthquake is about $0.15Hz$, it seems adequate to set the low frequency limit about $0.10/0.15Hz$. There is no evidence of noise contamination in the high frequency range up to $25Hz$.

3.4.5 Examination of Reliable frequency bands

The examination of the *fig. III.24a,b,c,d* shows the importance of the digitization quality. For the particular values chosen for $\Delta\sigma$, F_{max} and Q, they give an evolutionary picture of the distance and magnitude effects on the reliable frequency range. Whereas at short distances and/or for large Magnitude the reliable frequency band seems as wide as expected, this is not true anymore when the station distances increase. It becomes almost impossible to rely on a recovered signal at more than 200 km, even for Magnitudes as large as 7 when the digitization quality is poor (categories I or II). For good quality digitization, the reliable frequency band remain wide, even for shocks of Magnitude 7 at more than 200 km away from the epicenter. But shocks of Magnitude 6 or below can hardly be detected.

It must be pointed out, however, that these conclusions refer to a signal-to-noise amplitude ratio criterion ($s/n = 2$ here), and that any less demanding level would widen the frequency limits significantly. The results may also vary if another separation criterion, like a signal-to-noise energy ratio, is chosen. The same comment applies to the choice of the source and propagation parameters which have been fixed for the illustration. A larger stress drop $\Delta\sigma$, a higher F_{max}, or even a smoother high frequency decay would increase the upper limits in large proportions. It is believed, however, that the trend of the observations would remain the same.

The quality of earthquake ground motion records in the near field are very sensitive to the digitization phase and an accurate knowledge of the processing methods and equipments is certainly required for each record. It is thus suggested, in order to be able to assess the quality of the 3 component uncorrected ground acceleration records, that a 4th component should be provided, i.e., the digitization of the associated "zero acceleration" or noise function. This supplementary time history should be considered as a quality index for the record set. In any subsequent correction or analysis, values of N_1 and b may be computed by fitting to the proposed noise model. The knowledge or assessment of the source and propagation parameters, together with the FAS model, would then help in the determination of the reliable frequency band. A decision concerning the separation criterion would also have to be made: the signal-to-noise amplitude ratio or the signal-to-noise energy ratio may be chosen.

Surely, one may not be fully satisfied with the quality of the currently available records, even when treated with advanced digitization techniques. In many cases, low frequency information, like the corner frequency or permanent ground displacement are still masked. In the high frequencies, Fmax and the FAS decay are not always visible for small earthquakes, or at lage distances. Further quality improvement lies in the use of the new generation of recording instruments of digital technology. In the meantime and for the treatment of all records obtained in the past or still to come from optical-mechanical instruments, one must make sure that poor quality of digitization is avoided.

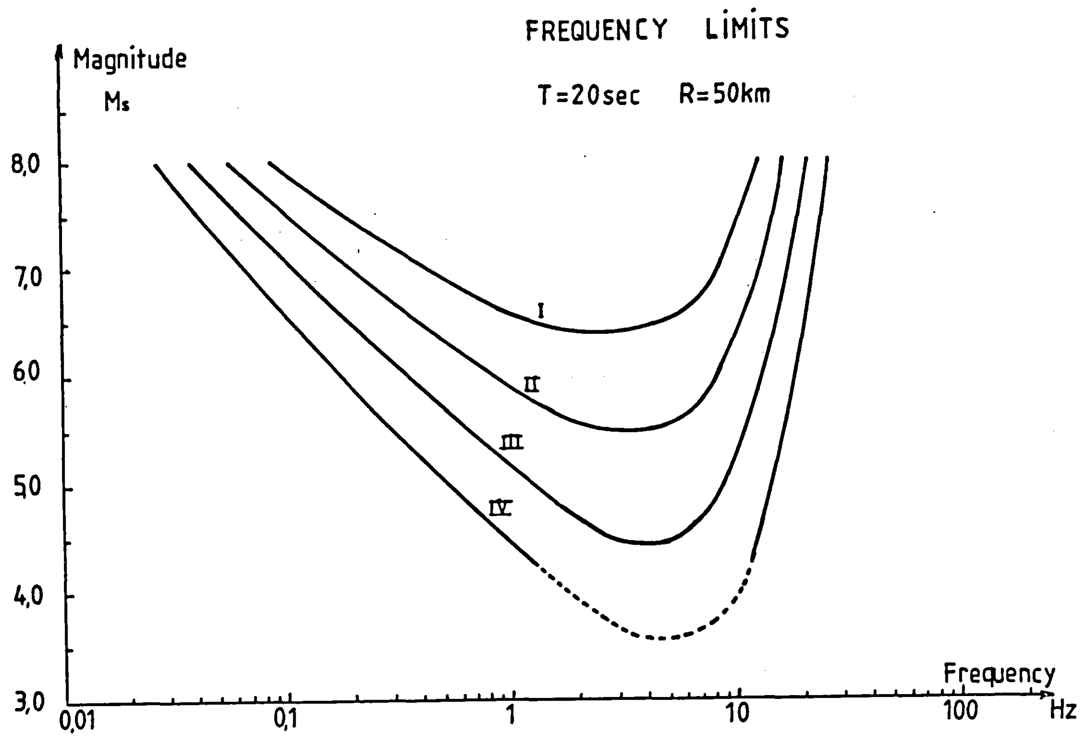

Fig.III.24a

Results showing Frequency cutoffs complying with a signal-to-noise ratio of at least 2, as a function of surface wave Magnitude, for the 4 digitization categories.

a- signal duration $T = 20sec$, distance $R = 50km$

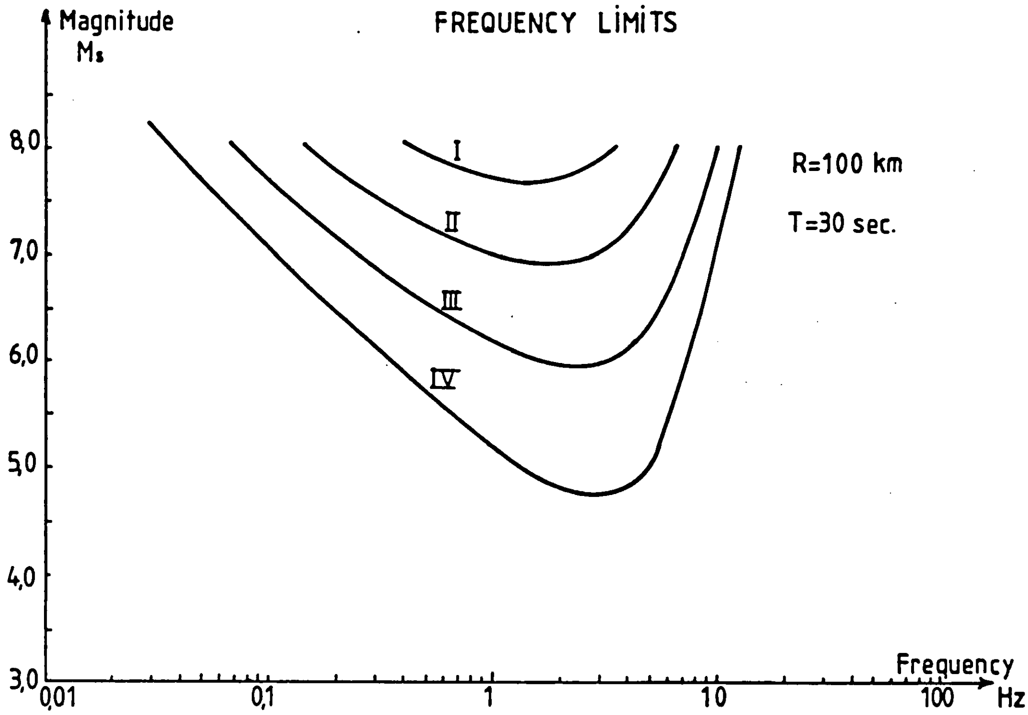

Fig.III.24b

b- signal duration $T = 30sec$, distance $R = 100km$

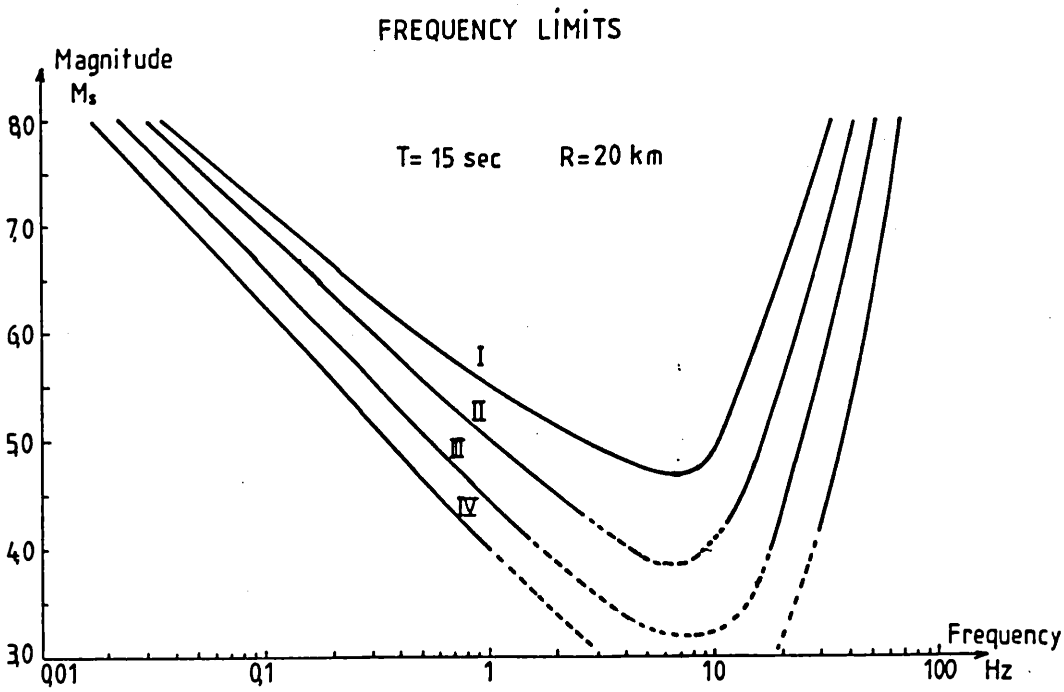

Fig.III.24c

c- signal duration $T = 15sec$, distance $R = 20Km$

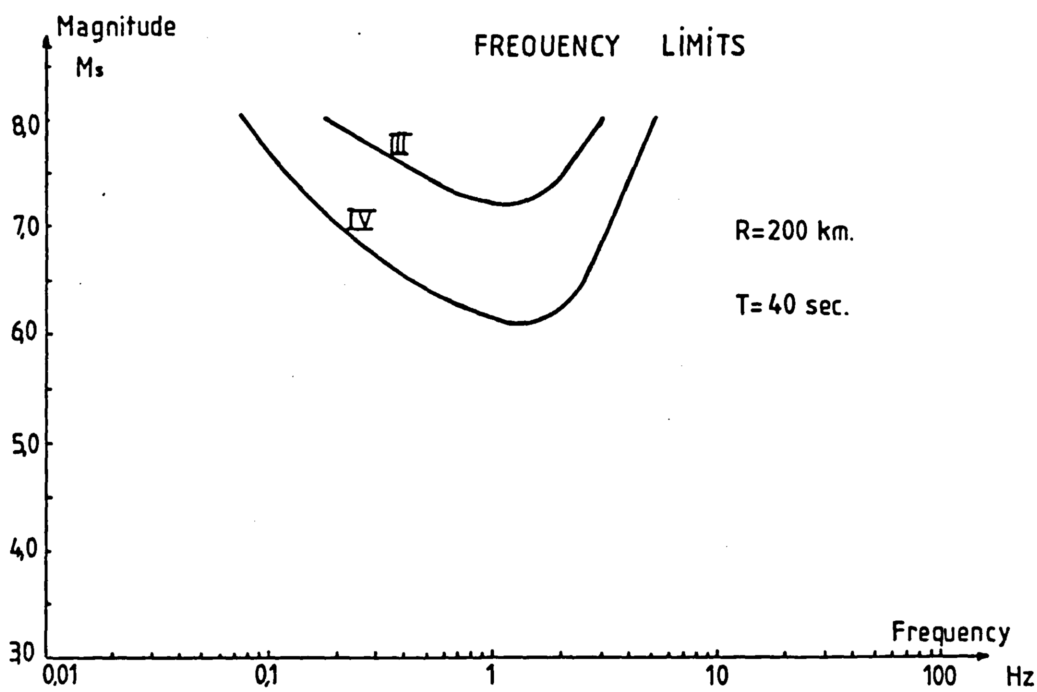

Fig.III.24d

d- signal duration $T = 40 sec$, distance $R = 200 km$

CHAPTER IV

POLYNOMIAL ADJUSTMENTS AND INTERPOLATIONS

4.1 INTRODUCTION

The necessitiy of correcting a strong motion record for base line has been recognised from the early days of acceleration motion recordings. This appeared in particular when integration of the acceleration time histories were performed to produce the associated velocity and displacement time histories. Obtained displacements were nowhere near the expected value. Several meters of displacement were obtained for small shocks at large distances where it was difficult to believe in more that a few cm. The main reason for such discrepencies, was the uncertainty relating to the base line of the acceleration trace. Today it is admitted that instrument imperfection and digitization contribute for a large part in the composition of the errors. However, in the early days of strong motions analysis, it was considered that most of the error was located in the low frequency range of the spectrum. The principal suggested explaination was the irregular motion of the driving spring (*SMAC*) or motor (*AR-240*, *SMA-1*, etcæ.) as seen on *fig. IV. 1*. As a consequence, a first approximation for a error model has been a low degree polynomial, and its corrective effect is shown on *fig. IV. 2*.

On *fig. IV. 3* the acceleration, velocity and displacement functions of our designed signal and the acceleration Fourier Amplitude spectrum are drawn in the case where no correction for base line has been achieved. Little or no difference can be detected on the acceleration time histories. But, it can be seen, from the velocity and displacement time histories, that the low frequency content has become more dominant, when we compare it with true level given by *fig. II. 5d*.

Simple processing procedures have attempted to correct for this base line position uncertainty. The various studies were initiated by *Housner (1967)*, but it was in the sixties that the method became 'standard'. *Berg and Housner (1961)*, *Berg (1963)*, *Shiff and Bogdanoff (1967)*, *Poppitz (1968)* and *Boyce (1970)* developed the technique based on polynomial fitting to assess the base line location. We shall present here the various methods of correction, based on polynomial detrending, and with a uniform mathematical treatment.

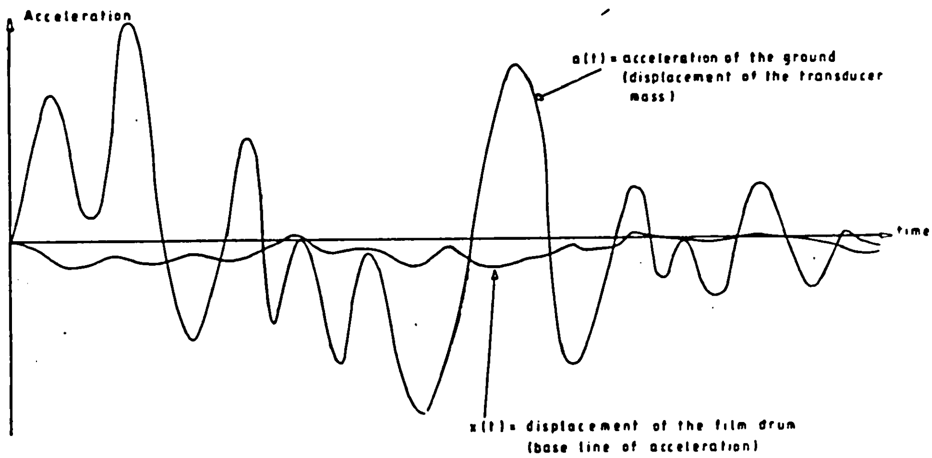

Fig.IV.1

Example of low frequency baseline produced
by an irregular instrument driving spring.

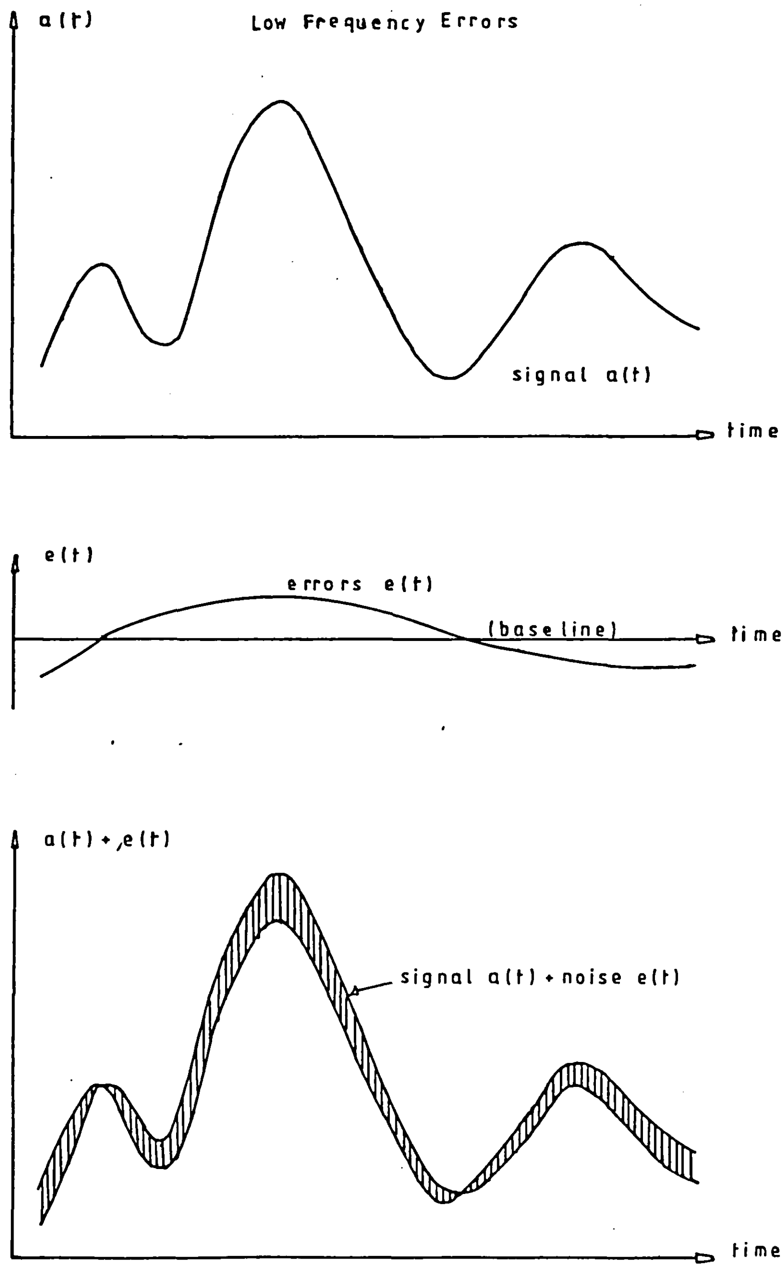

Fig.IV.2
Effect of low frequency error on
a recorded acceleration signal

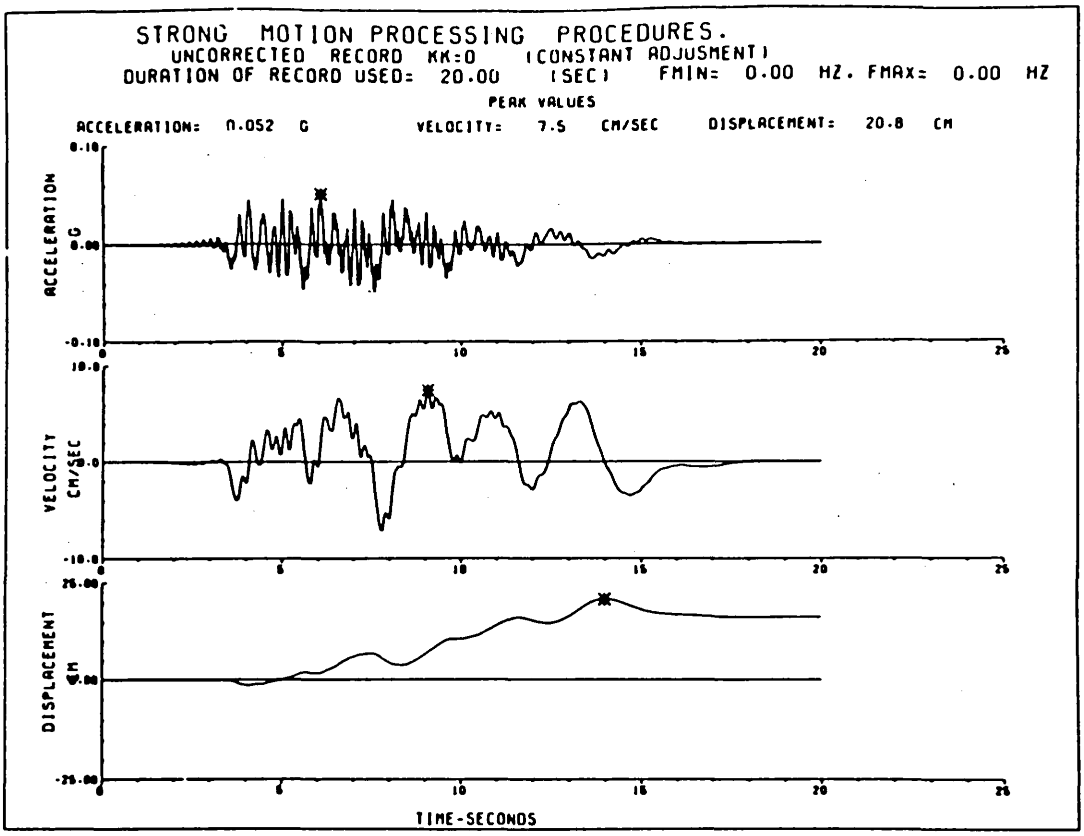

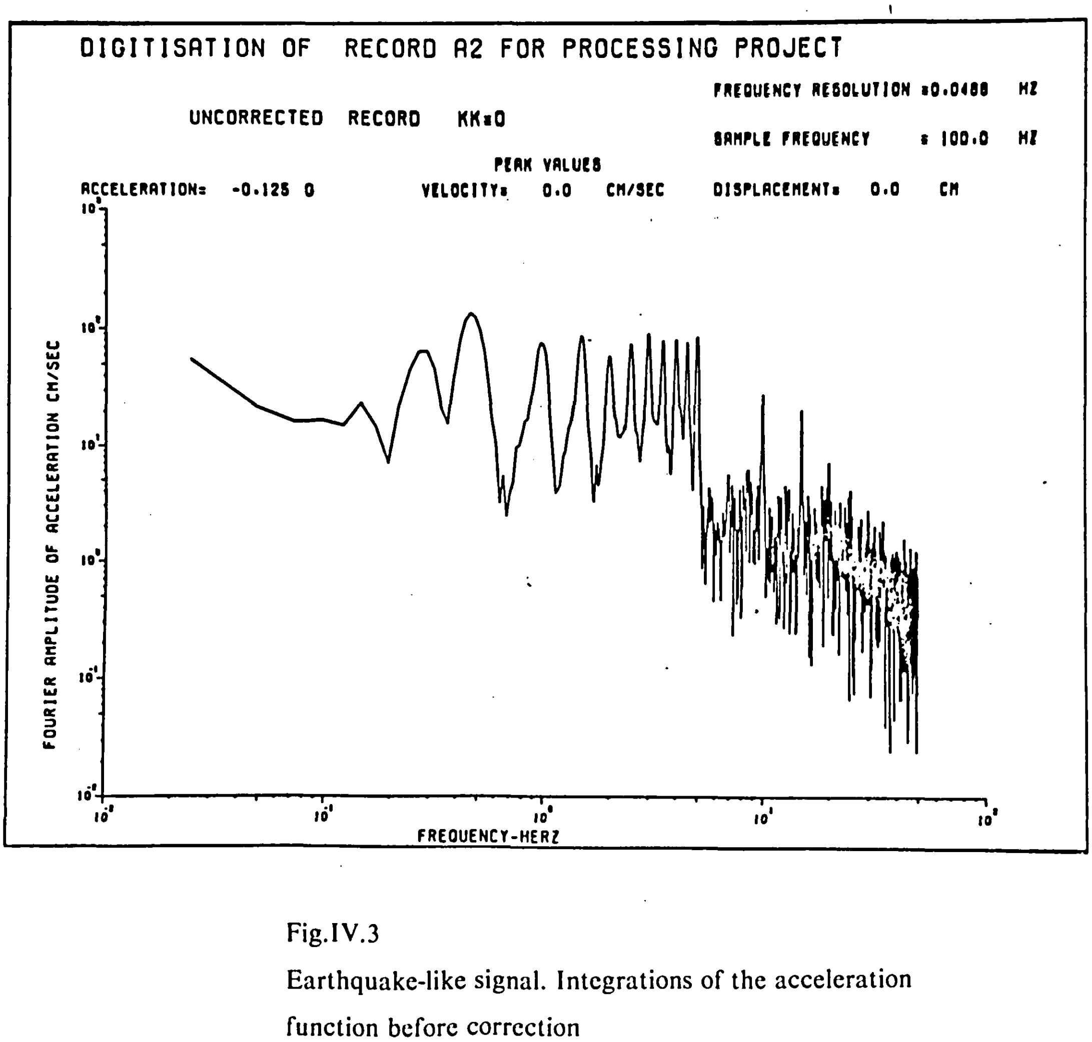

Fig.IV.3

Earthquake-like signal. Integrations of the acceleration function before correction

4.2 PRINCIPLE OF POLYNOMINAL FITTING

In the search for a base line model as a polynomial of low degree, we express the error $e(t)$ as the difference between the uncorrected accelerogram $a(t)$ and the corrected one $a_c(t)$:

$$e(t) = a(t) - a_c(t) \tag{4.1}$$

The actual error function $e(t)$ is unknown but is modelled as:

$$e(t) = c_0 + c_1 t + c_2 t^2 + \ldots + c_n t^n \tag{4.2}$$

The correction principle then consists of computing the coefficients of this polynomial, for a given degree, such that the deviation between the true error and its approximation is minimized in the mean square sense. The minimization can be performed on any time history (acceleration, velocity or displacement). However, it has been common practice to treat either acceleration or velocity.

4.2.1 Adjustment on Acceleration

The error $e(t)$ is the acceleration base line. The minimization of the 'distance' between $e_a(t)$ and its model $\hat{e}_a(t)$ is mathematically expressed by saying that the continuous sum of the squares of the deviations:

$$R_a = \int_o^T \left[e_a(t) - \hat{e}_a(t)\right]^2 dt \tag{4.3}$$

viewed as a function of the polynomial coefficients is minimum, where T is the duration of the record. When $e_a(t)$ has been determined, the corrected acceleration may be written:

$$a_c(t) = a(t) - \hat{e}_a(t) \tag{4.4}$$

4.2.2 Adjustment on Velocity

Similarly if the ground motion is described by its velocity time history, obtained by integration of the acceleration, the actual error function is $e_v(t)$ can be modelled by the polynomial $\hat{e}_v(t)$. There is a direct link between the polynomial models $\hat{e}_v(t)$ and $\hat{e}_a(t)$, since the error on velocity is the integration of the error on acceleration. There is an advantage to operate on velocity since the integration process emphasizes the low frequencies and as a result a lower degree for the polynomial may be used. There is, on the other hand, the supplementary problem of dealing with V_0, the unknown constant of integration.

Again, the search for the polynomial of degree n is achieved by minimizing:

$$R_v = \int_0^T \left[e_v(t) - \hat{e}_v(t) \right]^2 dt \tag{4.5}$$

and the corrected acceleration is given by:

$$a_c(t) = a(t) - \frac{d}{dt}\hat{e}_v(t) \tag{4.6}$$

4.2.3 Various Cases Retained for Base Line Search

Polynomial corrections distort the original acceleration in an attempt to improve it. As mentioned by *Hudson et al. (1967)*, however, the only physically justified function for $e_a(t)$ is the straight line, $c_0 + c_1 t$. It only operates an approximate rotation of the acceleration signal as a whole in restoring a zero-mean in the acceleration, lost either due to the lack of the initial part of the signal (with no pre-event memory instrument) or due to a non perfect alignment of the time axis during digitization. In the following, this case is referred to as $KK = 0$. However, one can invoke multiple other considerations to depart from the simple straight line. The fitting is usually improved if a parabola is assumed to be the base line ($KK = 1$). A linear adjustment on acceleration is similar to a parabolic adjustment on velocity. This can be envisaged, first by assuming that the unkown initial velocity $V_0 = 0$ ($KK = 2$ and *Hudson's standard procedure*), second by considering that V_0 is unkown and has to be determined ($KK = 3$). Finally we also shall consider the method originally suggested by *Poppitz (1967)* which seeks the base line of acceleration as a polynomial of degree 3. ($KK = 4$). This case results from the consideration that, fixing the initial and final conditions for acceleration, velocity and displacement functions yield 6 conditions, (for example all initial and final values to be zero). These conditions enable a polynomial of degree $n = 5$ to be determined as a displacement error function.

For all these cases, calling $P_n(t)$ the polynomial to be determined, one has:

$$a_c(t) = a(t) - \frac{d^s}{dt^s}\{P_n(t)\} \tag{4.12}$$

$s = 0$ for the acceleration cases: $KK = 0$ and $KK = 1$,

$s = 1$ for the velocity cases: $KK = 2$ and $KK = 3$,

$s = 2$ for the displacement case: $KK = 4$.

4.2.4 The Least-Squares Approximation of Polynomials

This approximation problem is a classical problem of numerical analysis and the normal equations will be written here for completion. The polynomial $P_n(t)$ (representing here $\hat{e}_a(t)$, $\hat{e}_v(t)$ or $\hat{e}_d(t)$):

$$P_n(t) = \sum_{k=0}^{n} c_k t^k \tag{4.7}$$

of degree at most n, is such that it minimizes R:

$$R = \int_0^T \left[f(t) - f_c(t) - P_n(t) \right]^2 dt \tag{4.8}$$

the difference between the actual error function and its model in the mean square sense.

$f(t)$ is the analogue ground motion (acceleration, or velocity or displacement).

$f_c(t)$ is the unknown corrected form of $f(t)$.

The problem is to find the coefficients of $P_n(t)$ through the necessary conditions:

$$\frac{\partial R}{\partial c_j} = 0 \tag{4.9}$$

for each $j = 0, 1, \ldots, n$

This leads to:

$$\int_0^T t^j \left[f(t) - f_c(t) \right] dt - \sum_{k=0}^{n} c_k \int_0^T t^{j+k} dt = 0 \tag{4.10}$$

$j = 0, 1, \ldots, n$

This is a system of n+1 linear equations which can be letter viewed as:

$$\sum_{k=0}^{n} c_k \int_0^T t^{j+k} dt = \int_0^T t^j f(t) dt - \int_0^T t^j f_c(t) dt \tag{4.11}$$

$j = 0, 1, \ldots, n$

In order to compute the coefficients c_k, the second integral in the right hand side is assumed to be zero. The significance of this assumption is worth examining since it gives the physical interpretation of what is commonly regarded as "fitting" of strong motion records. In doing so, we are actually implicitly stating that the correction polynomial is equivalent to the general trend of the ground motion. The various polynomial corrections are then nothing else that a simple low degree detrending. The operation consists of averaging the various statistical moments of the function up to an order n. It will be seen further that this is not, in general, what should be achieved since it may destroy some of the recorded information and in particular the dissymetric character of the motion in the near field.

Eq.(4.11) expressed in matrix form is:

$$\{C\}\{D\} = \{M\} - \{M_c\} \tag{4.12}$$

where

$$\{C\} = \{c_k\} \tag{4.13a}$$

$$\{D\} = \{d_{jk}\} \tag{4.13b}$$

$$\{M\} = \{m_j\} \tag{4.13c}$$

$$\{M_c\} = \{m_{c_j}\} \tag{4.13}$$

$$j = 0,...,n \qquad k = 0,...,n$$

We have:

$$\{D\} = \left\{\int_0^T t^{j+k}\,dt\right\} \tag{4.14a}$$

$$\{M\} = \left\{\int_0^T t^j f(t)\,dt\right\} \tag{4.14b}$$

$$\{M_c\} = \left\{\int_0^T t^j f_c(t)\,dt\right\} \tag{4.14c}$$

The assumption previously discussed, is expressed by $\{M_c\} = 0$ and the corrected time history is:

$$f_c(t) = f(t) - \left\{t^k\right\}\{c_k\} \tag{4.15}$$

with

$$\{c_k\} = \{C\} = \{D\}^{-1}\{M\} \tag{4.16}$$

From the previous section, this means that:

$$a_c(t) = a(t) - \left\{t^k\right\}\{c_k\} \qquad \text{for } KK = 0 \text{ and } KK = 1,$$

$$a_c(t) = a(t) - k\left\{t^{k-1}\right\}\{c_k\} \qquad \text{for } KK = 2 \text{ and } KK = 3,$$

$$a_c(t) = a(t) - k(k-1)\left\{t^{k-2}\right\}\{c_k\} \qquad \text{for } KK = 4.$$

$$k = 0,...,n$$

4.3 POLYNOMIAL CORRECTIONS USED IN PRACTICE

Eq. 4.15 and 4.16 are valid for all corrections of polynomial type. We shall now give the expressions for the matrices $\{D\}$ and $\{M\}$ for the various KK cases defined above. At the same time, the meaning of the assumption $\{M_c\} = 0$ will be explicitely described. We shall also replace $f(t)$ by $a(t)$ or $v(t)$ when acceleration or velocity are considered.

4.3.1 $KK = 0$: Straight line adjustment through acceleration

The matrices $\{M\}$ and $\{D\}$ are of order $n + 1 = 2$:

$$\{M\} = \begin{bmatrix} \int_0^T a(t)\,dt \\ \int_0^T ta(t)\,dt \end{bmatrix} \tag{4.17}$$

$$\{D\} = \begin{bmatrix} T & \frac{T^2}{2} \\ \frac{T^2}{2} & \frac{T^3}{3} \end{bmatrix} \tag{4.18}$$

The inverse of matrix $\{D\}$ is:

$$\{D\}^{-1} = \begin{bmatrix} \frac{4}{T} & -\frac{6}{T^2} \\ \frac{-6}{T^2} & \frac{12}{T^3} \end{bmatrix} \tag{4.16}$$

The conditions $\{M_c\} = 0$ written explicitely are:

$$\int_0^T a_c(t)\,dt = 0 \tag{4.20}$$

$$\int_0^T ta_c(t)\,dt = 0 \tag{4.21}$$

Eq. 4.20 shows that the corrected acceleration is now symetrically distributed about the arithmetic mean of the corrected acceleration. This is also expressed by:

$$v_c(T) = v_c(0) \tag{4.22}$$

and *Eq.4.21* shows in a similar way that one has imposed:

$$d_c(T) = d_c(0) + T v_c(T) \tag{4.23}$$

If $v_c(0) = 0$ and $d_c(0) = 0$ are assumed (usual case, even though the initial part of the motion is not recorded), then also the final velocity and displacement are forced to be zero.

4.3.2 $KK = 1$: Parabolic adjustment through acceleration

The matrices $\{M\}$ and $\{D\}$ are of order $n + 1 = 3$:

$$\{M\} = \begin{bmatrix} \int_0^T a(t)\,dt \\ \int_0^T t a(t)\,dt \\ \int_0^T t^2 a(t)\,dt \end{bmatrix} \tag{4.24}$$

$$\{D\} = \begin{bmatrix} T & \frac{T^2}{2} & \frac{T^3}{3} \\ \frac{T^2}{2} & \frac{T^3}{3} & \frac{T^4}{4} \\ \frac{T^3}{3} & \frac{T^4}{4} & \frac{T^5}{5} \end{bmatrix} \tag{4.25}$$

The inverse of matrix $\{D\}$ is:

$$\{D\}^{-1} = \begin{bmatrix} \frac{9}{T} & \frac{-36}{T^2} & \frac{-30}{T^3} \\ \frac{-36}{T^2} & \frac{-192}{T^3} & \frac{-180}{T^4} \\ \frac{-30}{T^3} & \frac{-180}{T^4} & \frac{180}{T^5} \end{bmatrix} \tag{4.26}$$

In the derivation of $\{D\}^{-1}$, the conditions $\{M_c\} = 0$ are the same as in the previous case (*Eq.4.20* and *Eq.4.21*) but with a supplementary one:

$$\int_0^T t^2 a_c(t)\,dt \tag{4.27}$$

The latter condition adds the following constraint on the corrected displacement function:

$$W_c(T) = T d_c(T) - \frac{1}{T^2} v_c(T) \tag{4.28}$$

where $W_c(t)$ is the algebraic area of the displacement curve. As in the previous case, if $v_c(0) = 0$ and $d_c(0) = 0$, the displacement curve area will be also equally distributed about the new base line.

4.3.3 $KK = 2$: Parabolic adjustment through velocity with $V_0 = 0$

The matrices $\{M\}$ and $\{D\}$ are still of order $n + 1 = 3$:

$$\{M\} = \begin{bmatrix} \int_0^T t v(t)\, dt \\ \int_0^T t^2 v(t)\, dt \\ \int_0^T t^3 v(t)\, dt \end{bmatrix} \tag{4.29}$$

The matrices $\{D\}$ and $\{D\}^{-1}$ are:

$$\{D\} = \begin{bmatrix} \frac{T^3}{3} & \frac{T^4}{8} & \frac{T^5}{15} \\ \frac{T^4}{4} & \frac{T^5}{10} & \frac{T^6}{18} \\ \frac{T^5}{5} & \frac{T^6}{12} & \frac{T^7}{21} \end{bmatrix} \tag{4.30}$$

$$\{D\}^{-1} = \begin{bmatrix} \frac{300}{T^3} & \frac{-900}{T^4} & \frac{630}{T^5} \\ \frac{-1800}{T^4} & \frac{5760}{T^5} & \frac{-4200}{T^6} \\ \frac{1890}{T^5} & \frac{-6300}{T^6} & \frac{4725}{T^7} \end{bmatrix} \tag{4.31}$$

The conditions imposed by $\{M_c\} = 0$ still reflect a stronger averaging of the displacement curve.

$$W_c(T) = T d_c(T) \tag{4.32a}$$

$$X_c(T) = \frac{T^2}{2} d_c(T) \tag{4.32b}$$

$$Y_c(T) = \frac{T^3}{6} d_c(T) \tag{4.32c}$$

where:

$$W_c(t) = \int_0^t d_c(\tau)\, d\tau \tag{4.33a}$$

$$X_c(t) = \int_0^t W_c(\tau)\, d\tau \tag{4.33b}$$

$$Y_c(t) = \int_0^t X_c(\tau)\, d\tau \tag{4.33c}$$

This case does not implicitly impose a final displacement but the extent of the smoothing is clearly seen in the case where $d_c(T) = 0$ (when the distance to the source is sufficiently large). It can be seen that the displacement curve is highly averaged since:

$$W_c(T) = X_c(T) = Y_c(T) = 0 \tag{4.34}$$

The above conditions can also be viewed as rendering minimum:

$$\int_0^T v_c^2(t)\, dt \tag{4.35}$$

with $V_0 = 0$ which corresponds to the *Hudson's standard procedure (1969).*

4.3.4 $KK = 3$: Parabolic adjustment through velocity with $V_0 \neq 0$

This case is similar to the $KK = 2$ case, but the unknown constant of integration is determined from an extra condition:

$$\frac{\partial R_v}{\partial V_0} = 0 \tag{4.36}$$

This is equivalent to saying that we are searching for the matrices $\{M\}$ and $\{D\}$ of order $n + 1 = 4$: we get:

$$\{M\} = \begin{bmatrix} \int_0^T v(t)\,dt \\ \int_0^T tv(t)\,dt \\ \int_0^T t^2 v(t)\,dt \\ \int_0^T t^3 v(t)\,dt \end{bmatrix} \tag{4.37}$$

$$\{D\} = \begin{bmatrix} T & \frac{T^2}{2} & \frac{T^3}{3} & \frac{T^4}{4} \\ \frac{T^2}{2} & \frac{T^3}{3} & \frac{T^4}{8} & \frac{T^5}{5} \\ \frac{T^3}{3} & \frac{T^4}{4} & \frac{T^5}{5} & \frac{T^6}{6} \\ \frac{T^4}{4} & \frac{T^5}{5} & \frac{T^6}{6} & \frac{T^7}{7} \end{bmatrix} \tag{4.38}$$

The inverse of matrix $\{D\}$ is:

$$\{D\}^{-1} = \begin{bmatrix} \frac{16}{T} & \frac{-120}{T^2} & \frac{240}{T^3} & \frac{-140}{T^4} \\ \frac{-120}{T^2} & \frac{1200}{T^3} & \frac{-2700}{T^4} & \frac{1680}{T^5} \\ \frac{240}{T^3} & \frac{-2700}{T^4} & \frac{6480}{T^5} & \frac{-4200}{T^6} \\ \frac{-140}{T^4} & \frac{1680}{T^5} & \frac{-4200}{T^6} & \frac{2800}{T^7} \end{bmatrix} \tag{4.39}$$

The conditions carried by $\{M_c\} = 0$ are given by *Eq. 4.32a/b/c* and:

$$\int_0^T v_c(t)\,dt = 0 \tag{4.40}$$

which means that $d_c(T) = d_c(0)$ is imposed. As previously, the case is equivallent to saying that:

$$\int_0^T v_c^2(t)\,dt \tag{4.41}$$

is minimized, but here with $V_0 = 0$.

4.3.5 $K = 4$: Zero and End Time Correction

We saw in a previous paragraph that, if we assume known the values of acceleration, velocity and displacement at time $t = 0$ and $t = T$, we can define a 3rd order polynomial which will be used to correct for the acceleration base line.

Matrices $\{M\}$ and $\{D\}$ are of the order 6:

$$\{M\} = \begin{bmatrix} a(0) \\ v(0) \\ d(0) \\ a(T) \\ v(T) \\ d(T) \end{bmatrix} \tag{4.43}$$

$$\{D\} = \begin{bmatrix} 1 & 0 & 0 & 0 & 0 & 0 \\ 0 & 1 & 0 & 0 & 0 & 0 \\ 0 & 0 & 1 & 0 & 0 & 0 \\ 1 & 0 & 0 & T & T^2 & T^3 \\ T & 1 & 0 & \frac{T^2}{2} & \frac{T^3}{3} & \frac{T^4}{4} \\ \frac{T^2}{2} & T & 1 & \frac{T^3}{3} & \frac{T^4}{4} & \frac{T^5}{5} \end{bmatrix} \tag{4.44}$$

The inverse of $\{D\}$ has for expression:

$$\{D\}^{-1} = \begin{bmatrix} 1 & 0 & 0 & 0 & 0 & 0 \\ 0 & 1 & 0 & 0 & 0 & 0 \\ 0 & 0 & 1 & 0 & 0 & 0 \\ \frac{-9}{T} & \frac{-36}{T^2} & \frac{-60}{T^3} & \frac{3}{T} & \frac{-24}{T^2} & \frac{-60}{T^3} \\ \frac{18}{T^2} & \frac{96}{T^3} & \frac{180}{T^4} & \frac{-12}{T} & \frac{84}{T^2} & \frac{180}{T^3} \\ \frac{-10}{T^3} & \frac{-60}{T^4} & \frac{-120}{T^5} & \frac{10}{T^3} & \frac{-60}{T^4} & \frac{120}{T^5} \end{bmatrix} \tag{4.45}$$

and

$$\{M_c\} = \begin{bmatrix} a_c(0) \\ v_c(0) \\ d_c(0) \\ a_c(T) \\ v_c(T) \\ d_c(T) \end{bmatrix} \tag{4.46}$$

4.4 RECOVERY OF THE ORIGINAL ANALOGUE ACCELERATION

4.4.1 The Digital to Analogue conversion

In this section, we shall discuss the ways the original recorded acceleration signal may be recovered after digitization, in an analogue form. We shall not analyse again the accuracy with which digitization is achieved (see chapter III), but we shall generate an analogue function from the set of digitized points obtained from a particular, known as imperfect digitization. The starting point of the study is then an ensemble $a(n\Delta t_n)$ $n = 0, 1, ..., N-1$, where the interval between points Δt_n may be constant or not.

The case of a constant interval of time, however, allows a preliminary insight into the problem. The transformation of the equi-spaced data $a[n]$ into a continuous function $a(t)$ may be assimilated to the passage of the sequence through a continuous low pass filter with cutoff $\omega_N = \pi/\Delta t$. The interpolated function becomes, in the frequency domain:

$$A(i\omega) = \Delta t \, A_S(i\omega) \, H(i\omega) \tag{4.47}$$

where $A_S(i\omega)$ is the Fourier Transform of the sequence $a[n]$, and $H(i\omega)$ is the frequency function of the filter:

$$|H(i\omega)| = \begin{cases} 1 & |\omega| < \pi/\Delta t \\ 0 & |\omega| \geq \pi/\Delta t \end{cases} \tag{4.48}$$

This time domain representation is the expression of the sampling theorem (see chapter III):

$$a(t) = \sum_{n=0}^{N-1} a[n] \frac{\sin\omega_N(t - n\Delta t)}{\omega_N(t - \Delta t)} \tag{4.49}$$

The process, valid for all time can be visualised on *fig. IV.4*. It is a theoretical interpolation which is not used for strong motion recovery. Instead the "hold" interpolation or the "linear" interpolation are used. We shall describe here these procedures and in:roduce the more accurate "cubic" interpolations. They are all time domain interpolations and can be seen on *fig. IV.7*.

a) *The hold interpolation*

The hold interpolation is performed by holding the digitized points along the corresponding Δt as shown on *fig. IV.5a*. Unless the interval of time is very small, this type of interpolation is not very accurate, and large errors may be introduced which will contaminate further processing. *Fig. IV.6* shows the distorsion due to sampling hold. It is apparent, that this error is reduced by inceasing the sampling frequency ω_S by comparison with the maximum expected frequency ω_M. It must be realized that the hold interpolation is implicit in any signal treatment of digital type. Therefore, it requires, before processing a change in Δt compatible with the analysis.

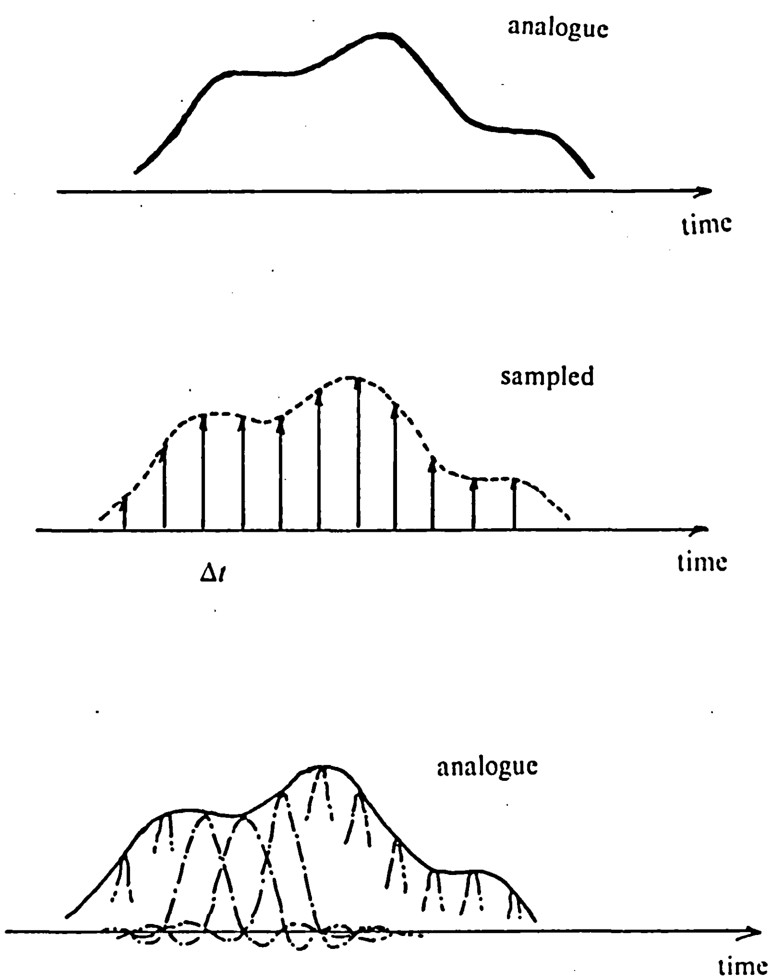

Fig.IV.4

The theoretical digital to analogue conversion
expressed by the Sampling Theorem

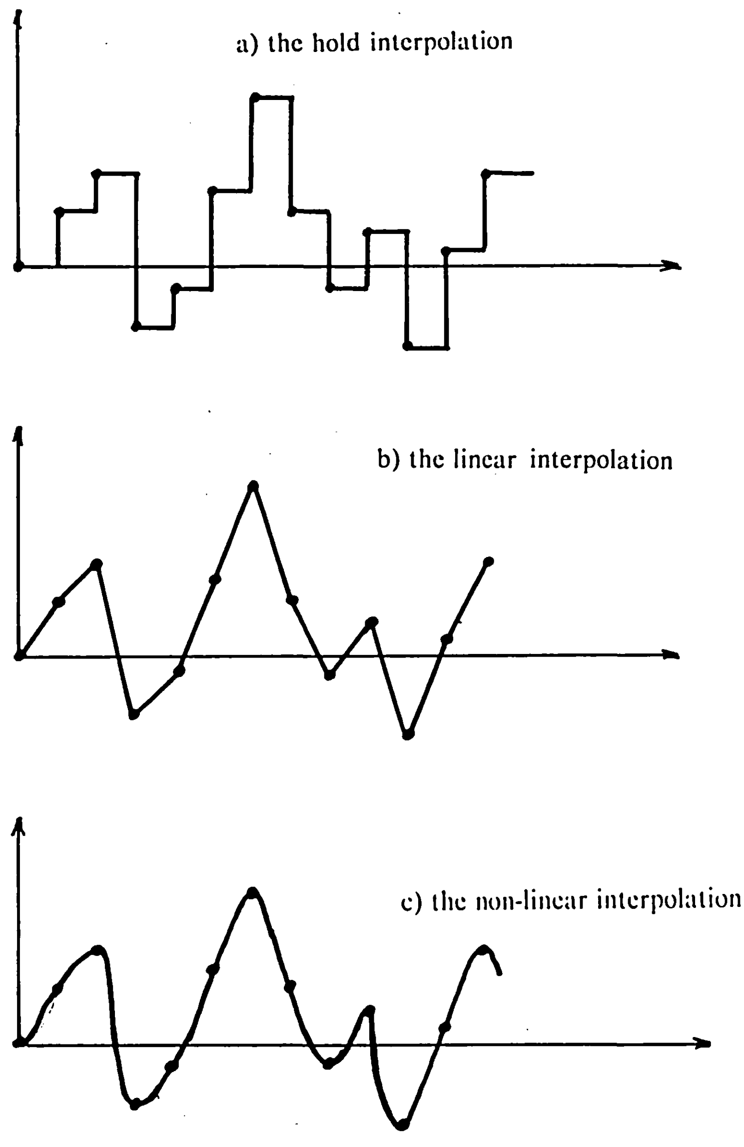

Fig.IV.5

Various cases of polynomial interpolation used
to recover the analogue signal from its digital form

b) *The linear interpolation*

The linear interpolation is the type of interpolation currently used. It consists (*fig. IV. 5b*) of considering that the signal which has been digitized may be adequately recovered by assuming that it follows a sraight line between digitized points. In particular, because of its simplicity, this assumption is being used in all standard computer codes to calculate the responses of linear and non linear systems. The well known Response Spectra, are also computed according to this assumption. It is an improvement by comparison with the hold interpolation, but cannot be used as such in further analysis of digital type. Although the obtained function is continuous, its successive derivatives are not. It has been observed (see also chapter VII) that this approximation may have an effect on the velocity and displacement functions wich are calculated by integration of the recovered analogue signal.

c) *The non-linear interpolation*

A new approach in signal interpolation, and developed here is the non-linear interpolation (*fig. IV. 5c*). Many hypotheses may be set in order to find an appropriate curve between the digitized points. We shall limit ourselves to the "cubic interpolations". The motivation for non-linear interpolation originates from the poor accuracy obtained with the hold interpolation in digital signal treatment when the actual measured points are used. The idea is to perform first, from the digitized points an interpolation of good quality and then re-sample the signal to a new constant and smaller Δt compatible with digital treatment. As we shall see further it can also perform a much better integration of the acceleration function when we wish to obtain velocity and displacement functions.

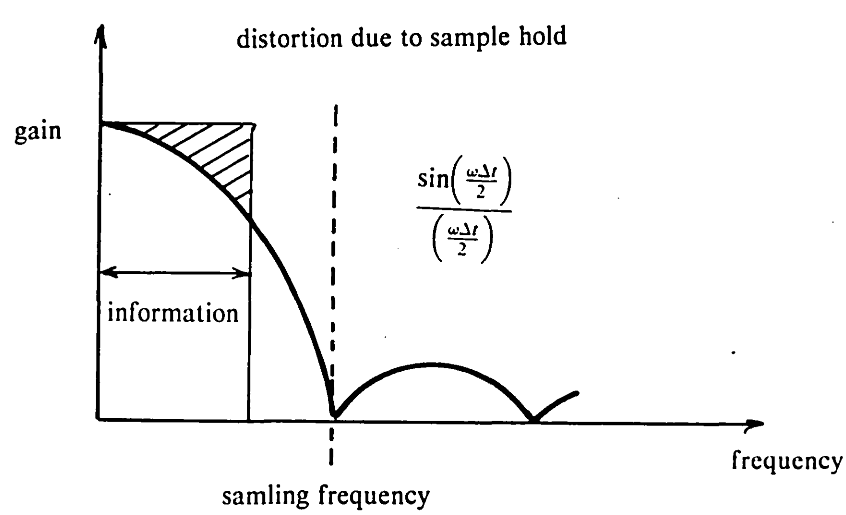

Fig.IV.6

Frequency effect of the hold interpolation

4.4.2 Non-linear interpolations

In the search for a better acceleration signal interpolation, the following cases were investigated.
1) the spline interpolation
2) the Hermite interpolation
3) the Maude interpolation.

For the three cases, a polynomial of degree at least three insures the gap between measured points. Unlike the linear interpolation, continuity of the first and second derivatives are satisfied at any point of the interpolating curve.

Let us consider an interval ot time $\left[t_j, t_{j+1}\right]$. The amplitudes of the signal are measured only at its boundaries and are a_j and a_{j+1}. The piecewise interpolation polynomial of degree n can be written as:

$$\mathcal{I}_j(t) = \alpha_j + \beta_j \frac{(t-t_j)}{(t_{j+1}-t_j)} + \gamma_j \frac{(t-t_j)^2}{(t_{j+1}-t_j)^2} + \delta_j \frac{(t-t_j)^3}{(t_{j+1}-t_j)^3} + \dots \tag{4.50}$$

In the following, the interpolation parameter

$$\lambda = \frac{t-t_j}{t_{j+1}-t_j} \tag{5.51}$$

will be used as well as the interval length

$$h_j = t_{j+1} - t_j \tag{4.51}$$

The Spline interpolation

The attraction of the cubic spline interpolation resides in the fact that a piecewise cubic function with continuous first and second derivative can be obtained without assumption other than the knowledge of the boundary conditions at $t = 0$ and $t = T$ of the signal.

Given a set of digitized points (t_j, a_j) $j = 1, \dots, N$ -the spline interpolation $\mathcal{S}(t)$ is an ensemble of cubic polynomials denoted $\mathcal{S}_j(t)$ on each interval (t_j, t_{j+1}) $j = 1, \dots, N-1$ satisfying the following conditions:

$$\mathcal{S}(t_j) = a_j \qquad j = 1, \dots N \tag{4.53a}$$

$$\mathcal{S}_{j+1}(t_{j+1}) = \mathcal{S}(t_{j+1}) \qquad j = 1, \dots, N-1 \tag{4.53b}$$

$$\mathcal{S}_{j+1}(t_{j+1}) = \mathcal{S}_j(t_{j+1}) \qquad j = 1, \dots, N-1 \tag{4.53c}$$

$$\ddot{\mathcal{S}}_{j+1}(t_{j+1}) = \ddot{\mathcal{S}}_j(t_{j+1}) \qquad j = 1, \dots, N-1 \tag{4.53d}$$

The boundary conditions may be either

$$\ddot{\mathcal{S}}(t_1) = \ddot{\mathcal{S}}(t_N) = 0 \qquad \text{free boundaries} \tag{4.54a}$$

or

$$\mathcal{S}(t_1) = \dot{a}_1 \quad \text{and} \quad \mathcal{S}(t_N) = \dot{a}_N \qquad \text{clamped boundaries} \tag{4.54b}$$

The cubic spline $\mathcal{S}(t)$ is the sum of local polynomials (*fig. IV. 7a*):

$$\mathcal{S}_j(t) = \sigma_{0,j} + \sigma_{1,j}(t - t_j) + \sigma_{2,j}(t - t_j)^2 + \sigma_{3,j}(t - t_j)^3 \tag{4.55}$$

for each $j = 1, \ldots, N - 1$

By application of the condition (4.53) and (4.54*a*) (we assumed free boundary conditions since nothing permits to impose derivatives at extreme points), we obtain:

$$\sigma_{0,j} = a_j \tag{4.56a}$$

$$\sigma_{1,j} = \frac{1}{h_j}(a_{j+1} - a_j) - \frac{h_j}{3}(\sigma_{2,j+1} + 2\sigma_{2,j}) \tag{4.56b}$$

$$\sigma_{3,j} = \frac{1}{3h_j}(\sigma_{2,j+1} - \sigma_{2,j}) \tag{4.56c}$$

where the $\sigma_{2,j}$ are solution of the diagonally dominant linear system:

$$h_{j-1}\sigma_{2,j-1} + 2(h_{j-1} + h_j)\sigma_{2,j} + h_j\sigma_{2,j+1} = \frac{3}{h_j}(a_{j+1} - a_j) - \frac{3}{h_j}(a_j - a_{j-1}) \tag{4.56d}$$

Expressed in terms of the coefficients of *Eq. 4.50* this gives:

$$\alpha_j = a_j \tag{4.57a}$$

$$\beta_j = \frac{1}{h_j}(a_{j+1} - a_j) - \frac{1}{3h_j}(\sigma_{2,j+1} + 2\sigma_{2,j}) \tag{4.57b}$$

$$\gamma_j = \frac{\sigma_{2,j}}{h_j^2} \tag{4.57c}$$

$$\delta_j = \frac{1}{3h_j}(\sigma_{2,j+1} - \sigma_{2,j}) \tag{4.57d}$$

The physical interpretation of the spline interpolation is the minimization of the second derivative $\ddot{\mathcal{S}}(t)$ along the curve:

$$\frac{\partial}{\partial t} \int_0^T \ddot{\mathcal{S}}(\tau)\, d\tau = 0 \tag{4.58}$$

This property is particularly apparent at peaks and throughs points where $\mathcal{S}(t)$ approaches the largest osculating circle compatible with other digitized points. As a consequence, spline interpolation requires extra points in the vicinity of these peaks to control the actual curvature.

The Hermite interpolation

The constraint of minimized integrated curvature, although very convienient, is not always suitable. It requires that the digitized points are chosen at certain optimized locations and this is relatively difficult for an operator with little experience in particular when the frequency of the various pulses changes along the record. The Hermite polynomial interpolation does not require such an optimisation. It relies on the knowledge of the slope of the acceleration trace as well as the amplitude at a given time.

Routine digitization, however does not measure the slopes and this information is unknown. It is believed that the measurement of such slopes would improve considerably the quality of the recovered analogue in the future. What is required for this, is a particular cursor on the digitization table, able of measuring them at the same time as the amplitudes. An uncorrected record, in this condition would be given by a set of triplets $(t_j, a_j, \dot{a}_j)$ measuring the time, the amplitude and the slope. In the meantime, only an approximation of the required slope may be used. We have chosen the simplest one: the average of the two secants on each side of the digitized point. In the particular but important case where the two secants are of opposite sign, the point must be considered as an exact extremum and therefore the slope must taken to be zero.

The piecewise cubic Hermite interpolation is composed of a set of unique polynomials of degree three on the interval (t_j, t_{j+1}) agreeing with a_j, $\dot{a}_j$ and a_{j+1}, $\dot{a}_{j+1}$ at time t_j and t_{j+1} resectively *(fig. IV.7b). It can be expressed as:*

$$\mathcal{H}_j(t) = \sum_{k=j}^{j+1} a_k \left[1 - 2(t - t_k) L_{1,k-j+1}{}'(t_k) \right] L^2_{1,k-j+1}(t) + \sum_{k=j}^{j+1} \dot{a}_k (t - t_k) L^2_{1,k-j+1}(t) \tag{4.59}$$

where L_{1j} and $L_{1j}{}'$ are the first order Lagrange polynomial and its derivative. We can easily verify that $L_{1,1}(t) = 1 - \lambda$, $L_{1,2}(t) = \lambda$ and $L_{1,2}{}' = -1/h_j = -L_{1,2}{}'$. After some algebra we can write $\mathcal{H}_j(t)$ in the form:

$$\mathcal{H}_j(t) = \eta_{0j} + \eta_{1j}(t - t_j) + \eta_{2j}(t - t_j)^2 + \eta_{3j}(t - t_j)^3 \tag{4.60}$$

where

$$\eta_{0j} = a_j \tag{4.61a}$$

$$\eta_{1j} = \dot{a}_j \tag{4.61b}$$

$$\eta_{3j} = \frac{1}{h_j} \quad \frac{a_{j+1} - a_j}{h_j} - \dot{a}_j \tag{4.61c}$$

$$\eta_{3j} = \frac{1}{h_j^2} \quad \dot{a}_{j+1} + \dot{a}_j - 2\frac{a_{j+1} - a_j}{h_j} \tag{4.61d}$$

As before $\mathcal{H}_j(t)$ can take the form of Eq. 4.50 with:

$$\alpha_j = a_j \tag{4.62a}$$
$$\beta_j = \dot{a}_j \tag{4.62b}$$
$$\gamma_j = 3(a_{j+1} - a_j) + 2h_j(\dot{a}_{j+1} + \dot{a}_j) \tag{4.62c}$$
$$\delta_j = -2(a_{j+1} - a_j) + h_j(\dot{a}_{j+1} + \dot{a}_j) \tag{4.62d}$$

One can show that, as for the case of the spline interpolation, the curvature is also continuous at each digitized point.

The Maude interpolation

The method was first proposed by *Maude (1973)* to be used by a computer for plotting accurately a function on a graph plotter. We consider here the one-dimensional case in the range $\left[t_j, t_{j+1}\right]$ where two compatible functions $f_j(t)$ and $f_{j+1}(t)$ are used. The interpolating function in the interval is given by their weighted average:

$$\mathcal{M}_j(t) = W_M(t)f_j(t) + \left[1 - W_M(t)\right]f_{j+1}(t) \tag{4.63}$$

$W_M(t)$ is the chosen weighting function:

$$W_M(t) = (1 - \lambda)^2(1 + 2\lambda) \tag{4.64}$$

which has the following properties:

$$W_M(t_j) = 1 \tag{4.65a}$$
$$W_M(t_{j+1}) = 0 \tag{4.65b}$$
$$W_M(1 - \lambda) = 1 - W_M(\lambda) \tag{4.65c}$$
$$W_M(t_j) = W(t_{j+1}) \tag{4.65d}$$

The values of $f_j(t)$ can simply be chosen as the known a_j, but this yields the trivial case where the final interpolation $\mathcal{M}_j(t)$ possesses horizontal slopes at each digitized point (see *fig. IV.7c*). This case provides a suitable interpolation when the actual digitized points are only peaks or throughs:

$$\mathcal{M}_j(t) = (1 - \lambda^2)(1 + 2\lambda)a_j + \lambda^2(3 - 2\lambda)a_{j+1} \tag{4.66}$$

A more general interpolation is achieved when the function $f_j(t)$ and $f_{j+1}(t)$ are two polynomials of second order: one $f_j(t)$ fitting exactly a_{j-1}, a_j, a_{j+1} and the other $f_{j+1}(t)$ fitting exactly a_j, a_{j+1}, a_{j+2}. Both functions can be expressed in terms of the second order Lagrange polynomials:

$$f_j(t) = \sum_{k=j-1}^{j} a_k L_{2j-k+1}(t) \tag{4.67}$$

and $W_M(t)$ takes the form:

$$W_M(t) = \sum_{k=j-1}^{j} 1 - 2(t-t_k)L_{1,k-j+1}{}'(t_k)\, L^2_{1,k-j+1}(t_k) \tag{4.68}$$

The explicit Maude interpolation may be written:

$$\mathcal{M}_j(t) = (1-\lambda)^2(1-2\lambda)(A_j\lambda^2 + B_j\lambda + a_j) + \lambda^2(3-2\lambda)(C_j\lambda^2 + D_j\lambda + a_j) \tag{4.69}$$

where

$$A_j = \frac{a_{j+1}\dfrac{h_{j-1}}{h_j} - a_j\left(\dfrac{h_{j-1}}{h_j} + 1\right) + a_{j-1}}{\dfrac{h_{j-1}}{h_j}\left(\dfrac{h_{j-1}}{h_j} + 1\right)} \tag{4.70a}$$

$$B_j = \frac{a_{j+1}\left(\dfrac{h_{j-1}}{h_j}\right)^2 - a_j\left[\left(\dfrac{h_{j-1}}{h_j}\right)^2 - 1\right] - a_{j-1}}{\dfrac{h_{j-1}}{h_j}\left(\dfrac{h_{j-1}}{h_j} + 1\right)} \tag{4.70b}$$

$$C - j = \frac{a_{j+2} - aj + 1\left(\dfrac{h_{j+1}}{h_j} + 1\right) + a_j\dfrac{h_{j+1}}{h_j}}{\dfrac{h_{j+1}}{h_j}\left(\dfrac{h_{j+1}}{h_j} + 1\right)} \tag{4.70c}$$

$$D_j = \frac{-a_{j+2} - aj + 1\left(\dfrac{h_{j+1}}{h_j}\right)^2 - a_j\left[\left(\dfrac{h_{j+1}}{h_j}\right)^2 - 1\right]}{\dfrac{h_{j+1}}{h_j}\left(\dfrac{h_{j+1}}{h_j} + 1\right)} \tag{4.70d}$$

Expressed in terms of *Eq. 4.50*, we get:

$$\alpha_j = a_j \tag{4.71a}$$

$$\beta_j = B_j \tag{4.71b}$$

$$\gamma_j = A_j \tag{4.71c}$$

$$\delta_j = -3(B_j - D_j) \tag{4.71d}$$

$$\epsilon_j = -3(A_j - C_j) + 2(B_j - D_j) \tag{4.71c}$$

$$\zeta_j = 2(A_j - C_j) \tag{4.71f}$$

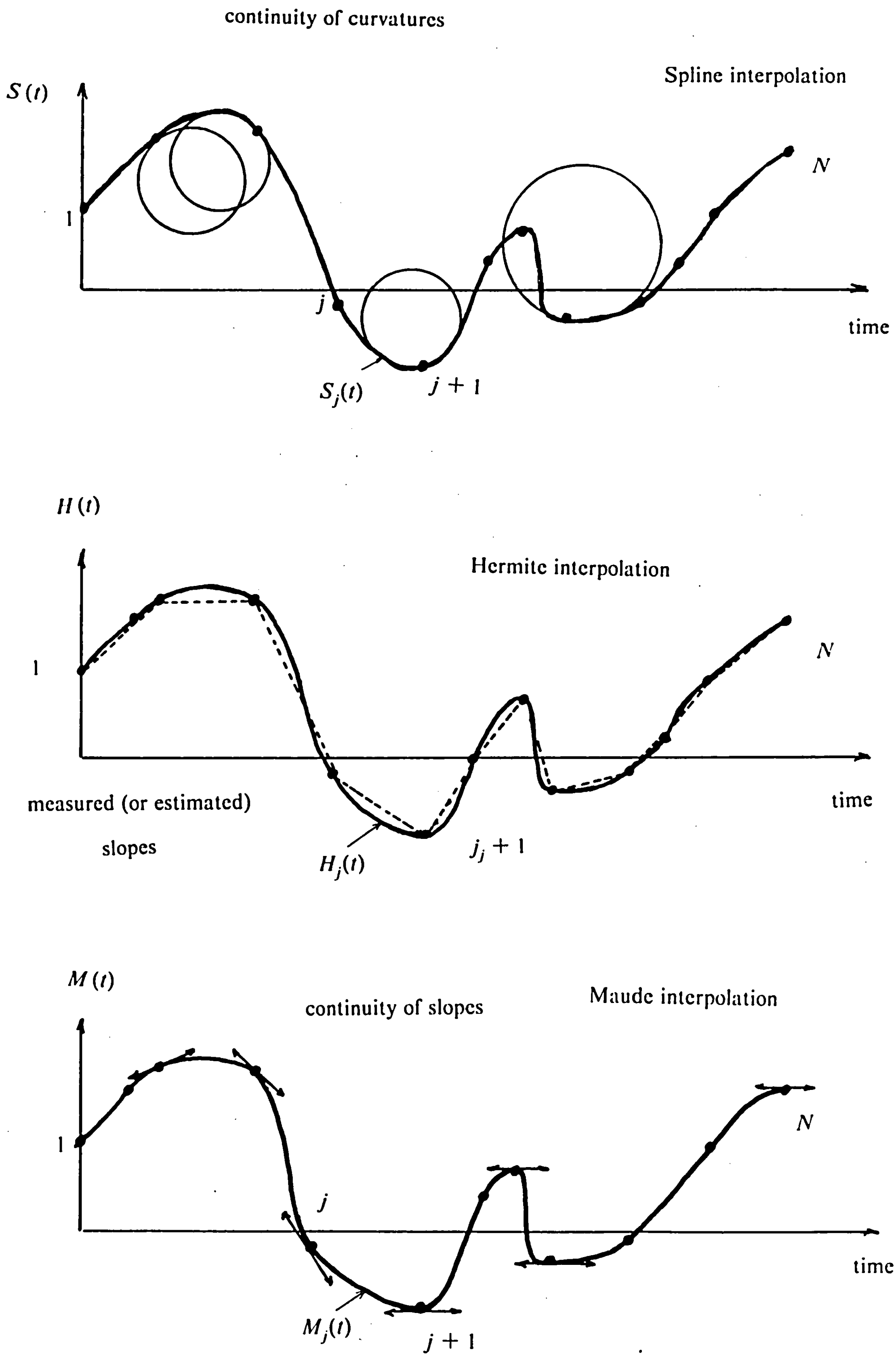

Fig.IV.7

The 3 types of non-linear interpolation

4.4.3 Comparison of the non-linear interpolations

In order to assess the improvement achieved by non-linear interpolations and to compare between them, an experiment was performed with a testing function: The Berlage Function:

$$B(t) = te^{-t}\sin \pi t \qquad (4.72)$$

and its interval $0-5$ sec was studied. The Berlage function provides large similarities with simple acceleration signals and depends only on a few parameters. The particular case retained here gives a predominant frequency of the order of 1 sec. But this choice does not affect the analysis since any compression of the time axis will yield the same results at another frequency. Only peaks of this function were taken as "pseudo-digitized points" for the comparison as this choice worsens the signal recovery. The different interpolations are shown on *fig. IV. 8a/b/c* and the quantitative comparison is presented on table VIII a and b.

The chosen quality criteria were the L_2-norm and the L_∞-norm usually used to compare the "distance" between two functions. They are defined respectively as:

$$L_2\text{-norm} = \int_0^T \left[B(t) - B(t)\right]^2 dt \qquad (4.73a)$$

$$L_\infty\text{-norm} = \int_0^T \mid B(t) - B(t) \mid dt \qquad (4.73b)$$

where $B(t)$ is the analogue recovered function.

It is immediately visible that the Maude interpolation provides a very good signal recovery whereas the spline interpolation lacks from accuracy near the peaks. Numerically the "goodness" of fit of the latter is of the same order as the linear interpolation, but for different reasons. The linear interpolation is functionaly insufficient (too simple) whereas the spline interpolation requires a particular choice for the points to be picked-up and the peaks are not particularly good ones. The zero locations of the Tchebichev function would certainly be a solution but this choice is unrealistic as regard to the actual process of human digitization. An automatic sampling could be advantageouly used.

The Hermite interpolation is very promissing, although only approximate values for slopes have been introduced. If reasonable values for these slopes at digitized points can be obtained, this method should be retained since it shapes the acceleration function according to a measured information. In the meantime, the very satisfactory Maude interpolation should be used.

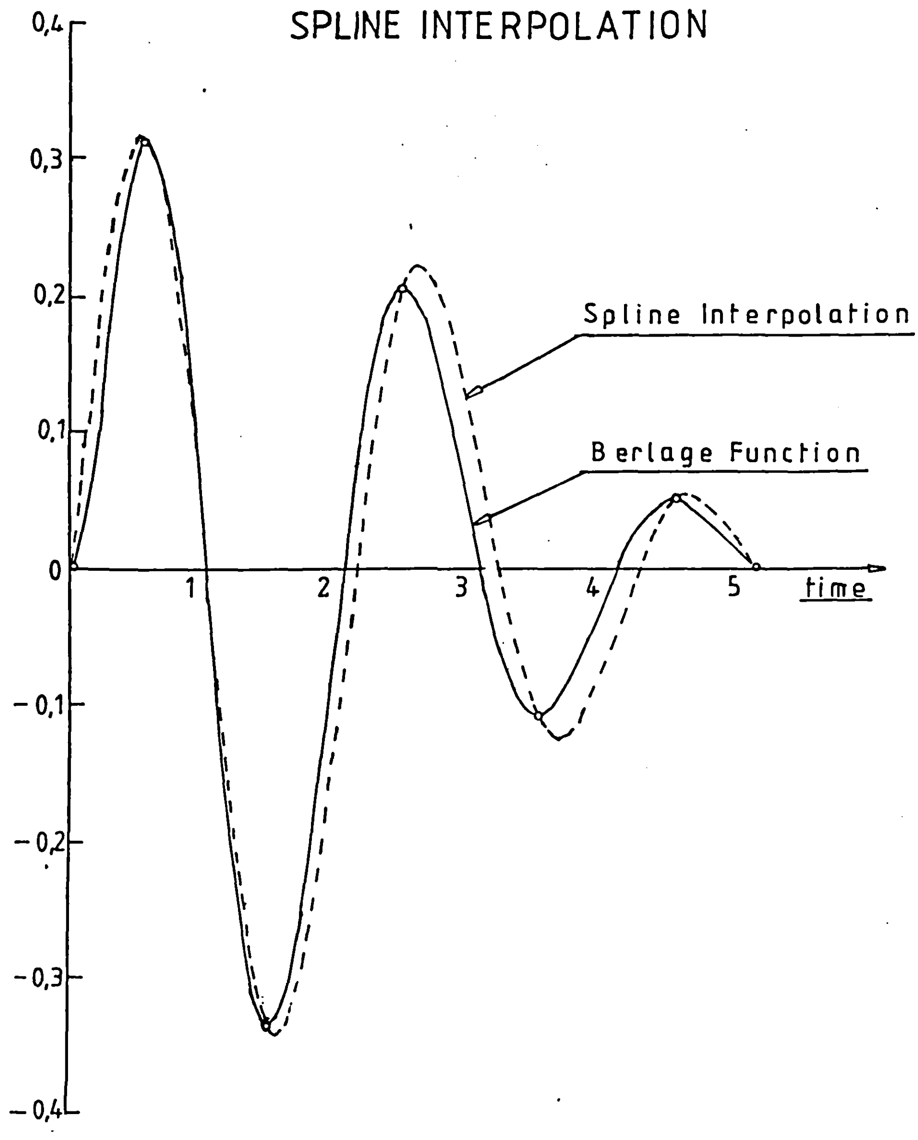

Fig.IV.8a
Comparison of the Berlage function
with a Spline interpolation

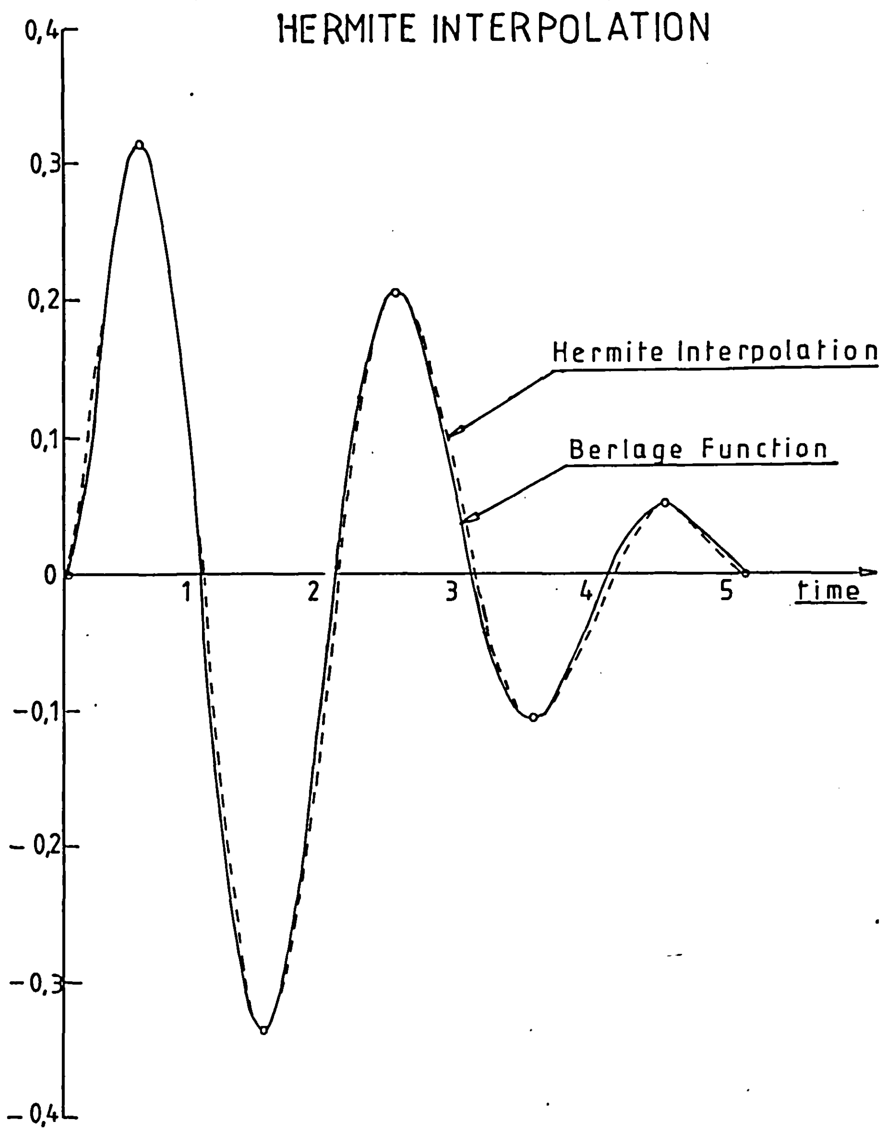

Fig.IV.8b
Comparison of the Berlage function
with a Hermite interpolation

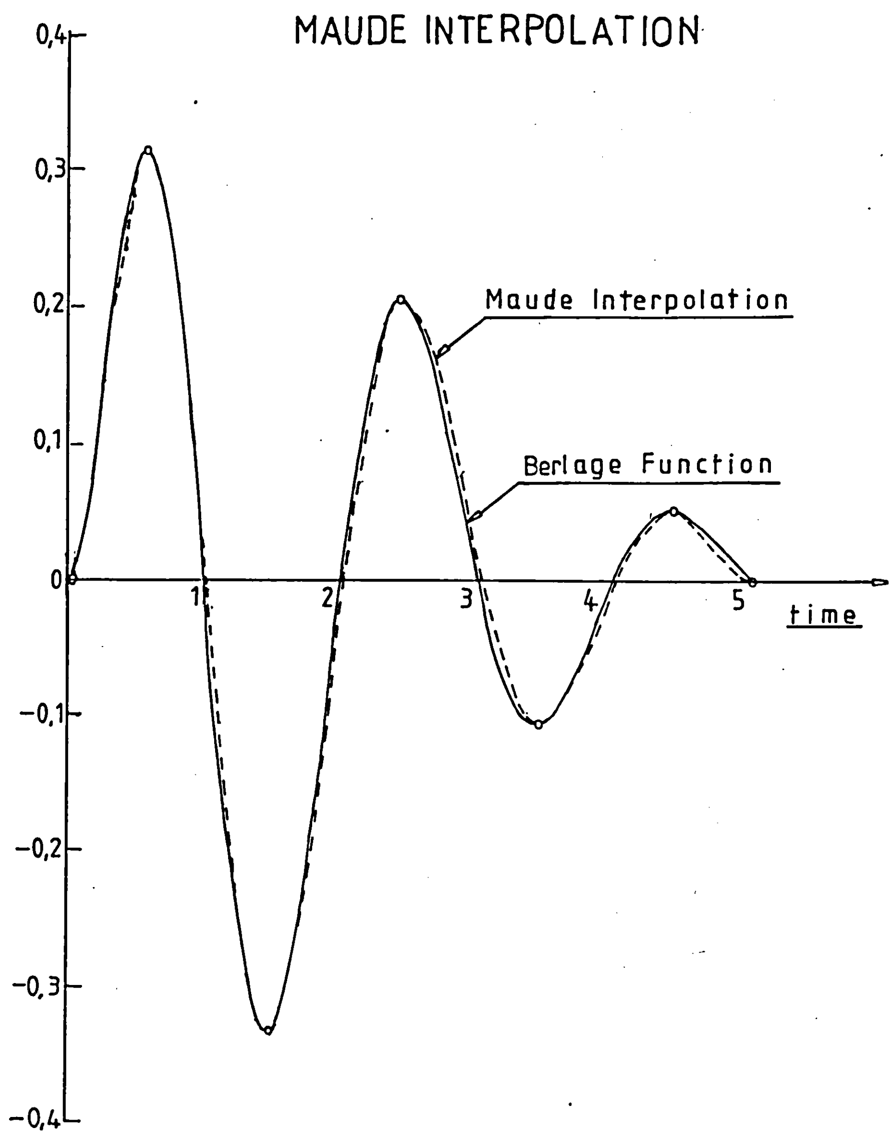

Fig.IV.8c

Comparison of the Berlage function with a Maude interpolation

Table VIII a

Comparison of non-linear Interpolations

L_2-norm $\sigma \times 10^2$

zones / *methods*	1	2	3	4	5	6	*total*
Linear	2.378	5.047	5.202	2.637	1.359	0.574	3.5
Spline	5.123	1.906	5.895	5.724	3.589	0.963	4.400
Hermite	0.968	0.958	1.561	1.188	0.676	0.340	1.063
Maude	0.739	0.958	1.561	1.188	0.676	0.592	1.054

Table VIII *b*

Comparison of non-linear Interpolations

L_∞-norm $|\delta|$

zones / *methods*	1	2	3	4	5	6	*total*
Linear	0.340	0.785	0.900	1.211	1.380	0.471	0.810
Spline	1.002	0.614	0.911	1.015	0.666	0.782	
Hermite	0.105	0.085	0.130	0.151	0.102	0.079	0.109
Maude	0.070	0.091	0.141	0.137	0.095	0.091	0.098

4.4.4 Adjustments and integrations of non-linearly interpolated accelerations

In the various cases of non-linear interpolated acceleration functions studied in the previous section, the results are expressed by an ensemble of coefficients at each particular value of time:

$$(a_j,\ t_j) \qquad \text{measured values}$$

$$(\alpha_j,\ \beta_j,\ \gamma_j, ... \qquad \text{coefficients of polynomial}$$

$$j = 1, ..., N-1$$

The recovered analogue function is then expressed by *Eq. 4.50.* The different types of adjustments described at the beginning of this chapter and the successive integrations of acceleration are straightforward. We obtained the following formulae.

Linear adjustment

The only required terms are those entering in expession of *Eq. 4.14b* For instance, the column matrix $\{M\}$ in *Eq. 4.17* has its terms given by:

$$\int_0^T a(t)\,dt = \sum_{j=1}^{N-1} \int_0^1 \left[\alpha_j + \beta_j\lambda + \gamma_j\lambda^2 + ...\right] h_j\,d\lambda \tag{4.74a}$$

$$= \sum_{j=1}^{N-1} h_j\left[\alpha_j + \frac{\beta_j}{2} + \frac{\gamma_j}{3} + ...\right] \tag{4.74b}$$

$$\int_0^T ta(t)\,dt = \sum_{j=1}^{N-1} \int_0^T (t_j + h_j\lambda)\left[\alpha_j + \beta_j\lambda + \gamma_j\lambda^2 + ...\right] h_j\,d\lambda \tag{4.75a}$$

$$= \sum_{j=1}^{N-1} h_j\left[\alpha_j\frac{t_j + t_{j+1}}{2} + \beta_j\frac{t_j + 2t_{j+1}}{6} + \gamma_j\frac{t_j + 3t_{j+1}}{12} + ...\right] \tag{4.75b}$$

All other terms are obtained in the same way but their formulae are still more lengthy.

Simple and Double Integrations

The velocity and displacement functions are simply given by the integrations of *Eq. 4.50.* Denoting by τ the time in the interval $m+1$ at which velocity is computed:

$$t_m < \tau = \lambda_1 h_m < t_{m+1}$$

We have the following expressions, very easy to compute for each interval on a computer:

$$v(\tau)\int_0^{\tau} a(t)\,dt = \sum_{j=1}^{m}\int_0^{1}\left[\alpha_j + \beta_j\lambda + \gamma_j\lambda^2 + \dots\right]h_j\,d\lambda + \int_0^{\lambda_1}\left[\alpha_m + \beta_m\lambda + \gamma_m\lambda^2 + \dots\right]h_m\,d\lambda \tag{4.76a}$$

$$v(\tau) = \sum_{j=1}^{m} h_j\left[\alpha_j + \frac{\beta_j}{2} + \frac{\gamma_j}{3} + \dots\right] + h_m\left[\alpha_m\lambda_1 + \beta_m\frac{\lambda_1}{2} + \gamma_m\frac{\lambda_1}{3} + \dots\right] \tag{4.76b}$$

$$d(\tau) = \int_0^{\tau} v(t)\,dt = \sum_{j=1}^{m}\int_0^{1}\int_0^{\lambda}\left[\alpha_j + \beta_j\kappa + \gamma_j\kappa^2 + \dots\right]h_j\,d\lambda\,d\kappa + \int_0^{\lambda_1}\int_0^{\lambda}\left[\alpha_m + \beta_m\kappa + \gamma_m\kappa^2 + \dots\right]h_m\,d\lambda\,d\kappa \tag{4.77a}$$

$$d(\tau) = \sum_{j=1}^{m} h_j\left[\frac{\alpha_j}{2} + \frac{\beta_j}{3} + \frac{\gamma_j}{4} + \dots\right] + h_m\left[\alpha_m\frac{\lambda_1^2}{2} + \beta_m\frac{\lambda_1^3}{3} + \gamma_m\frac{\lambda_1^4}{4} + \dots\right] \tag{4.77b}$$

CHAPTER V

THE USE OF FILTERS

5.1 INTRODUCTION

In the previous chapter, attempts were made to remove low frequency contamination by subtraction of some low degree polynominals, assumed to carry most of the undesired noise. Accurate analysis of acceleration noise was performed by *Trifunac et al. (1973)* and a Digitization Noise model was proposed in Chapter III. These studies have shown that the frequency content of the time acceleration noise is relatively high, both in the low frequency and in the high frequency ranges. *Fig. III. 22* showed this noise by comparison to the Fourier Spectrum and *Fig. V. 1* also adjusts it relatively to various cases, at a fixed distance for shocks of magnitude 4 to 7. *Fig. V. 2* shows a similar graph but this time emphasizing the epicentral distance effect for a constant magnitude of 6. In chapter III, we noticed that most of this noise could be explained by digitization, and that a noise model has been proposed, with the digitization equipment as principal parameter.

Even though other sources of noise are added, it is clear that the noise is predominant both in the low and high frequencies. In the middle range of the spectrum, its relative influence is much less noticable. In order to minimize its influence in the acceleration signal, filtering of both the extremes of the spectrum, where the noise/signal ratio is too high, was therefore suggested (*Trifunac, 1971*).

The determination of the frequency limits, where one may say that it is judicious to operate this filtering, is not a simple matter since it depends on the noise level, on one hand and in the magnitude and distance of the earthquake, on the other. In an attempt to standardize the processing procedure, *Trifunac* proposed to filter at the fixed values of 0.07 Hz and 25 Hz, but it must be recognized that these values are strongly dependent on the type of digitizing equipment used (a Benson-Lehrer 099D Datareducer in that case). A better approach consists in assessing these limits, as a function of the Magnitude of the shock, the distance of the recording station, the digitizing equipment and the operator experience, as developed in section 3.4.3.

By filtering, it is hoped to recover accurately the ground motion, not only in its acceleration form but also in its velocity and displacement form. It is vital to realise that efficient filtering must be performed since we cannot accept a procedure which would contaminate the records beyond non admissible bounds and therefore would render the correction process illusive.

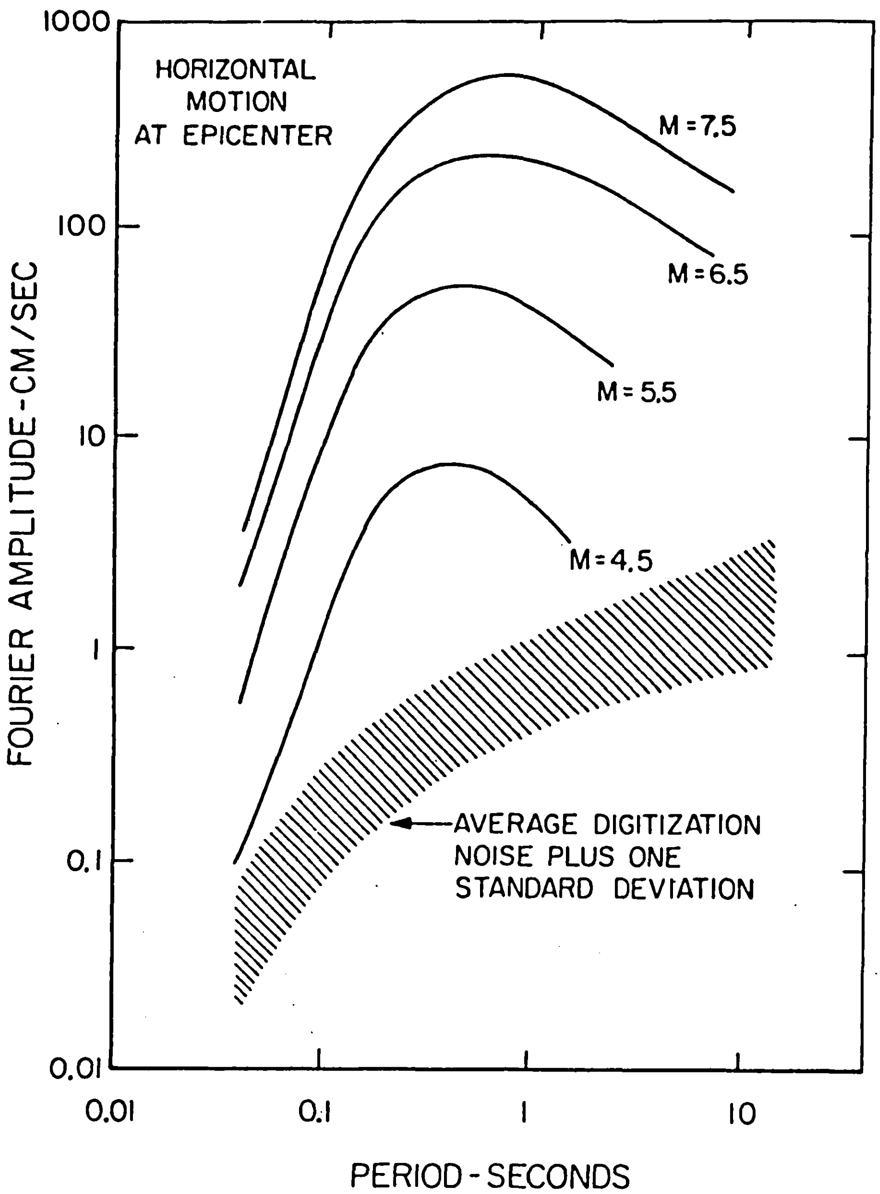

Fig.V.1

Typical FAS of ground acceleration at the epicenter, for various Magnitudes, by comparison with digitization noise. (after *Trifunac (1976)*

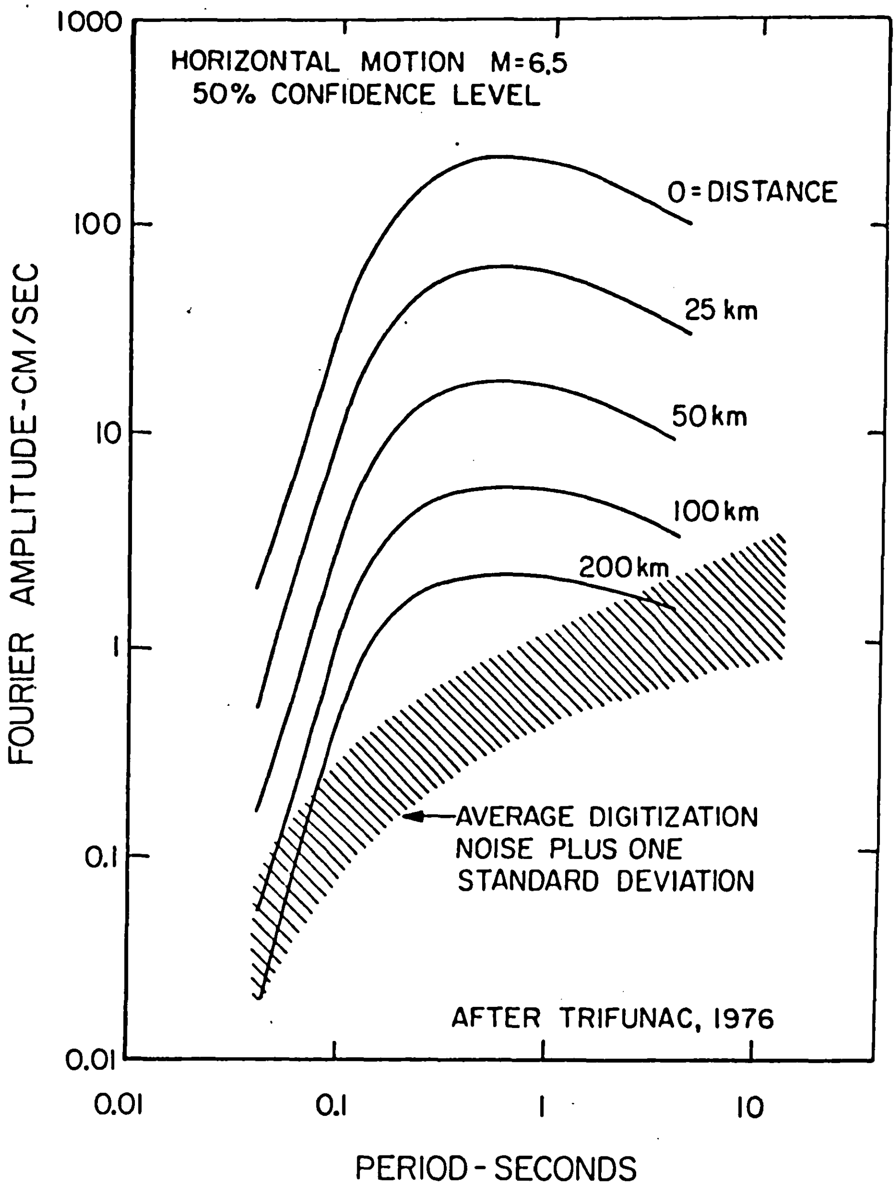

Fig.V.2

Typical FAS of ground acceleration of Magnitude $M_L = 6.5$ at various distances, by comparison with digitization noise. (after *Trifunac (1976)* blank page

5.2 THE TRIFUNAC BASE-LINE CORRECTION

The method was first proposed in 1971 as the Caltech new standard strong motion data processing procedure. After a few years of extensive use, it was noticed that it suffered from built-in distorsions due to the difficult implementation of the filter particularly in the low frequency range. *Fletcher et al. (1977)* recognised that improvements were needed and several investigators suggested modifications (*Basili and Brady 1978*). Today changes of minor extent are still introduced (*Lee, 1984*). The full procedure can be divided into two correction phases:

1. a transducer correction in the time domain, using a central difference approximation and a sampling period of 0.02 sec (see chapter VI). 2. a base line correction including a sucessive series of smoothings and filterings as shown in *Fig. V.3.*

The filter used by *Trifunac*, known as the *Ormsby* filter, was developed in the early sixties for application to missile data processing. The pass-band filter is implemented as a combination of low-pass *Ormsby* filters and consequently it suffices to evaluate the performance of the low pass version of this filter and apply the result successively to low and high frequency (*fig. V.4*)

5.2.1 The digital filtering equations

A general linear filtering process of a causal analogue signal $x(t)$ is achieved in the time domain by a linear weighting operation relating the input $x(t)$ to the output $y(t)$ by means of inpulse response function $h(t)$ through the causal convolution integral:

$$y(t) = \int_{-\infty}^{t} x(\tau)h(t-\tau)\,d\tau \tag{5.1}$$

where

$$h(t) = \frac{1}{\pi}\int_{0}^{\infty} |H(i\omega)|\cos[\omega t - \theta(\omega)] \tag{5.2}$$

In this equation

$$H(i\omega) = |H(i\omega)|e^{-i\theta(\omega)} \tag{5.3}$$

is the complex filter function. The problem consists then of the determination of the impulse response $h(t)$ for a given $H(iw)$.

The amplitude and phase shift of the ideal low-pass filter without phase distorsion are such that (*fig. V.5*):

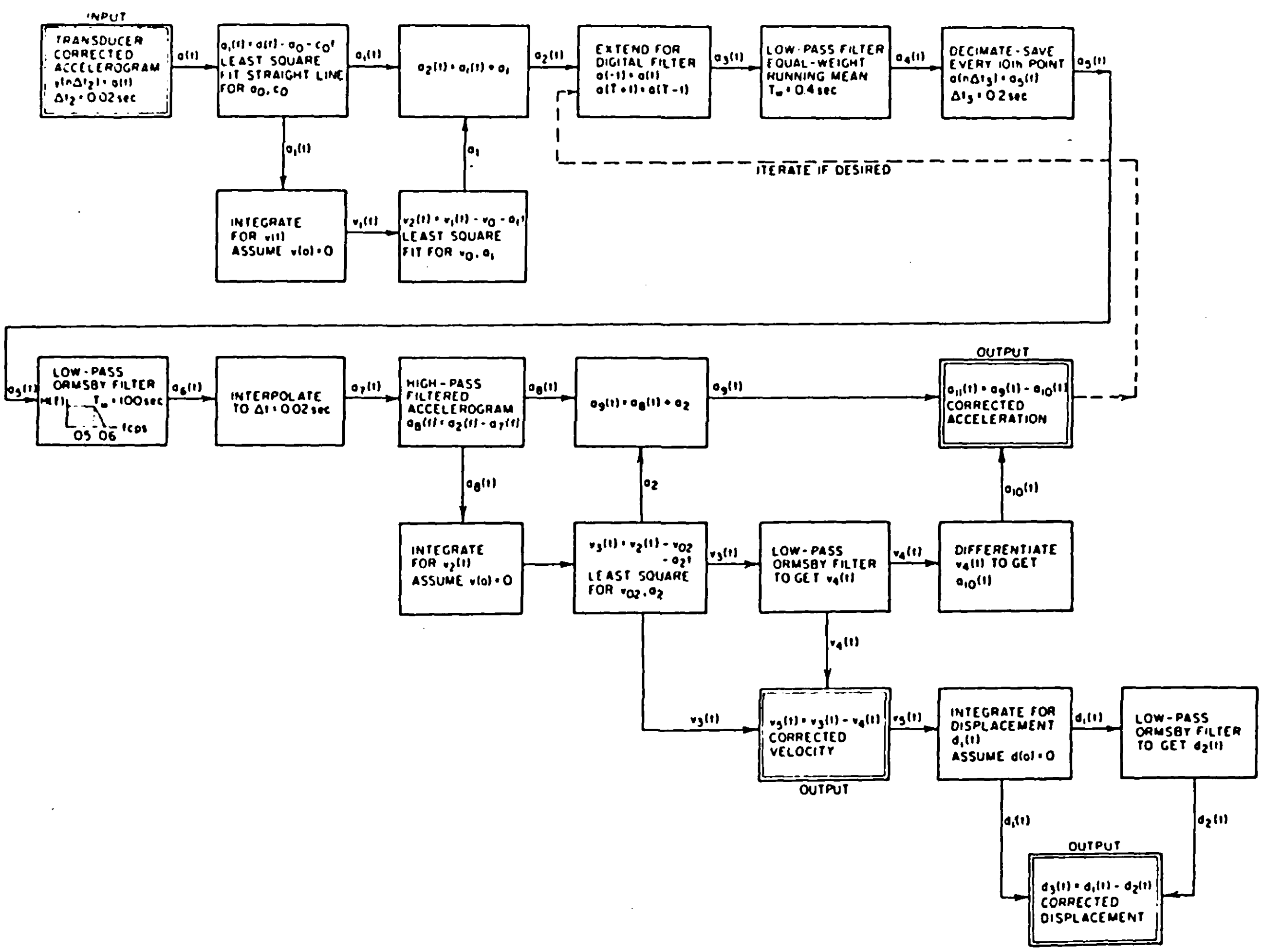

Fig.V.3

Schematic diagram of the Standard Correction Procedure

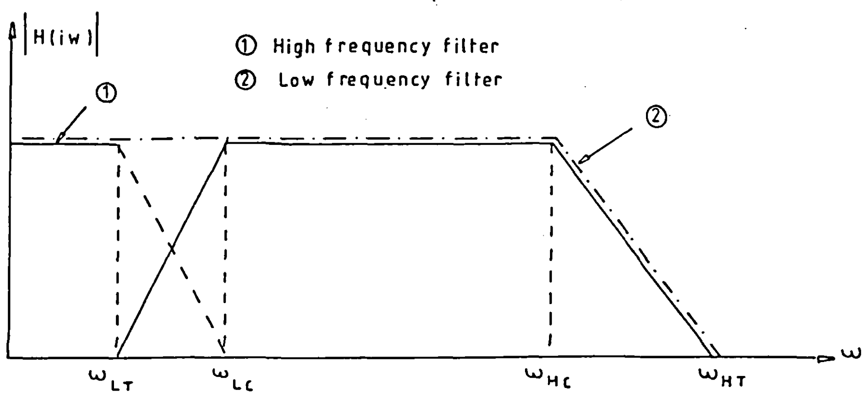

b) combination of the filters to achieve a pass-band filter

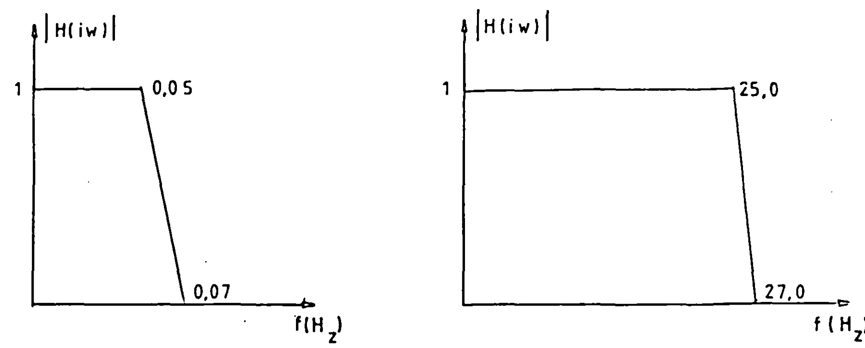

Fig.V.4

Representation of the high and low frequency filters of the *Ormsby* type

a) individual filters with typical cutoffs

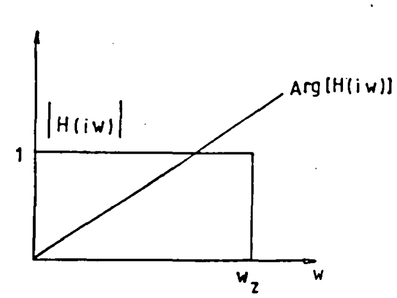

Fig.V.5

Amplitude and phase of a perfect low-pass filter

$$|H(i\omega)| = \begin{cases} 1 & \text{for } |\omega| \le \omega_C \\ 0 & \text{for } |\omega| \ge \omega_C \end{cases} \qquad \begin{matrix}(5.4a)\\(5.4b)\end{matrix}$$

$$\theta(\omega) = \omega t_0 \qquad (5.4c)$$

ω_C is the perfect circular frequency cutoff.

This yields a weighing function:

$$h(t) = \frac{1}{\pi}\int_0^{\omega_C} \cos\omega(t-t_0)\,d\omega = \frac{\sin\omega_C(t-t_0)}{\pi(t-t_0)} \qquad (5.5)$$

This $h(t)$ is not realisable since it has a continuous analytic expression which extends from $-\infty$ to $+\infty$. In order to implement this filter on a numerical computer, two alterations have to be carried out.

1. the limitation of its duration since infinity is not accessible.

2. the discretisation of the impulse response $h(t)$, for digital computer treatment.

In doing so, the charateristics of the ideal filter are modified (*fig. V.6*):

- the frequency function has become $H_r(i\omega)$ the convolution of the original $H(i\omega)$ with the Fourier Transform of the applied box-car window $w(t)$ of length T:

$$H_r(i\omega) = \frac{1}{2\pi}\left[H(i\omega) \quad * \quad \frac{2\sin\omega T/2}{\omega}\right]e^{-i\omega T/2} \qquad (5.6)$$

- the sampling in time at a frequency ω_s has rendered the frequency function periodic with period $2\pi/\omega_s$.

The observable roll-off about $\omega = \pm\,\omega_C$ and the undesirable ripples in the pass-band and the stop-band are dependent on the type and length of the applied time window $w(t)$. The phase characteristic has remained unchanged.

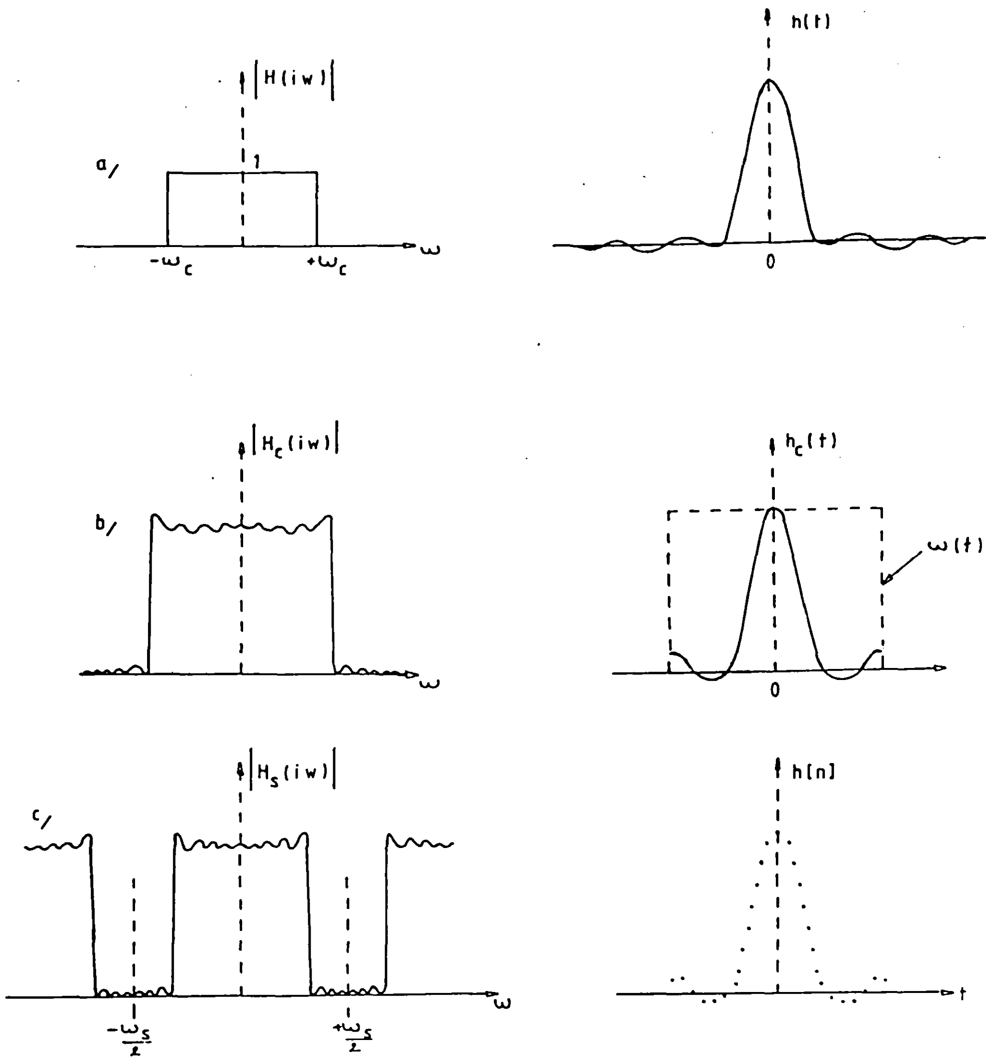

Fig.V.6

Amplitude distorsions of a real digital filter

a) the perfect target filter

b) frequency effect of time truncation

c) frequency effect of time discretization

5.2.2 The Ormsby filter

In order to achieve such a filter with unity gain and zero phase shift, *Ormsby* suggested, for the controlling frequency function $H(i\omega)$, the following expression (*fig. V.7*):

$$|H(i\omega)| = \begin{cases} 1 & \text{for } |\omega| \leq \omega_C \\ sgn(\omega)\dfrac{\omega_T - \omega}{\omega_T \omega_C} & \text{for } \omega_C < |\omega| < \omega_T \\ 0 & \text{for } |\omega| \geq \omega_T \end{cases} \tag{5.7}$$

ω_C = cutoff frequency

ω_T = roll-off termination frequency

$\omega_T - \omega_C$ = roll-off width (transition band).

The true frequency function $H_r(i\omega)$ exhibits ripples in the pass-band and the stop-band; they are controlled by widening the transition band. *Trifunac* (1971) suggested a roll-off of $\Delta f = 2\pi/(\omega_C - \omega_T) =$ 0.02 Hz between $f_T = 0.05$ Hz and $f_C = 0.07$ Hz in the low frequency. In the high frequency a roll-off of 2 Hz between $f_C = 25$ Hz and $f_T = 27$ Hz has been chosen.

In terms of discrete data the expression for linear digital filter is obtained by introducing $h[n]$, the sampled version of $h(t)$ for $= n\Delta t$, $n = -\infty, ..., -1, 0, +1, ..., +\infty$, and the continous convolution (*Eq. 5.1*) becomes:

$$y[n] = \sum_{k=-\infty}^{+\infty} h[k]x[n-k] \tag{5.8}$$

The impulse response $h(t)$ associated with $H(i\omega)$ is given by:

$$h(t) = \frac{1}{2\pi} \int_{-\infty}^{+\infty} H(i\omega)e^{i\omega t}\, d\omega \tag{5.9}$$

and, after some algebra is found to be:

$$h(t) = \frac{\cos \omega_C t - \cos \omega_T t}{\pi(\omega_T - \omega_C)t^2} \tag{5.10}$$

Its sampled version $h[n]$ is readily evaluated from $h(n\Delta t)$ where $\Delta t = 2\pi/\omega_s$ is the constant sampling period:

$$h[n] = \frac{\cos 2\pi n\lambda_C - \cos 2\pi n\lambda_T}{2\pi^2 n^2(\lambda_T - \lambda_C)} \tag{5.11}$$

where $\lambda_C = \omega_C/\omega_s$ and $\lambda_T = \omega_T/\omega_s$.

Finally, for the filter to be realisable, it is necessary to window the infinite impulse response sequence within a duration $T = N\Delta t$; it becomes:

$$h_r[n] = h[n] \quad \text{only for} \quad -\frac{N-1}{2} \leq n \leq \frac{N+1}{2} \tag{5.12}$$

It follows that the discrete filter output is now expressed by:

$$y[n] = \sum_{k=-(N-1)/2}^{(N+1)/2} h[k]x[n-k] \tag{5.13}$$

Ormsby studied empirically the error

$$\epsilon = \max\{|H_r(i\omega)| - |H(i\omega)|\}$$

when a limited number of points $N = 2M + 1$ is used, as a function of the sharpness of the roll-off

$$\lambda_R' = c\frac{\omega_T - \omega_C}{\omega_s} \tag{5.14}$$

The c values 1.2, 1.5, 2.0 were investigated and the number M was half the number of required points.

His numerical results covered:

$$0 < \lambda_C < 0.4 \tag{5.15a}$$

$$0.05 < \lambda_R < 0.1 \tag{5.15b}$$

$$10 < M < 100 \tag{5.15c}$$

and he produced the graph of the *fig. V.8*. From it, he suggested an approximate formula to help in the determination of the window length:

$$M\lambda_R' \approx \frac{0.012}{\epsilon} \tag{5.16}$$

This shows that the number of points required $2M + 1$ is inversely proportional to the roll-off width.

With the roll-off widths of 0.02 Hz and 2 Hz chosen respectively for the low and high frequencies, and assuming $f_s = 50$ Hz ($\Delta t = 0.02$ sec), the values $2M + 1$ and the duration L of the impulse response can be computec ' table IX').

It is visible that the low frequency filter involves a large number of points. As a consequence the length of the impulse response may become larger than most of the acceleration records to be treated. Furthermore the accepted error ϵ is certainly not always accurate, since, in this case, M is out of range of the *Ormsby's* investigation. A partial solution would be to work with a smaller interval of time Δt. To overcome this difficulty *Trifunac* prefered to operate a preliminary low pass filter using an equally weighted running mean filter, with a window width $T_{w_C} = 0.40$ sec (*fig. V.9*).

The transfer function $H(i\omega)$ of such a filter is:

$$H_1(i\omega) = \int_{-T_w/2}^{+T_w/2} \frac{1}{T_w} e^{-i\omega t} dt \tag{5.17a}$$

$$= \frac{\sin \omega T_w/2}{\omega T_w/2} \tag{5.17b}$$

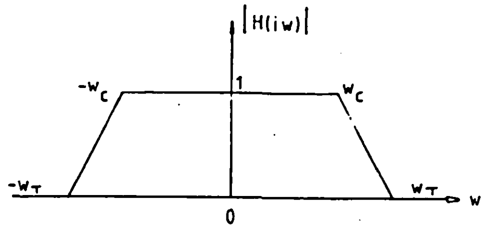

Fig.V.7

The roll-off of the *Ormsby* filter
used to reduce frequency distorsions

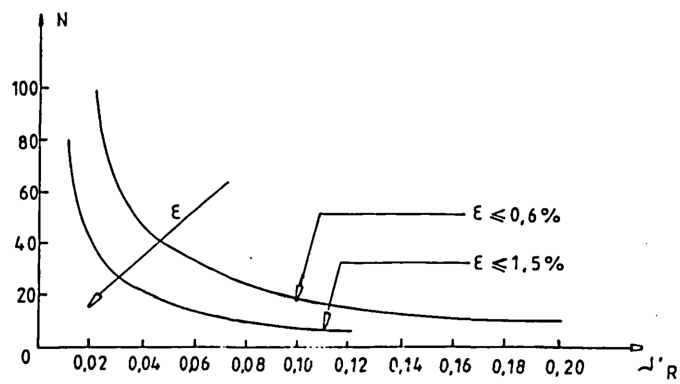

Fig.V.8

Half the number of points required in the *Ormsby* filter
to achieve an accuracy ϵ as a function of the roll-off

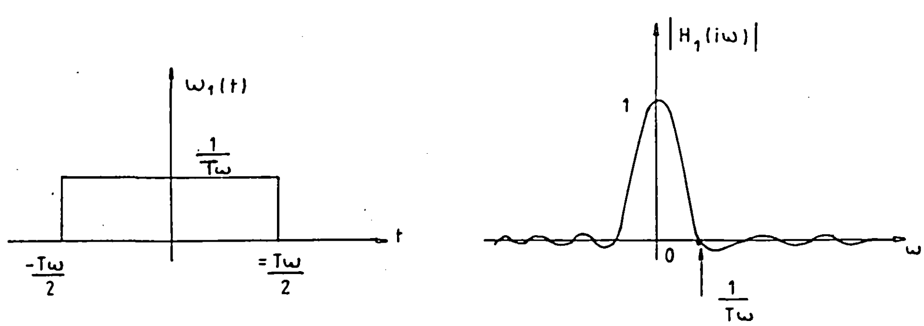

Fig.V.9

Principle of the mean running filter

When $w_1(t)$ is sampled at time interval Δt and the discrete weights are $w[n] = w(n\Delta t).\Delta t$, the frequency function becomes periodic with period $\omega_s = 2\pi/\Delta t$:

$$H_{1,\Delta t}(i\omega) = \frac{1}{\pi T_w} \sum_{n=-\infty}^{+\infty} \frac{\sin \pi T_w (\lambda - n)/\Delta t}{(\lambda - n)} \tag{5.18}$$

where $\lambda = \omega/\omega_s$ is the normalised frequency.

Fig. V.10a and b show the actual frequency functions of the *Ormsby* filter designed for a cutoff frequency $f_C = 0.07$ Hz and a roll-off frequency termination $f_T = 0.05$ Hz with a sampling interval $\Delta t = 0.2$ sec. *Fig. V.11* is a representation of the obtained frequency function corresponding to a box-car window of length $T_w = 0.40$ sec. with $\Delta t = 0.02$ sec. The maximum error in the low frequency is of the order of 6 % of the unit gain, whereas, with 3 %, the performance is slightly better in the high frequency, due to the smoother, in comparison, discontinuity.

In both cases the phase shift is strictly linear.

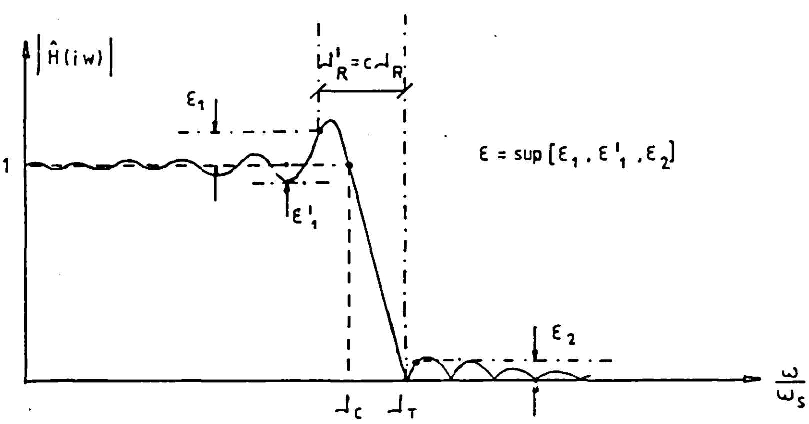

a) low frequency

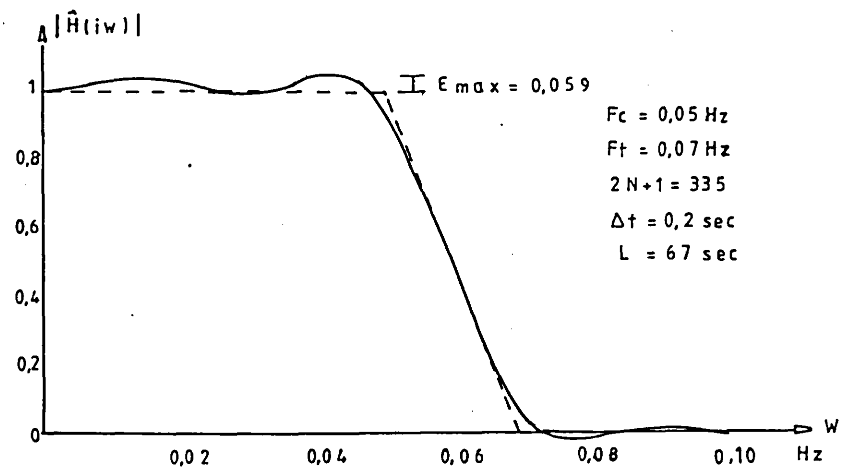

Ormsby filter in low frequencies

b) high frequency

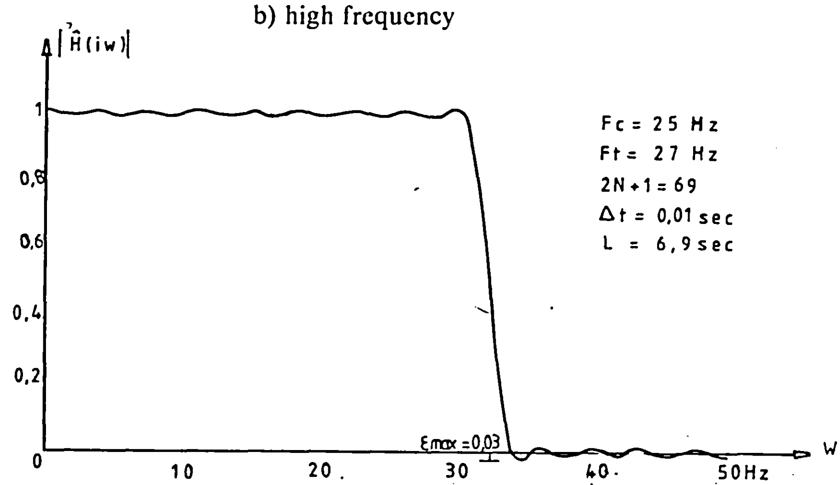

Ormsby filter in high frequencies

Fig.V.10

Numerical values and performances of the *Ormsby* filter commonly used:

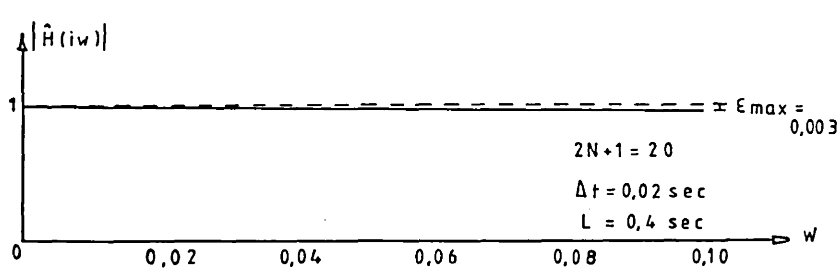

Mean running filter

Fig.V.11

Numerical values and performance of the mean running filter

5.2.3 Limitations and improvements of the method.

The *Trifunac* base line correction suffers however from some limitations which are in some cases very significant. It is frequently observed that the corrected displacements still contain unexpected low periods which should have been eliminated after the records have been treated. To avoid this, it is necessary to filter the three time histories (acceleration, velocity, displacement) successively and to detrend each of them. This procedure has the regrettable effect of masking the near field information which migth be included in the records. The process can only be justified when the station is located far away from the fault and when no local permanent displacement is likely to be present. In this condition, the assumption of zero mean and zero first moment is fulfilled since the propagation path has been long enough to transform the displacement function into an oscillation more or less symetric about the base line.

In all steps of the procedure, to high-pass filter acceleration, velocity or displacement, the routine uses decimation to reduce the length of the window and the computing time. If the original time interval between the data points is 0.02 sec, then the effective Nyquist frequency is 25 Hz. After decimation by ten, this frequency drops to 2.5 Hz. Thus some aliasing of high frequency would be expected when no suitable low-pas filter, is used before decimation. Such filter, in the form of a simple running mean filter is used before decimation in the high-pass filter of acceleration. But no similar anti-aliasing filter is applied on the velocity and displacement computations.

To correct for these insufficiencies, *Fletcher et al. (1980)* have proposed to operate three changes to improve the calculation of velocity and displacement.

1-a broadening of the ramp in the response of the high-pass filter in order to limit the ripples due to a sharp discontinuity.

2-the removal of the high-pass filter of displacement to keep the near field information included in the signal. 3-the removal of all decimation in filtering to be free from aliasing errors.

In particular point 1) had been previously thoroughly investigated by *Basili and Brady (1978)*. They also proposed a methodology for the selection of the low frequency cutoffs of the accelerograms according to seismological information and a limitation of the Fourier spectrum distorsion. Their results are mainly based on tests and are expressed with a two priority levels:

priority 1:

$$f_C \geq \frac{4}{L_R} \tag{5.19a}$$

$$f_C \geq \frac{0.125}{e} \tag{5.19b}$$

$$f_C \geq 0.07\,Hz \tag{5.19c}$$

$$f_T \geq \frac{2}{L_R} \tag{5.19d}$$

$$LD_f \geq 1 \quad \text{for } \epsilon = 1.2\% \tag{5.19e}$$

$$LD_f \geq 2 \quad \text{for } \epsilon = 2.4\% \tag{5.19f}$$

priority 2:

$$f_C \leq \frac{1}{d} \tag{5.20a}$$

$$L \leq 3L_R \tag{5.20b}$$

$$f_C(orig) - f_T(final) \geq 0.8D_f(final) \tag{5.20c}$$

In this table, the cutoff frequency f_C and the roll-off frequency f_T in the low frequency range are searched for in function of:

L_R = length of the record in sec.

L = length of the *Ormsby* window in sec.

d = an estimate of the strong motion portion of the record in sec.

$D_f = f_C - f_T$ = the transition bandwidth in Hz.

Values of e refer to the study (*Hanks 1975*) of the possible spread of displacement to be expected at particular frequencies due to digitizing noise. The length of the average coherent fault rupture can be estimated from other seismological information. A crude assessment can be made from the inverse of the corner frequency (*Brune 1970, Hanks 1975*).

The bounds of the various parameters are to be treated with a reasonable amount of judgement. Even for a record whose digitization is considered ideal, it will be readily seen to be impossible to allow all parameters to assume their desirable limiting values. Judgement is therefore necessary in the selection of the parameters to insure that each is equally close to its limiting value.

Fig. V.12 shows the typical case of the Chilean earthquake of 9 July 1971 recorded at Santiago. *Fig. V.12a* represents the result of the analysis of the N10W component, treated by the unmodified *Trifunac* correction procedure. *Fig. V.12b* results from using the scheme detailed above with f_T = 0.05 Hz and f_C = 0.15 Hz. A clear improvement in the first 10 sec of the velocity function can be seen as well as the removal of large displacement value of 10 cm associated with a 20 sec period which was prove to be mostly noise.

Fig. V.13 also shows the effect of the other suggested improvements. *Fig. V.13a* is the displacement trace of the unmodified version of the afterschok of 6 August 1975 recorded at the *Oroville station DWR*

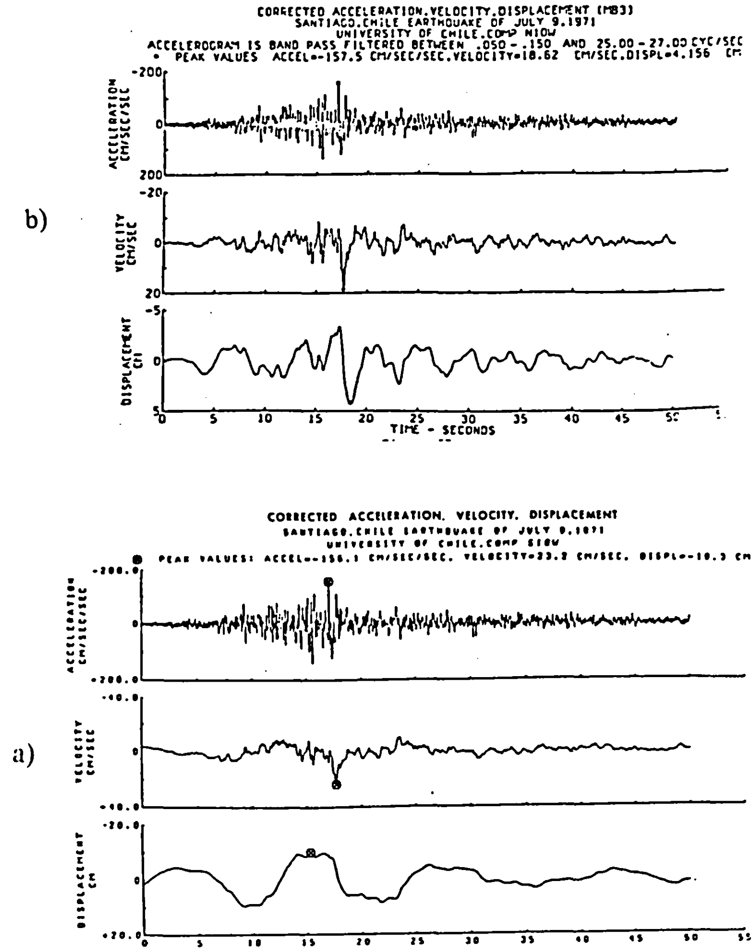

Fig.V.12

Improvement of accellration correction using the *Basili and Brady* technique

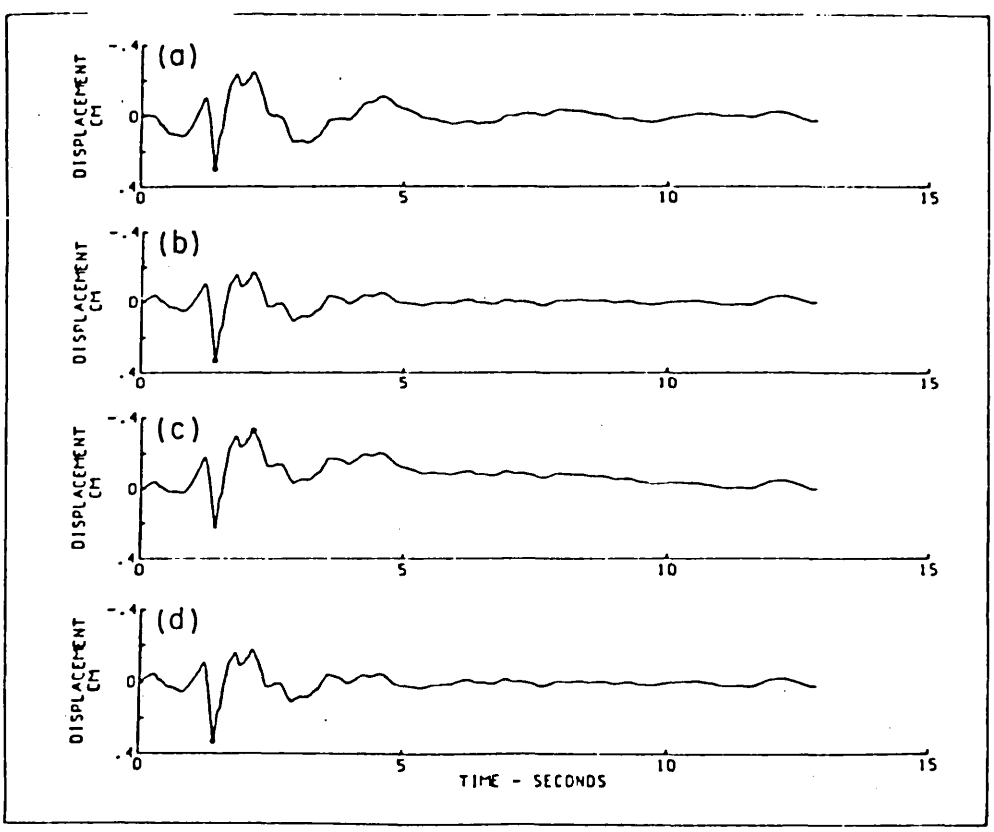

Fig.V.13

Improvement achieved by suppressing the aliasing effect of the mean running filter

(EW component). Although, the low frequency limit are $f_C = 0.33$ Hz and $f_T = 0.23$ Hz, a significant 3-4 sec oscillation is still present in the record, particularly visible in the tail of the motion.

When f_C is changed to 0.5 Hz, increasing the bandwith from 0.1 Hz to 0.27 Hz, the result in *fig. V.13b* exhibits a fair reduction of this oscillation. The case *fig. V.13c* represents the displacement when the filtering of displacement has been removed. Again spurious periods of 2-4 sec are present. This time, they are due to aliasing caused by decimation. These oscillations are surpressed when no decimation is carried out (*fig. V.13d*).

5.3 THE DISCRETE FOURIER TRANSFORM METHOD

The Discrete Fourier Transform method has been studied as soon as it was advanced that the implementation of the Ormsby filter to acceleration record processing generated unacceptable distorsions, not only due to its intrinsic inaccuracy but also due to the effect of decimation required to limit the number of points before low-pass filtering. The so called *Stanford Method* proposed by *Khemici and Shah (1982)* is based on the Discrete Fourier Method implemented with a FFT.

Once the acceleration trace has been processed in its first stage (uncorrected record), and transformed into an equally-spaced sequence, a discrete representation of its Fourier Transform can be obtained. Calling $a[n]$, $n = 0, 1, ..., N-1$, this acceleration sequence, its Fourier Transform is a complex function which can be written as:

$$A(i\omega) = \Delta t \sum_{n=0}^{N-1} a[n] e^{i\omega n \Delta t} \tag{5.21}$$

$A(i\omega)$ is such that both its amplitude and phase function are continuous (although $a[n]$ is discrete), and exhibits an even amplitude symmetry and an odd phase symmetry due to the fact that the source function is real. Furthermore, it is periodic with period $1/\Delta t$ due to the discrete character of its time sequence.

A sampled approximation of this spectrum, at constant frequency intervals $\Delta\omega$ is known as the Discrete Fourier representation of the signal and is expressed as:

$$A[k] = \Delta t \sum_{n=0}^{N-1} a[n] e^{-i2\pi kn/N} \tag{5.22}$$

where

$$\omega = k\Delta\omega = \frac{2\pi k}{N\Delta t}$$

has been used.

The range of k can be limited to the positive frequencies due to the symmetry mentioned above.

In terms of its Fourier coefficients and within the frequency range defined by the Nyquist frequency $F_N = 1/2\Delta t$, the time sequence $a[n]$ can be exactly recovered by the inverse Discrete Fourier Transform:

$$a[n] = \frac{1}{N} \sum_{k=0}^{N/2} A[k] ei 2\pi kn/N \tag{5.23}$$

The coefficients $A[k]$ are readily computed by the efficient Fast Fourier Transform, at a large number of particular frequencies. It is then a simple matter to modify these coefficients according to a predetermined frequency function $H(i\omega)$ of a filter before returning in the time domain through the inverse transformation.

Calling $H[k]$ a discrete approximation of $H(i\omega)$ at the same frequency points as $A[k]$, the corrected signal has for new time sequence:

$$a_c[n] = \frac{1}{N}\sum_{k=0}^{N/2} A[k]H[k]e^{i2\pi kn/N} \tag{5.24}$$

Unfortunately, it is well known that this simple procedure is subjected to large distorsion since it is impossible to predict the actual frequency response between the frequency points of the FFT. Moreover, the behaviour within these intervals is not very satisfactory. This effect is produced by the aliasing in the time domain and the ripples must be reduced to become more acceptable. *Fig. V.14* shows the particulrly simple case of a low-pass filter performed by this frequency sampling method. The circle points are the imposed frequency points of the discrete representation $H[k]$ of $H(i\omega)$, whereas the continuous line is the actually achieved filter $H_r(i\omega)$.

It is apparent that the distorsion introduced by the approximation of the sampling is caused by the discontinuity in the frequency response, and is accentuated for a very small transition band between the last sample in the pass-band taken to be unity and the first sample in the stop-band taken to be zero. This discontinuity in frequency domain implies a long impulse response and hence the error is caused by aliasing in the time domain due to the time limited nature of the impulse response. The reduction of this error, which increases for long records, if all capabilities of the D.F.T. are used, can be performed by frequency windowing. The width of the transition band is increased to make the discontinuity less abrupt.

One realises immediately, that the accuracy in the gain of the filter is achieved at the expense of the bandwith.*Khemici and Shah* have suggested to use the same frequency limits as those chosen in the *Trifunac method* . They achieved this frequency smoothing by replacement of the linear transition of the *Ormsby* filter by two half cosine functions controlled by the cutoff and roll-off frequencies in the low and high frequencies (*fig. V.15*).

Using the same notations as in the previous section, the expression of the filter in the frequency domain can be written (in the positive frequency half plane):

$$|H(i\omega)| = \begin{cases} 0 & \text{for } \omega < \omega_{LT} \quad \text{or } \omega > \omega_{HT} \\ 1 & \text{for} \quad \omega_{LC} \le \omega \le \omega_{HC} \\ \frac{1}{2}\left\{1 - \cos\left[\frac{1}{2D_L}(\omega - \omega_{LT})\right]\right\} & \text{for} \quad \omega_{LT} \le \omega \le \omega_{LC} \\ \frac{1}{2}\left\{1 + \cos\left[\frac{1}{2D_H}(\omega - \omega_{HC})\right]\right\} & \text{for} \quad \omega_{HT} \le \omega \le \omega_{HT} \end{cases} \tag{5.25}$$

where $D_L = \omega_{LC} - \omega LT$ and $D_H = \omega_{HT} - \omega_{HC}$ are the low anf high frequency transition bandwiths respectively. The actual transfer function of such a filter is best obtained from its Z-transform representation. The time sequence $h[n]$ corresponding to the discrete Fourier coefficients of the filter is:

$$h[n] = \frac{1}{N} \sum_{k=0}^{N/2} H[k] e^{i2\pi kn/N} \tag{5.26}$$

The Z-transform of the filter can then be written:

$$H_r(z) = \sum_{n=0}^{N-1} h[n] z^{-n} \tag{5.27a}$$

$$= \sum_{n=0}^{N-1} \left\{ \frac{1}{N} \sum_{k=0}^{N-1} H[k] e^{i2\pi kn/N} \right\} z^{-n} \tag{5.27b}$$

$$= \frac{1 - z^{-N}}{N} \sum_{k=0}^{N-1} \frac{H[k]}{1 - e^{i2\pi k/N} z^{-1}} \tag{5.27c}$$

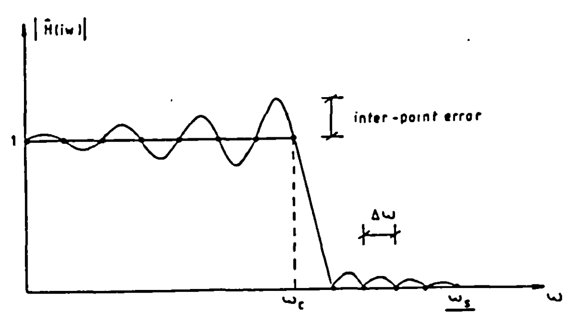

Fig.V.14

Ripples of the frequency response of a DFT filter

By substitution of

$$z = e^{i\omega t} = e^{i2\pi kn}$$

in this equation, we obtain both the time frequency response as:

$$| H_r(i\omega) | = \frac{H[0]}{N}\frac{\sin\omega N/2}{\sin\omega/2} + \sum_{k=1}^{N/2-1}\frac{H[k]}{N}\left[\frac{\sin\left[N\left(\frac{\omega}{2}-\frac{\pi k}{N}\right)\right]}{\sin\left[\frac{\omega}{2}-\frac{\pi k}{N}\right]}+\frac{\sin\left[N\left(\frac{\omega}{2}+\frac{\pi k}{N}\right)\right]}{\sin\left[\frac{\omega}{2}+\frac{\pi k}{N}\right]}\right] \qquad (5.28a)$$

and the phase function as:

$$\Phi(i\omega) = -\pi k\frac{N-1}{N} \qquad (5.28b)$$

$$k = 0,...,N/2-1.$$

In the previous derivation, it has been considered that the number of points N was even (since in practice, the FFT with a power of two number of points is required) and that the spectrum exhibited symmetry about the $\omega = 0$ axis (since the acceleration signal is purely real).

Fig. V. 16 shows the actual frequency function obtained for $f_{LT} = 0.05$ Hz, $f_{LC} = 0.07$ Hz, $f_{HC} =$ 25 Hz and $f_{HT} = 27$ Hz for a $\Delta t = 0.01$ sec. The phase function is here again strictly linear as *Eq. 5. 28b* shows.

The imp

rovement in the filtering, by comparison with a cascade *Ormsby* filter is certain. There is no need to perform any decimation of points to achieve the critically sensitive low frequency filtering. However, the chosen bandwith are the same as in the Californian procedure. The order of magnitude of the intrinsic error which was not studied by the authors is given here, through application of *Eq. 5. 28a.* We get an absolute deviation of 1.5% for the first lobe in the low frequency and 0.3% in the high frequencies for a filter similar to the *Ormsby's* one. These values are to be compared with 6% and 3% respectively, obtained at the same critical points in the *Trifunac method.*

The method possesses also the advantage of being very easily coupled with the instrument correction (see chapter VI) as the wished filter $H(i\omega)$ can be generalised and multiplied by the inverse transfer function of the SDOF transducer.

As we shall see in Chapter VII, it does not seem that the technique offers enough accuracy to recover properly the displacement function. Although the actual frequency response follows more precisely the ideal function, the bandwiths remain the same; or if one wishes to reduce them, then the previouly computed error would increase. This fact was implicitely recognised by the authors as they keep on filtering succesively (in the frequency domain) the three representations of the ground motion. In so doing, they too, loose the near field information included in the acceleration record.

If still more accuracy is to be obtained, by following the same line of thougths, the choice of the frequency points in the transition bands should not be simply computed by a pre-determined function like a double cosine taper (actually by any function whatsoever). The amplitudes of these points should be optimised as to yield an accepted error both in the pass-band and in the stop-band at the same time as searching for a minimum bandwidth. Proposed methods have been developed based on a steepest descent algorithm (*Rabiner et al. 1970*) or more efficiently by formulating the optimisation as a linear programming problem. None of these possible improvements have been followed here as we felt that the use of optimisation could be more advantageous with a very efficient type of filter like the elliptic filter.

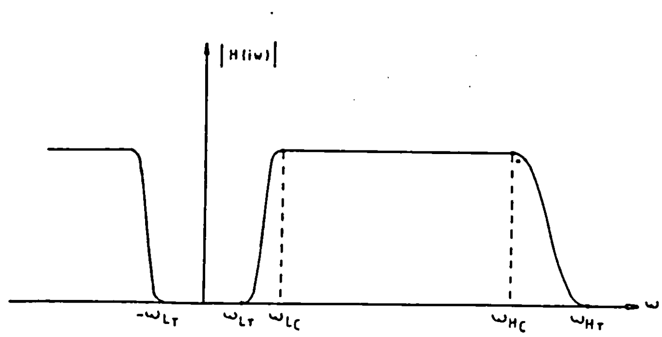

Fig.V.15

The roll-off of the DFT filter are achieved by two half-cosines at the extremities of the pass-band

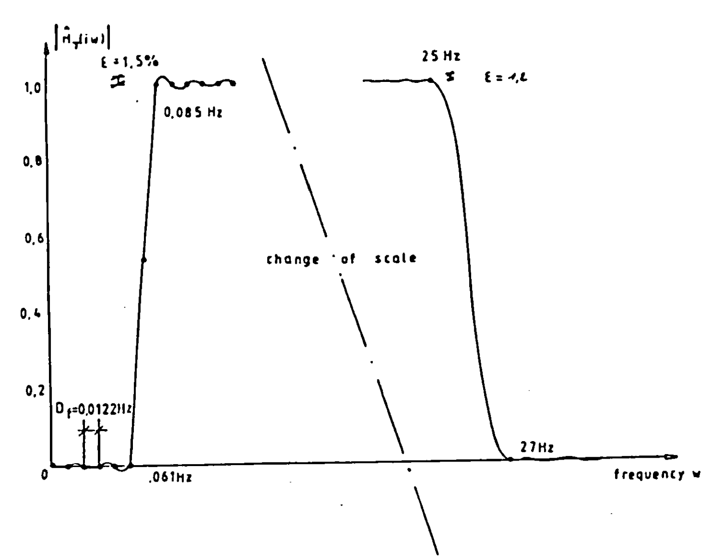

Fig.V.16

Performance of the DFT processing procedure

5.4 THE ELLIPTIC FILTER

In the search for an efficient filter, we are faced with the following criteria:

1. the filtering should be achieved simply, incorporating both low-pass and high-pass filtering.

2. the stop-band level of leakage should be very small, in particular in the low frequency since it is wished to avoid performing the filtering again on velocity and displacement.

3. the transient phase at the beginning and at the end of the record should be as small as possible, and hence should involve a minimum length for the impulse response function.

4. the phase function of the filter should be stictly linear.

Points 2) and 3) led us immediately to the class of elliptic filters known to be very efficient with minimum ripple both in the pass-band and in the stop-band. It is a simple matter to apply the technique of frequency transformation to achieve point 1). Point 4), however is not realised since this type of infinite impulse response (IIR) filter strongly distorts the phase linearity. We shall describe a technique which will restore a strict linearity.

5.4.1 Digital filter formulation

The design of this filter follows the implementation proposed by *Gray and Markel (1976)* which allows the best optimisation of the required filter according to a pre-defined accuracy in the pass-band and the stop-band. The filtering is performed in the time domain; it is expressed in analogue form by *Eq.5.1* and in discrete form by *Eq.5.8* which is rewritten here as:

$$y[n] = \sum_{k=0}^{+\infty} h[k]x[n-k] \tag{5.29}$$

for a causa6 filter impulse response:

Its Z-tranform expression is:

$$Y(z) = H(z)X(z) \tag{5.30}$$

where

$$X(z) = \sum_{n=0}^{N-1} x[n]z^{-n} \tag{5.31}$$

and

$$Y(z) = \sum_{n=0}^{+\infty} y[n]z^{-n} \tag{5.32}$$

are respectively the Z-transform of the imput and output sequences. For an IIR filter of the elliptic type, the filter transfer function $H(z)$ has the form:

$$H(z) = \sum_{n=0}^{+\infty} h[n]z^{-n} = \frac{\sum_{r=0}^{M} b_r z^{-r}}{1 + \sum_{k=1}^{P} a_k z^{-k}} \tag{5.33}$$

We see that, in this case, once $H(z)$ is known through the coefficients b_r $(r = 0, 1, ..., M)$ and a_k $(k = 1, 2, ..., P)$, the filtering process can be performed directly in the time domain through the discrete convolution:

$$y[n] = \sum_{r=0}^{M} b_r x[n-r] - \sum_{k=1}^{P} a_k y[n-k] \tag{5.34}$$

The output $y[n]$ is not only computed from the input sequence $x[n]$ as in the finite impulse response (FIR) type of filter, but also involves values of output itself previously computed. This is this feedback operation wich makes it very efficient in reducing the required filter order (number of filter points).

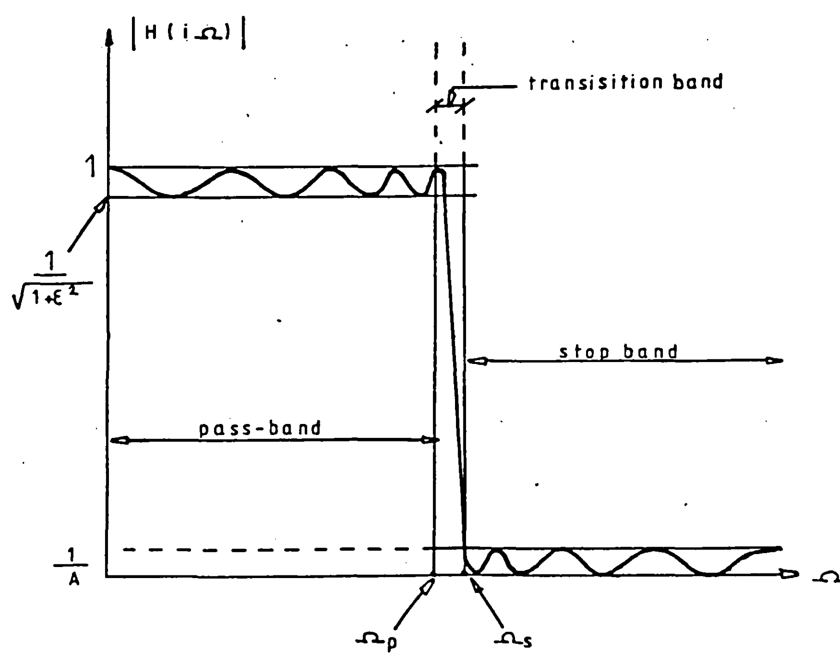

Fig.V.17

Representation of the low-pass elliptic filter

5.4.2 The analogue elliptic filter

The design of the discrete elliptic filter consists of finding a function $H(z)$ (to be transformed in a discrete sequence) capable of approximating the transfer function of a continuous elliptic filter. Such a function is fully defined by its squared gain and has the form:

$$|H(i\Omega)|^2 = \frac{1}{1 + \epsilon^2 sn(\Omega, k)} \tag{5.35}$$

where $sn(\Omega, k)$ is the first *Jacobian elliptic* function (*Abramowitz and Stegun, 1965*) noted:

$$sn(\Omega, k) = \sin\theta \tag{5.36}$$

where θ is such that:

$$\Omega = \int_0^\theta \frac{d\phi}{\sqrt{1 - k^2 \sin^2\phi}} \tag{5.37}$$

Ω is the frequency axis of a complex s-plane. k and ϵ are filter parameters.

In the design of the elliptic filter in its analogue version, the following coeeficients are also used:

$$k = \frac{\Omega_S}{\Omega_P} \tag{5.38a}$$

$$k_1 = \frac{\epsilon}{\sqrt{A^2 - 1}} \tag{5.38b}$$

Ω_P = cutoff frequency

Ω_S = stop-band frequency

$\sqrt{1 + \epsilon^2}$ = pass-band attenuation

A = stop-band attenuation

The process of finding this elliptic filter originates from the search of a complex rational function, $H_n^*(s)$ which approximates up to a certain order n, the transfer function $H^*(s)$ of the continuous low-pass filter in the complex s-plane. Such a target function is drawn on fig.V.17 with a normalised frequency cutoff $\Omega_P = 1$.

The actual transfer function $H(z)$ of the digital filter will be deduced from $H^*(s)$ by frequency transformation (*Constantinides 1968-1969*).

If $H_{LP}(z)$, $H_{HP}(z)$, $H_{BP}(z)$, and $H_{BR}(z)$ are respectively the Z-tranforms of the low-pass, high-pass, band-pass and band-reject filters, they are obtained by application of the double mapping descibed in table VII.

The complex potential analogy technique provides the method. It is such that poles and zeros are uniformly spaced and the poles can be located very near the pass-band limit. In this operation, the complex frequency Ω is linked to s through the two successive conformal mappings:

$$\lambda = i\,\frac{K(k)\Omega}{nK(k_1)} \tag{5.39a}$$

$$s = i\,\Omega_P sn(-i\lambda, k) \tag{5,39b}$$

where the complex λ is only an intermediate variable.

In order to construct the rational function $H^*_n(s)$, one needs to compute the poles and zeros of $H^*(s)$ up to the order n and to express it as:

$$H^*_n(s) = p_s \frac{\Pi^n_{q=1}(s - s_q)}{\Pi^n_{q=1}(s - \bar{s}_q)} \tag{5.40}$$

where p_s is a normalising factor yielding a unit gain for the filter, and s_q and $\bar{s}_q$ are the first q zeros and poles respectively of the function $H^*(s)$.

The minimum order n of the normalised continuous low-pass filter required to achieve the conditions of *fig. V. 17* is given by:

$$n = \frac{K(k)\ \ K'(k_1)}{K(k_1)\ \ K'(k)} \tag{5.41}$$

where

$$K(k) = \int_0^{\pi/2} \frac{d\phi}{\sqrt{1 - k^2 \sin^2\phi}} \tag{5.42}$$

and

$$K'(k) = K\left(\sqrt{1-k^2}\right) \tag{5.43}$$

are the quater-periods of the elliptic functions.

This value of n may also be approximated (Storer 1957) by:

$$n \approx \frac{2}{\pi^2} \ln\left\{\frac{4A}{\epsilon}\right\} \ln\left\{\frac{8\Omega_P}{\Omega_S - \Omega_P}\right\} \tag{5.44}$$

From *Eq. 5.35*, we see that the zeros of $H^*(s)$ are the poles of $sn(\Omega, k)$ known to be located (*Abramovitz and Stegun*) at:

$$\Omega_{m,l} = (2l + 1)i\,K'(k_1) + 2mK(k) \tag{5.45}$$

where m and l are integers.

The poles of $H^*(s)$ are the zeros of:

$$1 + \epsilon^2 sn(\Omega, k_1) \tag{5.46}$$

and are located at:

$$\bar{\Omega}_m = sn^{-1}\left(\frac{i}{\epsilon}, k\right) + 2mK(k) \tag{5.47}$$

The mapping of the left hand side of the s-plane required for stability of the filter imposes $l = 0$.

Expressing the zeros and poles locations in the complex λ-plane through *Eq. 5.39a* and making use of *Eq 5.41* one obtains (*fig. V.19*):

$$\lambda_m = -K'(k) + \frac{2m}{n} i K(k) \tag{5.48a}$$

$$-\frac{n-1}{2} < m < \frac{n-1}{2} \qquad \text{if } n \text{ odd}$$

$$\lambda_m = -K'(k) + \frac{2m}{n} i K(k) \tag{5.48b}$$

$$-\frac{n}{2} < m < \frac{n}{2} - 1 \qquad \text{if } n \text{ even}$$

$$\bar{\lambda}_m = i \frac{K(k)}{nK(k_1)} sn^{-1}\left(\frac{i}{\epsilon}, k_1\right) + \frac{2m}{n} K(k) \tag{5.49a}$$

$$-\frac{n-1}{2} < m < \frac{n-1}{2} \qquad \text{if } n \text{ odd}$$

$$\bar{\lambda}_m = i \frac{K(k)}{nK(k_1)} sn^{-1}\left(\frac{i}{\epsilon}, k_1\right) + \frac{2m+1}{n} K(k) \tag{5.49b}$$

$$-\frac{n}{2} < m < \frac{n}{2} - 1 \qquad \text{if } n \text{ even}$$

Finally, the desired zeros and poles in the s-plane can be obtained by the the transformation of *Eq. 5.39b.*

It can be shown (*Guillemin 1957*), by writting $s = \Sigma + i\Omega$ and $\lambda = u + iv$, that this tranformation can also be expressed as:

$$\Sigma = \frac{sn(u,k')\,cn(u,k')\,cn(v,k)\,dn(v,k)}{1 - sn^2(u,k')\,dn^2(v,k)} \tag{5.50}$$

$$\Omega = \frac{sn(v,k)\,dn(u,k')}{1 - sn^2(u,k')\,dn^2(v,k)} \tag{5.51}$$

where $cn(.)$ and $dn(.)$ are the Jacobian elliptic functions copolar to $sn(.)$ and such that:

$$cn^2(.) = 1 - sn^2(.) \tag{5.52a}$$

$$dn^2(.) = 1 - k^2 sn^2(.) \tag{5.52b}$$

The computation of each $s_m = \Sigma_m + i\Omega_m$ is performed numerically to yield the desired approximation expressed by *Eq. 5.40.*

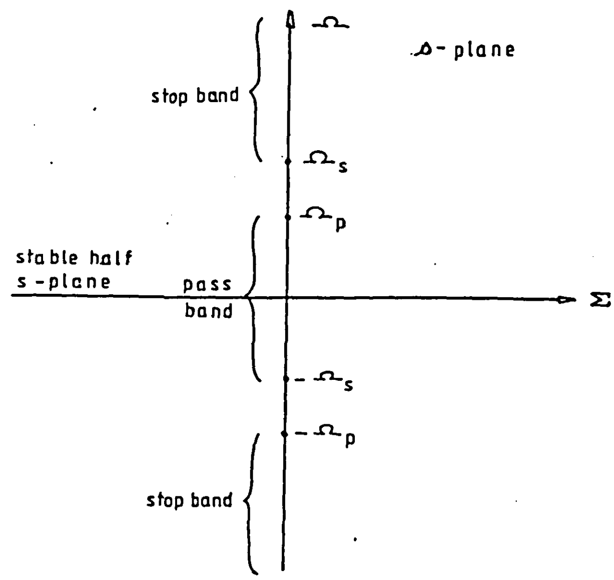

Fig.V.18

Location of the cutoff frequency and the stop-band frequency in the complex frequency plane

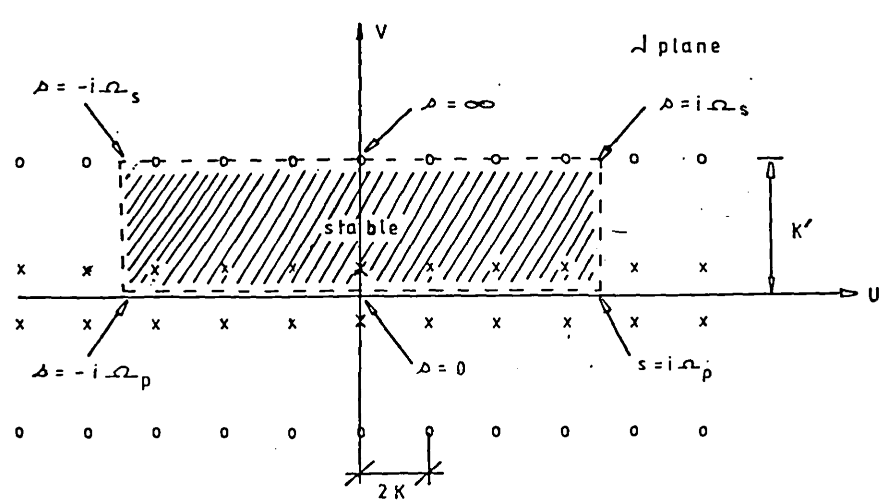

Fig.V.19

Mapping of the poles and zeros of the frequency function an the intermediate λ-plane

5.4.3 The digital elliptic filter

As mentionned previously, the transfer function of the digital filter is deduced from the analogue transfer function given by *Eq.5.40* through the application of the frequency transforms of table VII.

$$\begin{array}{ccc} H_n^{\bullet}(s) & \longrightarrow & H_N(z) \\ s-plane & & z-plane \end{array}$$

The obtained expression for $H_N(z)$ is:

$$H_N(z) = p_z \frac{\Pi_{q=1}^{n'}(z - z_q)}{\Pi_{q=1}^{n'}(z - \bar{z}_q)} \tag{5.53}$$

n' being the true filter order, after tansformation (usually $n' = 2n$ for band-pass filter).

$H_N(z)$ is advantageously written in the form which associates the conjugate poles and zeros yielding a transfer function in the complex z-plane with real coefficients and consisting of a cascade of first and second order systems:

$$H_N(z) = p_z \prod_{q=1}^{n''} \frac{1 + a_q z^{-1} + b_q z^{-2}}{1 + c_q z^{-1} + d_q z^{-2}} \tag{5.54}$$

n'' being the integer part of $(n' + 1)/2$;

here also p_z is the normalising coefficient producing a unit gain pass-band filter when expressed in the z-plane.

For use in its direct form implementation *Eq.5.34*, $H_N(z)$ may be expressed with numerator and denominator expanded into their polynomial:

$$H_N(z) = \frac{\sum_{q=0}^{M} BB_q z^{1-q}}{\sum_{q=0}^{M} AA_q z^{1-q}} \tag{5.55}$$

where we recognise:

$$BB_q = b_r \quad ; \quad AA_q = a_k \quad ; \quad AA_1 = 1$$

$$n' = M - 1 = P \qquad \text{and} \qquad q = r + 1 = k$$

The simple direct implementation expressed by *Eq.5.34* provides the filtered sequence $y[n]$. The computer program developed by *Gray and Markel (1976)* has served as a basis for our elliptic filter design.

5.4.4 Phase linearity

Point 4) of the introduction, however was not considred at this stage and we know that this efficient IIR filter exhibits a strong non-linear characteristic which is unacceptable in the processing of earthquake acceleration records. It is known that the linear phase is preserved only when a poles-zeros configuration includes reciprocal pole and zero pairs (*Lynn 1972*). as shown on *fig. V. 20.*

For the transfer function $\mathcal{H}_N(z)$ to be composed of poles and zeros pairs only, it should satisfy the relation :

$$\mathcal{H}_N(z) = H_N(z)\, H_N(z^{-1}) \tag{5.56}$$

The use of such function will produce instability in a real time process because, at least one pole of each pair, will be situated outside the unit circle. On the contrary, as in our case, we know the complete record before processing it, we can make use of values in the signal which are "in the future" of the point to be processed.

As the time sequence $x[n]$ has a z-transform $X(z)$, the time sequence $x[-n]$ has a z-transform $X(z_{-1})$. This leads to a stable time reversal procedure (*Rabiner and Gold, 1975*).

This procedure which consists of applying an IIR filter $H(z)$ twice on reversed time sequences, achieves an equivalent phase linearity as the following shows. In the time domain, the input sequence $x[n]$ becomes succesively:

$$a[n] = x[-n] \tag{5.57a}$$

$$f[n] = \sum_{m=1}^{n'} h[m]a[n-m] \tag{5.57b}$$

$$b[n] = f[-n] \tag{5.57c}$$

$$y[n] = \sum_{m=1}^{n'} h[m]b[n-m] \tag{5.57d}$$

In the z-domain, this corresponds to:

$$A(z) = X(z^{-1}) \tag{5.58a}$$

$$F(z) = H(z)A(z) = H(z)X(z^{-1}) \tag{5.58b}$$

$$B(z) = F(z^{-1}) = H(z^{-1})X(z) \tag{5.58c}$$

$$Y(z) = H(z)B(z) = H(z)H(z^{-1})X(z) \tag{5.58d}$$

We see that the combined result has now a transfer function of the type $\mathcal{H}_N(z)$. The implementation of this technique restores a linear phase to the signal. The "price" is that the magnitude characteristic is squared. Since our processing deals with a unit pass-band, there is no significant effect. However, some slight correction should be carried out.

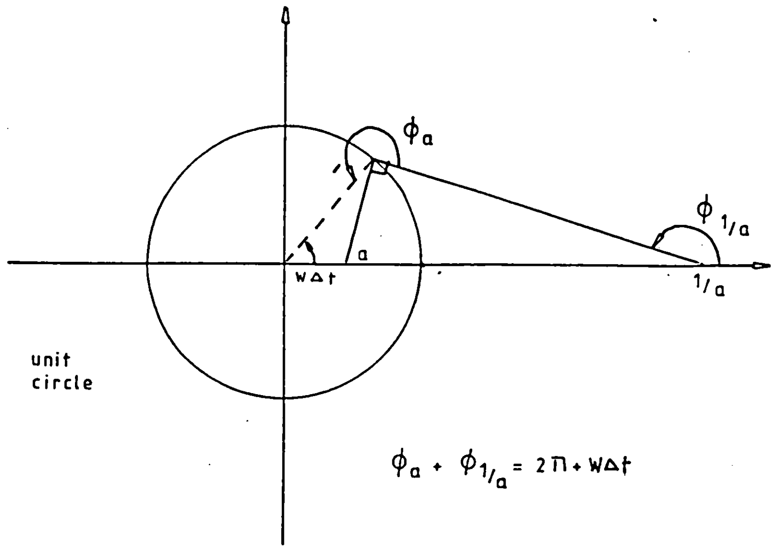

Fig.V.20

Diagram showing the reciprocal character of pole-zero pairs of a linear phase filter

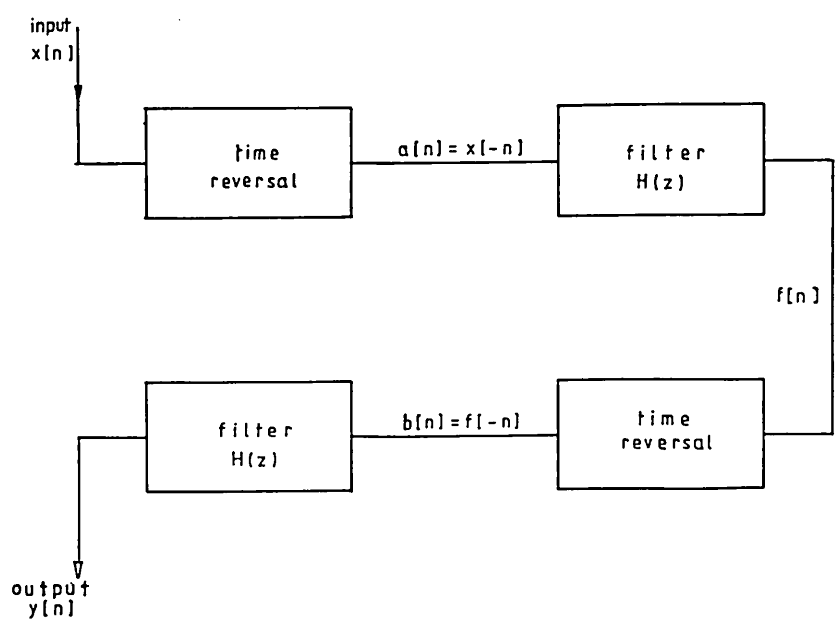

Fig.V.21

The time reversal procedure used to achieve phase linearity

5.4.5 Choice of the parameters

The design of the normalised elliptic filter requires three basic parameters to perform the optimisation:

$k = \Omega_P/\Omega_S$ the relative bandwith

$k_1 = \epsilon/\sqrt{A^2-1}$ the relative attenuation

$F_s =$ the sampling frequency

The filter order N is the deduced from *Eq. 5.44* . In practice, it is more convenient to formulate the problem in terms of the allowable ripple δ_1 in the pass-band and the allowable leakage δ_2 in the stop-band. *Fig. V. 22* shows the square of the normalised filter and its final version after frequency tranformation. The square of the designed filter represents the actual frequency function which operates on the raw acceleration signal since the convolution is performed twice *Eq. 5.57 and 5.58.*

The values to input in the computer programme are: k, δ_1, $\delta 2$, and F_s. For the choice of δ_1 and δ_2 we must have present in mind that, within certain limits, a strong stop-band attenuation δ_2 is more appropriate than a small ripple δ_1. The reason for this is that we are looking for a level of leaked energy as small as possible in the stop-band in order to remain free from filtering noise in the double integration process. This is this strong attenuation which will enable to avoid performing again the filtering on velocity and displacement.

In terms of δ_1 and δ_2, the coefficients ϵ and A express as:

$$\epsilon = \sqrt{\frac{\delta_1}{1-\delta_2}} \tag{5.59a}$$

$$A = \frac{1}{\sqrt{\delta_2}} \tag{5.59b}$$

$$\text{and } K_1 \approx \sqrt{\delta_1 \delta_2} \tag{5.59c}$$

for the geometric average of the errors in the pass-band and the stop-band.

We are retaining, for working area of the elliptic filter, the zone defined by:

$$1.02 \leq k \leq 1.06 \tag{5.60a}$$

$$5.10^{-3} \leq \sqrt{\delta_1 \delta_2} \leq 5.10^{-4} \tag{5.60b}$$

which is approximately shown on *fig. V. 23.* We feel that reasonable values of these parameters should be about:

$$k = 1.04 \tag{5.61a}$$

$$\delta_1 = 0.0025 \tag{5.61b}$$

$$\delta_2 = 10^{-5} \tag{5.61c}$$

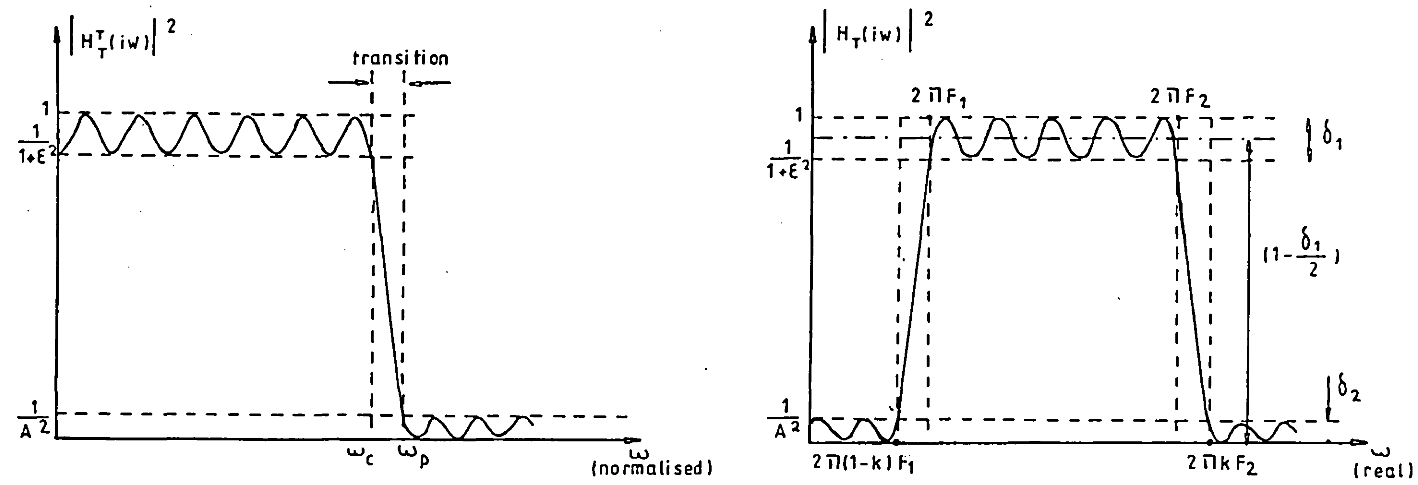

Fig.V.22

Frequency transformation of a low-pass elliptic filter to a band-pass elliptic filter

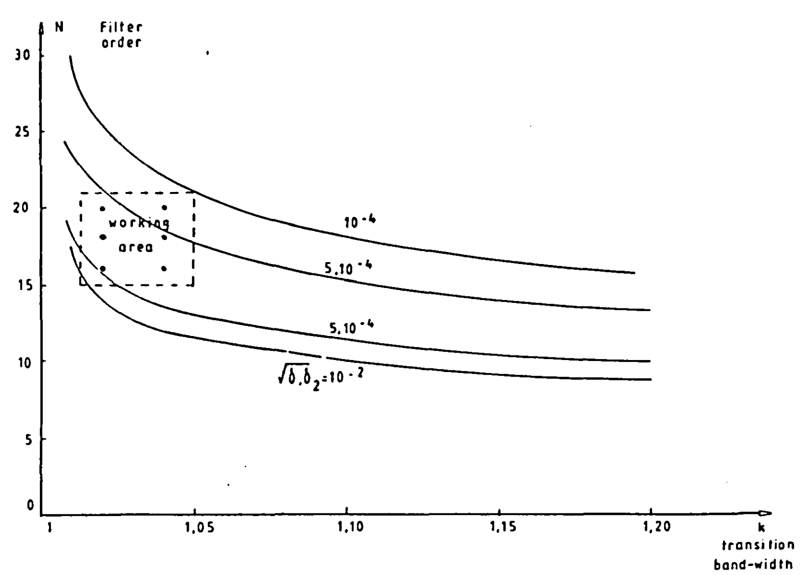

Fig.V.23

Working area of the elliptic filter used to correct strong motion accelerograms which yields:

$$\sqrt{\delta_1 \delta_2} = 5.10^{-4} \tag{5.61d}$$

The associated order of the filter is N=20.

Numerical instability may occur when too much accuracy is demanded with a high order filter to achieve a precise low relative frequency filtering. As an example, we found that, on the Imperial College CDC 855 computer, working with Fortran single precision, results at F_s = 100 Hz were not reliable when the low frequency cutoff were positionned at 0.07 Hz, unless the accuracy was less than δ_1 = 0.001.

In this particularly extreme case the instability introduced an error of the order of 5%. It amplified very rapidly when the parameters are still more severe and tends to infinity.

Such limits are not necessary in the processing of earthquake acceleration records. A warning has been introduced in the programme itself when the final gain of the filter departs of more than 0.1% from the expected unity. A final correction is also performed to minimize the error in the pass-band. As can be seen on *fig. V.19*, the maximum value of the ripple in the pass-band is 1. The oscillation δ_1 is forced below this value. The correction consists in modifying the normalising coefficient p_z by the term $1/(1-\delta_1/2)$. The pass-band oscillation is then reduced to the very small value $\delta_1/2$ above or below the unit value.

Table IX

Bilinear transformations

Filter type	*Frequency cutoff*	*replace s by*	*where*
low − pass	ω_{LP}	$\frac{z-1}{c(z+1)}$	$c = \tan\frac{\omega_{LP}\Delta t}{2}$
high − pass	ω_{HP}	$c\frac{z+1}{z-1}$	$c = \tan\frac{\omega_{HP}\Delta t}{2}$
band − pass	ω_{LP}, ω_{HP}	$\frac{z^2-2\alpha z+1}{c(z^2-1)}$	$\alpha = \frac{\cos(\omega_{LP}+\omega_{HP})\Delta t/2}{\cos(\omega_{HP}-\omega_{LP})\Delta t/2}$
band − reject	ω_{LP}, ω_{HP}	$\frac{c(z^2-1)}{z^2-2\alpha z+1}$	$c = \tan\frac{(\omega_{HP}-\omega_{LP})\Delta t}{2}$

CHAPTER VI

RECORDING INSTRUMENT DECONVOLUTION

6.1 THEORY OF THE SDOF ACCELERATION TRANSDUCER

Most of the acceleration transducers are based on the oscillation of a pendulum, which can be modelled as a SDOF system, with viscous damping (*fig. VI. 1*). When a ground acceleration input $a(t)$ activates such a system, the displacement $x(t)$ of the mass of the pendulum is governed by the second order differential equation:

$$\ddot{x}(t) = 2\lambda\omega_0\dot{x}(t) + \omega_0^2 x(t) = -a(t) \tag{6.1}$$

where λ = % of critical damping and $\omega_0 = 2\pi/f_0$ = natural circular frequency of the pendulum.
The trace $y(t)$ drawn by the light beam on the film of the recording instrument is proportional to this displacement. The term SEN is the proportionality factor, called sensitivity of the instrument and expressed in mm/g (typically SEN = 25 to 100 mm/g; (see also chapter III).

The design of strong motion instruments is such that the terms $\ddot{x}(t)$ and $2\lambda\omega_0\dot{x}(t)$ are small in comparison with $\omega_0^2 x(t)$. In this case, a first approximation of the unknown ground acceleration $a(t)$ is given by:

$$a(t) \approx -\frac{y(t)}{SEN} \tag{6.2}$$

Since SEN is simply a scaling factor, it will be taken to be ω_o^2 in what follows. The approximation is achieved in practice through a particular choice of the value ofλ, the % of critical viscous damping.

On *fig. I. 1*, we represented the frequency response of SDOF system of natural circular ω_0 and various percentages of critical damping λ. We also drew the "perfect" instrument frequency response, as an horizontal straight line passing through 1. Such an ideal frequency response gives a perfect replica of the input signal for all frequencies from $\omega = 0$ to $\omega = +\infty$. However, real SDOF transducers cannot be as perfect; their frequency response is:

$$| H(i\omega) |^2 = \frac{1}{(\omega_0^2 - \omega^2)^2 + 4\lambda^2\omega_0^2\omega^2} \tag{6.3}$$

This function approaches the desired straight line for a value of critical damping of $\sqrt{2}/2 = 0.707$. This is the case for wich the frequency response $| H(i\omega) |$ is the closest to the straight line. It is associated with an inflection point at $\omega = 0$ and hence remains longer identical to its target.

This value, however is not the optimised value for the design of a SDOF acceleration transducer as explained on *fig. VI. 2a/b, 3 and 4*. The first reason is that, although $\lambda = 0.707$ gives a good response in the vicinity of $\omega = 0$, this deteriorates as the frequency increases. Its use would require a very large natural frequency ω_0 and this is difficult and expensive to achieve. Instead, if we accept a sligtly smaller damping, and then introduce a positive maximum error δ in the low frequency range, we can transfer this error beyond the crossing point and define a frequency range F_1 within wich the relative error is less than δ. This workable frequency range is always wider than for the $\lambda = 0.707$ case for a given natural frequency ω_0. On *Fig. VI. 3* we have also indicated the workable frequency ranges F_2 and F_3 which correspond to a 2δ and 3δ acceptable transducer error.

The second reason is that the phase response should also be linear to avoid distorsion in time of the pulse sequences. The SDOF transducer cannot achieve such a perfect straigth line either. The best approximation from the phase view point is not reached with $\lambda = 0.707$. On *fig. VI 2b*, we have also presented the frequency ranges F_1', F_2' and F_3' for wich the acceptable error in phase is 1, 2 or 3 times the maximum deviation in the lower part of the diagram.

A tradeoff value for λ, which complies both with a reasonable finite natural frequency ω_0 and an acceptable error is a value close to $\lambda = 0.6$.

Fig. VI. 3 and 4 show in a different way, the workable frequency ranges in amplitude and in phase as a function of critical damping for different values of acceptable transducer errors. For example, a critical damping of 0.6 produces in the lower frequency range a relative error of 0.041. The frequency range extends to $0.8\omega_0/2\pi$ if the same maximum error is also imposed in the high frequency range. It becomes approximately $F_3 = \omega_0/2\pi$ if three times this error ($3x0.042 = 0.126$) is accepted.

Fig. VI. 4 is a similar graph for the phase accuracy. Here, the maximum of the two factors δ_1 and δ_2 must be considered. It can be seen that at $\lambda = 0.6$, the frequency ranges F_1', F_2' and F_3' are wider, but the relative error is bigger.

This value of $\lambda = 0.6$ has now been chosen for the typical SDOF transducer as it provides a satisfactory frequency range of about $F = 2\pi\omega_0$ with an associated relative error both in phase and frequency of about 0.1.

This systematic error due to the mechanics of the transducer may not be always acceptable. In particular, when accurate information is needed in the frequencies around the natural frequency of the instrument or beyond, the error becomes large very rapidely. Various methods have been suggested to correct for transducer response. We shall describe the finite difference method (used in our polynomial corrections and in the *Trifunac correction*) and the inverse DFT filter method (used in the *Stanford procedure*) and show their limitations. Associated with our procedure, we developed the use of a minimax FIR filter to achieve the required differentiations. It will be seen that, at least after the transients have vanished, (a fraction of second), the results are more satifactory.

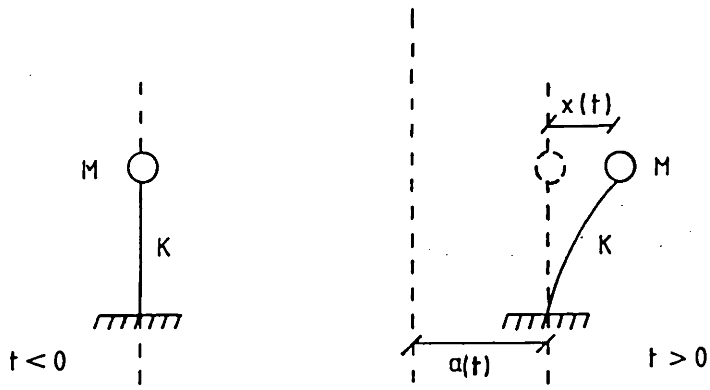

Fig.VI.1

SDOF system excited by a ground acceleration $a(t)$

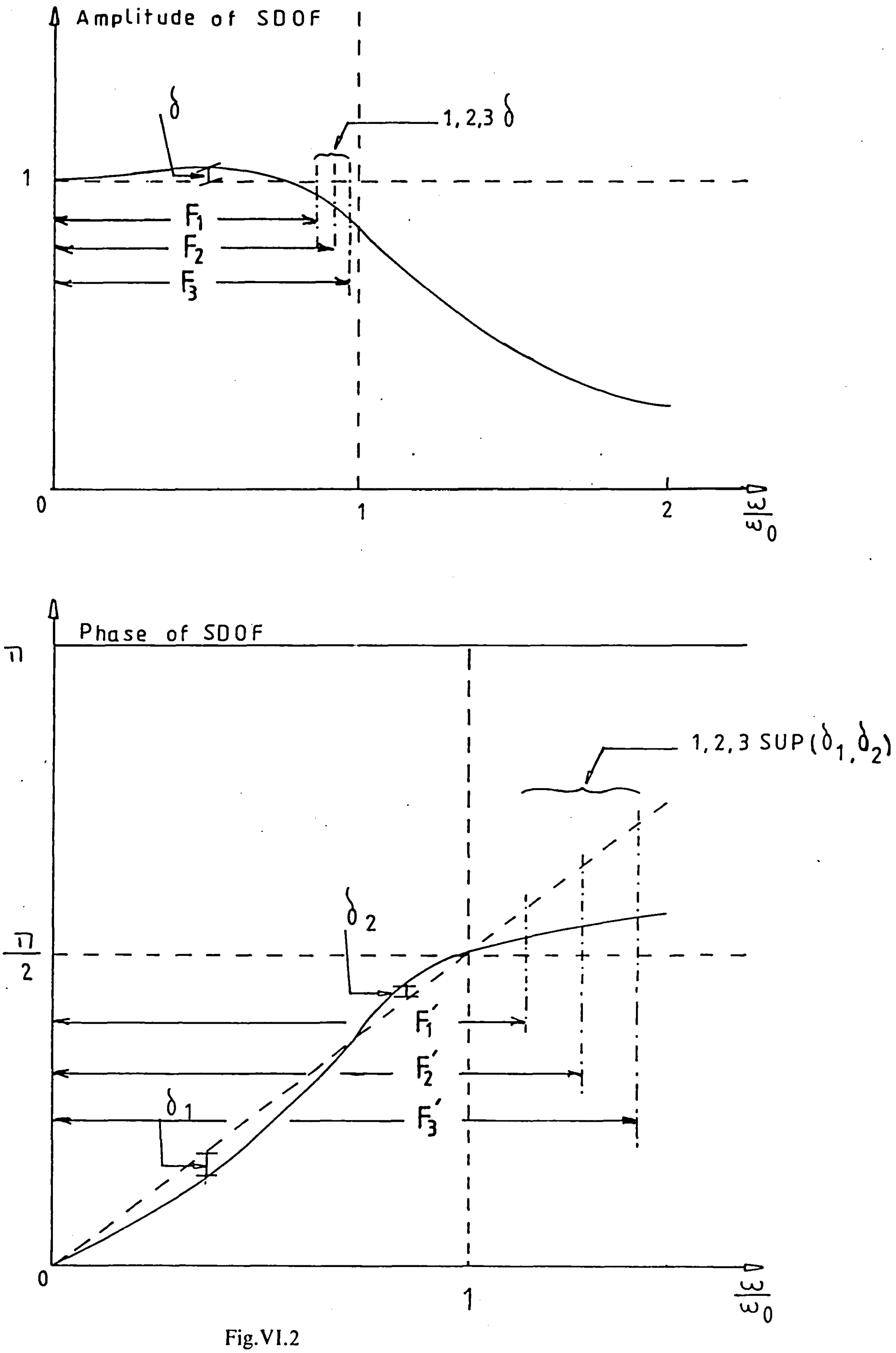

Fig.VI.2

Frequency ranges of a SDOF acceleration transducer

a) in amplitude:

F_1, F_2 and F_3 correspond to 1δ, 2δ and 3δ respectively

b) in phase:

F_1', F_2' and F_3' correspond to $1\delta'$, $2\delta'$ and $3\delta'$ resperctively

where $\delta' = SUP\,[\delta_1, \delta_2]$

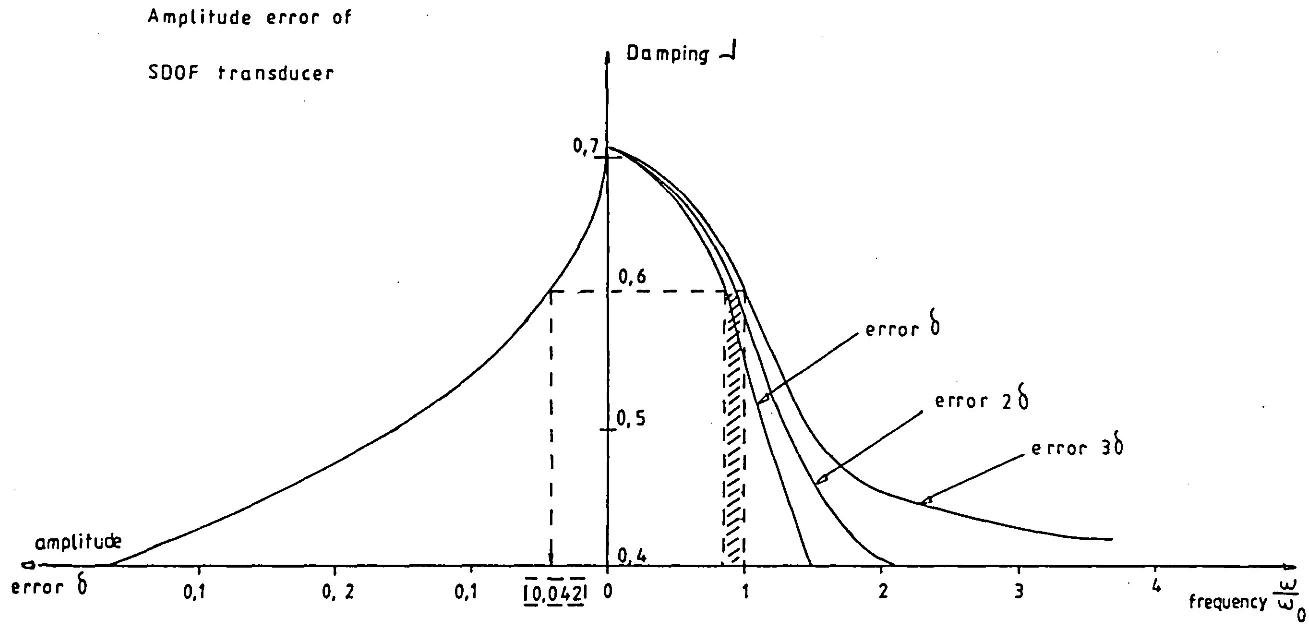

Fig.VI.3

Frequency range and amplitude error δ as a function of critical damping λ

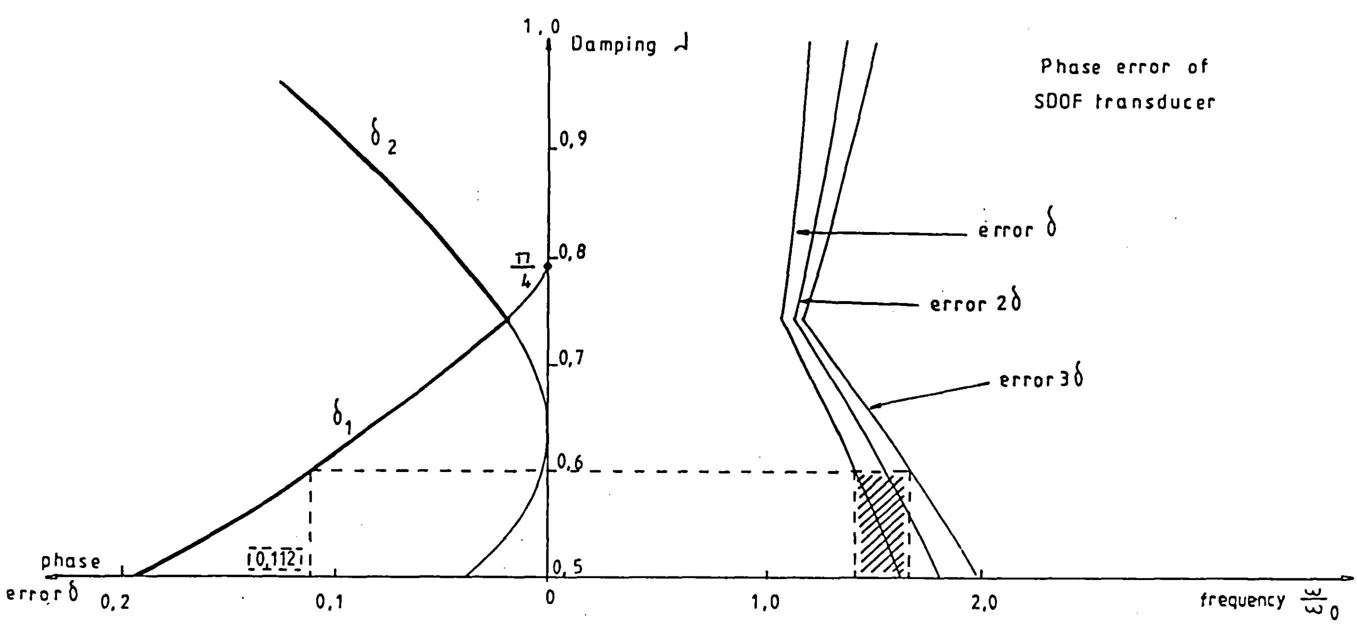

Fig.VI.4

Frequency range and phase error δ as a function of critical damping λ

6.2 THE FINITE DIFFERENCE DECONVOLUTION

Since we are working with a discrete description of the acceleration signal, *Eq.6.1* must be written in its digital form, where a interval of time Δt is implied:

$$\ddot{x}[n] + 2\lambda\omega_0\dot{x}[n] + \omega_0^2 x[n] = a[n] \tag{6.4}$$

$$n = 0, 1, ... N - 1$$

The finite difference deconvolution method consists of computing the terms $\ddot{x}[n]$ and $\dot{x}[n]$ from their finite difference formulation:

$$\dot{x}[n] = \frac{x[n+1] - x[n-1]}{2\Delta t} \tag{6.5a}$$

$$\ddot{x}[n] = \frac{x[n+1] - 2x[n] + x[n-1]}{(\Delta t)^2} \tag{6.5b}$$

Introducing *Eq.6.5a and 6.5b* into *Eq.6.4*, we obtain a sequence $a[n]$ corrected for transducer error:

$$a[n] = \omega_0^2 x[n] + \lambda\omega_0 \frac{x[n+1] - x[n-1]}{\Delta t} + \frac{x[n+1] - 2x[n] + x[n-1]}{(\Delta t)^2} \tag{6.6}$$

Eq.6.6 is used in the *Californian Standard Procedure.* However, it is not always recognised how badly the problem is resolved in the high frequencies. This can be seen on *fig. VI.5, VI.6 and VI.7*, where the effects of the finite difference correction are shown for various types of transducer and for various intervals of time Δt and are compared with the expected true correction.

The Z-transform $A(z)$ of the corrected sequence $a[n]$ is:

$$A(z) = \left[\omega_0^2 + \lambda\omega_0 \frac{z - z^{-1}}{\Delta t} + \frac{z - 2 + z^{-1}}{(\Delta t)^2} \right] X(z) \tag{6.7}$$

where $X(z)$ is the Z-transform of the digitized record. This finite difference operation may be assimilated to a digital tranformation through a linear system with transfer function $H_T^{*-1}(i\omega)$ approximating the analogue inverse transfer function $H_T^{-1}(i\omega)$. It is obtained by the substitution (see also section 3.2.5):

$$z = e^{i\omega\Delta t} \tag{6.8}$$

We get:

$$H_T^{*-1}(i\omega) = \frac{2}{(\Delta t)^2}(1 - \cos\omega\Delta t) - \omega_0^2 + 2i\lambda\omega_0 \frac{\sin\omega_0\Delta t}{\Delta t} \tag{6.9}$$

whereas:

$$H_T^{-1}(i\omega) = \omega_0^2 + \omega^2 + 2i\lambda\omega_0\omega \tag{6.10}$$

The *fig. VI.5, VI.6 and VI.7* show the differences, i.e, how the instrument correction is actually achieved when Δt varies, by comparison with the target $H_T^{-1}(i\omega)$. Curves have been drawn for instruments charac-

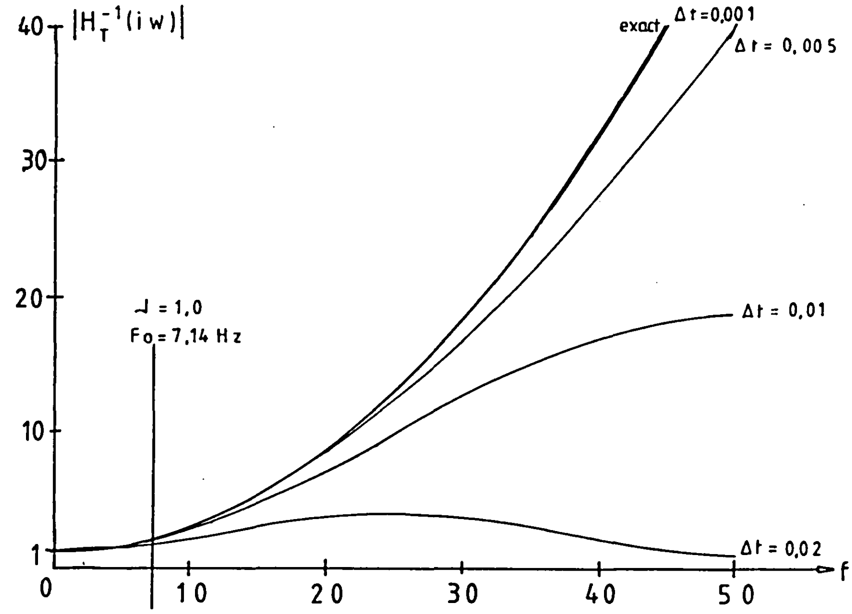

Fig.VI.5

Variations with Δt for $F_0 = 7.14$ Hz and $\lambda = 1.0$

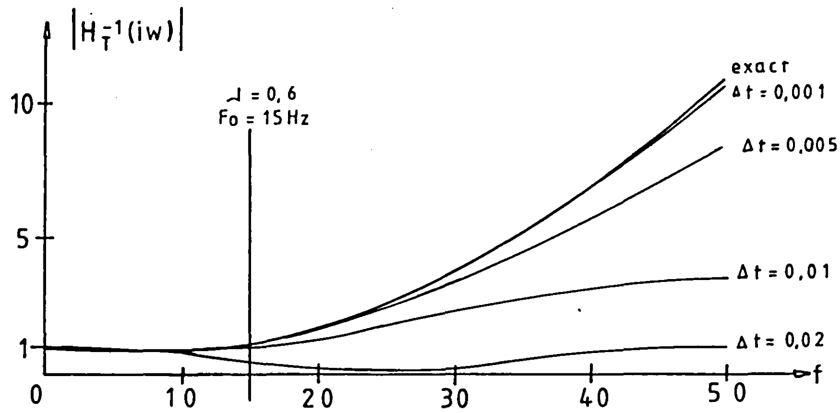

Fig.VI.6

Variations with Δt for $F_0 = 15$ Hz and $\lambda = 0.6$

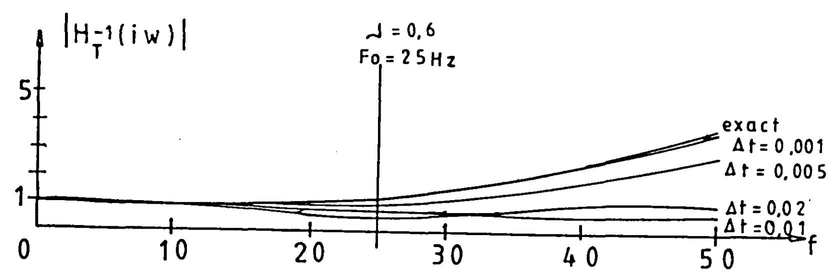

Fig.VI.7

Variations with Δt for $F_0 = 25$ Hz and $\lambda = 0.6$

Transducer correction achieved by comparison with the exact correction teristics $\omega_0 = 7.14$ Hz $\lambda = 1.0$ (Smac, Japan), $\omega_0 = 15$ and 25 Hz $\lambda = 0.6$ (SMA1, USA).

It can be seen that the correction factor becomes predominant when one wishes to correct beyond, say, 1.5 times the transducer natural frequency. Furthermore, the interval of time Δt used affects drastically the results. The *Standard Californian Procedure* suggests to use a $\Delta t = 0.02$ sec. With this value, most of the transducer correction is illusive. At least a $\Delta t = 0.005$ sec is required to yield a good correction within 2% error up to twice the natural frequency of the instrument. The periodicity observed corresponds to the Nyquist frequency $\omega_N = \pi/\Delta t$.

6.3 DECONVOLUTION USING THE DFT FILTER

The method used here follows exactly the principle of the DFT procedure of section 5.3.

We saw that the corrected acceleration sequence is the Inverse Discrete Fourier Transform of the uncorrected signal $A[k]$ multiplied, in the frequency domain, by the frequency function of some band-pass filter $H[k]$ (see *Eq.5.24*). Using the same approach, it is straightforward to operate the deconvolution of the transducer. We know that its transfer function $H_T(i\omega)$ is given by *Eq.6.3.* The deconvoluted signal, in the frequency domain is then obtained by a further multiplication by $H_T^{-1}(i\omega)$ or in digital form $H_T^{-1}[k]$:

$$H_T^{-1}[k] = - \left[1 - \left(\frac{k}{k_0}\right)^2 - 2i\lambda\frac{k}{k_0} \right] \tag{6.11}$$

where $k_0 = \omega_0/2\pi$ and $k = 0, 1, ..., N/2$ The final acceleration including transducer correction, is given by:

$$a_c[n] = \frac{1}{N} \sum_{k=0}^{N/2} A[k]H[k]H_T^{-1}[k]\, e^{i2\pi kn/N} \tag{6.12}$$

$$n = 0, 1, ..., N-1$$

which replaces *Eq.5.24.*

6.4 CORRECTION BY DIGITAL DIFFERENTIATOR

The terms $\dot{x}[n]$ and $\ddot{x}[n]$ are obtained as the outputs of a discrete convolution of $x[n]$ with a differentiator sequence $h_D[n]$. $h_D[n]$ is a limited time sequence approximating, in the minimax sense, the continuous differentiator $i\omega$. Its time expression is the inverse Fourier transform:

$$h_D(t) = \frac{1}{2\pi} \int_{-\infty}^{+\infty} i\omega e^{i\omega t} d\omega \tag{6.13}$$

The design of such sequences can be achieved using various approaches. The procedure suggested by *McClellan et al. (1973)* was used. The resulting sequence exhibits the required strictly linear phase function whose slope depends of the number of points retained (delay).

The expressions for $\dot{x}[n]$ and $\ddot{x}[n]$ are:

$$\dot{x}[n] = \sum_{k=-M/2}^{M/2} h_D[k]x[n-k] \tag{6.14a}$$

$$\ddot{x}[n] = \sum_{k=-M/2}^{M/2} h_D[k]\dot{x}[n-k] \tag{6.14b}$$

The instrument corrected sequence $a_c[n]$ is then obtained by substituting *Eq. 6.14a and 6.14b* into *Eq. 6.4*:

$$a_c[n] = - \left\{ x[n] + 2\lambda\omega_0 \sum_{k=-M/2}^{M/2} h_D[k]x[n-k] + \omega_0^2 \sum_{k=-M/2}^{M/2} h_D[k] \sum_{\kappa=-M/2}^{M/2} h_D[\kappa]x[n-\kappa] \right\} \tag{6.15}$$

$$n = 0, 1, ..., N-1$$

The case of an even sequence is advantageous since it yields good approximation of the differentiator up to the Nyquist frequency $F_N = F_s/2$, whereas the case of an odd sequence is practically limited to $0.8F_N$ as shown on *fig. VI.8a and VI.8b.*

Fig. VI.9a and VI.9b show how this numerical differentiator works, for numbers of points $M = 31$ and $M = 32$ with intervals of time $\Delta t = 0.01$ sec and $\Delta t = 0.02$ sec. The input functions are the sine motion starting at $t = 0$. The output functions are the cosine delayed by $(M-1)\Delta t/2$. This delay is taken into

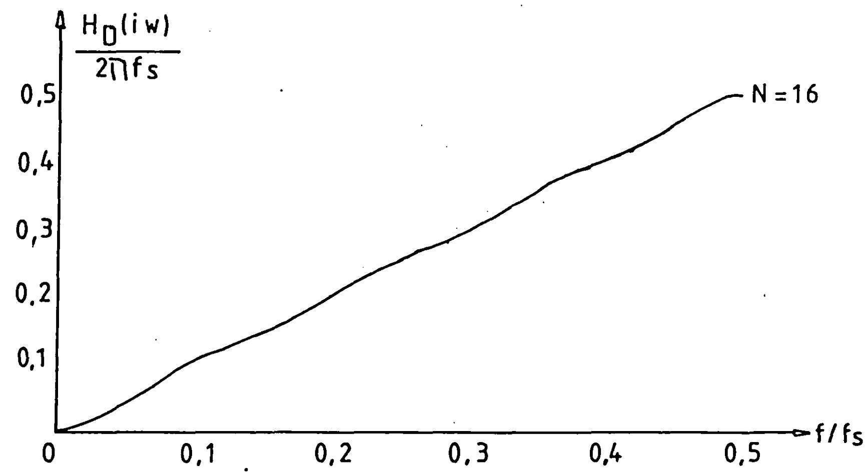

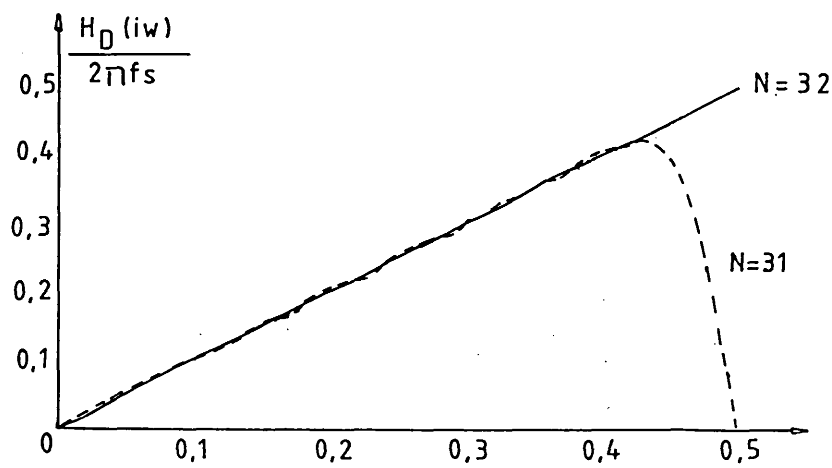

Fig.VI.8

Numerical differentiators

a) with $M = 16$ points

b) with $M = 31$ or 32 points

for an odd number of points, the differentiator is limited to about $0.8F_N$

consideration during implementation. Ripples are also visible at the bebinning of the output sequences. They refect the transient character due to zero amplitudes at negative times. This transient dies out very quickly (after a time of the order of the delay). The advantage of small Δt is then immediately perceived as the transient duration is reduced accordingly.

The purely imaginary character of a differentiator yield an odd symmetry for the sequence $h_D[n]$. The double differentiation is obtained by performing the numerical operation twice. *Fig. IV. 10* gives the result: a sine with a phase of π with respect to the input. The delay and the transient duration have also been doubled.

We have chosen to use a $M = 32$ filter; the 16 numerical values are given below. The actual frequency function is the DFT of the limited sequence (see *fig. VI. 8a and 8b*:

$$H_D(i\omega) = \sum_{k=-M/2}^{M/2} h_D[k] e^{-i\omega k \Delta t}$$

$$= -2i\, e^{-i(M-1)\omega\Delta t/2} \sum_{k=1}^{M/2} h_D[k] \ \sin(\frac{2k-1}{2}\omega\Delta t) \qquad (6.16)$$

for M even $\qquad h_D[k] = -h_D[M-1-k] \qquad k = 1, ..., \frac{M}{2}$

For an acceleration time history with an interval of time $\Delta t = 0.01$ sec, the delay and the transient duration are of 0.15 sec for the first derivative and 0.30 sec for the second derivative. Therefore distorsions in the corrected signal at the beginning and at the end of the signal are to be expected for a short duration.

Table X

Differentiator coefficients

$h_D(1) = -0.0006271309 = -h_D(32)$

$h_D(2) = +0.0008563343 = -h_D(31)$

$h_D(3) = -0.0004241855 = -h_D(30)$

$h_D(4) = +0.0003990152 = -h_D(29)$

$h_D(5) = -0.0004343727 = -h_D(28)$

$h_D(6) = +0.0004996945 = -h_D(27)$

$h_D(7) = -0.0005963496 = -h_D(26)$

$h_D(8) = +0.0007327703 = -h_D(25)$

$h_D(9) = -0.0009300268 = -h_D(24)$

$h_D(10) = +0.0012270042 = -h_D(23)$

$h_D(11) = -0.0017012820 = -h_D(22)$

$h_D(12) = +0.0025272341 = -h_D(21)$

$h_D(13) = -0.0041601159 = -h_D(20)$

$h_D(14) = +0.0081294555 = -h_D(19)$

$h_D(15) = -0.0225390974 = -h_D(18)$

$h_D(16) = +0.2026653505 = -h_D(17)$

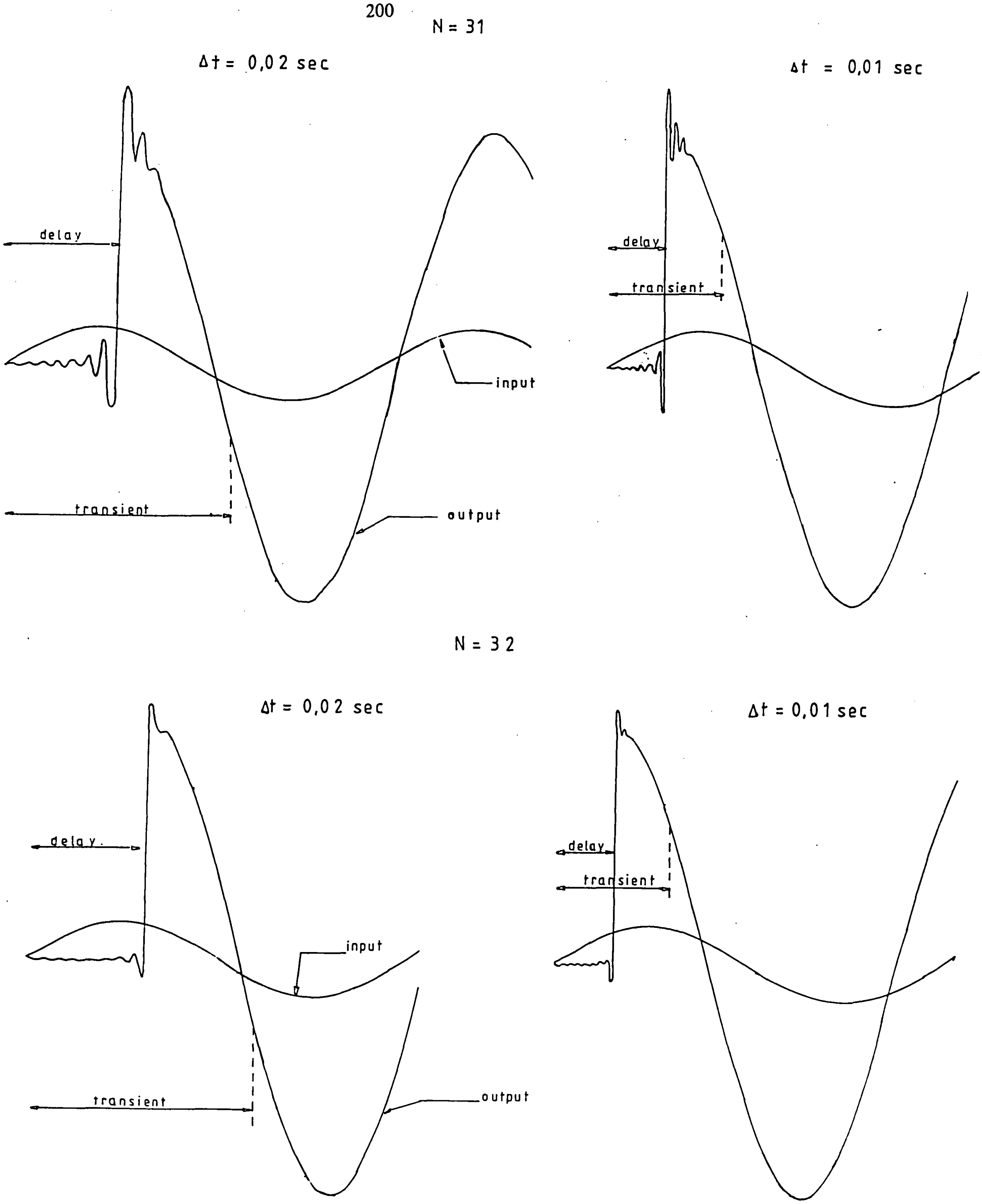

Fig.VI.9

Numerical differentiation of a sine function

a) number of points $M = 31$

b) number of points $M = 32$

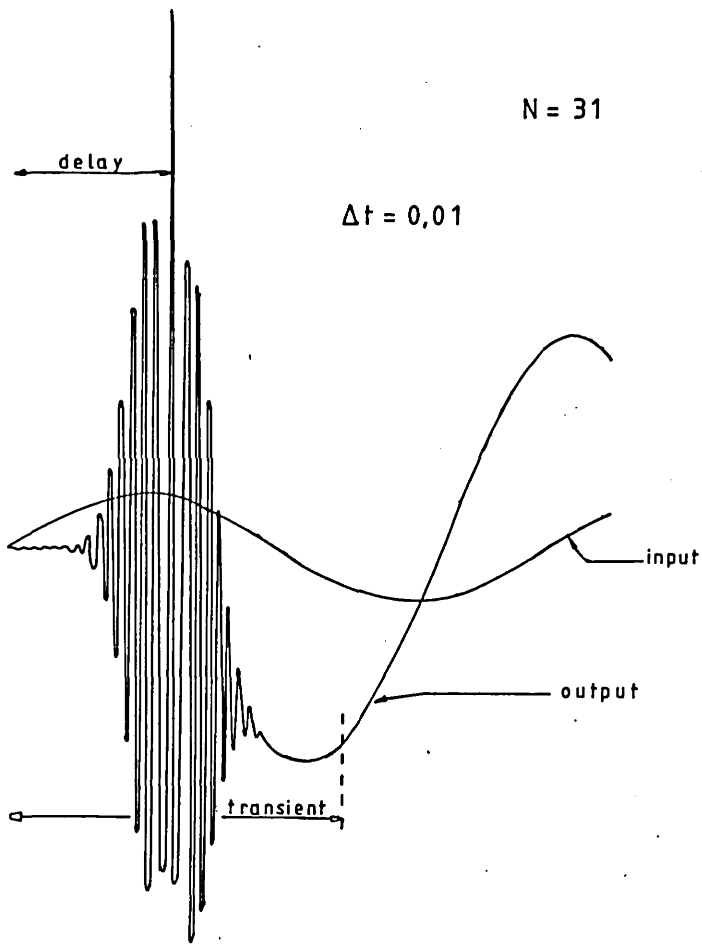

Fig.VI.10

Double numerical differentiation of a sine function $M = 31$

6.5 CHARACTERISTICS OF THE FORCE-BALANCE TRANSDUCER

It was mentioned in section 1.3.2 that better frequency and phase responses could be obtained by using the more sophisticated Force-Balance servo-type transducer. *Fig. I. 13 and I. 14* show schematically its principle. Such a transducer does not measure directly the displacement $x(t)$ of the mass m relative to the ground. Instead, it measures the force required to reduce $x(t)$ to a very small quantity. This force tends to cancel the inertia force produced by the ground motion. The recorded output is an analogue voltage proportional to the balancing force:

$$u(t) = DK[x(t) + \gamma\dot{x}(t)] \tag{6.17}$$

The system is composed of two sub-systems interacting with each other:

1) a mechanical system whose transfer function is:

$$H_M(i\omega) = \frac{1}{\omega_0^2 - \omega^2 + 2\lambda i\omega_0\omega} \tag{6.18}$$

representing the SDOF pendulum of *fig. 6. 1.*

2) an electrical system insuring the feedback of the balanced force whose transfer function is:

$$H_E(i\omega) = \frac{1}{\rho(1 + i\gamma\omega)} \tag{6.19}$$

representing the feedback of the force balance $u(t)$.

ρ is the proportionality coefficient depending on the electrical parameters and the mass m (*fig. I. 13*):

$$\rho = \frac{DKG}{mR_0} \tag{6.20}$$

If the composite system is looked upon as yielding relative displacement output $x(t)$, its frequency representation is proportional to the sum of the mechanical impedances:

$$Z_M(i\omega) = \frac{1}{H_M(i\omega)} \tag{6.21a}$$

and

$$Z_E(i\omega) = \frac{1}{H_E(i\omega)} \tag{6.21b}$$

This produces a response $X(i\omega)$ in frequency:

$$X(i\omega) = [Z_M(i\omega) + Z_E(i\omega)]A(i\omega) \tag{6.22}$$

$A(i\omega)$ being the ground acceleration.

This equation is equivalent to the time domain differential equation:

$$\ddot{x}(t) + i(2\lambda\omega_0 + \rho\gamma)\dot{x}(t) + (\omega_0^2 + \rho)x(t) = -a(t) \tag{6.23}$$

It is seen that the transducer behaves exactly as a SDOF system but its dynamic characteristics have been modified by the electrical circuitry. By making the electrical parameters variable and in particular the capacity D, it is possible to adjust the system to a desired natural frequency ω_n and damping ratio ξ:

$$\omega_n^2 = \omega_0^2 + \rho \tag{6.24a}$$

$$\xi = \frac{1}{\omega_n}(2\lambda\omega_0 + \rho\gamma) \tag{6.24b}$$

But the transducer does not measure the displacement of the mass m. The measured output is the force-balance of *Eq.6.17*. The frequency expression for $u(t)$ involves clearly the feedback function of the system:

$$U(i\omega) = T_r(i\omega)A(i\omega) \tag{6.25}$$

where

$$T_r(i\omega) = \rho\frac{-\omega^2 H_M(i\omega)}{1-[-\omega^2 H_M(i\omega)][-\omega^2 H_E(i\omega)]} \tag{6.26}$$

is the resultant instrument transmissibility (*fig. VI.11*).

Now, substituting the expressions of $H_M(i\omega)$ and $H_E(i\omega)$, we get:

$$T_r(i\omega) = \frac{1 + i\gamma\omega}{\dfrac{\omega^2}{\rho} + \left(1 - \dfrac{\omega_0^2}{\omega^2} + 2\lambda i\dfrac{\omega_0}{\omega}\right)(1 + i\gamma\omega)} \tag{6.27}$$

This function is the complex frequency ratio between the acceleration input and the force-balance output. It depends not only on the parameters ω_0 and λ of the mechanical system, but also of ρ and γ characterising the electrical system. It is to be noted that the force-balance transducer acts to reduce the relative displacement $x(t)$ to a minimum value. This enables to limit distorsion due to non-linearity effect.

Fig. VI.11a and 11b, show the performance of the transmissibility function both in amplitude and phase, for typical values of the parameters. In practice, one arranges the system to render it electrically dominant, by increasing the proportionality coefficient ρ and/or by reducing the stiffness of the pendulum so that ω_0 becomes negligeable.

The transmissibility function becomes:

$$T_r(i\omega) = \frac{1 + i\gamma\omega}{\dfrac{\omega^2}{\rho} + 1 + i\gamma\omega} \tag{6.28}$$

This means that the electical parameters control the resultant SDOF system. Their values are related to the dynamic characteristics of the resultant systems through:

$$\rho = \omega_n^2 \tag{6.29a}$$

$$\gamma = \frac{2\xi}{\omega_n} \tag{6.29b}$$

The frequency function $H_{FB}(i\omega)$ and the phase function $\Phi_{FB}(i\omega)$ are given by:

$$| H_{FB}(i\omega) | = \frac{\sqrt{1 + \left(2\xi\frac{\omega}{\omega_n}\right)^2}}{1 - \left(\frac{\omega^2}{\omega_n^2}\right)^2 + \left(2\xi\frac{\omega}{\omega_n}\right)^2} \tag{6.30a}$$

$$\Phi_{FB}(i\omega) = \tan^{-1} \frac{2\xi\left(\frac{\omega}{\omega_n}\right)^3}{1 + \left(\frac{\omega}{\omega_n}\right)^2 (4\lambda^2 - 1)} \tag{6.30b}$$

The advantage of using large values for the apparent damping ξ is clear as the frequency function tends to a perfect tansmissibility equal to unity for all frequencies and the phase function tends to a straight line with slope $\xi\omega_0/2$.

Large values of damping also enable the transients to die out rapidely. In this case, the equivalent natural frequency of the instrument is not critical. The only limitation to "quasi-perfect" accuracy is the finiteness of the electrical coefficient γ. In the design or in the calibration of such transducers both ρ and γ should be made as large as possible.

On *fig. VI.11a and 11b* where the curves $H_{FB}(i\omega)$ and $\Phi_{FB}(i\omega)$ are drawn for $\omega_n = 2\pi \times 50$ Hz and $\xi = 7.0$, the maximum relative error is of 0.5% on the amplitude and 0.8% on the phase, in the $0 - 100$ Hz range.

For illustration purposes other transfer functions are also drawn.

Force-balance	$\omega_n = 2\pi \times 50$ *cps*	$\xi = 0.6$(with feed-back)
SDOF	$\omega_0 = 2\pi \times 50$ *cps*	$\lambda = 0.6$(without feed-back)

In the case of such a force balance transducer, no correction for instrument is therefore required.

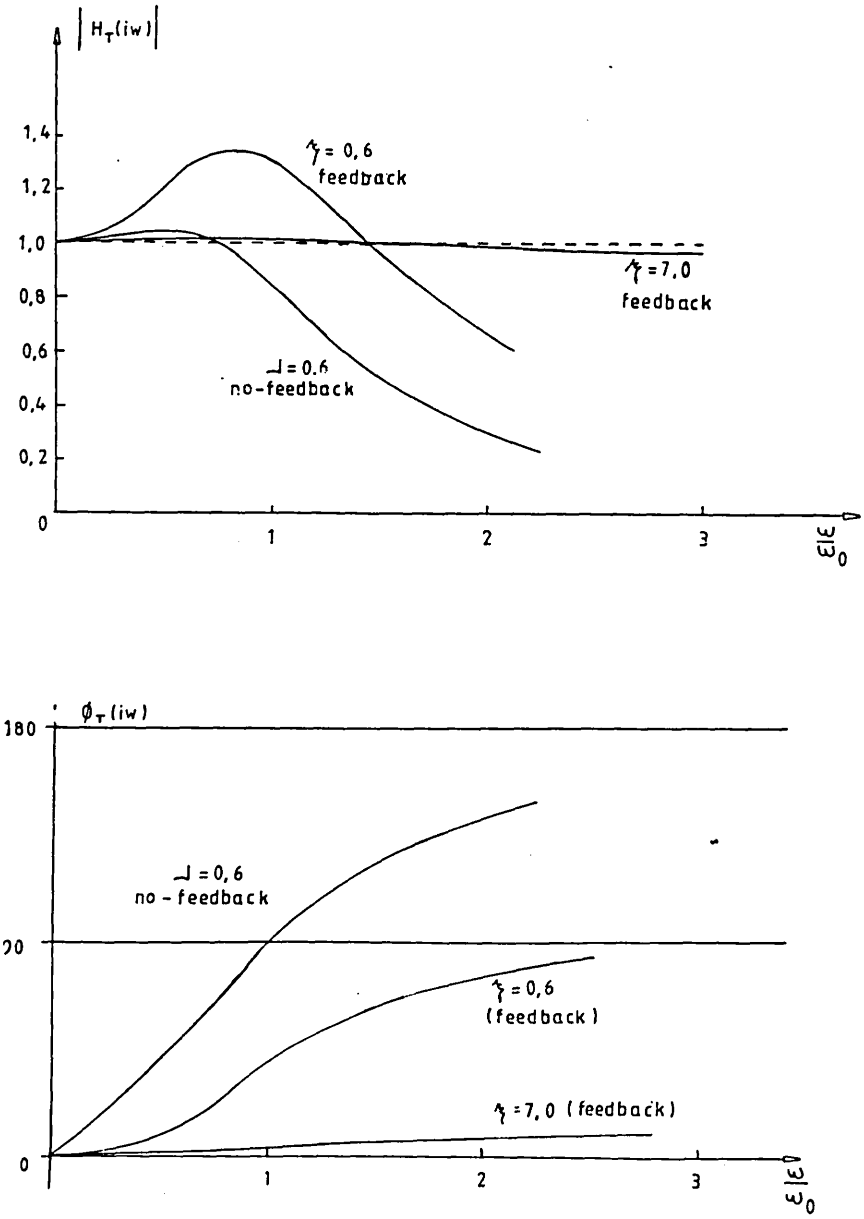

Fig. VI.11

Performances of a Force-balance acceleration transducer

a) amplitude

b) phase

CHAPTER VII

COMPARISON OF PROCESSING PROCEDURES

7.1.INTRODUCTION

In this chapter we are presenting comparisons between the various ground motion processing procedures It is worthwhile to recall here that we do not intend to compare the peak values only. This type of comparison is certainly of value for engineering purposes since peaks are the basic parameters of practical attenuation laws. What is also looked for, is a fair understanding of the reliability of the whole motion which is currently recorded. Strong motion records are not only peak values. Much information of seismological and geotechnical nature are included in the full time histories. It is therefore vital to know the confidence with which one may treat this information further.

The earthquake-like signal designed in chapter II has been processed by all the procedures described. Its analytic form will serve as the target ground motion.

Several types of comparisons are performed. The first described is an overall comparison once all the processing phases have been passed through:

1) the recording,

2) the digitization,

3) the correction process including:

- the digitization noise removal
- the base line search
- the correction for transducer error.

The individual effects will then be detected in particular cases.

It must be said at this stage that we realized how difficult a full comparison, involving all aspects of the recovery process, could be. It requires more than one single original signal, even when, as in our case, we attempted to introduce in it many common odd features. Nevertheless, it is believed that the conclusions reached are of large value to understand the actual level of quality for acceleration signal recovery. It should also permit to foresee what should be done in the future to improve ground motions acquisition.

7.2 OVERALL COMPARISON OF GROUND NOTION RECOVERY

The various procedures compared are refered by their code according to the various theories developed in the previous chapters.

$KK = 1$, Parabolic adjustment through acceleration,

$KK = 2$, Parabolic adjustment through velocity with $v_0 = 0$,

$KK = 3$, Parabolic adjustment through velocity with $v_0 \neq 0$,

$KK = 4$, Zero and end time correction,

$KK = 5$, Standard Californian Procedure (Trifunac),

$KK = 6$, The DFT procedure (Stanford),

$KK = 7$, The ImpCol Procedure (Elliptic filter),

The different results of recovered ground motions are shown on *fig. VII. 1, 2, 3, 4, 5, 6, 7* and are compared each time with the analytic target ground motion at the top of the page. The three ground motion representations are plotted. As in chapter IV, we attempted to quantify the closeness of each curve to the original one using several criteria such as the L_2-norm or the L_∞-norm. The results were widely spread and were very sensitive to the chosen criterion. Furthermore they only expressed a comparison for a specific feature emphasized by the criterion. Eventually, we prefered the visual comparison between the various cases as we thought that a more complete idea, although less quantitative, may be reached instantaneously. We have also given table XI in which we compared the peak values obtained and showed their expected spreads. *Fig. VII.8* gives its graphical view.

No significant differences are visible from the acceleration time histories. The table indicates that all the procedures reduce the value of the peak acceleration; the average is 0.7%. The filtering types of correction seem to reduce more the peak values than the polynomial types of correction.

Differences between the ground motions begin to appear on the velocity representations. The major distorsions originate, for the polynomial types of correction ($KK = 1$, $KK = 2$, $KK = 3$ and $KK = 4$), at the beginning and at the end of the records. They are affected, sometimes too much, by the correcting polynomial itself. Parabolic or cubic trends are visible except for the $KK = 2$ case where its importance is less. The filtering types of correction ($KK = 5$, $KK = 6$ and $KK = 7$) yield functions wich are much closer to the analytic target. In particular, their behaviour at the limits are in accordance with the true function.

In any case, the value of the peak velocity do not seem to be largely modified. This is possibly due to a double effect acting in opposite directions:

1) after digitization, some signal energy has been lost,

2) the correcting polynomial has re-amplified it.

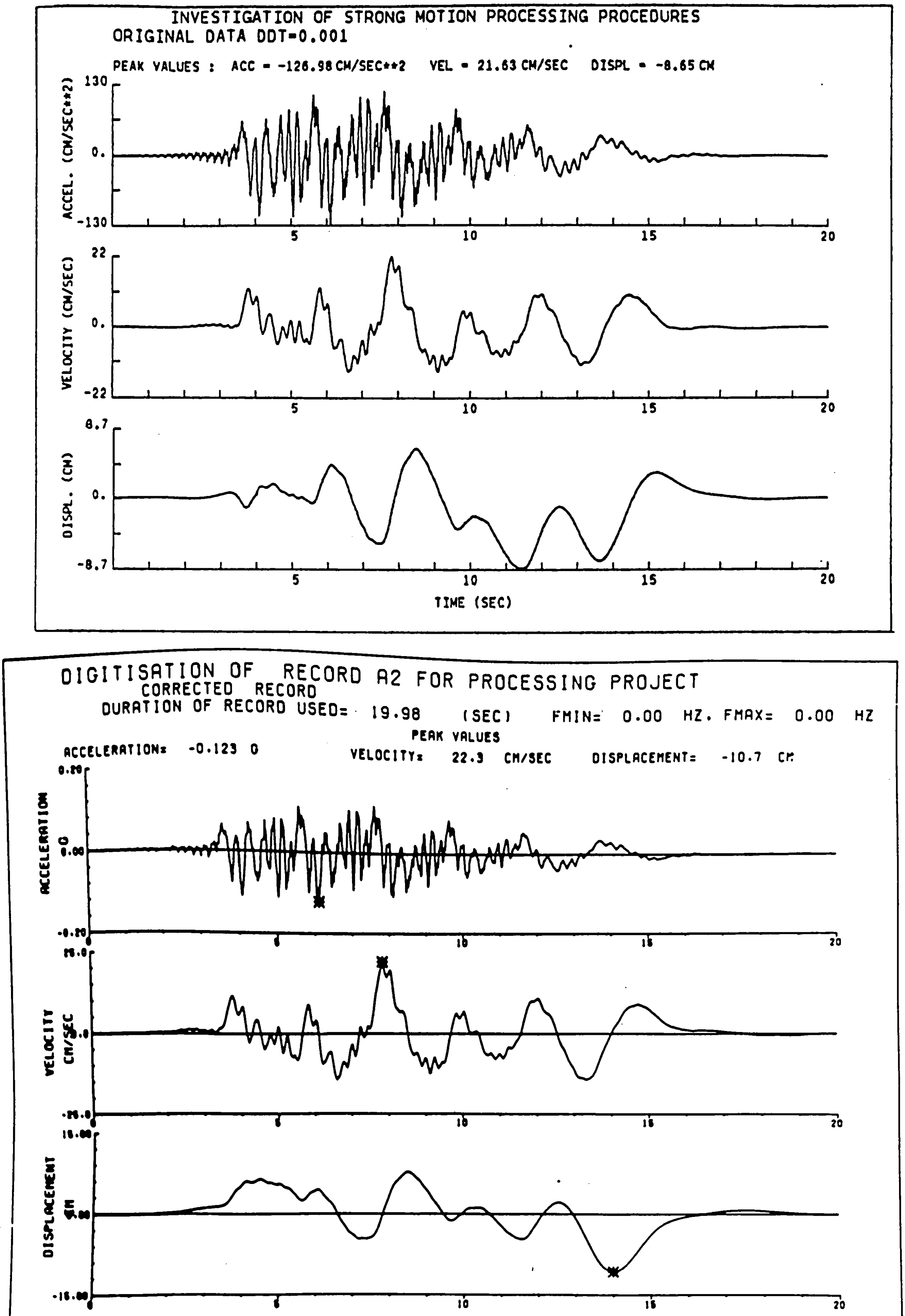

Fig.VII.1

Comparison of acceleration, velocity and displacement time histories of the original earthquake-like signal with the Procedure $KK = 1$

a) top: original signal

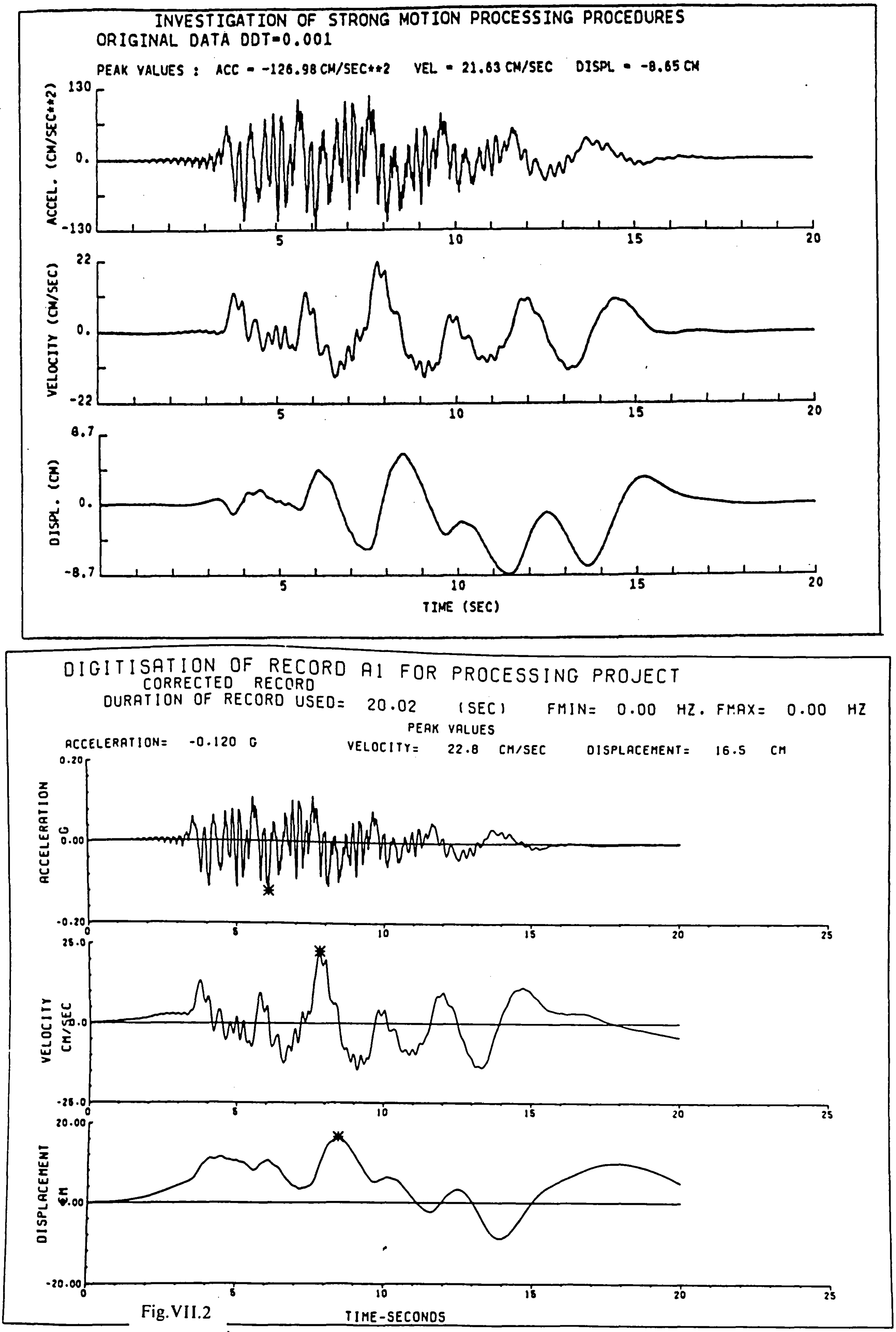

Fig.VII.2

Comparison of acceleration, velocity and displacement time histories of the original earthquake-like signal with the Procedure $KK = 2$

a) top: original signal

b) bottom: $KK = 2$ output

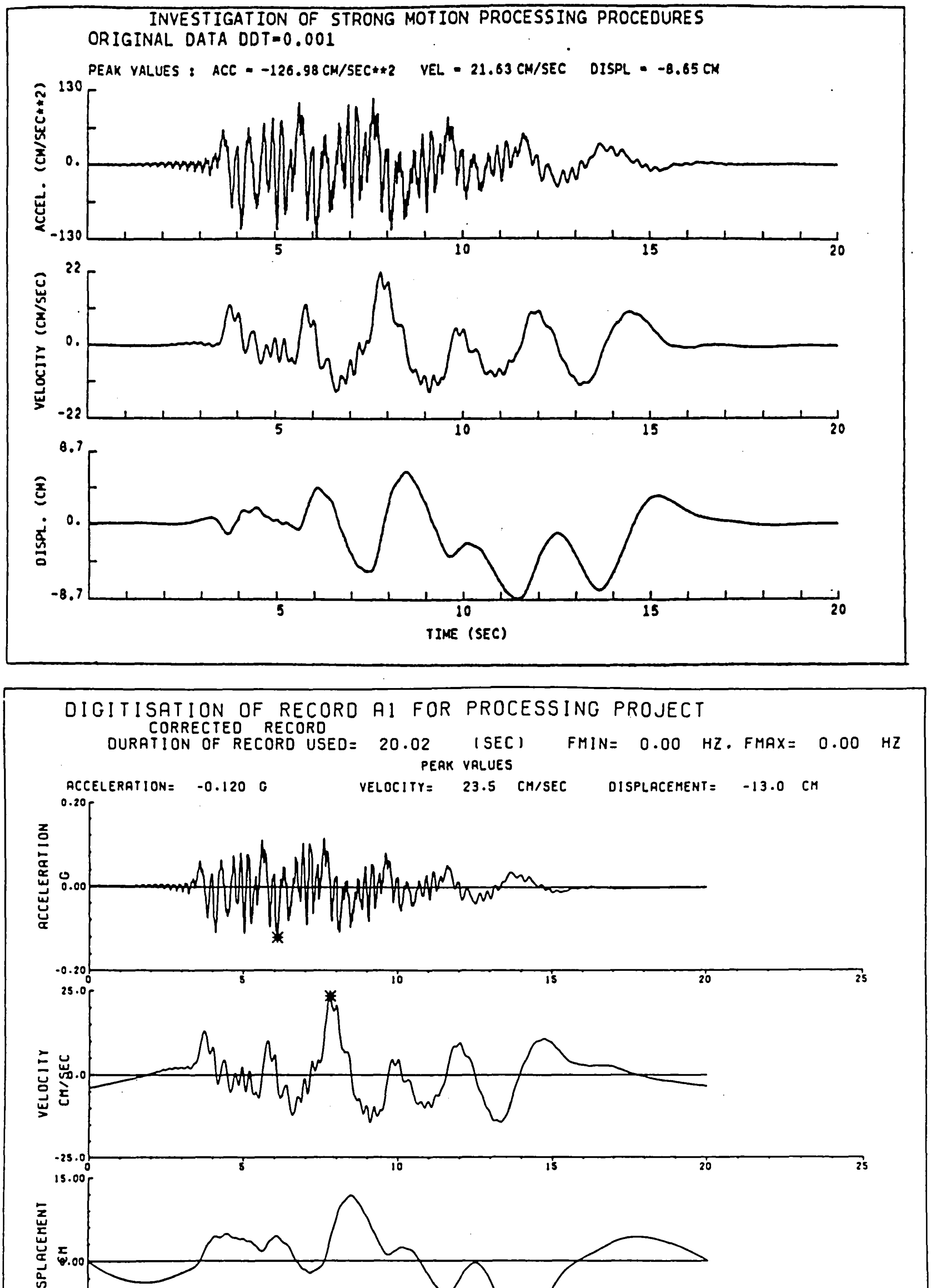

Fig.VII.3

Comparison of acceleration, velocity and displacement time histories of the original earthquake-like signal with the Procedure $KK = 3$

a) top: original signal

b) bottom: $KK = 3$ output

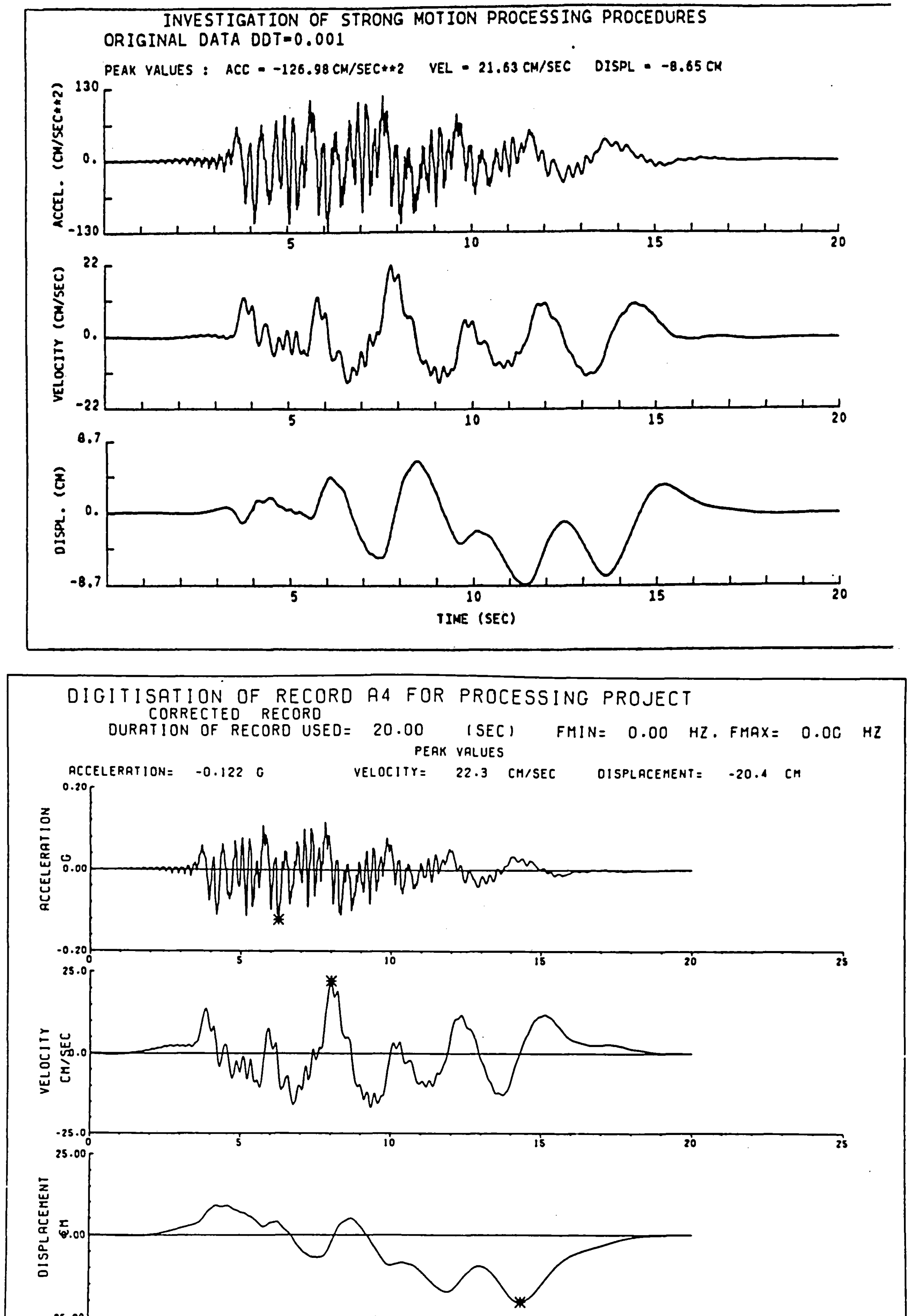

Fig.VII.4

Comparison of acceleration, velocity and displacement time histories of the original earthquake-like signal with the Procedure $KK = 4$

a) top: original signal

b) bottom: $KK = 4$ output

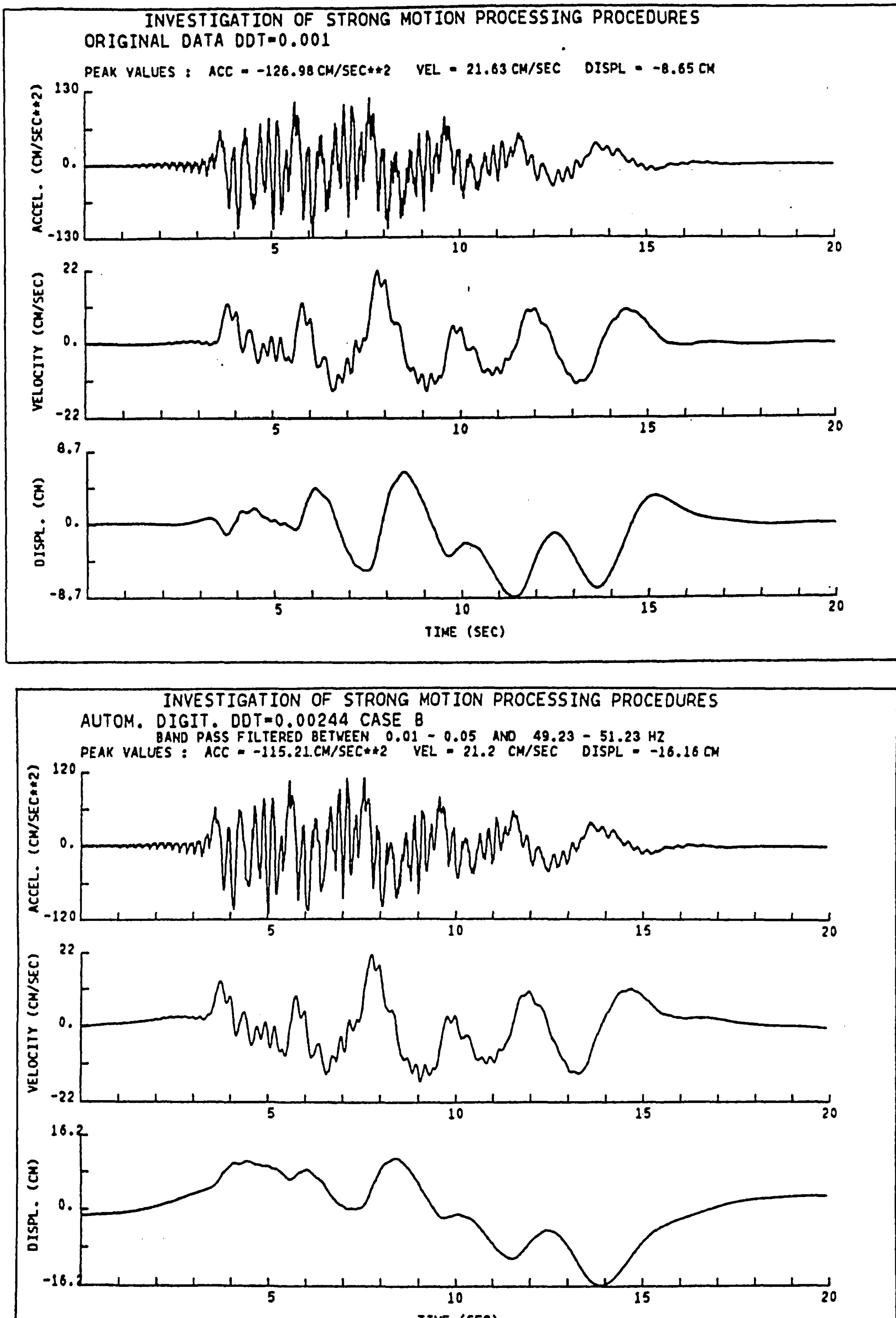

Fig.VII.5

Comparison of acceleration, velocity and displacement time histories of the original earthquake-like signal with the Procedure $KK = 5$

a) top: original signal

b) bottom: $KK = 5$ output

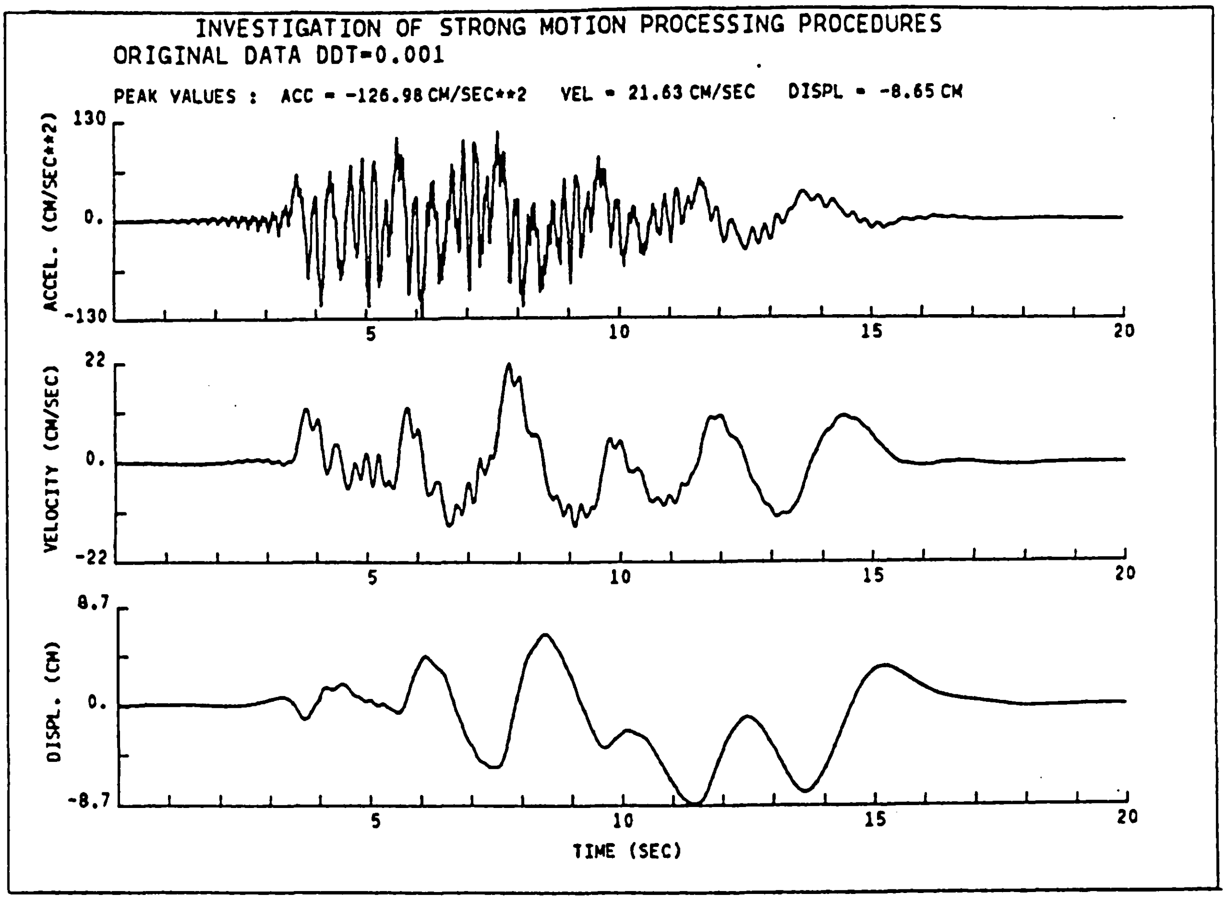

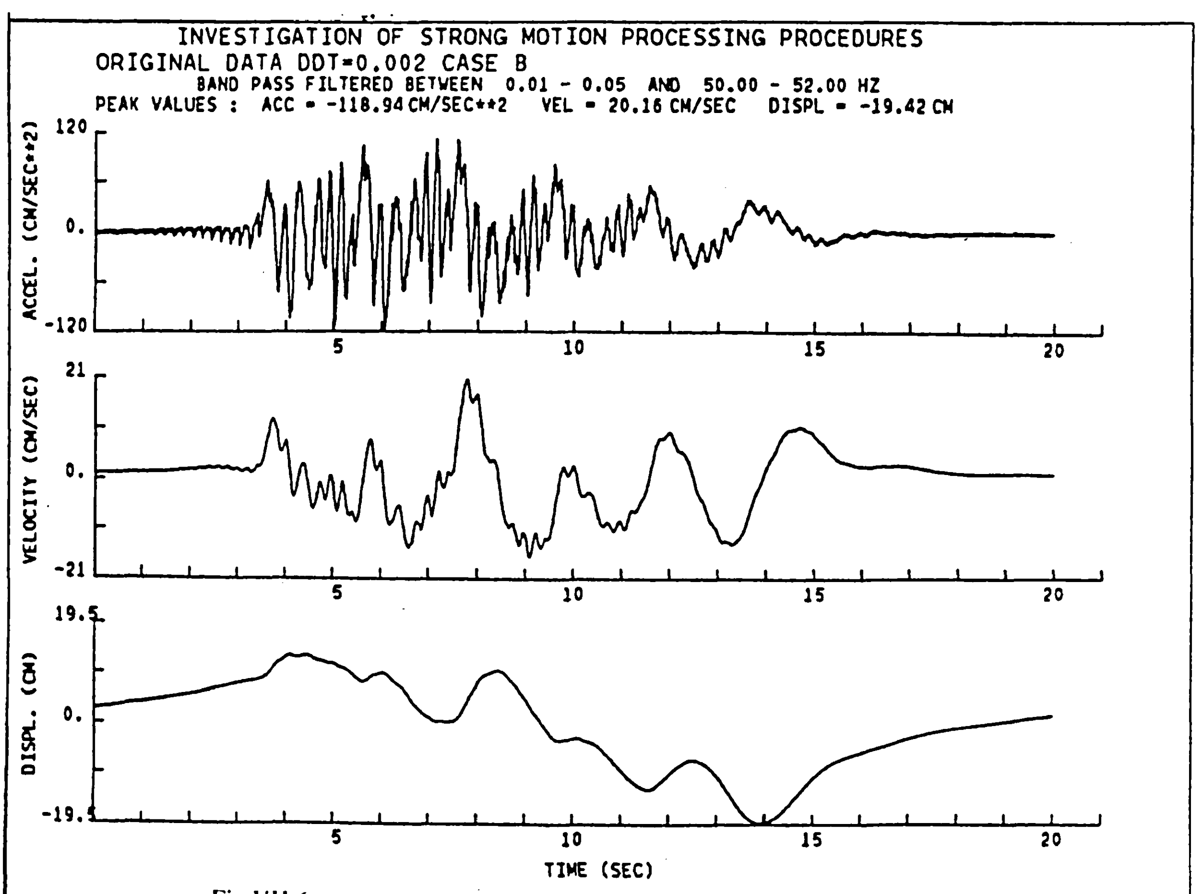

Fig.VII.6

Comparison of acceleration, velocity and displacement time histories of the original earthquake-like signal with the Procedure $KK = 6$

a) top: original signal

b) bottom: $KK = 6$ output

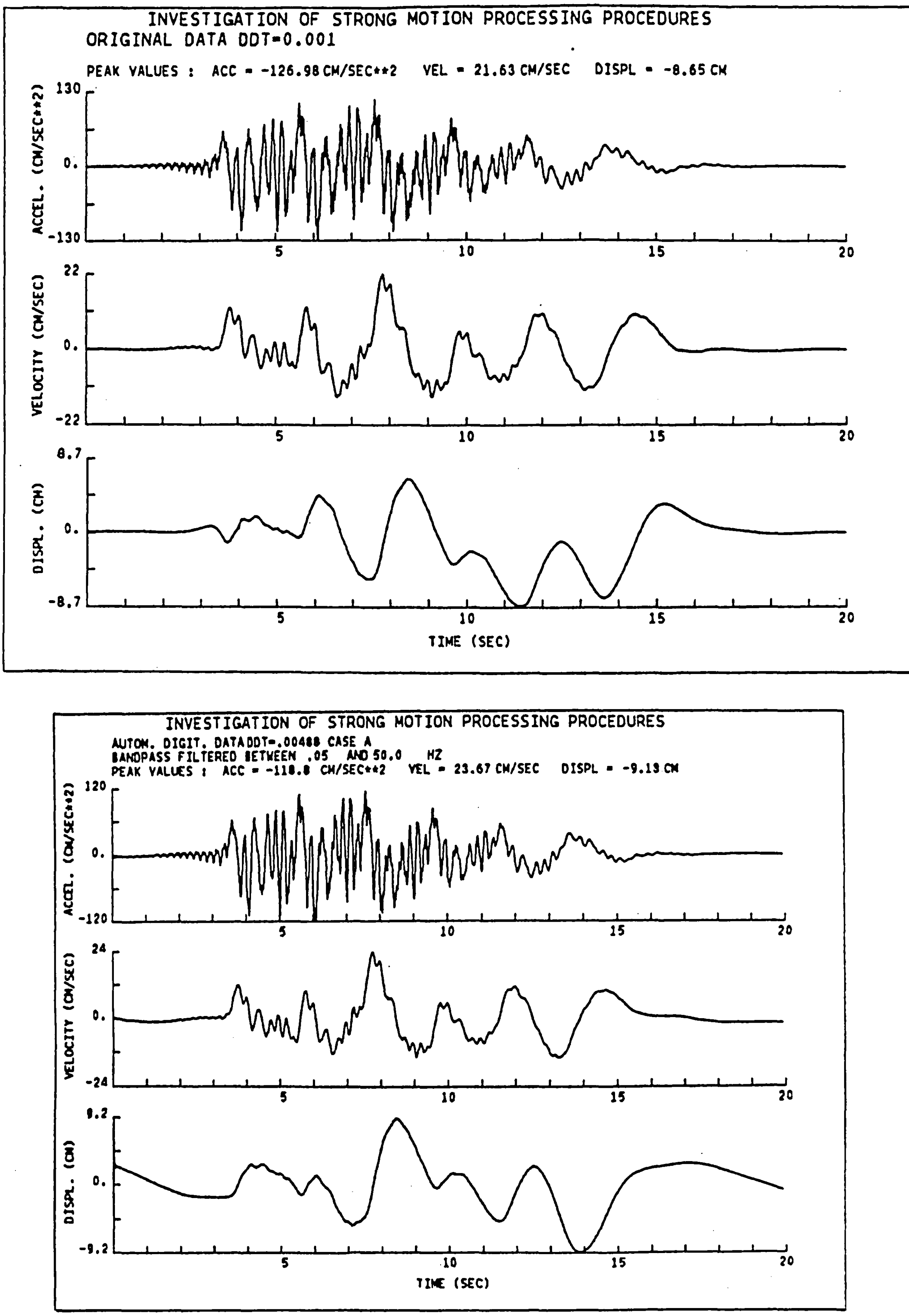

Fig.VII.7

Comparison of acceleration, velocity and displacement time histories of the original earthquake-like signal with the Procedure $KK = 7$

a) top: original signal

b) bottom: $KK = 7$ output

It is to be noted, however, that polynomial procedures do not always re-amplified the velocity RMS. They may also reduce it and then a much less accurate peak values is obtained.

The principal signal distorsions, however occur on the displacement time histories, for wich it was stated (*Schiff and Bogdanov (1967)*) that a recovery from acceleration records was almost impossible. The results may be classified in three groups:

Group 1: The polynomial types of correction ($KK = 1$, $KK = 2$, $KK = 3$, $KK = 4$),

Group 2: The early filtering procedures ($KK = 5$, $KK = 6$), Group 3: The new filtering procedure ($KK = 7$).

Displacements time histories of group 1 hardly bear any resemblance with the original signal. They are strongly affected by low frequencies coming from digitization noise and/or from the correcting polynomial itself. The pseudo-realistic shape of these motions are due to the artificial averagings of their $W(t)$, $X(t)$ and $Y(t)$ functions (see chapter IV). The peak values are far from the true value and even sometimes change their sign ($KK = 1$). As a whole, one should not rely on these functions as recovered ground displacement.

Displacements of group 2 are very similar to each other. They show a net improvement with respect to the displacement functions of group 1. They are still distorted by a low frequency component which is believed to come from the too sharp cutoff between 0.01 Hz and 0.05 Hz in the filtering process. In chapter V, we saw that a progressive smooth transition is required for such filters. *Fig VII 9a and VII 9b* show a possible improvement when the same roll-off transition band ($D_f = 0.05$ Hz) is used away from the DC value. We also note the unstable third digit in the peak acceleration, the increase of the peak velocity and the strong reduction of the peak displacement. These effects are due to the successive filterings and smoothings of acceleration, velocity and displacement that we shall discuss in section 7.4.

The displacement of group 3 exhibits immediately a fair similarity with the original displacement, although unrealistic start and end are visible. This function is comparable to those of the $KK = 5$ and $KK = 6$ cases but here neither successive filterings of velocity and displacement nor least square smoothings were performed. In section 7.4, we shall explain why such technique is preferable for final displacement recovery.

Table XI

Peak values for various correction types

correction type	acceleration g	velocity cm/sec	displaceme nt cm
original	0.130	21.8	8.7
$KK = 0$	0.130	18.7	52.0
$KK = 1$	0.123	22.3	10.7
$KK = 2$	0.120	22.8	16.5
$KK = 3$	0.120	23.5	13.0
$KK = 4$	0.122	22.3	20.4
$KK = 5$	0.115	21.2	16.2
$KK = 6$	0.119	20.2	19.4
$kk = 7$	0.117	23.6	9.1

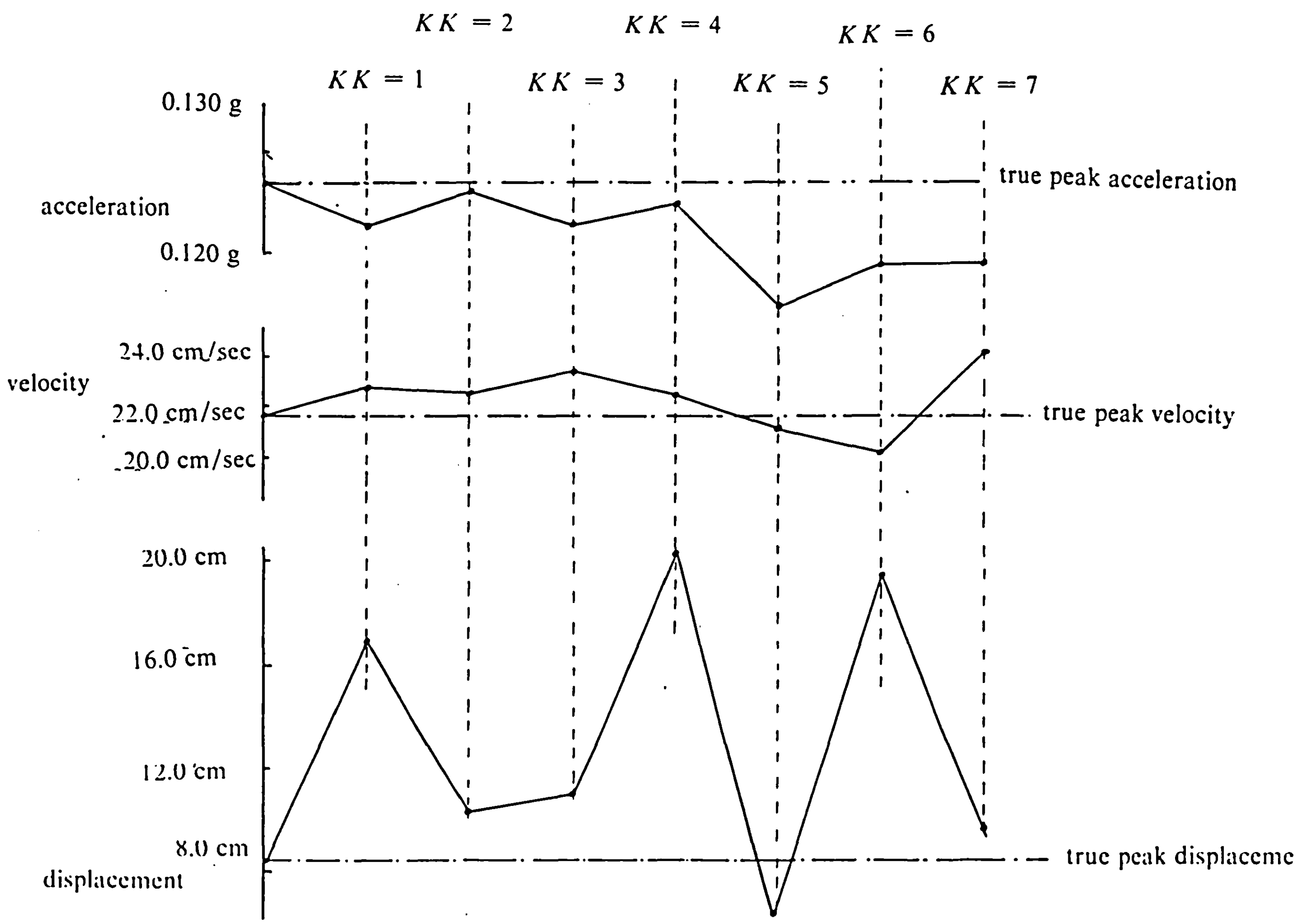

Fig.VII.8

Variations of peak values for the different Processing Procedures

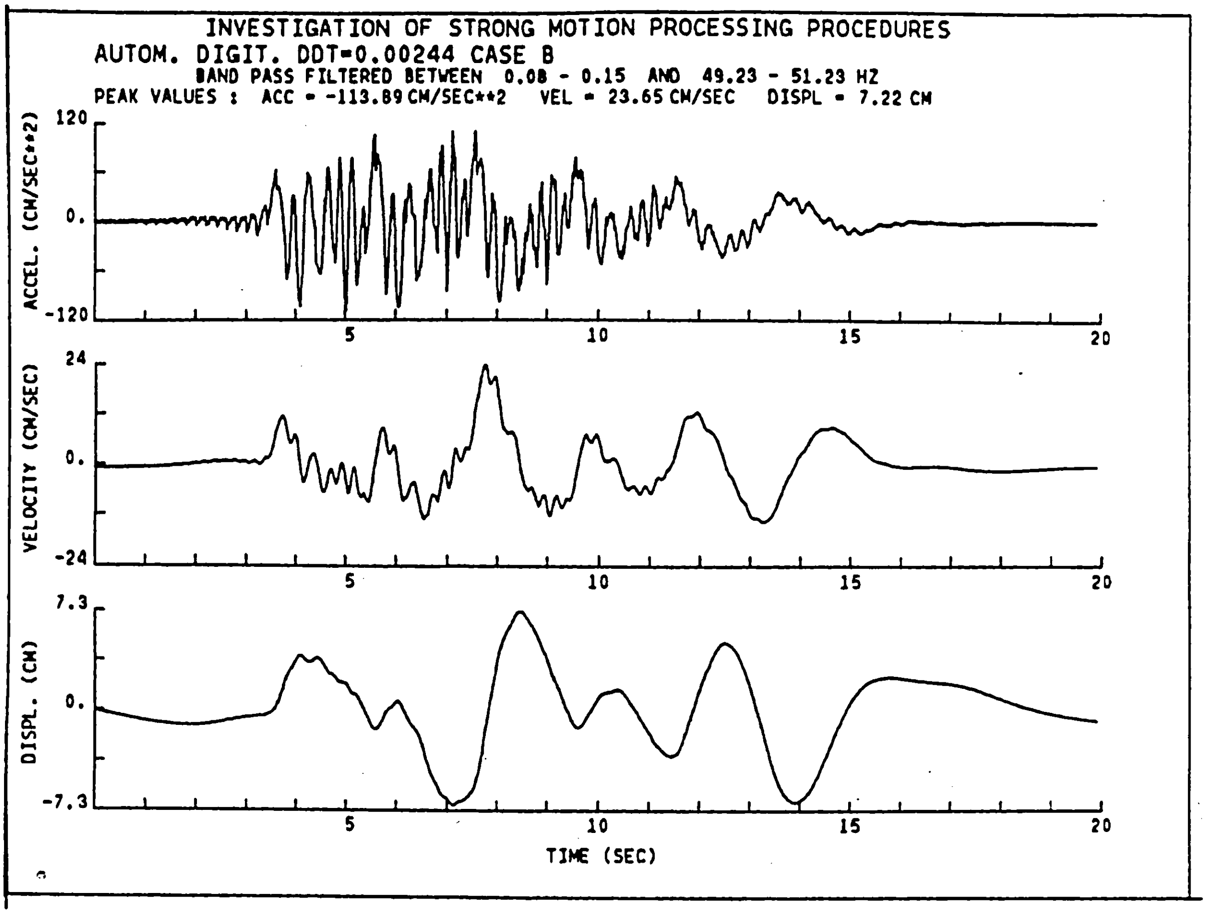

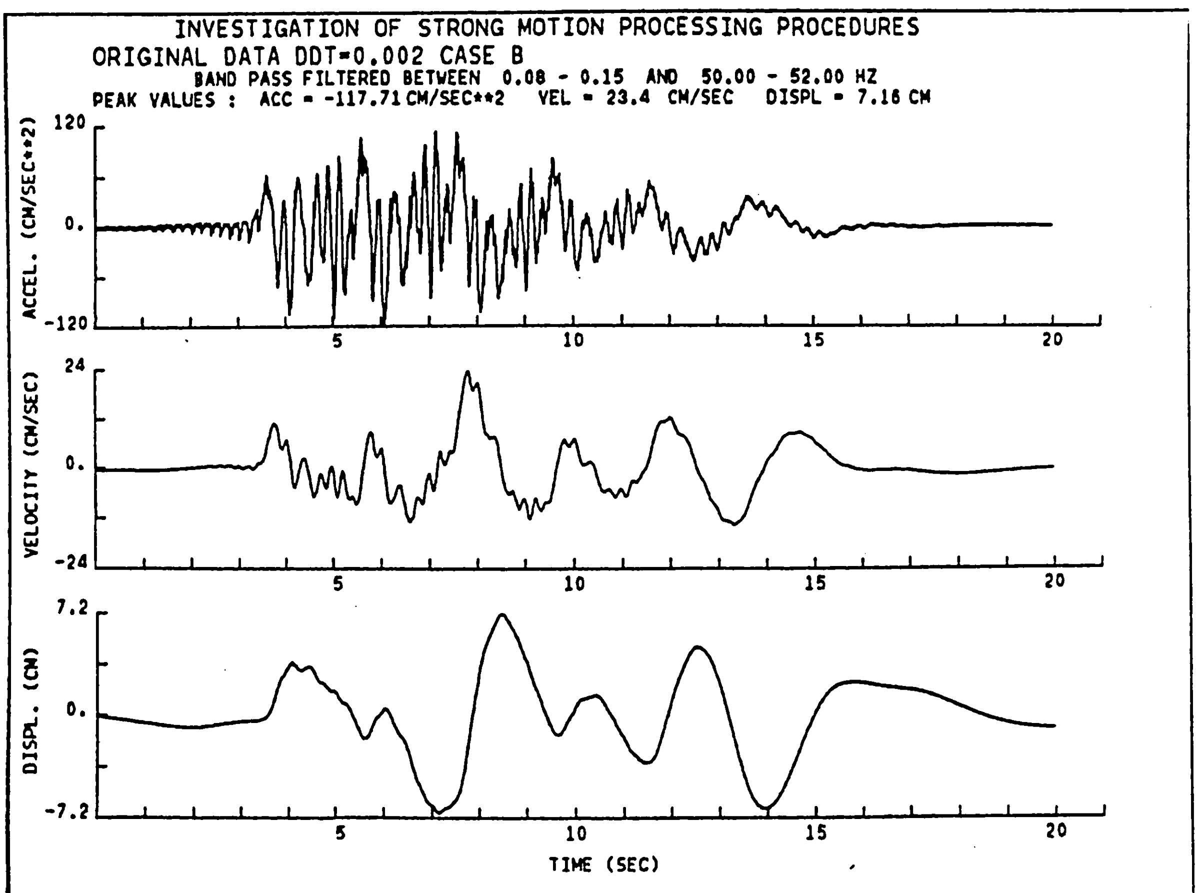

Fig.VII.9

Improvement of the ground motion time histories by increasing the low-pass transition band

a) Procedure $KK = 5$

b) Procedure $KK = 6$

7.3 SPECIFIC COMPARISONS

In this section, we shall examine successively the effects of the types of digitization, the instrument correction on the final ground motion. Also the influence of the correction programme will be evidenced.

7.3.1 Digitization effect

We saw in chapter III that digitization may have an important influence on the uncorrected motions, both in the low and in the high frequency ranges. After removal of the zones in wich the errors are significant, we are left with the central part of the spectrum where no significant differences are noticable. This is also seen on *fig. VII 10a and b* where we compare the final motions, initially digitized manually and automatically. No difference whatsoever is detectable. Only the least significant digits of the peak values are modified and do not deserve any particular attention.

7.3.2 Transducer correction

fig VII 11a and 11b show the treated signal with and without instrument correction, using the procedure of section 6.4. Here again, no major differences are worthwile noting. Unfortunately, this case must be regarded as favorable. The natural circular frequency of $\omega_0/2\pi = 25$ Hz and a critical damping of 60% are such that they do not require strong correction. On the other hand these values are now very common in transducer design and therefore this reflects the good final result which is now achieved.

7.3.3 Distorsions induced by the correcting programmes

This aspect of comparison deserves a closer examination. We have just said that, after correction, both digitization and transducer effects have not been detected. The final displacement, however, still does not copy exactly the original in its analytic form. We believe that this due to the correcting programme itself. In *fig. VII. 12a and b* we have compared the true ground motion representations with the same signal wich has only be submitted to a mock pass through the correcting procedure. No correction as such has been achieved and still the distorions that we observed at the beginning and the end of the displacement are already present. The correcting programme has contaminated the signal and this is the contamination wich remains in all the versions presented so far. The same conclusions, in a larger extent, are also valid for the other types of procedures.

This explains that there is a limit in the possibility of signal improvement by using such programmes. We also think that a reasonable level of quality has been achieved to date. Higher quality requirements would necessitate a far bigger effort, not in proportion with the expected results. It is certainly time to turn to other techniques of ground motion acquisition like the use of the second generation of recording instruments.

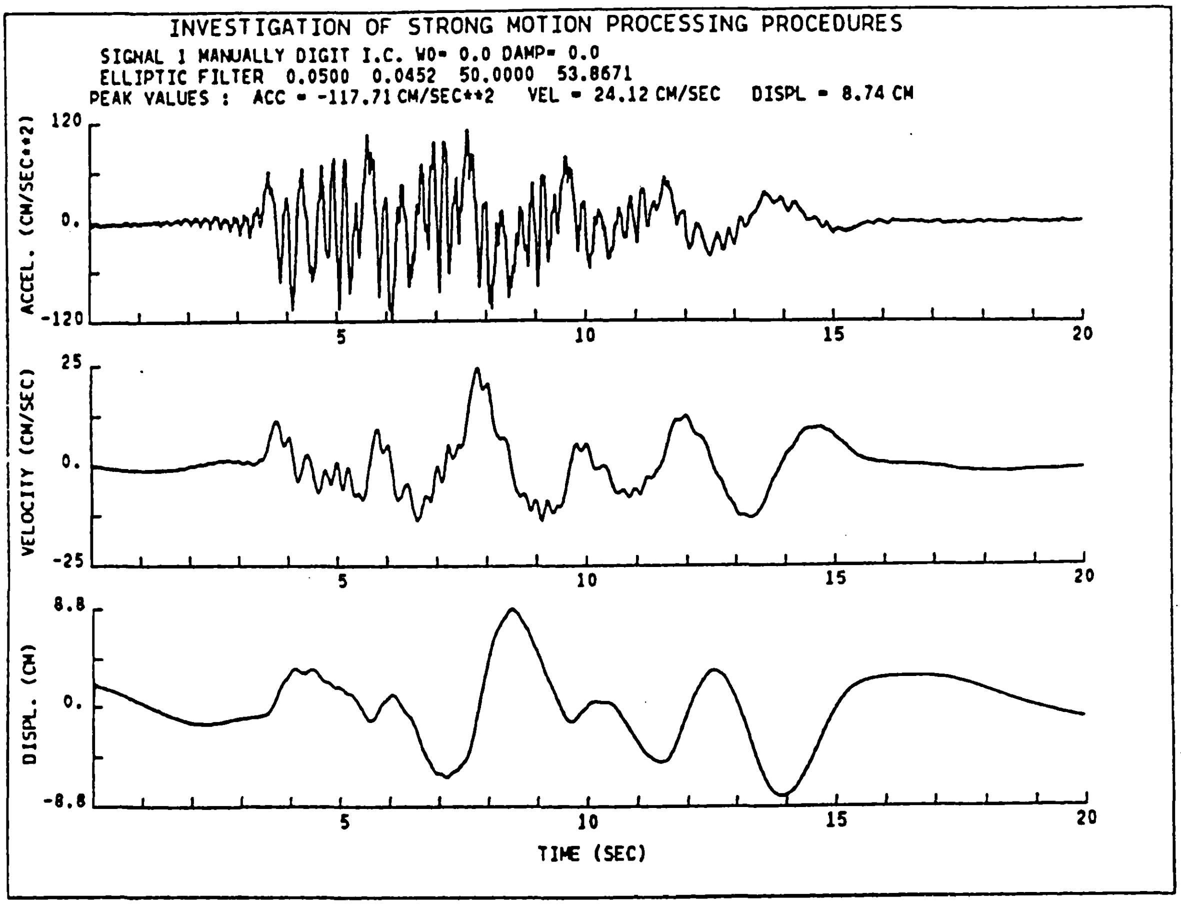

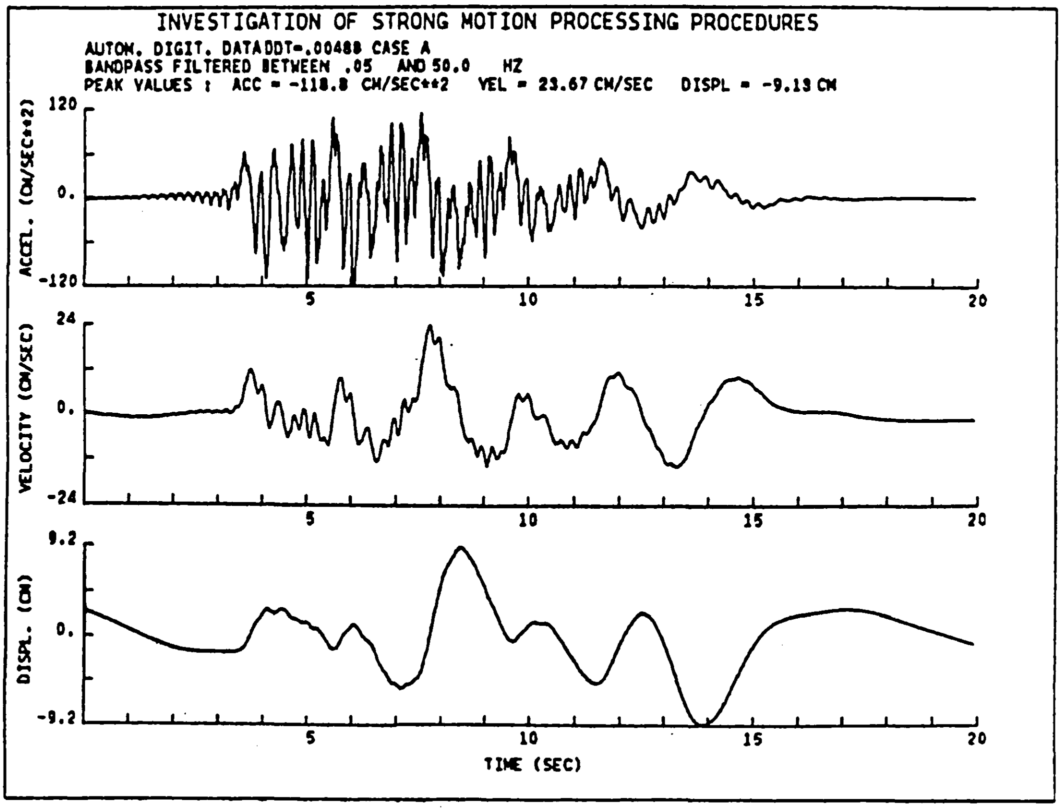

Fig.VII.10

No significant effect is noticed, after processing,

between two good quality digitizations

a) top: automatic digitization (DG1)

b) bottom: good quality semi-automatic digitization (DG4)

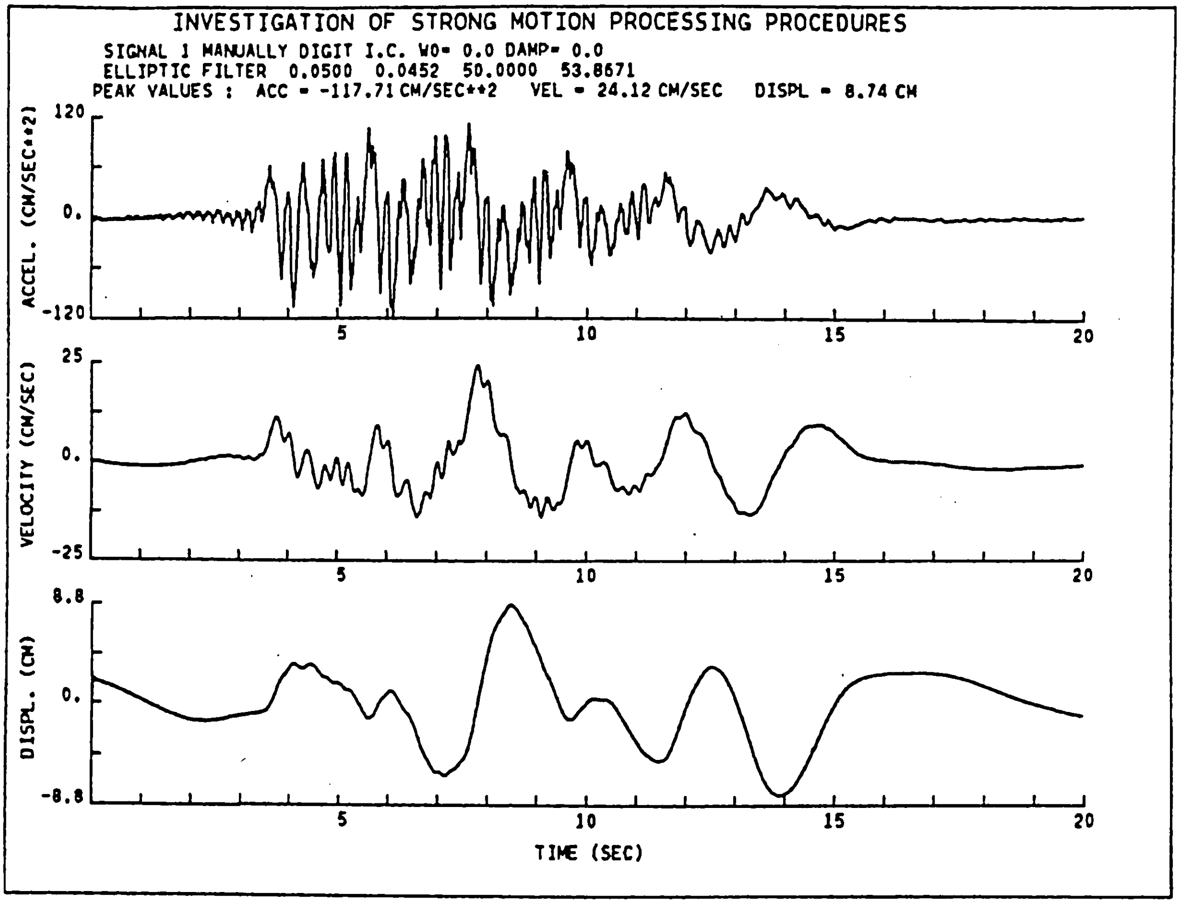

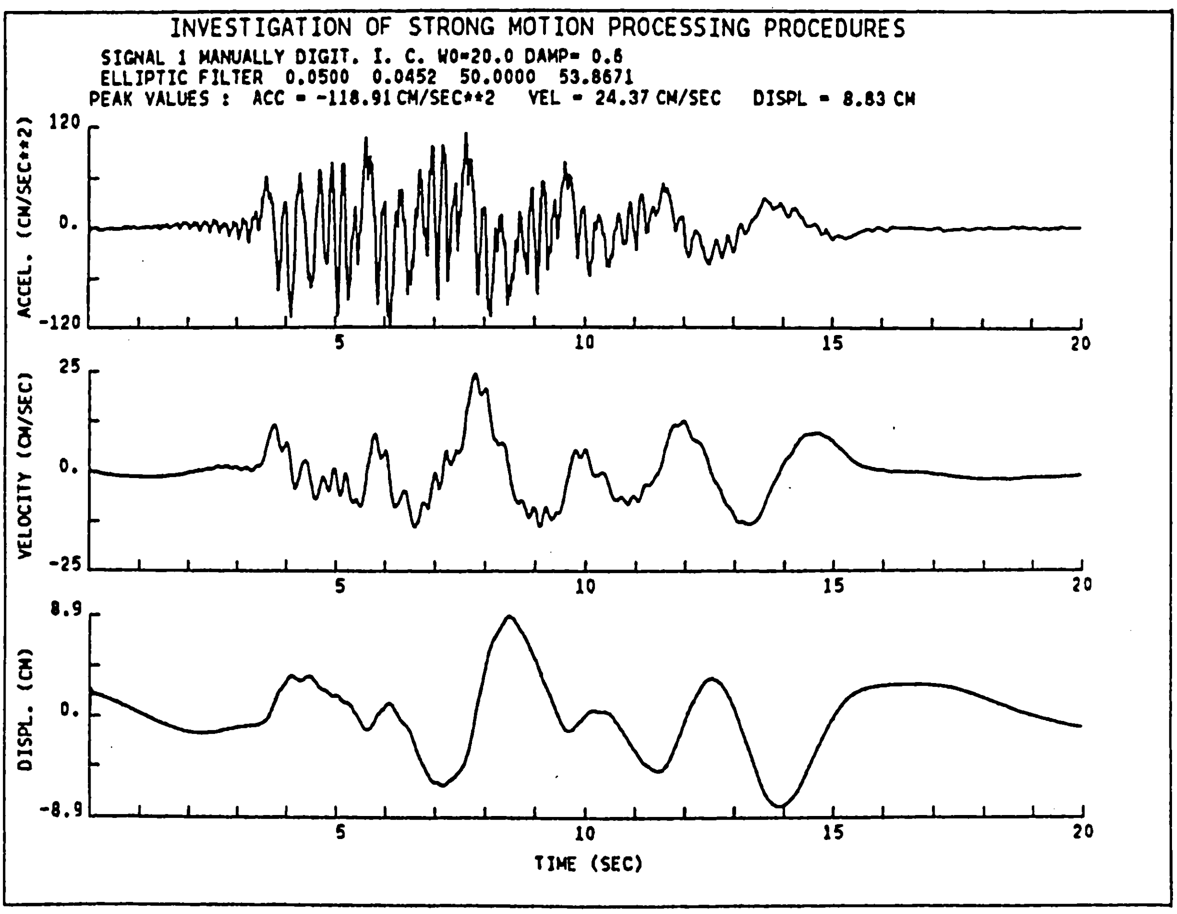

Fig.VII.11

Little effect is visible after transducer correction at $F_0 = 20$ Hz

a) without transducer correction

b) with transducer correction

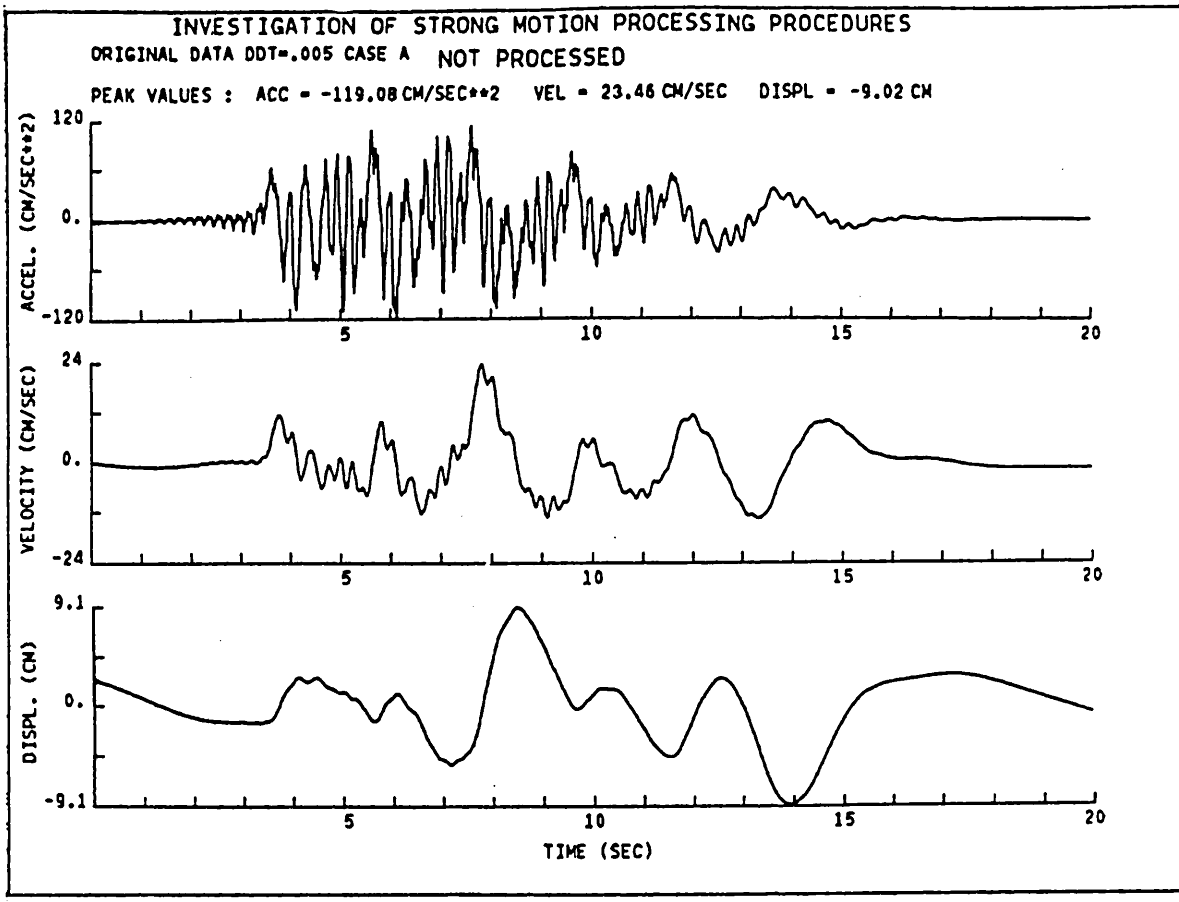

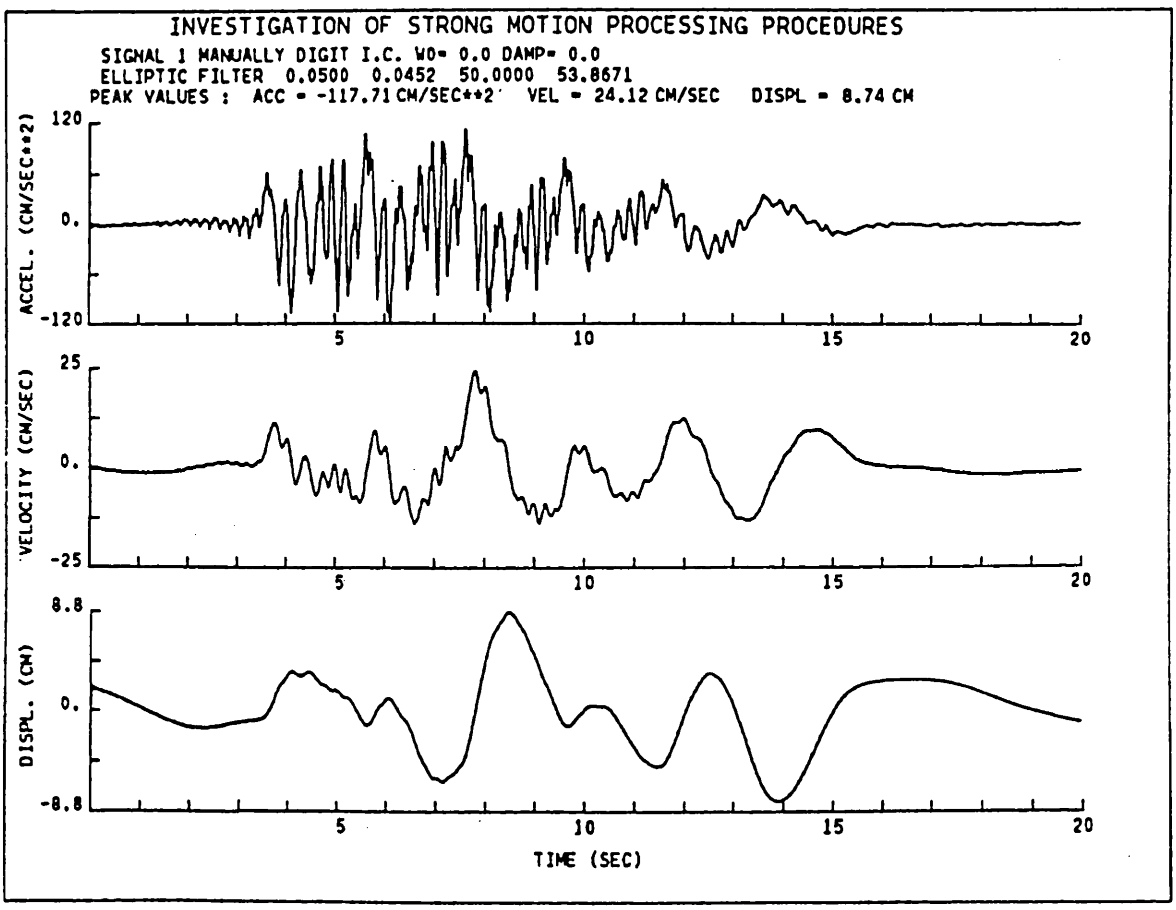

Fig.VII.12

The distorsion of the displacement time history is due to the correcting programme $KK = 7$

a) ground motion after a mock passage through $KK = 7$

b) ground motion processed typically

7.4 CONDITIONS OF PERMANENT DISPLACEMENT RECOVERY

7.4.1 Motivation and use

Although we do not have the material to present a permanent displacement recovery, it is of interest to give the necessary (but not sufficient) conditions for such a recovery.

These conditions are fulfilled in the *ImpCol Procedure* ($KK = 7$) but are not in any of the others. The use of such conditions may be useful when recording instruments are located very near the fault. Then fault offets may be measured. There are, however, major difficulties to perform sucessfully such a recovery. In essence, a permanent displacement originates from the coherent part of the rupture along the fault. It is a low frequency motion (see chapter X) and it is often unseparable from low frequency digitization noise. An important analytic effort associated with strict conditions may be required. The non respect of these conditions annilhilates all the chances of permanent displacement recovery.

7.4.2 The necessary conditions

In order to understand these conditions, let us consider a simple SDOF whose mass m is vibrating due to a sudden displacement of its base at time $t = 0$ (*fig. VI. 1*). The displacement function $x(t)$ (governed by *Eq. 6. 1*) is given by:

$$x(t) = x_0 \qquad 1 - e^{-\lambda\omega_0 t}\left[\cos\omega_1 t + \frac{\lambda\omega_0}{\omega_1}\sin\omega_1 t\right] \tag{7.1}$$

with the same notations as in chapter VI and where x_0 is the imposed intial displacement.

Velocity and acceleration functions $a(t)$ and $v(t)$ are immediately deduced by differentiations and the three representations of the motion are drawn on *fig. VII. 13a, b and c*. It is clear that the baselines of both the velocity and the displacement are not similar to their average linear trend. A linear fitting of acceleration requires that (see section 4.20 and 4.21):

$$\int_0^T a(t)\,dt = 0 \tag{7.2a}$$

$$\int_0^T t a(t)\,dt = 0 \tag{7.2b}$$

These equations are usually applied with $v(0) = d(0) = 0$, which may be questionable when no pre-event memory device has recorded the initial part of the motion. However, this assumption is sufficiently valid in a first approximation.

On the contrary, a linear fitting of velocity, is not always an acceptable assumption since it implies $d(T) = d(0) = 0$ and $W(T) = W(0) + Td(T) = Td(T) = 0$ (see *Eq.4.32*). This is not the case when a final displacement $d(T) \neq 0$ is expected. A linear fitting of the displacement function still accentuates the averaging of the higher moments $X(t)$ and $Y(t)$.

It can also be seen that any parabolic adjustment through acceleration imposes inacceptable constraints to the velocity and displacement curves. The only fitting which may be imposed is the linear fitting of the acceleration function. This is the first necessary condition of permanent displacement recovery.

There exits a second condition that the acceleration signal must fulfill. The digitization noise should be separable from the fault displacement information. Most of the information is certainly included about the period $T = T_f$, corresponding to the duration of the fault rupture:

$$T_f = \frac{D}{V_r} \tag{7.3}$$

where D is the fault length,

and V_r is the average rupture velocity.

If the low frequency cutoff ω_c is greater than $2\pi/T_f$ then, one has also eliminated the permanent displacement. An improved digitization and an accurate assessment of the low frequency cutoff are needed to keep this information in the corrected signal.

The first of these conditions is satisfied in the *ImpCol Procedure* ($KK = 7$). This has been achieved through the use of a very efficient filtering on the acceleration. In section 5.4.5 and *fig. V.23*, we suggested that the stop-band noise level should currently be around 60 dB attenuation. This renders unnecessary to operate successive filterings and smoothings on velocity and displacement functions, as required by the $KK = 5$ and $KK = 6$ procedures. The second condition is fulfilled when good quality digitization enables a very low frequency cutoff.

a) acceleration

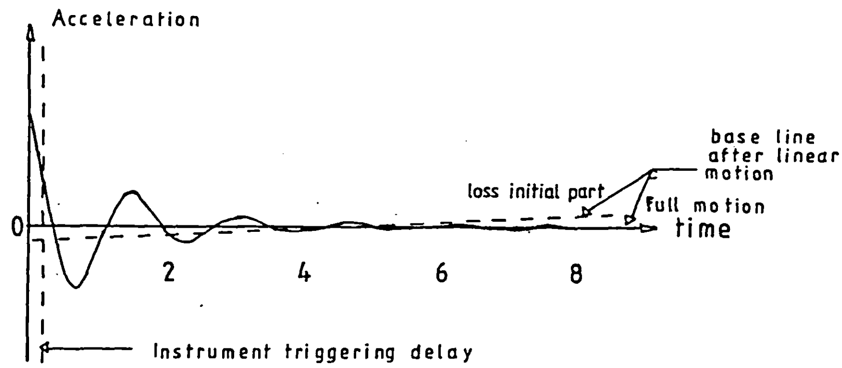

b) velocity

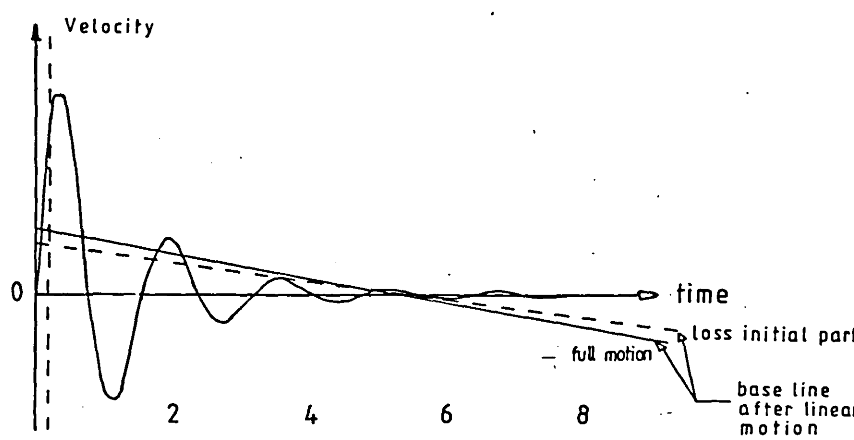

c) displacement

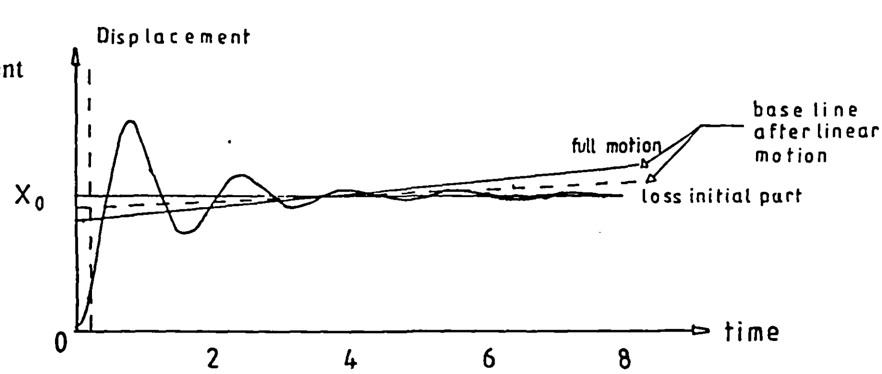

Fig.VII.13

Motion of a SDOF pendulum submited to an initial displacement x_0

Representation of the time history linear trends

with and without a loss of the record onset.

7.5 DISCUSSION

The successive analyses which have been carried out in the present chapter and in chapter 3 show the minimum spread for the signal recovery representing the reliability of earthquake strong motion records.

It is first apparent that the record processing affects the acceleration and the displacement time histories differently. In most cases a frequency range of reliability (0.1 Hz-10 Hz) may be defined which covers most the applications of engineering interest. These limits extend wider in the case of ground motions recorded at short distance where the signal energy is well above the noise energy. As the distance increases or the Magnitude decreases, this frequency range reduces. In the case of a digitization of average quality, the acceleration signal may be totally hidden by the noise at 200 km from the epicenter, even for a Magnitude of the order of 7. Significant improvement is achieved by extremely carefull manual or automatic digitization. With the same values for the distance and Magnitude, the frequency range may reach (1 Hz-5 Hz).

This effect (masking of signal by digitization noise) renders any type of correction or intrument deconvolution, illusive outside these frequency limits. The filtering of the extremes is necessary to remove a large amount of predominantly noise energy.

The displacement time history is also affected by digitization noise but a large contribution to the distorsion comes from the correcting programmes themselses. This limits considerably the usefulness of such near-field records as a backup for geophysical and seismological studies. Polynomial corrections add uncontrolled long period components which have the reverse effect for particular long records. The filtering techniques also bring spurious noise during the treatment due to the sharp cutoff required at very low frequency. This effect is mimimized in the $KK = 7$ case, where a very efficient elliptic filter is used. As a result, only acceleration filtering is sufficient and this permits to satisfy the neccessary conditions of permanent displacement recovery which cannot be obtained by any of the other methods.

Finally, we have to mention the significant advantage of the recording instruments of the second generation. It has been shown that, with such instruments, very reliable signals may be obtained. The dynamic range is about 20 times larger than for the mechanical-optical types of instruments. The onset of the signal is not lost, good signal reproduction is insured up to 50 Hz and digitization is not required. Although the present cost of such recorders seems excessive when only engeneering information is required, it is believed that they can provide a satisfactory answer for the accurate ground motion measurement in the near-field for a deeper understanding of the earthquake source mechanism.

blank page

PART II:

SIMULATION OF EARTHQUAKE STRONG MOTIONS

SCOPE OF PART II

In this second part, we analyse the present state of the art of engineering near-field ground motion simulation. The problem is very much influenced by the similar topic encoutered in conventional seismology but it also differs from it. Surely, it is of primar importance to understand the complexities of earthquake mechanism and wave propagation to be able to simulate any motion. However, the very purpose of engineering simulation is not to describe the mechanics of the rupture as accurately as possible. It is to make use of the fundamental knowledge, in order to improve the design techniques, without loosing on the safety or economic fronts.

We shall look at both aspects of engineering simulation: the empirical and the geophisical approaches. We do not intend to develop formaly a particular method. Our aim is rather to discuss on the topics and introduce new ideas in the conventional methods and provide the analytical formulation.

The empirical approach consists in dealing statistically with the recorded data. In this case, the simulation is an attempt to reproduce a motion possesing certain characteristics which have been detected in previous analyses. The advance in that direction is rather slow and rely on a large quantity of data. The difficult question which is posed at this stage of the research is to introduce, in a reliable manner, the strong non-stationary character of ground motion without the help of too sophisticated techniques. We shall see how "non-stationarity in time" may be simply integrated.

The second approach is not of common use in engineering, due to the many parameters involved. However, we believe that it can bring an interesting new view point for the understanding of the earthquake loading in design. We shall analyse thoroughly the topic and shall propose a methodology for a simulation largely constrained by all the kinematic and dynamic aspects of the crust rupture and seismic wave propagation. Since we are interested in the acceleration field, it is not possible to retain deterministic considerations for the whole procedure. We shall therefore propose a physico-stochastic method to take into account the unknown detailed behaviour on the rupturing fault.

CHAPTER VIII

BACKGROUND OF STOCHASTIC PROCESSES

8.1 INTRODUCTION

Before entering into the description of strong motion simulation of earthquakes, it is convenient to give a brief summary of some fundamental probabilistic concepts that will be used in the following chapters.

Most of the material of this chapter was obtained from *Papoulis (1981)* and *Newland (1984)*, but was rearranged to suit the earthquake strong motion study context.

8.2 RANDOM PROCESSES

8.2.1 Probability function of 1st and 2nd Order

Many phenomena in nature, and this also applies to near field accelerograms, are characterised by the unpredictable change in time, wich cannot be fully described before the phenomenon occur. Nevertheless, if the same phenomenon occurs several times, and if certain statistical regularities among occurences can be found, the phenomena can be described by a set of probability distributions and mean values of some characteristics can be estimated.

Let $X_i(t)$ be a real-valued function of time t. The index i identifies a particular function of an infinite set of functions, called ensemble and written $X(t)$. The *ensemble* constitutes a random process if we cannot predict their values at any instant during the time in which they take on finite values (*fig. VIII.1*). Usually it possible to characterise the process by the knowledge of a set of probability functions. At any fixed value of time t_j the random process defines a single random variable $x(t_j)$. The characteristics of the stochastic (or random) process is closely related to the random properties of the random variable $x(t)$.

Although a stochastic process is fully determined if one knows its n order distribution functions, for engineering purposes, only the first and second order statistics of the distribution are usually considered. The distribution function of the random variable $x(t)$ is denoted by $F(x;t)$, and we have:

$$F(x;t) = \mathrm{Prob}[X(t) \leq x\ ] \tag{8.1}$$

Given two real numbers x and t, the function $F(x;t)$ equals the probability of the event $X(t) \leq x$ consisting of all the outcomes such that, at the specified time t, the functions of the ensemble $X(t)$ do not exceed the given number x.

The function $F(x;t)$ is the first-order distribution of the process $X(t)$. The corresponding density is obtained by differentiating with respect to x:

$$f(x;t) = \frac{\partial F(x;t)}{\partial x} \tag{8.2}$$

Given two instances t_1 and t_2, we consider the random variables $x(t_1)$ and $x(t_2)$. Their joint distribution depends, in general, on t_1 and t_2. We shall denote it by:

$$F(x_1,x_2;t_1,t_2) = \mathrm{Prob}\Big[X(t_1) \leq x_1, X(t_2) \leq x_2\Big] \tag{8.3}$$

It is the second-order distribution of the process $X(t)$. The corresponding density is given by:

$$f(x_1,x_2;t_1,t_2) = \frac{\partial^2 F(x_1,x_2;t_1,t_2)}{\partial x_1 \partial x_2} \tag{8.4}$$

8.2.2 Parameters of stochastic processes

The mean function $\nu(t)$ of a process $X(t)$ is the expected value of the random variable $x(t)$ and is defined by:

$$\nu(t) = \mathrm{E}[X(t)] = \int_{-\infty}^{+\infty} x f(x;t)\,dx \tag{8.5}$$

where E[.] denotes expectation. It is in general a function of time (non stationary process).

The autocorrelation $R(t_1,t_2)$ of a process (the prefix "auto" refers to the fact that the two random variables belong to the same process) is the joint moment of the two random variables $x(t_1)$ and $x(t_2)$:

$$R(t_1,t_2) = \mathrm{E}\Big[X(t_1).X(t_2)\Big] = \int_{-\infty}^{+\infty} x_1 x_2 f(x_1,x_2;t_1,t_2)\,dx_1 dx_2 \tag{8.6}$$

It is in general a function of t_1 and t_2.

The autocovariance of $X(t)$ is the covariance of $x(t_1)$ and $x(t_2)$:

$$C(t_1,t_2) = \mathrm{E}\Big[\Big(x(t_1) - \nu(t_1)\Big)\Big(x(t_2) - \nu(t_2)\Big)\Big] \tag{8.7}$$

From the above we see that:

$$C(t_1,t_2) = R(t_1,t_2) - \nu(t_1)\nu(t_2) \tag{8.8}$$

When $t_1 = t_2 = t$, the covariance reduces to the the variance σ_X^2. We remark that:

$$\sigma_X^2(t) = C(t,t) = R(t,t) - \nu^2(t) \tag{8.9}$$

the variance of the process, may be obtained from the autocorrelation function.

$\sigma_X(t)$ is also called the Root Mean Square (RMS) of the process.

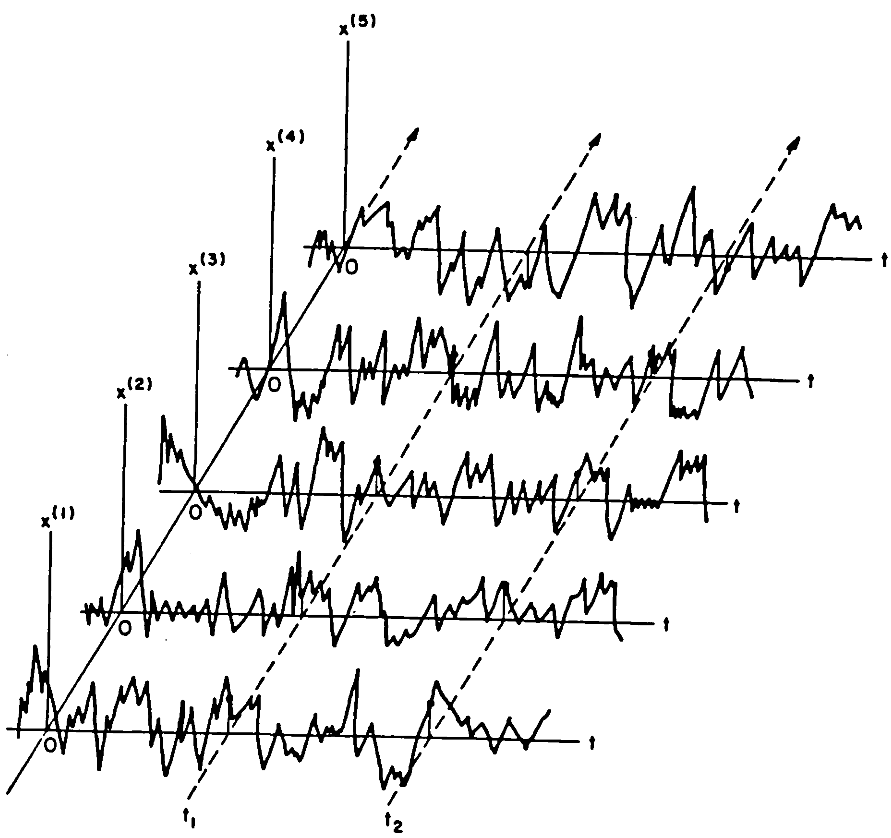

Fig.VIII.1

Schematic representation of a random process $X(t)$

Each $x^{(j)}(t)$ is a sample function of the ensemble

8.2.3 Stationarity and Ergodicity

A stochastic process is said to be stationary if its probability distributions are invariant under any shift in the time origin; otherwise the process is called non-stationary. In particular the first-order probability density $f(x; t)$ becomes independent of time; this implies that the expected value E[x] and the variance σ_X^2 are constants. The second probability density is also independent of time, whereas the autocorrelation becomes only function of the lag $\tau = t_2 - t_1$ and not of the individual values t_1 and t_2:

$$R(\tau) = \mathrm{E}[X(t)X(t+\tau)] \tag{8.10}$$

Truly, a stationarity in a strict sense involves the n order statistical moments. In practical engineering cases, where we do not consider order higher than two, we have what we call a weak stationarity. It must be recognized that any time limited process (like earthquake signals) is non-stationary. However the non-stationarity effects associated with starting and stopping are often neglected in practice if the duration of the stationary operation is long compared with the starting and stopping intervals.

A stationary stochastic process is called an ergodic process if its temporal averages along any representative sample function are equal to the ensemble averages. The assumption of ergodicity of a process is a very common one. It permits estimations of ensemble averages by taking time averages of single functions of the ensemble. This is in particular very useful with strong motion records, where it is difficult and expensive to obtain a large number of independent sample functions at a given site.

8.2.4 Harmonic Analysis

Fourier analysis is a very useful tool in the analysis of stationary stochastic process. The autocorrelation function of a stationary process was transformed by *Parzen (1962)* and expressed as:

$$R(\tau) = \frac{1}{2\pi} \int_{-\infty}^{+\infty} e^{i\omega t}\, dF(\omega) \tag{8.11}$$

where $i^2 = -1$ and $\tau = t_2 - t_1$,

ω = circular frequency.

For two frequencies $\omega_1 < \omega_2$, $F(\omega_2) - F(\omega_1)$ can be interpreted as a measure of the contribution of the frequency band $\omega_2 - \omega_1$, to the content of the stochastic process. If $F(\omega)$ is everywhere differentiable, its derivative, $S(\omega)$ is called the *spectral density function* of the outcome (*fig. VIII.2*). Then it can be written:

$$R(\tau) = \frac{1}{2\pi} \int_{-\infty}^{+\infty} S(\omega) e^{i\omega t}\, d\omega \tag{8.12}$$

It can be shown that the spectral density function and

$$S(\omega) = \int_{-\infty}^{+\infty} R(\tau) e^{-i\omega\tau} d\tau \tag{8.13}$$

Notice that, if $\tau = 0$ ($t_1 = t_2$),

$$R(0) = \frac{1}{2\pi} \int_{-\infty}^{+\infty} S(\omega)\, d\omega = \sigma_X^2 \tag{8.14}$$

and therefore the variance of the process is proportional to the sum over all frequencies of $S(\omega)\,d\omega$, and, $S(\omega)$ can be interpreted as a mean square spectral density (*fig. VIII. 3*). It can be shown that $S(\omega)$ is a non-negative even function of ω. Also the ensemble average $G(\omega)$ of the spectral densities for all sample functions equals the spectral density of the process,i.e.

$$\mathrm{E}\left[S_k'(\omega)\right] = G(\omega)$$

If the process is ergodic then

$$S_k(\omega) = G(\omega)$$

where $S_k(\omega)$ is the spectral density of any representative outcome.

In the literature both notations $S(\omega)$ and $G(\omega)$ are used to represent the SDF of the processes which are therefore implicitely assumed to be ergodic.

From the definitions above one can see the following interesting conclusions (*Crandall and Mark 1963*):

1) If the process contains no periodic components then $S(\omega)$ is finite everywhere.

2) if the process has a sinusoidal component of frequency ω_0 then the spectral density must be infinite at $\omega = \omega_0$. In particular if the process does not have zero mean then there is a finite, zero-frequency component and the spectrum will have a spike at $\omega = 0$.

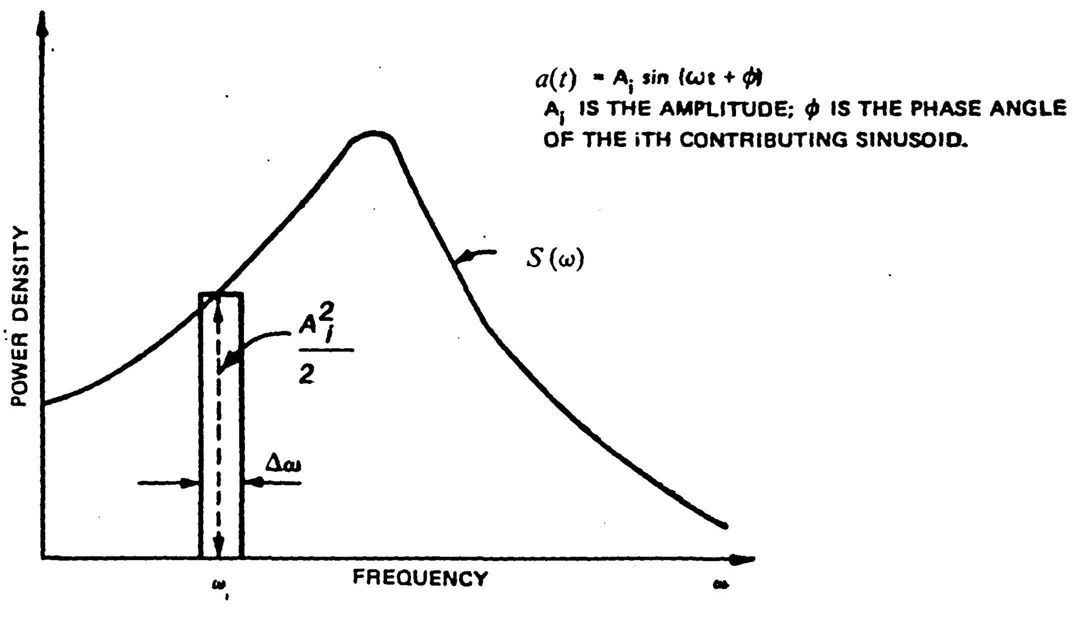

The PSD function $S(\omega)$

Fig.VIII.2
Typical spectral density of a stochastic process

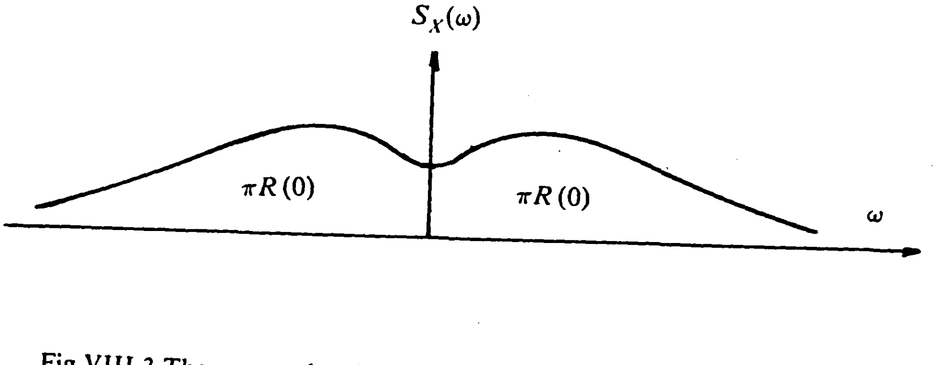

Fig.VIII.3 The area under the spectral density curve is equal to $2\pi\sigma^2$

8.3 STOCHASTIC PROCESSES USED IN S.M. SIMULATION

We shall describe now two well-known types of stochastic processes which find direct application in the simulation of earthquake strong motion simulation.

1) The *Gaussian Process* which is very commonly used in all branches of engineering and which is particularly adapted to time histories.

2) The *Poisson Process* which is usually encountered in the problems relating to queues and in seismology; it describes reasonably well most of the arrival processes of events.

Both these processes are mainly used in the context of stationary processes but extension to non-stationary processes have been developed.

8.3.1 Gaussian Process

The Gaussian, or normal process is of useful interest in practice since it is uniquely defined by the first and second order distribution functions. It originates from the probabilistic law of large numbers expressed by the Central Limit theorem and the *Moivre-Laplace* theorem. Successful tests of normality of earthquake accelerograms, viewed as stochastic processes, were performed by *Hanks and McGuire (1981)*.

With the notations given in the previous sections. In this case the probability function of a normal process is:

$$f(x) = \frac{1}{\sigma\sqrt{2\pi}} \; e^{-(x-\nu)^2/2\sigma^2} \tag{8.15}$$

The cumulative probability function is:

$$F(x) = \frac{1}{\sigma\sqrt{2\pi}} \int_{-\infty}^{x} e^{-(\xi-\nu)^2/2\sigma^2} \, d\xi \tag{8.16}$$

The non-stationary Gaussian process is obtained when both the mean ν and the variance σ are function of time.

A stationary Gaussian process with zero mean is completely characterised in the probabilistic sense by its power spectral density (*Eq. 8.13*) which is computed in practice through:

$$S(\omega) = \lim_{\substack{T_k \to \infty \\ n \to \infty}} \frac{1}{n} \sum_{k=1}^{n} \frac{2 \mid F_k(i\omega) \mid^2}{T_k} \tag{8.17}$$

in which $F_k(i\omega)$ is the Fourier Transform of $X_k(t)$ and T_k is the duration of the signal used. The variance of the process is obtained from:

$$\sigma_X^2 = 2 \int_0^{+\infty} S(\omega)\, d\omega \tag{8.18}$$

This shows that the RMS may be interpreted as a continuous sum of all the frequency contributions.

8.3.2 Poisson Process

The Poisson process is a counting process of events occuring in intervals of times $]t_i, t_{i+1}]$. A semi closed interval is used to treat t_i as belonging to the previous interval. Its probability function has the following properties:

1) independence of arrivals: the arrivals of events in the future are independent of the arrivals in the past.

2) the probability of simultaneous events is assumed nil: within an infinitesimal interval $]t, t+dt]$ the probability of two or more events is negligible compared with the probability of one event.

3) the average arrival rate of events is independent of time: the probability of one arrival in $]t, t+dt]$ is equal to the probability of one arrival in $]t+h, t+h+dt]]$. this rate is commonly denoted λ (=const).

If property 3) is removed the process is called Poisson process with non-stationary intervals. If besides property 2) is removed, and only property 1) is satisfied the process is called non-stationary Poisson process.

It can be shown, by deleloping the three mentioned properties that the probability of having N events in an interval of duration T is:

$$\text{Prob}[N;T] = e^{-\lambda T} \frac{(\lambda T)^N}{N!} \tag{8.19}$$

It is straitghtforward to check that the average arrival rate is λ:

$$\text{E}[N(T)] = \lambda$$

In the case of a non starionary arrival rate $\lambda = \lambda(T)$,the Poisson process has the more complicated expression:

$$\text{Prob}[N,T] = \frac{1}{N!} \left[\int_0^T \lambda(\tau)\, d\tau \right]^N \exp \left[-\int_0^T \lambda(\tau)\, d\tau \right] \tag{8.20}$$

8.4 TRANSMISION OF PROCESSES THROUGH LINEAR SYSTEMS

8.4.1 Power spectral density function of outputs

We shall examine now, how stochastic processes are transmitted through mechanical systems. Since we have in mind the subsequent study of Response Spectra, we shall limit our review to the linear SDOF systems. We are concerned here with the case of a stationary process $X(t)$ to be input to such systems; the output process is noted $Y(t)$.

It is well known that, when the randomness of a linear SDOF system is negligeable, the response of a deterministic input $x(t)$ is expressed by $y(t)$, the solution of the equation:

$$\ddot{y}(t) + 2\lambda\omega_0\dot{y}(t) + \omega_0^2 = x(t) \tag{8.21}$$

$y(t)$ can be obtained through the time domain using the convolution, or Duhamel integral:

$$y(t) = \int_{-\infty}^{t} x(\tau)h(t-\tau)\,d\tau \tag{8.22}$$

where τ is a dummy time variable and $h(t-\tau)$ is the free vibration response due to a unit impulse at time τ, that is due to:

$$x(t) = \delta(t-\tau) \qquad \delta(t) = \text{ Dirac function}$$

This response can also be expresned in the frequency domain using the relation:

$$y(t) = \frac{1}{2\pi}\int_{-\infty}^{+\infty} H(i\omega)X(i\omega)e^{i\omega t}\,d\omega \tag{8.23}$$

where $H(i\omega)$ is the complex frequency response function (transfer function).

and $X(i\omega)$ = the Fourier transform of the input function $x(t)$.

In the general case of stationary input, a function $x(t)$ is expanded in separate simple harmonics which cover the entire range $-\infty < t < +\infty$. For this reason the frequency response must be defined as the ratio of the steady-state output response $y(t)$ to in the common case where $0 \leq \lambda \leq 1$,

$$\omega_1 = \omega_0\sqrt{1-\lambda^2} = \quad \text{damped circular frequency.}$$

If a stochastic process $X(t)$ is input to the same system, the same *Eq. 8.21* may be used where $X(t)$ and $Y(t)$ are now stochastic processes and the coefficients are non random if the system is deterministic. Power density functions must be considered.

It can be shown that the power density function of the output process has become $S_Y(\omega)$ such that:

$$S_Y(\omega) = | H(i\omega) |^2 S_X(w) \tag{8.26}$$

where $S_X(\omega)$ is the power spectral density of the input process (*fig. VIII. 4*).

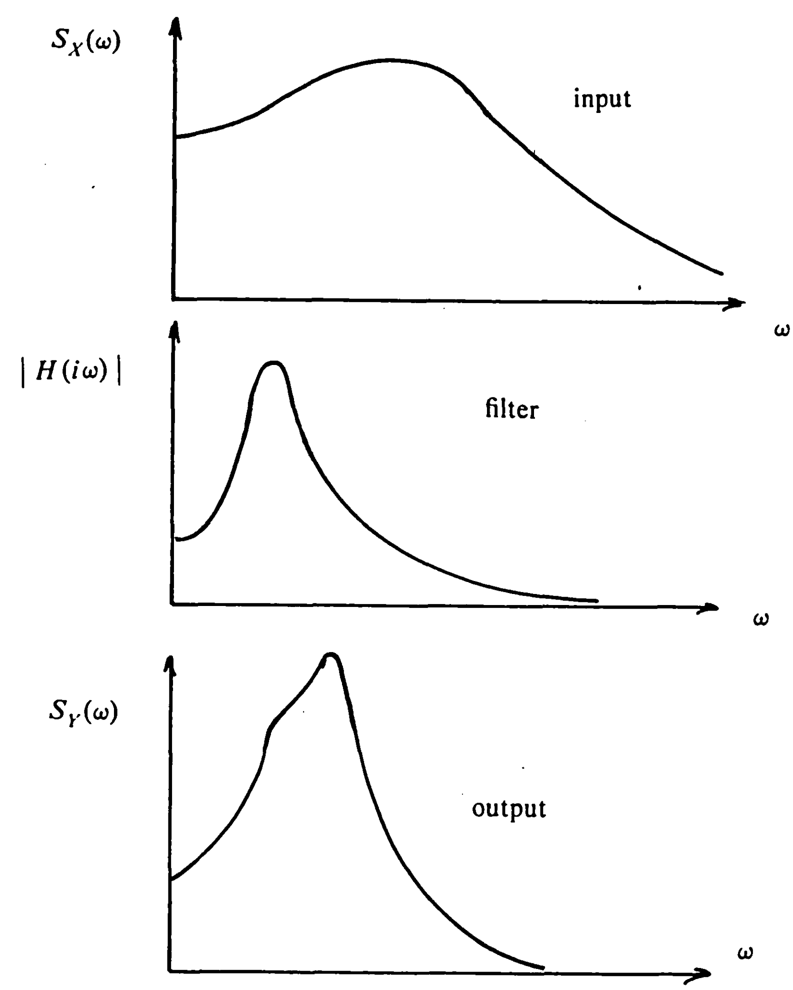

Fig.VIII.4

Output PSD $S_Y(\omega)$ for a system submitted to a input PSD $S_X(\omega)$

8.4.2 Non-stationatity effect due to time limited input process

The response previously defined for output processes are based on steady state conditions, that is those conditions which result when input processes are assumed to start at $t = -\infty$. In actual practice, and in particular with earthquake acceleration signals, input processes start at time $t = 0$ (causal signals). This results in a non-stationarity (or transient) effect at the beginning of the output signal. It may even happen that no stationary parts exist at all. This problem was studied by *Caughey and Stumpf (1961)*, for the case of Gaussian stationary input process of zero mean and power spectral density $S(\omega)$.

They gave the expression for the output variance in the form of an integral equation wich can be evaluated by contour integration if $S(\omega)$ is given analytically and numerically otherwise.

$$\begin{aligned}\sigma_Y^2(t) = \int_0^{+\infty} S(\omega) \mid H(i\omega) \mid^2 & \left[1 + e^{-2\omega_0\lambda t} \left\{ 1 + \frac{2\omega_0\lambda}{\omega_1} \sin\omega_1 t \cos\omega_1 t \right.\right. \\ & - e^{\omega_0\lambda t}\left(2\cos\omega_1 t + \frac{2\omega_0\lambda}{\omega_1} \sin\omega_1 t \right) \cos\omega t - e^{\omega_0\lambda t} \frac{2\omega}{\omega_1} \sin\omega_1 t \sin\omega t \\ & \left.\left. + \frac{(\omega_0\lambda)^2 - \omega_1^2 + \omega^2}{\omega_1^2} \sin^2\omega_1 t \right\} \right] d\omega\end{aligned} \tag{8.27}$$

An approximation may be obtained when the damping λ is small and $S(\omega)$ does not exhibit sharp peaks (case of engineering structures):

$$\sigma_Y^2(t) \approx \frac{\pi S(\omega_0)}{4\lambda\omega^3} \left[1 - \frac{e^{-2\omega_0\lambda t}}{\omega_1} \left\{ \omega_1^2 + \frac{(2\omega\lambda)^2}{2} \sin^2\omega_1 t + \omega_0\omega_1 \sin 2\omega_1 t \right\} \right] \tag{8.28}$$

This assumption reflects the fact that, when λ is small $\mid H(i\omega) \mid$ is strongly peaked at $\omega = \omega_0$ and the main contribution to the integral comes from the region of $\omega = \omega_0$.

Plots on *fig. VIII.5* show the transient responses of a dynamic SDOF system for $\lambda = 0, 0.025, 0.05$ and 0.1. It is seen that the asymptote (stationary level) is reached after approximately 12, 8 and 3 cycles respectively for $\lambda = 2.5$, 5 and 10 % damping.

This emphasizes the importance of the transient study for earthquake signals and more particularly when they are of very short duration with lightly damped structures. As pointed out by the authors, caution should be exercised in applying the distribution function for the probability of exceeding a given value since it is very sensitive to the tail of the distribution function.

The previous observations are illustrated on *fig. VIII.6* with the case of the Mexican earthquake of Septembre 1985. Such considerations may be used (but will not be developed here) to form the basis for the establishement of design response spectra on rock, in a given region where strong motions of short duration are expected (U.K.).

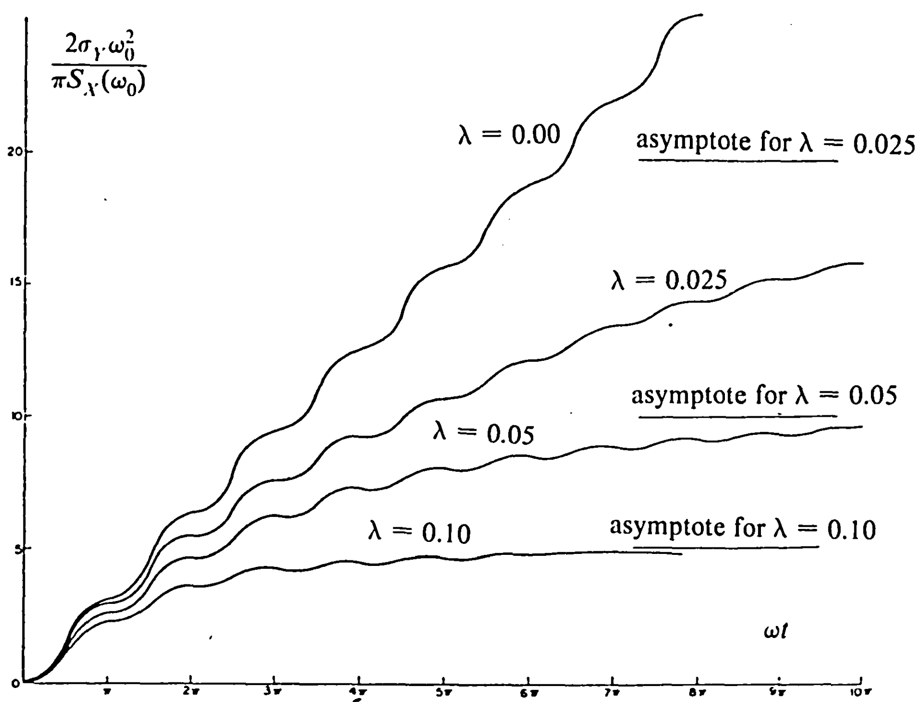

Fig.VIII.5

Transient response of a dynamic system under random excitation

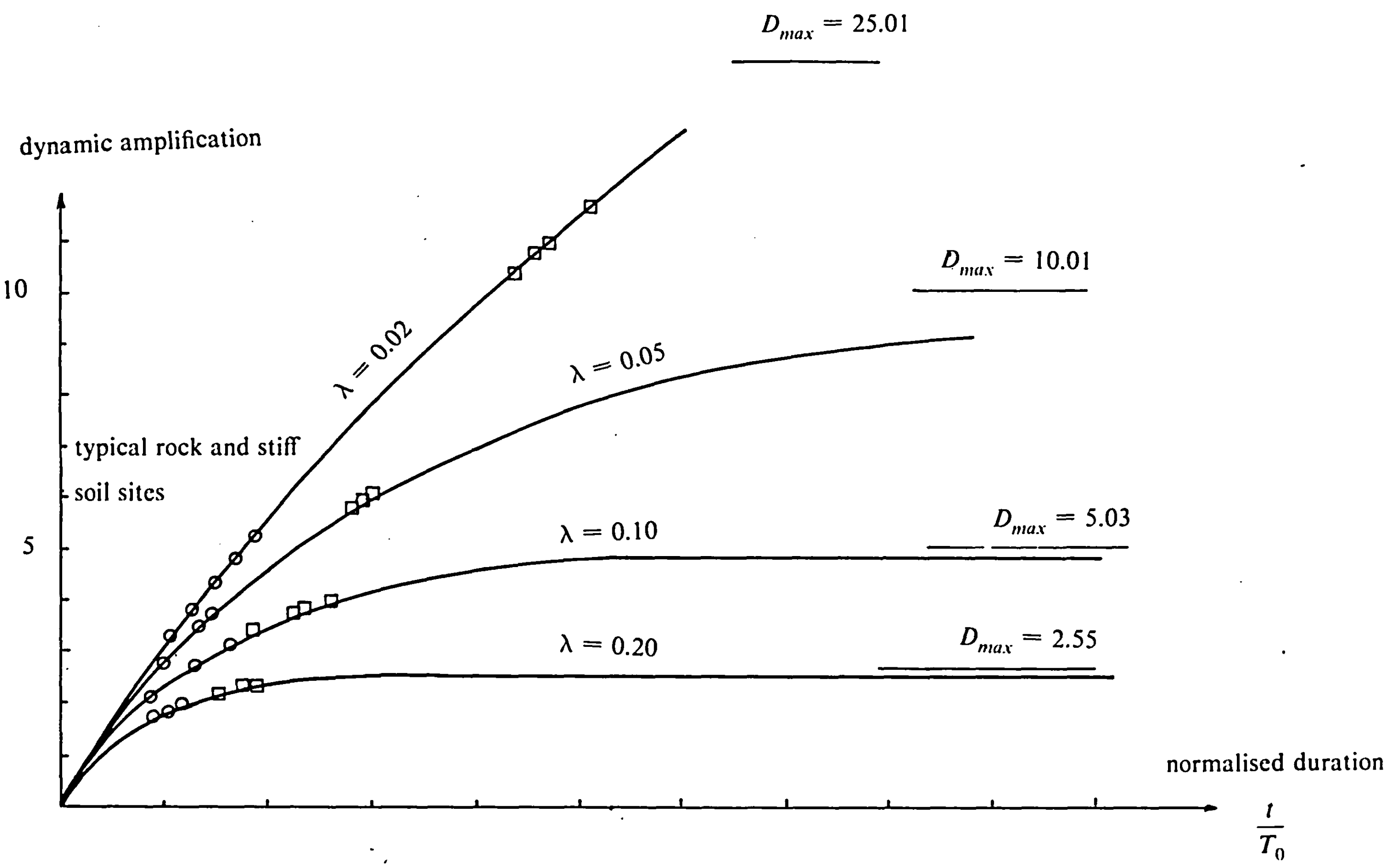

○ Parkfield, El-Centro, Friuli (Tolmezzo), etcæ.

□ Mexico-City site

Fig.VIII.6

Case of the Mexico earthquake of Septembre 1985 plotted

on the Caughey and Stumpf graph by comparison with other earthquakes

8.5 DISTRIBUTION OF PEAKS

Of interest for reliability analysis is the determination of the probability of exceedance of a structural response quantity above some pre-established level, refered to as "a". Since it is closely related to the probability of failure it will find direct application when we shall require to simulate time histories from Response Spectra. In the following we shall desbribe the necessary concepts linking the time description (Response spectra) with the frequency description (Power Spectra Density).

8.5.1 Crossing analysis

The crossing analysis is a technique which forms the basis of such investigations since it deals with the probability of crossings the just mentioned pre-defined barriers; it is also closely related to pulse distribution analysis. Unfortunately it has not produced large quantities of practical results yet, due to the extreme complexity of the problem specially in the non-stationary case. The usual assumptions used tend to oversimplify the problems exept in simple one dimensional processes, and therefore we shall limit the analysis to this case. We will see (chapter IX), through which transformation earthquake near field records may enter in this category.

Within such an approximation, the mean crossing rate in an interval of time dt, beyond a fixed barrier level "a" has been derived by *Rice (1944)*. His expression is:

$$\nu_a^+ = \frac{1}{dt} \int_0^\infty d\dot{x} \int_{a-\dot{x}dt}^{a} f(x,\dot{x})\, dx \tag{8.29}$$

where ν_a^+ is the frequency of crossing of the fixed barrier level $x = a$. The superscript $+$ indicates that only crossing with a positive slope are counted (upcrossings). $f(x,\dot{x})$ is the joint probability density function of x and its first derivative $\dot{x}$ (fig.VIII.7 and VIII.8).

If the process is stationary and Gaussian with zero mean, the joint probability density is:

$$f(x,\dot{x}) = \frac{1}{2\pi\sigma_X\sigma_{\dot{X}}} \exp\left[-\frac{1}{2}\left(\frac{x^2}{\sigma_X^2} + \frac{\dot{x}^2}{\sigma_{\dot{X}}^2}\right)\right] \tag{8.30}$$

Then *Eq.8.29* reduces to :

$$\nu_a^+ = \frac{1}{2\pi}\frac{\sigma_{\dot{X}}}{\sigma_X} \exp\left[-\frac{a^2}{2\sigma_X^2}\right] \tag{8.31}$$

A process that represents the output of a lightly damped SDOF oscillator is approximately narrow-band. In a narrow-band process the motion occurs in a narrow range or band of frequencies whose central frequency is large with respect to the bandwidth. For this type of Gaussian process it appears reasonnable to define a representative frequency of the process. This frequency which may be interpreted physically as

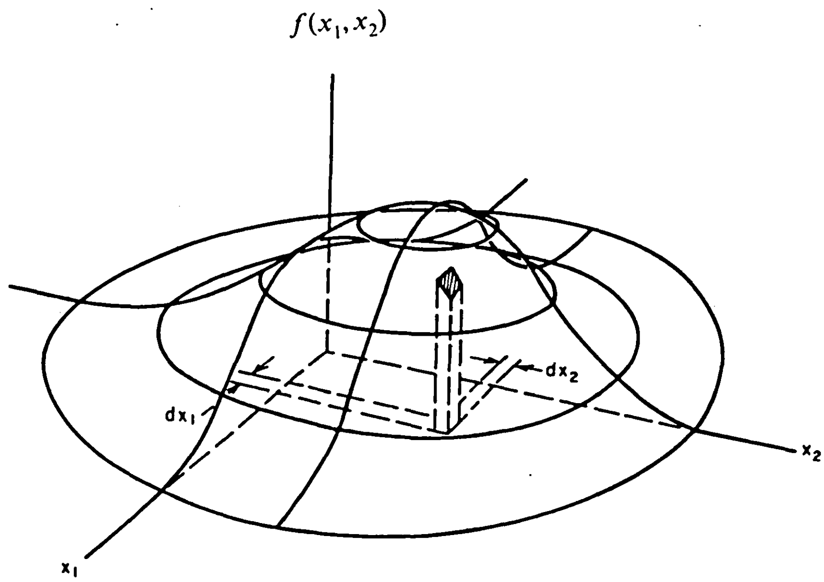

Fig.VIII.7

Joint normal probability distribution used to compute the "a" level crossing

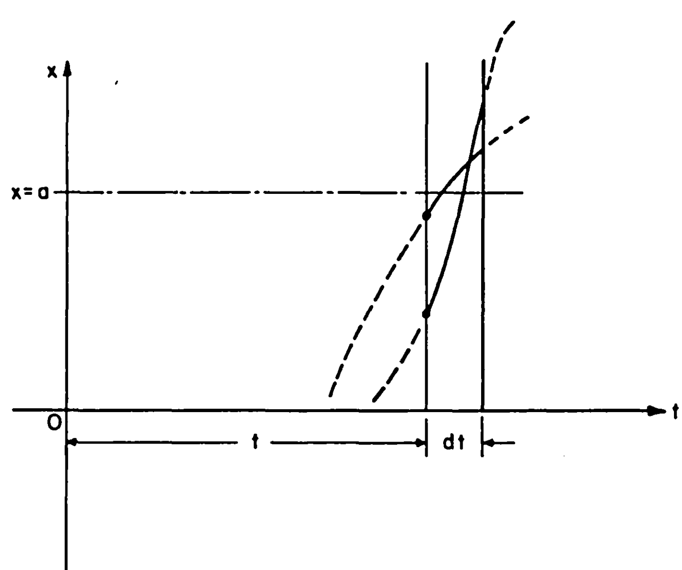

Fig.VIII.8

Sample function crossings $x = a^+$ during the interval dt

the frequency at which most of the energy in the spectrum is concentred (or predominant frequency), may be obtained by setting $a = 0$ in *Eq.8.31* to give the rate of zero crossings:

$$\nu_0^+ = \frac{1}{2\pi}\frac{\sigma_{\dot{x}}}{\sigma_x} \qquad (8.32)$$

The predominant period of the process is then:

$$T_0 = \frac{1}{\nu_0^+} \qquad (8.33)$$

We can now define the time to first passage of a process above a barrier level "a". Using *Eq.8.31* and *Eq.8.32* we see that the expected number of times N during a period T that a value $x = a$ is intercepted with a positive slope is:

$$N(a) = \nu_0 T \exp\left[-\frac{a^2}{2\sigma_X^2}\right] \qquad (8.34)$$

and the average rate of "a" level crossings is:

$$\lambda = \frac{N(a)}{T} = \nu_0 \exp\left[-\frac{a^2}{2\sigma_X^2}\right] \qquad (8.35)$$

When "a" is large compared with σ_X (tail of the distribution), the occurence of such interceptions constitutes a rare event and one may use the Poisson distribution to estimate the probability that there are given numbers of crossings at level "a". Therefore, by substituting *Eq 8 35* into *Eq 8 19* we get the probability of no interception over a duration T as:

$$f(0,T) = e^{-N(a)} \qquad (8.36)$$

This result will be used in section 8.5.3 to define the probability of extreme values.

The Poison's arrival assumption may not be valid for low level "a" in particular for low predominant frequency. *Vanmarke (1976)* has proposed, based on the work of *Crandall (1966)* an empirical relation to improve the classical results.

Still further improvements may be considered (*Vanmarke 1976*) but their application require non-stationarity functions which have not, in the present state of the art, been strongly established. It is clear that the steady-state analysis remain on the safe side, especially for small damping. That is why we shall keep on using the well established development of stationarity just described. We shall see in the next chapter how we propose to deal with the non-stationarity.

8.5.2 Probability distribution of maxima

Cartwright and Longuet-Higgins (1956) have computed the probability density function for the maxima x_m of a stationary random process $X(t)$ (ensemble of $x(t)$) having a normal probability distribution:

$$f_m(x_m) = \frac{1}{\sqrt{2\pi}} \left[\epsilon e^{-\eta^2/2\epsilon^2} + (1-\epsilon^2)^{1/2} \eta\, e^{-\eta^2/2} \int_{-\infty}^{\eta(1-\epsilon^2)^{1/2}/\epsilon} e^{-x^2/2} dx \right] \quad (8.37)$$

$$\eta = \frac{x_m}{m_0^{1/2}} \quad \text{is the non-dimensional maximum ordinate} \quad (8.38)$$

$$\epsilon = \frac{m_0 m_4 - m_1^2}{m_0 m_4} \quad \text{is a frequency content parameter} \quad (8.39)$$

The different m_i are the successive moments of the spectral density function $S(\omega)$ defined as:

$$m_i = \int_0^{+\infty} \omega_i S(\omega)\, d\omega \quad (8.40)$$

Its cumulative probability $F_m(x_m)$ is obtained by integrating *Eq. 8.37*:

$$F_m(x_m) = \frac{1}{\sqrt{2\pi}} \left[\int_{\eta/\epsilon}^{+\infty} e^{-x^2/2}\, dx + (1-\epsilon^2)^{1/2}\, e^{\eta^2/2} \int_{-\infty}^{\eta(1-\epsilon^2)^{1/2}/\epsilon} e^{-x^2/2}\, dx \right] \quad (8.41)$$

Graphs of *Eq. 8.37* and *Eq. 8.41* are plotted on *fig. VIII. 9* and *fig. VIII. 10* respectively for different values of ϵ. For a narrow band process, approching the single harmonic process (very near source records or records strongly affected by the soil layers like in Mexico-City (1985)), ϵ tends to zero and the peak distribution reduces to the *Rayleigh* distribution:

$$f_m(x_m) = \frac{\eta}{\sigma_X} e^{\eta^2/2} \quad (8.42)$$

When the process is a white noise or a band limited white noise (for records away from the source, on rock when heavy scattering has occured), one can show that ϵ tends to 2/3. The limiting case $\epsilon = 1$ is the Gaussian process; it is obtained when random noise is predominant in the signal (Low energy acceleration records strongly contaminated by digitization noise).

The value of ϵ may be more simply estimated for a given sample $x(t)$ than by computing *Eq. 8. 39*. It suffices to count the total number of maxima (+ and −) N^+ and the number of negative maxima (+ and −) N^- occuring in the "stationary-modified" signal (*fig. VIII. 11*). Dividing N^- by N^+ gives the proportion r of negative maxima present in the total which must be equal to the area under the probability function $f_m(x_m)$ to the left of the origin in *fig. VIII. 9*. It can be shown that ϵ is related to this area by:

$$\epsilon = \sqrt{1-(1-2r)^2} \quad (8.43)$$

By substitution in *Eq. 8. 37* we get the probability distribution of peaks.

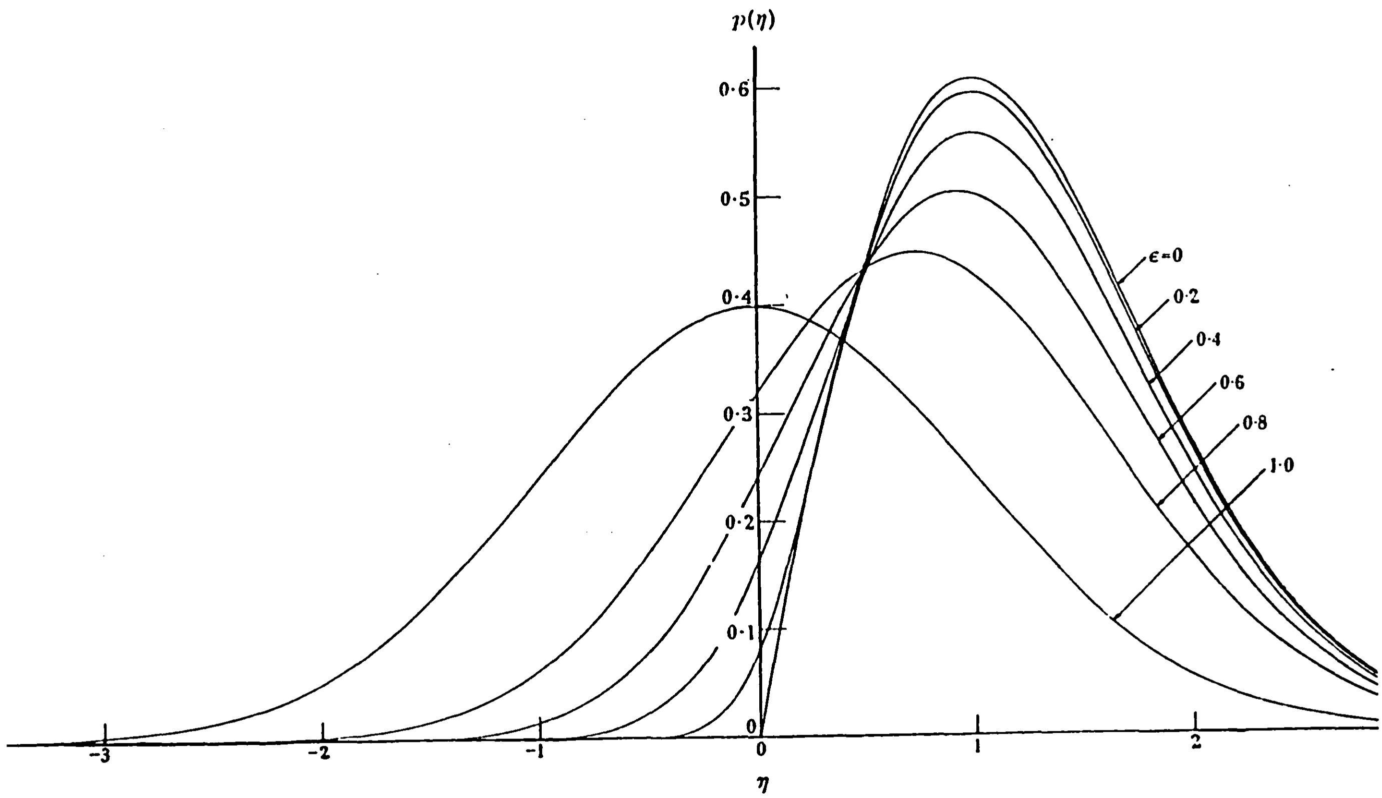

Fig.VIII.9

Graphs of the probability distributions of maxima

for different values of the width ϵ of the energy spectrum

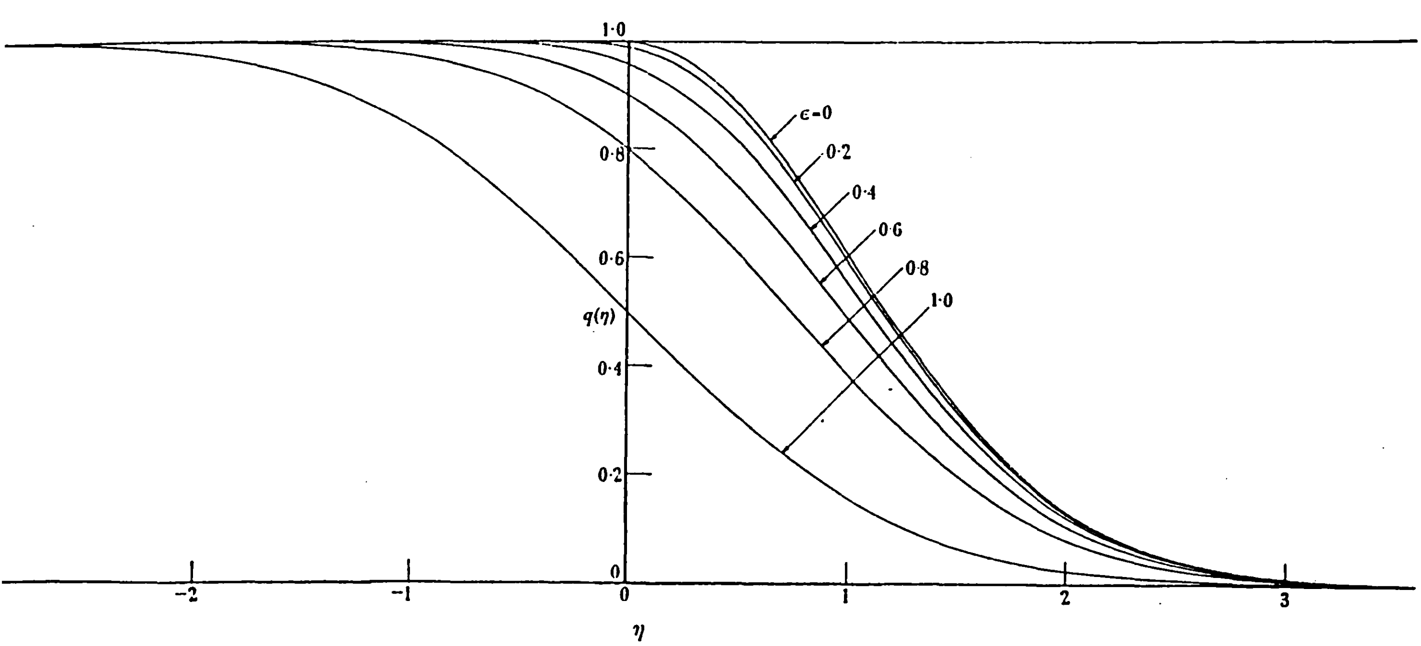

Fig.VIII.10

Graphs of the cumulative probability of maxima

for different values of ϵ

8.5.3 Probability distribution of extreme values

In strong motion studies, we are limited to a signal of duration T and only the largest values of the maxima during this time interval should be retained. Considering a sample of N maxima, the probability that the largest of them has the value x_M, has an asymptotic form, valid for large N. It is given by *Eq 8.36* which also expresses the probablity that the extreme value x_M must be less than "a"; we get:

$$f_M(x_M) = \exp\left[-\nu_0 T \; e^{-\eta^2/2} \right] \tag{8.44}$$

This result could have been obtained by using *Eq.8.37* for $\epsilon \rightarrow 0$ (assumption of narrow band process). Also other models for the tail of $\exp(-\eta^2/2)$ may have been used, like the *Gumbel Type I* distribution to reduce computation.

Using this expression, we get the mode of the extreme value x_M:

$$\mathrm{mode}(x_M) = \sigma_X \sqrt{2 \ln \nu_0 T} \tag{8.45}$$

Its expected maximum (probability $p = 0.5$) is found to be (*Davenport 1964*):

$$x_{MAX} = \mathrm{E}\left[x_M \right] = \int_0^{+\infty} x_M f_M(x_M)\, d x_M \approx \sigma_X \left[\sqrt{2 \ln 2\nu_0 T} + \frac{\gamma}{\sqrt{2 \ln 2\nu_0 T}} \right] \tag{8.46}$$

where $\gamma = 0.57724$ is the *Euler's constant*

and its variance:

$$\sigma_M^2 = \mathrm{E}\left[(x_M - x_{MAX})^2 \right] = \int_0^{+\infty} (x_M - x_{MAX})^2 f_M(x_M)\, d x_M = \sigma_X^2 \frac{\pi^2}{12 \ln 2\nu_0 T} \tag{8.47}$$

Vanmarke (1976) proposed the following relation to reflect the departure from the Poisson's assumption:

$$x_{MAX,p} \approx 2 \ln \left\{ 2n \left[1 - \exp\left(-\delta \sqrt{\pi \ln 2n} \right) \right] \right\}^{1/2} \tag{8.48}$$

where

$$n = \frac{\nu_0 T}{2\pi} \left(\ln \frac{1}{p} \right)^{-1} \tag{8.49}$$

and p is the probability for x_M not to exceed x_{MAX} over the duration T.

δ is a bandwith parameter (similar to ϵ) defined as :

$$\delta = \left[\frac{m_0 m_2 - m_1^2}{m_0 m_2} \right]^{0.6} \tag{8.50}$$

In any case, we call *peak ratio* the factor:

$$r_{T,p} = \frac{x_{MAX}}{\sigma_X} \tag{8.51}$$

It is represented on *fig. VIII.12* for its expected value ($p = 0.5$) and its 95% confidence. For large values of δ or ϵ the peak ratio approaches an upper bound (Poisson's assumption):

$$r_{T,p} = \sqrt{2 \ln 2\nu_0 T \left(\frac{1}{p}\right)^{-1}} \tag{8.52}$$

It is clearly seen that, in the range of interest for earthquake near field records ($\nu_0 T = 10$ to $\nu_0 T = 1000$), the peak acceleration is expected to be 2 to 3.5 times the RMS of the signal depending mainly on the frequency content. The plot shows to what extent a high peak ratio is more likely to occur when high predominant frequency and/or long duration are expected. It is also seen that the peak will remain, below 4.8 times the RMS, even for high frequency and/or long duration, with a confidence of 95%.

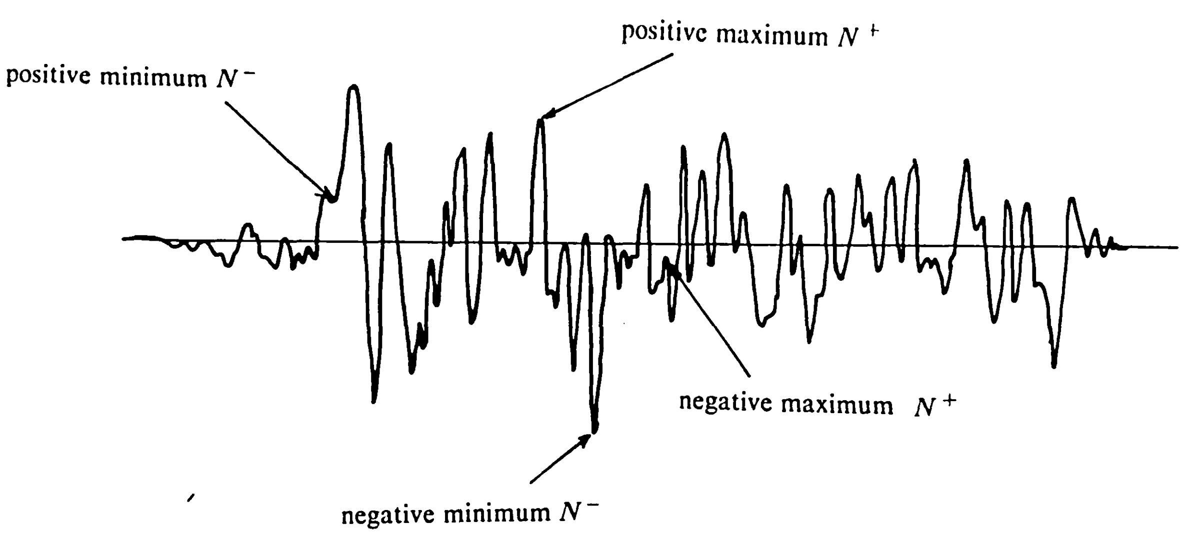

Fig.VIII.11
Positive and negative maxima and minima
of a stochastic process

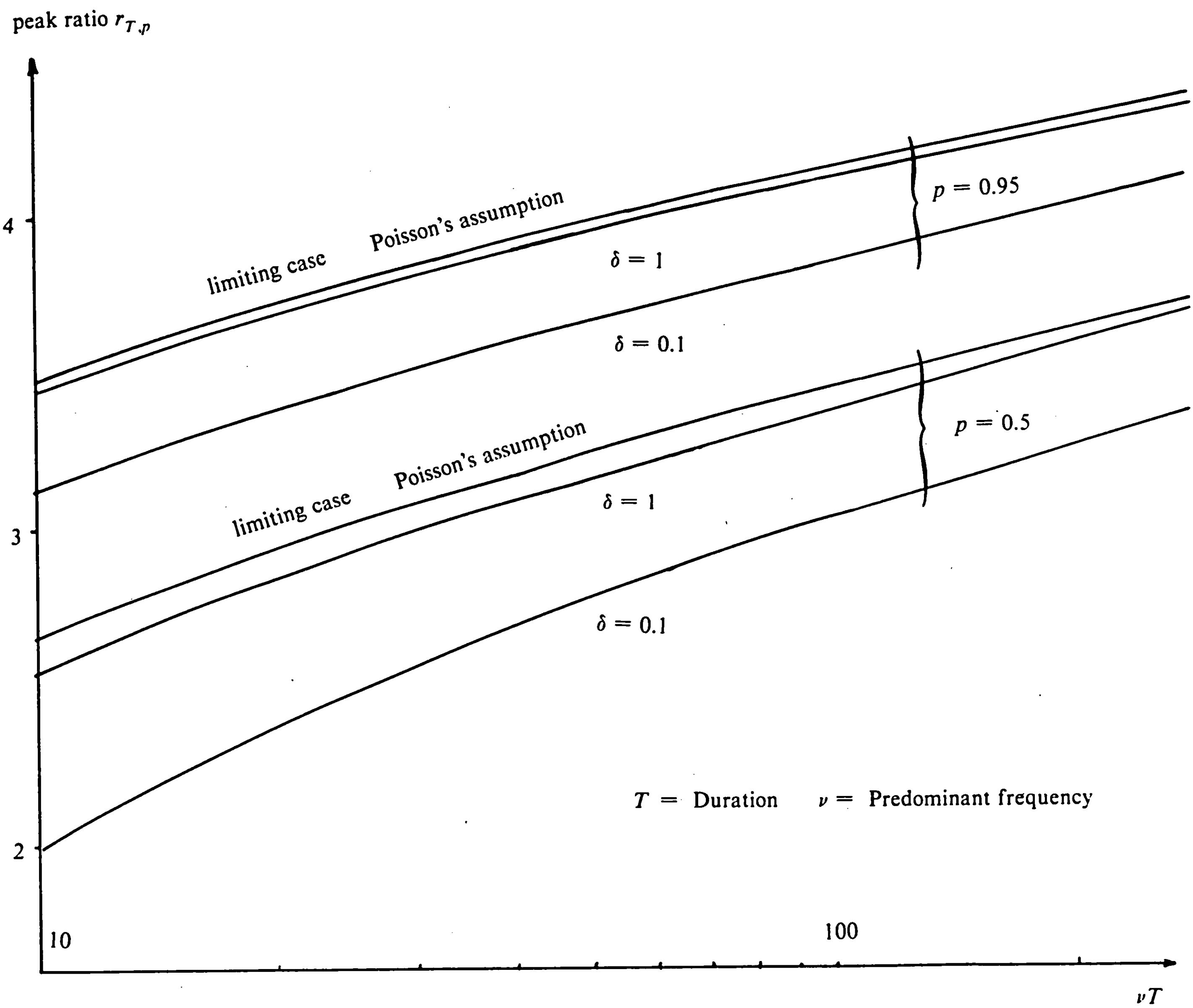

Fig. VIII.12

Variations of Peak ratios of a stationary process with its frequency content parameters

CHAPTER IX

EMPIRICAL STRONG MOTION SIMULATION FROM THEIR SPECTRUM

9.1 PURPOSE AND DEFINITION

9.1.1 Motivation

Amongst the spectral descriptions of earthquake strong motions, the Response Spectrum is certainly the most popular. The Response Spectrum method is a widely used approximate procedure to determine the maximum values of structural response quantities under dynamic excitations. The loads are characterised by their Response Spectra and the structural quantities are calculated by combining the maximum modal contributions. The Response Spectrum of a time-dependent load like earthquake strong motion is obtained from the corresponding maximum displacement of a simple oscillator at different values of its natural frequency and its damping ratio. The technique has been very successful for the design of many structures, but today one is trying to depart softly from it because of some limitations. These limitations are due to the three main following reasons:

1) Response Spectra represent the maximum responses of linear structures, and as such may not always be a good indication of structural behaviour near collapse.

2) For multi-degree of freedom systems the simple addition rule (or any other empirical rule like the addition of the squares of the maximum responses, etcæ.) is too conservative for large structures.

3) The structures are assumed to be fixed on a rigid foundation, (although correction are sometimes provided in codes of practice). This makes it uneasy to introduce the soil effects or the soil-structure interactions which are known to be very significant when large structures are rigid or semi-rigid by comparison to their foundation (Nuclear power plants, underground tanks, concrete dams,etcæ.)

Strictly speaking, the only appropriate method to perform valuable research or accurate design is to make use of time histories. Indeed, we are still very far from being able to generate physically reliable strong motion time histories. Chapter X of this thesis will propose a possible approach making use of theoretical developments and geophysical and seismological information. But the amount of input data required is so large that such a model depends mainly on the actual numerical values that we are asked to provide.

In the mean time, empirical methods may also give interesting approximate results. The determination of simulated strong motion time histories from response spectra has also the advantage of yielding a ground motion compatible with the well accepted Response Spectrum method. There are several solutions to the problem as many different time histories may produce the same spectrum, but at least the final product reflects the frequency characteristics of the given "load". In particular, it will have the peak responses imposed by the spectrum at the different frequencies. This time history may then be used in any structural analysis, integrating non-linearity, multi-mode analysis or soil-structure interaction.

In the next section, we shall develop a strategy to determine such time histories. It will be shown, in particular that the passage from Response Spectrum to time history is not unique; there are four levels of indeterminacy:

1) the statistical distribution of the peaks (see chapter VIII),

2) the choice of the phases for all frequencies,

3) the non-stationarity of the signal in time,

4) the non-stationarity of the signal in frequency (see chapter II).

Assuming that the other data are known accurately (which is not the case), the final time history is affected by a four-dimensional indeterminacy.

9.1.2 Strategy of the method

The proposed method is represented on *fig.IX.1*. The conventional starting point is the Response Spectrum usually given. It may have been determined from the well known studies by *Mohraz (1976)*, *Trifunac and Anderson (1978)* or by any derived method to represent more closely the local effects. In any case, the Response Spectrum has the average shape similar to those shown in *fig.IX.2* which have been proposed for different regions of the U.S.A. Such spectra are commonly scaled by the peak ground acceleration, also refered to as the zero-period acceleration; they are very dependent on the particular attenuation laws.

Fig.IX.3 shows the spread of some published laws where it can be seen that an uncertainty of two on the median value expands for all distances. A still much wider range must be expected in the peak acceleration assessment if we want a specific value within, say a 90% interval of confidence. To illustrate the poor reliability of such a parameter, the case of the Mexican earthquake of Septembre 1985 provides another striking example. *Fig.IX.4* shows the peak ground acceleration attenuation proposed by *Joyner and Boore (1981)* (usually recognized as accurate) for this particular shock. At the distance of 360 km from the epicenter, the expected A_{MAX} is 0.007 g and should have remained below 0.014 g with a probability of 80%. In fact, all the acceleration peaks recorded in Mexico-city varied between 0.028 g and 0.168 g

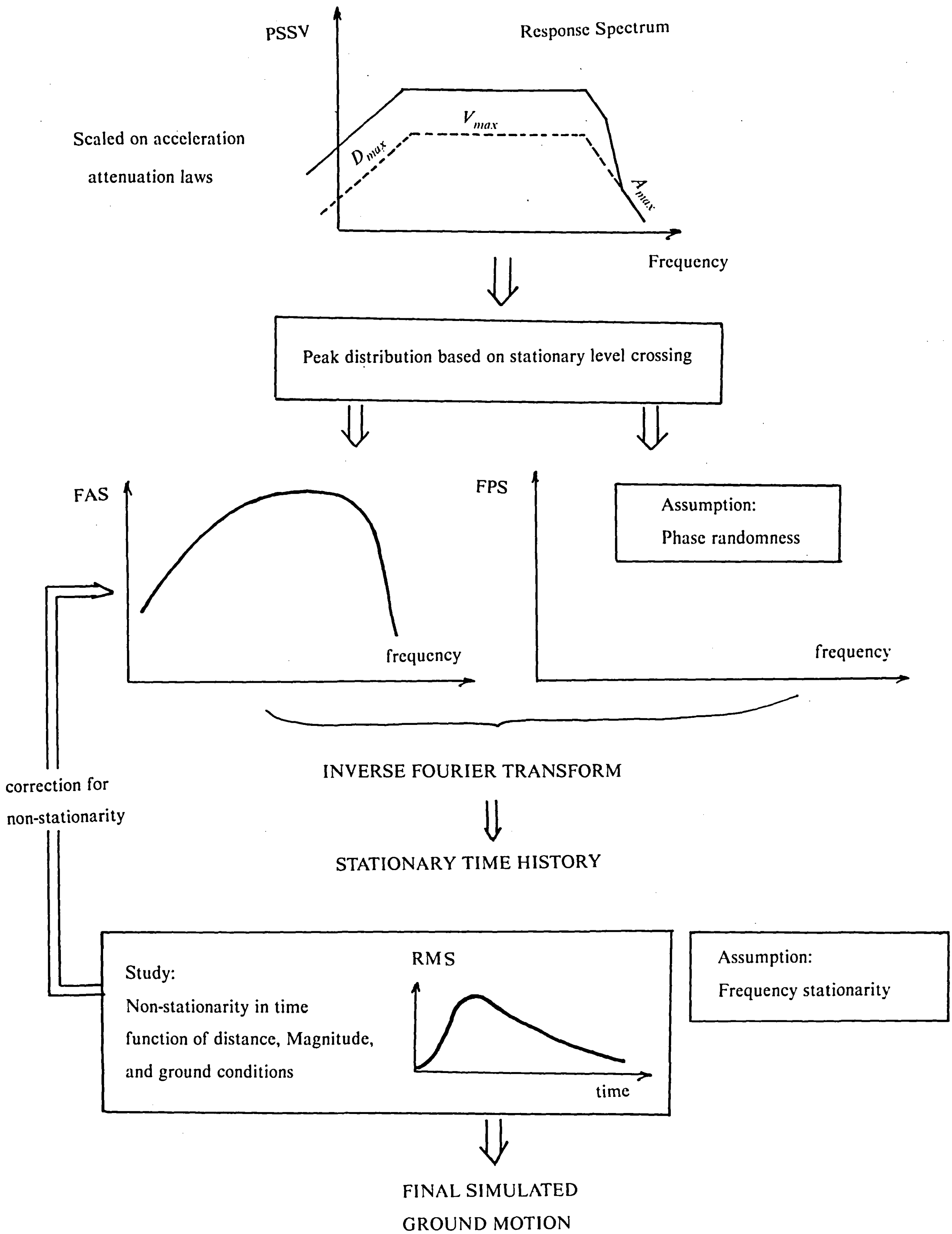

Fig.IX.1

Methodology for empirical simulation of earthquake strong motion

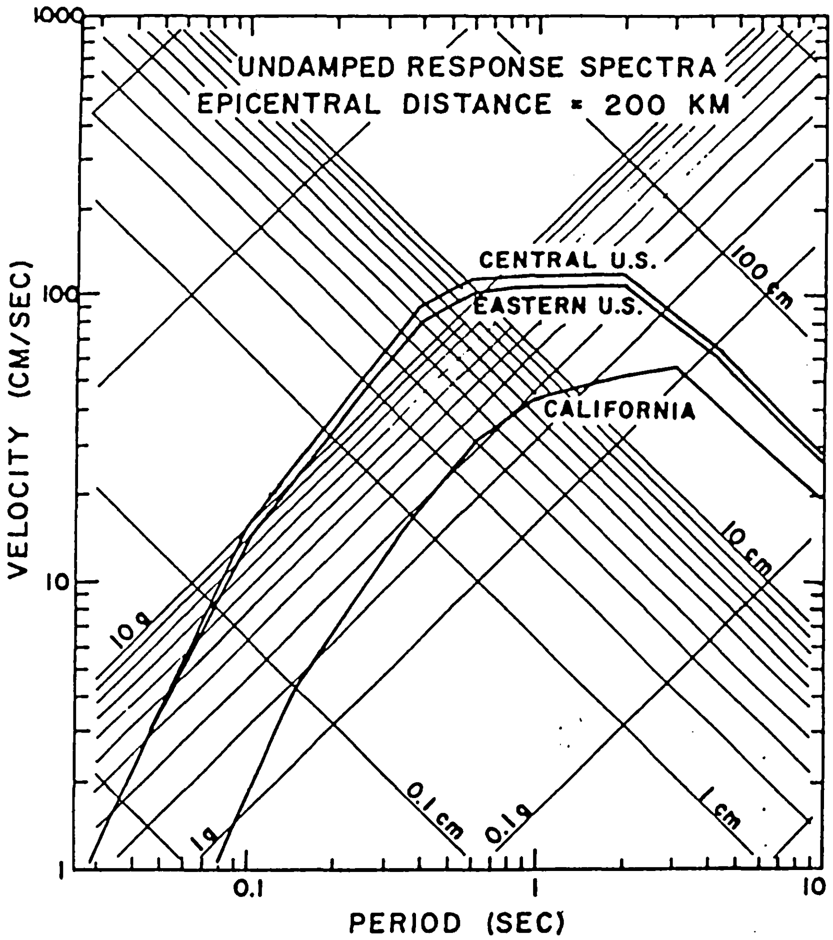

Fig.IX.2

Typical given response spectra specific of a region

Here the case of the USA

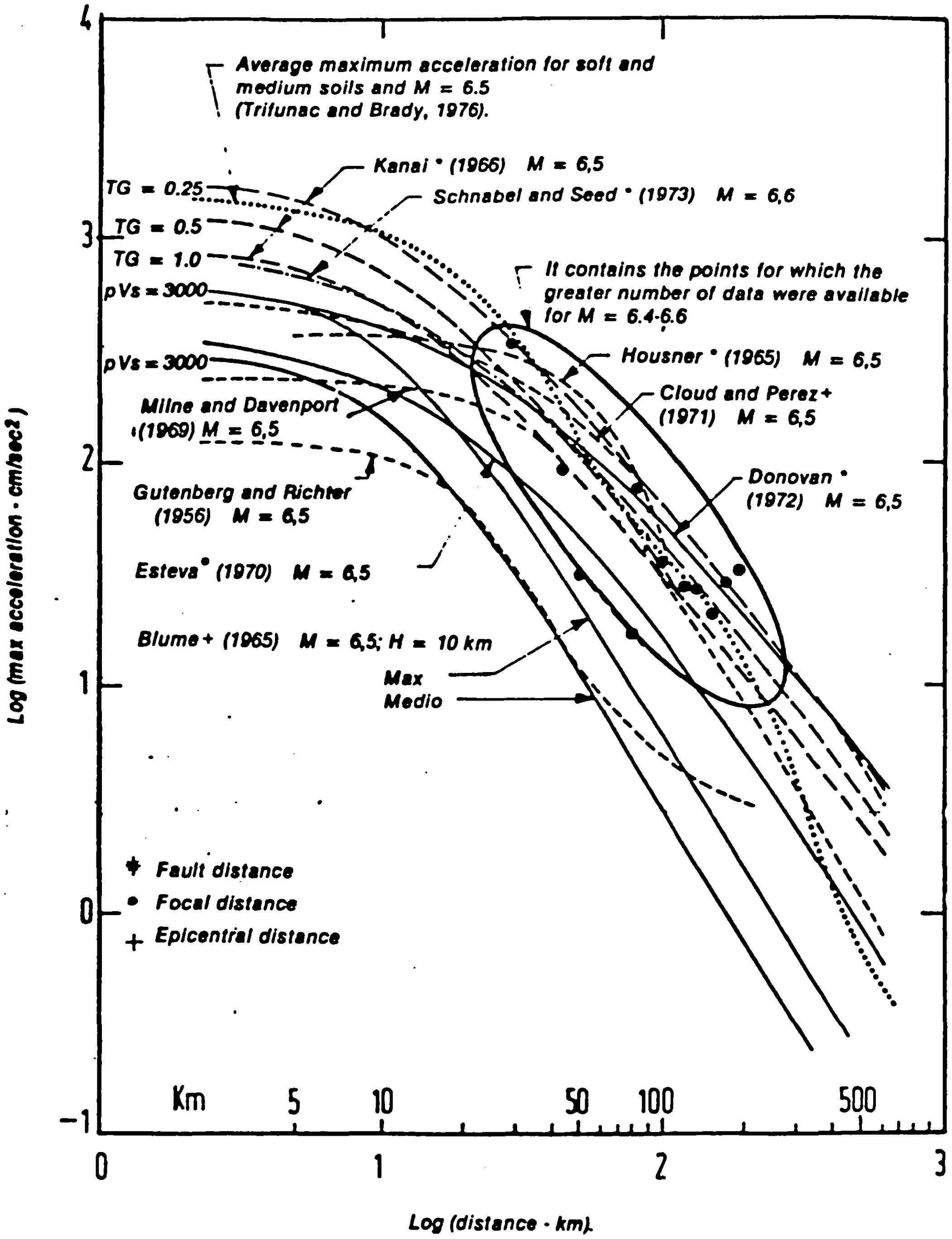

Fig.IX.3

Some of the published peak acceleration attenuation with distance exhibiting an increase of 4 to 24 times the predicted value. Surely, Mexico-city is a particular case, with very poor ground conditions, but such a phenomenon may happen again in similar conditions. We shall see in section 9.4.2 with *Eq.9.16* how we propose to scale the strong motion total energy.

The first step of the procedure consists of obtaining, a ground motion Fourier Spectrum. Once this is determined, the passage to time can be achieved by Inverse Fourier Transform.

The Fourier Spectrum of a signal is a complex function of frequency. It is uniquely defined when both its Fourier Amplitude Spectrum and its Phase Spectum are known. In the described procedure there is no possibility to deduce the phase function. Only the FAS can be assessed. The first of our assumptions will therefore be to fix the phases at the various frequencies. An examination of phase diagrams of recorded motions shows no simple rule for the phase behaviour, specially in the high frequencies (beyond 0.5-1.0 Hz). In the low frequency range, one may be able to detect a pattern known as the the group velocity dispersion curves. In a simulation process, the dispersion curves are not usually available. A crust velocity model is required in the vicinity of the particular site, and this is not easily defined. For those two reasons, we are compelled to assume that the phases $\Phi(\omega)$ are randomly distributed over their mathematical range $(0, 2\pi)$.

A better understanding of the phase function is certainly needed for the future. It may be approached through the use of the *Hilbert Transform* making use of the properties of causality of the near field ground motions.

There is, however, the possibility to link, in a probabilistic sense, the Response Spectra with the Fourier Amplitude Spectra, since both have connection with the distribution of energy over the frequencies. The key point of this link resides in the relation between the amplitude of harmonic wave and the peak its produces when it is input in a simple oscillator. Introducing the stochatic concepts of such transformations, a relation between the variance of a process with the peak response may be determined. This is known as the peak ratio studied in section section 8.5.3 for stationary processes.

Once the complex Fourier Spectrum is determined, one can easily generate a stationary time history by Inverse Fourier Transform (see also *Eq.2.3* and *Eq.5.23*). We shall write it here in its real and discrete form as:

$$a(n\Delta t) = \sum_{k=1}^{M} \mid A(k\Delta\omega) \mid \cos\Big[kn\Delta\omega\Delta t + \Phi(k\Delta\omega)\Big] \tag{9.1}$$

$$n = 0, 1, ..., N-1$$

The frequency range covers:

$$F_{min} = \Delta\omega \qquad to \qquad F_{max} = M\Delta\omega$$

and the duration is $T = N\Delta t$.

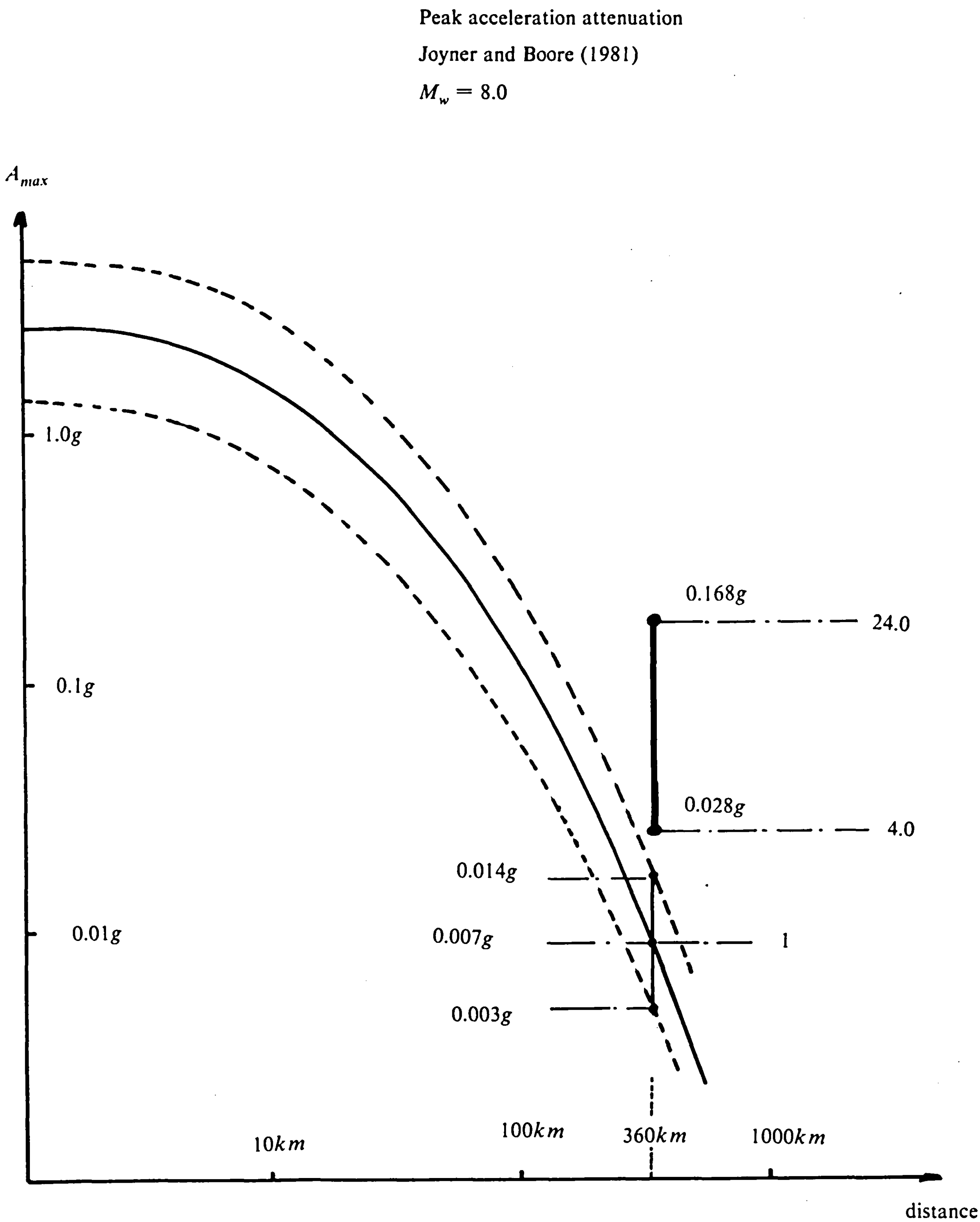

Fig.IX.4
Comparison of the *Joyner and Boore* attenuation law
with the measured peak accelerations at Mexico-city
Septembre 1985

Finally a time shaping function is applied to the stationary motion to integrate its non-stationary character. This time window is described in section 9.4.2 and depends primarily on Magnitude and distance.

The loop between the shaped motion and the FAS is required since any modification of the amplitudes in time affects also the amplitudes in frequency. The final simulated ground motion is then obtained after an iterative process.

9.2 THE PASSAGE TO THE FOURIER AMPLITUDE SPECTRUM

9.2.1 Pseudo-Velocity Spectrum models

Several models for Pseudo-Velocity Response Spectra have been proposed in recent literature. We shall describe here the two that we find the most representative; they do not apply to a particular region.

The Mohraz Response spectrum

Mohraz (1976) studied the statistics of the various Response Spectra both for horizontal and vertical motions. His study is an extension of his early analysis (*Mohraz et al. (1972)*). The latter produced later the well known *Newmark's Design spectrum* which has intensively been used for the nuclear power plants design in the USA. He distinguished between three different frequency bands: the amplified acceleration (high frequency) region, the amplified velocity (intermediate frequency) region and an amplified displacement (low frequency) region and he assumed a constant dynamic amplification factor over each region. For each group he calculated statistics of the ratios v/a and ad/v^2 (a, v, d = peak ground acceleration, velocity and displacement respectively) and of the acceleration, velocity and displacement amplification factors A_f, V_f, D_f. They were found to have a log-normal distribution.

Mohraz's results may be used to define an average Response Spectrum for rock motion. A median ($p = 0.5$) Pseudo-Velocity Spectrum normalised to a peak acceleration of 1.0 g is:

$$PSSV[\omega,\lambda] = (13.37 - 8.77 \ln\lambda)\omega \qquad \text{in the displacement region} \qquad (9.2a)$$

$$PSSV[\omega,\lambda] = (18.07 - 21.94 \ln\lambda) \qquad \text{in the velocity region} \qquad (9.2b)$$

$$PSSV[\omega,\lambda] = (-2435.8 - 1489.0 \ln\lambda)\frac{1}{\omega} \qquad \text{in the acceleration region} \qquad (9.2c)$$

$$\text{valid for } 0.005 \le \lambda \le 0.10$$

in wich λ is the damping ratio, and ω is the circular frequency. PSSV is expressed in cm/sec. A smooth transition is performed from 8 Hz to reach progressively the peak ground acceleration at 30 Hz. To investigate the effect of spectrum uncertainty, the following variance function may be used:

$$\sigma_{PSSV} = \exp\left[\sqrt{0.043 - 0.0406\lambda^{0.38}}\ \ln\left(2\pi\frac{30.0}{\omega}\right)\right] \quad \text{for} \quad \frac{\omega}{2\pi} < 30 \text{ Hz} \qquad (9.2d)$$

Fig. IX.5 shows such a spectrum for a rock site and its $\pm\,\sigma_{PSSV}$ fractiles.

The Trifunac Response Spectrum

Trifunac and Anderson (1978) proposed also a preliminary empirical model for scaling Pseudo-Velocity Spectra. They operate a muliple regression analysis on a set of 57 earthquakes on various bands of frequency. They expressed their results in terms of Magnitude by the relation:

$$\log\{PSSV[\omega,\lambda,p]\} = M + \log\{A_0(R)\} - A_M(\omega)p - B_M(\omega)M - C_M$$

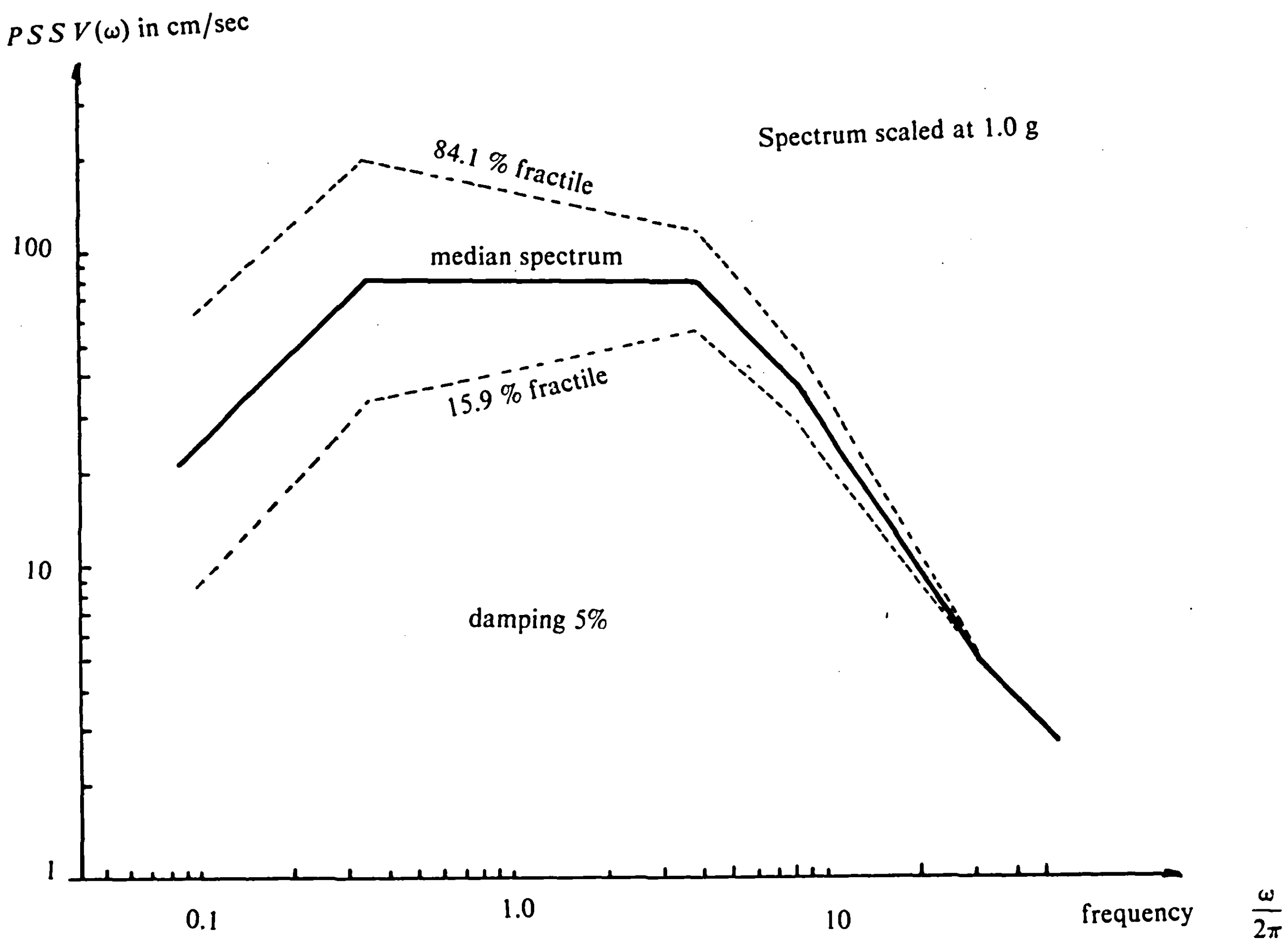

Fig.IX.5
Mohraz's response spectra on bedrock
and $\pm\ \sigma$ fractiles
Spectral pseudo-velocity *cm/sec*
natural frequency Hz

$$-D_M(\omega)s - E_M(\omega)v - F_M(\omega)M^2 - G_M(\omega)R \qquad (9.3)$$

and in terms of Intensity by the relation:

$$\log\{PSSV[\omega,\lambda,p]\} = A_I(\omega)p + B_I(\omega)I_{MM} + D_I(\omega)s + E - I(\omega)v \qquad (9.4)$$

In *Eq.9.3*, M represents the published Magnitude (Local Magnitude if $M < 6$ and Surface wave Magnitude if $M > 6$) and $\log\{A_0(R)\}$ the wave amplitude attenuation with epicentral distance given in table XII. It should be noted that this conventional attenuation given by Richter for its local Magnitude definition, includes anelastic attenuation as well as geometric attenuation and has been corrected across the frequency range by the function $G_M(\omega)$.

In *Eq.9.4*, I_{MM} is the *Modified Mercalli* Intensity at the site.

In both equations, v stands for the component direction:

$v = 0$ for horizontal,

$v = 1$ for vertical,

and s describes local geological site classification:

$s = 0$ for alluvium sites,

$s = 1$ for intermediate sites,

$s = 2$ for rock sites.

The parameter p, varying from 0.1 to 0.9 approximates the probability that $PSSV[\omega,p]$ will not be exceeded.

The frequency dependent coefficients A_M, B_M, C_M, D_M, E_M, F_M and G_M of *Eq.9.3* are tabulated in table XIII for various damping ratios. In a similar way, table XIV gives the frequency dependent terms A_I, B_I, C_I, D_I, and E_I, of *Eq.9.4*.

Examples of these spectra are given in *fig.IX.6* and *fig.IX.7* respectively for the Magnitude controlled and the Intensity controlled cases.

9.2.2 Computation of FAS from PSSV

In practice, the Response Spectra curves are computed from the maximum relative displacement response of simple oscillators i.e., from $SD[\omega_0,\lambda]$ where both the natural circular frequency ω_0 and the damping ratio λ vary ($p = 0.5$).

$$SD[\omega_0,\lambda] = \max\left[\frac{1}{\omega_1}\int_0^t \ddot{a}_G(\tau)e^{-\lambda\omega_0(t-\tau)}\sin\omega_1(t-\tau)\,d\tau\right] \qquad (9.5)$$

with $\omega_1 = \omega_0\sqrt{1-\lambda^2}$ = damped natural circular frequency. The Pseudo-Velocity spectrum is then given by:

$$PSSV[\omega_0,\lambda,p] = \omega_1 SD[\omega_0,\lambda,p] \tag{9.6}$$

Now, writting the displacement response peaks as a function of the variance of the stationary output process $\sigma_Y(\omega_0,\lambda)$, we get:

$$SD[\omega_0,\lambda,p] = R_{T,p}(\nu_0 T)\,\sigma_Y(\omega_0,\lambda) \tag{9.7}$$

This equation forms the kernel of the computation procedure, as the left hand side is known through the specified PSSV:

$$SD[\omega-0,\lambda,p] = \frac{PSSV]\omega_0,\lambda,p]}{\omega_0\sqrt{1-\lambda^2}} \tag{9.8}$$

and the right hand side depends on the searched Power Spectra Density $S_X(\omega)$ of the input motion.

$S_Y(\omega_0,\lambda)$ depends on $S_X(\omega)$ through *Eq.8.14* and *Eq.8.26*:

$$\sigma_Y(\omega_0,\lambda) = \frac{1}{\pi}\cdot\int_0^\infty S_Y(\omega_0,\omega,\lambda)\,d\omega \tag{9.9}$$

where

$$S_Y(\omega_0,\omega,\lambda) = \frac{S_X(\omega)}{(\omega_0^2-\omega^2)^2-4\lambda\omega_0^2\omega^2} \tag{9.10}$$

$R_{T,p}(\nu_0^+ T)$ depends on $S_X(\omega)$ through the predominant frequency of the output ν_0^+ defined by *Eq 8.32* and explicitely written as:

$$\nu_0^+ = \frac{1}{2\pi}\,\frac{\int_0^\infty \omega^2 S_Y(\omega_0,\omega,\lambda)\,d\omega}{\int_0^\infty S_Y(\omega_0,\omega,\lambda)\,d\omega} \tag{9.11}$$

In practice, a very good approximation for ν_0^+ valid for small structural damping is obtained directly from $\nu_0^+ = \omega_0/2\pi$.

The practical steps of the computation are as follows:

From a given damped (or undamped) Response Spectrum $PSSV[\omega_0,\lambda,p]$ one computes $SD]\omega_0,\lambda,p]$ and then divides by the peak ratio $R_{T,p}(\nu_0^+ T)$ at a set of target frequencies ω_j. This yields the RMS-spectrum $\sigma_Y(\omega_j,\lambda)$ from wich $S_X(\omega)$ can be obtained by a non-linear fitting procedure based on *Eq 9.8* and *Eq.9.9*. Having obtained $S_X(\omega)$, one can deduce the Amplitude Fourier Spectrum through the approximate relation:

$$|A(i\omega)| \approx \sqrt{\frac{S_X(\omega)T}{2}} \tag{9.12}$$

derived from *Eq.8.17* for the chosen duration T.

One then procedes to simulate a stationary motion by *Eq.9.1* whose computed Response Spectrum will match the specified smooth Pseudo-Velocity Spectrum.

9.3 DIRECT METHODS FOR FAS DETERMINATION

9.3.1 PSD models

Instead of defining the ground motion from a Pseudo-Response Spectrum, it is possible, of course, to work directly from Power Spectral Density function models. This has the obvious advantage to avoid the difficult computational step described in the last section. Unfortunately, there does not exist many studies on PSD and none of them have been suggested recently. One can mention the very simple limited white noise model (box-car model) (*fig. IX.8a*) but the *Kanai-Tajimi (1960-1961)* model is certainly the most used. Its PSD depends on three parameters S_0, ω_G and λ_G. It is given by:

$$S_{KT}(\omega) = S_0 \frac{1 + 4\lambda_G\left(\frac{\omega}{\omega_G}\right)^2}{\left[1 - \left(\frac{\omega}{\omega_G}\right)^2\right]^2 + 4\lambda_G^2\left(\frac{\omega}{\omega_G}\right)^2} \tag{9.13}$$

It can be interpreted as white noise filtered by a SDOF oscillator of natural circular frequency ω_G and damping ratio λ_G. The term S_0 is the scaling factor (*fig. IX.8b*) which can be related to the RMS of acceleration by:

$$\sigma^2 = \frac{1}{\pi}\int_0^{\infty} S_{KT}(\omega)\, d\omega = \frac{S_0\omega_G}{4\lambda_G}\sqrt{1 + 4\lambda_G^2} \tag{9.14}$$

In section 9.4.3 we shall give typical numerical values for the coefficients ω_G and λ_G for rock sites and soil sites (table XVII). The computation of the FAS is simply obtained from *Eq. 9.12*. The phases of the motion are also assumed to be randomly distributed in the range (0-π).

9.3.2 The Trifunac FAS model

In a study similar to the Pseudo-Velocity Spectrum study, *Trifunac (1976)* suggested that the Fourier Amplitude Spectrum (FAS) of strong motion acceleration could be scaled in terms of the Magnitude scale with the incorporation of various other effects. He improved the original work by providing a more continuous dependence of spectral amplitudes on the geological character of the site. The scaling factor s used in section 9.2.1 is now replaced by h the depth of sediments in kilometres beneath the site.

In terms of Magnitude the proposed model is:

$$\log\{FAS(\omega)\} = M + \log\{A_0(R)\} - B_M'(\omega)M - C_M'(\omega) - D_M'(\omega)h$$

$$- E_M'(\omega)v - F_M'(\omega)M^2 - G_M'(\omega)R \tag{9.15}$$

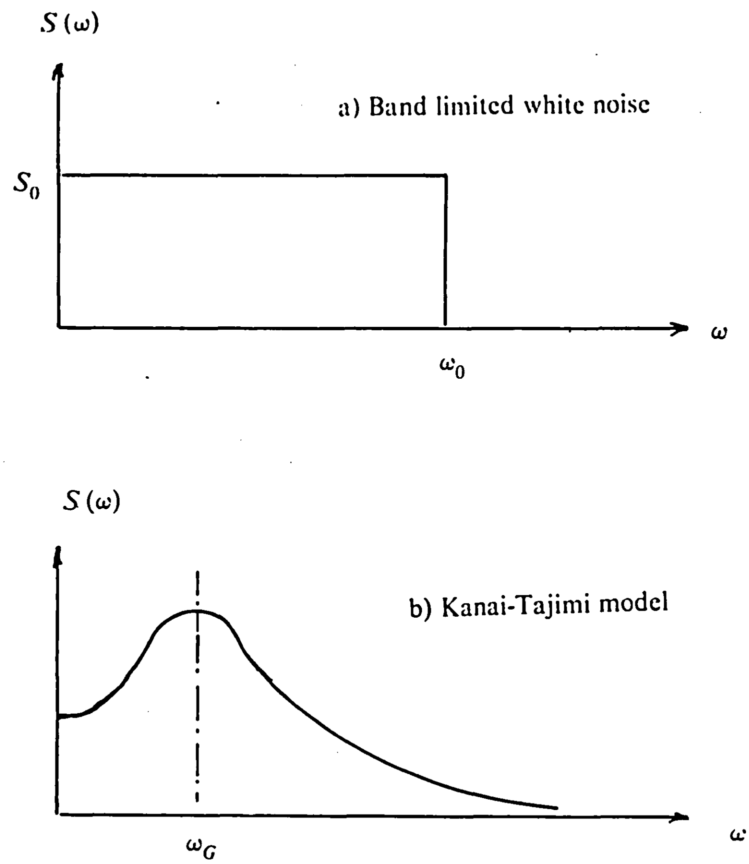

Fig.IX.8
Frequency contribution to the RMS σ of a process

Table XII

Attenuation term $\log\{A_0(r)\}$ in *Eq. 9.3 and 9.15*
based on Richter's local Magnitude scale

$R\,(km)$	$-\log\{A_0(R)\}$	$R\,(km)$	$-\log\{A_0(R)\}$	$R\,(km)$	$-\log\{A_0(R)\}$
0	1.40	140	3.23	370	4.34
5	1.50	150	3.28	380	4.38
10	1.61	160	3.33	390	4.41
15	1.72	170	3.38	400	4.45
20	1.83	180	3.43	410	4.49
25	1.96	190	3.48	420	4.52
30	2.08	200	3.53	430	4.55
25	2.20	210	3.58	440	4.58
40	2.31	220	3.63	450	4.61
45	2.42	230	3.68	460	4.63
50	2.52	240	3.73	470	4.66
55	2.60	250	3.78	480	4.69
60	2.68	260	3.83	490	4.71
65	2.75	270	3.88	500	4.73
70	2.81	280	3.93	510	4.76
80	2.92	290	3.98	520	4.78
85	2.96	300	4.02	530	4.80
90	2.99	310	4.07	540	4.82
95	3.02	320	4.12	550	4.84
100	3.04	330	4.16	560	4.86
110	3.09	340	4.21	570	4.87
120	3.14	350	4.25	580	4.89
130	3.18	360	4.30	590	4.90

Table XIII

Regression parameters for PSSV Model
based on Magnitude ($Eq.9.3$)

$Damping\lambda = 0.00$

$Frequency$ Hz	$\log(\omega)$	A_M	B_M	C_M	D_M	E_M	$10F_M$	$1000G$
25.00	2.196	−1.521	−1.857	9.224	−0.047	−0.020	1.961	−1.20
14.72	1.966	−1.469	−1.836	8.654	−0.099	−0.033	1.912	−1.21
8.67	1.736	−1.340	−1.539	7.086	−0.083	0.065	1.644	−1.21
5.11	1.506	−1.241	−1.327	5.960	−0.011	0.227	1.456	−1.04
3.00	1.275	−1.247	−1.195	5.348	0.079	0.321	1.332	−0.74
1.77	1.046	−1.310	−1.105	5.097	0.157	0.329	1.227	−0.54
1.04	0.815	−1.343	−1.365	6.085	0.194	0.338	1.390	−0.600
0.612	0.584	−1.359	−1.905	8.014	0.202	0.330	1.781	−0.872
0.360	0.354	−1.405	−2.363	9.636	0.203	0.297	2.126	−1.111
0.212	0.124	−1.479	−2.459	10.240	0.191	0.307	2.304	−1.045
0.125	−0.105	−1.566	−2.339	9.570	0.173	0.330	2.169	−0.721

Table XIII (continued)

Regression parameters for PSSV Model
based on Magnitude (*Eq. 9.3*)

Damping $\lambda = 0.02$

Frequency *Hz*	$\log(\omega)$	A_M	B_M	C_M	D_M	E_M	$10F_M$	$1000G_M$
25.00	2.196	−1.290	−1.225	7.222	−0.066	0.068	1.490	−1.173
14.72	1.966	−1.286	−1.357	7.178	−0.118	0.019	1.579	−1.181
8.67	1.736	−1.213	−1.612	7.331	−0.104	0.100	1.770	−1.236
0.196	1.506	−1.130	−1.664	6.988	−0.037	0.251	1.791	−1.102
3.00	1.275	−1.138	−1.435	6.094	0.043	0.339	1.575	−0.769
1.77	1.046	−1.212	−1.181	5.405	0.108	0.350	1.315	−0.478
1.04	0.815	−1.250	−1.241	5.787	0.141	0.354	1.309	−0.510
0.612	0.584	−1.253	−1.691	7.340	0.155	0.345	1.640	−0.837
0.360	0.354	−1.294	−2.219	9.104	0.170	0.316	2.047	−1.104
0.212	0.124	−1.391	−2.447	9.878	0.172	0.332	2.236	−1.000
0.125	−0.105	−1.511	−2.199	9.140	0.159	0.356	2.059	−0.630

Damping $\lambda = 0.05$

Frequency *Hz*	$\log(\omega)$	A_M	B_M	C_M	D_M	E_M	$10F_M$	$1000G_M$
25.00	2.196	−1.235	−1.275	7.391	−0.067	0.102	1.533	−1.283
14.72	1.966	−1.239	−1.376	7.295	−0.115	0.044	1.594	−1.202
8.67	1.736	−1.186	−1.487	7.045	−0.105	0.118	1.672	−1.111
5.11	1.506	−1.108	−1.523	6.645	−0.044	0.255	1.691	−0.987
3.00	1.275	−1.106	−1.392	6.022	0.031	0.342	1.556	−0.731
1.77	1.046	−1.172	−1.187	5.470	0.091	0.359	1.332	−0.467
1.04	0.815	−1.207	−1.207	5.711	0.120	0.369	1.294	−0.475
0.612	0.584	−1.203	−1.541	6.867	0.132	0.360	1.538	−0.773
0.360	0.354	−1.237	−2.039	8.508	0.150	0.330	1.923	−1.081
0.212	0.124	−1.331	−2.342	9.509	0.155	0.350	2.169	−1.103
0.125	−0.105	−1.445	−2.175	9.034	0.144	0.369	2.048	−0.869

Table XIII (continued)

Regression parameters for PSSV Model
based on Magnitude ($Eq.9.3$)

Damping $\lambda = 0.10$

$Frequency$ Hz	$\log(\omega)$	A_M	B_M	C_M	D_M	E_M	$10F_M$	$1000G_M$
25.00	2.196	−1.190	−1.132	6.972	−0.080	0.110	1.409	−1.097
14.72	1.966	−1.195	−1.337	7.193	−0.105	0.081	1.565	−1.065
8.67	1.736	−1.156	−1.426	6.922	−0.095	0.141	1.629	−1.052
5.11	1.506	−1.097	−1.458	6.545	−0.044	0.261	1.644	−0.969
3.00	1.275	−1.087	−1.367	6.036	0.023	0.343	1.543	−0.710
1.77	1.046	−1.139	−1.174	5.494	0.078	0.366	1.332	−0.397
1.04	0.815	−1.170	−1.150	5.571	0.106	0.379	1.259	−0.365
0.612	0.584	−1.166	−1.392	6.405	0.115	0.374	1.430	−0.698
0.360	0.354	−1.191	−1.876	7.968	0.130	0.348	1.813	−1.051
0.212	0.124	−1.279	−2.318	9.394	0.141	0.367	2.163	−1.049
0.125	−0.105	−1.400	−2.299	9.376	0.136	0.391	2.156	−0.781

Damping $\lambda = 0.20$

$Frequency$ Hz	$\log(\omega)$	A_M	B_M	C_M	D_M	E_M	$10F_M$	$1000G_M$
25.00	2.196	−1.144	−1.165	7.045	−0.074	0.127	1.445	−1.043
14.72	1.966	−1.152	−1.245	6.946	−0.099	0.122	1.494	−1.057
8.67	1.736	−1.120	−1.307	6.650	−0.090	0.171	1.535	−1.138
5.11	1.506	−1.076	−1.391	6.466	−0.046	0.264	1.595	−1.077
3.00	1.275	−1.068	−1.350	6.102	0.013	0.342	1.534	−0.744
1.77	1.046	−1.103	−1.165	5.547	0.061	0.372	1.331	−0.371
1.04	0.815	−1.132	−1.103	5.465	0.086	0.386	1.235	−0.323
0.612	0.584	−1.130	−1.247	5.972	0.096	0.385	1.332	−0.615
0.360	0.354	−1.138	−1.593	7.076	0.110	0.360	1.601	−0.925
0.212	0.124	−1.223	−2.031	8.458	0.212	0.374	1.951	−0.986
0.125	−0.105	−1.368	−2.174	8.972	0.177	0.412	2.066	−0.847

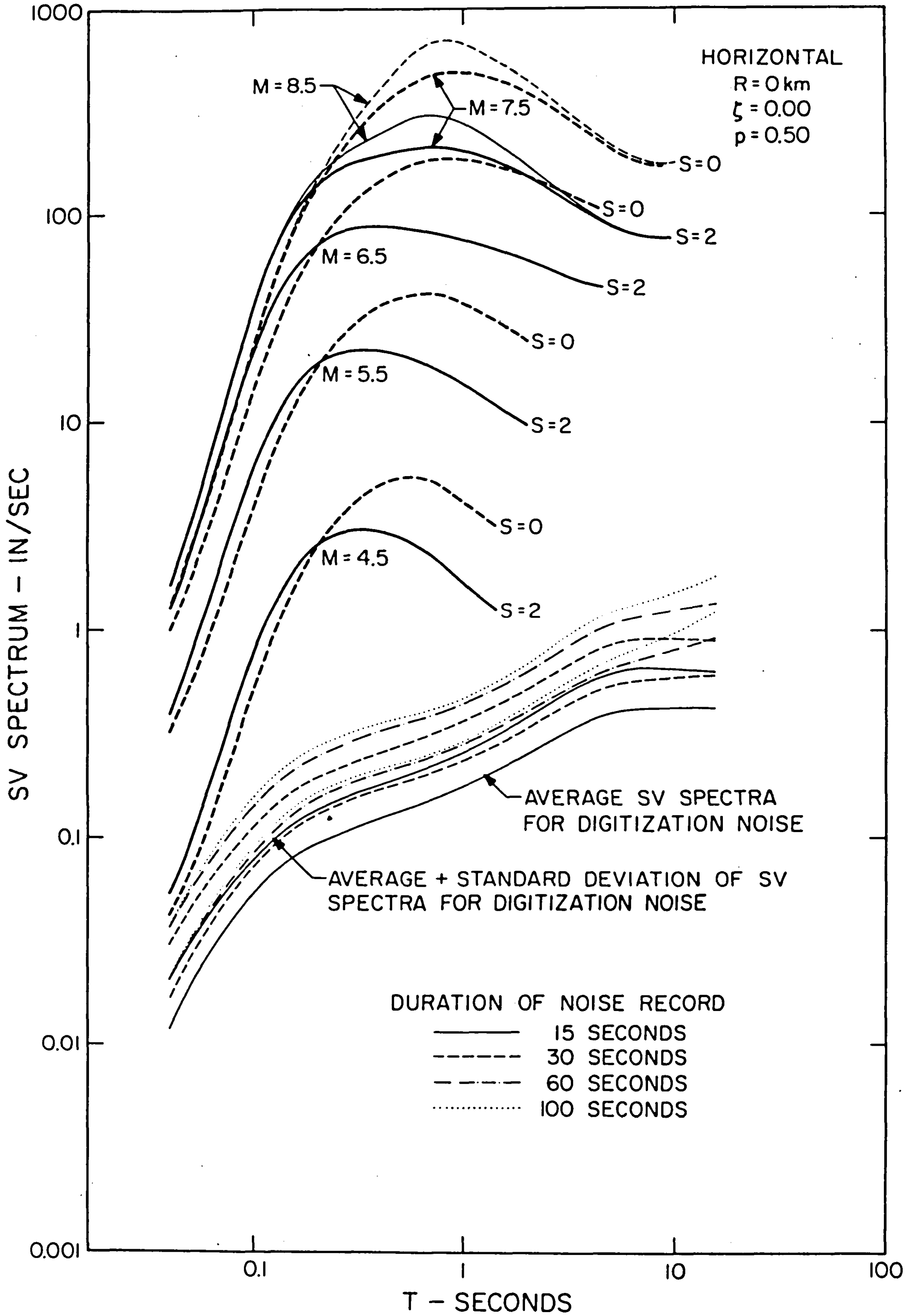

Fig.IX.6

Epicentral pseudo-velocity spectra scaled by Magnitude

(after Trifunac and Anderson 1978)

Table XIV

Regression parameters for PSSV Model

based on Intensity (*Eq. 9. 4*)

$Damping \lambda = 0.00$

Frequency *Hz*	log(ω)	A_I	B_I	C_I	D_I	E_I
25.00	2.196	1.562	0.339	−3.605	0.208	0.034
14.72	1.966	1.556	0.320	−3.237	0.203	0.032{
8.67	1.736	1.460	0.296	−2.117	0.173	−0.074
5.11	1.506	1.286	0.278	−1.454	0.115	−0.221
3.00	1.275	1.125	0.271	−1.068	0.049	−0.314
1.77	1.046	1.059	0.275	−0.953	−0.002	−0.342
1.04	0.815	1.106	0.296	−1.093	−0.031	−0.331
0.612	0.584	1.221	0.324	−1.369	−0.051	−0.287
0.360	0.354	1.349	0.333	−1.551	−0.070	−0.249
0.212	0.124	1.402	0.316	−1.557	−0.074	−0.268
0.125	−0.105	1.332	0.292	−1.526	−0.045	−0.308

Table XIV (continued)

Regression parameters for PSSV Model
based on Intensity (*Eq. 9.4*)

$Damping \lambda = 0.02$

Frequency Hz	log(ω)	A_I	B_I	C_I	D_I	E_I
25.00	2.196	1.371	0.341	−3.768	0.237	−0.077
14.72	1.966	1.393	0.331	−3.235	0.243	−0.031
8.67	1.736	1.358	0.311	−2.502	0.221	−0.098
5.11	1.506	1.222	0.291	−1.823	0.164	−0.230
3.00	1.275	1.066	0.282	−1.388	0.097	−0.323
1.77	1.046	0.999	0.287	−1.239	0.040	−0.348
1.04	0.815	1.028	0.307	−1.326	0.007	−0.338
0.612	0.584	1.113	0.332	−1.530	−0.016	−0.303
0.360	0.354	1.240	0.343	−1.673	−0.041	−0.270
0.212	0.124	1.329	0.330	−1.678	−0.056	−0.285
0.125	−0.105	1.308	0.307	−1.648	−0.034	−0.329

$Damping \lambda = 0.05$

Frequency Hz	log(ω)	A_I	B_I	C_I	D_I	E_I
25.00	2.196	1.325	0.340	−3.789	0.238	−0.107
14.72	1.966	1.349	0.328	−3.277	0.241	−0.057
8.67	1.736	1.321	0.307	−2.579	0.222	−0.118
5.11	1.506	1.193	0.288	−1.929	0.171	−0.241
3.00	1.275	1.040	0.282	−1.510	0.110	−0.328
1.77	1.046	0.968	0.290	−1.365	0.061	−0.355
1.04	0.815	0.986	0.310	−1.432	0.029	−0.349
0.612	0.584	1.058	0.333	−1.600	0.004	−0.319
0.360	0.354	1.168	0.347	−1.732	−0.024	−0.289
0.212	0.124	1.260	0.341	−1.769	−0.037	−0.295
0.125	−0.105	1.272	0.323	−1.764	−0.015	−0.327

Table XIV (continued)

Regression parameters for PSSV Model
based on Intensity (*Eq*.9.4)

$Damping \lambda = 0.10$

Frequency Hz	log(ω)	A_I	B_I	C_I	D_I	E_I
25.00	2.196	1.298	0.333	−3.779	0.237	−0.107
14.72	1.966	1.322	0.322	−3.296	0.237	−0.087
8.67	1.736	1.293	0.304	−2.647	0.219	−0.146
5.11	1.506	1.172	0.287	−2.036	0.174	−0.251
3.00	1.275	1.026	0.282	−1.630	0.119	−0.328
1.77	1.046	0.948	0.291	−1.476	0.077	−0.359
1.04	0.815	0.954	0.309	−1.512	0.048	−0.359
0.612	0.584	1.016	0.329	−1.630	0.016	−0.329
0.360	0.354	1.111	0.342	−1.737	−0.016	−0.297
0.212	0.124	1.190	0.343	−1.800	−0.021	−0.303
0.125	−0.105	1.221	0.334	−1.835	0.001	−0.335

$Damping \lambda = 0.20$

Frequency Hz	log(ω)	A_I	B_I	C_I	D_I	E_I
25.00	2.196	1.274	0.322	−3.734	0.226	−0.118
14.72	1.966	1.304	0.315	−3.303	0.225	−0.120
8.67	1.736	1.268	0.301	−2.723	0.211	−0.177
5.11	1.506	1.148	0.287	−2.192	0.173	−0.260
3.00	1.275	1.015	0.284	−1.777	0.127	−0.325
1.77	1.046	0.941	0.291	−1.609	0.093	−0.360
1.04	0.815	0.931	0.306	−1.603	0.068	−0.368
0.612	0.584	0.964	0.323	−1.669	−0.039	−0.345
0.360	0.354	1.031	0.336	−1.741	0.006	−0.314
0.212	0.124	1.106	0.340	−1.812	−0.004	−0.317
0.125	−0.105	1.170	0.340	−1.892	0.016	−0.351

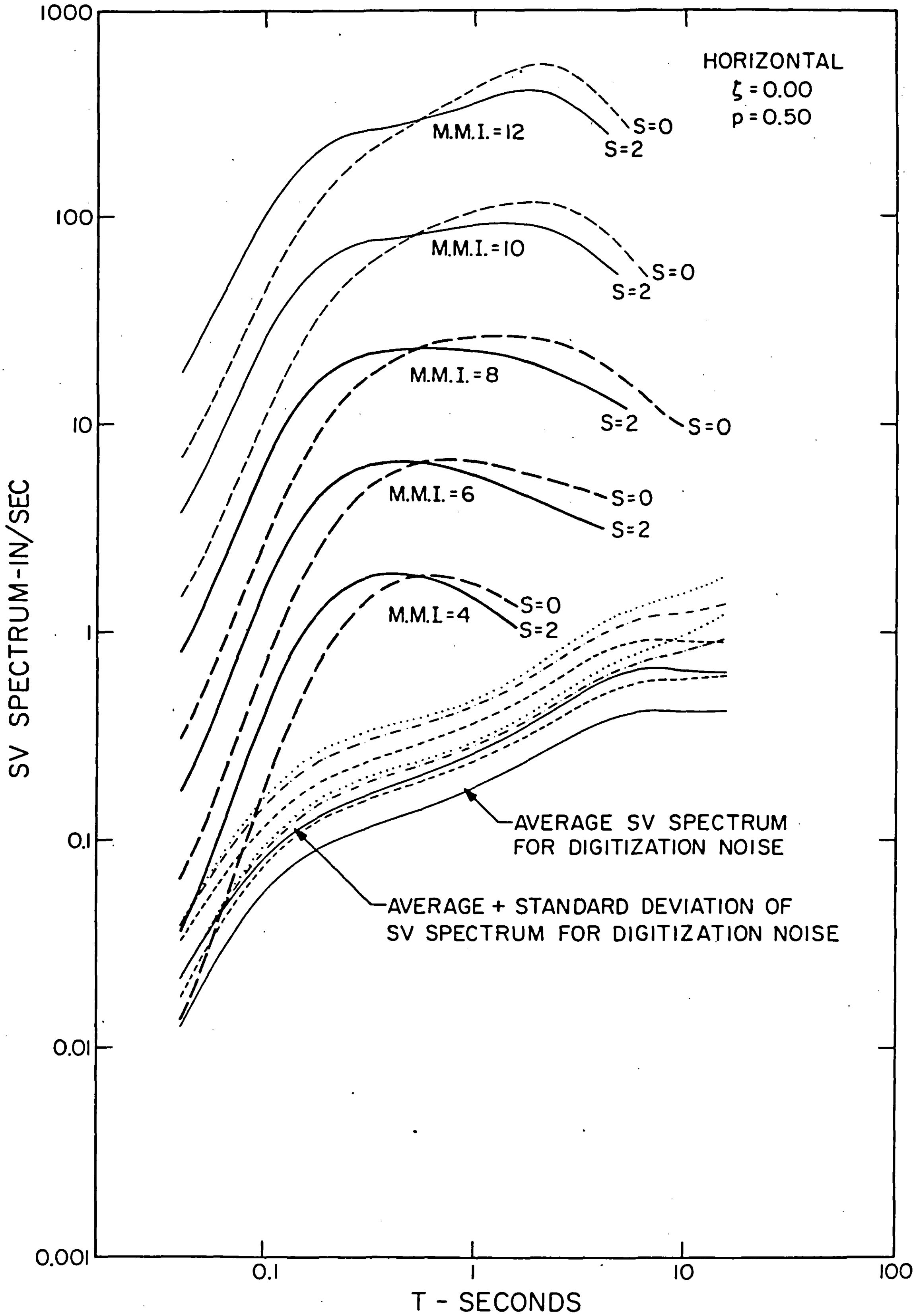

Fig.IX.7

Epicentral pseudo-velocity spectra
scaled by Intensity
(after Trifunac and Anderson 1978)

Table XV

Regression parameters for FAS Model
based on Magnitude (*Eq. 9.15 and 9.17*)

Frequency *Hz*	$\log(\omega)$	B_M'	C_M'	$10D_M'$	E_M'	F_M'	$1000G_M'$	μ
25.00	2.196	−1.187	6.648	0.044	−0.047	0.137	−0.410	0.003
15.38	1.985	−1.310	6.641	0.074	−0.026	0.146	−0.485	0.012
9.09	1.757	−1.420	6.253	0.102	0.067	0.154	−0.860	0.020
5.26	1.519	−1.065	4.688	0.015	0.223	0.126	−1.939	0.010
2.94	1.267	−0.589	3.091	−0.204	0.318	0.089	−3.260	0.01
2.00	1.099	−0.414	2.575	−0.364	0.328	0.074	−4.014	−0.00[illegible]
1.11	0.844	−0.467	2.964	−0.528	0.323	0.075	−4.525	0.003
0.625	0.594	−0.734	4.167	−0.654	0.273	0.089	−4.548	0.033
0.357	0.351	−1.079	5.451	−0.822	0.229	0.115	−4.991	0.078
0.227	0.155	−1.058	5.317	−0.876	0.249	0.119	−5.712	0.089
0.133	−0.077	−0.338	2.937	−0.754	0.217	0.070	−6.277	0.046

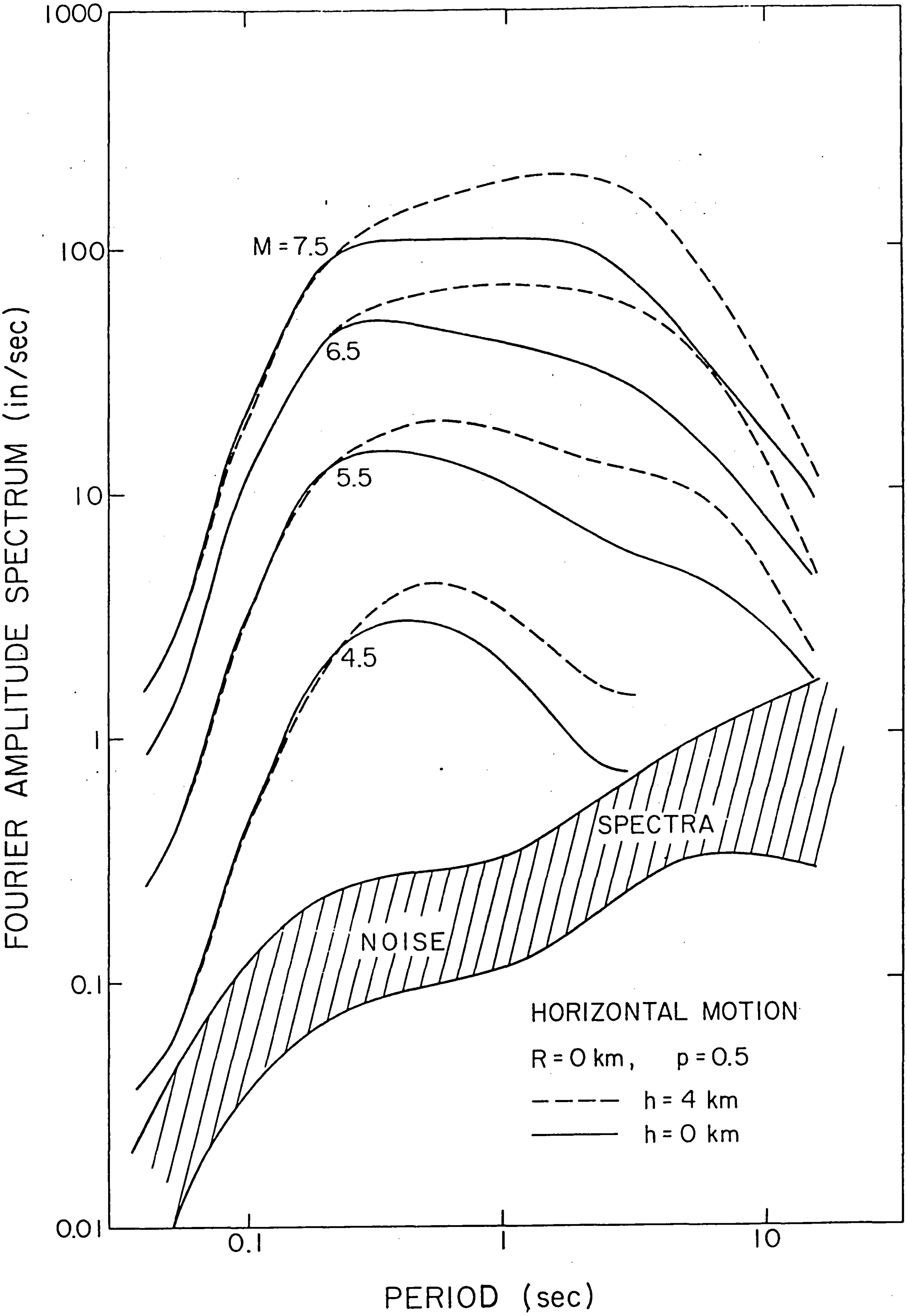

Fig.IX.9a

Epicentral Fourier Amplitude spectra

scaled by Magnitude

(after Trifunac 1976)

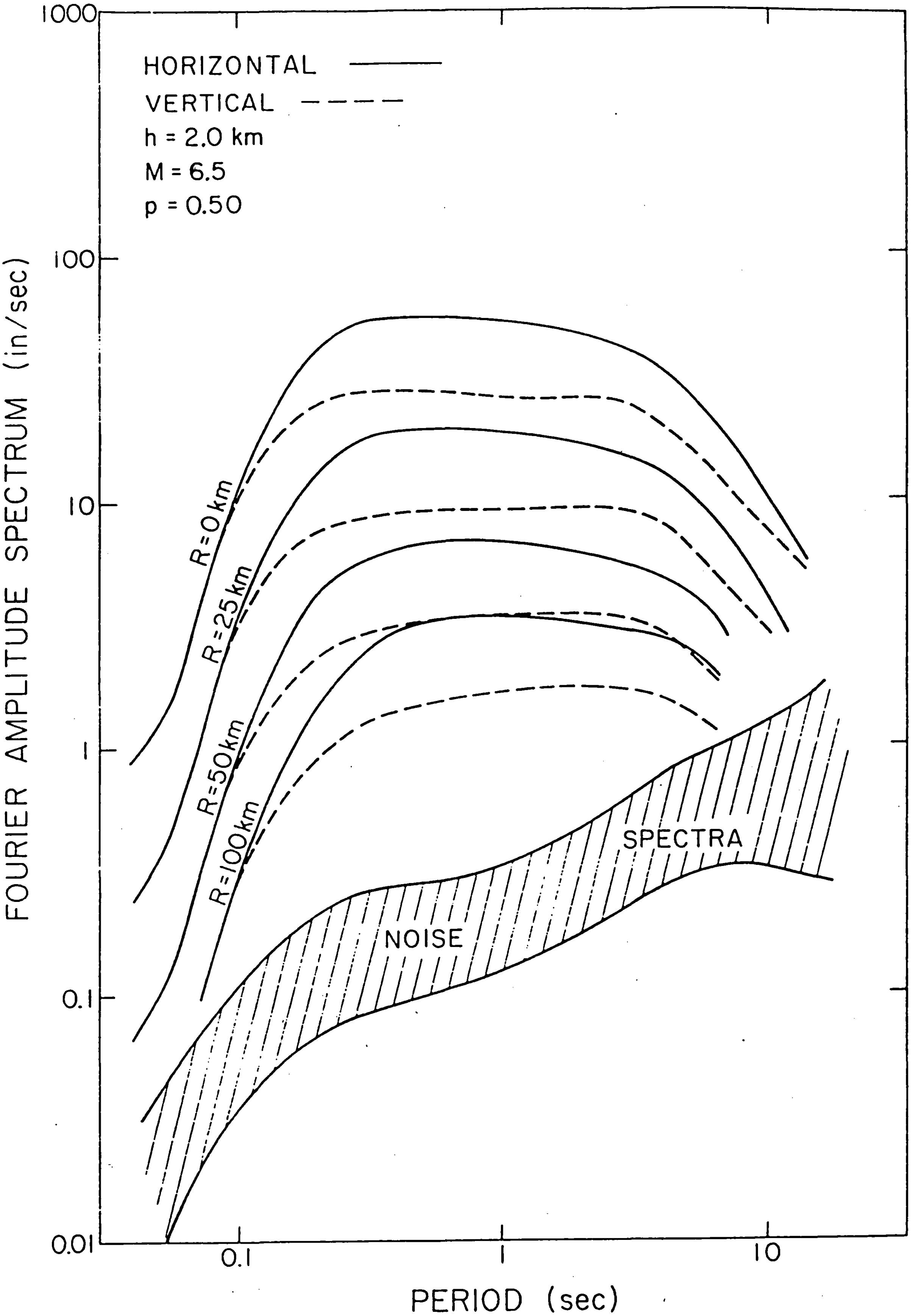

Fig.IX.9b

Variation with distance of a $M = 6.5$ Fourier Amplitude spectra (after Trifunac 1976)

Table XVI

Regression parameters for FAS Model
based on Intensity (*Eq.9.16 and 9.17*)

Frequency *Hz*	$\log(\omega)$	B_I'	C_I'	$10D_I'$	E_I'	μ	υ
25.00	2.196	0.340	−2.795	−0.337	0.039	−0.069	0.58
15.38	1.985	0.319	−2.254	−0.298	0.020	−0.052	0.57
9.09	1.757	0.286	−1.321	−0.236	−0.075	−0.028	0.54
5.26	1.919	0.270	−0.766	−0.078	−0.231	−0.021	0.47
2.94	1.267	0.268	−0.579	0.132	−0.329	−0.018	0.41
2.00	1.099	0.266	−0.539	0.260	−0.348	−0.016	0.39
1.11	0.844	0.283	−0.691	0.478	−0.340	−0.010	0.40
0.625	0.594	0.314	−1.032	0.744	−0.264	0.001	0.43
0.357	0.351	0.319	−1.185	1.010	−0.201	0.012	0.48
0.227	0.155	0.282	−1.016	1.060	−0.233	0.013	0.49
0.133	−0.077	0.214	−0.732	0.806	−0.243	−0.005	0.47

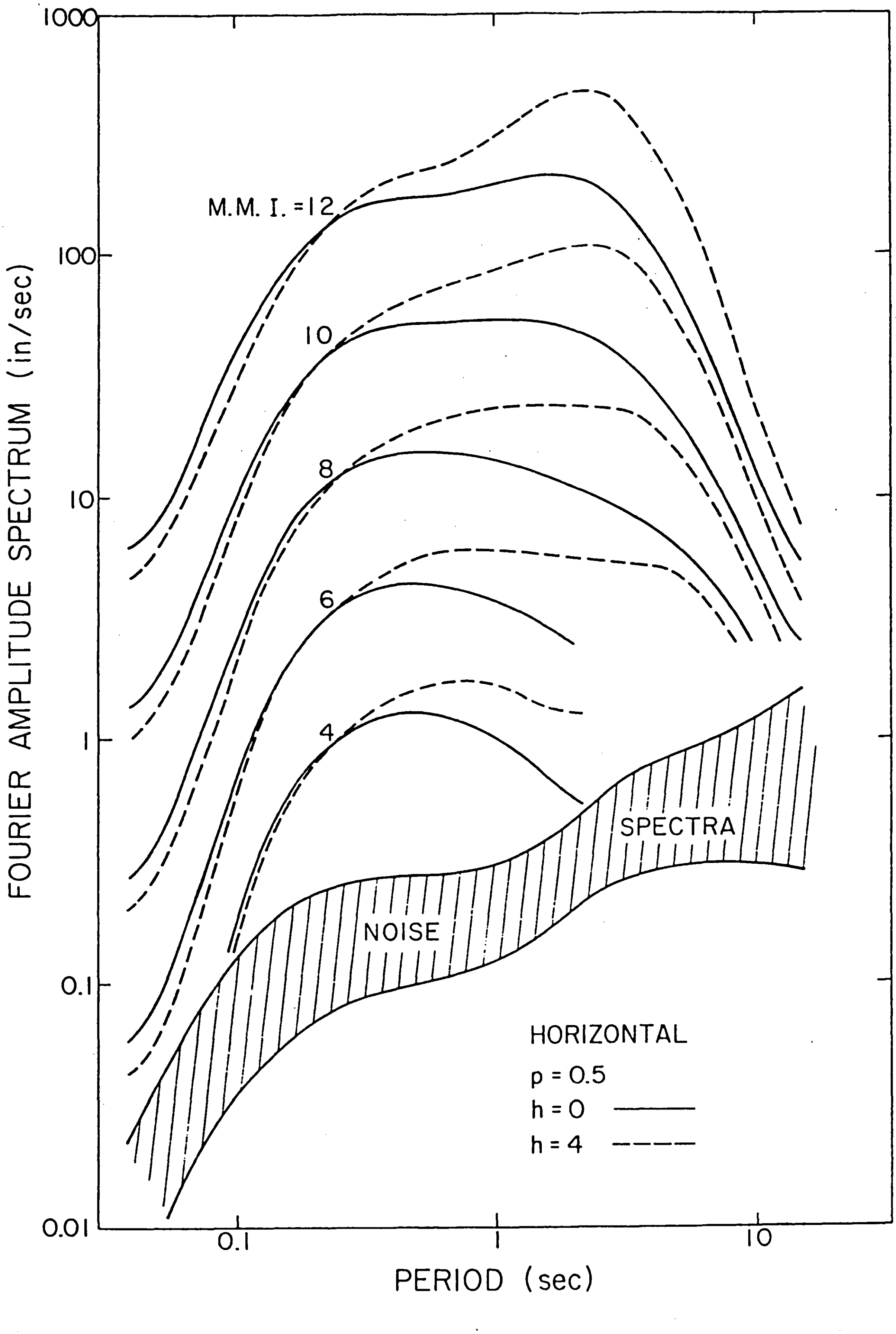

Fig.IX.10
Epicentral Fourier Amplitude spectra
scaled by Intensity
(after Trifunac 1976)

and in terms of Intensity is:

$$\log\{FAS(\omega)\} = B_I'(\omega)I_{MM} + C_I'(\omega) + D_I'(\omega)h + E_I'(\omega) \tag{9.16}$$

All the definitions given in section 9.2.1 are still valid here and the frequency dependent coefficients are given in table XV and table XVI at eleven selected frequencies. The overall trend of the amplitudes is to increase in the long period range for alluvium sites versus rock sites. The opposite trend can be observed in the high frequencies as shown in *fig. IX. 9a and b.* The terms $\mu(\omega)$ and $\upsilon(\omega)$ given in the tables describe the assumed normal probability distribution of the residuals. They can be used to determine the probability $p(e,\omega)$ that an error e will not be exceeded.

$$p(e,\omega) = \frac{1}{\upsilon(\omega)\sqrt{2\pi}} \int_{-\infty}^{e(\omega)} \exp\left[-\frac{1}{2}\left(\frac{x-\mu(\omega)}{\upsilon(\omega)}\right)^2\right] dx \tag{9.17}$$

Here again, for simulation purposes, the phases $\Phi(\omega)$ are assumed to be randomly distributed.

9.3.3 The Boore FAS model

The *Boore* FAS model has already been described in section 3.4.3 (see *Eq. 3.42*) and we shall only insist here on the required data which are neccessary in order to be able to use it. The principal assumptions of the model are the following:

Shear waves only

Far-field equations

Random phases

Linear propagation medium.

Then parameters have to be assessed, according to a fair knowledge of the local seismological and geotechnical conditions. We have to provide estimates for the following parameters:

Seismic moment	M_0
Crust rigidity	μ
Distance	R
Focal Depth	H
Stress drop	$\Delta\sigma$
"Hanks" limit	F_{max}
High frequency decay	s
attenuation	Q
S-wave velocity	β
Radiation pattern	$R_{\theta\phi}$

An example of such a FAS computation has been given in section 3.4.3 and is shown in *fig. III. 22* for an earthquake of Magnitude $M_S = 7$ at hypocentral distance of 20 km.

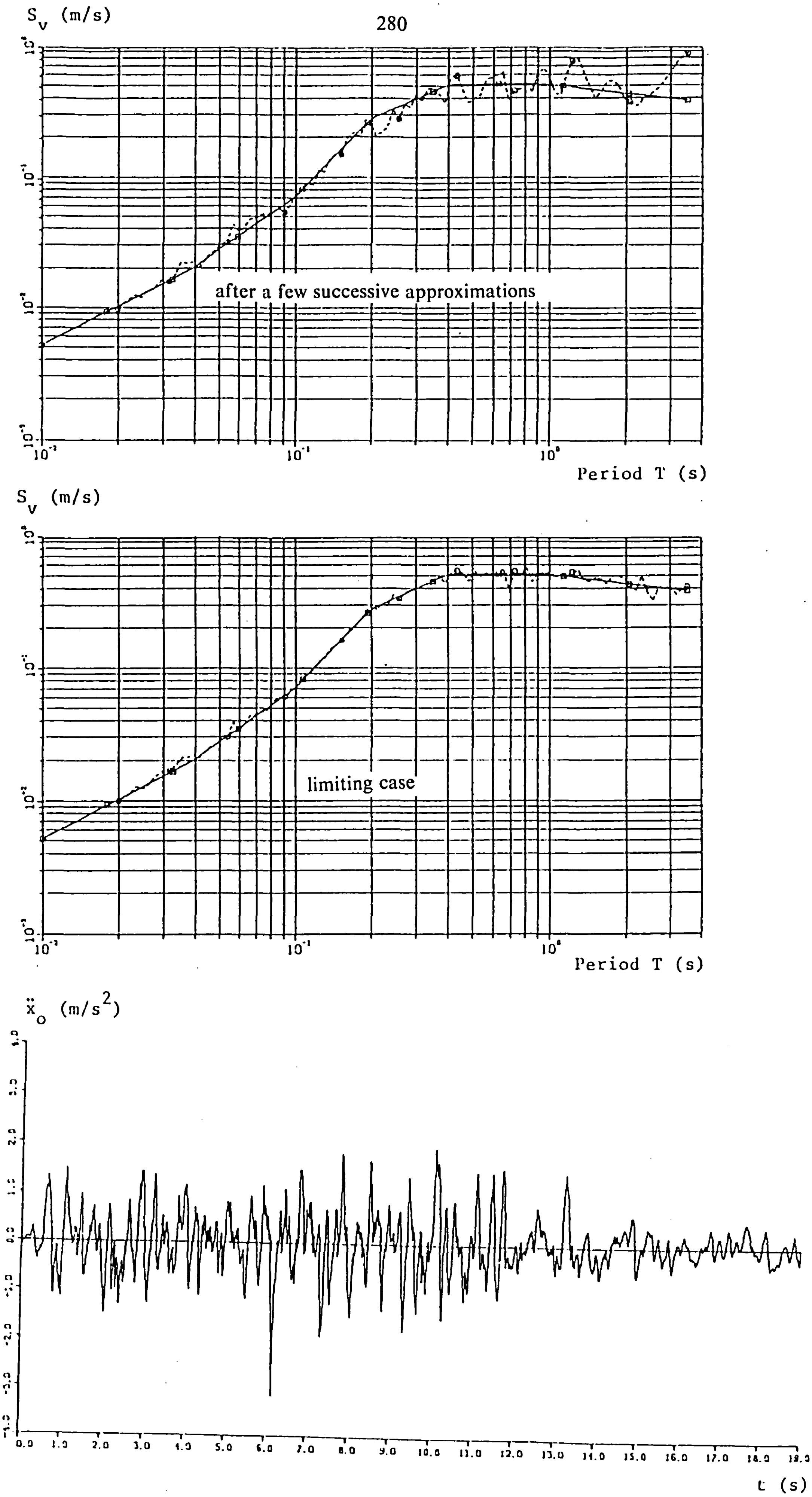

Fig.IX.11

Example of response spectrum fitting

9.4 NON-STATIONARITY IN TIME

9.4.1 Use of Chapter II method

In Chapter II we used a simple method to integrate the non-stationarity of a near field signal both in time and frequency. What has been achieved has consisted in fact of applying a shaping function which represented approximatively the observed buildup and decay of energy, for a particular frequency. Each group of frequencies was treated differently. For the designed signal of 20 sec duration, we assumed that the P-wave frequency content was present from $t = 0$ sec. to $t = 14$ sec. For the S-waves, and the T-waves (assumed to correspond to surface-waves) the windows began at $t = 3$ and $t = 0$ sec. and finished at $t = 18$ and $t = 20$ sec. respectively.

In this particular case, the shapes of the windows for the P-waves and the T-waves were symmetric with respect to their middle points and we used a function proposed by *Harris*. The purpose was to avoid frequency leakage, and to keep a "clean" signal. The S-waves, however, were multiplied by a more realistic non-symmetrical window, simulating, in some way, the initial burst of energy followed by a slow decay.

The same principle can be used to shape, in time, the presence of particular frequencies. There is, of course, no need to make use of mathematical functions like those employed in Chapter II to ease the signal analysis. Any empirical shape, determined from statistical analysis of filtered records may be used. We have not performed here such an analysis which must rely a complete earthquake strong motion data set. A limited study is however presented in the next section. It investigates this problem for all the frequencies included in the records.

The time history generation technique developed aims at achieving a time history of limited duration T with a specified amplitude spectrum. It must be realized that the intuitive procedure must be used with care. It consists in generating first a stationary process of known frequency content and then to shape it in time according to the function mentioned above. In doing so, the amplitudes of the different frequencies are modified and hence also the spectrum we started off with. A looping process is necessary to correct the distorsions introduced, as shown in *fig. IX. 1*. Other methods may also be used (*Boore 1983*) but we believe that results need not be pushed further since we face errors of the same order of magnitude as the uncertainty of the passage from PSSV to FAS.

9.4.2 Empirical time shaping

A preliminary analysis of a acceleration time shaping has been performed to introduce the non-stationary character of actual strong motions. Typical records exhibit a variation of their RMS with time (*fig. IX. 12*) This is also seen on the *Husid plots* which show a non-linear buildup. We have retained the mathematical expression:

$$w(t) = A\,t^{b}e^{-ct} \tag{9.18}$$

first proposed by *Sagaroni (1972)* to model the time dependence of the signal variance. This expression is attractive since it offers three parameters A, b and c to be determined for each acceleration record. The total signal "energy" described by the *Arias intensity* I_{max} is scaled by the parameter A:

$$A = (2c)^{b+1/2}\sqrt{\frac{I_{max}}{\Gamma(2b+1)}} \tag{9.19}$$

where $\Gamma[.]$ is the Gamma function.

The parameters b and c do not have a direct physical interpretation, but they are linked to the time T_m of expected acceleration maximum (or maximum slope of the *Husid plot*) and the distance between inflection points T_s which can be taken as a simple measure of the strong part of the motion.

After some algebra, we get:

$$T_m = \frac{b}{c} = \quad \text{expected time of maximum} \tag{9.20a}$$

$$T_s = \frac{\sqrt{b}}{c\sqrt{2}} = \quad \text{strong part duration} \tag{9.20b}$$

It is clear that A is a scaling factor describing the total energy at the recording site, and as such depends of Magnitude and hypocentral distance. The following preliminary results are based on 25 earthquake strong motion records (Italy, Greece and California) of limited characteristics.

$$5.0 < M_S < 6.5$$

$$10 < R < 80 \quad km$$

We found:

$$T_m = 0.15 \quad (\pm\, 0.51) \quad R \text{ in sec.} \tag{9.21a}$$

$$T_s = 1.26 \quad (\pm\, 0.29) + 0.11 \quad (\pm\, 0.03) \quad R \text{ in sec.} \tag{9.21b}$$

$$I_{max} = 0.15\,10^{-5}e^{2.55M}R^{-0.25} \tag{9.21c}$$

This gives the folllowing expressions, also represented in *fig. IX. 12* for the model parameters:

$$b = \frac{0.045R^2}{(1.26 + 0.11R)^2} \tag{9.22a}$$

$$c = \frac{b}{0.15R} \tag{9.22b}$$

and finally A can be computed through *Eq 9. 19*. Surely the proposed coefficients are not of strong value

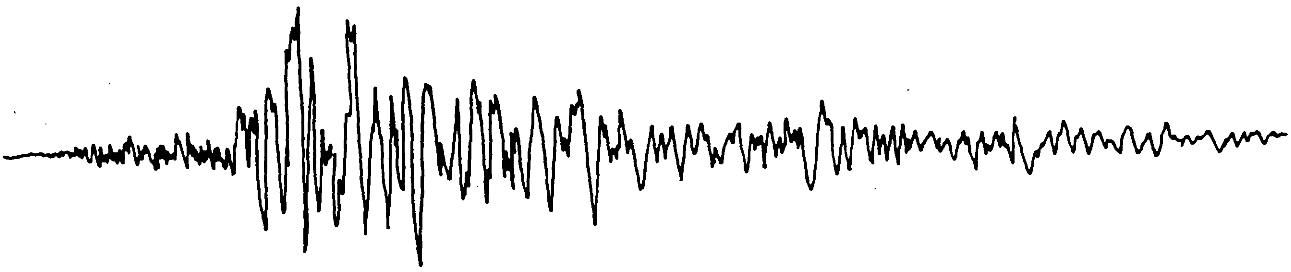

a) typical near-field non stationarity for ground acceleration

b) Husid plot: a possible representation of "energy" build-up

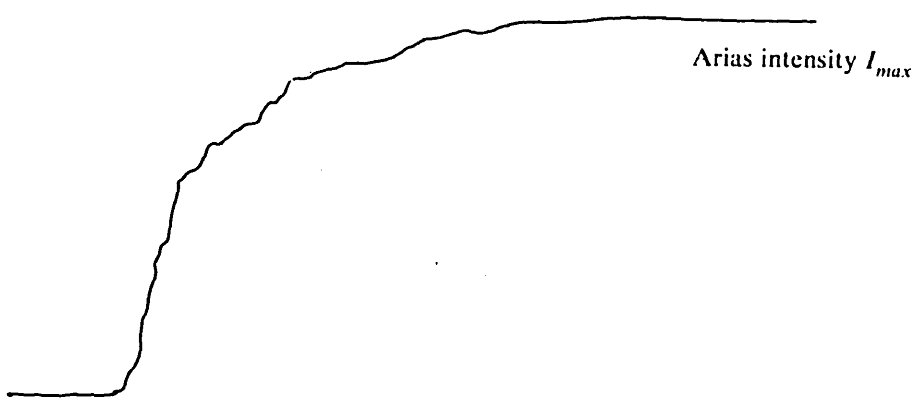

c) model for the time function of ground motion "energy" density

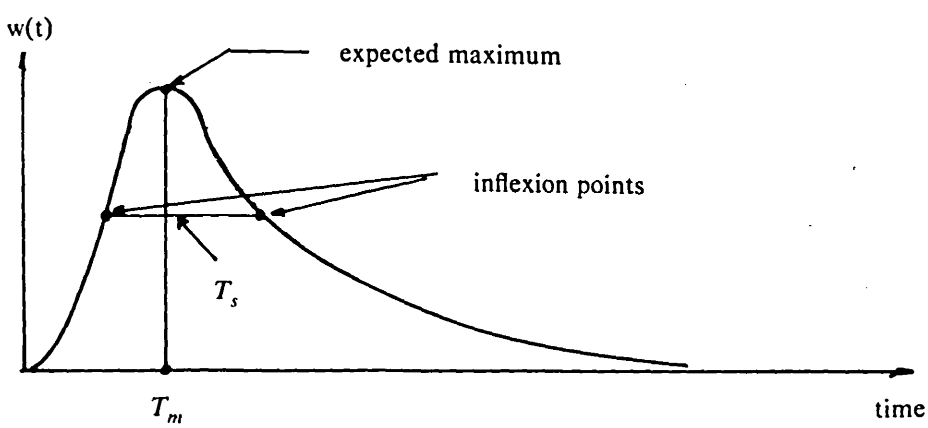

Fig.IX.12

Non-stationarity exhibited by a typical ground motion record since they only rely on a limited number of earthquakes, within limited magnitude and hypocentral range. It is however believed that a more complete statistical study should provide a good definition of the non-stationarity of the acceleration signals in this way. Furthermore, as mentioned in the last section it should be interesting for engineering application to perform such a study for different frequency band and apply the technique used in chapter II.

9.4.3 An equivalent stationary motion

In order to define an equivalent stationary motion, we shall make use of the shaping function in time $w(t)$ given by *Eq.9.18.* If we multiply the recorded acceleration time history by its inverse:

$$w^{-1}(t) = \frac{1}{A} t^{-b} e^{ct} \tag{9.23}$$

we obtain a process which may be considered as to have all the characteristics of a stationary process normalised to a unit RMS. Therefore, every development envisaged in chapter VIII can be applied to this "stationary modified" motion.

In particular, for the purpose of defining typical parameters for the *Kanai-Tajimi* PSD model, we used the data set mentioned in the last section. We have obtained the values included in table XVII

The *fig.IX.13a and b* show some of the acceleration time histories simulated by this method associated with the *Kanai-Tajimi* PSD. The two acceleration signals are 20 sec. long and are coming from a shock of Magnitude 6.5 at 50 km away. Their characteristics are written in table XVII

Table XVII

Average values for Kanai-Tajimi PS models

	Rock	Soil
$\omega_G/2\pi$	4.15 $\pm$ 0.09	1.55 $\pm$ 0.75
λ_G	0.51 $\pm$ 0.20	0.40 $\pm$ 0.25

Numerical values used for example of fig.IX.13

$\omega_G/2\pi$	4.00	0.80
λ_G	0.55	0.35
Magnitude	6.5	6.5
Distance	50	50

a) ground acceleration on rock

duration 20 sec

Max acceleration = 0.2783 g

RMS = 0.0640 g

frequency range F_{max} = 10 Hz F_{min} = 0.2 Hz

predominant frequency = 4.0 Hz damping = 0.55

b) ground acceleration on soil

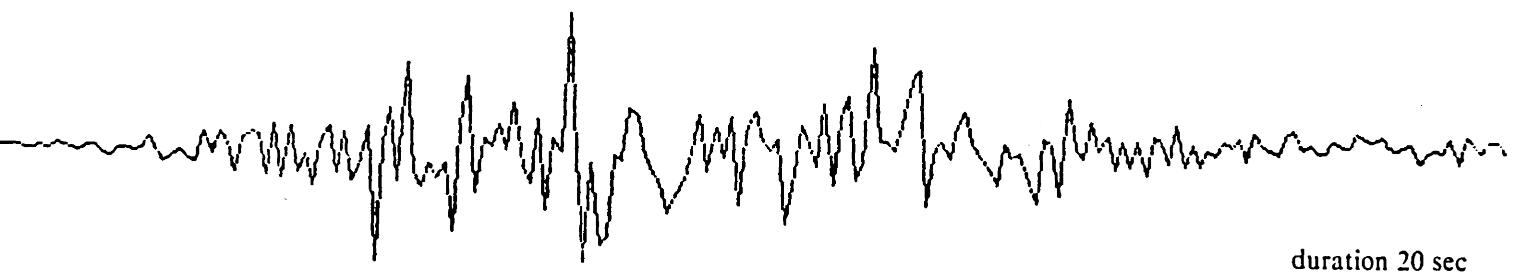

duration 20 sec

Max acceleration = 0.2802 g

RMS = 0.0640 g

frequency range F_{max} = 5 Hz F_{min} = 0.1 Hz

predominant frequency = 0.8 Hz damping = 0.35

Fig.IX.13

Simulated motion from non-stationry

Kanai-Tajimi model

Magnitude M = 6.5 at 50 km

CHAPTER X

BASIS FOR THE SIMULATION OF GROUND ACCELERATION FROM GEOPHYSICAL MODELS

10.1 INTRODUCTION

In this chapter, we intend to develop a theory necessary to generate ground acceleration in the near field of an earthquake. The method will be based on the physical aspects of fault rupture and of wave propagation. The complete geophysical theory is a immense task whose termination is not likely to be achieved before many years. Nevertheless, we think that the approach presented here covers more than is usually described.

Still many assumptions are included in the theories, both in the faulting mechanism and in the seismic energy radiation.

The generation of an acceleration field requires an accurate knowledge of the mechanism of rupture on the fault. The common method consists of using kinematic slip functions for the motions on the fault, which fit the far-field waveforms. We have reviewed these classical methods as well as showing how quasi-dynamic basic functions can be used. There is no question of satisfying the complete dynamic problem since this requires the knowledge of the still inaccessible state of tectonic stress in the crust and the rock characteristics in the vicinity of the expected fault. Furthermore, the specific details of the rupture, influenced for example by the variation of the material strength or its weakeness distribution can only be approached stochastically.

The propagating medium is assumed to be elastic with allowance for anelastic energy dissipation. This means that the present development is valid for energy radiating in rock or rock-like materials exclusively. However, unlike the conventional methods which consider the far-field terms of radiation only, we have retained all the terms of the elastic propagation. We have also integrated a full source-site geometry and an extensive formulation of the Doppler effect. On the other hand, we remain limited to the radiation of the body waves in an unbounded medium. If surface effect is allowed, this assumption may be considered as applicable for distance D less than $H \times \tan\theta$, where H is the depth of the radiating point (focus) and $\theta = \sin^{-1} V_R/V$, is dependent of the ratio of the Rayleigh wave velocity V_R and the P or S wave velocity V (*Nakano's condition*). This domain is precisely the very near-field where no surface waves are generated.

10.2 ELASTIC THEORY OF SHEAR DISLOCATION

10.2.1 Point source in an unbounded medium

The first theoretical approaches to the description of the source mechanism of an earthquake were based on the consideration of various simple point sources and couples on a surface (fault) of an elastic medium.

The displacements components (u_x, u_y, u_z) due to a single force of magnitude $G(t) = G_0 g(t)$ acting at the origin of a reference system of coordinates in the direction of the x-axis (*fig. X. 1*) were given by *Love (1944)* for an unbounded medium.

$$u_x = \frac{G_0}{4\pi\rho}\left\{ \frac{\partial^2 R^{-1}}{\partial x^2} \int_{R/V_P}^{R/V_S} \tau g(t-\tau)\,d\tau + \frac{1}{R V_S^2} g\left(t-\frac{R}{V_S}\right) + \frac{1}{R}\left(\frac{\partial R}{\partial x}\right)^2 \left[\frac{1}{V_P^2} g\left(t-\frac{R}{V_P}\right) - \frac{1}{V_S} g\left(t-\frac{R}{V_S}\right)\right]\right\} \tag{10.1a}$$

$$u_y = \frac{G_0}{4\pi\rho}\left\{ \frac{\partial^2 R^{-1}}{\partial y^2} \int_{R/V_P}^{R/V_S} \tau g(t-\tau)\,d\tau + \frac{1}{R}\frac{\partial R}{\partial x}\frac{\partial R}{\partial y} \left[\frac{1}{V_P^2} g\left(t-\frac{R}{V_P}\right) - \frac{1}{V_S} g\left(t-\frac{R}{V_S}\right)\right]\right\} \tag{10.1b}$$

$$u_z = \frac{G_0}{4\pi\rho}\left\{ \frac{\partial^2 R^{-1}}{\partial z^2} \int_{R/V_P}^{R/V_S} \tau g(t-\tau)\,d\tau + \frac{1}{R}\frac{\partial R}{\partial x}\frac{\partial R}{\partial z} \left[\frac{1}{V_P^2} g\left(t-\frac{R}{V_P}\right) - \frac{1}{V_S} g\left(t-\frac{R}{V_S}\right)\right]\right\} \tag{10.1c}$$

The amplitude G_0 of the force is, for the moment, constant; $g(t)$ represents the time dependence of the force. R is the distance from the acting force to the point $M(x, y, z)$ where the motion is expressed.

The elastic characteristics of the propagating medium are given through the P-wave velocity V_P and the S-wave velocity V_S. ρ is the medium density.

In spherical coordinates (r, ϑ, ϕ) at the source, (the choice of spherical coordinates eases the discussion as, at least for the far field equations, the radial component carries the P-wave and the tangential component carries the S-wave), the expressions become (*fig. X. 2*):

$$u_r = \frac{G_0 \cos\phi}{4\pi\rho R}\left[\frac{2}{R^2}\int_{R/V_P}^{R/V_S} \tau g(t-\tau)\,d\tau + \frac{1}{V_P^2} g\left(t-\frac{R}{V_P}\right)\right] \tag{10.2a}$$

$$u_\vartheta = 0 \tag{10.2b}$$

$$u_\phi = \frac{G_0 \sin\phi}{4\pi\rho R}\left[\frac{1}{R^2}\int_{R/V_P}^{R/V_S} \tau g(t-\tau)\,d\tau + \frac{1}{V_S^2} g\left(t-\frac{R}{V_S}\right)\right] \tag{10.2c}$$

It is convienient for the following to define $\dot{s}(t)$ and $s(t)$ the two successive integrations of the time function:

$$\dot{s}(t) = \int_0^t g(\tau)\,d\tau \tag{10.3a}$$

$$s(t) = \int_0^t \dot{s}(\tau)\,d\tau \tag{10.3b}$$

We have immediately:

$$\ddot{s}(t) = g(t) \tag{10.3c}$$

$s(t)$ is therefore the displacement time function on the fault, also called slip function. Then, integrating by parts, the term:

$$\int_{R/V_P}^{R/V_S} \tau g(t-\tau)\,d\tau \tag{10.4a}$$

takes the form:

$$\frac{R}{V_P}\dot{s}\left(t-\frac{R}{V_P}\right) + s\left(t-\frac{R}{V_P}\right) - \frac{R}{V_S}\dot{s}\left(t-\frac{R}{V_S}\right) + s\left(t-\frac{R}{V_S}\right) \tag{10.4b}$$

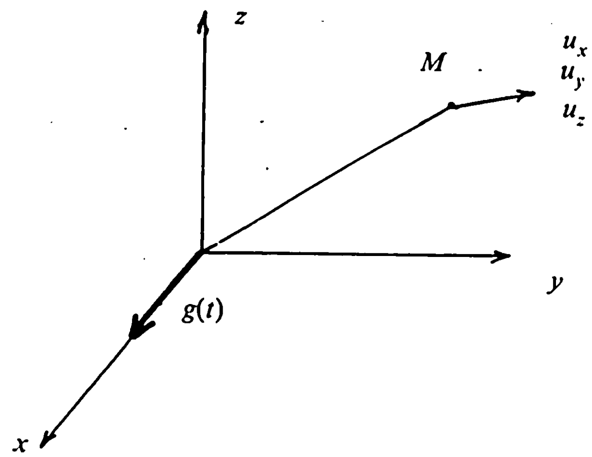

Fig.X.1 Force $g(t)$ acting in the direction of the x −axis.

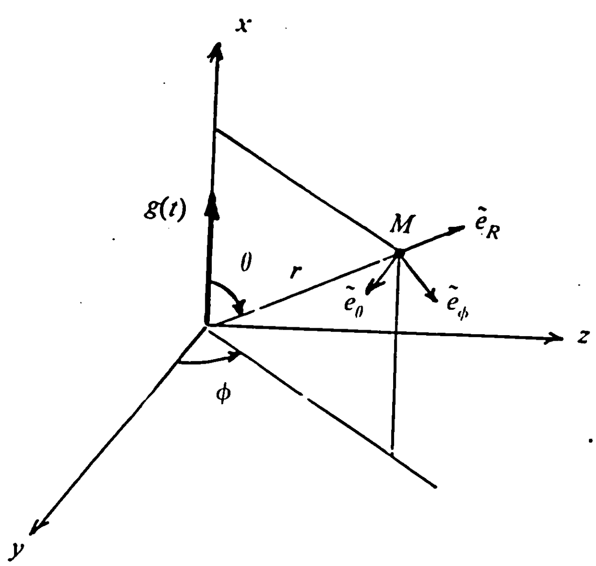

Fig.X.2

Spherical coordinate representation

We shall write *Eq. 10.2* as:

$$u_r = u_r^N + u_r^F \tag{10.5a}$$

$$u_\vartheta = 0 \tag{10.5b}$$

$$u_6 = u_6^N + u_6^F \tag{10.5c}$$

where the superscripts N and F stand for near-field and far-field respectively.

$$u_r^N = \frac{2G_0 \cos 6}{4\pi\rho R^3}\left[\frac{R}{V_P}s\left(t-\frac{R}{V_P}\right)+s\left(t-\frac{R}{V_P}\right)-\frac{R}{V_S}s\left(t-\frac{R}{V_S}\right)+s\left(t-\frac{R}{V_S}\right)\right] \tag{10.6a}$$

$$u_6^N = \frac{G_0 \sin 6}{4\pi\rho R^3}\left[\frac{R}{V_P}s\left(t-\frac{R}{V_P}\right)+s\left(t-\frac{R}{V_P}\right)-\frac{R}{V_S}s\left(t-\frac{R}{V_S}\right)+s\left(t-\frac{R}{V_S}\right)\right] \tag{10.6b}$$

$$u_r^F = \frac{G_0 \cos 6}{4\pi\rho R}g\left(t-\frac{R}{V_P}\right) \tag{10.6c}$$

$$u_6^F = \frac{G_0 \sin 6}{4\pi\rho R}g\left(t-\frac{R}{V_S}\right) \tag{10.6d}$$

This reflects the definition of the far-field which is clearly the displacement field attenuating in $1/R$. As can be seen the near-field terms are more complicated and attenuate in $1/R^2$ (for $s(t)$ terms) and in $1/R^3$ (for $s(t)$ terms). As mentioned before, it is seen that the radial term u_r^F is propagated with the velocity V_P, this is the P-wave and the tangential term u_6^F is propagated with the velocity V_S, this is the S-wave term.

In all analyses of earthquake waves, including in strong motion seismology, only the far-field terms are usually taken into account. The near-field terms are assumed to be negligeable. This assumption, which is quite admissible far away from the source in tele-seismology, deserves more attention when the stidied motions are very near the source. This is true, in particular, when the source dimension (fault length L) is of the same order of magnitude as the distance R involved.

From a deeper examination of the near-field terms one may observe that:

1) in the near field terms, both V_P and V_S are present in the radial expression u_r^N and the tangential expression u_6^N. This means that the concepts of radial and tangential radiation

breaks down and that both P and S waves are mixed in the near field.

2) the functions involved are not proportional to the force waveform $g(t)$ but are proportional to its first and second integrals $s(t)$ and $s(t)$. These formulae show that the displacement field is proportional to the active source displacement function in the very near field; it becomes influenced by the source velocity function at larger distance before being directly proportional to the source force as the distance R increases towards infinity.

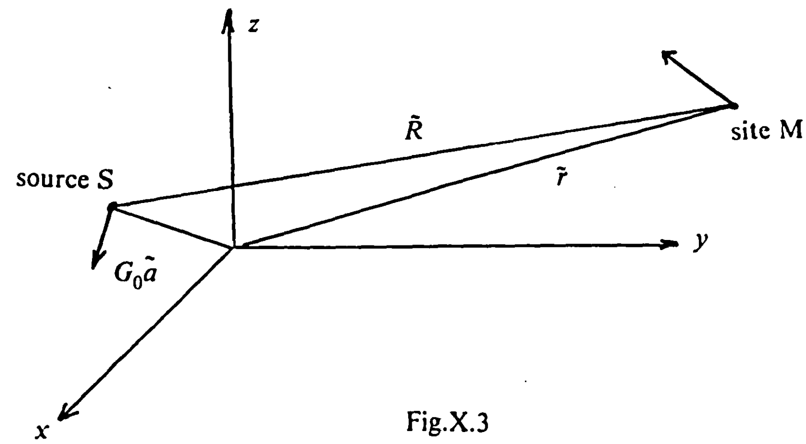

Fig.X.3

General source-site geometry

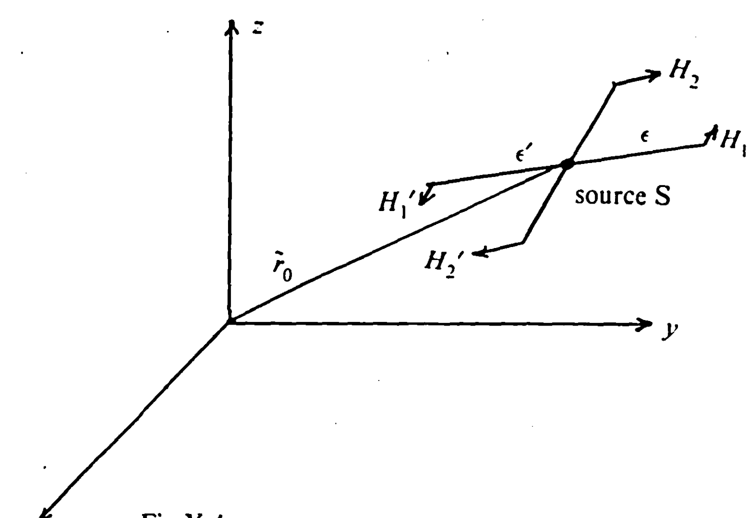

Fig.X.4

Equivalence of a shear dislocation with a double couple of forces

10.2.2 Vectorial formulation and Green's tensor

Eq. 10.1 may also be written more generally in vectorial form as (*fig. X.3*):

$$\tilde{u}(\tilde{r},t) = \frac{G_0}{4\pi\rho}\, \tilde{grad}\; div\left[\frac{\tilde{a}}{R}s\left(t-\frac{R}{V_P}\right)\right] - \tilde{curl}\,\tilde{curl}\left[\frac{\tilde{a}}{R}s\left(t-\frac{R}{V_S}\right)\right] \tag{10.7}$$

which can be directly derived from the dynamic *Navier* equation of motion. Its advantage lies in the fact that the source site relative geometry is also included (see section 10.3). The time function $s(t)$ acts at the source in the direction $\tilde{a}$, and the motion is carried by the vector $\tilde{u}$ at the site. The respective distances from the reference origin are the vectors $\tilde{r}_0$ and $\tilde{r}$. R is the distance between the point source H and the site S:

$$\tilde{R} = R.\tilde{e}_R = \tilde{r} - \tilde{r}_0 \tag{10.8}$$

It can be shown that:

$$\tilde{grad}\; div\left[\frac{\tilde{a}}{R}s\left(t-\frac{R}{V}\right)\right] = \frac{\tilde{R}(\tilde{R}.\tilde{a})}{V^2R^3}\ddot{s}\left(t-\frac{R}{V}\right) + \left[\frac{3\tilde{R}(\tilde{R}.\tilde{a})}{R^5} - \frac{\tilde{a}}{R^3}\right]\left\{s\left(t-\frac{R}{V}\right) + \frac{\tilde{R}}{V}\dot{s}\left(t-\frac{R}{V}\right)\right\} \tag{10.9}$$

and using:

$$\nabla^2\left[\frac{\tilde{a}}{R}s\left(t-\frac{R}{V}\right)\right] = \frac{\tilde{a}}{R\,V^2}\ddot{s}\left(t-\frac{R}{V}\right) \tag{10.10}$$

derived from:

$$\tilde{curl}\,\tilde{curl}\,[.] = \tilde{grad}\; div[.] - \nabla^2[.] \tag{10.11}$$

we obtain:

$$\begin{aligned}\tilde{u}(\tilde{r},t) = \frac{G_0}{4\pi\rho}\quad & \left[\frac{3\tilde{R}(\tilde{R}.\tilde{a})}{R^5} - \frac{\tilde{a}}{R^3}\right]\int_{R/V_P}^{R/V_S} \tau s(t-\tau)\,d\tau \\ + \frac{\tilde{R}(\tilde{R}.\tilde{a})}{R^3} & \left[\frac{1}{V_P^2}\ddot{s}\left(t-\frac{R}{V_P}\right) - \frac{1}{V_S^2}\ddot{s}\left(t-\frac{R}{V_S}\right)\right] + \frac{\tilde{a}}{R\,V_S^2}\ddot{s}\left(t-\frac{R}{V_S}\right)\end{aligned} \tag{10.12}$$

This is the 3 −dimensional displacement field for a single force $G(t) = G_0 \ddot{s}(t)$ acting at a point H in the direction $\tilde{a}$. This is commonly written (*Morse and Feshbach 1953*):

$$\tilde{u}(\tilde{r},t) = G_0 \tilde{\tilde{\mathcal{G}}}\left[\tilde{r}/\tilde{r}_0, t\right].\tilde{a} \tag{10.13}$$

where

$$\begin{aligned} \tilde{\tilde{\mathcal{G}}}\left[\tilde{r}/\tilde{r}_0, t\right] = \frac{1}{4\pi rho} & \left[\frac{3\tilde{R}\tilde{R}}{R^5} - \frac{\tilde{\tilde{\mathcal{I}}}}{R^3}\right] \int_{R/V_P}^{R/V_S} \tau \ddot{s}(t-\tau)\, d\tau \\ & + \frac{\tilde{R}\tilde{R}}{R^3}\left[\frac{1}{V_P^2}\ddot{s}\left(t - \frac{R}{V_P}\right) - \frac{1}{V_S^2}\ddot{s}\left(t - \frac{R}{V_S}\right)\right] + \frac{\tilde{\tilde{\mathcal{I}}}}{R V_S^2}\ddot{s}\left(t - \frac{R}{V_S}\right) \end{aligned} \tag{10.14}$$

is the *Green's displacement tensor* in the time domain.

We recognise *Eq. 10. 1* as a particular case where the vector $\tilde{a}$ is carried by one of the axis of the cartesian reference system. The advantage of the vectorial formulation expressed by *Eq. 10. 7, 10. 13 and 10. 14* is that that they are independent of the system of reference. This will be very useful when we shall be expressing the *Green's tensor* for any source-site relative geometry.

10.2.3 Expression of the point shear dislocation

We shall now write the *Eq. 10. 14* for a point shear dislocation. Using the equivalence theorem proved by *Maruyama (1963)*, we express that a shear displacement is equivalent to a double couple (*fig. X. 4*). This theorem is valid for any elastic anisotropic but unbounded medium.

The displacement at the point $S(\tilde{r})$ induced by a concentrated force $\tilde{a}.G(t) = \tilde{a}.G_0 s(t)$ acting at an hypocenter $H(\tilde{r}_0)$ in the direction of a unit vector $\tilde{a}$ is given by:

$$\tilde{u}(\tilde{r},t) = G_0 \tilde{\tilde{\mathcal{G}}}\left[\tilde{r}/\tilde{r}_0, t\right].\tilde{a} \tag{10.15}$$

If we consider two forces of the same magnitude G_0 acting at points $H_1(\tilde{r}_0 + \Delta\epsilon\tilde{n}/2)$ and $H_2(\tilde{r}_0 - \Delta\epsilon\tilde{n}/2)$ in opposite directions, the resultant displacement at S is:

$$\Delta\tilde{u}(\tilde{r},t) = G_0 \quad \tilde{\tilde{\mathcal{G}}}\left[\tilde{r}/(\tilde{r}_0 + \Delta\epsilon\tilde{n}/2), t\right] - \tilde{\tilde{\mathcal{G}}}\left[\tilde{r}/(\tilde{r}_0 - \Delta\epsilon\tilde{n}/2), t\right] \;.\tilde{a} \tag{10.16}$$

and as $\Delta\epsilon \rightarrow 0$, $G_0 \rightarrow \infty$, but their product is finite. The shear force G_0 at S, over an elementary surface $\Delta\Sigma$ is:

$$G_0 = \mu \frac{d(\Sigma)}{\Delta\epsilon} \Delta\Sigma \tag{10.17}$$

where

$\frac{d(\Sigma)}{\Delta\epsilon}$ is the shear strain and

μ is the propagating material shear modulus

Then,

$$m_0 = \lim_{\Delta\epsilon \rightarrow 0} G_0 \Delta\epsilon = \mu d(\Sigma)\Delta\Sigma \tag{10.18}$$

We obtain:

$$\Delta\tilde{u}(\tilde{r},t) = m_0(\tilde{a}\tilde{n} + \tilde{n}\tilde{a}) : \widetilde{grad}\, \tilde{\tilde{\mathcal{G}}}\left[\tilde{r}/\tilde{r}_0, t\right] \tag{10.19}$$

(:) is the double dot product of 2nd order moment tensor $\tilde{\tilde{m}}_o$ with the 3rd order tensor:

$$\widetilde{grad}\, \tilde{\tilde{\mathcal{G}}} = \lim_{\Delta\epsilon \rightarrow 0} \frac{\tilde{\tilde{\mathcal{G}}}_1 - \tilde{\tilde{\mathcal{G}}}_2}{\Delta\epsilon} \tag{10.20}$$

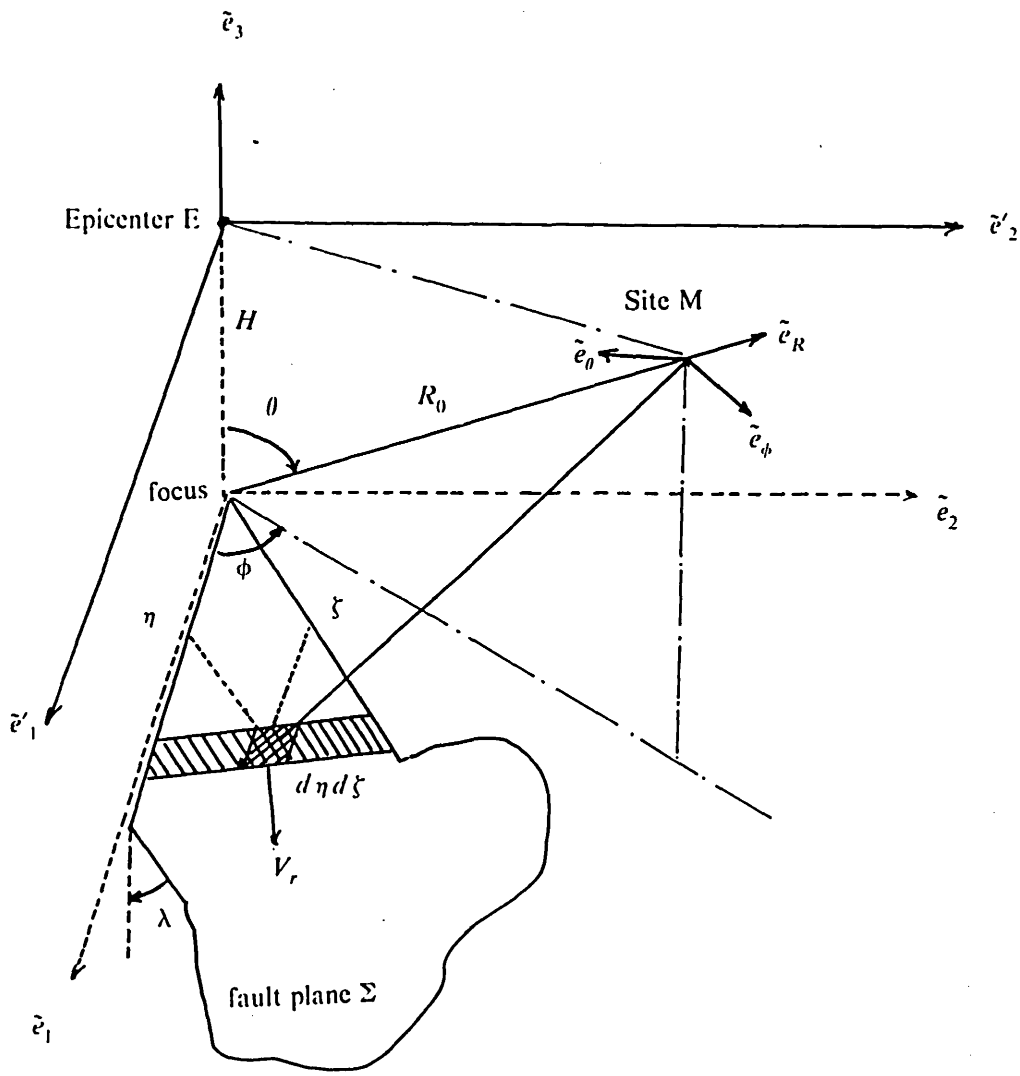

Fig.X.5

Fault-site relative location for acceleration field determination

10.2.4 Displacement field for an entire fault

For an entire fault of area Σ, the displacement field is obtained by integrating *Eq. 10.20* over the entire surface Σ:

$$\tilde{u}(\tilde{r},t) = \mu \int_{\Sigma} d(\Sigma,t)(\tilde{a}\tilde{n} + \tilde{n}\tilde{a}) : gr\tilde{a}d\, \tilde{\tilde{\mathcal{G}}}\, d\Sigma \tag{10.21}$$

Furthermore, since one is often led to assume that the slip function of space and time $d(\Sigma,t)$ is separable over the fault $d(\Sigma,t) = G(\Sigma) \times s(t)$, one may introduce the overall seismic moment:

$$M_0 = \mu \int_T \int_{\Sigma} d(\Sigma,\tau)\, d\tau\, d\Sigma = \mu \overline{d}\, \Sigma \tag{10.22}$$

where $\overline{d}$ is the average fault displacement, Σ its area and T the train wave duration; then we re-write *Eq. 10 21* more simply as:

$$\tilde{u}(\tilde{r},t) = M_o(\tilde{a}\tilde{n} + \tilde{n}\tilde{a}) : gr\tilde{a}d\, \tilde{\tilde{\mathcal{G}}} \tag{10.23}$$

In the case where the fault is too large, it must be considered as a sum of elementary rupture zones limited by barriers (*Das and Aki (1977)*); the surface Σ is then only one of the induvidual coherent patches. This will be used in section 10.4 to describe the stochatic fault rupture model.

Eq. 10. 21 is the closed form solution for the displacement field in an elastic unbounded medium. We shall give now its expression on a more computational form. We see from *Eq. 10. 20* that the elementary displacement at a site due to a point shear dislocation is composed of three terms:

$m_0 =$ the elementary seismic moment

$(\tilde{a}\tilde{n} + \tilde{n}\tilde{a}) =$ the geometric radiation pattern

$\tilde{\tilde{\mathcal{G}}}[.] =$ the Green function or radiation function

After some lengthy algebra, consisting in expanding the gradient term and projecting on the spherical system, we get for the acceleration field (*fig. X. 5*):

$$
\begin{bmatrix} d\ddot{u}_R \\ d\ddot{u}_\theta \\ d\ddot{u}_\phi \end{bmatrix}
= \frac{\mu d(\Sigma)\, d\Sigma}{4\pi\rho}
\begin{bmatrix} (\tilde{n}.\tilde{e}_R) & 0 & 0 \\ (\tilde{n}.\tilde{e}_\theta) & (\tilde{n}.\tilde{e}_R) & 0 \\ (\tilde{n}.\tilde{e}_\phi) & 0 & (\tilde{n}.\tilde{e}_R) \end{bmatrix}
\begin{bmatrix} (\tilde{e}.\tilde{e}_R) \\ (\tilde{e}.\tilde{e}_\theta) \\ (\tilde{e}.\tilde{e}_\phi) \end{bmatrix} \times
$$

$$
\left\{
\begin{bmatrix} \dfrac{2}{V_P^3} & \dfrac{12}{V_P^2} & \dfrac{30}{V_P} & 30 \\ 0 & \dfrac{-2}{V_P^2} & \dfrac{-6}{V_P} & -6 \\ 0 & \dfrac{-2}{V_P^2} & \dfrac{-6}{V_P} & -6 \end{bmatrix}
\begin{bmatrix} \dfrac{1}{R}\dot{g}\left(t-\dfrac{R}{V_P}\right) \\ \dfrac{1}{R^2}g\left(t-\dfrac{R}{V_P}\right) \\ \dfrac{1}{R^3}\dot{s}\left(t-\dfrac{R}{V_P}\right) \\ \dfrac{1}{R^4}s\left(t-\dfrac{R}{V_P}\right) \end{bmatrix} +
\right.
$$

$$
\left.
\begin{bmatrix} \dfrac{-2}{V_S^3} & \dfrac{-12}{V_S^2} & \dfrac{-30}{V_S} & -30 \\ \dfrac{1}{V_S^3} & \dfrac{2}{V_S^2} & \dfrac{6}{V_S} & 6 \\ \dfrac{1}{V_S^3} & \dfrac{2}{V_S^2} & \dfrac{6}{V_S} & 6 \end{bmatrix}
\begin{bmatrix} \dfrac{1}{R}\dot{g}\left(t-\dfrac{R}{V_S}\right) \\ \dfrac{1}{R^2}g\left(t-\dfrac{R}{V_S}\right) \\ \dfrac{1}{R^3}\dot{s}\left(t-\dfrac{R}{V_S}\right) \\ \dfrac{1}{R^4}s\left(t-\dfrac{R}{V_S}\right) \end{bmatrix}
\right\}
\tag{10.24}
$$

This expression shows in detail that the required information to generate such an elementary accelerogram consists of:

1) the elementary seismic moment m_0,

2) the elastic properties of the medium V_P, V_S and ρ,

3) the source-site geometry which defines the radiation pattern,

4) the fault slip function $s(t)$.

It may be observed that the shear force associated with $s(t)$, e.i. $g(t)$, must be differentiable. We see that the P-waves and the S-waves have been decoupled. Written in a more compact manner, *Eq. 10.24* exhibits the various factors involved. Also, it is easily seen that one may express it easily in frequency domain by operating the Fourier Tranform on the slip function only. The acceleration field is:

$$\{A(R,i\omega)\} = \left\{A_{V_P}(R,i\omega)\right\} + \left\{A_{V_S}(R,i\omega)\right\} \tag{10.25a}$$

where

$$\{A_V(R,i\omega)\} = M.\left\{\mathcal{R}_{\theta\phi}\right\}.\{V\}.\{G_V(R,i\omega)\}.\{D_V(\Theta,i\omega)\}.\exp\left[\frac{-\omega R}{2Q(\omega)V}\right] \tag{10.25b}$$

V stand for V_P and V_S alternatively. The frequency expression is also convienient to deal with an anelastic attenuation term which is generaly frequency dependent.

$$\begin{aligned}
M &= \text{scaling factor} \\
\mathcal{R}_{\theta\phi} &= \text{radiation pattern} \\
\{V\} &= \text{velocity matrix} \\
\{G_V(R,i\omega\} &= \text{radiation column vector} \\
\{D_V(\Theta,i\omega)\} &= \text{Doppler effect} \\
\exp\left[\frac{-\omega R}{2Q(\omega)V}\right] &= \text{anelastic attenuation}
\end{aligned}$$

In the next sections we shall discuss possible approaches to assess these various terms.

10.3 ACCELERATION FIELD FROM A COHERENT PATCH

10.3.1 Introduction

For a long time, it has been known that shallow earthquake energy is not released by a sudden instantaneous rupture of the crust. It is rather a crack-like phenomenon, the tip of which propagates from an initial localised region, the focus, at a finite velocity in one and sometimes several directions. *Haskell (1966)* showed that some of the complexities of the rupture process could be accounted for by modeling it with a stochastic process with a spati-temporal auto-correlation. Thus, he introduced the idea of coherence in the rupture length. Some other authors, like *Boore and Joyner (1978)* or *Andrews (1980)* have tried to account for those irregularities in a purely statistical manner by considering a random field of strength, stresses and stress build-up across the fault. A more physical approach was taken by *Das and Aki (1977)* who assumed the rupture surface to be made of regions of low strength separated by regions of high strength called "barriers". Depending on the strength of the earthquake, the rupture can propagate through the low strength regions and eventually stop or break some of the barriers (*fig.X.6*). The concept is attractive because it may be used to interprete aftershocks as ruptures of barriers which have not been broken during the main shock, but nevertheless were not far from their breaking point.

In this section we shall look at one particular patch of the fault in the light of *Eq.10.25b*. Its successive main terms will be examined.

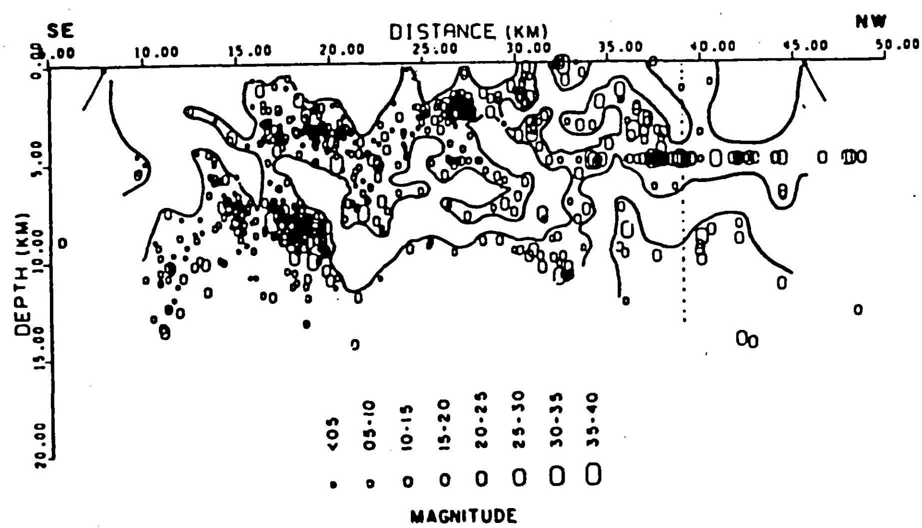

Fig.X.6

Projection of the Parfield aftershock hypocenters on a vertical plane
The region with no aftershocks has been broken during the main shock
(after Aki, 1979)

10.3.2 The geometric radiation pattern

The term $R_{\theta\phi}$ which describes the relative source-site geometry is a tensor of order 2, explicitely written in *Eq. 10.24. Fig. X.7a/b/c* show the various systems of coordinates usually used. The first system of coordinates is the "*source system*" ($\tilde{e}_1$, $\tilde{e}_2$, $\tilde{e}_3$) whose axes are defined with reference to the fault plane (Σ) and the initiation of the rupture, the hypocenter H.

$\tilde{e}_1$ is parallel to the strike of the fault,

$\tilde{e}_2$ is the horizontal parallel to the dip direction,

$\tilde{e}_3$ is the vertical directly deduced by $\tilde{e}_3 = \tilde{e}_2 \wedge \tilde{e}_2$

The positive direction of $\tilde{e}_1$ is the direction producing a positive component on this axis for the rupture propagation vector (*fig. X.7a*).

The second system is the "*slip system*" ($\tilde{a}$, $\tilde{m}$, $\tilde{n}$):

$\tilde{a}$ is the direction of the slip vector in the fault plane,

$\tilde{n}$ is the normal to the fault plane,

$\tilde{m}$ is uniquely defined by $\tilde{m} = -\tilde{a} \wedge \tilde{n}$

The positive direction for the $\tilde{n}$ normal is taken such that it leaves the foot wall on the negative side. The slip system of coordinates is obtained from the source system by:

-rotating the source system through δ about $\tilde{e}_1$.

-rotating the obtained system through λ about the new position of $\tilde{e}_3$.

δ = dip angle

λ = slip angle

The matrix of the transformation expressed in the source system is:

$$\begin{bmatrix} \tilde{a} \\ \tilde{m} \\ \tilde{n} \end{bmatrix} = \begin{bmatrix} \cos\lambda & \sin\lambda\cos\delta & \sin\lambda\sin\delta \\ -\sin\lambda & \cos\lambda\cos\delta & \cos\lambda\sin\delta \\ 0 & -\sin\delta & \cos\delta \end{bmatrix} \begin{bmatrix} \tilde{e}_1 \\ \tilde{e}_2 \\ \tilde{e}_3 \end{bmatrix} \tag{10.26}$$

At the site, we shall define the "*site spherical system*" ($\tilde{e}_R$, $\tilde{e}_\theta$, $\tilde{e}_\phi$). R, θ, ϕ are the spherical coordinates of the station by reference to the source system:

ϕ = azimut of station refered to the strike,

θ = latitude of the station refered to the hypocenter.

The matrix of transformation expressed in the source system is:

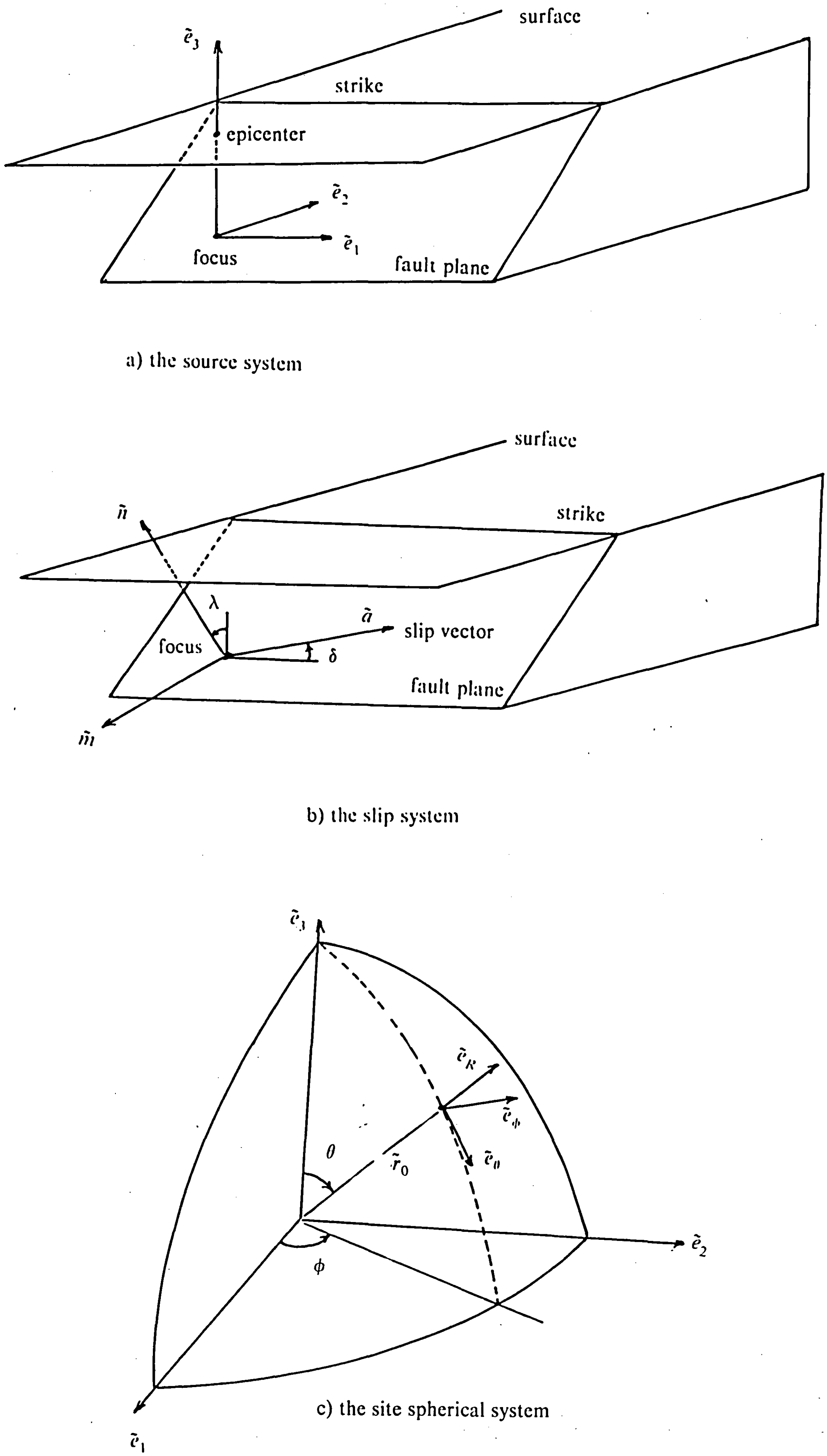

Fig.X.7

Various systems of coordinates used to describe the geometric radiation pattern

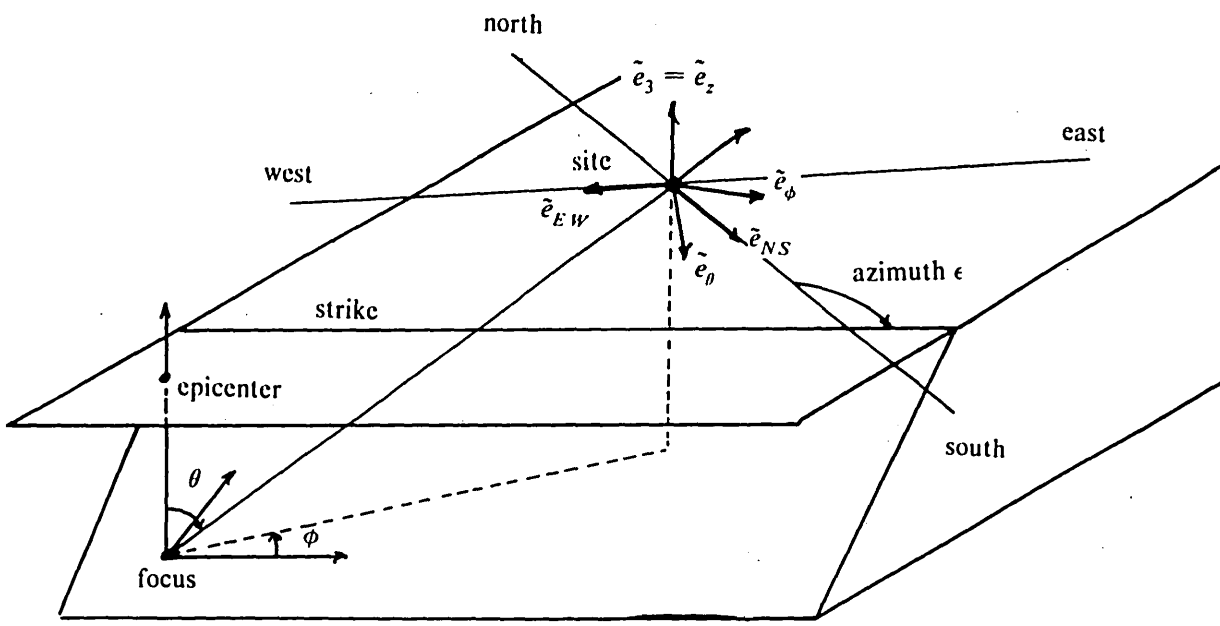

Fig.X.8

The relative position of the site cartesian system

$$\begin{bmatrix} \tilde{e}_R \\ \tilde{e}_\theta \\ \tilde{e}_\phi \end{bmatrix} = \begin{bmatrix} \sin\theta\cos\phi & \sin\theta\sin\phi & \cos\theta \\ \cos\theta\cos\phi & \cos\theta\sin\phi & -\sin\theta \\ -\sin\phi & \cos\phi & 0 \end{bmatrix} \begin{bmatrix} \tilde{e}_1 \\ \tilde{e}_2 \\ \tilde{e}_3 \end{bmatrix} \tag{10.27}$$

Finally, the *"site cartesian system"* is very useful since the recorded motions are refered to it (fig.X.8). In general, the geographic directions NS and WE are used.($\tilde{e}_{NS}$, $\tilde{e}_{WE}$, $\tilde{e}_Z$). This system is deduced from the source system by simple rotation $\kappa - \pi$ about the common $\tilde{e}_3$ axis. Its transformation matrix from the source system is:

$$\begin{bmatrix} \tilde{e}_{NS} \\ \tilde{e}_{WE} \\ \tilde{e}_Z \end{bmatrix} = \begin{bmatrix} -\cos\kappa & -\sin\kappa & 0 \\ \sin\kappa & -\cos\kappa & 0 \\ 0 & 0 & 1 \end{bmatrix} \begin{bmatrix} \tilde{e}_1 \\ \tilde{e}_2 \\ \tilde{e}_3 \end{bmatrix} \tag{10.28}$$

These various transformation matrices will be used to expressed the radiation pattern tensor in the different systems. Since they all represent transformations between unit orthogonal reference systems, they have the property of having their inverse equal to their transpose and thus simplifying the subsequent algebra.

Geologic fault types

	δ: 0 — 45	45 — 90	
λ			
0	strike-slip	strike-slip	
	left lateral thrust	left lateral reverse	
90	dip-slip	dip-slip	
	right lateral thrust	right lateral reverse	
180	strike-slip	strike-slip	
	right lateral normal	right lateral normal	
270	dip-slip	dip-slip	
	left lateral normal	left lateral normal	
360	strike-slip	strike-slip	

In particular, the expressions of the "slip system" unit vectors expressed in the "site spherical system" are:

$$\begin{aligned}\tilde{a} = &\Big[\cos\lambda\sin\theta\cos\phi + \sin\lambda\cos\delta\sin\phi\sin\theta + \sin\lambda\sin\delta\cos\theta\Big]\tilde{e}_R \\ &+ \Big[\cos\lambda\cos\theta\cos\phi + \sin\lambda\cos\delta\cos\theta\sin\phi - \sin\lambda\sin\delta\sin\theta\Big]\tilde{e}_\theta \\ &+ \Big[-\sin\lambda\sin\phi + \sin\lambda\cos\delta\cos\phi\Big]\tilde{e}_\phi\end{aligned} \tag{10.29}$$

$$\begin{aligned}\tilde{n} = &\Big[-\sin\delta\sin\theta\sin\phi + \cos\delta\cos\theta\Big]\tilde{e}_R \\ &+ \Big[-\sin\delta\cos\theta\sin\phi - \cos\delta\sin\theta\Big]\tilde{e}_\theta \\ &+ \Big[-\sin\delta\cos\phi\Big]\tilde{e}_\phi\end{aligned} \tag{10.30}$$

We have immediately:

$$\tilde{n}.\tilde{e}_R = -\sin\delta\sin\theta\sin\phi + \cos\delta\cos\theta \tag{10.31a}$$

$$\tilde{n}.\tilde{e}_\theta = -sin\delta\cos\theta\sin\phi - \cos\delta\sin\phi \tag{10.31b}$$

$$\tilde{n}.\tilde{e}_\phi = -\sin\delta\cos\phi \tag{10.31c}$$

and

$$\tilde{a}.\tilde{e}_R = \cos\lambda\sin\theta\cos\phi + \sin\lambda\cos\delta\sin\theta\sin\phi + \sin\lambda\sin\delta\cos\theta \tag{10.32a}$$

$$\tilde{a}.\tilde{e}_\theta = \cos\lambda\cos\theta\cos\phi + \sin\lambda\cos\delta\cos\theta\sin\phi - \sin\lambda\sin\delta\sin\theta \tag{10.32b}$$

$$\tilde{a}.\tilde{e}_\phi = -\cos\lambda\sin\phi + \sin\lambda\cos\delta\cos\phi \tag{10.32c}$$

Finally, the terms of the radiation tensor may be written:

$$\text{P-wave radiation pattern} = \mathcal{R}^{P}_{\theta\phi}$$

$$\text{SH-wave radiation pattern} = \mathcal{R}^{SH}_{\theta\phi}$$

$$\text{SV-wave radiation pattern} = \mathcal{R}^{SV}_{\theta\phi}$$

$$\begin{aligned}2\mathcal{R}^{P}_{\theta\phi} = &-\cos\lambda\sin\delta\sin^2\theta\sin 2\phi + \cos\lambda\cos\delta\sin 2\theta\cos\phi \\ &+ \sin\lambda\sin 2\delta\big[\cos^2\theta - \sin^2\theta\sin^2\phi\big] + \sin\lambda\cos 2\delta\sin 2\theta\sin\phi\end{aligned} \tag{10.33a}$$

$$\begin{aligned}2\mathcal{R}^{SH}_{\theta\phi} = &-2\cos\lambda\sin\delta\sin\theta\cos 2\phi - 2\cos\lambda\cos\delta\cos\theta\sin\phi \\ &- \sin\lambda\sin 2\delta\sin\theta\sin 2\phi + 2\sin\lambda\cos 2\delta\cos\theta\cos\phi\end{aligned} \tag{10.33b}$$

$$\begin{aligned}2\mathcal{R}^{SV}_{\theta\phi} = &\ 2\sin\lambda\cos 2\delta\cos 2\theta\sin\phi + 2\cos\lambda\cos\delta\cos 2\theta\cos\phi \\ &- \cos\lambda\sin\delta\sin 2\theta\sin 2\phi - \sin\lambda\sin 2\delta\sin 2\theta\big[1 + \sin^2\phi\big]\end{aligned} \tag{10.33c}$$

10.3.3 The source-slip functions

In many of the studies of earthquake mechanism, especially in tele-seismology, it has been assumed that the fault slip function can be decoupled in the product of a space function and a time function:

$$d(\Sigma, t) = G(\Sigma) \times s(t) \tag{10.34}$$

The space function describes the geometical movement across the fault and is partially covered by the term "focal mechanism". The time function gives the time dependence of the source action as for example a pulse, a step or a ramp function. This separation is mainly due to the ease with which mathematical treatments may be carried out, but does not correspond to any physical reality. It is indeed approximate to say that the space function would follow exactly the same time evolution for all points of the fault during the rupture process. This assumption means that the major dynamic constraints of the rupture are neglected giving too much emphasis on particular aspects of the kinetics of the motion.

In far-field studies, where the propagation path has smoothed the sharpness of the fault rupture characteristics, this may be founded. Only the gross features of the source can be detected in this case. In the near-field, on the other hand, the ground motions contain more apparent features of the rupture and the above assumption may not be valid anymore. This observation is particularly relevant when we are dealing with simulation of acceleration, since acceleration is primarily influenced by the high frequency content of the slip function.

Anderson and Richards (1975) have already concluded that modeling near field ground motion displacement from various slip function models does not affect significantly the final displacement time history. As far as acceleration is concerned, no results have been proposed so far. It is believed that acceleration time histories are predominantly influenced by the erratic rupture process itself and therefore the dynamic conditions on the fault cannot be neglected. A realistic acceleration simulation is less influenced by the well establised far-field conditions than the much less understood dynamics of the fault rupture. It is unfortunate that such data are so difficult to measure or assess. Thus, one is left with theoretical approaches which satisfy partially the dynamic necessary conditions.

From *Eq. 10.24*, we clearly see that, when only the far-field term is retained, the displacement field becomes (for each wave type):

$$\tilde{u}(\tilde{r}, t) = \frac{\mu}{4\pi\rho} \mathcal{R}_{\theta\phi} \frac{2}{R\, V^3} \int_{\Sigma} \dot{d}\left(t - \frac{R}{V}\right) d\Sigma \tag{10.35}$$

e.i., the far-field displacement waveform is proportional to the fault normalised slip velocity $\dot{s}(t)$. The available far-field displacement waveforms correspond therefore to the shape of the slip velocity on the fault and the other terms $s(t)$, $g(t)$ and $\dot{g}(t)$ can be deduced par integration or differentiation. Furthermore, if only the shear waveform is known, then all the factors, including the compressional waveforms may be obtained.

Radiation function derived from the Knopoff and Gilbert model

The first dislocation model was proposed by *Knopoff and Gilbert (1959)*. They expressed the displacement $d(t)$ on the fault as a *Heaviside* unit step function (*fig. X. 9a*). After space-time separation (*Eq. 10. 34*) and introducing a constant rupture propagation V_r, the slip function writes:

$$d(\Sigma, t) = G_0 H\left(t - \frac{R}{V_r}\right) \tag{10.36}$$

This model, apparently simple for the far field, raises some fundamental difficulties for the determination of the acceleration field in the near-field. The associated velocity slip is a δ-Dirac function and its successive derivatives are not defined. Therefore no high frequency is described by this too poor model.

Radiation function derived from the Haskell model

The *Haskell model* is an extension of the previous model. The *Heaviside* function is replaced by a ramp function, increasing linearly with time (*fig. X. 9b*). This model gave its name to the "rise time" of the slip function which is the duration of the dislocation. For the same reason, this function is still inadequate and therefore cannot be retained for acceleration simulation.

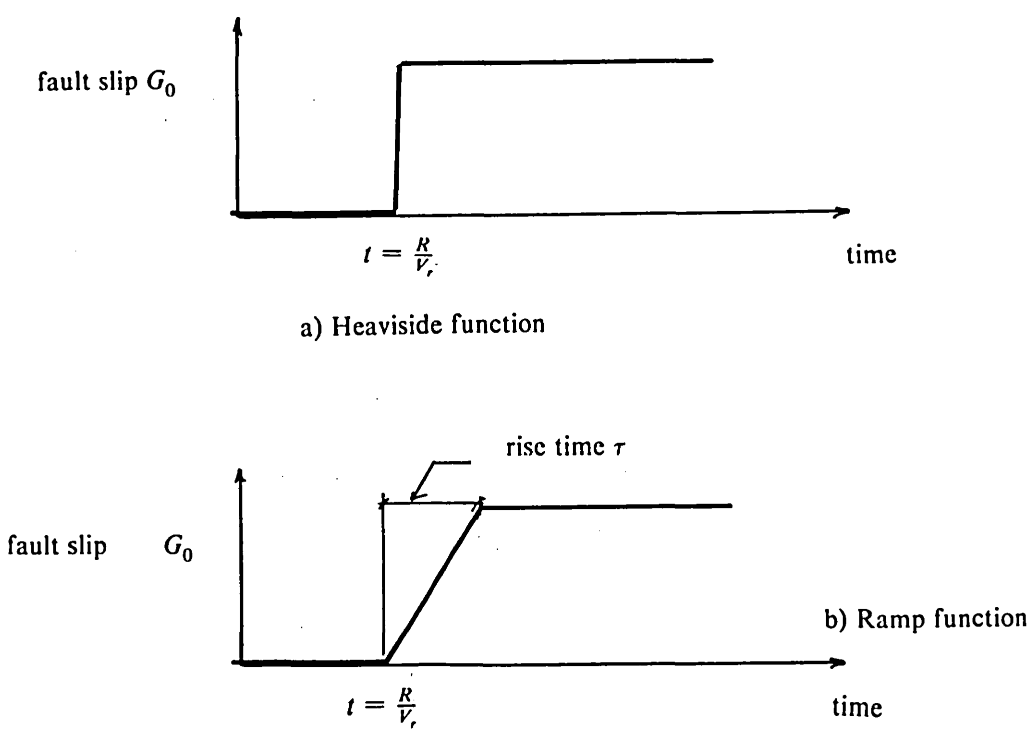

Fig.X.9

Elementary slip functions

Radiation function derived from the Brune mode

The *Brune model* is the simplest model which can be used for our purpose. In its formulation, a constant slip velocity on the fault is progressively attenuated by an exponential term $\exp(-t/\tau)$ to model the effects of fault finiteness at a current point. This is the healing process of the rupture that is taken into account and will be studied in more detail in a more refined model below. *Brune* made use of the time constant τ, equivalent to the travel time of the signal to the limit of the fault:

$$\tau = \frac{2}{\sqrt{7\pi}} \frac{a}{V_S} \tag{10.37}$$

where a is the equivalent radius of the fault. The radius a is related to the corner frequency $f_c = 1/2\pi\tau$ through:

$$a = \sqrt{\frac{7}{16\pi}} V_S f_c^{-1} \tag{10.38}$$

and located on a log-displacement versus log-frequency plot the junction between the low frequency and the high frequency trends of the spectrum (fig.X.10). The initial particule velocity on the fault results from an intantaneous stress drop $\Delta\sigma$ and can be computed by integration of:

$$\Delta\sigma = \mu \frac{\partial d}{\partial \Sigma} \tag{10.39}$$

We have:

$$d(\Sigma, 0) = G(\Sigma) \frac{\partial s(t)}{\partial t} \Big|_{t=0} = \frac{V_S \Delta\sigma}{\mu} \tag{10.40}$$

After multiplying by $\exp(-t/\tau)$ previously mentioned and integration,

$$D(\Sigma, t) = G(\Sigma)\left(1 - e^{-t/\tau}\right) \tag{10.41}$$

where $G(\Sigma) = 4/3\overline{d}$ is the final fault offset:

$$\overline{d} = \frac{\Delta\sigma}{\mu} V_S \tau = \frac{16}{7\pi} \frac{\Delta\sigma}{\mu} a \tag{10.42}$$

in accordance with the expression derived by *Keilis-Borock (1959)* for the static case.

Then, we obtain immediately:

$$s(t) = 1 - e^{t/\tau} \tag{10.43a}$$

$$\dot{s}(t) = \frac{1}{\tau} e^{-t/\tau} \tag{10.43b}$$

$$g(t) = -\frac{1}{\tau^2} e^{t/\tau} \tag{10.43c}$$

$$\dot{g}(t) = \frac{1}{\tau^3} e^{-t/\tau} \tag{10.43d}$$

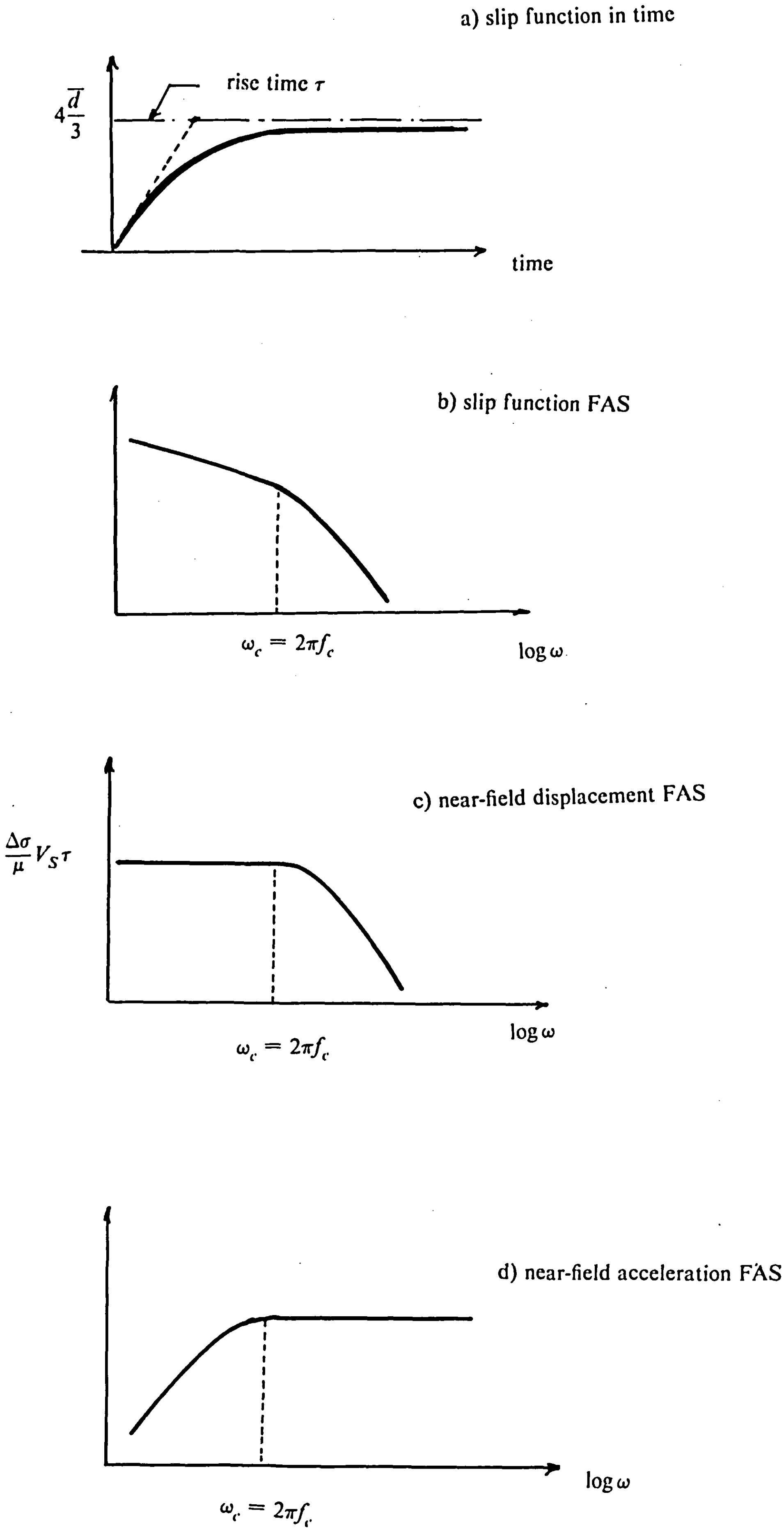

Fig.X.10

The Brune model

which can be used directly in *Eq. 10. 24.* The *Fourier Spectrum* of the slip function is (fig.X.10):

$$\overline{D}(\Sigma, i\omega) = \frac{\Delta\sigma}{\mu} V_S \tau \frac{1}{i\omega(1 + i\omega\tau)} \tag{10.44}$$

decaying in ω^{-2} in the high frequency. This leads to a ω^{-1} decay of the displacement spectrum in the far-field, and departs from the now commonly accepted $\omega{-2}$ to ω^{-3} decay (*Aki 1967*). This prompted *Brune* to modify the far-field expression of his model.

We may incidently note that the scaling factor and seismic moment M_0 may be expanded as:

$$M_0 = \mu \overline{d}\, \Sigma = \frac{16}{7} \Delta\sigma a^3 \tag{10.45}$$

i.e., the total energy released from the patch may originate either from high stress drop or from large patch dimensions. For simulation purposes, when no indication is available relating to the possible stress drops or the likely patch equivalent radius, there is no possibility to separate their respective influence. We shall develop more on this aspect in section 10.4.

Radiation function derived from the McGarr model

Although the source model developed by *McGarr (1981)* scales on peak acceleration and peak velocity in the near-field, it is of value to retain his assumption about the radiated pulse shape. It may be viewed as a generalised *Brune's* pulse except that the initial time dependence of the faulting is assumed to be more gradual. (*fig.X.11a*). His proposed function is:

$$d(\Sigma,t) = \frac{4\overline{d}}{3}\left\{1 - e^{-t/\tau}\left[1 + \frac{t}{\tau} + \frac{t^2}{2\tau^2} + \frac{t^3}{6\tau^3}\right]\right\} \qquad (10.46)$$

with the result that the far-field wave displacement is proportional to $t^3\exp(t/\tau)$. The relationship between a and f_c is assumed to be the same and hence the exponential decay of the displacement pulse is not affected. This time function also complies with the comment of *Savage (1966 and 1972)* who argued for an initial quadratic-like dependence for the initiation of rupture followed by a radial propagation at a constant velocity. Its *Fourier Spectrum* is (*fig.X.11b*):

$$\overline{D}(\Sigma,i\omega) = \frac{4\Delta\sigma V_S\tau^5}{\mu}\frac{1}{i\omega(1+i\omega\tau)^4} \qquad (10.49)$$

It produces a frequency decay in ω^{-4} for the displacement in the far-field. Although this seems contradictory with the above well accepted values, we believe that such a function explains partially the shape of the acceleration spectra beyond the so-called F_{max}. Not only, as stated by *Hanks (1981)*, this acceleration fall-off is due to strong anelastic attenuation in the vicinity of the fault, but also it reflects the smoothness of the slip function. In the limit, a pure impulse *Dirac* function (in a very brittle environment) will give rise to a ω^{-2} decay for the far-field displacement. A more physical pulse, smoothed by the ductility of the rock (as one goes deeper) and the healing process of the rupture may produce ω^{-3} or even ω^{-4} decays.

The slip function included in *Eq.10.24* write:

$$s(t) = 1 - e^{-t/\tau}\left[1 + \frac{t}{\tau} + \frac{t^2}{2\tau^2} + \frac{t^3}{6\tau^3}\right] \qquad (10.50a)$$

$$\dot{s}(t) = \frac{t^3}{2\tau^4}e^{-t/\tau} \qquad (10.50b)$$

$$g(t) = \frac{t^2}{2\tau 4}\left(1 - \frac{t}{3\tau}\right)^{-t/\tau} \qquad (10.50c)$$

$$\dot{g}(t) = \frac{t}{\tau^4}\left(1 - \frac{t}{\tau} + \frac{t^2}{6\tau^2}\right)e^{-t/\tau} \qquad (10.50d)$$

Fig.X.12 show the shapes of the resulting velocity and acceleration pulses for different values of the patch dimensions.

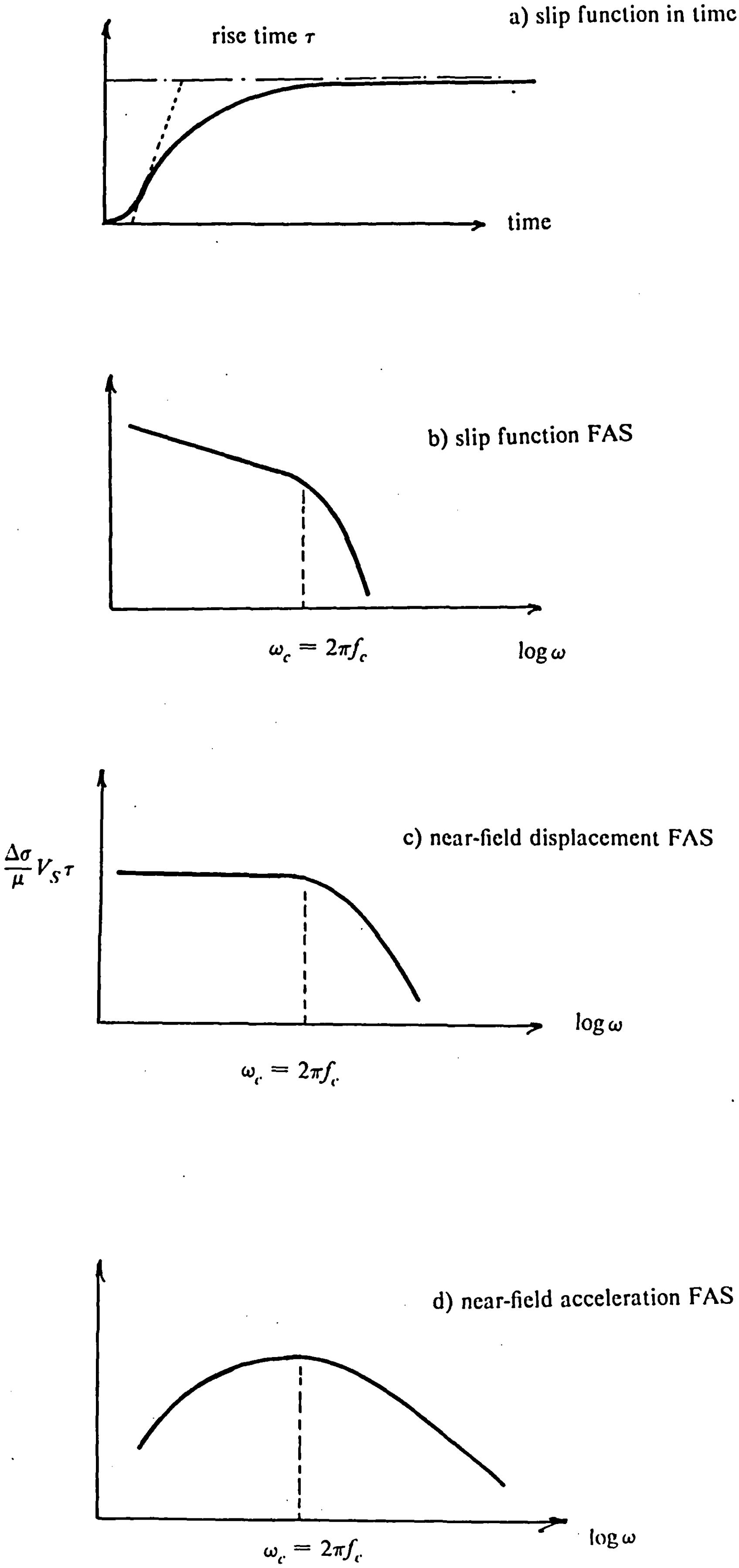

Fig.X.11

The McGarr model

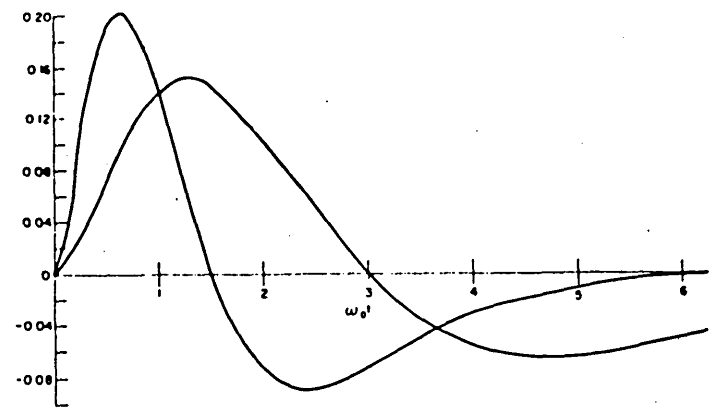

a) velocity pulses

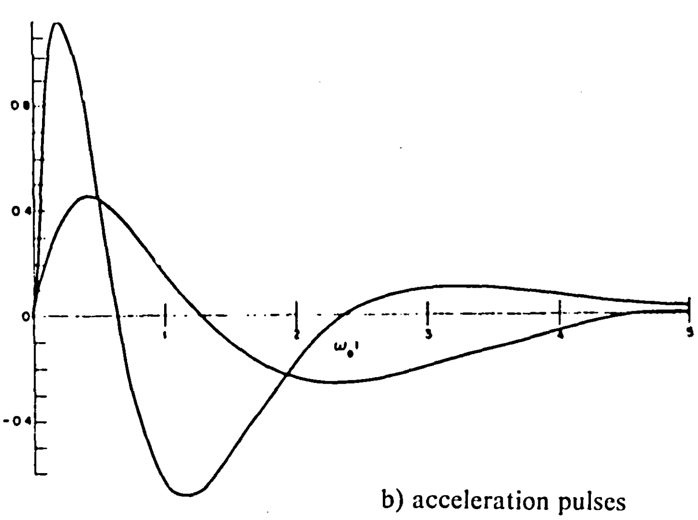

b) acceleration pulses

Fig.X.12

Examples of slip pulses according to the McGarr model.

Radiation function derived from the Sato-Hirasawa model

The *Sato-Hirasawa model* approaches the physics of the source dynamics still closer. It is based on the exact solution developed by *Kostrov (1966)* for the self-similar growth of rupture of a circular crack with uniform stress drop. It is a quasi-dynamic model which assumes that the *Eshelby's* static solution (1957) holds at every successive instant of the rupture. The relative slip of the faces of the crack under a uniform shear stress $\Delta\sigma$ is given by:

$$d(\Sigma, t) = d_{max}\sqrt{\xi^2 - \rho^2} \qquad \xi > \rho \tag{10.51}$$

$$\Sigma = \pi\rho^2 \qquad d_{max} = \frac{24}{7\pi}\frac{\Delta\sigma}{\mu}$$

(it can be seen by integration over the total area that the average displacement $\overline{d}$ is the same as in *Eq. 10.42*). The authors suppose that the rupture initiates at a point $t = 0$ and spreads outwards at constant velocity V_r. According to the assumption made, the relative displacement on the fault at time t is obtained by substituting $V_r t$ to the radius ξ:

$$d(\rho, t) = K\sqrt{(V_r t)^2 - \rho^2}\, H\left(t - \frac{\rho}{V_r}\right) \tag{10.52}$$

$$K = d_{max} = \frac{3\overline{d}}{2}$$

It is also assumed that the rupture stops abruptly at $\rho = a$ giving the complete form:

$$d(\rho, t) = K\sqrt{(V_r t)^2 - \rho^2}\, H\left(t - \frac{\rho}{V_r}\right)\left[1 - H(\rho - a)\right] \qquad V_r t < a \tag{10.53a}$$

$$d(\rho, t) = K\sqrt{a^2 - \rho^2}\left[1 - H(\rho - a)\right] \qquad V_r t > a \tag{10.53b}$$

Strictly speaking, *Eq. 10.53a and b* are not the solution for the dynamical stress relaxation problem. They represent, nevertheless, a first good approximation of the dynamical process. It may be observed that the space-time separation of *Eq. 10.34* has been dropped. *Fig. X.13* shows on a dimensionless plot the variation of displacement slips with time. The dashed line indicates the arrival time of the rupture front with respect to ρ/a.

The functions required for the computation of the acceleration waveform in the near-field must integrate $d(\Sigma)$ into $s(t)$:

$$d(\rho,t) = Z K\left[(V_r t)^2 - \rho^2\right]^{1/2} \tag{10.54a}$$

$$d(\rho,t) = Z V_r^2 t\left[(V_r t)^2 - \rho^2\right]^{-1/2} \tag{10.54b}$$

$$\ddot{d}(\rho,t) = -Z K V_r^2 \rho^2\left[(V_r t)^2 - \rho^2\right]^{-3/2} \tag{10.54c}$$

$$\dddot{d}(\rho,t) = -3K Z V_r^3 t\left[(V_r t)^2 - \rho^2\right]^{-5/2} \tag{10.54d}$$

$$\text{where} \qquad Z = H\left(t - \frac{\rho}{V_r}\right)\left[1 - H(\rho - a)\right] \tag{10.54e}$$

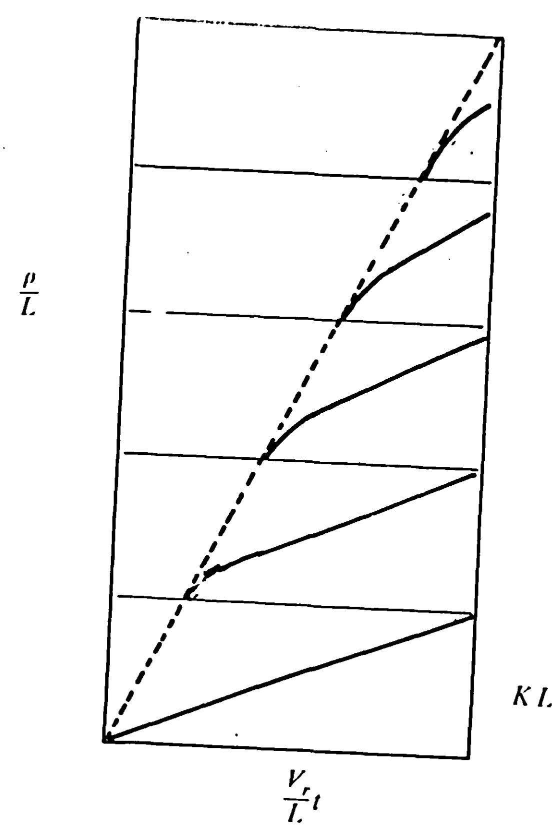

Fig.X.13

The Sato-Hirasawa model

Dimensionless slip function with no space-time separation

Radiation function derived from the Madariaga model

The model described now is derived from the study of the dynamics of an expanding circular fault of *Madariaga (1976)*. In a numerical solution, constant rupture velocities were used, ranging from $V - r = 0.6V_S$ to $V_r = 0.9V_S$. He noticed that the slip function was surprisingly simple and quite similar to that of *Burridge (1969)* for similar problems.

The rupture grows with a uniform rupture velocity until it reaches a fixed barrier where it stops abruptly. The movement at an interior point continues to grow until the P-wave generated by the stopping of the rupture front arrives and decelerates its motion. This stopping phase reaches internal points at time $T_{SP}(\rho)$ variable with the distance from the nucleation point. *Fig. X. 14* shows that this time is:

$$T_{SP} = \frac{a}{V_r} + \frac{a-\rho}{V_p} \tag{10.55}$$

As the rupture heals, the relative slip velocity decreases continuously towards zero. The initial part of the source function, before the arrival of the P-stopping phase is the same as the solution given by *Kostrov (1966)* for a self-similar circular shear crack:

$$d(\rho,t) = \dot{d}_0 \sqrt{t^2 - \frac{\rho^2}{V_r^2}} \qquad \rho < t < T_{SP} \tag{10.56}$$

where $\dot{d}_0$ is the initial particule velocity on the fault which depends on the stress drop. *Ambraseys (1973)* and others have given an upper limit for the value of $\dot{d}_0$, assuming that the rupture of the crack is instantaneous.

During healing the slip function takes the form:

$$d(\rho,t) = \dot{d}_0 \sqrt{t2 - V_H(t - T_{SP})^2 + \frac{\rho^2}{V_r^2}} \qquad T_{SP} < t < T_F \tag{10.57}$$

where V_H is the healing wave velocity and T_F the final time of sliding; both are function of the distance ρ.

According to *Madariaga*, the final slip overshoots the static solution by a factor nearly independent of the rupture velovity V_r. It varies slightly from $\alpha = 1.15$ at $V_r = 0.6V_S$ to $\alpha = 1.20$ at $V_r = 0.9V_S$. Due to this overshoot, the static stress drop that we considered up to now has no longer a satisfactory unique definition. We shall discuss its influence in section 10.4.

The final offset can be expressed as:

$$d_{max} = \dot{d}_0 \frac{a}{V_r} \alpha \sqrt{1 - \frac{\rho^2}{a2}} \qquad t > T_F \tag{10.58}$$

A closed form expression for $V_H(\rho)$ is then obtained by writing:

$$\frac{\partial d(\rho,t)}{\partial t}\Big|_{t=T_F} = 0 \tag{10.59}$$

We get:

$$V_H(\rho) = \frac{T_F(\rho)}{T_F(\rho) - T_{SP}(\rho)} \tag{10.60}$$

where all the times are ρ dependent. Substituting this expression into the identity

$$d(\rho, T_F) = d_{max} \tag{10.61}$$

yields:

$$T_H(\rho) = \frac{\alpha^2 a^2 + (1-\alpha^2)\rho^2}{V_r^2 T_{SP}(\rho)} \tag{10.62}$$

Finally, we are able to re-write the slip function as:

$$d(\rho, t) = d_0 \sqrt{t^2 - \frac{\rho^2}{V_r^2}} \qquad \frac{\rho}{V_r} < t < T_{SP} \tag{10.63a}$$

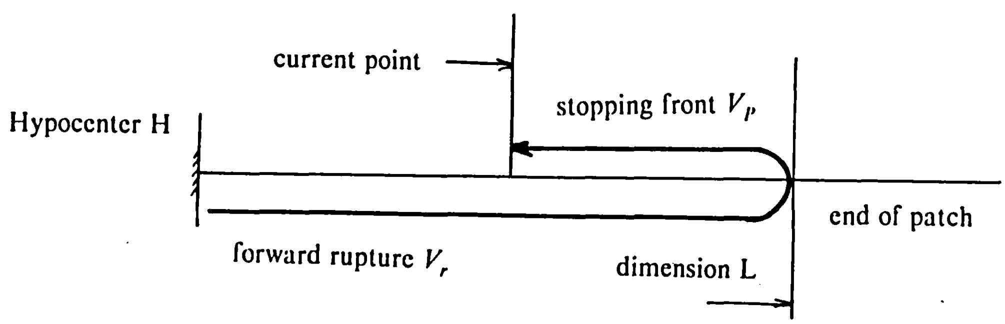

Fig.X.14
Definition of the stopping time of rupture
at an internal point of the slip surface

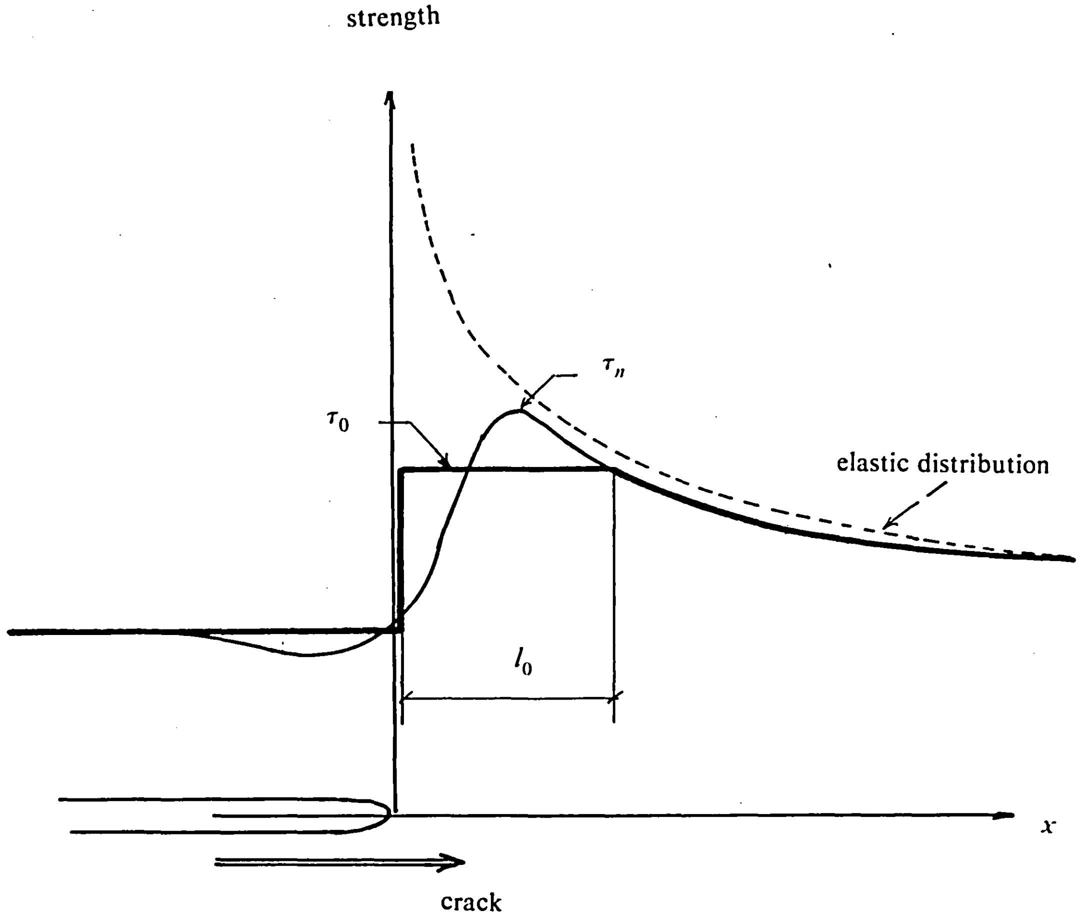

Fig.X.15

Average shear strength at the crack tip

One may observe that the velocity function posseses a square root singularity at the onset of the slip. This is due to the elastic assumption made in the shear crack model. Whereas this assumption may be perfectly acceptable at some distance away from the crack tip, it is incompatible with any realistic stress-strain law in the vicinity of the crack rupture front.

In this area, a plastified zone of limited extent develops which renders the elastic assumption erroneous. It is common, in crack theory, to treat this zone by introducing the fracture energy per unit area of newly created crack surface. This is also the energy barrier that the rupture front has to jump to overcome the stopping attempt in the fault resistant zones. The stresses at the tip of the crack are distributed accordingly to the stress-strain law of the ruptured rock and is limited to τ_n its ultimate shear strength (fig.X.15).

This singularity needs removing. For this purpose, we shall follow *Ida's (1973)* results giving order of magnitude for the maximum slip velocity d_{max} and the maximum acceleration $\ddot{d}_{max}$ as a function of the average plastic stress τ_0 and its extent l_0 at the tip of the crack before elastic theory may be re-joined.

The values of d_{max} and $\ddot{d}_{max}$ are dependent of the shape of the stress-strain law of the ruptured rock. Since it is almost impossible (at least at the present level of knowledge) to determine such shapes, some fair realistic assumptions have to be made and analysis, based on them, carried out.

Following this principle, *Ida* showed that a first estimation of d_{max} and $\ddot{d}_{max}$ can be obtained irrespectively of the shape of the stress-strain law and suggested:

$$d_{max} \approx \frac{\tau_0}{\mu} V_r \tag{10.67a}$$

$$\ddot{d}_{max} \approx \left(\frac{\tau_0}{\mu}\right)^2 \frac{V_r^2}{l_0} \tag{10.67b}$$

τ_0, the average plastic stress extends over a length l_0. He also gave the time T_{max} for the maximum velocity:

$$T_{max} \approx \frac{\mu}{\tau_0} \frac{l_0}{V_r} \tag{10.67c}$$

These expressions are not independent of each other and we shall write them:

$$d_{max} = \frac{\tau_0}{\mu} V_r \tag{10.68a}$$

$$\ddot{d}_{max} = \frac{d_{max}^2}{l_0} \tag{10.68b}$$

$$T_{max} = \frac{d_{max}}{\ddot{d}_{max}} \tag{10.68c}$$

Once the maximum velocity has been assessed from a fair estimation of the material characteristics, on one hand, and the rupture velocity V_r on the other, the maximum acceleration value can be computed by varying slightly T_{max} and l_o.

With the help of those considerations, we are able to introduce approximate physical values in the definition of the motion at the very start of the rupture. This will remove the non-physical discontinuity mentioned earlier. This process is important in the sense that, contrary to displacement analysis, simulation of acceleration requires realistic high frequency information. They are precisely included in the mechanism of the breakage of the cohesive bonds at the tip of the crack. And this is precisely what we attempted to do with this first approximation. Since d_{max} varies from 50 cm/sec to 100 cm/sec and considering that $\ddot{d}_{max}$ varies from 0.2 g to 2 g on the fault, we see that the smoothing correction of the velocity function is very limited in time. The values of T_{max} range from 0.025 to 0.5 sec. These are associated with the high frequency features between 2 Hz and 40 Hz that are required for realistic ground acceleration generation. It is clear that much experimental effort has to be made to determine more accurately the early start of the breakage.

The searched smoothing function $d(\rho, t)$ will also have to be constrained by the following continuity conditions: if $d_I(\rho, t)$ is valid for $0 < t < T_I$ only

$$d_I(\rho, 0) = 0 \tag{10.69a}$$

$$\ddot{d}_I(\rho, 0) = 0 \tag{10.69b}$$

$$\Big[d_I(\rho, t)\Big]_{max} = d_{max} \quad \text{at} \quad t = T_{max} \tag{10.69c}$$

$$\Big[\ddot{d}_I(\rho, t)\Big]_{max} = \ddot{d}_{max} \tag{10.69d}$$

Finally the $d(\rho, t)$ function must re-join the rupture growing phase tangentially at $t = T_I$.

Fig. X. 16a and b show the typical expected shapes of such slip functions. A proposed analytic expression able to meet the above conditions is of the form:

$$d_I(\rho, t) = A X^{\zeta} e^{-\eta X} \tag{10.70}$$

Where A, ζ and η have to be determine from the assessed d_{max} and $\ddot{d}_{max}$.

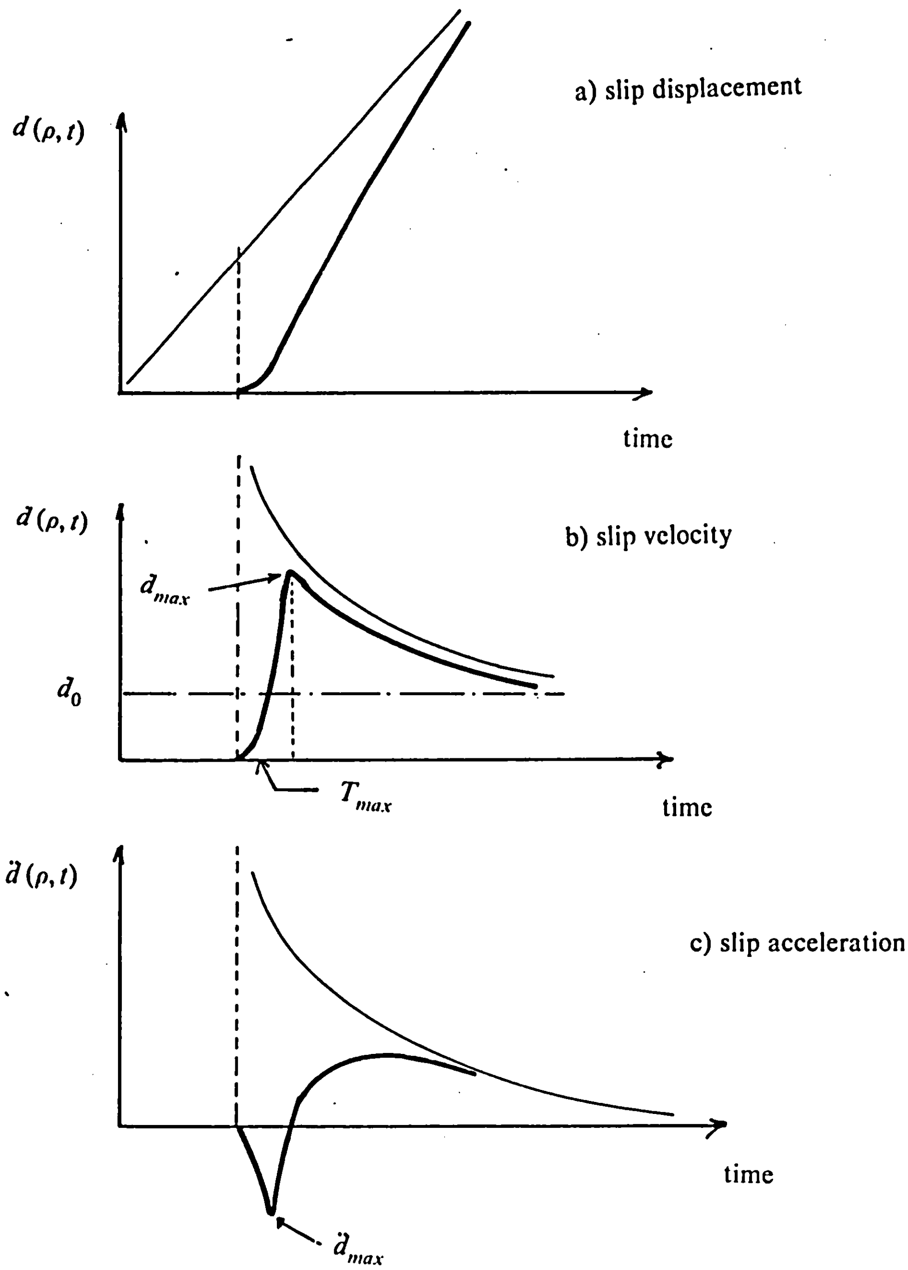

Fig.X.16

Proposed slip function, before the stopping phase arrival

10.3.4 Doppler effect

The *Doppler effect* is a phenomenon which occurs away from a moving source. We do not consider here the slippage on the fault, but its effect at some distance R in any direction. In *Eq.10.1, 10.2, 10.3 etc...*, the slip function $s(t)$ has become $s(t - R/V)$. This is a "retardated" function which gives rise to the *Doppler effect.* It is accounted for by the term $D_r(R, i\omega)$ in *Eq.10.25b* and depends mainly on the rupture velocity V_r and the azimuth of the site with respect to the strike of the fault.

The simplified equation *Eq.10.35* will enable us to describe its effect in a simple manner. It is also advantageous to deal with this problem in the frequency domain. *Eq.10.35* exhibits a term $d(\Sigma, t - R/V)$ under the integral sign, the significance of which is visible on *fig.X.17.* When the radiating point is Q, away from the hypocenter H, after some slippage has occured, the distance R is not equal to R_0 anymore but is:

$$R = (R_0 \sin\theta\cos\phi - \xi)^2 + (R_0 \sin\theta\cos\phi + \nu\cos\delta)^2 + (R_0\cos\theta + \nu\cos\delta)^2 \qquad (10.71)$$

and can be very different for sites very close to a large fault. The overall effect due to large fault cannot be computed in general except numerically. This is accounted for by adding the radiation of several patches, all of them with a different delay from the start (see section 10.4). We shall consider here only the *Doppler effect* due to a single patch, much smaller than the entire fault and therefore the *Fraunhofer approximation* is legitimate.

It consists in saying that $R >> \xi$ and $R >> \nu$, then *Eq.10.71* reduces to:

$$R \approx R_0 - \xi\sin\theta\cos\phi \qquad (10.72)$$

(we have left aside, for the moment, the *Doppler effect* in the νdirection),

Eq.10.35 then becomes:

$$\tilde{u}(\tilde{r}, t) = \frac{\mu}{4\pi\rho} \mathcal{R}_{\theta\phi} \frac{2}{R\,V^3} \int_\Sigma d\left\{\Sigma, t - \frac{R_0}{V} + \frac{\xi\sin\theta\cos\phi}{V} - \frac{\xi}{V-r}\right\} d\Sigma \qquad (10.72)$$

We shall use $\cos\Theta = \cos\theta\cos\phi$. Θ is the angle of HS with the slippage direction, which reduces to ϕ for very shallow shocks.

By a tranformation to the frequency domain we get:

$$\tilde{U}(\tilde{r}, i\omega) = \frac{\mu}{4\pi\rho} \mathcal{R}_{\theta\phi} \frac{2}{R\,V^3} i\omega D(\Sigma, i\omega) e^{-iR_0\omega/V} \int_\Sigma s(\lambda) \exp\left[-i\omega\frac{\xi}{V_r}\left(1 - \frac{V_r}{V}\cos\Theta\right)\right] d\lambda \qquad (10.74)$$

wheree recognise the particular case where:

$$G_V(R, i\omega) = i\omega D(\Sigma, i\omega) \qquad (10.75a)$$

and

$$D_r(A_z, i\omega) = e^{-iR_0\omega/V} \int_{\Sigma} s(\lambda) \exp\left[-i\omega\frac{\xi}{V_r}(1 - \frac{V_r}{V}\cos\Theta)\right] d\lambda \tag{10.75b}$$

the *Doppler effect* in the ν direction may also be integrated into $D_r(A_z, i\omega)$. For the simple case of a strike-slip fault of length L, it was expressed by *Bath* as:

$$D_r(A_z, i\omega) = \frac{\sin X}{X} \exp\left[-i\frac{R_0}{V} - iX\right] \tag{10.76a}$$

$$\text{where} \quad X = \frac{L\omega}{2V_r}\left(1 - \frac{V_r}{V}\cos\Theta\right) \tag{10.76b}$$

and is usually considered as a first approximation of more complicated situations.

The Doppler phenomenon affects both the amplitude and the phase of the motion. At a given site S, the duration of the forward wave train:

$$T_f = T_s\left(1 - \frac{V_r}{V}\cos\Theta\right) \tag{10.77a}$$

is reduced, wheras as the duration of the backward wawe train:

$$T_b = T_s\left(1 + \frac{V_r}{V}\cos\Theta\right) \tag{10.77b}$$

is increased with respect to the duration of the slip function on the fault T_s. Therefore the forward field becomes richer in high frequency and the backward field becomes richer in low frequencies. The amplitude is modulated depending of the frequency; this explains some of the peaks and valleys of the FAS of ground motion records. *Fig.X.17* shows the *Doppler effect* variations with azimuth for the simple case of a strike slip fault for two different V_r/V_s ratios.

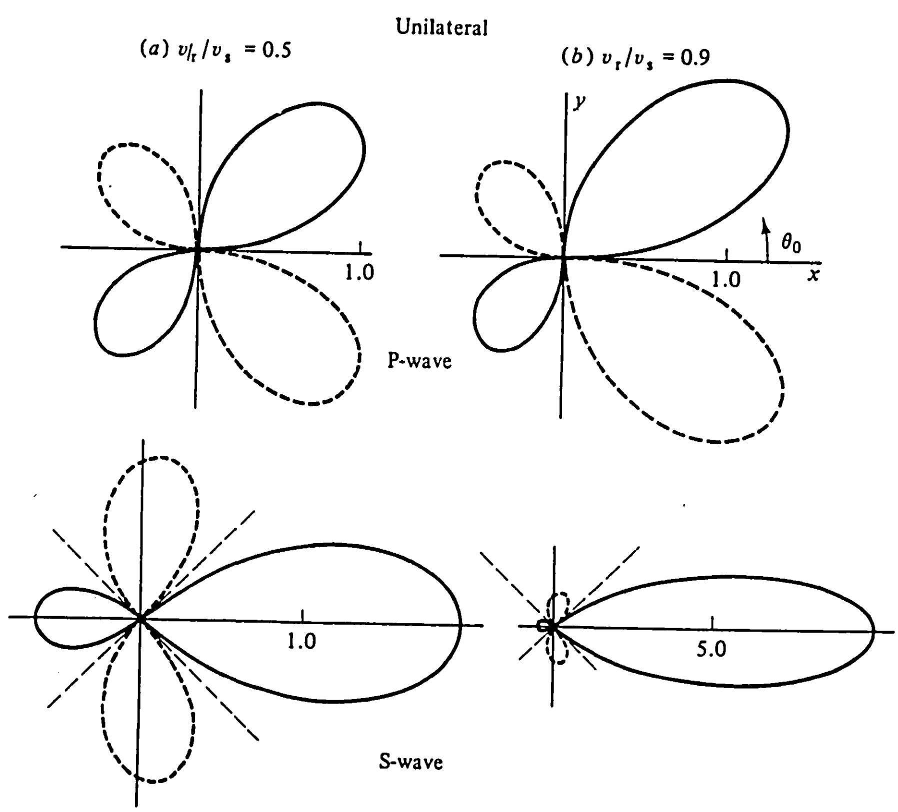

Fig.X.17

Radiation pattern due to Doppler effect

10.3.5 Anelastic attenuation

In the early part of this chapter, we were mainly concerned with the geometric attenuation of seismic waves in the near-field. The linear hypothesis for the propagating medium was retained. It is well known that the earth crust is not perfectly elastic and we shall now account for the difference. Unlike the wave propagation in soft soil, the propagation in rock medium is not strongly affected by the frictional non linearity. During the wave propagation, the stress-strain law remains very close to an elastic law. Therefore, it is sufficient to retain the equation developed previously with a correction for anelasticity. In particular the displacement field (*Eq. 10.21*) and the acceleration field (*Eq. 10.24*) may be improved only by:

1) considering the phase velocities V_S and V_P as frequency dependent,

2) allowing an attenuation term by multiplcation by $\exp[-\gamma(\omega)R]$, $\gamma(\omega)$ being the attenuation coefficient.

In practical terms, all the anelastic effects may be described by the quality factor Q of the propagating medium. Its definition originates from the equivalent linear assumption commonly accepted in geophysics and in seismology.

The anelastic attenuation of a seismic wave is related to the amplitude decay of a viscous SDOF pendulum, of natural frequency w_0 and percentage of critical damping ξ:

$$A = A_0 e^{-\xi\omega_0 t} \sin\omega_D t \tag{10.78}$$

$$\text{where} \qquad \omega_D = \omega_0\sqrt{1-\xi^2}$$

The first effect of such an attenuation is to smear the original frequency w_0, which becomes w_D. The second effect is to reduce the amplidude of the oscillation by a constant factor at each cycle. Both effects are reflected in the Q factor.

In 3 −dimensional media, the stress-strain law governing the propagation is, in its general form:

$$\tilde{\tilde{\tau}} = \tilde{\tilde{\tau}}\;[\;\tilde{\tilde{\epsilon}},\;\dot{\tilde{\tilde{\epsilon}}},\;\ddot{\tilde{\tilde{\epsilon}}},\;...] \tag{10.79}$$

where $\tilde{\tilde{\tau}}$ is the 2nd order stress tensor, and $\tilde{\tilde{\epsilon}}$ the associated strain tensor. This constitutive law is said to be linear if the coefficients involved in the right hand side are independent of the strain. The law is linear elastic when no time derivatives intervien; it is visco-linear when the first time derivative is involved. When the coefficients are strain dependent the law is said to be non linear. Two examples in one dimension are now given:

1) the *Kelvin-Voight* material (linear):

$$\tau(\epsilon,t) = \mu\epsilon(t) + \eta\frac{\partial\epsilon}{\partial t} = \mu\epsilon\left[1 + \frac{\eta}{\mu\epsilon}\frac{d\epsilon}{dt}\right] \tag{10.80a}$$

where μ is the shear modulus and η is the shear viscosity coefficient. In the frequency domain *Eq. 10.80a* writes:

$$T(i\omega) = \mu\epsilon\left[1 + i\frac{\eta}{\mu}\omega\right] \tag{10.80b}$$

2) the elasto-plastic material (non-linear):

$$\tau(\epsilon, t) = \mu(\epsilon)\epsilon(t) \tag{10.81a}$$

where μ is strongly strain dependent. In the frequency domain:

$$T(i\omega) = \mu(\epsilon)\epsilon(i\omega) \tag{10.81b}$$

We observe that, in *Eq. 10.80b* the frequency dependence is limited to the first term of the complex series in ω. In *Eq. 10.81b* the frequency dependency is much more complicated.

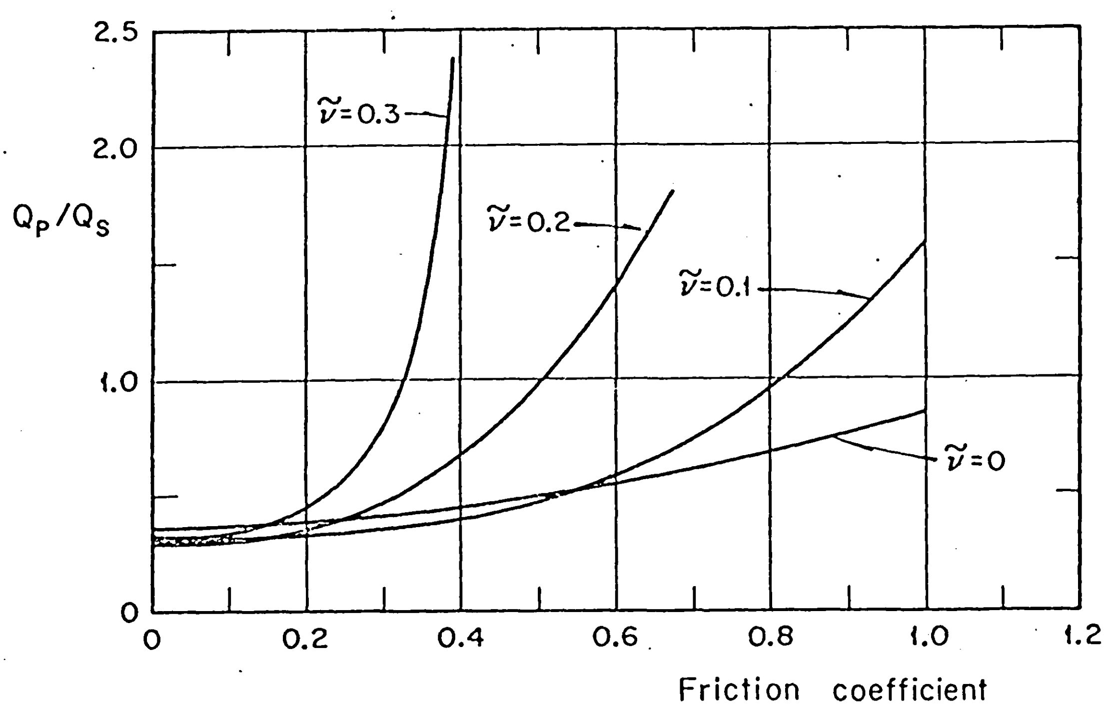

Fig.X.18

Variations of the ratio Q_P/Q_S for a frictional attenuation

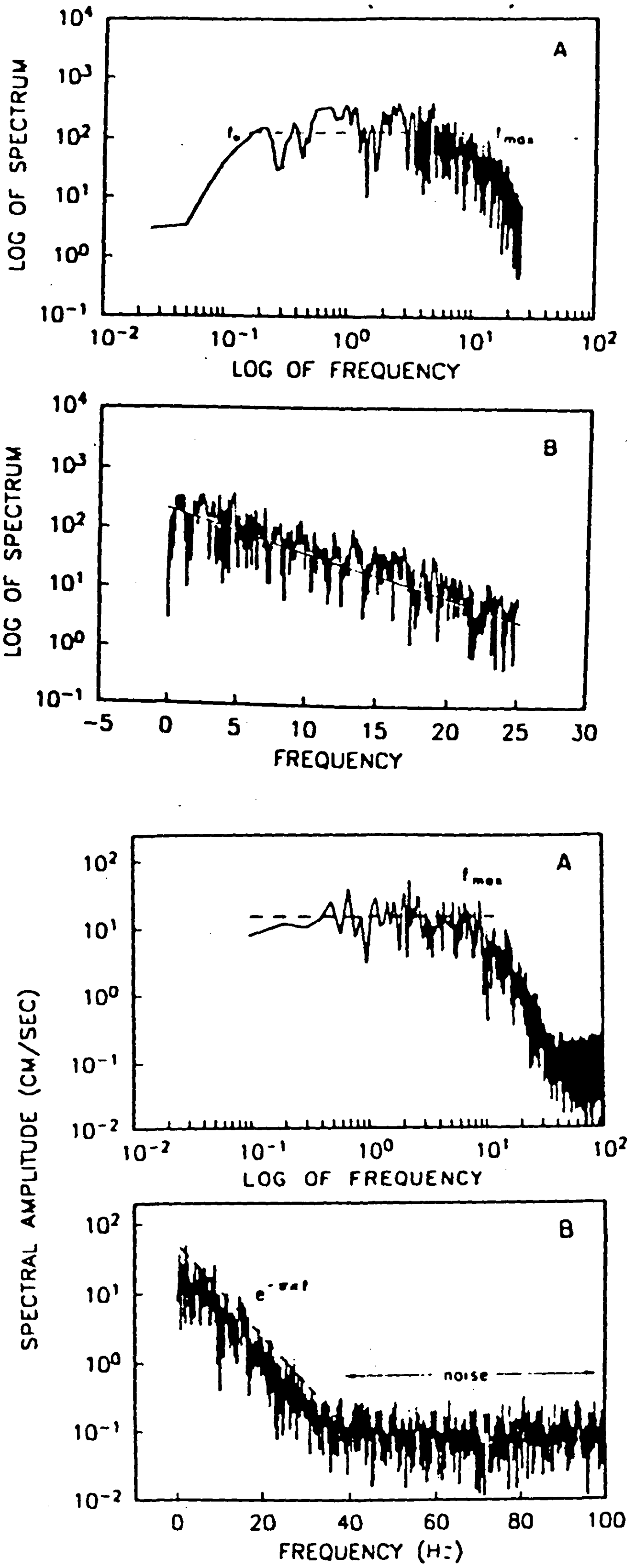

Fig.X.19

High frequency decay study of Anderson and Hough (1984)

The equivalent linear assumption consists in fitting the attenuation observations to a model of the *Kelvin-Voight* type (even if strong non-linearity are present). It is clear that this modelisation may reflect satifatorily weak non-linearity or visco-elasticity: this our case in rock material. It cannot reflect accurately the attenuation phenomenon in strongly non-linear media like soft soil deposits. In this case, specific studies are required, which should take into account the actual stress-strain law of the propagating material.

In the equivalent linear assumption, the *Lamé* coefficients λ and μ transfom into:

$$\lambda \quad \rightarrow \quad \lambda + \lambda' \frac{\partial}{\partial t} \qquad \text{or in frequency} \qquad \lambda^* = \lambda(1 + i\omega\alpha) \tag{10.82a}$$

$$\mu \quad \rightarrow \quad \mu + \mu' \frac{\partial}{\partial t} \qquad \text{or in frequency} \qquad \mu^* = \mu(1 + i\omega\beta) \tag{10.82}$$

where α and β are constant for material behaving strictly in a visco-elastic manner. They are frequency dependent when non-linearity is present.

Defining the non-dimensional Q factor as:

$$\frac{1}{Q} = \frac{1}{2\pi} \frac{\text{energy dissipated in one cycle}}{\text{peak energy stored during the cycle}} \tag{10.83}$$

we see that:

$$Q_P = \frac{1}{2\xi_P} = \alpha + 2\beta \tag{10.84a}$$

$$V^*_P(i\omega) = V_P \sqrt{1 + i\omega \frac{\alpha\lambda + 2\beta\mu}{\lambda + \mu}} \tag{10.84b}$$

and

$$Q_S = \frac{1}{2\xi_S} = \beta \tag{10.84c}$$

$$V^*_S i\omega) = V_S \sqrt{1 + i\omega\beta} \tag{10.84d}$$

Also, from *Eq. 10.78*:

$$A = A_0 e^{-\omega_0 t / 2Q(\omega)} \sin \omega_D t \tag{10.85}$$

and this gives for the P-waves and the S-waves alternatively:

$$\gamma(\omega) = \frac{\omega}{2Q(\omega) V^*(i\omega)} \tag{10.86}$$

where t was substituted by $R / V^*(i\omega)$. We see that the attenuation term is strongly influenced by a linear frequency trend for a viscous behaviour (Q = const and $V^* \approx V$). It exhibits a more complex relationship for non-linear behaviour $Q = Q(\omega)$.

Gutemberg (1958), using a large set of far-field earthquake records, concluded that the attenuation $\gamma(\omega)$ is frequency independent. He found no difference between the attenuation of shear and compresional

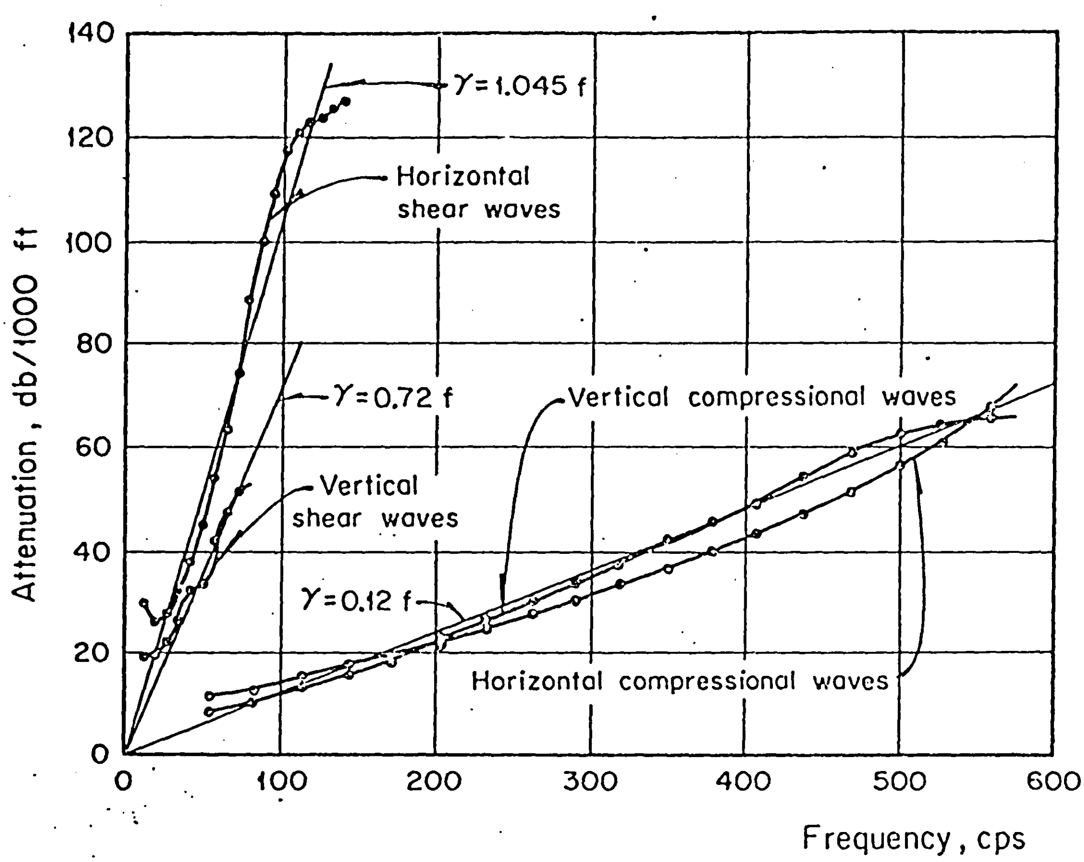

Fig.X.20

Variations of $\gamma(\omega)$ with frequency.

Average linear trends for P-waves and S-waves

waves and he proposed the value of $\gamma = 0.06 \quad 10^{-3} \quad km^{-1}$.

Other authors (reported in *White 1965*), found a linear dependency of $\gamma(\omega)$, in line with the $Q =$ const hypothesis. It also appeared that the frequency exponent n in $\gamma(\omega)$, i.e., ω^n decreases greatly with increase of confining pressure or depth. This shows that a complex attenuation mechanism involving many behaviour types is to be expected over large distances.

Walsh (1966) analysed the frictional type of attenuation and found that the Q_P/Q_S ratio varies from 0.4 to 2.5 for a ıPoisson's ratio of 0.25 when the friction coefficient ranges from 0.1 to 0.7 (*fig.X.18*).

For the earth crust a likely average value is $Q_S = 500$ with $Q_P = 2Q_S$, but it does not apply to the very-near field.

More recently, *Anderson and Hough(1984)* studied the high frequency decay of the acceleration FAS of many strong motions recorded at distances varying from 10 to 150 Km (*fig.X.19*). They found an average value for rock depending of distance:

$$Q = \frac{1}{V}\left[\frac{R}{0.040 + 0.00038R}\right] \tag{10.87}$$

where R is the epicentral distance (km) and V (km/sec) the average shear wave velocity and emphasized that Q inceases rapidely with depth in the shallow crustal layers. In average *Eq.10.87* corresponds to a frequency independant Q varying from $Q = 50$ to $Q = 500$ in the strong motion distances.

Also *fig.X.20* summarises partially the problem by showing fairly linear trends for $\gamma(\omega)$ both for the P-waves and the S-waves.

All these models may be used for the acceleration field generation. However we realise that no strongly established law is available for near-field studies. We think that models based on the combination of several attenuation mechanisms like:

$$\frac{1}{Q(\omega)} = \frac{1}{Q_0} + \frac{1}{Q_1\omega} + ... \tag{10.87}$$

should give a better description of near-field attenuation in the future.

10.4 A PHYSICO-STOCHASTIC SOURCE MODEL

10.4.1 General description of the model

In the previous sections, we have developed the means of generating a realistic seismic pulse, from a suitable slip function on the fault. We also computed the elementary acceleration field at a site whose relative location with respect to the fault is known. Various effects like anelastic attenuation or *Doppler* effect have also been introduced. Basically, two scaling factors were needed: the patch dimension and the patch stress drop. In this section we shall describe how to combine these elementary pulses to simulate the ground motion due to an entire fault.

When the expected earthquake is of small Magnitude (M about 4), there is little difference between the overall fault and an individual patch, since small earthquakes are often generated by a single coherent patch of fault. In general, however, for larger shocks, the total rupture is constituted from the addition of several patches triggering each other successively as the rupture front reach them (*fig.X.21*). The motion initiates at the hypocenter where a first fault patch is released. As the rupture front stops at the patch limit, it triggers immediately another one.

For the entire fault the same two parameters are required, but this time to describe the overall average earthquake characteristics. The first parameter needed is the total expected fault area Σ_T. It is directly assessed from the expected Magnitude, determined independently from seismic risk analysis. It may also be determined from seismotectonic studies when data are available. The second parameter is the average stress drop $\overline{\Delta\sigma}$. We shall give in 10.4.3 preliminary values for this independent scaling term as a function of the brittleness of the rupture zone.

Although these two parameters are fundamental and relate directly to the commonly known earthquake parameters, they are not assumed constant all over the fault. We shall propose in 10.4.4 a stochastic generation of the patch pulses based on elementary patch dimensions and patch stress drops. Their probability distributions will be made compatible with the imposed overall values of $\overline{\Delta\sigma}$ and Σ_T.

Eventually, all the patch pulses are added together, with their associated delay, to form the final acceleration time history. The stochatic nature of the model reflects the erratic character of the rupture on the fault. It is not actually possible to describe in a better way the complexities of the shear strength distribution or the variation of the tectonic forces along the fault. On the other hand the model integrates the overall values (total fault area and average stress drop) which are accessible from observations.

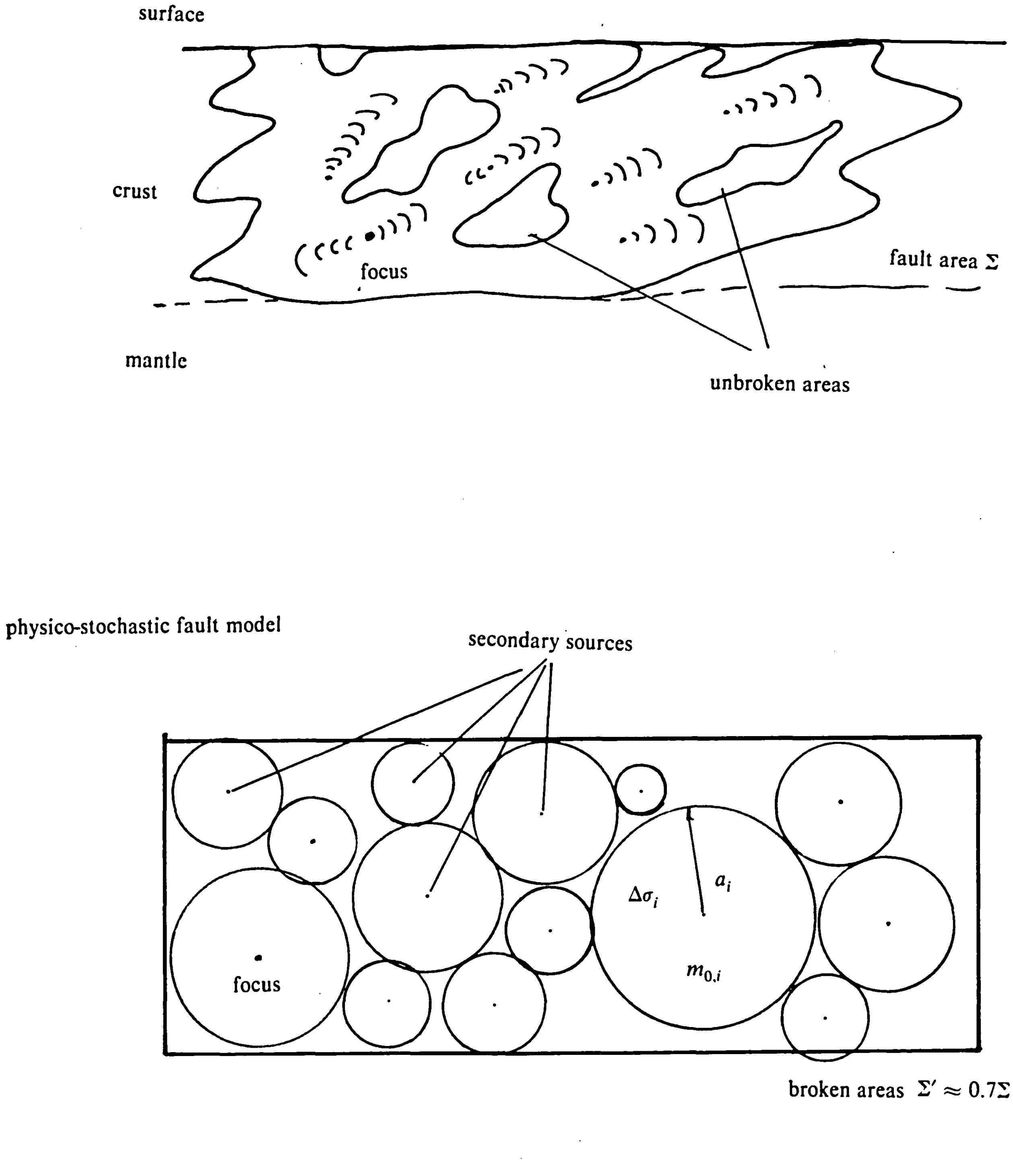

Fig.X.21

The entire fault is divided into several patches
of variable dimensions triggering each other successively

10.4.2 Discussion on the stress drop parameter

Before going into the proposed method which deals with the two inter-related parameters, Σ_T and $\overline{\Delta\sigma}$, it is necessary to look more closely at the definition of the stress drop itself. In fact, there are several concepts used in seismology to define the stress release and it is not always clear which of them is actually refered to. The original definition of the stress drop $\overline{\Delta\sigma}$ comes from the expression of the scalar seismic moment M_0 given by *Eq.10.18* or *Eq.10.22* and must be called "static stress drop". In terms of overall average values, M_0 may be re-written:

$$M_0 = \mu \overline{d} \Sigma_T \tag{10.89}$$

where μ = crust rigidity $\overline{d}$ = average fault offset Σ_T = total fault area

In order to obtain the stress drop from the seismic moment, a relation between $\overline{d}$ and $\overline{\Delta\sigma}$ on the fault is needed. Seismologists usually assume that the stress drop on the fault is constant and then compute the average slip for different geometries. Expressed in this form, the problem is that of a shear crack under uniform stress drop, i.e., uniform difference between tectonic stress σ_1 and final stress σ_2: $\overline{\Delta\sigma} = \sigma_1 - \sigma_2$. The solution of this problem may be written in the general form (fig.X.22):

$$\overline{d} = C \frac{\overline{\Delta\sigma}}{\mu} l \tag{10.90}$$

where l is a characteristic length associated with the narrowest dimension of the fault, usually different from L the largest dimension of the fault. For an elliptical fault of semi-major axis L and semi-minor axis l, C is found from the results of *Eshelby (1957)*. For tranversal slip (in the l direction):

$$C = \frac{4k^2}{(1-k^2)K(k) - (1-4k^2)K'(k)} \tag{10.91a}$$

and for the longitudinal slip (in the L direction):

$$C = \frac{4k^2}{(1+3k^2)K'(k) - (1-k^2)K(k)} \tag{10.91b}$$

$K(k)$ and $K'(k)$ are the complete elliptic integrals already defined in *Eq.5.42 and 5.43* and $k = \sqrt{1 - l^2/L^2}$. The Poisson ratio was assumed to be equal to 0.25.

When $L = l$, this the case of circular fault, then $C = 16/7\pi = 0.73$ (see *Eq.10.42*). For a very long, rectangular fault, $C = \pi/2 = 1.57$. All practical cases lie between these two values. Thus it appears that C varies within a factor of two for different fault geometries. This is also the uncertainty in the value of the average stress drop.

Other definitions have been proposed as a result of the various methods used for its computation. *Brune*, in his model for the body wave spectrum (section 10.3.3) considers in fact that the stress drop $\overline{\Delta\sigma}$ equals the "dynamic stress drop" or "effective stress" the difference between the static friction τ_s and

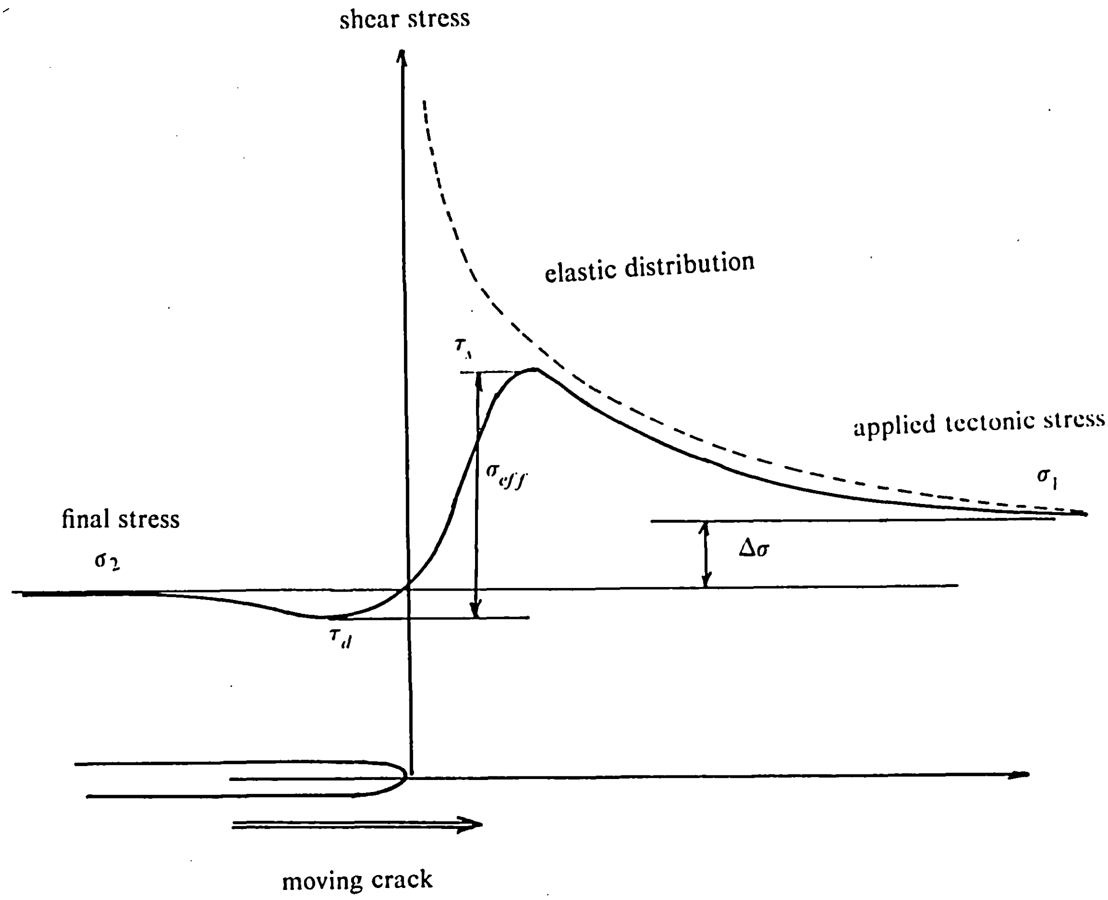

σ_1 = applied tectonic stress

σ_2 = final stress after slip

τ_s = static friction

τ_d = dynamic friction

$\sigma(d, \dot{d})$ = friction law

$\Delta\sigma = \sigma_1 - \sigma_2$ = stress drop

$\bar{\sigma} = \frac{1}{2}(\sigma_1 + \sigma_2)$ = average stress

$\sigma_{eff} = \tau_s - \tau_s$ = effective stress

$\bar{\sigma}_f$ = average frictional stress

$\sigma_a = \eta\sigma$ = apparent stress

Fig.X.22

Definition of the various stresses involved during faulting the dynamic friction τ_d. This is due to the instantaneous rupture assumption, expressed by $\sigma_1 = \tau_s$ of the model in a perfectly brittle material $\sigma_2 = \tau_d$ (also $= \sigma_f$). The interpretation of the *Brune* stress drop as a average stress drop requires that the imposed relation between corner frequency and source radius (which derives from the analytic expression of the model in frequency) be exact rather than approximate. Also, when the source radius is estimated using the duration between the P-wave onset and the first zero crossing, (*Frankel and Kanamori 1983*), the stress drop is very dependent on the azimuth of the station.

Boatwright (1980), using the *Sato and Hirasawa* model estimated the dynamic stress drop from:

$$\overline{\Delta\sigma} \approx \mu \frac{\dot{d}_0}{V_S} \tag{10.92}$$

by measuring the initial slope of the far field velocity waveform.

Also *Hanks and Macguire (1981)* defined the "root mean square stress drop" which is an estimate of the *Brune* effective stress derived from the high frequency seismic radiation. They also demonstrated that these estimates were uncorrelated with estimates of the average static stress drop. *Fig.X.23* shows various estimates of stress release for typical earthquakes of magnitude M_L between 4 and 5 (after *Boatwright 1984*). Facing this plethora of "stress drops" we have chosen to consider this parameter as a scaling factor giving the strength of the shock rather than an exact stress drop, and we call it "design stress drop". We shall assume that, within a factor of two, due to the geometry uncertainty and the definition uncertainty, all these values are identical.

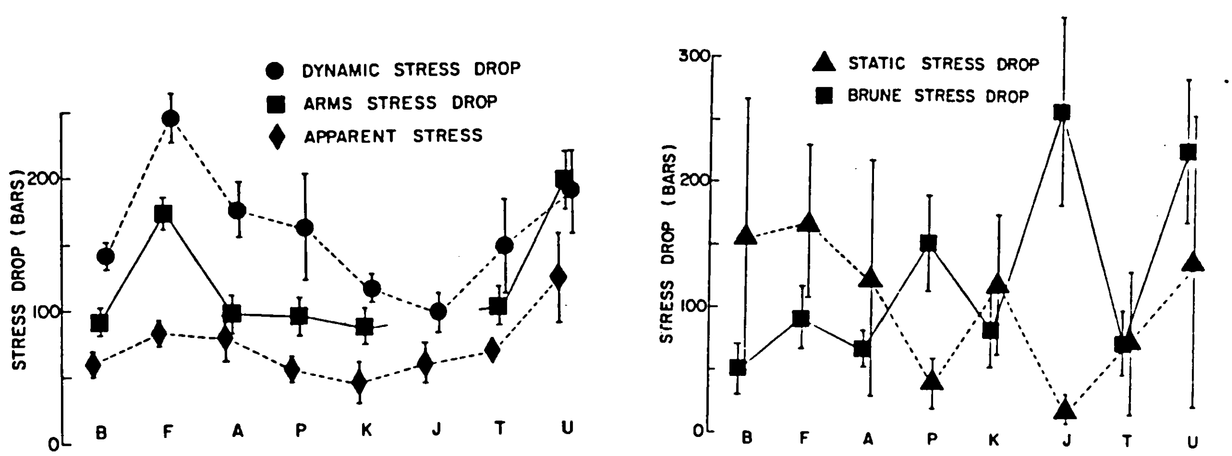

Fig.X.23

Various estimates of the stress drop for the same earthquakes using different methods

The design stress drop is then the scaling term which affects the sharpness of the earthquake. It is related to the rise time τ, as defined by *Brune*, through *Eq. 10.37 and 10.45* which give:

$$\tau = \frac{\text{contant}}{(\overline{\Delta\sigma})^{1/3}} \tag{10.93}$$

This equation shows that high design stress drop earthquakes have small rise time and conversely.

From an analysis of several data sets (*Kanamori and Anderson (1975), Frankel and Kanamori (1983), Fletcher et al. (1984), Frankel (1984), Mori and Shimazaki (1984)*), from many different earthquakes covering a wide range of Magnitudes, we found that design stress drops follow a lognormal distribution with:

$$\text{average stress drop (in bars):} \quad \log\overline{\Delta\sigma} = 1.69 \tag{10.94a}$$

$$\text{standard deviation (in bars):} \quad \log STD = 0.33 \tag{10.9ab}$$

Values of the average stress drop over the entire fault will be used to control the total fault area Σ_T. It may also be considered that potentially brittle regions are likely to see larger average stress drops and hence judgement should be exercised.

In the following, we shall also need the apparent stress σ_a defined by *Aki (1966)* as:

$$\sigma_a = \mu\frac{E_s}{M_0} \tag{10.95}$$

which originates from the equation of the energy balance on the fault:

$$E = E_s + E_f + E_c + E_g \tag{10.96}$$

E = total released energy

E_s = seismic wave energy

E_f = work dissipated by friction

E_c = fracture energy at the crack tip

E_g = work done against gravity

It is common practice to neglect the terms E_c and E_g to write the fault radiation efficiency:

$$\eta = \frac{E_s}{E} \approx \frac{E - E_f}{E} \tag{10.97}$$

The total energy released is:

$$E = \frac{1}{2}(\sigma_1 + \sigma_2)\overline{d}\Sigma_T = \overline{\sigma}\overline{d}\Sigma_T \tag{10.98}$$

where $\overline{\sigma}$ is the average stress on the fault,

while the frictional work is:

$$E_f = \overline{d}\Sigma_T\overline{\sigma}_f \tag{10.99}$$

$\overline{\sigma}_f$ is the average kinetic shear resistance during the slip as the frictional stress drops from the static friction τ_s down to the dynamic friction τ_d . For a sharp drop of the friction law encountered in very brittle rocks, $\overline{\sigma}_f = \tau_d$ whereas for more ductile materials $\Gamma\tau_s < \overline{\sigma}_f < \tau_d$.

From Eq.10.97 we deduce:

$$\eta = \frac{\overline{\sigma} - \overline{\sigma}_f}{\overline{\sigma}} \tag{10.100}$$

and we also see that:

$$\sigma_a = \text{ apparent stress } = \eta\overline{\sigma} \tag{10.101}$$

We can write:

$$\sigma_a = \frac{\overline{\Delta\sigma}}{2} + (\sigma_2 - \overline{\sigma}_f) \tag{10.102}$$

which shows that we always have:

$$\frac{\overline{\Delta\sigma}}{2} \geq \sigma_a \quad \text{(Savage and Wood inequality)} \tag{10.103}$$

The equality is met when $\overline{\sigma}_f = \sigma_2$ e.i., for brittle materials. This is the result that *Kanamori and Anderson (1975)* found from their data set. They also concluded that:

$$\overline{\Delta\sigma} \approx \text{effective stress } = \tau_s - \tau_d \tag{10.104}$$

It must be noted, however, that this relation considers, like in the *Brune* model, $\sigma_1 = \tau_s$. There is still no firm evidence for this simple assumption.

In their study of the 1975 Brawley Imperial Valley earthquake, using a spectral integration technique, *Hartzell and Brune (1977)* suggested $\overline{\Delta\sigma} = 4.02\sigma_a$. We shall reconcile these two proposals by writting:

$$\overline{\Delta\sigma} = 2(1 + \chi)\sigma_a \tag{10.105}$$

where χ is a ductility indicator:

$\chi = 0.0$ perfectly brittle

$\chi = 0.5$ intermediate

$\chi = 1.0$ ductile

In the limit, for a perfectly ductile material, $\tau_s = \tau_d$, no accelerating stress is available and all the quantities tend to zero.

10.4.3 Interaction between average stress drop and total fault area

We saw in section 10.2, that the total seismic moment M_0 was the energy scaling factor for the released energy on the fault. We also mentioned in 10.3.3 that two parameters contributed to M_0: the fault area and the stress drop. There is an infinity of $\overline{\Delta\sigma}$ and Σ_T combinations giving the same value for M_0. The same total energy may originate from a low stress drop over a large area Σ_T or conversely from a small area associated with a high sress drop. As far as the simulated waveform is concerned, the difference between the two cases is significant; therefore it is worthwhile to attempt to quantify this parameter interaction.

We make use, as a starting point, of the well established *Gutemberg* energy relation:

$$\log E_s = 1.5 M_S + 11.8 \qquad E_s \text{ in cgs} \tag{10.106}$$

M_S is the surface wave Magnitude and the radiated energy E_s is linked to the total energy released through:

$$E_s = \eta E = \eta \bar{\sigma} \bar{d}\, \Sigma_T \tag{10.107}$$

By introducing the expression of $\bar{d}$ from *Eq. 10.90*, and using *Eq. 10.106* to eliminate the energy term, we get:

$$M_S = \log \Sigma_T + \frac{4}{3} \log \overline{\Delta\sigma} + F \tag{10.108}$$

$$\text{where} \qquad F = \frac{1}{1.5}\left[\log \frac{C g(1 + \chi)}{\mu} - 11.8\right] \tag{10.109}$$

$$\text{in which} \qquad g = 1 \Big/ \sqrt{\frac{\pi}{2}\left(1 + \frac{l^2}{L^2}\right)} \tag{10.110}$$

is the fault shape ratio.

The term F depends on:

1) the rock stiffness μ and its ductility indicator χ,

2) the fault geometry through C and g.

Table XVIII gives typical and extreme values for F. It can be observed that, although many factors are involved, F is surprisingly constant. The value $F = 2.3$ will be used for numerical calculations.

Eq. 10.108 is the relation giving the total area as a function of magnitude and stress drop. It is in very good agreement with the expression proposed by *Utsu-Seki (1959)*:

$$M_S = \log \Sigma_T + 4 \tag{10.111a}$$

or by *Geller (1975)*:

$$M_S = \log \Sigma_T + 4.53 \tag{10.111b}$$

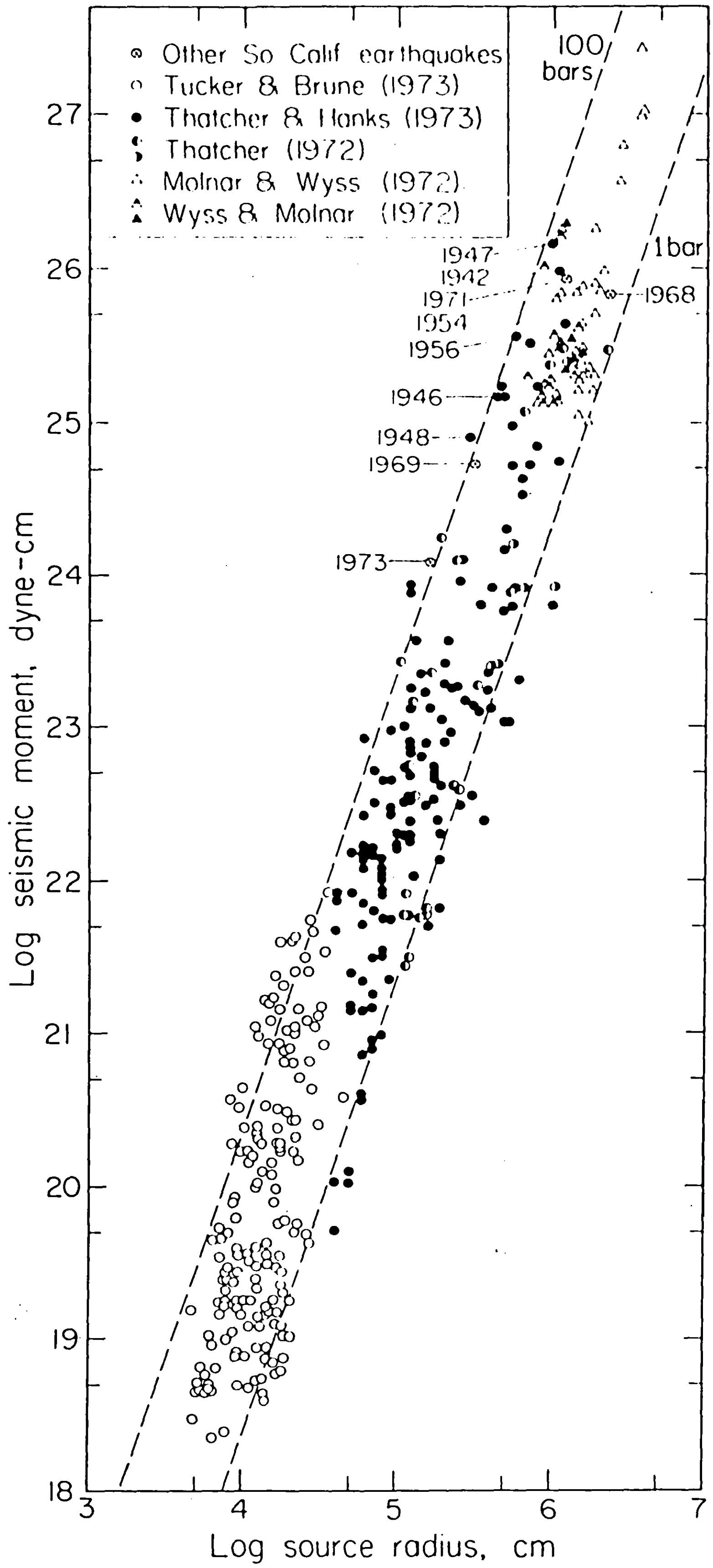

Fig.X.24

Relation between average source radius and seismic moment (after Hanks 1977)

They correspond to data sets having an average stress drop $\overline{\Delta\sigma} = 19$ bars and $\overline{\Delta\sigma} = 47$ bars respectively. It is apparent that the uncertainty on $\overline{\Delta\sigma}$ controls the uncertainty on Σ_T which is obtained within a factor of 2.0 to 2.5. Average values for $\overline{\Delta\sigma}$ may be chosen among the following:

$\overline{\Delta\sigma} = 20$ bars for (relatively) ductile rock or deep focus or on pre-establised fault like in interplate regions.

$\overline{\Delta\sigma} = 50$ bars for intermediate rock or focal depth. This value is also the average for large data sets.

$\overline{\Delta\sigma} = 100$ bars for very brittle rock or very superficial focus and also for the cases of fresh ruptures.

Table XVIII

Typical and extreme values for F

Geometry	*circle* $C = 0.73$ $g = 0.56$	$L/l = 2$ $C = 1.0$ $g = 0.36$	$L/l = 4$ $C = 1.57$ $g = 0.19$
brittle $d = 0.0,\ \mu = 3.5$	2.18	2.42	2.19
intermediate $d = 0.5,\ \mu = 3.0$	2.34	2.30	2.42
ductile $d = 1.0,\ \mu = 2.5$	2.48	2.44	2.39

10.4.4 Stochastic distribution of the patch parameters

We shall introduce now, the conditions of stochastic nature that the fault patches have to meet in order to satisfy the global parameters of the entire fault. Each individual patch composing the fault will generate its own seismic pulse scaled by its own area and its own stress drop. These individual values must be such that:

1) the sum of the areas of the patches should equal the previouly determined total area Σ_T (in fact a fraction p of the total area to account for the irregular barrier pattern),

2) the average of all the patch stress drops must equal the given average stress drop over the fault.

These two condi:ions will be satisfied, in a stochastic sense, as each patch is generated randomly. The stochastic law for the distribution of the patch dimensions and patch stress drops, is derived from the frequency Magnitude relationship:

$$\log N = A - bM \tag{10.112}$$

where N is the number of earthquakes of Magnitude greater or equal to M, and A and b are the well known seismic constants for a given area. This fundamental law describing the statistics of the seismicity has been found by *Mogi (1967)*, to be valid with the same factor b, not only at the macro-scale for all the earthquakes in an region, but also at the micro-scale for the rupture of rock samples. This relationship implies that an active fault undergoes tectonic slips through a vast number of seismic events over a wide range of Magnitude, many small ones and a few large ones. On a fault, "small earthquakes" occur, reflecting the same distribution of micro-events.

The Magnitude M of the "micro-events" is replaced here by the elementary seismic moment m_0 through a relation of the type:

$$\log m_0 = \alpha M + \beta \tag{10.113}$$

Finally, using its expression (see also *fig. X. 24*)

$$m_0 = \mu \overline{d} \Sigma = C g \pi^{3/2} \Delta\sigma a^3 \tag{10.114}$$

where a is the patch equivalent radius, we get:

$$\log N = \log K_1 - \frac{b}{\alpha} \log(\Delta\sigma a^3) \tag{10.115a}$$

$$\text{where} \qquad \log K_1 = \left(A + \frac{b\beta}{\alpha}\right) - \frac{b}{\alpha} \log C g \pi^{3/2} \tag{10.115b}$$

is a fault invariant.

Using, for example, the typical values $b = 1$ and $\alpha = 1.5$ (*Kanamori and Anderson (1975)*) *Eq. 10.115a* becomes:

$$N = \frac{K_1}{(\Delta\sigma)^{2/3} a^2} \tag{10.116}$$

but any observed value of $\nu = b/\alpha$ may be used.

This can be interpreted as the cumulative second order probability distribution of the random variables $\Delta\sigma$ and a. K_1 is determined by normalising the distribution. Let $\Delta\sigma_{min}$ and a_{min} be the minimum values of the patch stress drop and patch equivalent radius. They are arbritrarily chosen such that all elemetary seismic moments below:

$$m_0 = \kappa\Delta\sigma_{min}a^3_{min} \tag{10.117}$$

$$\text{where} \qquad \kappa = C g\pi^{3/2}$$

are considered negligible. Then the cumulatice probability distribution is:

$$F(\Delta\sigma, a) = 1 - \left(\frac{\Delta\sigma_{min}}{\Delta\sigma}\right)^{2/3}\left(\frac{a_{min}}{a}\right)^2 \tag{10.118}$$

Since the two random variables are independent their probability density function is:

$$f(\Delta\sigma, a) = \frac{\partial^2 F(\Delta\sigma, a)}{\partial\Delta\sigma\partial a} = \frac{4}{3}\Delta\sigma^{2/3}_{min}a^2_{min}\frac{1}{\Delta\sigma^{5/3}a^3} \tag{10.119}$$

and their marginal densities are respectively:

$$f_{\Delta\sigma}(x) = -\frac{2}{3}\frac{\Delta\sigma^{2/3}_{min}}{x^{5/3}} \tag{10.120a}$$

$$f_a(x) = -2\frac{a^2_{min}}{x^3} \tag{10.120a}$$

Fig.X.25 shows the joint probability density limited by a maximum elementary seismic moment $m_{0,max}$ whose value may be computed from the average stress drop constraint:

$$\overline{\Delta\sigma} = \int_{a_{min}}^{\infty}\int_{\Delta\sigma_{min}}^{m_0/\kappa a^3} f_a(x) f_{\Delta\sigma}(y)\,d\,x\,d\,y \tag{10.121}$$

We find:

$$\overline{\Delta\sigma} = 4\Delta\sigma^{2/3}_{min}\left\{\frac{1}{3a_{min}}\left[\frac{m_{0,max}}{\kappa}\right]^{1/3} - \frac{\Delta\sigma^{1/3}_{min}}{2}\right\} \tag{10.122}$$

Once $m_{0,max}$ is known, values of the maximum stress drop and the maximum patch radius may be obtained from:

$$\Delta\sigma_{max} = \frac{m_{0,max}}{\kappa a^3_{min}} \tag{10.123a}$$

$$a^3_{max} = \frac{m_{0,max}}{\kappa\Delta\sigma_{min}} \tag{10.123b}$$

Random values for the patch radius and the associated stress drop are then easily obtained from a double generation of numbers following the laws *10.120a and 10.120b*. If the number is sufficiently large, then the average stress drop will match the imposed $\overline{\Delta\sigma}$.

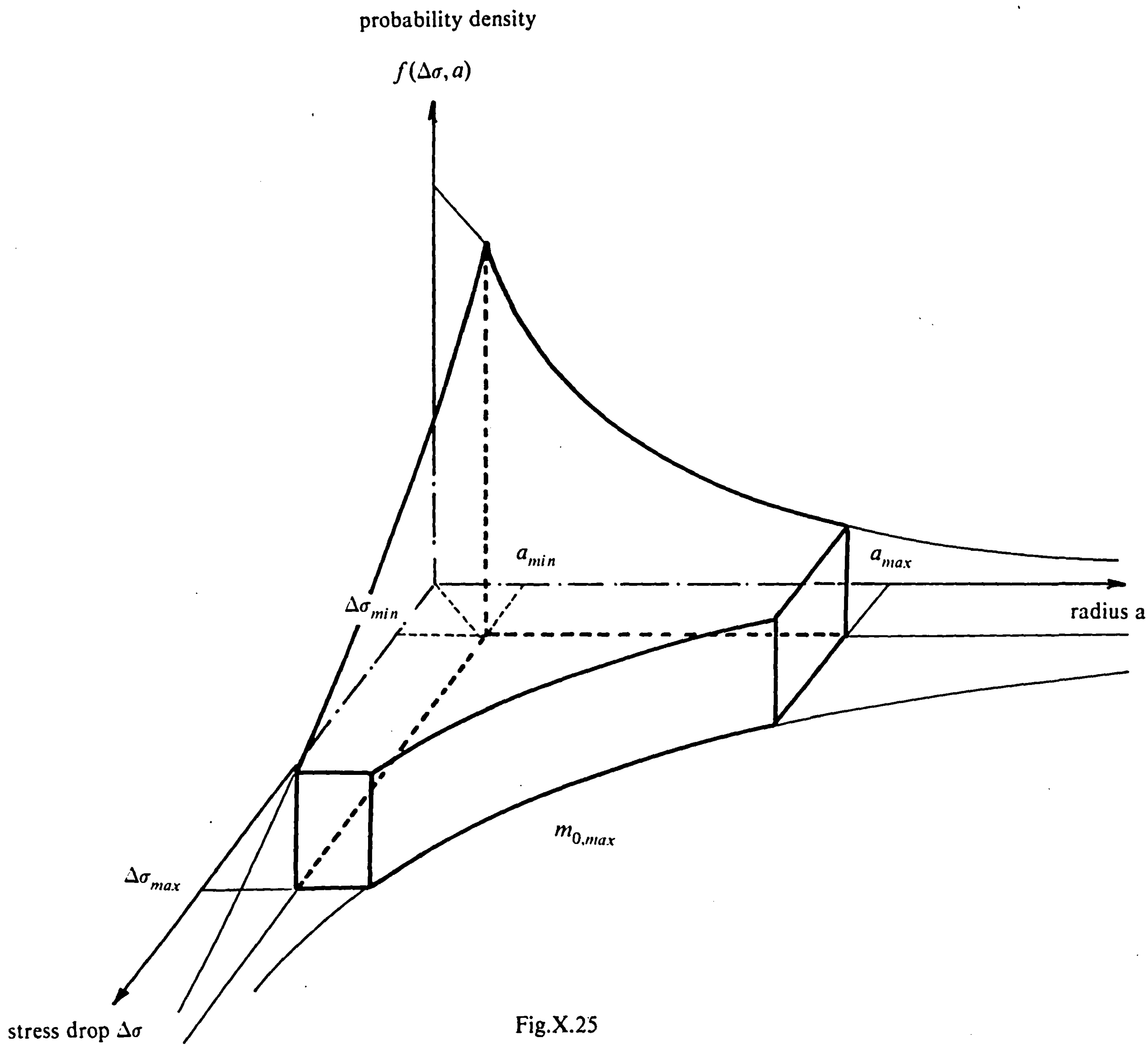

Fig.X.25
Joint probability of $\Delta\sigma$and a,
limited by the maximum seismic moment $m_{0,max}$

10.4.5 Flow-chart of the simulation procedure

In order to perform the acceleration simulation on a computer the succesive steps must be followed:

Step 1: Determine from a previous analysis the expected surface wave Magnitude M_S.

Step 2: Assess the average stress drop $\overline{\Delta\sigma}$ for the entire fault, if possible by integrating the brittleness indicator.

Step 3: Compute the total source area Σ_T from *Eq. 10.108* and correct to get the actual broken surface, $\Sigma_T' \approx 0.6\Sigma_T$.

Step 4: Decide on the smallest values for a_{min} and $\Delta\sigma_{min}$. As an example, one may choose a_{min} = 0.175 km and $\Delta\sigma_{min}$ = 0.1 bar giving an elementary Magnitude of the order of zero for the minimum patch.

Step 5: Compute the maximum elementary seismic moment $m_{0,max}$ from *Eq. 10.122.*

Step 6: Compute a_{max} and $\Delta\sigma_{max}$ from *Eq. 10.123a and 123b.*

Step 7: Generate random values for the current patch parameters $\Delta\sigma$ and a, according to the probability densities *10.120a and 10.120b.*

Step 8: Produce an acceleration pulse, for each patch using Eq.10.24), according to the selected slip function and the source-site geometry.

Step 9: Compute the successive patch delays from the patch rupture duratio and add the individual pulses at the site.

Step 10: Continue the patch generation until the sum of the elementary areas reach the total area Σ_T'.

In a preliminary attempt to generate an acceleration time history using this technique, we have chosen the parameters accordingly to the seismological data of the Tabas (Iran) earthquake of 16 Septembre 1978.

$$M_S = 7.6 \qquad \overline{\Delta\sigma} = 25 \text{ bars}$$

$$\phi = 120 \qquad \delta = 60 \qquad \lambda = 0 \qquad L = 85 \text{ km} \qquad l = 23 \text{ km}$$

The relative location of the station with respect to the fault and the hypocenter is drawn on *fig. 26.a and b.*

The computed total area was $\Sigma_T = 2754$ km and we retained the values $L = 90$ km and $l = 30$ km. The limits for the stress drops and the associated equivalent radii of the patches were:

$$\Delta\sigma_{min} = 0.4 \text{ bar} \qquad \Delta\sigma_{max} = 3000 \text{ bars}$$

$$a_{min} = 1 \text{ km} \qquad a_{max} = 40 \text{ km}$$

The maximum elementary seismic moment was $m_{0,max} = 9.7 \quad 10^25$ cgs, corresponding to a maximum coherent shock of magnitude $M_S = 6.7$. A constant value $Q = 300$ independent of frequency was chosen.

The slip function was an early version of the pulse derived from the Sato-Hirasawa model. Also, only the shear waves in *Eq. 10.24* have been propagated.

The obtained time history, can be seen on *fig. X. 27a* and compared with the motion actually recorded in Tabas presented in its corrected form (KK=7) on the *fig. X. 27a*. An overall resemblance between the two accelerations may be observed. Also the correspondance between the peak values is found satisfactory. However, a difference in the "shape" of the energy arrival is to be noted. It is certainly due to the phasing of the succesive arrivals which was not accurately fitted to the available fault dimension in the computer program.

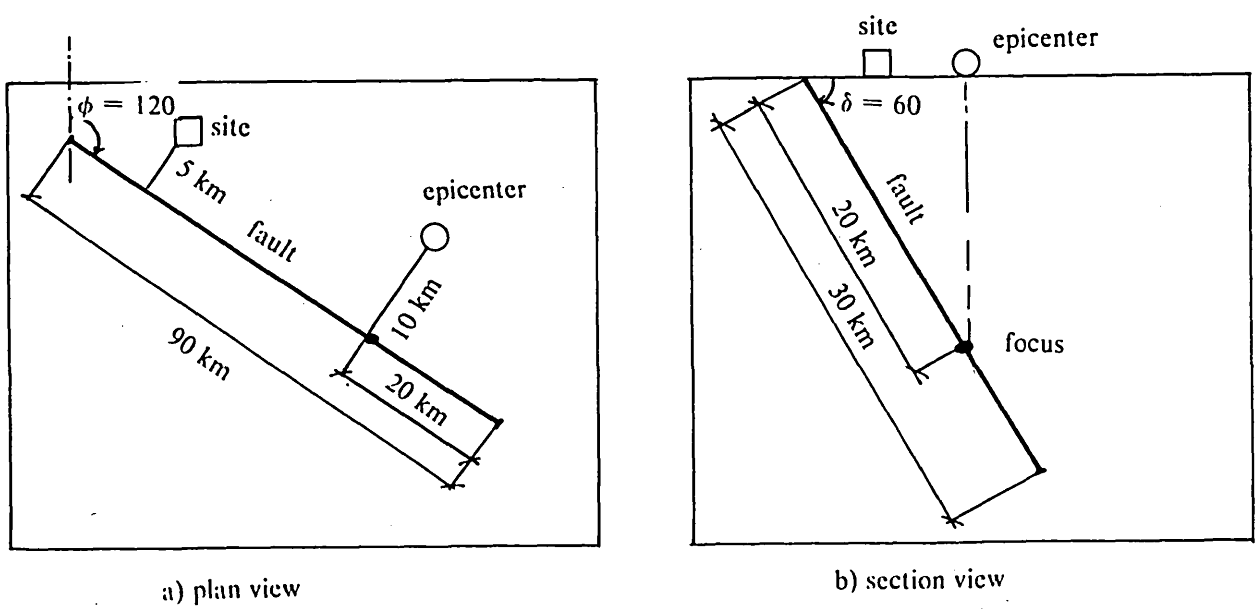

Fig.X.26

Relative location of the station with respect to the fault

a) actually recorded ground motion

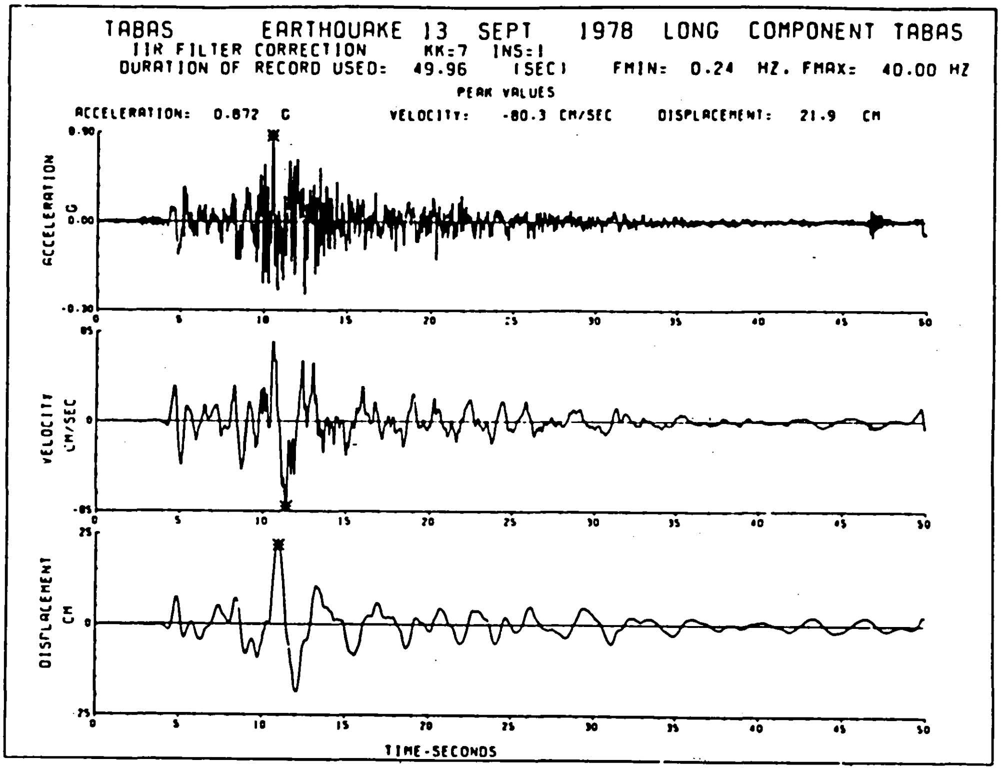

b) simulated ground motion

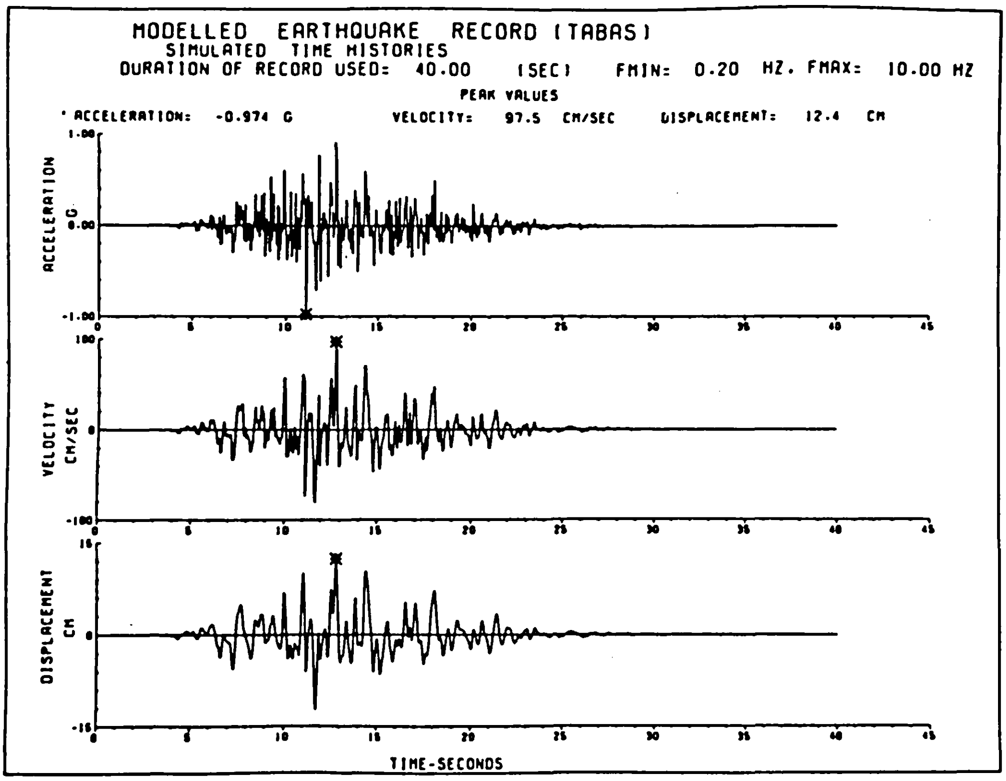

Fig.X.27

Horizontal ground motion component

of the Tabas (16 Septembre 1978) earthquake.

10.5 CONCLUSION

It is readily seen that, even in the limited case developed in this chapter, the generation of the ground acceleration from geophysical models requires many parameters. Most of them are badly known or even not known at all. In that sense, the use of the method seem to be of little use for engineering.

We think, however, that it is worth having such a method at hand, as it shows explicitely how little we must be confident in one particular motion. One should rather consider the obtained time history as one sample of a series of possible motions and then generate several other functions covering the range of possibilities for the parameters. When used in structural design, these motions will yield an envelope for the structural responses, more accurately than by any other methods; in particular, as it was said earlier, this enables a much better reliability assessment in the non-linear domain, in the vicinity of the collapse.

This approach is also very useful for applied research. In this area, it is needed to investigate the effects that the various parameters might have on the final acceleration. It provides the means to determine whether or not a particular variable has a predominant influence. Then, for engineering purposes the less influencial parameters may be dropped, to leave the engineer with the most significant ones for future simulations.

REFERENCES

1 Abramovitz,M. and Stegun,I. 1964 Hanbook of mathematical functions, Dover Publ.Inc.

2 Aki,K. 1979 Characterization of Barriers on an Earthquake fault. J.Geoph.Res., Vol:84,p.6140

3 Aki,K. 1968 Seismic Displacement near a fault. J.Geoph.Res., Vol:73,p.5359

4 Aki,K. 1966 Generation and propagation of G waves from the Niigata earthquake of June 16,1964. B.Earth.Res.Inst., Vol:44,p.73

5 Aki.K. 1982 Strong motion prediction using mathematical modelling techniques. BSSSA, No:72,p.529

6 Akima,H. 1970 On a new method of interpolationand smooth curve fitting based on local procedures. J.Assoc.Comput.Mach, No.17.p.589

7 Alford,J.L. Housner,G.W. and Martel,R.R. 1951 Spectrum analysis of strong motion earthquakes. Caltech, Earthq.Research Lab. Pasadena

8 Ambraseys,N.N. 1969 Maximum intensity of ground movements caused by faulting. Proc.4th WCEE, Chile,p.154

9 Ambraseys,N.N. 1985 Intensity attenuation and Magnitude-Intensity relationship for Northwest European earth. J.Earthq.Eng.Struc.Dyn. Vol:13,No:6,p.733

10 Ambraseys,N.N. Dynamics and response of foundation materials. Proc.4th WCEE, Rome,p.1

11 Amin,M. and Ang,A.H.S. 1966 A non-stationary stochastic model for strong motion earthquaques. Struct.Research Series No.306 Univ.of Illinois

12 Amini,A. and Trifunac,M.D. 1985 Analysis of a force balance accelerometer. Soil Dyn.and Earth.Eng. Vol.4,No.2

13 Anderson,D.L. Ben-Menahem,A. and Archambeau,C.B. 1965 Attenuation of seismic energy in the upper mantle J.Geoph.Res., Vol:70,p.1441

14 Anderson,J.G. and Hough,S.E. 1984 A model for the shape of the Fourier Amplitude Spectrum of acceleration at high frequencies. BSSA,Vol:74,No:5,p.1969

15 Anderson,J.G. and Richards,P.G 1975 Comparison of strong ground motions from several dislocation models. Geoph.J.Roy.Astr.Soc., Vol:42p.347

16 Andrews,D.J. 1980 A stochastic fault Model: Static case. J.Geoph.Res., Vol:85,p.3867

17 Andrews,D.J. 1976 Rupture velocity of plane strainshear cracks. J.Geoph.Res., Vol:81,p.5679

18 Andrews,D.J. 1980 A stochastic fault model: Static case. J.Geoph.Res., Vol:85,p.3867

19 Archambeau,C.B. 1968 General theory of elasto-dynamic source fields. Rev.Geoph., No:16,p.241

20 Arias,A and Sandoval,H. 1979 Muestreo e interpolacion de acelerogramas obtenidos en instr de registro optico o mecanico. Rep.UNAM, Mexico

21 Arias,A and Sandoval,H.S. 1980 Errores aleatorios de digitizacion. Rep.UNAM, Mexico.

22 Arias,A. 1970 A measure of earthquake intensity. Seismic Design of Nuclear Power Plants, R.Hansen Ed.

23 Basili,M. and Brady,A.G. 1978 Low frequency filtering and the selection of limits for accelerogram corrections. Proc.6th ECEE Yugoslavia.

24 Bath,M. 1974 Spectral analysis in geophysics. Elsevier,Amsterdam.

25 Bath,M. 1968 Mathematical aspects of seismology. Elsevier, Amsterdam

26 Bath,M. 1966 Earthquake energy and Magnitude. Physics and Chemistry of the Earth, No:7,p.115

27 Bazaraa,M.S. and Shetty,C.M. 1979 Nonlinear Programming. John Wiley and Sons.

28 Ben-Menahem,A and Singh,S.J. 1972 Computation of models of elastic dislocations in the earth. Methods Comp.Phys. (Bolt,Ed) Vol.12,p.299, Acad.Press,N.Y

29 Ben-Menahem,A. 1961 Radiation of seismic surface waves from finite moving sources. BSSA, No:51,p.401

30 Ben-Menahem,A. and Singh,S.H. 1981 Seismic waves and sources. Heidelberg:Springer

31 Benioff,H. 1934 The physical evaluation of seismic destructiveness. BSSA, Vol.24 p.398

32 Berg,G and Housner,G.W. 1961 Integrated velocity and displacement of strong earthquake ground motions. BSSA, Vol.51 No.2

33 Berg,G. 1963 A study of errors in response spectrum analysis. Prim.Jornados Chil. de Sismologia Vol.1 Chile

34 Berg,G.V. and Thomaides,S.S 1960 Energy consumption by structures in strong motion earthquakes. Proc.2nd WCEE Tokio and Kyoto

35 Berrill,J.B. and Hanks,T.C. 1974 High frequency amplitude errors in digitized strong motion accelerograms. Rep.Caltech, EERL No:14/104

36 Boatwright,J. 1980 A spectral theory for circular seismic sources. BSSA, Vol:70,p.1

37 Boatwright,J. 1984 The effect of rupture complexity on estimates of source size. J.Geoph.Res.Vol:89,p.1132

38 Boatwright,J. 1981 Quasi-dynamic models of simple earthquakes: Application to the aftershocks of the 1975 Oroville BSSA,No:71,p.69

39 Boatwright,J. 1975 A simplification in the calculation of motions near a propagating dislocation BSSA,No:65,p.133

40 Boatwright,J. 1980 A spectral theory for circular seismic sources: simple estimate of source dimension BSSA,Vol:70,p.1

41 Boore,D.M. 1983 Stochastic simulation of high frequency ground motion based on seismological models BSSA,Vol.73,No.6

42 Boore,D.M. and Joyner,W.B. 1978 The influence of rupture incoherence on seismic directivity BSSA,No:68,p.283

43 Boore,D.M. and Zoback,M.D. 1974 Near field motions from kinimatic model of propagating faults BSSA,No:64,p.321

44 Bouchon,M. 1979 Predictability of ground displacement and velocity at proximity of an earthquake J.Geoph.Res.Vol:84,p.6149

45 Bouchon,M. and Aki.K. 1977 Discrete wave-number representation of seismic source wave fields BSSA,No:67,p.259

46 Boyce,W.H. 1970 Integration of accelerograms BSSA,Vol.60,No.1

47 Brady,A.G. and Hudson,D.E. 1973 Standard data processing of strong motion accelerograms Proc.5th WCEE, Rome

48 Brune,J.N. 1970 Tectonic stress and the spectra of seismic shear waves from earthquakes J.Geophys.Res.75,p.4997

49 Brune,J.N. 1971 Correction J.Geophys.Res.76,p.5002

50 Burden,R.L. and Douglas Faires,J 1978 Numerical analysis Prindle, Weber and Schmidt

51 Burridge,R. and Halliday,G.S. 1971 Dynamic shear cracks with friction for shallow focus earthquakes Geoph.J.Roy.Astr.Soc.Vol:66p.261

52 Burridge,R. and Willis,J. 1974 The self-similar problem of the expanding elliptical crack in an anisotropic solid Proc.Cambr.Phil.Soc.Vol:66 p.443

53 Bycroft,G.N. 1960 White noise representation of earthquakes J.Eng.Mech.Div., Proc.ASCE no:86,(EM2)p.1

54 Cartwright and Longuet-Higgins,M.S. 1956 The statistical distribution of the maxima of a random function Proc.Roy.Soc.Vol:237,p.212

55 Caughey,T.K. and Stumpf,H.J. 1961 Transient response of a dynamic system under random excitation J.Appl.Mech.p.563

56 Cloud,W.I.K and Hudson,D.E. 1961 A simplified instrument for recording strong motion earthquakes. BSSA Vol.43 No.2

57 Clough,R.W. and Penzien,J. 1975 Dynamics of structures McGraw-Hill,New-York

58 Constantinides,A.G. 1970 Spectral transformations for digital filters Proc.IEEE Vol.117,p.1585

59 Converse,A.M. Brady,A.G. and Joyner,W.B. 1984 Improvements in strong motion data processing procedures Proc.8th WCEE,San-Francisco

60 Cormier,C.A. 1982 The effects of attenuation on seismic body waves BSSA,No:72,p.5169

61 Crandall,S.H. 1970 First-crossing Probabilities of the linear oscillator J.Sound Vib. Vol:12,p.285

62 Crandall,S.H. and Mark,W.D. 1963 Random vibrations in Mechanical Systems Academy Press, N.Y.

63 Das,S and Aki.K. 1977 Fault plane with barriers: a versatile earthquake model J.Geoph.Res.Vol:82,p.5648

64 Das,S. and Aki,K. 1977 Fault plane with barriers: a versatile earthquake model J.Geoph.Res.Vol:82,p.5658

65 Das,S. and Aki.K 1977 A numerical study of two-dimensional spontaneous rupture propagation Geoph.J.Roy.Ast.Soc.Vol:50 p.643

66 Davenport,A.G. 1964 Note on the distribution of the largest value of random function with application to gust loading p.187

67 Dean,W.C. 1964 Seismological application of Laguerre expansions BSSA,Vol.54,No.1

68 Der Kiureghian,A. 1980 Structural response to stationary excitation J.Eng.Mec. Div.ASCE, Vol:106, p.1195

69 Eisenberg,A. and McEvilly,T.V. 1971 Comparison of some widely-used strong motion earthquake accelerometers BSSA,Vol.61,No.2

70 Erdik,M. and Kubin,J. 1984 A procedure for the accelerogram processing Proc.8th WCEE,San-Francisco

71 Eshelby,J.D. 1957 The determination of the elastic field of an ellipsoial inclusion and related problems Proc.Roy.Soc.Lond.Ser.A, Vol:241,p.376

72 Ewing,W.M. Jardetzky,W.S. and Press,F. 1957 Elastic Waves in layered media McGraw Hill,Inc.

73 Fletcher,J. Boatwright,J. HaarL. Hanks,T. and McGarr,A. 1984 Source parameters for aftershockof the Oroville, California, earthquake. BSSA,Vol:74,p.1101

74 Fletcher,J.B. Brady,A.G. and Hanks,T.C. 1980 Strong motion accelerograms of the Oroville, California, aftershocks of 0350 Aug. 6, 1975 BSSA,Vol.70,No.1

75 Frankel,A. 1984 Source parameters of two Ml=5 earthquakes near Anza, and comparison with Imperial Valley BSSA,Vol:74, p.1509

76 Frankel,A. and Kanamory,H. 1983 Determination of rupture duration and stress drop for earthquake in Southern California BSSA,Vol:73, p.1527

77 Furuya,I. 1969 Predominant Period and Magnitude J.Phys.Earth,Vol:17,No:2 p.119

78 Geller,R.J. 1976 Scaling relations for earthquake source parameters and magnitudes BSSA,No:66, p.1501

79 Geller,R.J. 1976 Body force equivalents for stress-drop seismic sources BSSA,No:66,p.1801

80 Geller,R.J. 1976 Scaling relations for earthquake source parameters and magnitudes BSSA,Vol:66,p.1501

81 Georgiev,G. and Mutafov,D. 1982 Automatic digitization of strong motion records with line-scan camera. Proc.7th ECEE,Athens

82 Gilbert,F. and Backus,G. 1966 Propagator matrices in elastic wave and vibration problems Geophysics,Vol:31,p.326

83 Gray,H.A. and Markel,J.D. 1976 A computer program for designing digital elliptic filters IEEE Trans.Ac.Spe. and Sig. Pro, Vol.ASSP-24,No.6

84 Gutemberg,B. 1958 Attenuation of seismic waves in the earth's mantle BSSA,No:48,p.269

85 Halverton,H,T. 1971 Modern trends in strong motion movements instrumentation Dynamics Waves in Civ.Eng. Howwells et al.Eds,Wiley-I.

86 Halverton,H.T. 1965 The strong motion accelerograph Proc.3rd WCEE Vol.1 New Zealand

87 Halverton,H.T. 1974 A technical review of recent strong motion accelerographs Proc.5th WCEE, Rome

88 Hamming,R.W. 1977 Digital filters Prentice Hall,Inc.

89 Hammond,S.K. 1968 On the response of SDOF and MDOF systems to nonstationary random excitations J.Sound Vib.Vol:7,p.393

90 Hanks,T.C. 1975 Strong motion of the San-Fernando, California, earthquake: Ground displacements BSSA,Vol.65,No.1

91 Hanks,T.C. 1982 Fmax BSSA,Vol.72,p.1867

92 Hanks,T.C. 1979 b values and w-G seismic source models: implications for tectonic stress variations J.Geophys.Res.84,p.2235

93 Hanks,T.C. 1974 The faulting mechanism of the San-Fernando earthquake J.Geoph.Res.Vol:79,p.1215

94 Hanks,T.C. 1977 Earthquake Stress Drops, ambient tectonic stresses and stresses that drive plate motions Pure Appl.Geoph.Vol:115, p.441

95 Hanks,T.C. and Kamanori,H. 1979 A moment-Magnitude scale J.Geophys.Res.84,p.2348

96 Hanks,T.C. and McGuire,R.K. 1981 The character of high frequency strong ground motion BSSA,Vol.71,p.2071

97 Hanks,T.C. and McGuire,R.K. 1981 The character of high-frequency strong ground motions BSSA,No:71,p.2071

98 Harris,F,J. 1978 On the use of windows for harmonic analysis with the DFT Proc.IEEE,Vol.66,No.1

99 Hartzell,S.H. and Brune,J.N. 1977 Source parameters for the January 1975 Brawley Imperial Valley earthquake swarm. P.Appl.Geoph. Vol:115,p.333

100 Haskell,N.A. 1964 Total energy and energy spectral density of elastic wave radiation from propagating fault: I BSSA,No:54,p.1811

101 Haskell,N.A. 1966 Total energy and energy spectral density of elastic wave radiation from propagating fault: II BSSA,No:56,p.125

102 Himmelblau,D.M. 1972 Applied nonlinear programming McGraw Hill,Inc.

103 Hirasawa,T. and Stauder,W. 1965 On the seismic waves from a finite moving source. BSSA,No:55, p.1811

104 Holloway,L.J. 1958 Smoothing and filtering of time series and space fields Advances in Geophysics Vol.4

105 Housner,G.W. 1947 Characteristics of strong motion earthquakes BSSA Vol.45 No.1

106 Housner,G.W. 1955 Properties of strong ground motion earthquakes BSSA Vol.45 No.3

107 Housner,G.W. Martel,R.R. and Alford,J.L. 1953 Spectrum analysis of strong motion earthquakes BSSA Vol.43 No.2

108 Hudson,D.E et al. 1969 Strong Motion earthquake accelerograms: Digitized and plotted data, VOL.IA Rep.Caltech. No.EERL,69/20

109 Hudson,D.E et al. 1971 Strong motion earthquake Accelerograms: Digitized and plotted data, Vol.IIA Rep.Caltech, No.EERL,71/50

110 Hudson,D.E. 1966 Response spectrum technique in engineering seismology Proc.1st WCEE, Berkeley.

111 Hudson,D.E. 1962 Some problems in the application of spectrum techniques to strong motion BSSA Vol.52 No.2

112 Hudson,D.E. 1963 The measurement of ground motion of destructive earthquakes BSSA Vol.53

113 Hudson,D.E. 1970 Ground motion measurements Earthq.Eng. Ed. by Wiegel Ch.6 Prentice Hall,New-J.

114 Hudson,D.E. 1979 Reading and interpreting strong motion accelerograms EERI Nomographs

115 Hudson,D.E. 1982 Design of strong motion instruments, networks and arrays Proc.7th ECEE,Athens

116 Hudson,D.E. Wigan,N.C. and Trifunac,M.D. 1969 Analysis of strong motion accelerograph records Re8.Caltech, Pasadena

117 Hussieni,M.I. and Randall,M.J. 1976 Rupture velocity and radiation efficiency BSSA,No:66, p.1173

118 Iyengar,R,N. and Iyengar,K.T. 1969 A non-stationary randon process for earthquake accelerations BSSA,Vol.59, p.1163

119 Jarosh,H. 1975 Automatic digitazation of seismograms Geoph.J.R. Astr.Soc. Vol.42, p.565

120 Jenschke,V.A. and Penzien,J. 1964 Ground motion accelerogram analysis including dynamical instrumental correction BSSA,Vol.54, No.6

121 Jenschke,V.A. Clough,R.W. and Penzien,J. 1965 Characteristics of strong ground motions Proc.3rd WCEE,Vol.1 New-Zealand

122 Kajimi,H. 1960 A Standard method of determiningthe maximum response of a building during an earthquake Proc.2nd WCEE, Tokio

123 Kamanori,H. 1977 The energy release in great earthquakes J.Geoph.Res, Vol:82, p.2981

124 Kamanori,H. and Anderson,D.L. 1975 Theoretical basis of some empirical relations in seismology BSSA,No:65, p.1073

125 Kasahra,K. 1981 Earthquake Mechanics Cambr.Univ.Press.

126 Keilis-Borok,V. 1960 Investigation of the mechanism of earthquakes Soviet Res.Geoph. Vol:4 Engl.Trans. by Amer.Soc.Geo.

127 Keilis-Borok,V.I. 1959 On estimation of the displacement in an earthquake source and source dimensions Ann.Geofis. No:12, p.205

128 Khemici,O. and Chiang,W.L. 1984 Frequency domain corrections of earthquake accelerograms with experimental verifications Proc.8th WCEE, San-Francisco

129 Knopoff, L and Gilbert,F 1959 Radiation from a strike-slip fault BSSA,Vol:49, p.163

130 Kostrov,B.V. 1964 Self-similar problems in propagation of shear craks J.Appl.Math. Mech. Vol:30, p.1241

131 Kostrov,B.V. 1966 Unsteady propagation of longitudinal shear cracks J.Appl.Math. Mech. No:30, p.1241

132 Lee,V.W. 1984 Recent developents in data processing of strong motion accelerograms Proc.8th WCEE, San-Francisco

133 Lee,V.W. Trifunac,M.D. and Amini,A. 1982 Noise in earthquake accelerograms J.Eng.Mech. Div.ASCE Vol.108, No.EM6

134 Lin,Y.K. 1967 Probalistic Theory of structural dynamics McGraw-Hill N.Y.
135 Love, A.E.H. 1944 Treatise on the Mathematical Theory of Elasticity Dover Publ.N.Y.
136 Lynn,P.A. 1971 Recursive digital filters with linear phase characteristics The Computer Journal Vol.15.No.4
137 Madariaga,R. 1976 Dynamics of an expanding circular fault BSSA,No:66, p.639
138 Madariaga,R. 1978 The dynamic field of Haskell's rectangular dislocation fault model BSSA,No:68, p.869
139 Maruyama,T. 1969 On the force Equivalents of dynamical elastic dislocations with reference to earthquake B.Earth. Res.Ins., Tokio, Vol:41, p.467
140 Maude,A.D. 1973 Interpolation, mainly for graph plotters The Computer Journal, Vol.16,No.1
141 McGarr,A. 1981 Analysis of peak ground motion in terms of Model in Inhomogeneous faulting J.Geoph.Res. Vol:86, p.3901
142 McLennan,G.A. 1969 An exact correction for accelerometer error in dynamic seismic analysis BSSA,Vol.59, No.2
143 Menu,J.M.H. 1983 A computer programme to correct the strong motion accelerations by efficient filters: ELLICOR Research Report,I.C.
144 Menu,J.M.H. 1985 The Design of an earthquake-like signal Proc.Rome Workshop on "Inv. Strong Motion Proc.Proced.
145 Menu,J.M.H. 1985 A digitiz ation noise model for earthquake strong motion records Proc.Rome Workshop on "Inv. Strong Motion Proc.Proced."
146 Menu.J.M.H., Ambraseys,N.N. and Melville,C. 1985 On the seismicity of the south West of the british Isles Earthquake Engineering in Britain, p.227
147 Mogi,K. 1967 Earthquakes and fractures Tectonophysics, Vol:5, p.35
148 Mohraz,B. Hall,W.J. and Newmark,N.M. 1972 A study of vertical and horizontal earthquake spectra. USAEC Contact report, No: AT(49-5)-2667
149 Mori,J. and Shimazaki,K. 1984 High stress drops of short period subevents from the 1968 Tokach i-Oki earthquake BSSA,Vol:74, p.1529
150 Morse,P.M. and Fesbach,H. 1953 Methods of theoretical physics McGraw-Hill, N.Y.
151 Nakano,H. 1925 On Rayleigh waves Jap.J.Astr. Geoph. Vol:2, p.233
152 Naumosski,N. Petroski,D. Mihailov,V. and Kirijas,T. 1976 Strong motion earthquakes accelerograms: Digitized and plotted data Rep.Ins. EEES, Skopje

153 Newland,D.E. 1984 Random Vibrations and spectral analysis Longman Group Ltd

154 Newmark,N.M. and Rosenblueth,E. 1971 Fundamentals of earthquake engineering Prentice Hall,Inc.

155 Newmark,N.M. Blume,J.A. and Kapur,K.K. 1973 Seismic Design Spectra for Nuclear Power Plants J.Power Div., Proc.ASCE, 99 p.287

156 Nigam,N.C. and Jenning,P. 1966 Calculation of response spectra from strong motion earthquake records BSSA Vol.59, No.2

157 Nuttli,O.W. 1983 Average seismic source parameter relations for mid-plate earthquakes BSSA,No:73, p.519

158 Ohnaka, M. 1978 Earthquake source parameters related to magnitude Geoph.J.R. Astr.Soc. Vol:55 p.45

159 Oppenheim,A.V. and Shaffer,R.W. 1975 Digital signal processing Prentice Hall,Inc.

160 Ormsby,J.F.A. 1961 Design of numerical filters with application to missile data processing J.Assoc. Comp.Mach.8; p.440

161 Papageorgiou,A.S. and Aki,K. 1983 A specific model for the quantitative description of inhomogeneo us faulting. BSSA,No:73, p.693

162 Papoulis,A. 1962 The Fourier Integral and its applications McGraw-Hill,Inc.

163 Papoulis,A. 1981 Probability, random variables and stochastic processes McGraw Hill Int.

164 Pecnold,D.A. and Riddel,R. 1978 Effect of initial base motion on Response spectra. J.Eng.Mech. Div.ASCE, Vol.105, No.EM6

165 Petrovski,D. and Naumovski,N. 1979 Processing of strong motion accelerograms, Part I:Analytic Methods Rep.Inst. EEES, Skopje

166 Poppitz,J.V. 1968 Velocity and displacement of explosion induced earth tremors derived from acceleration BSSA Vol.58, No.5, p.1573

167 Priestley,M.B. 1967 Power spectral analysis of non-stationary random process. J.Sound Vib., Vol:6, p.86

168 Rabiner,L.R. and Gold,B. 1975 Theory and application of digital signal processing Prentice Hall,Inc.

169 Randall,M.J. 1973 Spectral peaks and earthquake source dimensions J.Geoph.Res. Vol:78, p.2609

170 Ravara,A. 1965 Spectral analysis of seismic actions Proc.3rd WCEE, New-Zealand

171 Rice,S.O. 1954 Mathematical analysis of random noise Noise and Stochastic Proces N.Wax, Ed.Dover

172 Richards,P.G. 1973 The dynamic field of a growing plane elliptical shear crack Int.J.Sol. Struct. Vol:9, p.843

173 Richards,P.G. 1976 Dynamic motion near an earthquake fault: A three dimensional solution BSSA,No:66, p.1

174 Richter,C.F. 1958 Elementary Seismology Freeman, San-Fran.

175 Rinaldis,D. Menu,J.M.H and Goula,X. 1986 A study of various uncorrected versions of the same ground acceleration Proc.8th ECEE, Lisbon

176 Ruge,A.C. and McComb,H.E. 1943 Tests of earthquake accelerometers on a shaking table BSSA,Vol.33, No.1

177 Saragoni,G.R. and Hart,G.C. 1974 Simulation of artificial earthquakes Earth.Eng. and Struc.Dyn. Vol.2, p.249

178 Sarma,S.K. 1970 Energy flux of strong earthquakes Tectonophysics

179 Sarma,S.K. 1970 Energy Flux of strong earthquakes Tectonophysics, No:11, p.159

180 Sato,R. 1972 Seismic waves in the near field J.Phys.Earth, Vol:20, p.357

181 Sato,R. 1979 Theoretical basis on relationships between focal parameters and magnitude J.Phys.Earth, Vol:27, p.372

182 Sato,T. and Hirasawa,T. 1973 Body wave spectra from propagating shear cracks J.Phys.Earth, Vol:21, p.415

183 Savage,J.C. 1966 Radiation from a realistic model of faulting BSSA,No:56, p.577

184 Savage,J.C. 1972 Relation of corner frequency to fault dimensions J.Geoph.Res. Vol:77, p.3788

185 Savage,J.C. and Wood,M.D. 1971 The relation between apparent and stress drop BSSA.Vol:61, p.1381

186 Scherer,R.J. and Schueller,G.I. 1982 On the correlation between XYZ-components of earthquake accelerations Proc.7th ECEE, Athens

187 Shakal,A.F. and Ragsdale,J.T. 1984 Acceleration, velocity and displacement noise analysis for the CSMIP digitization system Proc.8th WCEE, San-Francisco

188 Schiff,A. and Bogdanoff,J. 1967 Analysis of current methods of interpretating strong motion accelerograms BSSA,Vol.57, No.5, p.857

189 Shoja-Taheri,J. 1980 A new assessment of errors from digitization and base line corrections of SM accelerograms BSSA,Vol.70, No.1

190 Schteinberg,V.V. Ivanova,T.G. and Ponomareva,O.N. 1982 Ground motion during nearby earthquakes Proc. 7th ECEE, Athens

191 Shyam Sunder,J. and Connor,J.J. 1982 A new procedure for processing strong motion earthquake signals BSSA,Vol.73, p.643

192 Singh,S.J, Ben-Menahem,A. and Vered,M. 1973 A unified approach to the representation of seismic sources. Proc.Roy.Soc. (London), A331 p.525

193 Skinner,R.I and Stephenson,W.R. 1973 Accelerograph calibration and accelerogram correction Int.J.Earth. Eng. and Str. Dyn., Vol.2, No.1

194 Spottiswoode,S.M. and McGarr,A. 1975 Source parameters of tremors in a deep-level gold mine BSSA,Vol:65, p.93

195 Steketee,J.A. 1958 Some geophysical applications ofthe elasticity theory of dislocations Can.J.Phys. Vol:36, p.1168

196 Storer,J.E. 1957 Passive network synthesis McGraw Hill

197 Tajimi,H. 1960 A statistical mrthod of determining the maximum response of a building during an earthquake Proc.2nd WCEE, Tokio

198 Takahashi,R. 1956 The SMAC strong motion accelero-graph and other latest instruments for measuring earthquakes Proc.1st WCEE, Berkeley

199 Tolstoy,I. 1973 Wave propagation McGraw-Hill, N.Y.

200 Trifumac,M.D. 1971 Response envelope spectrum and interpretation of strong earthquake ground motion BSSA,Vol.61, No.2

201 Trifunac,M.D. 1970 Low frequency digitization error and a new method for zero base line correction Rep.Caltech, No.EER, 70/07

202 Trifunac,M.D. 1972 A note on the correction of SM accelerograms for instrument response BSSA, Vol.62, No.1

203 Trifunac,M.D. and Hudson,D.E. 1970 Laboratory evaluation and instrument correction of strong motion accelerograms Rep.Caltech No.EERL, 70/04

204 Trifunac,M.D. and Lee,V.W. 1973 Routine computer processing of strong motion accelerographs Rep.Caltech, No.EERL 73/03

205 Trifunac,M.D. and Lee,V.W. 1974 A note on the accuracy of computed ground displacements from SM accelerograms BSSA,Vol.64, No.4

206 Trifunac,M.D. Udwadia,F.E. and Brady,A.G. 1973 Analysis of errors in digitized strong motion accelerograms BSSA, Vol.63

207 Trifunac,M.D. Udwadia,F.E. and Brady,A.G. 1973 Recent developments in data processing and accuracy of eval- uation of acceleration measurement. Proc.5th WCEE, Rome

208 Trifunac.M.D. 1971 Zero base line correction of strong motion accelerograms BSSA, Vol.61

209 Udwadia,F.E. and Trifumac,M.D. 1974 Characteristerisation of response spectra through the stastistics of oscillator response BSSA,Vol.64, No.1

210 Udwadia,F.E. and Trifunac M.D. 1973 The Fourier transform, response spectra and their relationship through the statistics of oscillator Rep.Caltech, No.EERL 73/01

211 Udwadia,F.E. and Trifunac,M.D. 1973 Damped Fourier spectrum and response spectra BSSA, Vol.63, No.5

212 Utsu,T. and Seki,A. 1954 A relation between the areas of the aftershock region and the energy of main shock J.Seis.Soc. Japan, Vol:7, p.233

213 Vanmarke,E.H. 1976 Structural response to earthquakes Seismic Risk and Eng.Decision Lomnitz and Rosenblueth Ed.

214 Vanmarke,E.H. and Lai,S.P. 1980 Strong Motion duration of earthquakes BSSA,Vol.70, p.1293.

215 Walsh,J.B. 1966 Seismic wave attenuation in rock due to friction J.Geoph.Res. Vol:71, p.2591

216 White,J.E. 1965 Seismic waves radiation, transmission and attenuation McGraw-Hill, N.Y.

217 Wiggins,R.A. 1976 Interpolation of digitized curves BSSA.Vol.66. No.6

218 Wong,H.L. and Trifunac M.D. 1977 Effects of cross-axis sensitivity and misaligments on the response of accelerographs BSSA,Vol.67,No.3